New Series

LANDOLT-BÖRNSTEIN

Numerical Data and Functional Relationships in Science and Technology

GROUP VIII

Advanced Materials and Technologies

VOLUME 1

Laser Physics and Applications

SUBVOLUME B

Laser Systems

Part 2

Springer

Landolt-Börnstein
Numerical Data and Functional Relationships in Science and Technology
New Series / Editor in Chief: W. Martienssen

Group VIII: Advanced Materials and Technologies
Volume 1

Laser Physics and Applications

Subvolume B: Laser Systems

Part 2

Editors: W. Schulz, H. Weber, R. Poprawe

Authors:
R. Beigang, A. Bruns, E. Gornik, H.-J. Hoffmann, R. Iffländer, K.A. Janulewicz, M.J. Kelley, J. Limpert, G.R. Neil, P.V. Nickles, W. Sandner, A. Tünnermann, H. Wenzel

Springer

ISSN 1619-4802 (Advanced Materials and Technologies)

ISBN 978-3-540-44380-3 Springer Berlin Heidelberg New York

Library of Congress Cataloging in Publication Data:
Landolt-Börnstein: Numerical Data and Functional Relationships in Science and Technology, New Series.
Editor in Chief: W. Martienssen.
Group VIII, Volume 1: Laser Physics and Applications. Subvolume B: Laser Systems. Part 2.
Edited by W. Schulz, H. Weber, R. Poprawe.
Springer-Verlag, Berlin, Heidelberg, New York 2008.
Includes bibliographies.
1. Physics - Tables. 2. Chemistry - Tables. 3. Engineering - Tables.
I. Börnstein, Richard (1852-1913). II. Landolt, Hans (1831-1910).
QC 61.23 502'.12 62-53136

This work is subject to copyright. All rights are reserved, whether the whole or part of the material is concerned, specifically the rights of translation, reprinting, reuse of illustrations, recitation, broadcasting, reproduction on microfilm or in other ways, and storage in data banks. Duplication of this publication or parts thereof is permitted only under the provisions of the German Copyright Law of September 9, 1965, in its current version, and permission for use must always be obtained from Springer-Verlag. Violations are liable for prosecution act under German Copyright Law.

Springer is a part of Springer Science+Business Media.
springeronline.com
© Springer-Verlag Berlin Heidelberg 2008
Printed in Germany

The use of general descriptive names, registered names, trademarks, etc. in this publication does not imply, even in the absence of a specific statement, that such names are exempt from the relevant protective laws and regulations and therefore free for general use.

Product Liability: The data and other information in this handbook have been carefully extracted and evaluated by experts from the original literature. Furthermore, they have been checked for correctness by authors and the editorial staff before printing. Nevertheless, the publisher can give no guarantee for the correctness of the data and information provided. In any individual case of application, the respective user must check the correctness by consulting other relevant sources of information.

Cover layout: Erich Kirchner, Heidelberg
Typesetting: Authors and Redaktion Landolt-Börnstein, Darmstadt
Printing and Binding: AZ Druck, Kempten (Allgäu)

SPIN: 1078 5979 63/3020 - 5 4 3 2 1 0 – Printed on acid-free paper

Editors

Schulz, Wolfgang
Fraunhofer-Institut für Lasertechnik (ILT), Aachen, Germany

Weber, Horst
Technische Universität Berlin, Optisches Institut, Berlin, Germany

Poprawe, Reinhart
Fraunhofer-Institut für Lasertechnik (ILT), Aachen, Germany

Authors

Beigang, René
Technische Universität Kaiserslautern, Fachbereich Physik, Kaiserslautern, Germany

Bruns, Adlin
Fraunhofer-Institut, Angewandte Optik und Feinmechanik, Jena, Germany

Gornik, Erich
Technische Universität Wien, Institut für Festkörperelektronik, Wien, Austria

Hoffmann, Hans-Jürgen
Technische Universität Berlin, Institut für Werkstoffwissenschaften und -technologien, Fachgebiet "Glaswerkstoffe", Berlin, Germany

Iffländer, Reinhard
TRUMPF Laser GmbH, Schramberg, Germany

Janulewicz, Karol Adam
Max-Born-Institut für Nichtlineare Optik und Kurzzeitspektroskopie (MBI), Berlin, Germany

Kelley, Michael J.
Thomas Jefferson National Accelerator Facility, Newport News, VA, USA

Limpert, Jens
Friedrich-Schiller-Universität Jena, Institut für Angewandte Physik, Jena, Germany

Neil, George R.
Thomas Jefferson National Accelerator Facility, Newport News, VA, USA

Nickles, Peter V.
Max-Born-Institut für Nichtlineare Optik und Kurzzeitspektroskopie (MBI), Berlin, Germany

Sandner, Wolfgang
Max-Born-Institut für Nichtlineare Optik und Kurzzeitspektroskopie (MBI), Berlin, Germany

Tünnermann, Andreas
Fraunhofer-Institut, Angewandte Optik und Feinmechanik, Jena, Germany

Wenzel, Hans
Ferdinand-Braun-Institut für Höchstfrequenztechnik (FBH), Berlin, Germany

Landolt-Börnstein

Editorial Office
Gagernstraße 8
D-64283 Darmstadt, Germany
fax: +49 (6151) 171760
e-mail: Redaktion.Landolt-Boernstein@springer.com

Internet
www.landolt-boernstein.com

Preface

The three volumes VIII/1A, B, C document the state of the art of "Laser Physics and Applications". Scientific trends and related technological aspects are considered by compiling results and conclusions from phenomenology, observation and experiments. Reliable data, physical fundamentals and detailed references are presented.

In the recent decades the laser source matured to an universal tool common to scientific research as well as to industrial use. Today the technical goal is the generation of optical power towards shorter wavelengths, shorter pulses, higher efficiency and higher power for applications in science and industry. Tailoring the optical energy in wavelength, space and time is a requirement for the investigation of laser-induced processes, i.e. excitation, non-linear amplification, storage of optical energy, etc. According to the actual trends in laser research and development, Vol. VIII/1 is split into three parts: Vol. VIII/1A with its two subvolumes 1A1 and 1A2 covers laser fundamentals, Vol. VIII/1B with its three subvolumes 1B1, 1B2 and 1B3 deals with laser systems and Vol. VIII/1C gives an overview on laser applications.

In Vol. VIII/1B2 the following topics are treated in detail:

Part 4: Solid-state lasers

In four sections, the physical and engineering aspects of different solid-state lasers and laser active materials are presented. Solid-state lasers matured to versatile instruments applied for high-power industrial applications, enabling display technique providing the basic colors, becoming tools in medical surgery and dentistry, as well as entering scientific approaches for diagnosis of chemical reactions on the femto-second time scale. Glasses showing a strong inhomogeneous broadening and therefore facilitating laser excitation and tuning the wavelength are discussed in comparison with crystals. Promising alternatives to early concepts using bulk solid-state laser systems are rare-earth-doped fibers. Decades after the advent of low-loss fused silica fibers by Corning in 1970 an impressive development of beam power and quality happened. In 2004 kilowatt powers at diffraction-limited beam quality were demonstrated and actually multiple kilowatt high-power applications are in the focus of scientific research and industrial development of the corresponding applications.

Part 5: Diode lasers

Diode lasers represent the extreme with respect to compactness, efficiency and low laser threshold. Enabling physical properties, successful applications and promising perspectives are presented. The small spatial size below 500 μm allows their use for entertainment, data storage and printing as well as high-performance fiber-based communication systems. The impact of diode lasers spans from demonstrating single-frequency laser emission to giving perspectives for screening diagnostics in life-science. Flash lamps are substituted by high-power diode arrays to pump high performance solid-state lasers and enabling basically new laser design. Tuning the gain spectra with quantum-well structures laser diodes operate at wavelength not attainable with bulk material. Light from diode lasers in the visible spectral region enters our daily life. History and advances about multiple

hetero-structures having a thickness between 2 and 20 nm, made out of unstrained and strained, single or multiple quantum wells, emitting light in the visible spectral region are presented.

Part 6: Free-electron lasers

Free Electron Lasers (FEL's) are moving from an exotic tool of a few specialists to something broadly available. FEL's provide photon characteristics unobtainable from more conventional sources. Radiation comes directly from an oscillating bunch of electrons with relativistic properties instead of an inverted extra active medium. Physical principles and properties of ready-to-use machines with high average power from the InfraRed (IR) through Extreme Ultra-Violet (EUV) to X-ray are presented.

Part 7: X-ray lasers

The history and actual advances of concepts for population inversion deeply inside the atomic core are presented. Laser systems in the Extreme Ultra-Violet (EUV) spectral region, also called X-ray lasers, are taking up the challenge to control coherence of light where the emission wavelength matches the spatial dimensions of micro- and nano-scaled objects. With a wavelength between 2 and 60 nm these lasers approach the future needs of nano- and life-sciences, materials research as well as structuring.

February 2008 The Editors

Contents

Part 4 Solid-state lasers

4.1 Solid-state laser systems
R. Iffländer . . . 3

4.1.1 Solid-state laser systems . . . 3
4.1.1.1 Introduction . . . 3
4.1.1.2 Energy-level diagram and rate equations . . . 3
4.1.1.2.1 Rate equations for a 4-level system . . . 4
4.1.1.3 Amplifiers . . . 5
4.1.1.3.1 Stationary case for low intensities ($J \ll J_s$) . . . 6
4.1.1.3.2 Stationary case (or $T \gg \tau$) and $J \geq J_s$ . . . 6
4.1.1.3.3 Pulse operation for short pulses ($T \ll \tau$) . . . 7
4.1.1.4 Oscillator . . . 8
4.1.1.4.1 Oscillator condition . . . 10
4.1.1.4.2 Output power . . . 10
4.1.1.4.3 Optimal reflection coefficient . . . 11
4.1.1.5 Influence of the temperature . . . 12
4.1.1.6 Oscillator in pulsed operation . . . 14
4.1.1.6.1 Threshold . . . 14
4.1.1.6.2 High pump power $P_p \gg P_{th}$ . . . 14
4.1.1.6.3 Relaxation oscillation . . . 15
4.1.1.6.4 Spiking . . . 16
4.1.1.6.5 Long-pulse regime . . . 16
4.1.1.7 Q-switch operation . . . 16
4.1.1.7.1 Single Q-switch pulse . . . 17
4.1.1.7.2 Periodical Q-switch for high pulse repetition rate ($r\tau \gg 1$) . . . 19
4.1.1.8 The 3-level system . . . 21
4.1.1.8.1 Stationary case with $dN/dt = 0$ and $dJ/dt = 0$ . . . 22
4.1.1.9 Efficiency and optimization . . . 24
4.1.1.10 Stable resonators . . . 26
4.1.1.10.1 Eigenvalues for TEM-00 mode . . . 26
4.1.1.10.2 Introducing a virtual reference plane . . . 28
4.1.1.10.3 Beam parameter product . . . 29
4.1.1.11 Thermal effects . . . 29
4.1.1.11.1 Steady-state temperature profile . . . 30
4.1.1.11.2 Thermal load . . . 31
4.1.1.11.3 Thermal lensing . . . 33
4.1.1.11.4 Experimental determination of the refracting power . . . 34
4.1.1.12 Solid-state laser concepts . . . 35
4.1.1.12.1 Multicavity resonators . . . 35
4.1.1.12.2 Two external mirrors and two rods . . . 35

4.1.1.12.3 Multiple cavities with flat mirrors . . . 36
4.1.1.12.4 Thermally invariant resonators . . . 37
4.1.1.13 Excitation by diodes . . . 38
4.1.1.13.1 Rod . . . 38
4.1.1.13.1.1 Longitudinally pumped rod . . . 38
4.1.1.13.1.2 Transversally pumped rod . . . 39
4.1.1.13.2 Disk . . . 40
4.1.1.13.2.1 Longitudinal disk . . . 40
4.1.1.13.2.2 Transversally pumped disk . . . 40
4.1.1.13.3 Fiber . . . 40
4.1.1.13.3.1 Longitudinally pumped fiber . . . 40
4.1.1.13.3.2 Transversally pumped fiber . . . 41
4.1.1.13.4 Slab . . . 41
4.1.1.13.4.1 Transversally pumped slab . . . 42
4.1.1.13.4.2 Longitudinal slab . . . 42
4.1.1.13.5 Diode-pumped solid-state lasers in research and development . . . 42
4.1.1.14 Solid-state laser products . . . 43
4.1.2 Laser material parameter . . . 45
4.1.2.1 Parameter specification . . . 45
4.1.2.1.1 Laser data . . . 45
4.1.2.1.2 Optical properties . . . 46
4.1.2.1.3 Thermal parameters . . . 48
4.1.2.1.4 Mechanical properties . . . 49
4.1.2.1.5 Crystal properties . . . 49
4.1.2.1.6 Derived data . . . 52
4.1.2.1.7 Supplier data . . . 53
4.1.2.1.8 Measured values . . . 53
4.1.2.2 Active ions . . . 54
4.1.2.2.1 Overview . . . 54
4.1.2.2.2 Most important ions . . . 55
4.1.2.2.2.1 Chromium . . . 55
4.1.2.2.2.2 Erbium Er^{3+} . . . 57
4.1.2.2.2.3 Holmium Ho^{3+} . . . 59
4.1.2.2.2.4 Neodymium Nd^{3+} . . . 60
4.1.2.2.2.5 Praseodymium Pr^{3+} . . . 63
4.1.2.2.2.6 Titanium . . . 65
4.1.2.2.2.7 Thulium . . . 65
4.1.2.2.2.8 Ytterbium . . . 67
4.1.3 Laser crystals . . . 69
4.1.3.1 Alexandrite . . . 69
4.1.3.2 BEL (lanthanum beryllate) . . . 70
4.1.3.3 Emerald . . . 70
4.1.3.4 GGG (gallium gadolinium garnet) . . . 71
4.1.3.5 GSAG (gadolinium scandium aluminum garnet) . . . 72
4.1.3.6 GSGG (gadolinium scandium gallium garnet) . . . 73
4.1.3.7 GVO(4) (gadolinium (ortho)vanadate) . . . 74
4.1.3.8 KGW (potassium gadolinium tungstate) . . . 75
4.1.3.9 LICAF (lithium calcium aluminum fluoride) . . . 75
4.1.3.10 LNA (lanthanum neodymium hexa-aluminate), LMA (lanthanum magnesium hexa-aluminate) . . . 76
4.1.3.11 LSB (lanthanum scandium borate) . . . 77

4.1.3.12 NYAB (neodymium yttrium aluminum borate) . . . 77
4.1.3.13 Quartz . . . 78
4.1.3.14 Sapphire . . . 79
4.1.3.15 YAG (yttrium aluminum garnet) . . . 80
4.1.3.16 YAP (yttrium aluminum perovskite), YALO (yttrium aluminum oxide) . . . 82
4.1.3.17 YLF (yttrium lithium fluoride) . . . 83
4.1.3.18 YOS (yttrium ortho-silicate) . . . 84
4.1.3.19 YSAG (yttrium scandium aluminum garnet) . . . 84
4.1.3.20 YSGG (yttrium scandium gallium garnet) . . . 85
4.1.3.21 YVO(4) (yttrium (ortho)vanadate) . . . 86
References for 4.1 . . . 87

4.2 Glasses
H.-J. Hoffmann . . . 97
4.2.1 General properties of laser glasses . . . 97
4.2.1.1 Basic considerations . . . 97
4.2.1.2 Lanthanides as active ions . . . 98
4.2.1.3 Glasses doped with Nd^{3+} . . . 100
4.2.1.4 Radiative lifetime and concentration quenching . . . 102
4.2.1.5 Glasses doped with other active ions, codoping . . . 103
4.2.2 Temperature effects . . . 103
4.2.2.1 Thermal load of cylindrical rods . . . 103
4.2.2.2 Thermal lensing . . . 104
4.2.2.3 Increasing the maximum laser power . . . 105
4.2.3 Quantities to characterize properties of laser glasses . . . 107
4.2.3.1 Density of ions . . . 107
4.2.3.2 Refractive index . . . 107
4.2.3.3 The refractive index as a function of the temperature . . . 108
4.2.3.4 Photoelastic coefficients . . . 110
4.2.3.5 Nonlinear effects . . . 110
4.2.4 Properties of commercial laser glasses doped with Nd^{3+} (Er^{3+}) ions from different manufacturers . . . 113
4.2.4.1 Meaning of the symbols . . . 113
4.2.4.2 Manufacturer: Schott Glass Technologies . . . 114
4.2.4.3 Manufacturer: Hoya Optics . . . 116
4.2.4.4 Manufacturer: Kigre . . . 118
References for 4.2 . . . 120

4.3 Diode-pumped fiber lasers
A. Tünnermann, J. Limpert, A. Bruns . . . 125
4.3.1 Introduction . . . 125
4.3.2 Historical background of fiber lasers . . . 125
4.3.3 Basic principles of a fiber laser . . . 126
4.3.4 Fundamentals of fiber optics . . . 127
4.3.5 Double-clad fiber lasers . . . 128
4.3.6 Ytterbium-doped fiber lasers . . . 130
4.3.7 Fiber lasers versus bulk lasers . . . 131

4.3.8 Nonlinearity – the main performance limitation of a fiber laser . . . 132
4.3.9 Photonic crystal structures in a fiber laser . . . 134
4.3.10 Power scaling consideration for cw fiber lasers . . . 137
References for 4.3 . . . 138

4.4 Color-center lasers
R. Beigang . . . 141
4.4.1 Introduction . . . 141
4.4.2 Physics of color centers . . . 141
4.4.2.1 Classification of color centers . . . 141
4.4.2.2 Preparation of laser-active color centers . . . 142
4.4.2.3 Excitation and emission processes . . . 143
4.4.3 Laser systems . . . 143
4.4.3.1 Continuous-wave laser systems . . . 144
4.4.3.2 Pulsed laser systems . . . 145
References for 4.4 . . . 146

Part 5 Diode lasers

5.1 Fundamentals of diode lasers
E. Gornik . . . 151
5.1.1 Introduction . . . 151
5.1.2 Basic diode laser operational principles . . . 151
5.1.2.1 Gain in semiconductors . . . 152
5.1.2.2 Round-trip condition . . . 153
5.1.2.3 Rate equations . . . 154
5.1.2.4 Threshold behavior and optical output . . . 155
5.1.2.5 Thermal aspects . . . 156
5.1.3 Lateral light/current confinement . . . 156
5.1.3.1 Longitudinal mode control – single-mode lasers . . . 157
5.1.4 Laser modulation . . . 158
5.1.4.1 Large-signal amplitude modulation . . . 159
5.1.4.2 Small-signal amplitude modulation . . . 159
5.1.5 Line width . . . 160
References for 5.1 . . . 161

5.2 Diode lasers in the visible spectral region
H. Wenzel . . . 163
5.2.1 Introduction . . . 163
5.2.2 Diode lasers based on III-nitrides . . . 164
5.2.2.1 Material properties . . . 164
5.2.2.2 Substrate . . . 165
5.2.2.3 Doping . . . 165
5.2.2.4 Active region . . . 166
5.2.2.5 Waveguide and cladding layers . . . 166
5.2.2.6 Contact layer . . . 167
5.2.2.7 Distributed Bragg reflectors in VCSELs . . . 167

5.2.2.8 Epitaxial structure . . . 167
5.2.2.9 Results . . . 167
5.2.3 Diode lasers based on II-VI sulfo-selenides . . . 168
5.2.3.1 Material properties . . . 168
5.2.3.2 Substrate . . . 169
5.2.3.3 Doping . . . 169
5.2.3.4 Active region . . . 169
5.2.3.5 Waveguide and cladding layers . . . 169
5.2.3.6 Contact layer . . . 170
5.2.3.7 Distributed Bragg reflectors in VCSELs . . . 171
5.2.3.8 Epitaxial structure . . . 171
5.2.3.9 Results . . . 171
5.2.4 Diode lasers based on I-III-IV_2 compounds . . . 172
5.2.5 Diode lasers based on phospho-arsenides . . . 173
5.2.5.1 Material properties . . . 173
5.2.5.2 Substrate . . . 173
5.2.5.3 Doping . . . 174
5.2.5.4 Active region . . . 174
5.2.5.5 Waveguide and cladding layers . . . 175
5.2.5.6 Contact layer . . . 176
5.2.5.7 Distributed Bragg reflectors in VCSELs . . . 176
5.2.5.8 Epitaxial structure . . . 176
5.2.5.9 Results . . . 176
References for 5.2 . . . 179

Part 6 Free-electron lasers

6.1 Free-electron lasers
M.J. Kelley, G.R. Neil . . . 187
6.1.1 Overview . . . 187
6.1.2 Components of a FEL . . . 188
6.1.2.1 Injector . . . 188
6.1.2.2 Accelerator . . . 189
6.1.2.3 Wiggler . . . 190
6.1.2.3.1 Processes in the wiggler . . . 191
6.1.3 Output . . . 193
6.1.4 Summary and outlook . . . 195
References for 6.1 . . . 198

Part 7 X-ray lasers

7.1 X-ray lasers
P.V. Nickles, K.A. Janulewicz, W. Sandner . . . 203
7.1.1 Introduction . . . 203
7.1.2 Principles of X-ray lasers . . . 205
7.1.2.1 Active medium . . . 205
7.1.2.1.1 Pump energy absorption . . . 205

7.1.2.1.2 Population inversion and gain . . . 206
7.1.2.1.3 Pump power requirements for soft X-ray lasers in plasmas . . . 207
7.1.2.1.4 Kinetics of the active medium – working regimes . . . 208
7.1.2.1.4.1 Steady-state approximation . . . 209
7.1.2.1.4.2 Quasi-steady-state approximation . . . 209
7.1.2.1.4.3 Non-stationary or transient approximation . . . 210
7.1.2.1.5 Medium size and output geometry – refraction . . . 210
7.1.2.1.5.1 Refraction . . . 211
7.1.2.2 Excitation mechanisms . . . 213
7.1.2.2.1 Electron collisional excitation . . . 213
7.1.2.2.1.1 Ne-like scheme . . . 213
7.1.2.2.1.2 Ni-like schemes . . . 214
7.1.2.2.2 Recombination X-ray lasers . . . 216
7.1.2.2.3 Inner-shell photoionization (ISPI) . . . 217
7.1.2.2.4 Photoresonant pumping . . . 218
7.1.2.2.5 Other excitation schemes . . . 219
7.1.2.2.5.1 Charge-transfer schemes . . . 219
7.1.3 Output characteristics . . . 220
7.1.3.1 Output intensity . . . 220
7.1.3.2 Output energy and conversion efficiency . . . 221
7.1.3.3 Saturation . . . 221
7.1.3.4 Wavelength . . . 222
7.1.3.5 Spectral linewidth . . . 223
7.1.3.6 Pulse duration . . . 223
7.1.3.7 Coherence . . . 223
7.1.3.7.1 Transverse (spatial) coherence . . . 224
7.1.3.7.2 Longitudinal (temporal) coherence . . . 224
7.1.4 Practical X-ray laser schemes . . . 225
7.1.4.1 Collisionally pumped X-ray lasers . . . 225
7.1.4.1.1 Quasi-steady state (QSS) scheme . . . 225
7.1.4.1.2 Low-energy prepulse pumping . . . 225
7.1.4.1.3 Multi-pulse pumping . . . 226
7.1.4.1.4 Transient excitation scheme . . . 226
7.1.4.1.4.1 Traveling-wave pumping . . . 228
7.1.4.1.4.2 Grazing incidence pumping (GRIP) . . . 228
7.1.4.1.4.3 XUV master oscillator–power amplifier (XMOPA) . . . 229
7.1.4.1.5 Fast capillary discharge . . . 230
7.1.4.1.6 Hybrid X-ray lasers . . . 231
7.1.4.1.7 Dense gases . . . 232
7.1.4.1.8 Review of realized collisional X-ray lasers . . . 233
7.1.4.2 Recombination-pumped X-ray lasers . . . 233
7.1.4.3 Optical-field ionization (OFI) X-ray lasers . . . 242
7.1.4.3.1 Optical-field ionization as a plasma source . . . 242
7.1.4.3.2 Propagation issues of OFI . . . 242
7.1.4.3.3 OFI with linearly polarized pumping pulse . . . 245
7.1.4.3.4 OFI with circularly polarized pumping pulse . . . 246
7.1.4.4 Inner-shell photoionization X-ray lasers . . . 247
7.1.5 Applications . . . 250
7.1.5.1 Diagnostics with X-ray lasers . . . 250
7.1.5.2 Interferometry . . . 253
7.1.5.3 Reflectometry . . . 254

7.1.5.4 Excitation of nonlinear processes 254
7.1.6 Conclusion 255
References for 7.1 256

Index 265

4.1 Solid-state laser systems

R. Iffländer

4.1.1 Solid-state laser systems

4.1.1.1 Introduction

The past decade has seen a steady increase of solid-state lasers in basic research, commercial, medical and military applications. Solid-state laser systems are installed in nearly all technical fields, in the automotive industry for welding and cutting applications with an average power up to 10 kW, in science to investigate chemical reactions with very short pulses in the femto-second regime, in medical therapeutics, to use different wavelengths and short pulses for skin resurfacing, in the display technique to provide the basic colors red, green and blue to display full color, brilliant and bright pictures.

Solid-state lasers are optically pumped. Semiconductor lasers, which directly convert the electrical power into radiation, will not be considered in this section. The most common pump sources in the past were noble-gas-filled arc- or flashlamps. In future the lamps will more and more be replaced by semiconductor diode lasers which operate with much higher efficiency and reduced heat load in solid-state laser materials.

The most important solid-state laser material used for material processing is Nd:YAG; followed by Ti:sapphire, Cr:LiSAF, Cr:ruby and Nd:glass. Possible new materials are Cr:alexandrite, Nd:GSGG, Nd:GGG, Nd:Cr:GGG and Yb:YAG.[1] For medical applications, holmium and erbium are used at different wavelengths in various host crystals or glasses.

Except for materials doped with Yb or Cr (YAG, alexandrite, ruby), they can be described as 4-level systems. Therefore, the derivation of the following equations is based on a 4-level system and the corresponding equations for the 3-level system will be given without derivation.

The material properties necessary for amplifiers and oscillators will be described. The emphasis is on the efficiency of the systems, which depends on the threshold and slope efficiency.

Given the results, estimations for new materials and systems can easily be carried out. Simple experiments make a comparison and an assessment of the materials possible.

4.1.1.2 Energy-level diagram and rate equations

Solid-state lasers are normally designed according to Fig. 4.1.1. The laser material interacts with the radiation field of its own or another resonator and is pumped by one or more excitation sources (lamps or diode lasers). The pump light may be incident on the laser material from any direction relative to the laser radiation.

[1] YAG: yttrium aluminum garnet, LiSAF: lithium strontium aluminum fluoride, GSGG: gadolinium scandium gallium garnet, GGG: gallium gadolinium garnet.

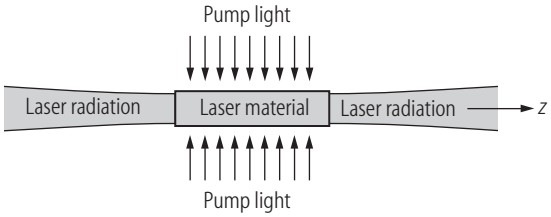

Fig. 4.1.1. Schematic setup of a solid-state laser.

4.1.1.2.1 Rate equations for a 4-level system

The stimulated and spontaneous emission processes are described by the simplified energy-level diagram of Fig. 4.1.2 and the corresponding rate equations.

By absorbing the pump light, atoms are excited from the ground state 0 to the absorption band 3. From there, a fast transition (10 ns) takes place to the upper laser state 2. At this level the atoms stay for a long time (1 to 1000 μs) and are available for stimulated emission. The following simplifications are invoked to derive the rate equations for a 4-level system:

- the transition from the upper absorption bands is rapid, and their populations can be neglected,
- the laser transition is homogeneously broadened,
- the intensity of the radiation field is assumed to be spatially constant,
- the density N_0 of the ground state population is large compared to the other states, so that the depletion by the pump can be neglected.

The rate equation for the upper level is

$$\frac{\mathrm{d}N_2}{\mathrm{d}t} = WN_0 - \frac{N_2}{\tau} - \frac{\sigma J}{h\nu}(N_2 - N_1) \tag{4.1.1}$$

with

N_i : density of the active ions in level i,
W : pump rate,
τ : lifetime of the upper laser level, consists of the fluorescence lifetime τ_{21} and of non-radiative transitions ($\frac{1}{\tau} \approx \frac{1}{\tau_{21}} + \frac{1}{\tau_{\mathrm{phonon}}}$),
J : intensity of the radiation field,
$h = 6.6 \times 10^{-34}$ J s : Planck constant,
ν : resonance frequency of the transition,
σ : cross section of the ion for induced emission.

Three mechanisms induce a change of the ion density N_2:

1. an increase caused by pumping, proportional to the ground-state density,
2. a decrease due to the finite lifetime of the upper laser level,

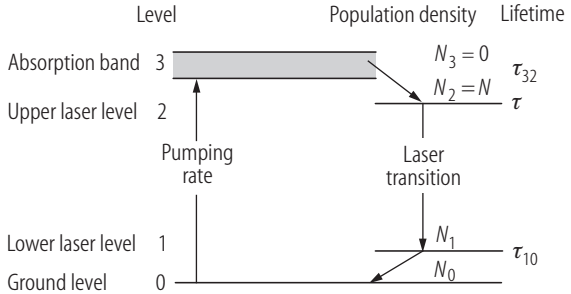

Fig. 4.1.2. Simplified energy-level diagram of a 4-level system.

3. a decrease due to the stimulated emission, proportional to the interacting radiation field, the cross section and the inversion $(N_2 - N_1)$. The energy difference is supplied to the radiation field.

For the lower laser level, one has

$$\frac{\mathrm{d}N_1}{\mathrm{d}t} = \frac{\sigma J}{h\nu}(N_2 - N_1) + \frac{N_2}{\tau} - \frac{N_1}{\tau_{10}} \tag{4.1.2}$$

with

τ_{10} : lifetime of the lower laser level.

The lower laser level population changes by spontaneous and stimulated emission from the upper state as well as by phonon transitions to the ground state.

The intensity of the radiation field in the medium is described by

$$\frac{\mathrm{d}J}{\mathrm{d}t} = \frac{\sigma c J(N_2 - N_1)}{n} - \frac{\sigma c J N_{\mathrm{th}}}{n} \tag{4.1.3}$$

with

N_{th} : term containing all losses,
c : light velocity in vacuum,
n : refractive index of the laser medium.

The intensity increases due to the inversion and decreases due to losses like absorption, scattering and outcoupled power, which are taken into account by the absorption coefficient.

If one assumes that the depletion of the lower laser level is very rapid, the rate equation (4.1.1) simplifies to

$$\frac{\mathrm{d}N}{\mathrm{d}t} = WN_0 - \frac{N}{\tau} - \frac{\sigma N J}{h\nu} \quad \text{for} \quad \tau_{10} \ll \tau \quad \text{and} \quad N := N_2 - N_1 \approx N_2 \; . \tag{4.1.4}$$

Introducing the saturation flux J_{s}, at which the population by spontaneous emission and phonon transitions equals stimulated emission,

$$J_{\mathrm{s}} = \frac{h\nu}{\sigma\tau} \; , \quad \textit{saturation flux} \; , \tag{4.1.5}$$

then (4.1.4) becomes

$$\frac{\mathrm{d}N}{\mathrm{d}t} = WN_0 - \frac{N}{\tau}\left(1 + \frac{J}{J_{\mathrm{s}}}\right) \; , \quad \textit{change of the inversion} \; , \tag{4.1.6}$$

and with $N_2 = N$, (4.1.3) is given as

$$\frac{\mathrm{d}J}{\mathrm{d}t} = \frac{\sigma c J}{n}(N - N_{\mathrm{th}}) \; , \quad \textit{change of the intensity} \; , \tag{4.1.7}$$

Equations (4.1.6) and (4.1.7) are the time-dependent rate equations for a 4-level system.

4.1.1.3 Amplifiers

Up to now the spatial dependence for inversion and intensity has been neglected. Taking into account the dependence in one coordinate (z direction), (4.1.6) and (4.1.7) change into

$$\frac{\partial}{\partial t}N(z,t) = WN_0 - \frac{N(z,t)}{\tau}\left(1 + \frac{J(z,t)}{J_{\mathrm{s}}}\right) \; , \tag{4.1.8}$$

$$\left(\frac{c}{n}\frac{\partial}{\partial z} + \frac{\partial}{\partial t}\right) J(z,t) = \frac{\sigma c J(z,t)}{n}(N(z,t) - N_{\mathrm{th}}) \; . \tag{4.1.9}$$

4.1.1.3.1 Stationary case for low intensities ($J \ll J_s$)

At low intensities of the input wave ($J \ll J_s$) its influence on inversion is small. The inversion $N(z,t) = N$ can therefore be considered as constant

$$N = \tau W N_0 = \text{const} , \tag{4.1.10}$$

and for the intensity we have the solution

$$J(z) = J_0 \, e^{\sigma(N - N_{th})z} . \tag{4.1.11}$$

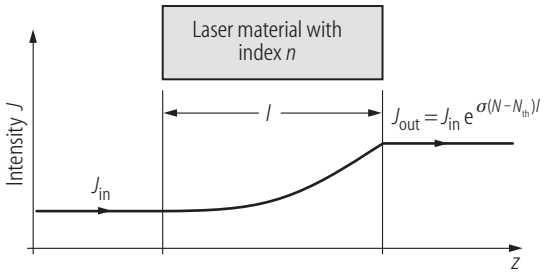

Fig. 4.1.3. Amplifier principle.

An incident field with the intensity J_{in} (Fig. 4.1.3) will be amplified by the laser material to the intensity J_{out},

$$J_{out} = J_{in} \, e^{\sigma(N - N_{th})l} , \quad \textit{intensity amplification for } J \ll J_s , \tag{4.1.12}$$

with

l: amplification length.

One therefore defines

$$G_0 = e^{\sigma N l} , \quad \textit{small-signal gain factor} , \tag{4.1.13}$$

$$g_0 = \sigma N , \quad \textit{small-signal gain coefficient} , \tag{4.1.14}$$

$$g_s = \frac{g_0}{1 + J/J_s} , \quad \textit{saturated gain coefficient} , \tag{4.1.15}$$

and, analogously,

$$V = e^{-\sigma N_{th} l} , \quad \textit{loss factor (in amplifiers)} , \tag{4.1.16}$$

$$\alpha = \sigma N_{th} , \quad \textit{loss coefficient (in amplifiers)} , \tag{4.1.17}$$

$$GV = J_{out}/J_{in} , \quad \textit{gain factor including the loss factor} . \tag{4.1.18}$$

The stationary case is even fulfilled for pulsed operation, provided the pulse duration T is large compared to the upper laser level lifetime.

4.1.1.3.2 Stationary case (or $T \gg \tau$) and $J \geq J_s$

At high input intensity the inversion N is reduced by the radiation field and becomes z-dependent

$$0 = W N_0 - \frac{N(z)}{\tau} \left(1 + \frac{J(z)}{J_s} \right) \tag{4.1.19}$$

and delivers for the inversion:

$$N(z) = \frac{W N_0 \tau}{1 + J(z)/J_s} \; . \tag{4.1.20}$$

The z-dependence of the intensity reads in the stationary case

$$\frac{\partial J(z)}{\partial z} = J(z)\,(g_s - \alpha) \; . \tag{4.1.21}$$

Neglecting the losses ($\alpha = 0$), (4.1.21) can be integrated, considering the intensity-dependent gain coefficient g_s and the boundary condition $J_{out} = J_{in}$ for $G_0 = 1$

$$\ln\left(\frac{J_{out}}{J_{in}}\right) + \frac{J_{out} - J_{in}}{J_s} = \ln G_0 \; . \tag{4.1.22}$$

For $G_0 - 1 \ll 1$ an approximate solution holds:

$$J_{out} = J_{in}\, G_0^{1/(1+J/J_s)} \; , \textit{intensity amplification} \; . \tag{4.1.23}$$

For $J_{in} \gg J_s$ (4.1.22) can be approximated by [99Koe]

$$J_{out} \approx J_{in} + J_s\, g_0\, l \; . \tag{4.1.24}$$

The high input intensity saturates the gain completely. The stored inversion energy is transformed into radiation energy and allows a high extraction efficiency. The maximum output intensity which can be extracted depends on the internal losses α of the amplifier and the gain coefficient g_0 [99Koe]

$$J_{out,max} = \left(\frac{g_0}{\alpha} - 1\right) J_s \; . \tag{4.1.25}$$

The results in both cases apply analogously for pulsed mode operation, provided the pulse duration T is large compared to the lifetime τ of the upper laser level.

4.1.1.3.3 Pulse operation for short pulses ($T \ll \tau$)

The energy amplification of short rectangular pulses is given in [99Koe] as

$$E_{out} = f H_s \ln\left(1 + \left[e^{E_{in}/f H_s} - 1\right] G_0\right) \tag{4.1.26}$$

with

E_{in} : input energy,
E_{out} : output energy,
$H_s = h\nu/\sigma$: saturation energy density,
f : cross section of the beam inside the laser material.

Losses have not been taken into account. Two limiting cases can be distinguished:

1. $E_{in} \ll f H_s$ results in

$$E_{out} = G_0 E_{in} \; . \tag{4.1.27}$$

The input energy is amplified linearly.

2. $E_{\mathrm{in}} \gg f H_{\mathrm{s}}$ results in

$$E_{\mathrm{out}} = E_{\mathrm{in}} + f H_{\mathrm{s}}\, gl = E_{\mathrm{in}} + h\nu N V_{\mathrm{ol}} \,, \tag{4.1.28}$$

with

V_{ol} : volume of the radiation field in the laser material.

In the latter case the output energy increases linearly with the pump length. The efficiency is more favorable than in the low-energy case, since the input energy is increased by the full stored energy $h\nu N V_{\mathrm{ol}}$ of the volume V_{ol}.

The small-signal gain factor and the amplification coefficient can be determined experimentally from (4.1.26)

$$G_0 = \frac{\mathrm{e}^{E_{\mathrm{out}}/f H_{\mathrm{s}}} - 1}{\mathrm{e}^{E_{\mathrm{in}}/f H_{\mathrm{s}}} - 1} \,. \tag{4.1.29}$$

No losses were taken into account so far and self-oscillation has to be avoided. Self-oscillation starts if the end-faces of the crystal are not completely AntiReflection (AR) coated and have remaining reflection.

4.1.1.4 Oscillator

First, the oscillator in the stationary case is discussed. Figure 4.1.4 shows the principle setup and the intensity distribution inside the oscillator [83Min].

The z-dependence of the two intensities J_+ and J_- is described by (4.1.21)

$$\frac{\partial J_+(z)}{\partial z} = J_+(z)(g_{\mathrm{s}} - \alpha) \,, \tag{4.1.30}$$

$$\frac{\partial J_-(z)}{\partial z} = -J_-(z)(g_{\mathrm{s}} - \alpha) \,. \tag{4.1.31}$$

In Fig. 4.1.4 z increases from left to right. The gradient $\partial J_-/\partial z$ is therefore negative. The sum of the two equations yields

$$\frac{1}{J_-(z)}\frac{\partial J_-(z)}{\partial z} + \frac{1}{J_+(z)}\frac{\partial J_+(z)}{\partial z} = 0 \,. \tag{4.1.32}$$

This is equivalent to

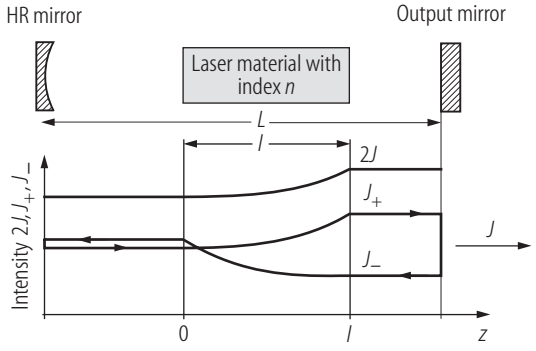

Fig. 4.1.4. Intensity distribution in an oscillator.

$$\frac{\partial\left(J_{+}(z)\times J_{-}(z)\right)}{\partial z}=0 \tag{4.1.33}$$

or

$$J_{+}\left(z\right)\times J_{-}\left(z\right)=\text{const}=J^{2}\ . \tag{4.1.34}$$

The product of the intensities for the back- and forward-running wave inside the resonator is constant and independent of the position z.

With the boundary conditions

$$J_{-}(0)=J_{+}(0)\quad\text{and}\quad J_{-}(l)=RJ_{+}(l) \tag{4.1.35}$$

it follows that

$$J_{-}(0)+J_{+}(0)=2J\quad\text{and}\quad J_{-}(l)+J_{+}(l)=\frac{1+R}{\sqrt{R}}\,J\ . \tag{4.1.36}$$

At the output mirror, with reflection R, there is, in general, the higher intensity. The difference of the average intensity $J_{-}(z)+J_{+}(z)$ from $2J$ is important only for low reflections. With $R=0.55$ it is approximately 10 %. Therefore, in the following only the average intensity $2J$ is considered. Exact solutions can be found for example in [78Rig, 80Sch].

For the stationary case the rate equations (4.1.6) and (4.1.7) become

$$0=W\tau-\frac{N}{N_{0}}\left(1+\frac{2J}{J_{\mathrm{s}}}\right)\ , \tag{4.1.37}$$

$$0=\frac{l}{L+l(n-1)}\,\sigma cJ\left(N-N_{\mathrm{th}}\right)\ , \tag{4.1.38}$$

with

L: resonator length,
l: length of the laser medium.

The change of the inversion is caused by the intensity $2J$ inside the laser material. The increased intensity of the radiation field caused by stimulated emission spreads out over the whole resonator length. The part that remains for stimulated emission in the medium is therefore only $nl/[L+l(n-1)]$.

For $J>0$, the last equation delivers

$$N=N_{\mathrm{th}}=\text{const}\ . \tag{4.1.39}$$

The inversion above threshold remains constant, independent of the excitation power, as soon as threshold inversion is reached. The excitation power above threshold increases the intensity in the resonator and the output power.

Equations (4.1.37) and (4.1.39) deliver the average intensity in the resonator. Introducing the threshold pump rate W_{th} for $J=0$,

$$W_{\mathrm{th}}=N_{\mathrm{th}}/\tau N_{0}\ , \tag{4.1.40}$$

one obtains

$$J=\frac{J_{\mathrm{s}}}{2}\left(\frac{W}{W_{\mathrm{th}}}-1\right)\ . \tag{4.1.41}$$

Figure 4.1.5 shows schematically the inversion N and the intensity J inside the resonator dependent on the pump rate W.

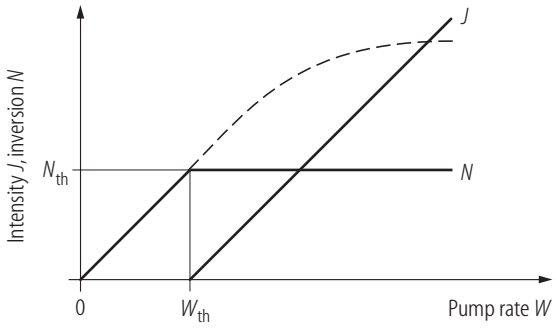

Fig. 4.1.5. Inversion N and intensity J in a 4-level laser.

4.1.1.4.1 Oscillator condition

For steady-state oscillation, an amplifier must fulfill the oscillator condition. The intensity of the wave J_+, starting at point 0, must be reproduced after a full round-trip. All losses such as absorption, scattering and laser output must be fully compensated by the amplification

$$(VG_0RVG_0)\,J_+ = J_+\ , \tag{4.1.42}$$

with

$R = R_1R_2$: average reflection coefficient,
V : loss factor for internal losses,
$G_0 = \exp(g_0 l)$: small-signal amplification factor ($J \ll J_\mathrm{s}$),

$$RV^2G_0^2 = 1\ , \quad \textit{oscillator condition}\ . \tag{4.1.43}$$

The inversion at laser threshold must not only compensate the internal losses in the laser material, but also the losses due to the output coupling. The threshold inversion follows from the oscillator condition as

$$\ln\left(RV^2\right) + 2\,\sigma N_\mathrm{th} l = 0, \quad N_\mathrm{th} = -\,\frac{\ln\left(V\sqrt{R}\right)}{\sigma l}\ . \tag{4.1.44}$$

4.1.1.4.2 Output power

To excite N_0 ions per volume to the upper level an excitation power of $V_\mathrm{ol}N_0\,h\nu W$ for a volume V_ol is required. This will be delivered by the pump power P_p with an excitation efficiency η_excit, assuming that the pump light homogeneously excites the whole volume:

$$V_\mathrm{ol}N_0\,h\nu W = \eta_\mathrm{excit}P_\mathrm{p}\ , \tag{4.1.45}$$

with

η_excit : excitation efficiency,
$h\nu$: photon energy,
$V_\mathrm{ol} = f \cdot l$: pumped volume.

Defining the pump power P_th at threshold analogously the average intensity in the resonator as a function of the electrical pump power P_p becomes

$$J = \frac{J_\mathrm{s}}{2}\left(\frac{P_\mathrm{p}}{P_\mathrm{th}} - 1\right)\ . \tag{4.1.46}$$

Behind the mirror with the reflection R the output laser intensity $J_{\rm cw}$ becomes

$$J_{\rm cw}(l) = (1 - R)\, J_+(l) \tag{4.1.47}$$

and the reflected part is

$$J_-(l) = R\, J_+(l)\ . \tag{4.1.48}$$

With $J^2 = J_+ J_-$ it follows that $J_+(l) = J/\sqrt{R}$ and therefore the output power $P_{\rm cw}$ is

$$P_{\rm cw} = f J_{\rm cw} = f\, \frac{1 - R}{\sqrt{R}}\, J\ . \tag{4.1.49}$$

With (4.1.46), the laser power behind the mirror can be expressed as

$$P_{\rm cw} = f J_{\rm s}\, \frac{1 - R}{2\sqrt{R}} \left(\frac{P_{\rm p}}{P_{\rm th}} - 1 \right)\ , \quad \frac{1 - R}{2\sqrt{R}} \approx -\ln \sqrt{R}\ , \tag{4.1.50}$$

which holds for reflectivities which are not too low. The usual form for the dependence of the laser power on the pump power, derived in [78Rig] under much stricter conditions, is

$$P_{\rm cw} = \eta_{\rm slope}\, (P_{\rm p} - P_{\rm th})\ , \tag{4.1.51}$$

with

$$\eta_{\rm slope} = \eta_{\rm excit}\, \frac{\ln \sqrt{R}}{\ln \left(V \sqrt{R} \right)} \quad \text{and} \quad P_{\rm th} = -\frac{f J_{\rm s}}{\eta_{\rm excit}} \ln \left(V \sqrt{R} \right)\ .$$

This linear dependence is shown in Fig. 4.1.6. The slope efficiency $\eta_{\rm slope}$ and the threshold $P_{\rm th}$ determine the efficiency of a laser. Both, however, are dependent on the reflection coefficient R of the output mirror.

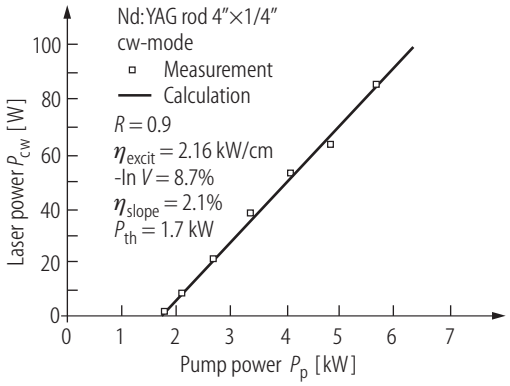

Fig. 4.1.6. Output power of a cw laser.

4.1.1.4.3 Optimal reflection coefficient

Equation (4.1.51) also describes the dependence of the laser power on the reflection coefficient of the output coupler, as shown for the cw case in Fig. 4.1.7. The optimal reflection coefficient decreases with increasing pump power and should therefore be optimized for the maximum output

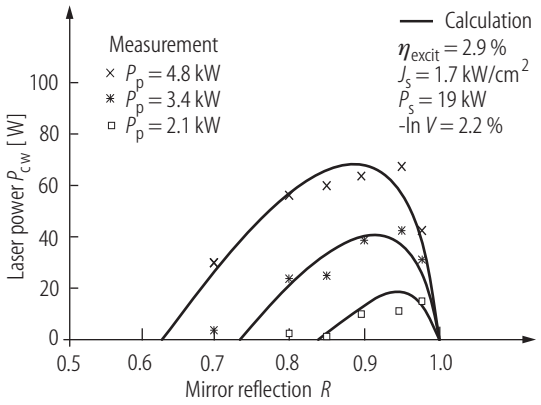

Fig. 4.1.7. Calculation of the laser power as a function of mirror reflection.

power. The optimal mirror reflection R_{opt} can be derived from (4.1.51). This yields the maximum laser power for a given input power P_{p}:

$$-\ln\sqrt{R_{\mathrm{opt}}} = \sqrt{\alpha l\,\frac{P_{\mathrm{p}}}{P_{\mathrm{s}}}} - \alpha l = (\sqrt{\alpha g_0} - \alpha)\,l\;, \tag{4.1.52}$$

$$P_{\mathrm{s}} = \frac{\eta_{\mathrm{excit}}}{f J_{\mathrm{s}}}\;,$$

$$R_{\mathrm{opt}} = \mathrm{e}^{-\sqrt{-\ln(V) P_{\mathrm{p}}/P_{\mathrm{s}}} + 2\,\ln(V)}\;, \quad \text{with} \quad \ln(V) = -\alpha l\;.$$

With the optimal reflection coefficient R_{opt} and the corresponding pump power P_{p}, the maximal laser output power P_{max} is

$$P_{\mathrm{max}} = \frac{f J_{\mathrm{s}}}{\alpha l}\left(\ln\sqrt{R_{\mathrm{opt}}}\right)^2 = f J_{\mathrm{s}}\left(\sqrt{g_0} - \sqrt{a}\right)^2 l\;, \quad \textit{optimized laser power}\;. \tag{4.1.53}$$

One selects the reflection coefficient of the output mirror with a safety margin towards larger values such that the efficiency is highest for the desired average power or energy. It should be noticed that with lower reflection coefficients, the resonator will be disturbed by back reflection from the workpiece, particularly during drilling and cutting.

4.1.1.5 Influence of the temperature

The temperature of the coolant and the heating due to the pump power determine the average temperature of the laser material. A higher average temperature in some cases is necessary to increase the efficiency, e.g. for alexandrite. In most other cases the material has to be operated at the lowest temperature possible. The temperature in the laser material has several effects:

- the lifetime of the upper and lower level can change,
- a noticeable increase in the population of the lower laser energy level takes place,
- the cross section changes,
- the center frequency shifts.

Since the influence of the thermal population in a 4-level system is significant, this will be discussed in more detail. The inversion is reduced by the thermal population N_{T} and the assumption $N_1 \approx 0$ (4.1.4) is no longer valid. For a constant average temperature of the laser medium the thermal population is given by:

$$N_1 = N_\mathrm{T} = \frac{N_0\, \mathrm{e}^{-\Delta E/k_\mathrm{B}T}}{\sum\limits_{i=0}^{n} \mathrm{e}^{-\Delta E_i/k_\mathrm{B}T}} \,, \tag{4.1.54}$$

with

k_B : Boltzmann constant,
ΔE : energy difference between ground state and lower laser energy level.

Example 4.1.1. Thermal population of the lower laser level in YAG.

With $N_0 = 1.4 \times 10^{20}/\mathrm{cm}^3$ and $T = 300$ K one finds:
the thermal population $N_\mathrm{T} = 1.91 \times 10^{15}/\mathrm{cm}^3$ for Nd with $\Delta E = 2110\ \mathrm{cm}^{-1}$ and
the thermal population $N_\mathrm{T} = 1.68 \times 10^{19}/\mathrm{cm}^3$ for Yb with $\Delta E = 612\ \mathrm{cm}^{-1}$.

With a rod length of 10 cm and a mirror reflectivity of about $R = 0.85$ the threshold inversion is typically $N_\mathrm{th} = 5 \times 10^{16}/\mathrm{cm}^3$ for Nd and $N_\mathrm{th} = 5 \times 10^{17}/\mathrm{cm}^3$ for Yb.

The rate equations for the oscillator in the stationary case become

$$0 = W\tau N_0 - N_2 - \frac{J}{J_\mathrm{s}}(N_2 - N_\mathrm{T}) \,, \tag{4.1.55}$$

$$0 = \frac{\sigma c J (N_2 - N_\mathrm{T} - N_\mathrm{th})}{L + l(n-1)} \,, \tag{4.1.56}$$

from which follows

$$P_\mathrm{cw} = \frac{\ln \sqrt{\mathrm{R}}}{\ln\left(V\sqrt{R}\right)} \left(\eta_\mathrm{excit} P_\mathrm{p} + f J_\mathrm{s} \ln(V\sqrt{R}) - \sigma\, l f J_\mathrm{s} N_\mathrm{T}\right) \,, \tag{4.1.57}$$

$$P_\mathrm{cw} = \eta_\mathrm{slope}\,(P_\mathrm{p} - P_\mathrm{th} - P_\mathrm{T}) \,.$$

Increasing the temperature will, depending on the pump power, decrease the laser power. The threshold power P_th is increased by $P_\mathrm{T} = P_\mathrm{s}\, \sigma\, l N_\mathrm{T}$.

In Fig. 4.1.8 the result of such a measurement is represented. The laser output power was measured as a function of the coolant temperature. The average crystal temperature is increased due to the pump-light absorption in the material and by the temperature jump between the coolant and the laser material. This increase of approximately 2 °C per kW pump power was taken into account in the theoretical curves in Fig. 4.1.8.

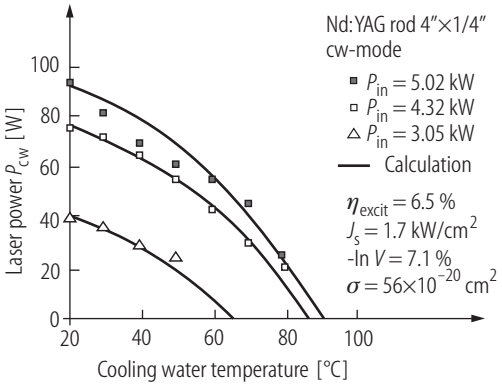

Fig. 4.1.8. Temperature dependence of a Nd:YAG laser in cw-mode.

4.1.1.6 Oscillator in pulsed operation

The pulse length varies from the ns region in Q-switched mode up to approximately 10 ms for pulse welding applications. When the pulse length is large compared to the upper laser lifetime, the system can be treated as in the stationary case.

4.1.1.6.1 Threshold

The pump light is switched on and the intensity J in the resonator is very low up to the time T_{th}. It consists only of spontaneous emission which is emitted into the laser modes. For $0 < t < T_{\mathrm{th}}$ with $J = 0$, the rate equation (4.1.8) reads

$$\frac{\mathrm{d}N(t)}{\mathrm{d}t} = WN_0 - \frac{N(t)}{\tau} \ . \tag{4.1.58}$$

With a constant pump rate W this may be integrated to

$$N(t) = W\tau N_0 \left(1 - \mathrm{e}^{-t/\tau}\right) \ . \tag{4.1.59}$$

Threshold inversion is reached at $t = T_{\mathrm{th}}$, which delivers

$$W_{\mathrm{th}} = W \left(1 - \mathrm{e}^{-T_{\mathrm{th}}/\tau}\right) \ , \tag{4.1.60}$$

and for the threshold itself

$$P_{\mathrm{th}} = P_{\mathrm{p}} \left(1 - \mathrm{e}^{-T_{\mathrm{th}}/\tau}\right) \tag{4.1.61}$$

with $P_{\mathrm{p}} = \mathrm{const}$.

This equation only holds for rectangular pump light. A universal method is described in [99Koe]. The time T_{th} to reach the threshold inversion is

$$T_{\mathrm{th}} = \tau \ln\left(\frac{P_{\mathrm{p}}}{P_{\mathrm{p}} - P_{\mathrm{th}}}\right) = \tau \ln\left(\frac{E_0}{E_0 - P_{\mathrm{th}}T_{\mathrm{th}}}\right) \ . \tag{4.1.62}$$

E_0 is the pump energy, which is needed up to the onset of lasing,

$$E_0 = P_{\mathrm{p}}T_{\mathrm{th}} \ . \tag{4.1.63}$$

The total threshold energy E_{th} during the pump pulse T_{p} consists of the energy to reach the inversion and the energy to cover the losses in this quasistationary regime:

$$E_{\mathrm{th}} = P_{\mathrm{p}}T_{\mathrm{th}} + P_{\mathrm{th}}(T_{\mathrm{p}} - T_{\mathrm{th}}) = P_{\mathrm{th}}T_{\mathrm{p}} - (P_{\mathrm{p}} - P_{\mathrm{th}})\tau \ln\left(1 - P_{\mathrm{th}}/P_{\mathrm{p}}\right) \ , \tag{4.1.64}$$

threshold energy in the pulsed operation.

4.1.1.6.2 High pump power $P_{\mathrm{p}} \gg P_{\mathrm{th}}$

At high pump power (4.1.62) and (4.1.64) may be approximated by

$$T_{\mathrm{th}} \approx \tau P_{\mathrm{th}}/P_{\mathrm{p}} \tag{4.1.65}$$

and

$$E_{\rm th} \approx P_{\rm th} T_{\rm p} + \tau P_{\rm th} - \tau P_{\rm th}^2 / P_{\rm p} \quad \text{with} \quad P_{\rm th} \ll P_{\rm p} \; . \tag{4.1.66}$$

The pulse energy E of a laser pulse averaged over the spikes and for a constant pump pulse power during the pulse length $T_{\rm p}$ then follows from (4.1.61)

$$E = P_{\rm cw}(T_{\rm p} - T_{\rm th}) = \eta_{\rm slope}(P_{\rm p} - P_{\rm th}) \left(T_{\rm p} - \tau \, \frac{P_{\rm th}}{P_{\rm p}} \right) \; , \tag{4.1.67}$$

$$E = \eta_{\rm slope} \left(E_{\rm p} - P_{\rm th} T_{\rm p} - \tau P_{\rm th} - \tau \frac{P_{\rm th}^2}{P_{\rm p}} \right) \; , \quad \textit{energy in the pulsed operation} \; . \tag{4.1.68}$$

With short pulses a good efficiency can only be reached at high pump power.

4.1.1.6.3 Relaxation oscillation

After the threshold time $T_{\rm th}$ a radiation field can establish itself. The time-dependent differential equations (4.1.37) and (4.1.38) are now applicable:

$$\frac{{\rm d}N}{{\rm d}t} = W N_0 - \frac{N}{\tau} \left(1 + \frac{2J}{J_{\rm s}} \right) \; , \tag{4.1.69}$$

$$\frac{{\rm d}J}{{\rm d}t} = \frac{\sigma l J \, (N - N_{\rm th})}{\tau_{\rm R}} \; , \tag{4.1.70}$$

with

$$\tau_{\rm R} = \frac{L + l(n-1)}{c} \; , \quad \text{resonator decay time} \; .$$

In the following, small deviations from the stationary values ΔN and ΔJ are considered. Inversion and radiation field are assumed to be

$$N = N_{\rm th} + \Delta N \; , \tag{4.1.71}$$

$$J = J_{\rm cw} + \Delta J \; , \quad \text{with} \quad J_{\rm cw} = \frac{J_{\rm s}}{2} \left(\frac{P_{\rm p}}{P_{\rm th}} - 1 \right) \; , \quad \text{according to (4.1.46)} \; . \tag{4.1.72}$$

Inserting these into the rate equations (4.1.69) and (4.1.70), eliminating ΔJ and neglecting terms of second order the differential equation for the damped harmonic oscillator follows

$$0 = \tau \, \frac{{\rm d}^2 \Delta N}{{\rm d}t^2} + \frac{P_{\rm p}}{P_{\rm th}} \frac{{\rm d}\Delta N}{{\rm d}t} + \frac{P_{\rm p} - P_{\rm th}}{\tau_{\rm R} P_{\rm s}} \Delta N \; , \tag{4.1.73}$$

with the solution

$$N = N_{\rm th} + \Delta N \, \cos(2\pi f t) \exp(-t/\tau_{\rm D}) \; . \tag{4.1.74}$$

The damping time $\tau_{\rm D}$ for the relaxation oscillation is

$$\tau_{\rm D} = \frac{P_{\rm th}}{P_{\rm p}} \, \tau \; , \quad (\tau_{\rm D} = T_{\rm th} \text{ according to (4.1.65)}) \; , \tag{4.1.75}$$

and the frequency f

$$4 \, \pi^2 f^2 = \frac{P_{\rm p} - P_{\rm th}}{\tau_{\rm R} \tau P_{\rm s}} - \frac{P_{\rm p}^2}{4 P_{\rm th}^2 \tau^2} \approx \frac{P_{\rm p} - P_{\rm th}}{\tau_{\rm R} \tau P_{\rm s}} \; . \tag{4.1.76}$$

The condition for damped oscillations is

$$\left(\frac{P_{\rm p}}{P_{\rm th}} \right)^2 < 4 \, \frac{\tau}{\tau_{\rm R}} \, \frac{P_{\rm p} - P_{\rm th}}{P_{\rm s}} \; . \tag{4.1.77}$$

If the oscillation condition is fulfilled, and for small disturbances, the intensity and the inversion will perform damped oscillations around the stationary value. With Nd:YAG the damping time is in the 100 μs range and the period is about 10 μs.

4.1.1.6.4 Spiking

The linear approximative equations do not hold for transient effects and are also not valid for strong disturbances, in which case (4.1.69) as well as (4.1.70) must be solved numerically.

Anharmonic oscillations appear, which are called spikes. When switching on a high pump power, the inversion quickly exceeds the threshold, without a sufficiently strong radiation field having been built up. The intensity then increases rapidly and reaches a value much higher than in the stationary case. The inversion is reduced below threshold and the radiation field drops again to a small value. As in the case of small perturbations, the stationary case is reached.

The temporal behavior of the laser radiation and the flash lamp light after switch-on for nearly monomode is shown in Fig. 4.1.9. Second harmonic generation inside the resonator may suppress or damp the spiking [91Jey].

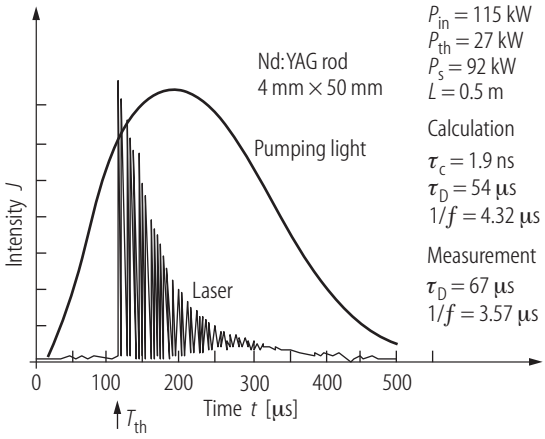

Fig. 4.1.9. Spiking in monomode operation [88Hod1].

4.1.1.6.5 Long-pulse regime

For long pulses with $T_p \gg T_{th}$ and at high excitation the threshold energy becomes

$$E_{th} = P_{th} T_p \ , \quad \textit{threshold energy} \ . \tag{4.1.78}$$

The laser pulse duration T is equal to the pump pulse time T_p and the laser energy is given to a good approximation by

$$E = P_{cw} T = \eta_{slope} (E_p - E_{th}) \ . \tag{4.1.79}$$

The amount of energy until the onset of laser activity is negligible with respect to the total threshold energy E_{th}. The temperature dependence is described analogously to the cw case, see (4.1.57):

$$E = \eta_{slope} (P_p - P_{th} - P_T) \, T \ . \tag{4.1.80}$$

4.1.1.7 Q-switch operation

For material surface treatments such as depainting, scribing and marking, short laser pulses with high peak power are required to ablate the surface layers. The thermal impact on the bulk material

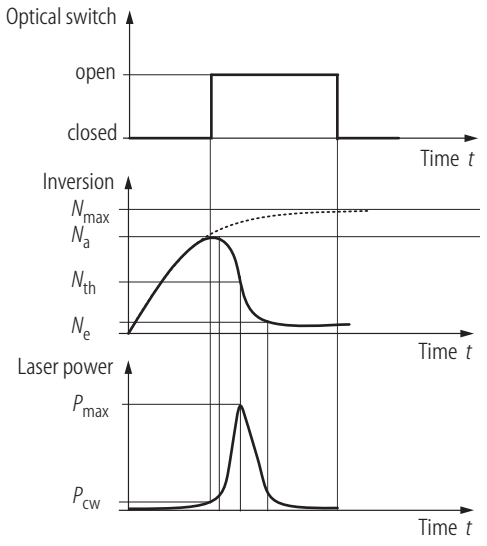

Fig. 4.1.10. Principle behavior of optical switch, inversion, and output power in the Q-switch mode.

is low. One method which is employed is focusing and scanning the laser beam in the so-called Q-switch mode [87Wil], in which the quality of the resonator alternates rapidly between two extreme values with the help of a suitable optical switch.

In the ideal case the light path is interrupted in the resonator for a certain time and at a constant pump rate a maximal inversion is reached, limited only by the spontaneous emission. If the light path is then restored, a fast rising pulse is built up from the spontaneous emission and the inversion is reduced, creating a short, intense light pulse. Figure 4.1.10 shows the principle temporal behavior.

Two cases can be discussed in an approximate way. On the one hand the single-pulse operation, in which the time between two pulses is long compared to the upper laser level lifetime and allows the maximal inversion. On the other hand the pulse operation with a frequency so high that the inversion varies only slightly around a stationary value before and after the Q-switch pulse. The range between these two extremes can be described only numerically. The rate equations were solved numerically in [71Bal] and the theoretical results for pulse energy and average laser power were compared with the experimental results.

4.1.1.7.1 Single Q-switch pulse

Equation (4.1.59) describes the temporal buildup of the inversion without induced emission:

$$N(t) = W\tau N_0(1 - \mathrm{e}^{-t/\tau}) \quad \text{for} \quad W = \text{const} . \tag{4.1.81}$$

The maximum inversion after a sufficiently long pumping time ($T_\mathrm{p} \gg \tau$) is for $J = 0$ with (4.1.45)

$$N_\mathrm{max} = N_0 W\tau = \eta_\mathrm{excit} \frac{\tau}{h\nu V_\mathrm{ol}} P_\mathrm{p} , \tag{4.1.82}$$

and the maximum energy E_max which can be stored is

$$E_\mathrm{max} = h\nu N_\mathrm{max} V_\mathrm{ol} = \eta_\mathrm{excit}\tau P_\mathrm{p} . \tag{4.1.83}$$

Once the inversion has attained N_max the optical feedback is opened by a fast shutter. The buildup time of the laser pulse in normal resonators is much shorter than the upper laser level lifetime τ and the pumping time constant $1/W$. The rate equations (4.1.69) and (4.1.70) then can be approximated as

$$\frac{\mathrm{d}N}{\mathrm{d}t} = -\frac{2NJ}{\tau J_\mathrm{s}} = -\frac{2NJ}{H_\mathrm{s}} \ , \quad \textit{rate equations for a fast Q-switch} \ , \tag{4.1.84}$$

$$\frac{\mathrm{d}J}{\mathrm{d}t} = \frac{\sigma l}{\tau_\mathrm{c}} \, J(N - N_\mathrm{th}) \ , \tag{4.1.85}$$

$$\tau_\mathrm{c} = \frac{L + l(n-1)}{c} \ , \quad \textit{resonator transit time} \ . \tag{4.1.86}$$

At the beginning of the pulse $N_\mathrm{a} \approx N_\mathrm{max}$ is assumed to be constant for a short time. The intensity inside the resonator and the pulse power increase exponentially

$$J(t) = J_\mathrm{a} \, \mathrm{e}^{\sigma l (N_\mathrm{max} - N_\mathrm{th}) t/\tau_\mathrm{c}} \quad \text{for} \quad J \ll J_\mathrm{s} \ . \tag{4.1.87}$$

J_a is the spontaneous (initial) emission in the laser mode. Dividing (4.1.85) by (4.1.84) and integrating with the initial conditions $J(0) = J_\mathrm{a}$ and $N(0) = N_\mathrm{a}$ for $t = 0$ gives

$$J = \frac{lh\nu}{2\tau_\mathrm{c}} \left[N_\mathrm{a} - N + N_\mathrm{th} \ln(N/N_\mathrm{a}) \right] \ . \tag{4.1.88}$$

The maximum of the intensity in the resonator is reached for $N = N_\mathrm{th}$ and (4.1.88) becomes

$$J_\mathrm{max} = \frac{lh\nu}{2\tau_\mathrm{c}} \left[N_\mathrm{a} - N_\mathrm{th} + N_\mathrm{th} \ln(N_\mathrm{th}/N_\mathrm{a}) \right] \quad \text{neglecting } J_\mathrm{a} \ . \tag{4.1.89}$$

However, since the intensity is considerably higher than in the stationary case, the inversion is further reduced and the output power falls back to zero. The optical shutter is closed rapidly. After a certain time the inversion again reaches values larger than N_th, the switch can be opened again and the cycle starts once more.

With (4.1.49) and (4.1.89) the maximum of the available laser pulse power P_max can be estimated, to be

$$P_\mathrm{max} = -\ln\left(\sqrt{R}\right) \, f J_\mathrm{max} \ . \tag{4.1.90}$$

At sufficiently long pump duration, and with $N_\mathrm{a} = N_\mathrm{max}$, the laser power is

$$P_\mathrm{max} = -\ln\left(\sqrt{R}\right) \, f \, \frac{lh\nu}{2\tau_\mathrm{c}} \, N_\mathrm{max} \left(1 - \frac{N_\mathrm{th}}{N_\mathrm{max}} + \frac{N_\mathrm{th}}{N_\mathrm{max}} \ln\left(\frac{N_\mathrm{th}}{N_\mathrm{max}} \right) \right) \tag{4.1.91}$$

and with (4.1.82) it follows that

$$P_\mathrm{max} = -\ln\left(\sqrt{R}\right) \, \frac{\tau}{\tau_\mathrm{c}} \, \eta_\mathrm{excit} P_\mathrm{p} \left(1 - \frac{P_\mathrm{th}}{P_\mathrm{p}} + \frac{P_\mathrm{th}}{P_\mathrm{p}} \ln\left(\frac{P_\mathrm{th}}{P_\mathrm{p}} \right) \right) \ , \tag{4.1.92}$$

which is the maximum attainable peak power of a Q-switch pulse.

The second zero of (4.1.88) gives the final inversion N_e:

$$0 = N_\mathrm{a} - N_\mathrm{e} + N_\mathrm{th} \ln(N_\mathrm{e}/N_\mathrm{a}) \ . \tag{4.1.93}$$

The output energy results from

$$E = \int_0^\infty P \, \mathrm{d}t = -f \ln\left(\sqrt{R}\right) \int_0^\infty J \mathrm{d}t = f H_\mathrm{s} \ln\left(\sqrt{R}\right) \int_{N_\mathrm{a}}^{N_\mathrm{e}} \frac{\mathrm{d}N}{N} = f H_\mathrm{s} \ln\left(\sqrt{R}\right) \ln \frac{N_\mathrm{e}}{N_\mathrm{a}} \tag{4.1.94}$$

and reads with (4.1.93)

$$E = -fH_s \ln\left(\sqrt{R}\right) \frac{N_a - N_e}{N_{th}} = \frac{V_{ol}\, h\nu}{-\ln(V\sqrt{R})}(N_{max} - N_e) \quad \text{for} \quad N_a \approx N_{max} \,. \tag{4.1.95}$$

At high pump power N_e can be neglected compared to N_{max} and (4.1.95) with (4.1.92) therefore gives

$$E_{max} = \eta_{excit} \frac{\ln\sqrt{R}}{\ln\left(V\sqrt{R}\right)} \tau P_p = \eta_{slope} \tau P_p \,, \tag{4.1.96}$$

the maximum energy of a single Q-switch pulse. The peak power P_{max} and the pulse energy E can be used to define the laser pulse duration T:

$$T = \frac{E}{P_{max}} = \tau_c \frac{P_p}{-\ln\left(V\sqrt{R}\right)\left[P_p - P_{th} - P_{th}\ln(P_p/P_{th})\right]} \,. \tag{4.1.97}$$

4.1.1.7.2 Periodical Q-switch for high pulse repetition rate ($r\tau \gg 1$)

In the periodical Q-switch mode the laser is continuously pumped and the Q-switch is switched on and off rectangularly with the pulse repetition rate r. The inversion varies slightly around the threshold inversion N_{th} between N_a and N_e (Fig. 4.1.11). In the interval T_p where $J \approx 0$ the evolution of the inversion is with (4.1.59)

$$N(t) = N_e + (N_{max} - N_e)\left(1 - e^{-t/\tau}\right) \,. \tag{4.1.98}$$

With the approximation,

$$T_p \approx 1/r \,, \tag{4.1.99}$$

the inversion at the end of a pump cycle is

$$N_a = N_e + (N_{max} - N_e)\left(1 - e^{-1/(r\tau)}\right) \,. \tag{4.1.100}$$

For small values of the inversion oscillations, $\Delta N \ll N_{th}$, (4.1.93) delivers in second order

$$\Delta N = N_a - N_{th} = N_{th} - N_e \,, \tag{4.1.101}$$

the amplitude of N can then be described as

$$\Delta N = \left(\frac{1 - e^{-1/(r\tau)}}{1 + e^{-1/(r\tau)}}\right)(N_{max} - N_{th}) \,. \tag{4.1.102}$$

With (4.1.95) the energy of a pulse in the periodical Q-switching mode becomes

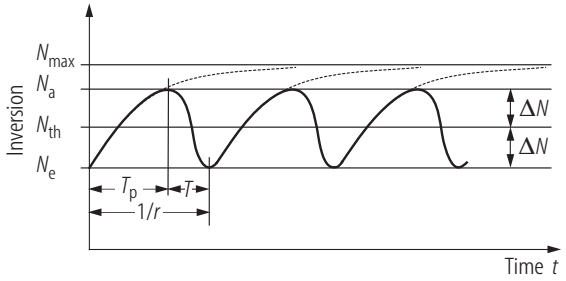

Fig. 4.1.11. Inversion for the periodical Q-switch versus time ($\Delta N \ll N_{th}$).

$$E = -f H_s \ln\sqrt{R}\ \frac{2\Delta N}{N_{th}} \tag{4.1.103}$$

and the peak power with (4.1.91) and (4.1.83)

$$P_{max} = -V_{ol}\ \ln\sqrt{R}\ \frac{h\nu}{\tau_R}\left[\Delta N - N_{th}\ln\left(1+\frac{\Delta N}{N_{th}}\right)\right] \approx \frac{-V_{ol}\,h\nu}{2\tau_R}\ \ln\sqrt{R}\ \left(\frac{\Delta N}{N_{th}}\right)^2 \tag{4.1.104}$$

with the resonator decay time $\tau_R = \tau_c \Big/ \left(-\ln\left(V\sqrt{R}\right)\right)$. The pulse duration T can be estimated to be

$$T = \frac{E}{P_{max}} = \frac{4\tau_R}{l\sigma\Delta N}\ . \tag{4.1.105}$$

The product of pulse energy and pulse duration in the periodical Q-switch is a system constant

$$(ET) = 8\,\eta_{slope} P_s \tau \tau_R = C_Q\ . \tag{4.1.106}$$

Example 4.1.2. Nd:YAG Q-switch parameter.

With the following experimental parameters

$\tau = 200$ µs,	$\eta_{excit} = 5$ %,	$\eta_{slope} = 2$ %,	$L = 1$ m,
$P_p = 5$ kW,	$P_{th} = 1$ kW,	$R = 0.9$,	$l = 10$ cm,

and the above equations one obtains:

stored energy	$E_{max} = 50$ mW s,	maximum laser energy	$E = 20$ mW s,
resonator transit time	$\tau_c = 3.3$ ns,	peak pulse power	$P_{max} = 0.4$ MW,
pulse duration	$T = 50$ ns.		

An increase of the pulse energy results in a shorter pulse duration. Equation (4.1.101) inserted into (4.1.102) gives for the energy with N_{max}, according to (4.1.82), and with N_{th}, according to (4.1.50):

$$E = 2\left(\frac{1-\mathrm{e}^{-1/(r\tau)}}{1+\mathrm{e}^{-1/(r\tau)}}\right)\tau P_{cw}\ , \tag{4.1.107}$$

and for the average power

$$P_{av} = Er\ , \quad T, T_p \text{ and } 1/r \text{ according to Fig. 4.1.11}\ . \tag{4.1.108}$$

At high pulse repetition rate r the average power in Q-switch mode approaches the cw laser power. With the help of the system constant C_Q the pulse duration and peak power follow as

$$T = \frac{(ET)}{E} = \frac{C_Q}{E} \tag{4.1.109}$$

and

$$P_{max} = \frac{E}{T} = \frac{E^2}{(E\times T)} = \frac{E^2}{C_Q}\ . \tag{4.1.110}$$

Figure 4.1.12 shows experimental results [71Bal] for the average power and for the pulse energy.

The relation between pump duration, laser pulse duration and Q-switch repetition rate determine how regular the pulse train is. If the Q-switch is opened quickly after reaching the threshold, a small pulse arises, changing the inversion insignificantly. In the next pump cycle a high inversion can then be reached, which leads to a large pulse and low initial inversion. Small pulses alternate therefore with large ones. Pulse patterns are possible that recur more or less regularly. Since the thresholds are different for the various modes, a mode hopping can be observed [87Non].

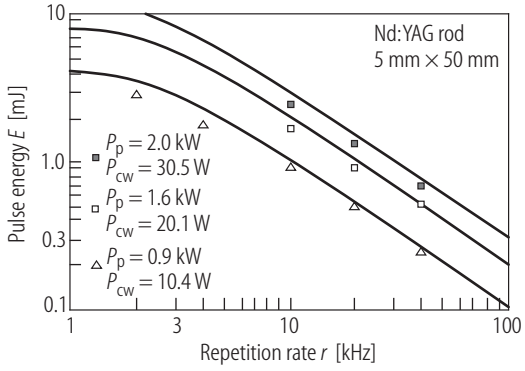

Fig. 4.1.12. Pulse energy versus the repetition rate in the Q-switch mode [71Bal].

4.1.1.8 The 3-level system

Using a simplified energy diagram of a 3-level system as in Fig. 4.1.13, the differences with respect to the 4-level system will be derived.

The rate equations for the upper laser energy level and the intensity are

$$\frac{\mathrm{d}N_2}{\mathrm{d}t} = WN_1 - \frac{N_2}{\tau} - \frac{\sigma J}{h\nu}\left(N_2 - N_1\right) \ , \tag{4.1.111}$$

$$\frac{\mathrm{d}J}{\mathrm{d}t} = \frac{\sigma cJ}{n}\left(N_2 - N_1\right) - \frac{\sigma cJ}{n}N_{\mathrm{th}} \ . \tag{4.1.112}$$

With the help of the following definitions:

$N = N_2 - N_1$, the *inversion*,

$N_0 = N_2 + N_1$, the total *density* of the active ions, and

$J_{\mathrm{s}} = \dfrac{h\nu}{2\sigma\tau}$, the *saturation intensity*,

the densities N_1 and N_2 in (4.1.111) and (4.1.112) can be eliminated and one obtains the rate equations for the 3-level system

$$\frac{\mathrm{d}N}{\mathrm{d}t} = W\left(N_0 - N\right) - \frac{1}{\tau}\left(N_0 - N\right) - \frac{J}{J_{\mathrm{s}}}N \ , \tag{4.1.113}$$

$$\frac{\mathrm{d}J}{\mathrm{d}t} = \frac{\sigma cJ}{n}\left(N - N_{\mathrm{th}}\right) \ . \tag{4.1.114}$$

Inversion requires $N \geq 0$, i.e. half of the ions must be excited into the upper laser level, $N_2 \geq N_0/2$.

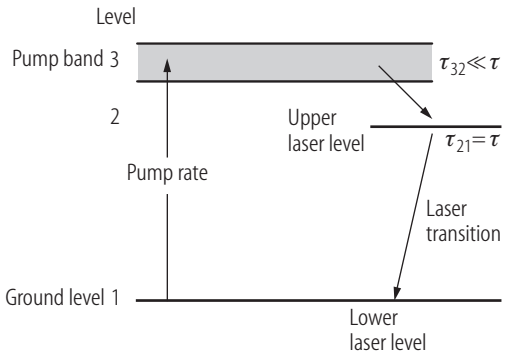

Fig. 4.1.13. Simplified energy diagram of a 3-level system.

4.1.1.8.1 Stationary case with $dN/dt = 0$ and $dJ/dt = 0$

The stationary case is the same as for the 4-level system

$$N = N_{\text{th}} \; . \tag{4.1.115}$$

The steady-state inversion equals the threshold inversion. The intensity in the resonator follows with (4.1.113)

$$J = J_{\text{s}} \left[W\tau \left(\frac{N_0}{N_{\text{th}}} - 1 \right) - \left(\frac{N_0}{N_{\text{th}}} + 1 \right) \right] \; . \tag{4.1.116}$$

The threshold pump rate reads:

$$W_{\text{th}} = \frac{1}{\tau} \, \frac{N_0 + N_{\text{th}}}{N_0 - N_{\text{th}}} \; . \tag{4.1.117}$$

Figure 4.1.14 shows schematically the intensity J and the inversion N as a function of the normalized pump rate τW. The stationary laser power P_{cw} becomes

$$P_{\text{cw}} = \eta_{\text{slope}} \left[P_{\text{p}} - P_{\text{s}} \left(\sigma N_0 l - \ln \left(V\sqrt{R} \right) \right) \right] \tag{4.1.118}$$

with

$$P_{\text{s}} = \frac{f J_{\text{s}}}{\eta_{\text{excit}}} \quad \text{and the slope-efficiency} \quad \eta_{\text{slope}} = \eta_{\text{excit}} \, \frac{\ln \sqrt{R}}{\ln \left(V\sqrt{R} \right)} \; .$$

In contrast to the 4-level-system, the threshold is increased by $\sigma N_0 l$. The pump power P_{p} has to be larger by the amount $\sigma N_0 l P_{\text{s}}$ than in the 4-level system. Because of the larger thermal load 3-level lasers are mainly used in pulsed operation.

The laser's pulse energy is

$$E = \eta_{\text{slope}} \left[P_{\text{p}} - P_{\text{s}} \left(\sigma N_0 l - \ln \left(V\sqrt{R} \right) \right) \right] T \; , \tag{4.1.119}$$

with the threshold energy

$$E_{\text{th}} = P_{\text{s}} \left(\sigma N_0 l - \ln \left(V\sqrt{R} \right) \right) T \; , \quad T : \text{pulse duration } (T \gg \tau) \; . \tag{4.1.120}$$

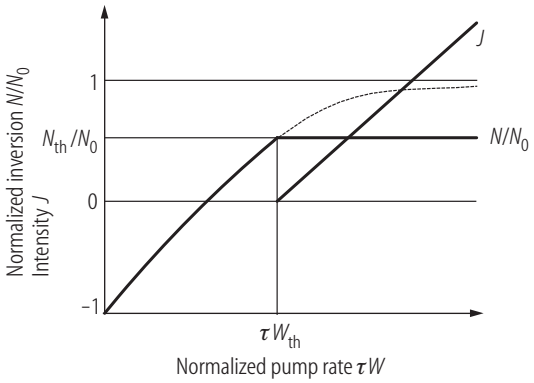

Fig. 4.1.14. Schematic diagram of inversion and intensity in the 3-level system.

Example 4.1.3. Ruby rod with 1 cm diameter and 10 cm length with a 0.05 wt% Cr doping.

With the supplier data

$\sigma = 2 \times 10^{-20}$ cm^2,	$N_0 = 0.16 \times 10^{20}$ cm^{-3},	$l = 10$ cm,	$r_0 = 0.5$ cm,
$R = 0.5$,	$V = 0.9$,	$\eta_{\text{excit}} = 0.8$ %,	

the parameters are calculated to be

$\sigma N_0 l = 3.2$,	$-\ln(V\sqrt{R}) = 0.45$,	$J_\text{s} = 1.9$ kW/cm^2,	$f \approx 0.8$ cm^2,
$P_\text{s} \approx 190$ kW,	$E_\text{th} \approx 3.4$ kW s,	$\eta_\text{slope} \approx 0.7$ %,	

and yield a laser energy of approximately 5 W s at 10 kW s pump energy.

By measuring the threshold energy E_th for the corresponding reflection R of the output mirror losses ($\ln V - \sigma l N_0$) can be determined. The influence of the reflection coefficient R on the threshold compared to the absorption $\sigma l N_0$, e.g. for ruby, is insignificant. The optimal reflection R_opt of the output mirror, for which the maximum laser pulse energy E_max can be extracted, is, analogous to (4.1.52),

$$\ln\sqrt{R_\text{opt}} = -2\sqrt{\left(\frac{P_\text{p}}{P_\text{s}} - \sigma N_0 l\right)\ln V} + 2\ln V \tag{4.1.121}$$

and the maximum laser energy is

$$E_\text{max} = f J_\text{s} T \left(\sqrt{\frac{P_\text{p}}{P_\text{s}} - \sigma N_0 l} - \sqrt{-\ln V}\right)^2 . \tag{4.1.122}$$

All equations for the 3- and 4-level systems were derived under simplified assumptions and can basically be validated by measurements. Some restrictions, however, have to be discussed in more detail:

- The inversion is not created and reduced homogeneously over the material cross section. The radiation field generally has a transverse structure. There is a mutual influence of the radiation field and the inversion. The longitudinal radiation field does not necessarily agree with the geometry of the laser medium. This is taken into account basically by the extraction efficiency η_extr [87Hod].
- As the laser preferably oscillates near threshold in the regions of highest inversion, the laser energy or power as a function of excitation (at low pump power) is nonlinear.
- For a high reflection coefficient and high excitation power the linear dependence of the laser energy or power on the excitation no longer holds. A saturation effect occurs.

All of these effects cause losses and heating of the laser material. However, they have not been examined in the equations explicitly but are taken into account by the loss terms $\ln V$ and P_s. They are discussed in detail in [80Sch, 87Web]. All essential equations for 4- and 3-level systems are compiled in Table 4.1.1.

The following loss mechanisms for pump light and laser radiation field in 3- and 4-level systems exist:

- amplification of spontaneously emitted ASE (Amplified Spontaneous Emission) light outside the utilizable area,
- inversion reduction by thermal population of the lower laser level,
- radiation field absorption in the medium by the upper laser energy level and excitation of higher energy states, Excited State Absorption (ESA),
- scattering of the radiation field in the material and at the mirrors,
- diffraction of the radiation field by the finite aperture of the laser medium,
- radiation field and inversion are not adapted to each other.

Table 4.1.1. Essential equations.

	4-level (Nd:YAG)	3-level (Cr:ruby)
saturation intensity	$J_s = \frac{h\nu}{\sigma\tau}$	$J_s = \frac{h\nu}{2\sigma\tau}$
saturation energy density	$H_s = \frac{h\nu}{\sigma}$	$H_s = \frac{h\nu}{2\sigma}$
small-signal gain factor	$G_0 = \exp(\sigma N l)$	$G_0 = \exp(\sigma N l)$
inversion	$N = N_2$	$N = N_2 - N_1$
saturated gain coefficient	$g_s = g_0/(1 + J/J_s)$	$g_s = g_0/(1 + J/J_s)$
loss factor per round trip	$V = \exp(-\alpha l)$	$V = \exp(-\alpha l)$
system constant	$P_s = f J_s/\eta_{excit}$	$P_s = f J_s/\eta_{excit}$
threshold (inversion)	$N_{th} = -\frac{\ln\left(V\sqrt{R}\right)}{\sigma l}$	$N_{th} = -\frac{\ln\left(V\sqrt{R}\right)}{\sigma l}$
threshold (pump power)	$P_{th} = -P_s \ln(V\sqrt{R})$	$P_{th} = P_s(\sigma l N_0 - \ln(V\sqrt{R}))$
threshold (temperature)		$P_T = P_s \sigma l N_T$
slope efficiency	$\eta_{slope} = \frac{\eta_{excit} \ln\sqrt{R}}{\ln(V\sqrt{R})}$	$\eta_{slope} = \frac{\eta_{excit} \ln\sqrt{R}}{\ln(V\sqrt{R})}$
laser power	$P_{cw} = \eta_{slope}(P_p - P_{th})$	$P_{cw} = \eta_{slope}(P_p - P_{th})$
laser energy (rectangular pulse)	$E = P_{cw}T$, $\tau \ll T$	$E = \eta_{slope}(E_p - E_{th})$

f : beam cross section, J : intensity of the laser beam, h : Planck's constant,
J_s : saturation intensity, l : length of the laser medium, N : inversion density,
α : loss coefficient, N_T : thermal population, η_{excit} : excitation efficiency,
P_p : pump power, σ : cross section, R : reflection coefficient,
τ : upper level lifetime, V : loss factor, T : pulse duration.

4.1.1.9 Efficiency and optimization

The different efficiencies from the power supply to the useable process laser power are explained and defined by the power transfer diagram, Fig. 4.1.15. An analogous definition of the power efficiency is valid for pulsed lasers if the pulse duration is large compared to the lifetime of the upper laser level and the laser is pumped far above the threshold. The efficiency determines the size of the power supply and the cooling unit and thus also fundamentally the price of the complete laser equipment.

The total efficiency of a laser system starting with the electrical power input up to the usable laser power combines from the various efficiencies of the components and process steps:

- The electrical power is provided by a power supply in a suitable form for the excitation source. In the case of pulsed operation the necessary energy is stored at first in capacitors (except Q-switch). Power for control circuits as well as for the cooling unit are not taken into account initially.
- The excitation sources convert the electrical power, both into radiation within the pump levels, and also to nonutilizable radiation and to heat.

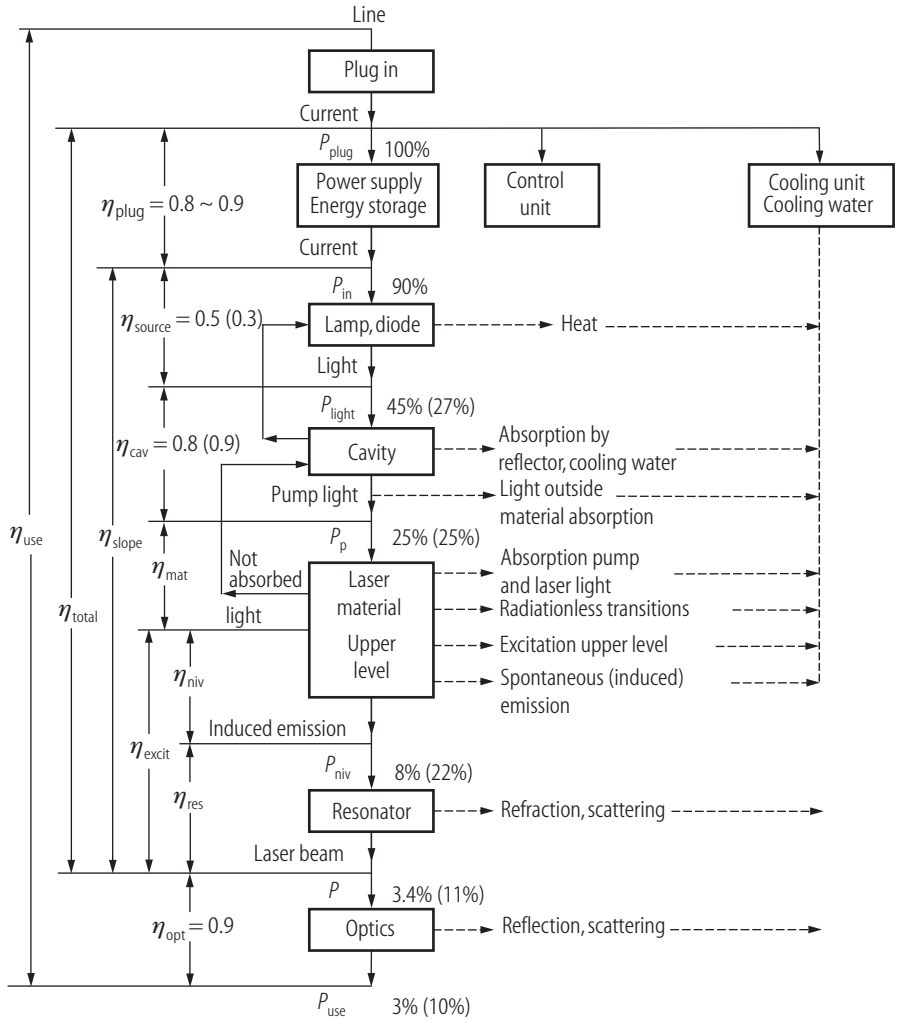

Fig. 4.1.15. Efficiencies of lamp- or laser-diode-pumped solid-state lasers, numerical values for laser diodes in round brackets.

- The pump light in the cavity is concentrated by a reflector onto the laser medium. Geometric and absorption losses by reflector, flow tubes and coolants occur. The radiation inside the laser material can then be utilized for optical pumping.
- Losses in the energy level diagram that can occur in the pump levels and in the upper laser energy level are nonradiative transitions (quantum efficiency, η_Q), multiphoton excitation activation directly from the already excited upper laser level (excited state absorption, ESA), spontaneous and amplified spontaneous emission (ASE).
- The pump light, absorbed by the laser material into the pump levels excites the upper laser level. All effects that cause losses of the pump radiation are contained in the efficiency η_{mat} of the laser material. One can distinguish the following single loss mechanisms: absorption of the pump light by color centers, nonradiative transitions from the upper levels (quantum efficiency η_Q), parts of the pump light not being absorbed, the quantum defect η_{QD}, i.e. the energy difference between pump and laser light. The energy losses of the above effects heat the laser material.
- The excitation energy available in the upper laser level cannot be fully coupled out. The resonator prescribes a radiation structure longitudinally and radially. Parts of the laser medium

that are not exposed to the radiation field of the resonator cannot contribute to the energy from the upper laser level by stimulated emission. In addition scattering, diffraction and absorption also occur in the resonator. These losses are included in the resonator efficiency.

– The optical system transforms the laser beam for the application as far as focus diameter and focus depth are concerned. There are losses due to reflection, e.g. at the lens surfaces or fiber ends, or by geometric restrictions.

The total efficiency is defined as the ratio of average laser output power to electrical input power:

$$P = \eta_{\mathrm{tot}} P_{\mathrm{in}} \,, \tag{4.1.123}$$

$$\eta_{\mathrm{tot}} = \eta_{\mathrm{excit}}\, \eta_{\mathrm{cav}}\, \eta_{\mathrm{mat}}\, \eta_{\mathrm{niv}}\, \eta_{\mathrm{res}} \,,$$

$$\eta_{\mathrm{tot}} = \eta_{\mathrm{excit}}\, \eta_{\mathrm{cav}}\, \eta_{\mathrm{extr}} \,, \quad \eta_{\mathrm{tot}} \approx 0.04 \,.$$

Since the total efficiency depends on the operating point, one uses the slope efficiency η_{slope}

$$\mathrm{d}P_{\mathrm{L}} = \eta_{\mathrm{slope}}\, \mathrm{d}P_{\mathrm{in}} \,, \quad \eta_{\mathrm{slope}} \approx 0.05 \,, \tag{4.1.124}$$

$$\mathrm{d}E_{\mathrm{L}} = \eta_{\mathrm{slope}}\, \mathrm{d}E_{\mathrm{in}} \,.$$

4.1.1.10 Stable resonators

Today stable resonators are almost exclusively used in commercial solid-state lasers. The resonator is defined as stable if the mode diameter of the TEM-00 mode is confined and remains finite for unlimited mirrors and unlimited medium size. The stationary intensity distribution can be described within the paraxial approximation and the matrix formalism can be applied. For details see Hodgson, N.: Optical resonators, Chap. 8.1, in: Landolt-Börnstein Vol. VIII/1 "Laser Physics and Applications", Subvol. A2 "Laser Fundamentals, Part 2", 2006, pp. 147–218.

4.1.1.10.1 Eigenvalues for TEM-00 mode

The beam is described by the complex beam parameter $q(z)$:

$$\frac{1}{q} = \frac{1}{R} - \frac{\mathrm{i}\lambda}{\pi w_0^2} \tag{4.1.125}$$

with

$R = R(z)$: curvature of the wavefront,
$w_0 = w_0(z)$: beam radius of 00-mode.

The divergence θ_0 of the fundamental beam TEM_{00} is defined as

$$\theta_0 = \lim_{z\to\infty} \frac{w_0(z)}{z} = \frac{\lambda}{\pi} \,, \quad \textit{divergence} \,. \tag{4.1.126}$$

For stationary conditions q must be reproduced after a round-trip of the wave (Fig. 4.1.16):

$$q = q_1 \,. \tag{4.1.127}$$

The ABCD law for a round-trip,

$$q = \frac{\mathsf{A}q + \mathsf{B}}{\mathsf{C}q + \mathsf{D}} \,, \quad \begin{vmatrix} \mathsf{A} & \mathsf{B} \\ \mathsf{C} & \mathsf{D} \end{vmatrix} = \textit{matrix for a full round-trip} \,, \tag{4.1.128}$$

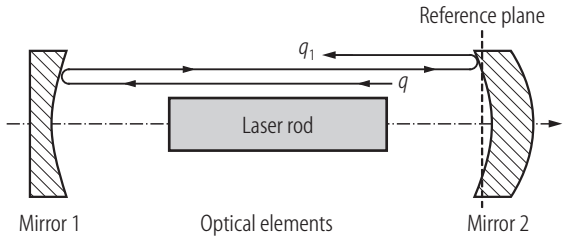

Fig. 4.1.16. Stable resonator.

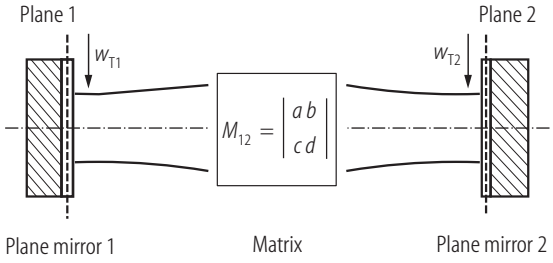

Fig. 4.1.17. Modified matrix representation.

leads with $\mathsf{AD} - \mathsf{BC} = 1$ to the solution

$$\frac{1}{q} = \frac{\mathsf{D} - \mathsf{A}}{2\mathsf{B}} \pm \frac{\mathrm{i}}{2\mathsf{B}} \sqrt{4 - (\mathsf{A} + \mathsf{D})^2} \,. \tag{4.1.129}$$

The expression under the square root must be positive in order for the beam radius to remain real. Therefore, the stationary value of the beam parameter in a stable resonator requires

$$-2 < \mathsf{A} + \mathsf{D} < 2 \,, \quad \textit{stability criterion} \,. \tag{4.1.130}$$

Such a resonator is called stable. Choosing the position of the reference plane, such that there is a flat wavefront (plane mirror), we have

$$\frac{1}{R} = \mathrm{Re}\left(\frac{1}{q}\right) = \frac{\mathsf{D} - \mathsf{A}}{2\mathsf{B}} = 0 \,. \tag{4.1.131}$$

The beam waist and the Rayleigh length at mirror 2 follow as

$$w_{\mathrm{T}2}^2 = \frac{\lambda}{\pi} \sqrt{-\frac{\mathsf{B}}{\mathsf{C}}} \,, \tag{4.1.132}$$

$$z_{\mathrm{R}2}^2 = -\frac{\mathsf{B}}{\mathsf{C}} \,. \tag{4.1.133}$$

In Fig. 4.1.17 M_{12} is defined as the beam matrix for a single transition from reference plane 1 to plane 2. M_{12} contains all optical elements including the plane mirror surfaces.

The matrix for a complete round-trip from plane 2 to mirror 2 through the resonator to mirror 1 and back to plane 2 reads

$$\begin{vmatrix} \mathsf{A} & \mathsf{B} \\ \mathsf{C} & \mathsf{D} \end{vmatrix} = \begin{vmatrix} a & b \\ c & d \end{vmatrix} \begin{vmatrix} 1 & 0 \\ 0 & 1 \end{vmatrix} \begin{vmatrix} d & b \\ c & a \end{vmatrix} \begin{vmatrix} 1 & 0 \\ 0 & 1 \end{vmatrix} = \begin{vmatrix} ad + bc & 2ab \\ 2cd & ad + bc \end{vmatrix} \,. \tag{4.1.134}$$

Since $\mathsf{A} = \mathsf{D}$, (4.1.133) and (4.1.134) give the following expressions for the Rayleigh lengths and waist radii:

$$z_{\mathrm{R}2}^2 = -\frac{ab}{cd} \,, \quad z_{\mathrm{R}1}^2 = -\frac{db}{ca} \,, \quad \textit{Rayleigh lengths} \,[69\mathrm{Bau}] \,, \tag{4.1.135}$$

$$w_{T1} = \sqrt{\frac{\lambda z_{R1}}{\pi}}\,, \quad w_{T2} = \sqrt{\frac{\lambda z_{R2}}{\pi}}\,, \quad \textit{waist radii}\,.$$

The stability condition (4.1.130) with (4.1.134) delivers

$$abcd < 0\,, \quad \text{the } \textit{stability criterion}\,. \tag{4.1.136}$$

As soon as one of the parameters a to d is zero, the resonator becomes unstable. This simplified description of the full round-trip with flat wavefronts in the reference planes will be used in the following to consider various resonators.

4.1.1.10.2 Introducing a virtual reference plane

The position of the reference plane can be chosen such that a flat wavefront apparently lies inside it. Since a curved mirror can be represented by a combination of a lens and a flat mirror (Fig. 4.1.18), the mirror matrix can be written in the form

$$\begin{vmatrix} 1 & 0 \\ -2/R & 1 \end{vmatrix} = \begin{vmatrix} 1 & 0 \\ -1/f & 1 \end{vmatrix} \begin{vmatrix} 1 & 0 \\ 0 & 1 \end{vmatrix} \begin{vmatrix} 1 & 0 \\ -1/f & 1 \end{vmatrix} = \begin{vmatrix} 1 & 0 \\ -2/f & 1 \end{vmatrix}\,, \tag{4.1.137}$$

with $R = f$. The virtual plane mirror is located inside the real mirror.

For the beam radius w_2 at the mirror it follows analogously that

$$w_2 = \sqrt{-\frac{\lambda}{\pi}\,\frac{ab}{cd}}\,. \tag{4.1.138}$$

The part of the beam transmitted by the partially reflecting mirror (Fig. 4.1.19), enters the mirror with the refractive index n, gets transformed with the corresponding mirror matrix and enters air with the curvature R_3.

The correct sign of the curvatures R_i has to be chosen according to whether R_i is regarded as a lens radius or a curvature for the wave front:

$$M_{24} = \begin{vmatrix} 1 & 0 \\ \dfrac{n-1}{R_3} & n \end{vmatrix} \begin{vmatrix} 1 & 0 \\ \dfrac{-1}{R_2} & 1 \end{vmatrix} \begin{vmatrix} 1 & 0 \\ 0 & \dfrac{1}{n} \end{vmatrix} = \begin{vmatrix} 1 & 0 \\ \dfrac{n-1}{R_3} - \dfrac{n}{R_2} & 1 \end{vmatrix}\,. \tag{4.1.139}$$

For adapted mirrors, which also produce a flat wavefront in plane 3 [66Gra], not only the matrix element B in R_2 of (4.1.139) has to vanish, but also the matrix element C. Therefore, the transition matrix of reference plane 2 to plane 4 with adapted mirrors requires $R_3 = R_2\,(1 - 1/n)$.

The matrix elements a to d result from the optical elements inside the resonator. In general, a laser crystal shows a lens effect due to the optical pumping. This is taken into account to a first approximation by the corresponding refracting power. The matrix for a thermal, thin lens is

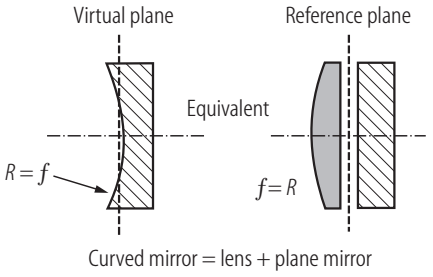

Fig. 4.1.18. Equivalence of a curved mirror and lens with a plane mirror.

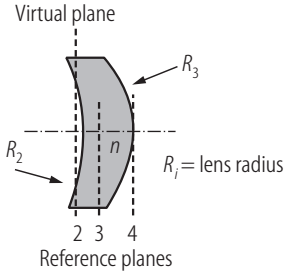

Fig. 4.1.19. Reference planes in the output mirror.

$$\mathsf{M} = \begin{vmatrix} 1 & 0 \\ -D & 1 \end{vmatrix} \tag{4.1.140}$$

with

D: refractive power.

The matrix elements a to d for a single transit are dependent on the refracting power D. The values of D are called critical refracting powers D_i, whenever one of the corresponding matrix element a, b, c or d vanishes:

$$i(D_i) = 0 \tag{4.1.141}$$

with

D_i: critical refracting power, $i = a, b, c, d$.

In order to calculate the beam radius and the divergence of a given resonator, the following steps have to be performed:

- The resonator matrix from plane 1 to 2, with the elements a to d is determined from the elements of the corresponding resonator. The critical refracting power D_i is calculated.
- The resonator parameters at the two mirrors are calculated with (4.1.135).
- The mode order is determined by calculating the beam radius at the position of the aperture. The ratio of the squares of the radii then yields the mode order M^2.
- Thus, with the mode order and the Rayleigh length, the multimode radius is known in the reference plane.
- The multimode divergence in the mirror plane is determined with (4.1.142), and for the output divergence the mirror itself has to be taken into account.

4.1.1.10.3 Beam parameter product

Transforming a beam waist of $w_{\mathrm{T}1}$ into a new waist $w_{\mathrm{T}2}$, one can show that for the product of waist and divergence one has

$$w_{\mathrm{T}2}\theta_2 = w_{\mathrm{T}1}\theta_1 = \text{const} , \quad w_{\mathrm{T}2}, w_{\mathrm{T}1}: \text{waist radius} . \tag{4.1.142}$$

This product is constant in ideal first-order optical systems (Abbe's sine law) and cannot be reduced by passive optics without any losses. The product of the divergence angle θ and the waist w_{T} is therefore a convenient measure for the optical beam quality of a laser system. The smaller this product or the mode order, the higher is the quality of the laser beam:

$$w_{\mathrm{T}}\theta = \frac{\mathsf{M}^2\lambda}{\pi} , \quad \textit{beam parameter product} . \tag{4.1.143}$$

4.1.1.11 Thermal effects

During optical pumping the laser material is heated [85Kru] and must be cooled. The temperature gradient in the laser material initially induces a degradation of the beam quality and finally a fracture of the crystal. The heating therefore determines the beam quality and the maximal laser output power. The exact knowledge of the various heating mechanisms is therefore important and will be discussed in some detail.

The average laser medium temperature influences the term population. Depending on the operation mode there is an optimal or maximal operating temperature. The laser efficiency can increase

initially with increasing temperature for alexandrite up to approximately 130 °C in the pulsed operation or decrease as for Nd:YAG and Nd:GGG. In laser glass the amplification is also reduced with increasing temperature due to the increasing population of the lower laser energy level. This reduction depends on the average temperature in the medium and on the ion concentration.

4.1.1.11.1 Steady-state temperature profile

Let the laser material with volume V be pumped with a power P_{in}. The amount P_{H} is heating the laser material. The surface is held at a constant temperature T_{r_0}. A temperature profile establishes itself in the material and a temperature step occurs at the surface (Fig. 4.1.20).

The Poisson equation describes the temperature profile in the range $T_{r_0} \geq T \geq T_0$:

$$\frac{\mathrm{d}T}{\mathrm{d}t} = \frac{k}{\rho c}\Delta T + \frac{P_{\mathrm{H}}}{V\rho c} \tag{4.1.144}$$

with

k: heat conductivity,
ρ: specific weight,
c: specific heat,
$P_{\mathrm{H}} \sim \eta_{\mathrm{H}} P_{\mathrm{p}}$: heating power,
η_{H}: heat efficiency,
V: material volume.

The stationary case for cylindrical symmetry reads [70Fos]

$$0 = \frac{\mathrm{d}^2T}{\mathrm{d}r^2} + \frac{1}{r}\frac{\mathrm{d}T}{\mathrm{d}r} + \frac{P_{\mathrm{H}}}{kV} \,. \tag{4.1.145}$$

At the surface $r = r_0$ Newton's cooling law applies

$$\left.\frac{\mathrm{d}T}{\mathrm{d}r}\right|_{r=r_0} = \frac{\lambda}{k}(T_{\mathrm{k}} - T_{r_0}) \tag{4.1.146}$$

with

r_0: rod radius,
T_{k}: cooling temperature.

The heat transfer coefficient λ is defined by

$$P_{\mathrm{H}} = \lambda O(T_{r_0} - T_{\mathrm{k}}) \,, \tag{4.1.147}$$

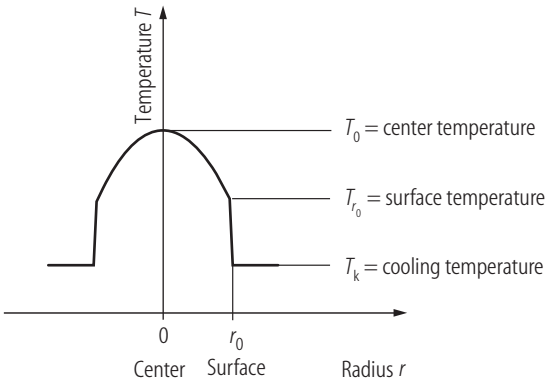

Fig. 4.1.20. Temperature distribution in the laser medium.

with

O: cooling surface,

and can be regulated in certain limits by coolant, flow tube diameter and coolant velocity. The temperature difference $(T_0 - T_{r_0})$ inside the material determines the material load as well as the lens effect. The average temperature T_{av} controls the population of the lower laser level. Depending on the pump light distribution in the crystal and the cooling, a temperature profile is established in the laser material.

In the stationary case and for a homogeneous heating in rod and slab systems, a parabolic temperature profile arises:

$$T_0 - T_{r_0} = \frac{1}{4}\,\frac{d_0}{O}\,\frac{1}{k}\,P_{\mathrm{H}} \tag{4.1.148}$$

with d_0: material thickness in cooling direction,

$$T_0 - T_{\mathrm{k}} = \frac{1}{\lambda k} P_{\mathrm{H}}\ . \tag{4.1.149}$$

The temperature difference between center and cooling surface is proportional to the heating power P_{H}, to the total material thickness d_0 in direction of the temperature gradient and inversely proportional to the heat conductivity k and the cooling surface O.

The system-specific efficiency η_{H} determines the material load and the lens effect, the heat-transfer coefficient λ with η_{H} the average temperature and thus the laser efficiency. Both quantities have to be determined experimentally [88Man].

4.1.1.11.2 Thermal load

Due to the temperature difference $(T_0 - T_{r_0})$ a surface tension σ is induced:

$$\sigma = F\frac{\alpha E}{1-\nu}\,(T_0 - T_{r_0}) \tag{4.1.150}$$

with

F: geometry factor, $F(\mathrm{rod}) = 1/2$, $F(\mathrm{slab}) = 1/3$ [86Bro],
α: thermal expansion coefficient,
E: modulus of elasticity (Young's modulus),
ν: Poisson number.

For safety reasons the tension should be smaller than the fracture tension by a factor of at least 5 [87Hag]

$$\sigma \le \frac{1}{5}\sigma_{\max}\ . \tag{4.1.151}$$

The maximum temperature difference between the center and the surface of a rod may therefore not be larger than

$$(T_0 - T_{r_0}) \le \frac{(1-\nu)}{5}\,\frac{\sigma_{\max}}{F\alpha E}\ . \tag{4.1.152}$$

For homogeneous heating it follows

$$\frac{\sigma_{\max}}{5} = \frac{F}{4}\,\frac{\alpha E}{(1-\nu)}\,\frac{d_0}{kO}\,P_{\mathrm{H}} \tag{4.1.153}$$

with d_0 : material thickness in direction of temperature gradient.

The thermal shock parameter R_T is defined as

$$R_T = \frac{k(1-\nu)}{\alpha E}\sigma_{max} \ . \tag{4.1.154}$$

The maximal heating power $P_{H,max}$ in the laser medium can be expressed as

$$P_{H,max} = \frac{4}{5F}\frac{O}{d_0}R_T \ , \tag{4.1.155}$$

and the corresponding acceptable pump power $P_{p,max}$ as

$$P_{p,max} = \frac{1}{\eta_H}\frac{4}{5F}\frac{O}{d_0}R_T \ . \tag{4.1.156}$$

Material properties and surface processing methods determine the thermal shock parameter $R_T = \sigma_{max}k(1-\nu)/\alpha E$. The material parameter R_T is dependent only on material properties. The fracture tension σ_{max} depends also strongly on the surface finish.

The maximal average laser power P_{max} for pulsed operation, limited by the safe thermal load, can then be estimated, as

$$P_{max} = \frac{4}{5F}\,\frac{O}{d_0}\,\frac{\eta_{extr}}{\eta_H}\,R_T \ , \tag{4.1.157}$$

$P = \eta_{extr}P_{niv}$,
for YAG: $\eta_{extr} \approx 0.5$ [88Hod2],
$F(\text{rod}) = 1/2$, $F(\text{slab}) = 1/3$ [86Bro].

If measurements of the slope-efficiency of a laser system are available, the maximal attainable laser power P_{max} can also be estimated as

$$P_{max} = \frac{4}{5F}\,\frac{O}{d_0}\,\frac{\eta_{slope}}{\eta_H}\,R_T \quad \text{with} \quad P_{max} \approx \eta_{slope}P_p \ . \tag{4.1.158}$$

High average laser power without fracture can only be obtained by a large cooling surface O or by a short cooling distance d_0. However, the statistical risk increases with the dimension of the surfaces. For a large surface a fracture induced by surface defects occurs already at a smaller load. For a large surface the acceptable load should be lowered. The maximal attainable laser power therefore does not increase linearly with the cooling surface. The allowed load by flash lamp pumping is considerably lower than the comparable pure thermal load, according to [87Hag]. This is taken into account by the empirical safety factor of 5.

The slope efficiency and the heat efficiency are correlated. An improvement in the pump setup will increase both unless a spectral selection does not improve the ratio. If the pumping direction is parallel to the direction of cooling (in the direction of d_0), one has a minimal d_0 because of the necessary absorption depth. High laser powers can then only be obtained with a large surface O or with other materials (R_T).

For rods, (4.1.158) reads

$$\frac{P_{max}}{l} = \frac{8\,\pi}{5}\,\frac{\eta_{slope}}{\eta_H}\,R_T \quad \text{with} \quad P_{max} \approx \eta_{slope}P_p \ . \tag{4.1.159}$$

The permitted laser power can only be increased by longer rods.

The maximal attainable laser power P_{max}/l can be increased by surface treatment. [85Mar] reports an increase of the fracture limit by almost an order of magnitude due to polishing and a special etching process for glass, GSGG and YAG.

4.1.1.11.3 Thermal lensing

The temperature difference $(T_0 - T_{r_0})$ between center and surface of the laser medium causes a lens effect. Three effects contribute to the refracting power:

1. the endface deformation by longitudinal expansion (α),
2. the radial temperature gradient of the refractive index ($\mathrm{d}n/\mathrm{d}T$), and
3. the photoelastic effect ($C_{r,\phi}$).

α, $\mathrm{d}n/\mathrm{d}T$ and $C_{r,\phi}$ are the characterizing quantities.

Due to the temperature distribution, the refractive index of the laser material becomes space-dependent. Neglecting the z dependence, one has:

$$n(r) - n_0 = \frac{\mathrm{d}n}{\mathrm{d}T}\,(T(r) - T_0) \tag{4.1.160}$$

with

n_0 : refractive index in the center,
$\mathrm{d}n/\mathrm{d}T$: temperature coefficient of the refractive index.

If a homogeneous heat distribution is assumed, a parabolic refractive index profile arises in a rod:

$$n(r) = n - \frac{\mathrm{d}n}{\mathrm{d}T}\,\frac{P_\mathrm{H}}{4kV}\,r^2\ . \tag{4.1.161}$$

Mechanical stress in tangential ϕ and in radial r directions also induces a change in the refractive index. Since the stress is quadratically dependent on the radial coordinate r for homogeneous heating, the photoelastic part of the refractive index acquires the same dependence [99Koe]:

$$n_r = \frac{n^3\alpha\,P_\mathrm{H}C_r}{2kV}\,r^2\ , \tag{4.1.162}$$

$$n_\phi = \frac{n^3\alpha\,P_\mathrm{H}C_\phi}{2kV}\,r^2\ . \tag{4.1.163}$$

Differences in n_r and n_ϕ cause birefringence. The tension coefficients C_r and C_ϕ are calculated for YAG with the photoelastic coefficients p_{ij} as follows [85Wal]:

$$C_r = \frac{(17\nu - 7)p_{11} + (31\nu - 17)p_{12} + 8(\nu + 1)p_{44}}{48(\nu - 1)}\ , \tag{4.1.164}$$

$$C_\phi = \frac{(10\nu - 6)p_{11} + 2(11\nu - 5)p_{12}}{48(\nu - 1)}\ . \tag{4.1.165}$$

The two essential changes in the refractive index add up to

$$n_{r,\phi}(r) = n - \left(\frac{\mathrm{d}n}{\mathrm{d}T}\,\frac{P_\mathrm{H}}{4\,kV} + \frac{n^3\alpha P_\mathrm{H}C_{r,\phi}}{2kV}\right)r^2 = n\left(1 - \frac{r^2}{2\beta_{r,\phi}^2}\right)\ , \tag{4.1.166}$$

$\beta_{r,\phi}$ is the characteristic focal length of the thermal lens. The material and geometrical constants can be combined as

$$\frac{1}{\beta_{r,\phi}^2} = \frac{P_\mathrm{H}}{kV}\left(\frac{1}{2n}\,\frac{\mathrm{d}n}{\mathrm{d}T} + n^2\alpha C_{r,\phi}\right) = \frac{P_\mathrm{H}M_{r,\phi}}{V} \tag{4.1.167}$$

and the material parameter $M_{r,\phi}$ is given by

$$M_{r,\phi} = \frac{1}{k}\left(\frac{1}{2n}\,\frac{\mathrm{d}n}{\mathrm{d}T} + n^2\alpha C_{r,\phi}\right)\ . \tag{4.1.168}$$

The term due to the thermal refractive index change normally dominates and to a good approximation one has

$$\frac{1}{\beta^2} = \frac{1}{2nk}\frac{\mathrm{d}n}{\mathrm{d}T}\frac{P_\mathrm{H}}{V} \ . \tag{4.1.169}$$

The thermal lens of a laser rod influences the beam quality of the resonator. For stable resonators the beam parameter product of rods in the multimode operation has a maximum:

$$\max(w\theta) \geq \frac{M_{r,\phi}\Delta P}{4\pi} \tag{4.1.170}$$

with ΔP: maximum pump power range.

4.1.1.11.4 Experimental determination of the refracting power

An experimental setup, as in Fig. 4.1.21, allows a simple determination of the average refracting power D_d for YAG or glass rods.

For a plane–plane resonator the critical refracting power is $D_\mathrm{d} = 1/d_1$. The average laser power as a function of the pumping power with the distance d_1 as parameter is measured.

When the critical pumping power is achieved, the laser power decreases since the resonator becomes unstable. For different distances d_1 the resonator becomes unstable at different pump powers P_crit. From the gradient of $1/d_1$ as a function of P_crit the thermal lens coefficient can be extracted

$$D_\mathrm{d} = \eta_\mathrm{H}\frac{M_{r,\phi}P_\mathrm{crit}}{\pi r_0^2} \ . \tag{4.1.171}$$

One defines $D_\mathrm{d}/P_\mathrm{crit}$ as the *lens coefficient*.

In Fig. 4.1.22 the laser power has been measured as a function of the pumping power for different reflecting distances d_1. Deviations from the straight line indicate the beginning of the unstable region for the r or ϕ component of the refracting power.

Another method [86Dri] is the determination of the focal length of a He–Ne test laser or Moiré reflectometry [84Hor]. These methods allow the investigation of the transient behavior.

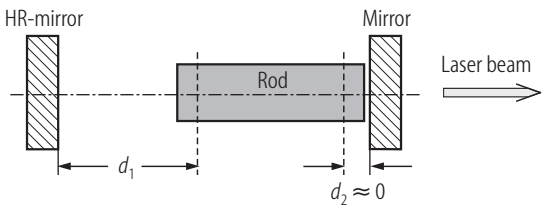

Fig. 4.1.21. Resonator to determine the critical refracting power.

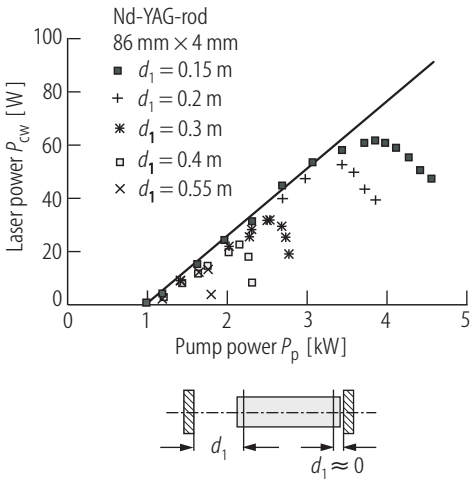

Fig. 4.1.22. Determination of the average refracting power for Nd:YAG rods.

4.1.1.12 Solid-state laser concepts

4.1.1.12.1 Multicavity resonators

Solid-state lasers with a single rod are limited due to the thermal load in their output power and beam quality. YAG rods only exist up to a length of 200 mm with a maximal output power per rod of about 500 W. By using several pump cavities in series inside or outside the resonator the power can be increased to the kW-range.

4.1.1.12.2 Two external mirrors and two rods

In Fig. 4.1.23 a resonator with two cavities is shown.

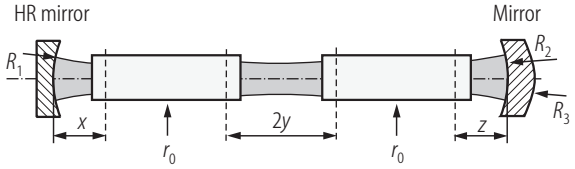

Fig. 4.1.23. Resonator with two cavities.

Resonator matrix:

$$\begin{vmatrix} a & b \\ c & d \end{vmatrix} = \begin{vmatrix} 1 & 0 \\ -1/R_2 & 1 \end{vmatrix} \begin{vmatrix} 1 & z \\ 0 & 1 \end{vmatrix} \begin{vmatrix} 1 & 0 \\ -D & 1 \end{vmatrix} \begin{vmatrix} 1 & 2y \\ 0 & 1 \end{vmatrix} \begin{vmatrix} 1 & 0 \\ -D & 1 \end{vmatrix} \begin{vmatrix} 1 & x \\ 0 & 1 \end{vmatrix} \begin{vmatrix} 1 & 0 \\ -1/R_1 & 1 \end{vmatrix} . \tag{4.1.172}$$

Mirror matrix for transmitted beam:

$$\mathsf{M}_{23} = \begin{vmatrix} 1 & 0 \\ \dfrac{n-1}{R_3} - \dfrac{n}{R_2} & 1 \end{vmatrix} , \quad \text{sign for } R_2 \text{ and } R_3 \text{ as lens radii} . \tag{4.1.173}$$

In the case of almost identically rods and the plane mirrors very close to the rods $R_1 = R_2 = \infty$ and $x = z = 0$, the following simplifications result:

Matrix elements: $a = 1 - 2yD , \quad b = 2y ,$ (4.1.174)

$$c = 2D(yD - 1) , \quad d = 1 - 2yD .$$

Critical refracting power: $D_a = D_d = 1/(2y) , \quad D_c = 0 \quad \text{or} \quad D_c = 1/y .$ (4.1.175)

Resonator parameter: $$p^2 = -\frac{ab}{cd} = -\frac{y}{D(yD-1)} .$$ (4.1.176)

Multimode divergence: $$\frac{\theta^2}{r_0^2} = \frac{1}{p^2} = -\frac{D(1-yD)}{y} .$$ (4.1.177)

Multimode radius: $w = r_0 .$ (4.1.178)

Beam quality: $$\max(\theta w) = \frac{r_0^2}{2y} .$$ (4.1.179)

Since the same power is distributed between two rods, the refracting power of each single rod is only half the value. The range of stable operation ΔD with the same beam quality is double that of a single rod. In the middle of the stable range, however, is an unique unstable point, $D = 1/(2y)$. In general, it can be proved [88Dri] that in the case of n rods the range of operation with the same beam quality increases by a factor n.

4.1.1.12.3 Multiple cavities with flat mirrors

The optical matrix of a resonator with several cavities (Fig. 4.1.24) is of the type

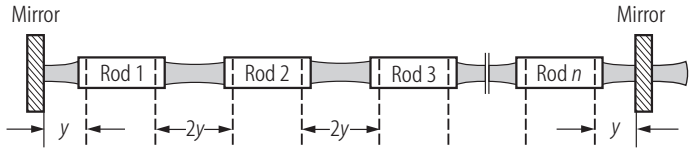

Fig. 4.1.24. Resonator with several pumping cavities.

$$\mathsf{M}^n = \left(\begin{vmatrix} 1 & y \\ 0 & 1 \end{vmatrix} \begin{vmatrix} 1 & 0 \\ -D & 1 \end{vmatrix} \begin{vmatrix} 1 & y \\ 0 & 1 \end{vmatrix} \right)^n . \tag{4.1.180}$$

With the help of the theorem of Sylvester [70Pip] this matrix can be evaluated

$$\mathsf{M}^n = \begin{vmatrix} a & b \\ c & d \end{vmatrix}^n = \frac{1}{\sin\varphi} \begin{vmatrix} a\sin(n\varphi) - \sin(n-1)\varphi & b\sin(n\varphi) \\ c\sin(n\varphi) & d\sin(n\varphi) - \sin(n-1)\varphi \end{vmatrix} \tag{4.1.181}$$

and $\cos\varphi = (a+d)/2$.

For matrices with $\det(\mathsf{M}) = 1$ the standardized critical refracting power can be calculated. Some values are given in Table 4.1.2.

For unequal distances between the cavities or differences in the refracting powers of the rods the output power is reduced and instabilities may occur. Due to the symmetrical construction ($a = d$) the resonator parameter for all resonators following this scheme is given by

$$p^2 = -\frac{b}{c} = \frac{2y - y^2 D}{D} . \tag{4.1.182}$$

For distances which are large compared to the rod length the beam quality can be estimated to be

$$\frac{\theta^2 w^2}{r_0^4} = \frac{D(2 - yD)}{4y} \tag{4.1.183}$$

with the maximum being

$$\max(\theta w) = \frac{r_0^2}{2y} . \tag{4.1.184}$$

Table 4.1.2. Normalized critical refracting powers for symmetrical setups.

Rods	$yD_a = yD_d =$	$yD_b =$	$yD_c =$
1	1	2	0
2	$1 \pm 0.5\sqrt{2}$	1, 2	0, 1
2	0.29, 1.71	1, 2	0, 1
3	$1, 1 \pm 0.5\sqrt{3}$	1/2, 3/2, 2	0, 1/2, 3/2
3	0.13, 1, 1.87	0.5, 1.5, 3	0, 0.5, 1.5
4	$1 \pm 0.5\sqrt{2 \pm \sqrt{2}}$	$1, 1 \pm 0.5\sqrt{2}$, 2	$1, 1 \pm 0.5\sqrt{2}$, 2
4	0.08, 0.62, 1.38, 1.92	0.29, 1, 1.71, 2	0.29, 1, 1.71, 2
5	$1, 1 \pm \sqrt{2}\ \sqrt{5 \pm \sqrt{5}}/4$	$2, (5 \pm \sqrt{5})/4, (3 \pm \sqrt{5})/4$	$0, (5 \pm \sqrt{5})/4, (3 \pm \sqrt{5})/4$

4.1.1.12.4 Thermally invariant resonators

The lens effect on the laser beam during operation can be avoided, in principle, if the temperature gradient is parallel to the beam propagation. Solutions of this kind are "disk amplifiers" or "active mirrors" [87Kel] (Fig. 4.1.25).

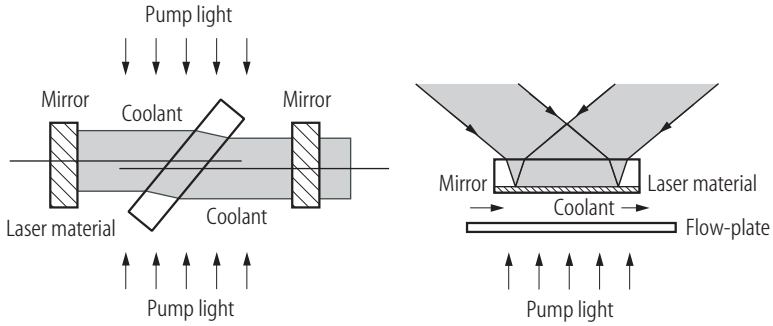

Fig. 4.1.25. Thermally invariant constructions.

A disadvantage of these solutions is that the laser beam has to traverse the cooling medium. This leads to disturbances and absorption by water or gas. Combining several active mirrors leads to the "multislab laser" [87Hug], i.e. a "slab" [72Mar] with multiple internal reflections (Fig. 4.1.26).

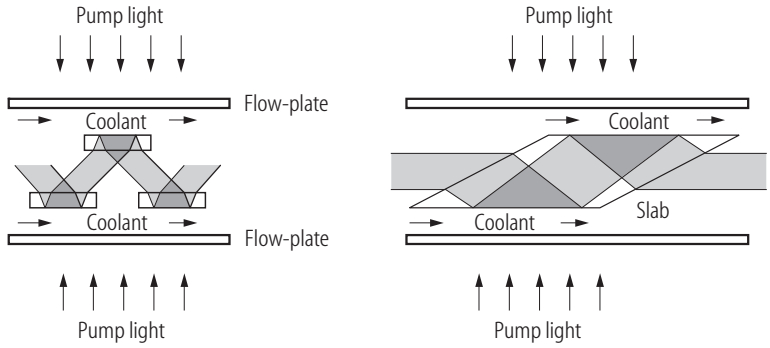

Fig. 4.1.26. Disk resonator and slab.

The slab is thermally isolated in the y-direction, and therefore the temperature remains constant in the y-direction. The external cooling is in the x-direction, creating a temperature gradient. Due to the zigzag path in the z-direction these influences average out to a first order and the laser beam is not disturbed by thermal effects, except for those that are caused by the temperature distribution at the slab tips.

Transparent cooling media with good heat conductivity are suggested in [87Hof1], where sapphire plates are alternated with the active laser material (Fig. 4.1.27). The heat flow occurs mainly in the beam direction.

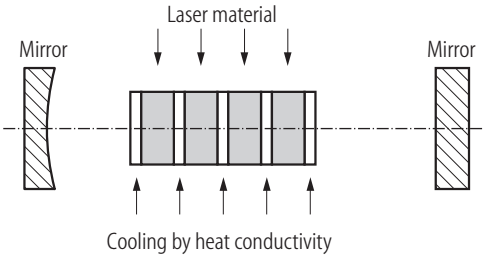

Fig. 4.1.27. Contact-cooled laser.

4.1.1.13 Excitation by diodes

Semiconductor or diode lasers are exceptional in their high electrical/optical efficiency. Therefore, they are of increasing importance for pumping solid-state lasers. The wavelength of the diodes can be tuned to an absorption band of the laser crystals slightly above the upper level. The efficiency of the pump process is higher and simultaneously the thermal load is less than in the case of excitation by lamps. If the diodes can be produced at lower costs, the solid-state laser will increasingly be used in new fields, even in those which are dominated at present by CO_2 lasers and replace the most common lamp-pumped solid-state laser in the near future.

Depending on the geometry of the laser medium, the direction of the excitation and the coupling of the diode radiation to the crystal, several concepts can be distinguished. In Table 4.1.3 these concepts with their distinctive characteristics are listed. In the following they are discussed each in turn.

Table 4.1.3. Concepts for diode-pumped solid-state lasers.

Geometry of the laser medium	**Rod**	**Disk**	**Fiber**	**Slab**
Direction of the pump radiation relative to the laser radiation	perpendicular longitudinal	parallel	perpendicular	perpendicular
Optics for pump radiation	reflector	fibers	glass plate	reflector
Pump radiation	divergent	2 axes collimated	1 axis collimated	divergent
Temperature gradient relative to the laser radiation	perpendicular	parallel	perpendicular	perpendicular
Cooling of the laser medium	liquid	contact cooling	air	contact cooling

4.1.1.13.1 Rod

4.1.1.13.1.1 Longitudinally pumped rod

A longitudinally pumped laser rod is excited at the endfaces by optically or fiber-coupled diodes. An example is given in Fig. 4.1.28. By matching of the pump light distribution to the desired mode volume and due to the almost complete absorption of the pump light a high efficiency with a good beam quality can be reached. Until now the achieved power, however, lies only in the 10 W range.

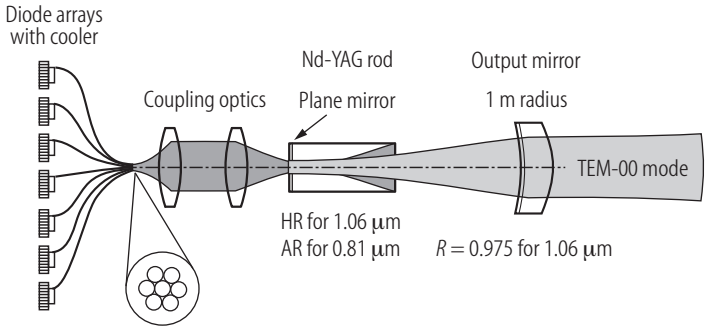

Fig. 4.1.28. Longitudinal diode-pumped rod laser [88Ber].

4.1.1.13.1.2 Transversally pumped rod

By transversal pumping, the pumped volume is extended and thus the attainable total power can be increased considerably. Figures 4.1.29 to 4.1.31 provide some examples for the direct pumping and for the transfer of the diode light with fibers.

It is plausible to arrange the pump modules, the laser-diode arrays, including the cooler without further optics directly around a laser rod. In this case, the flow tube with the laser rod acts as a cylinder lens.

A particularly simple construction is shown in Fig. 4.1.30. A stack of laser arrays is arranged at one rod side. By a suitable shape of the reflector on the opposite side the desired homogeneous pump light distribution can be achieved in the laser rod.

If the pump light is transmitted to the laser material with fibers, the mechanical construction can be separated completely from the laser head and the pump diodes. With a radial odd number

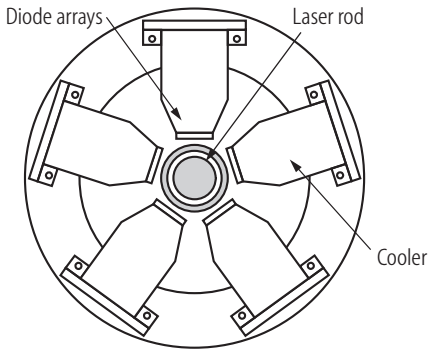

Fig. 4.1.29. Transversal diode-pumped rod laser without optics [93Bur].

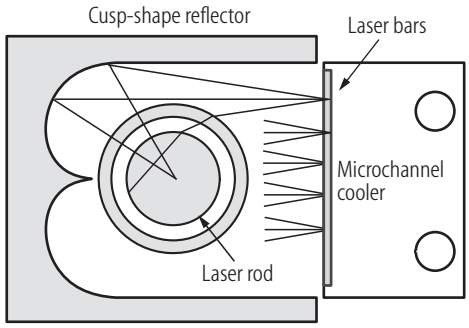

Fig. 4.1.30. Diode-pumped rod laser with cusp-shaped reflector [94Bra1, 94Bra2].

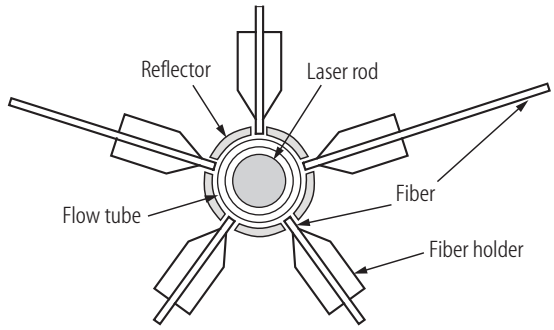

Fig. 4.1.31. Diode-pumped laser rod, pumping light supplied through fibers [96Gol].

of pump diodes and a reflector opposite to the fibers the absorption length in the laser rod is doubled. In [93Gol] the experience with three- and five-fold geometry is reported.

The cooling of transversally pumped rods is carried out perpendicular with respect to the laser radiation and therefore the thermal lens influences the laser beam. With other concepts the thermal lens can be avoided also at high powers, or at least significantly reduced.

4.1.1.13.2 Disk

4.1.1.13.2.1 Longitudinal disk

Due to the geometry of a disk the cooling and the lasing take place via the faces. This by itself ensures a good beam quality. For longitudinal excitation the laser material should have a high absorption to reach a good efficiency. Ytterbium can be doped in YAG with considerably higher concentrations than neodymium, however, due to its energy level diagram it must be cooled to low temperatures [00Tue]. The cooling can be carried out either in direct contact with a cooler or by a liquid. An example from [76Sar, 93Mor] is shown in Fig. 4.1.32.

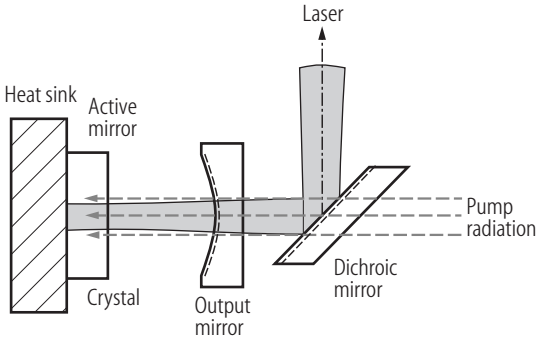

Fig. 4.1.32. Longitudinally pumped disk, according to [76Sar, 93Mor].

4.1.1.13.2.2 Transversally pumped disk

To increase the absorption of the disk, it can be pumped from the edge, using the full diameter for absorption. To reduce the influence of the thermal lens the cooling should therefore be carried out in the direction of the radiation. Setups of this kind have not yet been realized.

4.1.1.13.3 Fiber

4.1.1.13.3.1 Longitudinally pumped fiber

A thin, doped fiber core in a second undoped one with relatively large diameter shows a noticeable absorption. The focused diode pump radiation at the endface is absorbed by the doped core due to multiple total reflection in the second core over the whole fiber length. With a mirror at both endfaces a laser can be realized. In [95Zel] a design was reported in which a 12 μm Nd-doped core was pumped longitudinally in a 400 μm fiber. An output power of 10 W in the fundamental mode was obtained. The principle of this design is outlined in Fig. 4.1.33.

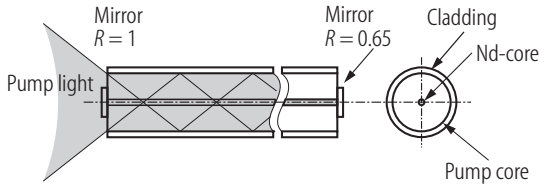

Fig. 4.1.33. Longitudinally pumped fiber laser [95Zel].

4.1.1.13.3.2 Transversally pumped fiber

Longitudinal pumping is limited by the endface diameter of the fiber. If one succeeds, by suitable preparation of the fiber cladding, to feed the pump radiation at periodic distances transversally into the doped core, the attainable laser power could be increased. Integrating a rectangular laser fiber in a disk shape and pumping the fiber transversally by a light guide a cw-power of 106 W and a peak power of 1 kW was achieved [01Sek]. Fig. 4.1.34 shows a schematic sketch of the disk shaped fiber laser.

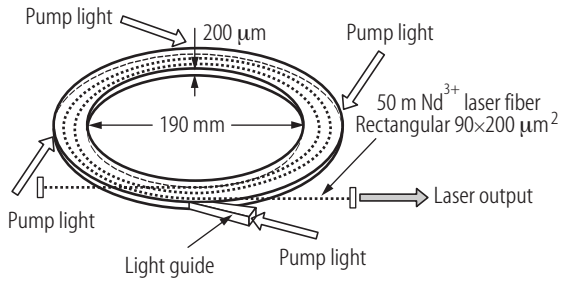

Fig. 4.1.34. Schematic sketch of the disk shaped fiber laser, after [01Sek].

4.1.1.13.4 Slab

In [87Hof2] and [91Coy] a slab design (Fig. 4.1.35) with internal total reflection is used to achieve a long path in the laser material. The slab offers a large cooling surface and also a large surface for the pump light. Due to the internal total reflection, however, the suppression of parasitic modes is difficult. A slight tilt of the polished side faces or drilling holes outside the resonator path of the laser beam has been proposed.

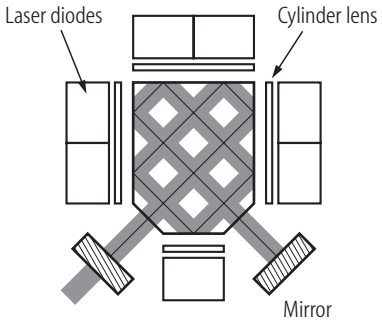

Fig. 4.1.35. Slab resonator [87Hof2, 91Coy].

4.1.1.13.4.1 Transversally pumped slab

With the slab concept a high pump power can be supplied to the side faces without complicated optics. A good beam quality can be achieved with the slab principle. However, no high cw power with good beam quality has been reached with this approach up to now.

Cooling is essential for the obtainable output power. Since the permissible temperature range is very narrow, the cooling must be designed to be as efficient as possible. With the diodes directly assembled on a microchannel cooler (Fig. 4.1.36), a diode-pumped solid-state laser can be scaled to the kilowatt range.

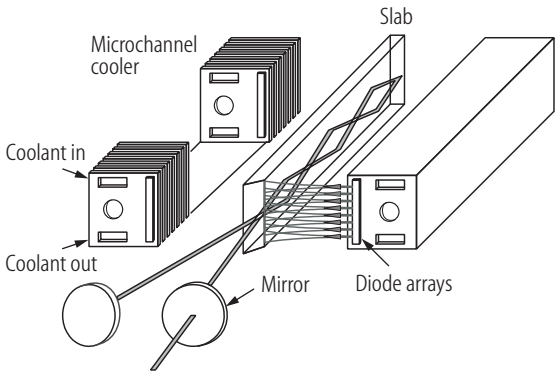

Fig. 4.1.36. Diode-pumped slab laser with microchannel cooling, according to [91Com, 92Com].

4.1.1.13.4.2 Longitudinal slab

A setup for a variant of a longitudinally pumped slab is shown in Fig. 4.1.37.

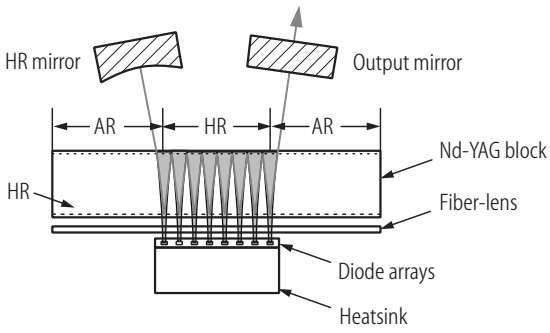

Fig. 4.1.37. Diode-pumped slab laser [90Bae].

4.1.1.13.5 Diode-pumped solid-state lasers in research and development

Some more details and parameters on the different concepts of diode-pumped lasers are given in Table 4.1.4.

Table 4.1.4. Diode-pumped solid-state lasers in research and development.

Concept	Crystal	Efficiency η [%]	Power P_{av} [W]	Mode $M^2 \approx$	Remark	Ref.
Rod						
long.	Nd:YAG	4.4[a]	0.6	1	00-mode	[88Ber]
transv.	Nd:YAG	17.8[a]	196		400 µs pulsed operation, 0.675 J	[93Bur]
transv.	Nd:YAG	26[b]	390		multimode, cusp reflector	[94Bra1, 94Bra2]
transv.	Nd:YAG	44[b]	320		multimode, fiber-pumped	[93Gol]
transv.	Nd:YAG	20[b]	80	1	00-mode, fiber-pumped	[93Gol]
transv.	Nd:YAG	22[a]	12000		six rods, 8 × 203 mm, 0.6 %Nd	[01Aki]
transv.	Nd:YAG	23	1050	8.2	compensated resonator	[01Fuj1, 01Fuj2]
transv.	Nd:YAG	25[b]	180	1.2	1 kHz, birefringence compensated, 2 rods	[02Ost]
Disk						
long.	Tm:Ho:YAG		0.5		Ti-sapphire pumped	
long.	Nd:YAG	50[b]	50	5	one disk, scalable	[00Tue]
long.	Yb:YAG	48[b]	500	5	one disk, scalable	[00Tue]
Fiber						
long.	Nd	25[b]	9.2	2		[95Zel]
long.	Nd	46[b]	30	1.3		[00Tue]
long.	Yb	38[b]	20	1.3	single frequency, MOPA, 1064 nm	[01Hoe]
long.	Yb	15[b]	5	3	Q-switch, 2.3 mJ, 1090 nm, 36 m long	[00Alv]
long.	Yb	58[b]	110	1.7	1120 nm	[99Dom]
long.	Yb	45[b]	135	1.05	1086 nm, 60 m fiber with 9 µm core	[02Pla]
transv.	Nd:quartz	20[a]	106		fiber in disk shape, 50 m long, 1 kW peak	[01Sek]
Slab						
transv.	Nd:YAG	23[b]	275		100 µs pulsed operation, 0.11 W s	[91Com, 92Com]
transv.	Nd:YAG	16[a]	2400	60	16.7 kW pulse peak at 0.5 ms	[01Sat]
transv.	Nd:YAG	23[b]	5400	2.4	5 slab modules, 400 Hz, 13.5 J per pulse	[02Mac]
long.	Nd:YAG	43[b]	500	6	unstable/stable resonator	[02Sch]
long.	Nd:YAG	30[b]	200	1.5	unstable/stable resonator	[02Hod]

[a] Optical to electrical conversion efficiency; [b] optical to optical conversion efficiency; long.: longitudinally pumped, transv.: transversally pumped.

4.1.1.14 Solid-state laser products

Depending on laser design, material and operation mode a broad range of operating parameters can be achieved. The average power in continuous-wave operation ranges from a few Watt to more than five kW, which determines the process speed. The peak power governing the application process in pulse (ms) and very short pulse (fs) mode starts with a few kW to up to 1 GW, which allows X-ray generation. Generation of shorter wavelengths allows to scale the beam quality even in diffraction-limited mode with the wavelength. Table 4.1.5 summarizes the typical parameter range of available products.

Table 4.1.5. Typical data of industrial solid-state lasers available on the market.

Excit.	Concept	Crystal	Oper. mode	Average power [W]	Peak power	Pulse length	Pulse energy [mJ]	Wave-length [nm]	Repet. rate [kHz]	Beam param. [mm mrad]
Welding, cutting										
		Nd:YAG	cw	100		ms–∞		532		30
Lamp	multi-rod	Nd:YAG	cw	500–5000	5 kW	50 ms-∞		1064		12–25
Diode	multi-rod	Nd:YAG	cw	500–5000	5 kW	10 ms-∞		1064		12–25
Diode	multi-disk	Yb:YAG	cw	500–10000	10 kW	10 ms-∞		1030		3
Spot welding, drilling										
Lamp	single-rod		pulsed		100 kW			1064		
Marking, scribing, micro-cutting										
Lamp	single-rod	Nd:YAG	Q-switch	10	100 kW	5–10 ns	700	1064	0.01	4
Lamp	single-rod	Nd:YAG	Q-switch	2			200	532	0.01	2
Lamp	single-rod	Nd:YAG	Q-switch	1			100	355	0.01	1
Diode			Q-switch	40	1 MW	6–100 ns	2–20	1064	10–100	
			Q-switch	25		15 ns		532	10	
			Q-switch	10		15 ns		355		
			Q-switch	2		6–20 ns		266	20–80	
Diode			locked	30		10 ps		1064		
			locked	5		1 ps		780		
			locked	4		10 ps		355		
Diode		Nd:YAG	locked	5	50 MW	10–20 ps	0.1–1	1064	5	0.76
	slab	Nd:YAG						1064		
	slab	Nd:YAG						532		
X-ray generation, micro machining										
Diode		Cr:LiSAF		0.5	1 GW	0.1 ps	0.1	840	2–5	

"Locked" means mode-locked.
To characterize the beam quality we use the beam parameter product instead of the mode order because the wavelength is already taken into account.

4.1.2 Laser material parameter

In the following, the specifications for the most important parameters are defined and listed for various laser materials. Only those materials are taken into account, for which laser activity has been proven for pulse or cw-operation at room temperature with an efficiency of about 1 % lamp or diode pumped and which are commercially available. Further details are provided in the subsequent Sects. 4.1.2.1–4.1.3.21.

4.1.2.1 Parameter specification

The most essential parameters used for characterizing laser materials are taken from the previous sections or defined anew in this section. These parameters are then listed in the following tables for the various laser materials.

4.1.2.1.1 Laser data

λ : lasing wavelength, in general the laser wavelength of the intensity maximum. The fluorescence wavelength is smaller.
$\Delta\lambda$: halfwidth of the laser transition.
λ_p : pumping wavelength.
λ_FZ : wavelength, below which color center generation has been observed or is possible.

σ : effective cross section of stimulated emission:

$$\sigma = \frac{\lambda^4}{4\pi^2 n^2 c \Delta\lambda} \,, \quad \Delta\lambda\text{: halfwidth of fluorescence .}$$

The effective cross section can be determined from absorption measurements $\alpha(\lambda)$ according

$$\sigma = \frac{\alpha(\lambda)}{N_0}\frac{Z_0}{Z_1}\mathrm{e}^{(E-h\nu)/k_\mathrm{B}T},$$

with

N_0 : concentration of the active ions,
Z_i : branching of the energy levels,
E : energy gap of the corresponding lowest branching.

The effective cross section is reduced by further excitation of the higher levels

$$\sigma = \sigma_\mathrm{e} - \sigma_\mathrm{ESA} \,,$$

σ_e = effective cross-section for spontaneous emission,
σ_ESA = effective cross-section for excited state absorption,

$$\sigma_\mathrm{e}(\lambda) = \sigma_\mathrm{a}(\lambda)\, \mathrm{e}^{(E-h\nu)/k_\mathrm{B}T} \,, \quad [91\mathrm{Min}] \,.$$

τ_0 : lifetime of the upper laser level, extrapolated to low concentrations of the active ion.
τ : lifetime of the upper level, at standard concentration. The natural decay of the upper laser level population is approximately exponential with time. In the literature, this decay is given as

$$N_2(t) = N_2(0)\, \mathrm{e}^{-t/\tau - f(t)} \,, \quad [89\mathrm{Rot}] \,.$$

For exponential depletion $\tau/\tau_0 = \eta_Q$ yields the quantum efficiency. The doping dependence becomes

$$\tau = \frac{\tau_0}{1 + (C/C_{0.5})^2} ,$$

with

C : concentration of the active ions,
τ_0 : extrapolated lifetime for $C = 0$,
$C_{0.5}$: concentration at which the lifetime is half τ_0 .

4.1.2.1.2 Optical properties

n_{rel} : refractive index (relative) at the indicated laser wavelength relative to air:

$$n_{rel}^2 = A + \frac{B\lambda^2}{\lambda^2 - C} + \frac{D\lambda^2}{\lambda^2 - E} .$$

The special notation for selected refractive indices are given in Table 4.1.6. A to E are the Sellmeier coefficients, tabulated for the most common materials in Table 4.1.7.

Table 4.1.6. Labeling of the refractive indices for various wavelengths.

λ [nm]	1014	852	706	656	644	589	588	546	481	480	436	405	365
Notation	n_t	n_s	n_r	n_C	$n_{C'}$	n_D	n_d	n_e	n_F	$n_{F'}$	n_g	n_h	n_i
Line				A	Cd		He			Cd			
Color				red	red	yellow	yellow	green		blue			

Table 4.1.7. Sellmeier coefficients for various crystals [90Fil].

Crystal	A	B	C	D	E
YAG	1	2.2779	0.01142	0	0
LaLuGG	1	2.3891	0.03781	0	0
GdScAG	1	2.510	0.0153781	0	0
YScAG	1	2.4118–2.420	0.01477–0.01520	0	0
GdGG	2.39841	1.35724	0.03027	2.37981	165.753
GdScGG	2.11233	1.63589	0.02620	0.99161	62.87
YGG	1	2.5297	0.019694	0	0
LuGG	1	2.2573	0.022833	0	0
LuAG	1	2.4822	0.009066	0	0
GdAG	1	2.0055	0.014559	0	0

dn/dT : temperature coefficient of the refractive index.

The light wave inside a material is influenced by the absolute refractive index change dn/dT in the material. However, the values of the refractive index change dn_{rel}/dT provided in the literature have been measured relative to air. With the definition of the refractive index the absolute change dn_{abs}/dT can be calculated:

$$n_{rel} = \frac{n_{abs}}{n_{air}} . \qquad (4.1.185)$$

Differentiating and setting $n_{\mathrm{air}} = 1$ gives

$$\frac{\mathrm{d}n_{\mathrm{abs}}}{\mathrm{d}T} = \frac{\mathrm{d}n_{\mathrm{rel}}}{\mathrm{d}T} + n_{\mathrm{rel}} \frac{\mathrm{d}n_{\mathrm{air}}}{\mathrm{d}T} \,. \tag{4.1.186}$$

For $\lambda = 1060$ nm Fig. 4.1.38 gives the temperature coefficient $\mathrm{d}n_{\mathrm{air}}/\mathrm{d}T$, [88Hof].

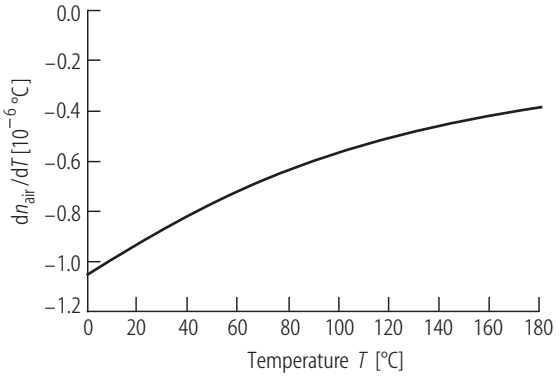

Fig. 4.1.38. Temperature coefficient of $\mathrm{d}n_{\mathrm{air}}/\mathrm{d}T$, according to [88Hof].

n_2 = nonlinear refractive index.

The nonlinear refractive index n_2 is given either as a function of the field strength E

$$n(E) = n_0 + n_2 \langle E^2 \rangle = n_0 + n_2 \frac{E^2}{2} \tag{4.1.187}$$

with

$$[n_2] = \mathrm{esu}\,,$$

$$E\,[\mathrm{esu}] = 3 \times 10^4 E \left[\frac{\mathrm{V}}{\mathrm{m}}\right] \,,$$

esu: electrostatic units,

or as a function of the intensity J

$$n(J) = n_0 + \gamma_2 J \,,$$

$$\gamma_2 \left[\frac{\mathrm{m}^2}{\mathrm{W}}\right] = 0.9 \times 10^9 \; n_2\,[\mathrm{esu}] \,,$$

with n_2 and γ_2 being the nonlinear refractive indices.

With the help of the Abbe number ν_{d} and the refractive index n_{d} for the Fraunhofer line the nonlinear refractive index can be calculated approximately, according to [78Bol], as

$$\frac{n_2}{[10^{-13}\ \mathrm{esu}]} = \frac{n_{\mathrm{d}} - 1}{\nu_{\mathrm{d}}^{5/4}} \,. \tag{4.1.188}$$

Table 4.1.8 provides in addition to the nonlinear refractive index the corresponding self-focusing length z_{F} and the critical damaging power P_{c} for some laser materials.

Table 4.1.8. Wavelength λ, nonlinear refractive index n_2, γ_2, critical power P_c and self-focusing length z_F.

Medium	λ [nm]	n	n_2 [10^{-13} esu]	γ_2 [10^{-20} m^2/W]	P_c [MW]	z_F [cm]	Ref.
Air (1 atm)	1064	1	0.2	0.84	10.75	7	
Water	1064	1.33	7	22.06	0.31	10	
BK-7	1064	1.517	1.24	3.43	1.73	11	
Quartz	1064	1.456	0.95	2.73	2.26	11	
Si-glass	1064	1.769	4.4	10.43	0.49	13	
LaSF-7	1064	1.914	6.2	13.58	0.35	14	
Alexandrite	750	1.55	0.83	2.24	1.29	16	[88Pen]
BEL	1070	1.99	2.1	4.42	1.04	15	[88Pen]
GGG	1064	1.943	4	8.63	0.54	14	
GSGG	1064	1.925	8	17.42	0.27	14	
Ruby	694.3	1.755	1.1	2.63	0.83	20	[88Pen]
YAG	1064	1.823	3.525	8.10	0.61	14	[88Pen]
YLF	1053	1.448	0.595	1.72	3.54	11	[77Mil]
APG-1	1061	1.526	1.12	3.08	0.91	11	
LG-650	1061	1.511	1.415	3.93	1.51	11	
LG-670	1061	1.567	1.41	3.77	1.52	12	
LG-680	1061	1.56	1.6	4.30	1.34	12	[88Pen]
LG-750	1053.5	1.516	1.08	2.99	1.95	11	
LG-760	1053	1.508	1.02	2.84	2.06	11	[88Pen]
LG-810	1051	1.5	0.515	1.44	4.07	11	[88Pen]
LG-812	1054	1.426	0.49	1.44	4.30	11	
LHG-5	1054	1.541	1.16	3.16	1.82	12	[81Bro]
LHG-6	1054	1.532	1.01	2.76	2.09	11	[81Bro]
Q-88	1054	1.536	1.14	3.11	1.85	12	[81Bro]

z_F was calculated for a diameter of 1 mm and a power $P = 100 \times P_c$ using a Gaussian distribution.

The conversion from electrostatic units [esu] to SI-units can be carried out [77Mil] with

$$\frac{\gamma_2}{[\mathrm{m^2/W}]} = \frac{40\,\pi}{c n_0}\,\frac{n_2}{[\mathrm{esu}]} = 4.19 \times 10^{-7}\,\frac{1}{n_0}\,\frac{n_2}{[\mathrm{esu}]}\ , \tag{4.1.189}$$

$$\frac{n_2}{[\mathrm{esu}]} = \frac{c n_0}{40\,\pi}\,\gamma_2 = 2.386 \times 10^6\ n_0\,\frac{\gamma_2}{[\mathrm{m^2/W}]}\ .$$

p_{ij} photoelastic constants.

These are in most cases not available at the laser wavelength. In isotropic media such as glass one has

$$p_{44} = (p_{11} - p_{12})/2\ . \tag{4.1.190}$$

4.1.2.1.3 Thermal parameters

c_p : specific heat (at constant pressure).

k : heat conductivity.

The heat conductivity is temperature dependent.

α : thermal expansion coefficient for the temperature range of 20 °C to 100 °C.

4.1.2.1.4 Mechanical properties

ρ : specific weight.
ν : Poisson number.
E : modulus of elasticity (Young's modulus).

$\sigma_{\max}$: fracture tension,
which may not be exceeded during laser operation. No safety margin is taken into account. This value depends strongly on the surface finish and decreases with increasing surface area. It can only be taken as a reference value.

σ_{f} : fracture tension due to microcracks in the material.

K_{c} : fracture toughness is correlated with the fracture tension via

$$\sigma_{\mathrm{f}} = \frac{Y K_{\mathrm{c}}}{\sqrt{\pi a}} \tag{4.1.191}$$

with

Y : geometry factor,
a : flaw depth [87Mar, 89Mar].

H_{K} : Knoop hardness as an indicator for polishing the material.

4.1.2.1.5 Crystal properties

T_{m} : melting temperature
for crystals, or for glasses the transformation temperature. This temperature may not be exceeded during normal handling and processing, e.g. when coated with dielectric layers.

C [at%] : concentration in atom per cent
is the part of the respective element relative to the total molecular weight. Manufacturers of crystals normally specify only the percentage share of the doping ions, which replace a crystal ion in the host. The at% details used in the following refer to this manufacturer definition.

C [wt%] : concentration in weight percentage
is the part of the atomic weight of the respective element relative to the molecular weight of the complete chemical formula.

F_{A}, F_{W}, F_{AW} : conversion factors for the calculation of the absolute ion number
N_0 [10^{20} ions/cm^3] $= F_{\mathrm{W}} \times C$ [wt%] , wt% = weight percentage ,
N_0 [10^{20} ions/cm^3] $= F_{\mathrm{A}} \times C$ [at%] , at% = atom percentage , at% $= F_{\mathrm{AW}} \times$ wt% .

The number of the ions per volumes can be calculated for a given weight percentage C [wt%] as

$$N_0 \left[\frac{1}{\mathrm{cm}^3}\right] = \frac{N_{\mathrm{A}} \rho}{M} \, \frac{C\,[\mathrm{wt\%}]}{100} \, ,$$

with

$N_{\mathrm{A}} = 6.022 \times 10^{23}$ mol^{-1},
M : atomic weight of the doping ion,
C : concentration in weight%,
ρ : specific weight.

For the specifications of the weight percentage one has to consider whether the part of the pure active ion or the part of the oxide is meant relative to the crystal material. In the case of Nd:YAG whether the pure neodymium or the neodymium oxide Nd_2O_3 is meant with respect to $Y_3Al_5O_{12}$.

Example 4.1.4. Atom per cent of concentration of Nd in YAG.

The atom% concentration $C(\mathrm{Y})$ of yttrium in YAG is given as

$$C(\mathrm{Y}) = \frac{3_\mathrm{Y}}{3_\mathrm{Y} + 5_\mathrm{Al} + 12_\mathrm{O}} = \frac{3}{20} \times 100\ \% = 15\ \mathrm{at}\% \ .$$

If one per cent of the Y^{3+} ions is replaced by Nd^{3+} ions (manufacturer's specification at% = 1 %!), then the chemical formula of $Y_3Al_5O_{12}$ changes into $Nd_{0.03}Y_{2.97}Al_5O_{12}$. The absolute atom per cent concentration of Nd in YAG becomes therefore

$$C(\mathrm{Nd}) = \frac{0.03_\mathrm{Nd}}{0.03_\mathrm{Nd} + 2.97_\mathrm{Y} + 5_\mathrm{Al} + 12_\mathrm{O}} = \frac{0.03}{20} \times 100\ \% = 0.15\ \mathrm{at}\% \ .$$

Example 4.1.5. Ruby with 1 at% chromium.

Here, the aluminum ion Al^{3+} is replaced by the chromium ion Cr^{3+}, chemical formula: $Cr_{0.02}Al_{1.08}O_3$, atomic weights: Al = 26.981, O = 16, Cr = 52, specific weight (ruby): ρ = 3.98 g/cm^3:

$$\frac{C}{\mathrm{at}\%} = \frac{(0.02 \times 52_\mathrm{Cr})}{(0.02 \times 52_\mathrm{Cr}) + (1.08 \times 26.981_\mathrm{Al}) + (3 \times 16_\mathrm{O})}\ 100\ \% = 1.33\ \ [\mathrm{wt}\%] \ ,$$

$$\frac{N_0}{\mathrm{at}\%} = \frac{(6.022 \times 10^{23} \times 3.98)}{52}\ \frac{1.33}{100}\ \frac{1}{\mathrm{cm}^3} = 6.13 \times 10^{20}\mathrm{cm}^{-3} \quad \text{or}$$

$$\frac{N_0}{\mathrm{wt}\%} = 4.61 \times 10^{20}\mathrm{cm}^{-3} \ .$$

Example 4.1.6. Nd:YAG with 1 at% Nd (manufacturer specification).

1 % of the Y^{3+} ions are replaced by Nd^{3+} ions. The chemical formula $Y_3Al_5O_{12}$ of the pure garnet is changed into $Nd_{0.03}Y_{2.97}Al_5O_{12}$. With the atomic weights Y = 88.905, Al = 26.981, O = 16 and Nd = 144.24 the weight concentration follows as

$$C_\mathrm{Nd} = \frac{(0.03 \times 144.24_\mathrm{Nd})}{(0.03 \times 144.24_\mathrm{Nd}) + (2.97 \times 88.9_\mathrm{Y}) + (5 \times 26.98_\mathrm{Al}) + (12 \times 16_\mathrm{O})}\ 100\ \% = 0.729\ \ [\mathrm{wt}\%] \ .$$

This means: 1 at% $\equiv$ 0.729 wt% or 1 wt% $\equiv$ 1.37 at%. With the specific weight $\rho = 4.56$ g/cm^3 of YAG follows for the absolute ion density

$$\frac{N_0}{\mathrm{wt}\%} = 1.89 \times 10^{20}\ \mathrm{cm}^{-3} \ .$$

Table 4.1.9 provides the number of the ions per cubic cm for one atom percentage (F_A) and Table 4.1.10 for one weight percentage (F_W).

Table 4.1.9. Conversion factor F_A of an atom percentage into the absolute ion number.

10^{20} cm^{-3}/%	Cr	Ho	Nd	Tm	Yb
Atom weight	52	165	122.2	169	173
Alexandrite	3.51			3.69	
Ruby	1.14				
BEL			1.94	6.061	
GGG	0.84	2.59	1.26	2.53	
GSAG	0.84	2.13	1.26	2.08	
GSGG	0.81	2.35	1.22	2.30	
Al_2O_3	4.07				
YAG	0.92	1.67	1.38	1.63	1.38
YAP	1.97		1.95		
YLF			1.39		
YSAG	0.86	1.67	1.30	1.63	
YSGG	0.83	1.91	1.25	1.86	
YVO_4			1.54		

Partially the values are dependent on the stoichiometry, for details see [88Lit2, 92Lit1, 92Lit2].
Atom per cent, according to manufacturer specifications.

Table 4.1.10. Conversion factor F_W of a weight percentage into the absolute ion number.

10^{20} cm^{-3}/%	Cr	Er	Ho	Nd	Ti	Tm	Yb
Ruby	3.24						
GGG	8.20		1.26	2.95	1.26	7.08	
GSAG	6.74		1.26	2.43	1.26	5.82	
GSGG	7.47		1.21	2.69	1.21	6.59	
YAG	5.28		1.39	1.90	1.39		1.59
YSAG	5.27		1.31	1.90	1.31		
YSGG		1.24		1.24			

For atom per cent specifications relative to the complete chemical formula the conversion is

$$N_0 = Z_{EZ} \times Z_{FE} \times Z_{EF} \frac{\text{at\%}}{100} = \frac{Z_{EZ} \times Z_{FE}}{V_{EZ}} \frac{\text{at\%}}{100} \tag{4.1.192}$$

with

Z_{EZ} : number of the formula units per elementary cell EZ,
Z_{FE} : number of the atoms per formula unit FE,
Z_{EF} : number of the elementary cells per cm^3,
V_{EZ} : volume of the elementary cell EZ.

Also, one has to consider whether the specifications refer to the pure ion (Nd) in relation to all other atoms including (O_2) or to the ion (Nd) in relation to the substitution ion (3Y). Table 4.1.11 gives the necessary data for the conversion.

Table 4.1.11. Crystal data for the calculation of the absolute ion numbers.

Crystal	ρ [g/cm^3]	Z_{EZ}	$V_{EZ} = a \times b \times c$ [Å × Å × Å]
Alexandrite	3.69	4	9.40 × 5.48 × 4.42
BEL	6.061	4	7.53 × 7.35 × 7.44
YAP	5.35	4	5.33 × 7.37 × 5.18
YLF	4.03	4	5.17 × 10.74
Al_2O_3	3.98	6	4.76 × 13.00
GGG	7.08	8	12.383
GSAG	5.82	8	12.393
GSGG	6.59	8	12.5453
YAG	4.55	8	12.013
YSAG		8	12.283
YSGG	5.383	8	12.433

K : distribution coefficient,

indicates the ratio of the doping concentration in the already grown crystal to the concentration in the melt. At $K = 1$ the concentration in the melt and crystal are the same. At $K < 1$ the concentration increases in the crystal with increasing grown crystal length. A distribution coefficient $K \neq 1$ results in an axial doping gradient along the pulling axis.

The concentration C of the crystal follows from the melt concentration

$$C = C_m K (1 - g)^{K-1} \ , \tag{4.1.193}$$

with g: mass ratio of the material crystallized relative to the initial melt.

4.1.2.1.6 Derived data

The results for the derived data have been calculated according to the following equations.

$h\nu = \dfrac{hc}{\lambda}$, laser photon energy , $h = 6.626 \times 10^{-34}$ J s , $c = 2.998 \times 10^8$ m/s ,

$J_s = \dfrac{h\nu}{\sigma\tau}$, saturation intensity for a 4-level system ,

$J_s = \dfrac{h\nu}{2\sigma\tau}$, saturation intensity for a 3-level system ,

$H_s = \dfrac{h\nu}{\sigma}$, saturation energy density for a 4-level system ,

$H_s = \dfrac{h\nu}{2\sigma}$, saturation energy density for a 3-level system ,

$\phi_B = \arctan(n)$, Brewster angle ,

$R_T = \dfrac{\sigma_{max}\, \kappa(1-\nu)}{\alpha E}$, thermal shock parameter .

It is an indication of the stress a laser material can take and is close to the value a rod per unit length can be loaded with pumping light.

$\dfrac{\tau}{r_0^2} = \dfrac{c_p \rho}{k}$, the reciprocal thermal diffusivity

taken as the time for thermalization within an area of 1 mm^2.

The photoelastic coefficients $C_{r,\phi}$ are required for calculation of the refracting power parameters $M_{r,\phi}$:

$$C_r = \frac{(17\nu - 7)p_{11} + (31\nu - 17)p_{12} + 8(\nu + 1)p_{44}}{48(\nu - 1)} ,$$

$$C_\phi = \frac{(10\,\nu - 6)p_{11} + 2(11\nu - 57)p_{12}}{32(\nu - 1)} \quad \text{(only for garnets such as YAG or GSGG)} .$$

p_{ij} = elastooptical coefficients from the literature.

The absolute dependence of the refractive index on the temperature

$$\frac{\mathrm{d}n}{\mathrm{d}T} = \frac{\mathrm{d}n_{\mathrm{rel}}}{\mathrm{d}T} + n_{\mathrm{rel}}\frac{\mathrm{d}n_{\mathrm{air}}}{\mathrm{d}T} .$$

Material parameters for the thermal lens

$$M_{r,\phi} = \frac{1}{2k}\left(\frac{\mathrm{d}n}{\mathrm{d}T} + 2n^3\alpha\, C_{r,\phi} + \alpha(n-1)\frac{l_x}{l}\right) .$$

In the tables $\mathrm{d}n_{\mathrm{air}}/\mathrm{d}T = -0.9$ is used for $T = 25\,^\circ\mathrm{C}$ and $l_x/l \approx 1/30$ is assumed.

4.1.2.1.7 Supplier data

With these data the capabilities of the suppliers are listed, as far as they are known:
$l_{\max}$: maximal deliverable length,
$d_{\max}$: maximum diameter or thickness,
C: offered doping concentration of the laser ion or the codoping.

4.1.2.1.8 Measured values

Measured values provide the best comparison of the various materials. We have attempted to find particularly favorable values for the respective material:
η_{slope}: slope efficiency, electrical to optical, lamp-pumped,
η_{excite}: excitation efficiency,
η_{extr}: extraction efficiency,
η_{H}: heat efficiency,
$-\ln V$: resonator losses per unit length and round trip,
$\kappa = \eta_{\mathrm{H}}/\eta_{\mathrm{excite}}$: heat coefficient,
$E_{\max}$: maximum output energy per pulse,
T: corresponding pulse length,
P_{av}: maximum average power in the pulsed operation,
P_{cw}: maximum cw power,
$d \times l \times h$: dimensions of the laser material used (diameter times thickness or length times height).

4.1.2.2 Active ions

The wavelength of the laser transition is determined by the active ion embedded in the solid. The imbedded ion can broaden the laser line, shift the line – such as in glasses – or can change the lifetime of the transition. Major properties, however, such as absorption and laser transitions, are determined by the active ion only and modified by the host crystal.

4.1.2.2.1 Overview

Table 4.1.12 gives an overview of the active elements in various solid materials and the corresponding laser wavelengths. The selection is restricted to materials that are commercially available at present. The transitions for the various ions are arranged according to the wavelength in Table 4.1.13.

Table 4.1.12. Typical laser parameters of various ions in solids.

Ion	λ [nm]	σ [10^{-20} cm^2]	τ_0 [µs]	ΔE [cm^{-1}]	Transition
Cr	700	0.7	200	100	$^4T_2 \rightarrow {}^4A_2$
Er^{3+}	2800				$^4I_{11/2} \rightarrow {}^4I_{13/2}$
	1640	0.4	64000	400	$^4I_{13/2} \rightarrow {}^4I_{15/2}$
	850	1.4	25		$^4S_{3/2} \rightarrow {}^4S_{13/2}$
Ho^{3+}	2000	1	10000	300	$^5I_7 \rightarrow {}^5I_8$
	750	97	65		$^5S_2 \rightarrow {}^5I_7$
Nd^{3+}	1320				$^4F_{3/2} \rightarrow {}^4I_{13/2}$
	1064	50	240	2000	$^4F_{3/2} \rightarrow {}^4I_{11/2}$
	950				$^4F_{3/2} \rightarrow {}^4I_{9/2}$
Pr	640	0.17	56	522	$^3P_0 \rightarrow {}^3F_2$
Tm^{3+}	1600	1.3	830		$^3H_4 \rightarrow {}^3H_6$
	780	0.5	6	586	$^3F_4 \rightarrow {}^3H_6$
Yb^{3+}	1030	2	1100	612	$^2F_{5/2} \rightarrow {}^2F_{7/2}$

ΔE: energy difference between the lower laser energy level to the ground state.

Further bibliographical references can be found in the following tables.

Table 4.1.13. Laser wavelengths of various ions in solids [76Kam, 91Kam].

Wavelength λ [μm]	Laser ion	Transition
0.544	Tb^{3+}	$^5D_4 \rightarrow {}^7F_5$
0.598–0.622	Pr^{3+}	$^3P_0 \rightarrow {}^3H_6$
0.66–1.08	Ti^{3+}	$^2E \rightarrow {}^2T_2$
0.637–0.65	Pr^{3+}	$^3P_0 \rightarrow {}^3F_2$
0.68–0.704	Cr^{3+}	$^2E \rightarrow {}^4A_2$
0.694–0.7221	Pr^{3+}	$^3P_0 \rightarrow {}^3F_3$
0.679–0.745	Sm^{2+}	$^5d, {}^5D_0 \rightarrow {}^7F_1$
0.717–0.7496	Pr^{3+}	$^3P_0 \rightarrow {}^3F_4$
0.74–0.89	Cr^{3+}	$^3E, {}^4T_2 \rightarrow {}^4A_2$
0.75–0.761	Ho^{3+}	$^5S_2 \rightarrow {}^5I_7$
0.843–0.863	Er^{3+}	$^4S_{3/2} \rightarrow {}^4I_{13/2}$
0.891–0.947	Nd^{3+}	$^4F_{3/2} \rightarrow {}^4I_{9/2}$
0.9017–0.931	Pr^{3+}	$^3P_0 \rightarrow {}^1G_4$
0.979–1.018	Ho^{3+}	$^5F_5 \rightarrow {}^5I_7$
0.996	Pr^{3+}	$^1D_2 \rightarrow {}^3F_3$
1.014–1.031	Ho^{3+}	$^5S_2 \rightarrow {}^5I_6$
1.023–1.038	Yb^{3+}	$^5F_{5/2} \rightarrow {}^2F_{7/2}$
1.037–1.123	Nd^{3+}	$^4F_{3/2} \rightarrow {}^4I_{11/2}$
1.0465–1.0664	Pr^{3+}	$^1D_2 \rightarrow {}^3F_4$
1.229–1.34	Er^{3+}	$^4S_{3/2} \rightarrow {}^4I_{11/2}$
1.306–1.415	Nd^{3+}	$^4F_{3/2} \rightarrow {}^4I_{13/2}$
1.391–1.408	Ho^{3+}	$^5S_2 \rightarrow {}^5I_5$
1.462–1.482	Tm^{3+}	$^3F_4 \rightarrow {}^3H_4$
1.58	Tm^{3+}	$^1G_4 \rightarrow {}^3F_3$
1.645–1.777	Er^{3+}	$^4S_{3/2} \rightarrow {}^3I_{9/2}$
1.965–2.0025	Er^{3+}	$^4F_{9/2} \rightarrow {}^4I_{11/2}$
1.933–2.171	Ho^{3+}	$^5I_7 \rightarrow {}^5I_8$
2.274–2.424	Tm^{3+}	$^3F_4 \rightarrow {}^3H_5$
2.689–3.01	Er^{3+}	$^4I_{11/2} \rightarrow {}^4I_{13/2}$
2.845–3.018	Ho^{3+}	$^5I_6 \rightarrow {}^5I_7$
2.972–3.022	Dy^{3+}	$^6H_{13/2} \rightarrow {}^6H_{15/2}$
3.369	Ho^{3+}	$^5S_2 \rightarrow {}^5F_5$

Laser transitions demonstrated at room temperature and flash lamp excitation.

4.1.2.2.2 Most important ions

For the most important ions the corresponding energy level diagram for absorption or emission and further information, as well as examples, are given in the following.

4.1.2.2.2.1 Chromium

Due to the energy band structure in the energy level diagram the Cr-doped vibronic lasers are tunable between 750 and 900 nm with a tuning range of around 100 nm, depending on the specific crystal.

In Table 4.1.14 laser parameters of Cr in various solids are listed. In Fig. 4.1.39 the energy levels of chromium in ruby and alexandrite are shown. Figure 4.1.40 shows the absorption spectrum of chromium in ruby. In Fig. 4.1.41 the tuneability and temperature dependence of chromium in alexandrite are depicted.

Table 4.1.14. Laser parameters of Cr in various solids.

(**a**) Laser data.

Host	λ [nm]	$\Delta\lambda$ [nm]	σ [10^{-20} cm^2]	τ [μs]	τ_0 [μs]	ΔE [cm^{-1}]	Transition	Ref.
Ruby	649	0.5		3000		1500	$^2E \rightarrow {}^4A_2$	[86Uni]
Alex.	750		0.7[c]	260[c]			$^4T_2 \rightarrow {}^4A_2$	[86Lai, 87Lai]
Emerald	780		3.1	60				[86Lai, 87Lai]
GGG	745		0.6	380	159			[84Pet]
GSGG	770		0.8	50	115			[84Pet]
GSAG	784							[86Mei]
Mg_2SiO_2	1200[b]		0.2					[91Pet]

(**b**) Pump data.

Host	λ_p [nm]	σ_p [10^{-20} cm^2]	σ_{ESA} [10^{-20} cm^2]	η_H	Transition	Ref.
Alex.	410	13.6	2–7			[85All]
Ruby	404	22			$^4A_2 \rightarrow {}^4F_2$	[86Uni]
Ruby	554	22			$^4A_2 \rightarrow {}^4F_1$	[86Uni]
Emerald	650	8.26			$^4A_2 \rightarrow {}^4T_2$	[86Lai, 87Lai]
Emerald	600	5.6			$^4A_2 \rightarrow {}^4T_1$	[86Lai, 87Lai]
GSGG	650	3.6 ± 0.6		0.25[a]	$^4T_2 \rightarrow {}^4A_2$	[87See]

(**c**) Measurements.

Host	P_{av} [W]	T [ms]	E [W s]	η_{slope} [%]	$-\ln V/l$ [%/cm]	$d \times l$ [mm^2]	Ref.
Alex.	105	0.16	7	3.9	0.3	6.35×100	[86Ima]
Alex.			2.5	1.7	0.64	8.16×139	[85Rap]
GSAG			0.11	0.12	0.54	6.35×76	[86Mei]

[a] Without ESA, [b] pumped with 1064 nm, [c] temperature-dependent, at 290 °C: $\sigma = 3 \times 10^{-20}$ cm^2.

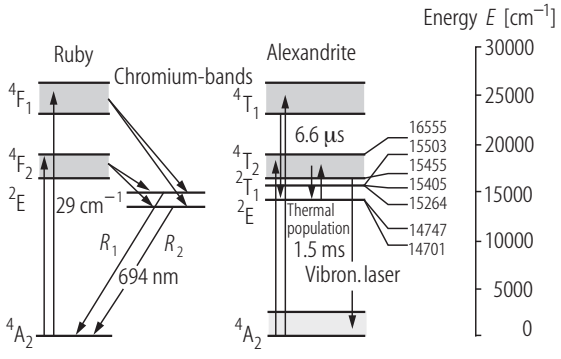

Fig. 4.1.39. Energy levels of chromium in ruby and alexandrite [99Koe, 80Wal].

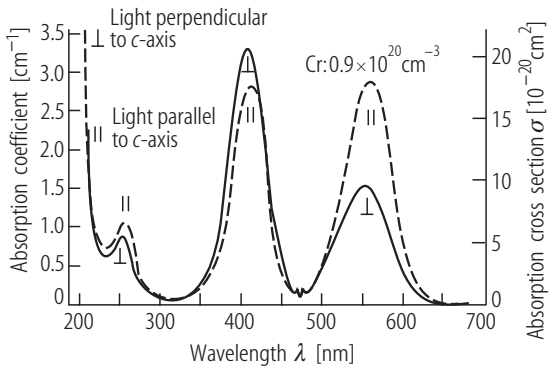

Fig. 4.1.40. Absorption spectrum of chromium in ruby [99Koe].

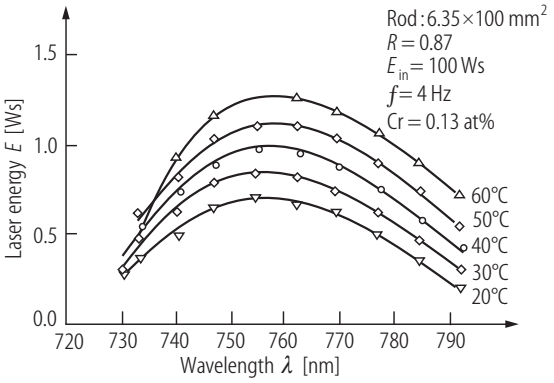

Fig. 4.1.41. Tuneability and temperature dependence of chromium in alexandrite [85Wal].

4.1.2.2.2 Erbium Er^{3+}

Figure 4.1.42 shows the energy level diagram of Er^{3+}.

In Table 4.1.15 laser parameters of Er in various solids are listed. Due to the lower thermal conductivity of YAP (5.5 W m^{-1} K^{-1}), compared with YAG (10 W m^{-1} K^{-1}) and the higher Er-doping (40 %) the thermal lens of Er:YAP is much stronger than of Nd:YAG.

The absorption spectrum of Erbium Er^{3+} in YAG is given in Fig. 4.1.43a [82Web] and Fig. 4.1.43b [93Hol]. Er^{3+} allows the interesting possibility via a 3-level excitation to achieve simultaneously transitions for blue $^2H_{9/2}$, green $^4S_{3/2}$ and red $^4F_{9/2}$, [93Tho, 92Ara].

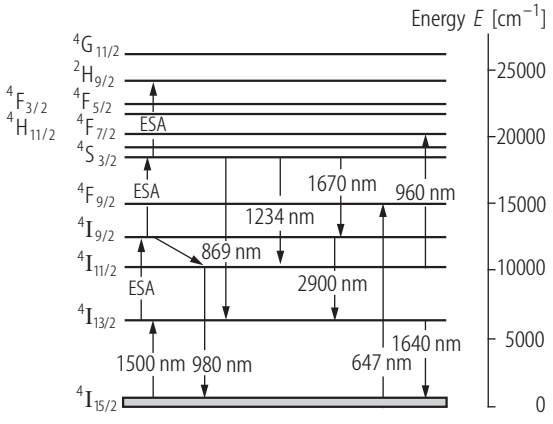

Fig. 4.1.42. Energy level diagram of Er^{3+} [89Sta, 93Tho, 92Ara, 90Kur, 86Bar, 87Dae].

Table 4.1.15. Laser parameters of Er in various solids.

(**a**) Laser data.

Host	λ [nm]	σ [10^{-20} cm^2]	τ_0 [μs]	ΔE cm^{-1}	Transition	Ref.
YAG	2940	3			$^4I_{11/2}\rightarrow{}^4F_{13/2}$	
	1640	0.45–0.49	64000	470	$^4I_{13/2}\rightarrow{}^4I_{15/2}$	[91Cha1, 91Cha2]
YAP	1640	0.28–0.31	450–510		$^4I_{13/2}\rightarrow{}^4I_{15/2}$	[91Cha1, 91Cha2]
YLF	2900					
	1730		400		$^4S_{3/2}\rightarrow{}^4I_{9/2}$	
	1640	0.33–0.42	64000	346	$^4I_{13/2}\rightarrow{}^4I_{15/2}$	[91Cha1, 91Cha2]
	1230					
	850	1.4	25		$^4S_{3/2}\rightarrow{}^4S_{13/2}$	[82Kni]
Glass		0.6			$^4I_{13/2}\rightarrow{}^4I_{15/2}$	[91Min]

(**b**) Pump data.

λ_p = 600–800 nm

(**c**) Measurements.

Host	λ [nm]	P_{av} [W]	T [ms]	E [W s]	η_{slope} [%]	C [at%]	$d \times l$ [mm^2]	Ref.
YAG	2940	1.1		0.3	0.8	40	6.35 × 75	[87Fra]
YAG	2940	10	0.242	1.4	2.1		6 × 80	[90Moc]
YAG	2940	0.8	0.170	0.6	0.28	50		[86Bas]

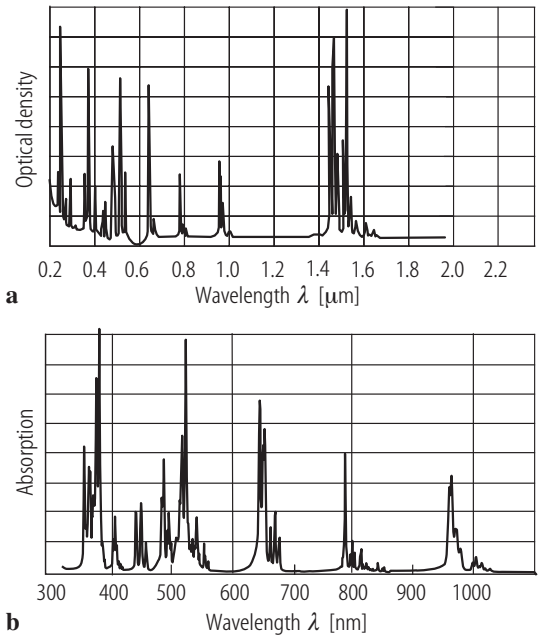

Fig. 4.1.43. Absorption spectrum of Erbium Er^{3+} in YAG, (**a**) [82Web], (**b**) [93Hol].

4.1.2.2.2.3 Holmium Ho^{3+}

In Fig. 4.1.44 the energy level diagram of Ho^{3+} in YLF is given. In Fig. 4.1.45 the excitation transfer via Cr and Tm to Ho in YAG is shown.

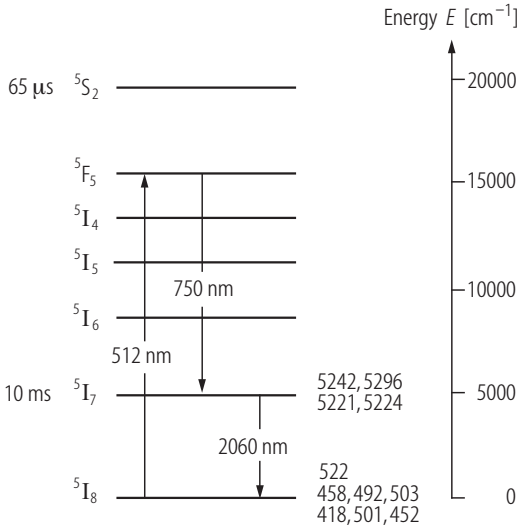

Fig. 4.1.44. Energy level diagram of Ho^{3+} in YLF [82Kni, 91Bow].

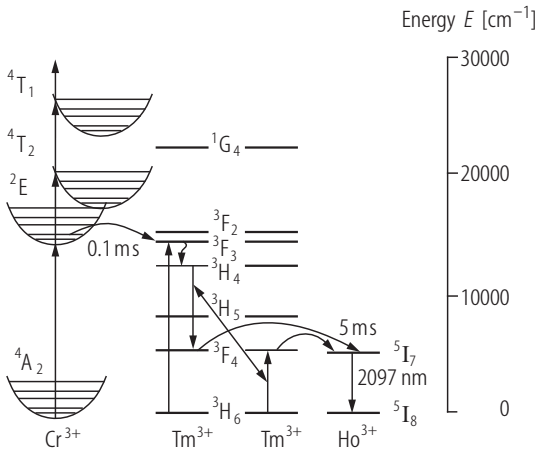

Fig. 4.1.45. Excitation transfer via Cr and Tm to Ho in YAG [89Qua, 90Qua2].

Table 4.1.16 lists typical laser parameters of holmium in solids.

By additional doping with other elements, for example additional Cr, and broadband pumping the absorption bands of these elements may also be used for excitation. An energy transfer takes place from the levels of the codoping into the energy levels of the real laser ion; this can increase the excitation efficiency considerably. The relationship of excitation efficiency to heat efficiency, however, becomes more unfavorable than without codoping.

Holmium must be doped low – 0.5 at% typically – to avoid absorption losses by reabsorption at the laser wavelength. Therefore, crystals for holmium lasers will be codoped with chromium and thulium or erbium and thulium to increase the efficiency with the help of the energy transfer.

Table 4.1.16. Typical laser parameters of holmium in solids.

(**a**) Laser data.

Host	λ [nm]	σ [10^{-20} cm^2]	τ_0 [μs]	ΔE cm^{-1}	Transition	Ref.
YAG	2000	0.94–1.6	10000	458	$^5I_7 \rightarrow {}^5I_8$	[91Cha1, 91Cha2]
	2127	3.9	522		$^5I_7 \rightarrow {}^5I_8$	[91Bow]
	2120	5.4	503		$^5I_7 \rightarrow {}^5I_8$	[91Bow]
	2096	10.1	458		$^5I_7 \rightarrow {}^5I_8$	[91Bow]
	2089	14.3	458		$^5I_7 \rightarrow {}^5I_8$	[91Bow]
	2091	0.9	8500		$^5I_7 \rightarrow {}^5I_8$	[87Fan, 88Fan]
YLF	2060	1.5	282		$^5I_7 \rightarrow {}^5I_8$	[82Kni]
YAP	2000	0.84	316–460		$^5I_7 \rightarrow {}^5I_8$	[91Cha1, 91Cha2]
YLF	750	97	65		$^5S_2 \rightarrow {}^5I_7$	[82Kni]

(**b**) Measurements.

Host	λ [nm]	P_{av} [W]	T [ms]	E [W s]	η_{slope} [%]	D/P [1/(m kW)]	$d \times l$ [mm^2]	Ref.
YAG	2100	20	0.2	3	2	1.52	4×102	[90Ima]
YAG	2080	7.5	1.5	17	2		5×60	[88Tei1, 88Tei2]
YAG[a]	2100		0.54	1.2	5.1		5×73	[89Qua, 90Qua2]
YLF	2060	10		0.1	3.5		5×50	[85Kni]

[a] Optimal doping Cr^{3+}: 7.7×10^{19} cm^{-3}, Tm^{3+}: 8.0×10^{20} cm^{-3}, Ho^{3+}: 5.0×10^{19} cm^{-3}.

4.1.2.2.2.4 Neodymium Nd^{3+}

In Fig. 4.1.46 the energy level diagram of Nd^{3+} in YAG is shown. Table 4.1.17 lists typical laser parameters of neodymium in solids.

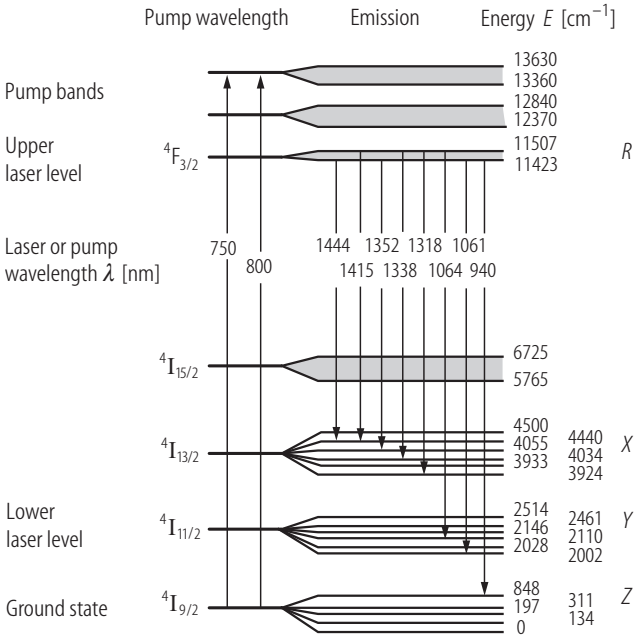

Fig. 4.1.46. Energy level diagram of Nd^{3+} in YAG [90Kam].

Table 4.1.17. Typical laser parameters of neodymium in solids.

(**a**) Laser data.

Host	λ [nm]	σ [10^{-20} cm^2]	C_0 [10^{20} cm^{-3}]	τ_0 [μs]	ΔE [cm^{-1}]	σ_e [10^{-20} cm^2]	Ref.
$^4F_{3/2}\rightarrow{}^4I_{11/2}$ at 1.0 μm							
YAG	1064	46–88	2.7	240–272	2000	34	[87Fuh, 90Kam]
GGG	1060	29	3.46	282			[78Kam, 84Mae]
GSGG	1061	31		281		11	[86Kru1]
KGW	1067	38		109			[95Esm]
BEL	1070	21		150			[76Jen]
BEL	1079	15					[76Jen]
YAP	1079	37		210			[72Mas]
YLF σ	1047	18		570		26	[82Pol]
YLF π	1053	12		520		37	[82Pol]
YVO	1063	120	3.85	116		62	[77Tuc, 74DeS]
NYAB	1064	100					[90Sch]
SiO_2	1089	0.82		512			[93Nak]
$^4F_{3/2}\rightarrow{}^4I_{13/2}$ at 1.3 μm							
YAG	1381	10					[90Kam]
GGG	1331	5.5					[78Kam]
GSGG	1335	7.3					[84Mae, 86Kru1]
YVO	1342	60–70					[77Tuc, 88Jai]

(**b**) Pump data.

Host	λ_{FZ} [nm]	Ref.
GGG	500	[87Hay]

(**c**) Measurements.

Host	P_{av} [W]	P_{cw} [W]	T [ms]	E [W s]	η_{slope} [%]	$d \times l \times h$ [mm^3]	Pumped by	Ref.
$^4F_{3/2}\rightarrow{}^4I_{11/2}$ at 1.0 μm								
GGG	230		3	23	2.4	$9 \times 35 \times 177$	lamp	[87Hay]
BEL		9	0.125		2.5	6.35×76		[76Jen]
YAG	800	400–1000	0–20	60	3–4	8×200	lamp	
YAG		1720			14	8×200	diode	[02Lu]
YAG ceramics		1460			12	8×200	diode	[02Lu]
YAP		163			3.16	5.8×111	lamp	[90Hon]
SiO_2	5	5			15		diode	[93Cao]
YVO		50			15		diode	[02Hua]
$^4F_{3/2}\rightarrow{}^4I_{13/2}$ at 1.3 μm								
YAG	165		8			8×150		[86Tho]
YAP		82.8		2.02		5.8×111		[86She]
YVO		6.5			12	3×10	diode	[02Lie]

The lifetime of the lower laser energy level $^4I_{11/2}$ is stated in [90Hov] to be approximately 10 ns.

Figure 4.1.47 shows the absorption spectrum of Nd^{3+} in YAG and integrated intensity.

Figure 4.1.48 shows the wavelength range around 800 nm with greater resolution which is particularly interesting for pumping with laser diodes.

In addition to the wavelength around 1.064 μm other lasing transitions have been shown to exist for Nd^{3+}. In Table 4.1.18 the corresponding relative intensities of the transitions are indicated.

The fluorescence spectrum of Nd^{3+} in YAG is depicted in Fig. 4.1.49.

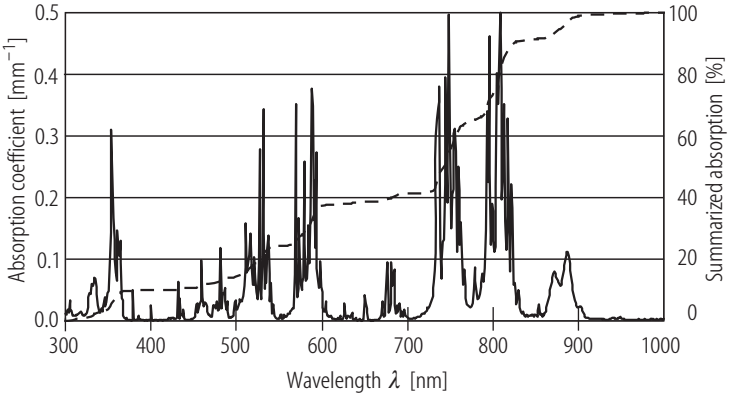

Fig. 4.1.47. Absorption spectrum of Nd^{3+} in YAG and integrated intensity [01Iff].

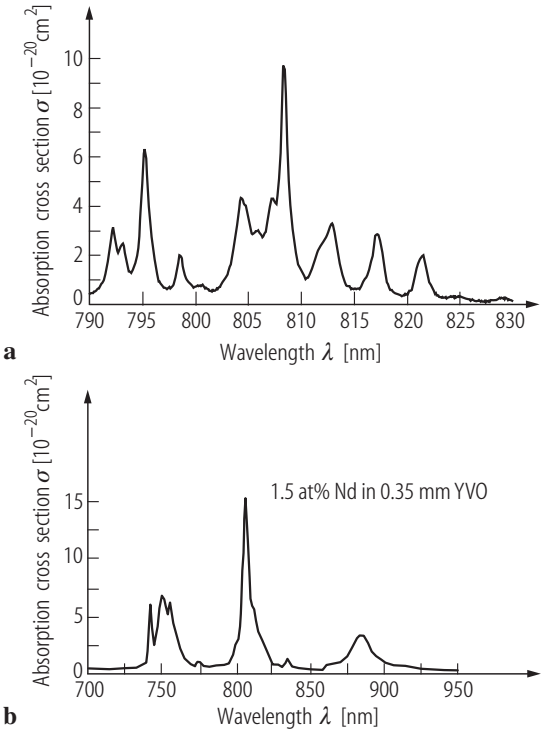

Fig. 4.1.48. (**a**) Absorption spectrum of Nd in YAG in the range 790 to 830 nm [93Hol]. (**b**) Absorption spectrum of Nd in YVO in the range 700 to 950 nm [93Hol].

Table 4.1.18. Laser transitions of Nd in YAG.

Wavelength [μm]	Relative intensity	σ [10^{-20} cm^2]	J_s [kW/cm^2]	$R_{1.44}$	Ref.
1.05205	0.46				[99Koe]
1.06152	0.92				[99Koe]
1.06415	1.00	41	2	0.1	[93Hod, 90Won]
1.0646	≈ 0.5				[99Koe]
1.0738	0.65				[99Koe]
1.0780	0.34				[99Koe]
1.1054	0.09				[99Koe]
1.1121	0.49				[99Koe]
1.1159	0.46				[99Koe]
1.12267	0.40				[99Koe]
1.3187	0.25	9.5	6.7	0.63	[93Hod, 90Won]
1.3200	0.09				[99Koe]
1.3335	0.13	5	13.1	0.82	[93Hod]
1.3351	0.15	6	10.9	0.78	[93Hod]
1.3381	0.33	9	7.2	0.65	[93Hod, 90Won]
1.3410	0.09				[99Koe]
1.3572	0.35	7.5	8.6	0.71	[90Won]
1.4150	0.62				[90Won]
1.4444	0.54	4.5	13.4	0.85	[93Hod, 90Won]

$R_{1.44}$ is the maximal permitted reflection of the respective wavelength for which pure 1.44 μm radiation with $R = 0.85$ can still be reached [93Hod].

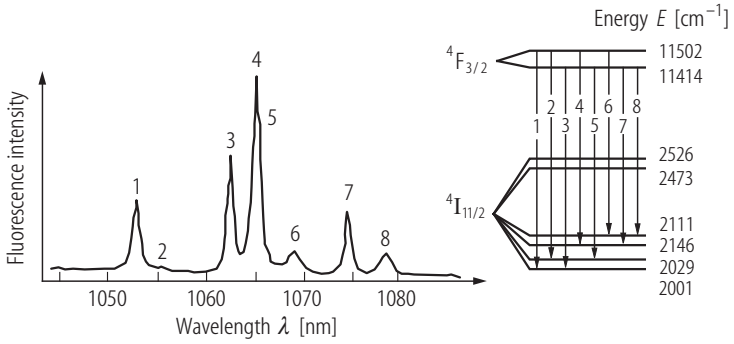

Fig. 4.1.49. Fluorescence spectrum of Nd^{3+} in YAG [99Koe].

4.1.2.2.5 Praseodymium Pr^{3+}

In Table 4.1.19 typical laser parameters of Pr ions in solids are listed.

The level scheme of Pr^{3+} in a fluoride fiber is shown in Fig. 4.1.50. Figure 4.1.51 shows the absorption of Pr^{3+}, Fig. 4.1.52 the luminescence spectrum around the laser line of Pr^{3+}.

Table 4.1.19. Typical laser parameters of Pr ions in solids.

(**a**) Laser data.

Host	λ [nm]	σ [10^{-20} cm^2]	C_0 [at%]	τ_0 [μs]	ΔE [cm^{-1}]	Transition	Ref.
YLF	639.5	0.17	0.5	56	5223	$^3P_0 \rightarrow {}^3F_2$	[93Eic, 93Kam]

(**b**) Measurements $^3P_0 \rightarrow {}^3F_2$ at 0.64 μm.

Host	P_{av} [W]	C [at%]	T [μs]	E [W s]	η_{slope} [%]	$d \times l$ [mm^2]	Ref.
YLF	0.8	0.5	0.14	0.09	0.3	6.3 × 95	[93Eic, 93Kam]

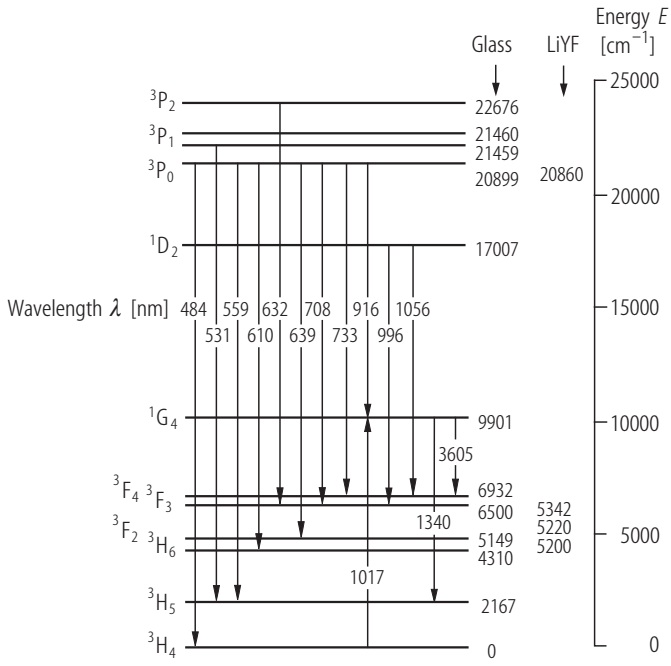

Fig. 4.1.50. Level scheme of Pr^{3+} in a fluoride fiber [93Eic, 93Kam, 91Ohi, 93Net].

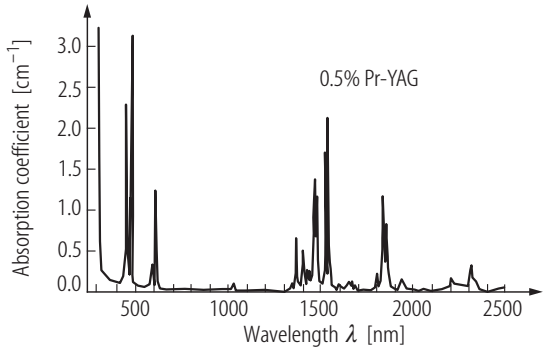

Fig. 4.1.51. Absorption of Pr^{3+} [94Pet].

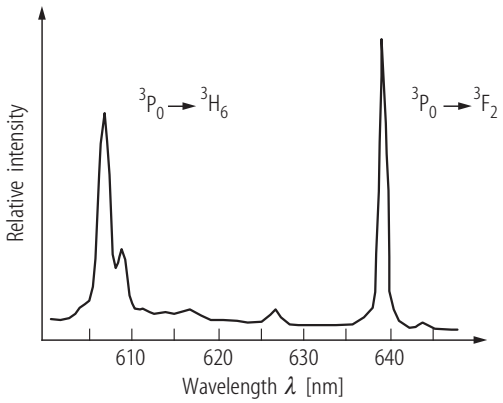

Fig. 4.1.52. Luminescence spectrum around the laser line of Pr^{3+} [93Eic, 93Kam].

4.1.2.2.2.6 Titanium

Table 4.1.20 lists typical laser parameters of Ti ions in sapphire. Figure 4.1.53 shows the absorption spectrum of titanium in sapphire.

Table 4.1.20. Typical laser parameters of Ti ions in sapphire.

(**a**) Laser data.

λ [nm]	σ [10^{-20} cm^2]	τ_0 [µs]	Ref.
720–920	0.17–0.32	3.9	[85Alb]

(**b**) Measurements.

P_{av} [W]	C [at%]	T [µs]	E [W s]	η_{slope} [%]	$-\ln V/l$ [%/cm]	$d \times l$ [mm^2]	Ref.
2	0.1	0.15	0.3–3	0.5–2	0.4–0.7	6.3 × 100	[85Lac, 86San, 89Car1, 89Car2]
220	0.1 wt%	5		1.9			[94Hof]

Ti sapphire is tunable, cw laser operation until now is only reached by pumping with an Ar-ion laser.

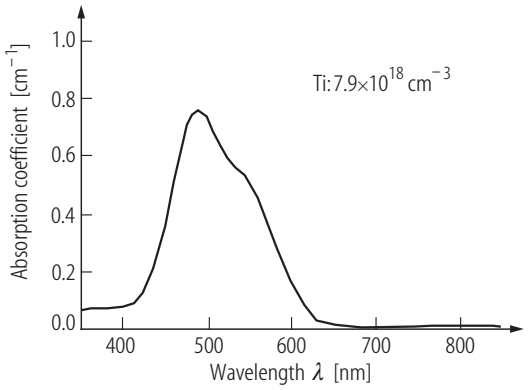

Fig. 4.1.53. Absorption spectrum of titanium in sapphire [86San].

4.1.2.2.2.7 Thulium

In Table 4.1.21 typical laser parameters of Tm ions in solids are listed.

The thulium absorption in YAG codoped with chromium and holmium is shown in Fig. 4.1.54. Figure 4.1.55 depicts the energy level scheme of thulium in ZBLAN.

Table 4.1.21. Typical laser parameters of Tm ions in solids.

(**a**) Laser data.

Host	λ [nm]	σ [10^{-20} cm^2]	C_0 [at%]	τ_0 [µs]	ΔE [cm^{-1}]	Ref.
$^3\mathbf{H}_4 \rightarrow {}^3\mathbf{H}_6$						
YAG	1600	1.3	1.2	740		[91Cha2, 90Arm, 91Arm]
YLF			1.06	2550		[91Arm]
$^3\mathbf{H}_4 \rightarrow {}^3\mathbf{F}_4$						
YLF	1500					
$^3\mathbf{F}_4 \rightarrow {}^3\mathbf{H}_6$						
GSGG	1986	0.13				
YAG	2014	0.16–1.3		586		[90Qua1, 90Qua2, 91Cha2]
YAG	1965	0.1				[90Qua1, 90Qua2]
YAP		0.5		6	461	[91Cha2]
YLF		0.32			355	[91Cha2]

(**b**) Measurements.

Host	λ [nm]	C(Tm) [10^{20} cm^{-3}]	C(Cr) [10^{20} cm^{-3}]	T [ms]	E [W s]	η_{slope} [%]	$d \times l$ [mm^2]	Ref.
$^3\mathbf{F}_4 \rightarrow {}^3\mathbf{H}_6$								
YAG	2014	8	0.5–2.5	1.2	2.2	4.5	5 × 76	[90Qua1, 90Qua2]
YAG	2066	8	0.5–2.5	1.2	0.3	1	5 × 76	[90Qua1, 90Qua2]
YAG	1965	8	0.5–2.5	1.2	0.9	0.7	5 × 76	[90Qua1, 90Qua2]
GSGG	1986	8	0.9	1.2	0.3	0.4	5 × 76	
YSGG	2010	8	0.8–2.5	1.2	0.6	0.6	5 × 76	[90Qua1, 90Qua2]

Host	λ [nm]	C(Tm) [%]	P_{cw} [W]		η_{slope} [%]	$d \times (h) \times l$ [mm × (mm) × mm]	Ref.
YLF	1910–2060	3.5	10	slab in multimode	37	2.6 × 6 × 22	[02Der]
YLF	1910–2060	3.5	6	slab in monomode	27	2.6 × 6 × 22	[02Der]
YLF	2000	4	140	rod, $M^2 \approx 34$	27	3 × 105	[02Lai]

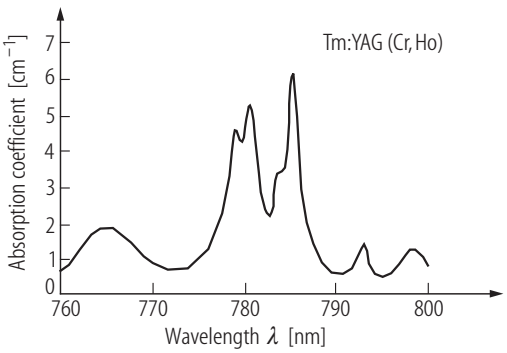

Fig. 4.1.54. Thulium absorption in YAG codoped with chromium and holmium [87Fan, 88Fan].

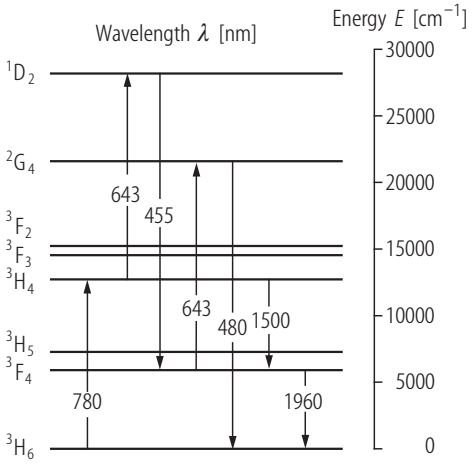

Fig. 4.1.55. Energy level scheme of thulium in ZBLAN [93Cth].

4.1.2.2.2.8 Ytterbium

In Table 4.1.22 typical laser parameters of Yb ions in solids are listed. Laser parameters of Yb ions in different host crystals are listed in Table 4.1.23.

Table 4.1.22. Typical laser parameters of Yb ions in solids.

(**a**) Laser data.

Host	λ [nm]	σ [10^{-20} cm^2]	τ_0 [μs]	ΔE [cm^{-1}]	Transition	Ref.
YAG	1030	2.3	950	612	$^2F_{5/2}\rightarrow{}^2F_{7/2}$	[91Lac1, 91Lac2]
FAP	1030	5.6	1100			[91Lac1, 91Lac2, 92Pay]
LuAG		2.7	925			[95Sum2]

(**b**) Pump data.

Host	σ_p [10^{-20} cm^2]	Ref.
LuAG	0.77 max	[95Sum1]
YAG	0.75	[95Sum1]

(**c**) Measurements.

Host	λ [nm]	C [at%]	P [W]	η_{slope} [%]	$d \times l$ [mm^2]	Ref.
$^2\mathbf{F}_{5/2}\rightarrow{}^2\mathbf{F}_{7/2}$						
YAG	1031	19	2	72	3×0.7	[94Gie]
	1049	19				[94Gie]

Diode-pumped at 942 nm.

Table 4.1.23. Laser parameters of Yb ions in different host crystals [93DeL].

Host	λ_p [nm]	λ [nm]	σ [10^{-20} cm^2]	τ_0 [ms]	H_s [W s/cm^2]	J_s [kW/cm^2]	E [cm^{-1}]	ΔE [10^{-20} W s]	ΔE/K [10^{-20} W s/K]
$LiYF_4$	962	1020	0.81	2.21	24	10	480	0.95	690
LaF_3	975	1009	0.36	2.16	54	25	353	0.70	508
SrF_2	967	1025	0.16	9.20	121	13	593	1.18	853
BaF_2	967	1024	0.14	8.00	138	17	578	1.15	831
$KCaF_3$	973	1031	0.22	2.70	87	32	593	1.18	853
KY_3F_{10}	976	1011	0.44	1.87	44	23	369	0.73	531
Rb_2NaYF_6	962	1012	0.10	10.8	196	18	372	0.74	535
BaY_2F_8	961	1018	0.67	2.04	29	14	458	0.91	659
Y_2SiO_5	979	1042	0.33	1.04	57	55	617	1.23	887
$Y_3Al_5O_{12}$	942	1031	2.03	1.01	9.5	9.4	628	1.25	903
$YAlO_3$	962	1014	1.31	0.43	15	35	353	0.70	508
$Ca_5(PO_4)_3F$	905	1043	5.90	1.20	3.23	2.69	603	1.20	867
$LuPO_4$	975	1011	0.53	0.83	37.1	44.7	349	0.69	502
$LiYO_2$	908	1020	0.56	1.13	34.8	30.8	474	0.94	682
$ScBO_3$	966	1022	0.19	4.80	102	21.3	472	0.94	679

Figure 4.1.56 shows the energy level scheme of Yb in YAG at 77 K. The absorption spectrum of Yb in YAG in the range 850 to 1050 nm, doping 6.5 at% Yb, is shown in Fig. 4.1.57.

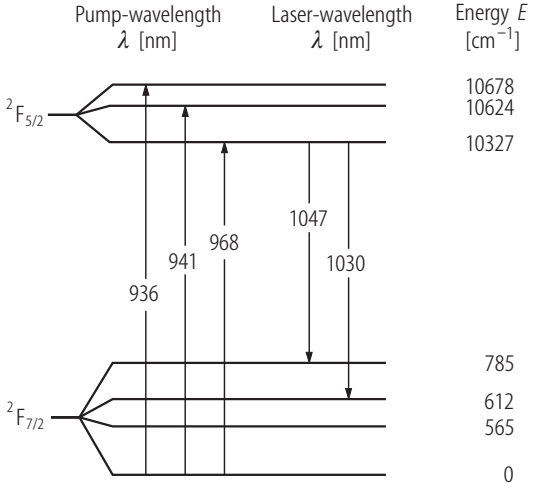

Fig. 4.1.56. Energy level scheme of Yb in YAG at 77 K [91Lac1, 91Lac2].

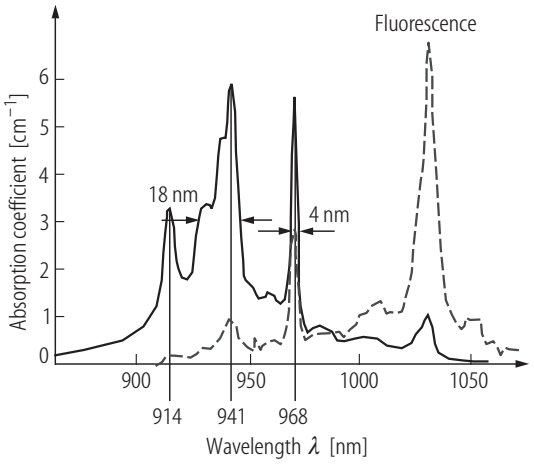

Fig. 4.1.57. Absorption spectrum of Yb in YAG in the range 850 to 1050 nm, doping 6.5 at% Yb [91Lac1, 91Lac2].

4.1.3 Laser crystals

4.1.3.1 Alexandrite

Material		$BeAl_2O_4$				Ref.
Active ion		Cr^{3+}				
Optical properties			$E \parallel a$-axis	$E \parallel b$-axis	$E \parallel c$-axis	
n		1.74	1.736	1.742	1.735	[85Wal, 84Wal, 85All]
dn_{rel}/dT	$10^{-6}/°C$	8.3–9.41	9.4	8.3		[85All, 85Wal, 90Cha]
n_2	10^{-20} m^2/W	2				[85All]
Thermal properties			$\parallel a$-axis	$\parallel b$-axis	$\parallel c$-axis	
k	W/(m °C)	23				[85Wal]
α	$10^{-6}/°C$		5.9–6	6.1–6.8	6.7–6.9	[84Wal, 90Cha]
Mechanical properties						
ρ	g/cm^3	3.69				[85All]
ν		0.3				[86Kru2]
E	GPa	469				[85All]
P_{max}	MPa	400–900	457–948	520		[85Wal, 85All]
H_K	MPa	19.6				[84Wal]
γ	MPa $m^{1/2}$	2.6				[86Kru2]
Crystal properties						
Structure		orthorhombic				[85All]
Space group		D_{2h}^{16}–Pnma				[85All]
Lattice const.	a/nm	0.9404				[85All]
	b/nm	0.5476				[85All]
	c/nm	0.4427				[85All]
T_m	°C	1870				
F_A	10^{20} cm^{-3}/at%	3.51				[85All]
Derived data			Literature values			
R_T	kW/m	2–5	3.5–7.4	2.35		[85All, 86Kru2]
dn_{abs}/dT	$10^{-6}/°C$	6.7–7.8				
Supplier data		Cr				
l_{max}	mm	120				[85Wal]
d_{max}	mm	15				[85Wal]
C (ion)	at%	0.05–0.2				[85Wal]

Alexandrite with Cr is tunable from 710 to 800 nm. Efficiency and wavelength increase linearly with the temperature to about 200 °C (750 nm at 20 °C to 790 nm at 300 °C). However, the lifetime decreases with temperature (260 µs at 20 °C to 100 µs at 150 °C).

4.1.3.2 BEL (lanthanum beryllate)

Material		$La_2Be_2O_5$	Lanthanum beryllate			Ref.
Active ion		Nd^{3+}				
Optical properties		$E \parallel x$	$E \parallel y$	$E \parallel z$		
n		1.964	1.997	2.035		[86Chi]
dn_{rel}/dT	$10^{-6}/°C$	2.86	1.53	−6.23		[86Chi]
n_2	10^{-13} esu	6				
Thermal properties			a-axis	b-axis	c-axis	
k	W/(m °C)	4.7–5				[75All, 86Chi]
α	$10^{-6}/°C$	8	7.0	7.9	9.5	[86Chi, 89Rap]
Crystal properties						
Structure		monoclinic		biaxial		
Space group		C^6_{2h}–C2/c				[89Rap]
Lattice const.	a/nm	0.75356				
	b/nm	0.73476				
	c/nm	0.74387				
T_m	°C		1360			[86Chi]
F_A	10^{20} cm^{-3}/at%	1.94				[89Rap]
Distribution coefficient			0.66 (Nd)			[86Chi]
Derived data			Literature values			
R_T	kW/m		0.22			[86Chi]
Supplier data						
l_{max}	mm	> 76				
d_{max}	mm	> 7				

In a suitable direction ($z - 62°y$) the crystal behaves almost athermally [86Chi]. The damage threshold is about 500 W/cm per rod length in cw operation, according to [89Rap]. The laser radiation is polarized due to the crystal structure [75All].

4.1.3.3 Emerald

Material		$Be_3Al_2Si_6O_{18}$			Ref.
Active ion		Cr^{3+}			
Optical properties		n_o	n_e		
n		1.57–1.60	1.56–1.59	dependent on Cr-concentration	
Crystal properties					
Structure	hexagonal				
Supplier data					
C (ion)	at%	3			[86Lai, 87Lai]

Tunable in the range from 720 nm to 842 nm [86Lai, 87Lai].

4.1.3.4 GGG (gallium gadolinium garnet)

Material	$Gd_2Ga_5O_{12}$	Gallium Gadolinium Garnet			Ref.
Active ion		Nd	Codoping	Cr	
Optical properties					
n		1.943			[85Hoe, 88Hoe]
dn_{rel}/dT	$10^{-6}/°C$	20.5			[85Hoe, 88Hoe]
p_{11}		−0.086			[85Kit]
p_{12}		−0.027			[85Kit]
p_{44}		−0.078			[85Kit]
λ_{FZ}	nm	500			[87Hay]
Thermal properties					
c_p	W s/(g °C)	0.38			[86Kru2]
k	W/(m °C)	7.4	7.05		[85Kit, 86Kru2]
α	$10^{-6}/°C$	8.96			[85Hoe, 88Hoe]
Mechanical properties					
ρ	g/cm^3	7.088			[86Kru2]
ν		0.28			[85Kit]
E	GPa	225			[85Kit]
P_{max}	MPa	440			
Crystal properties			Nd	Cr	
Structure			cubic		
Lattice const.	a/nm		1.238		[85Kit]
Orientation			⟨111⟩		[89Wac]
T_m	°C		2000		[85Kit]
F_A	10^{20} cm^{-3}/at%	1.265	0.84		[88Lun]
Distribution coefficient			0.4	3.0	[89Wac]
Derived data					
C_r			0.011		
C_ϕ			−0.016		
dn_{abs}/dT	$10^{-6}/°C$		18.75		
M_r	10^{-6} m/W		1.375		
M_ϕ	10^{-6} m/W		1.49		
Supplier data		Nd	Cr		
l_{max}	mm		200		[89Wac]
d_{max}	mm		80		[89Wac]
C	$10^{-20}/cm^3$	2.4	0.4		[89Wac]

4.1.3.5 GSAG (gadolinium scandium aluminum garnet)

Material		$Gd_3Sc_2Al_3O_{12}$		Ref.
Active ion		Cr^{3+}		
Optical properties				
n		1.88		[85Hoe, 88Hoe]
dn_{rel}/dT	$10^{-6}/°C$	5.20		[85Hoe, 88Hoe]
Thermal properties				
α	$10^{-6}/°C$	6.92		[85Hoe, 88Hoe]
Mechanical properties				
ρ	g/cm^3	5.822		[86Mei]
Crystal properties			Cr	
Structure			cubic	
Lattice const.	a/nm		1.242	[86Mei]
Orientation			⟨111⟩	
T_m	°C		1815	[86Mei]
Distribution coefficient			≈ 1	[86Mei]

4.1.3.6 GSGG (gadolinium scandium gallium garnet)

Material		$Gd_3Sc_2Ga_3O_{12}$			Ref.
Active ion		Nd^{3+}	Cr^{3+}	Codoping	
Optical properties		Nd	Nd (Cr)		
n		1.94	1.942		[85Hoe, 88Hoe, 87Lee]
dn_{rel}/dT	10^{-6}/°C	10.45	10.9		[85Hoe, 88Hoe, 87Lee]
n_2	10^{-13} esu	8			[86Kru2]
p_{11}		−0.012	−0.097		[85Kit]
p_{12}		0.019	−0.040		[85Kit]
p_{44}		−0.066	−0.066		[85Kit]
λ_{FZ}	nm	550–590			[86Pay]
Thermal properties		Nd	Nd (Cr)	Cr	
c_p	W s/(g °C)	0.40	0.40	0.40	[85Kit, 86Kru2]
k	W/(m °C)	4.86	6.02	5.63	[85Kit, 86Kru2]
α	10^{-6}/°C	7.32–7.39	7.5		[85Hoe, 88Hoe, 86Kru2]
Mechanical properties					
ρ	g/cm^3	6.46			[88Lit1]
ν		0.28			[86Kru2]
E	GPa	210			[86Kru2]
P_{max}	MPa	144	164[a]		[86Kru2, 88Hod2]
γ	MPa m$^{1/2}$	1.2			[86Kru2]
Crystal properties			Nd^{3+}	Cr^{3+}	
Structure		cubic			[88Lit1]
Lattice const.	a/nm	1.26			[88Lit1]
Orientation		⟨111⟩			
Debye Temp.	K	503			
T_m	°C	1800–2133			
F_A	10^{20} cm^{-3}/at%	1.265	0.84		
Distribution coefficient			0.65		[86Kru2]
Derived data		Nd	Nd (Cr)	Literature values	
R_T	kW/m	0.33–0.45	0.66		[86Kru2, 88Lit1]
τ/f	s/mm^2	0.43–0.53	0.435		[88Lit1]
C_r		0.02	0.004	0.024	[86Kru2]
C_ϕ		0.001	−0.02	0.0015	[86Kru2]
dn_{abs}/dT	10^{-6}/°C	8.75–9.15			
M_r	10^{-6} m/W	1.18	0.81		
M_ϕ	10^{-6} m/W	0.94	0.60		
Supplier data		Nd		Cr	
l_{max}	mm	152.4			[88Lit1]
d_{max}	mm	12.7			[88Lit1]
C (ion)	10^{20} cm^{-3}	2		1.2–2	[88Lit1]

[a] Depends on surface finish.

4.1.3.7 GVO(4) (gadolinium (ortho)vanadate)

Material		$GdVO_4$				Ref.
Active ion		Nd^{3+}	Tm^{3+}	Tm^{3+}	Yb^{3+}	
Codoping				Ho		
Mechanical properties						
ρ	g/cm^3	5.47				[93Ram]
Crystal properties						
Lattice const.	a/nm	0.721				[93Ram]
	b/nm	0.721				[93Ram]
	c/nm	0.635				[93Ram]
F_A	10^{20} cm^{-3}/at%	1.2				[93Ram]
Supplier data		Nd	Yb	Tm		
l_{max}	mm	10				[93Ram]
d_{max}	mm	5				
C (ion)	at%	1	2	4.5–8.5		[93Ram]

4.1.3.8 KGW (potassium gadolinium tungstate)

Material		$KGd(WO_4)_2$				Ref.
Active ion		Nd^{3+}				
Optical properties			x	y	z	
n	@ 1.067 µm		1.937	1.986	2.033	[93Opt]
n	@ 1.180 µm		1.928	1.979	2.026	[93Opt]
dn_{rel}/dT	10^{-6}/°C	4–10				[93Alk]
Thermal properties			⟨100⟩	⟨010⟩	⟨001⟩	
k	W/(m °C)		2.8	2.2	3.5	[93Opt]
α	10^{-6}/°C		4.0	3.6	8.5	[93Opt]
Mechanical properties			a-axis	b-axis	c-axis	
ρ	g/cm^3	7.27				[93Opt]
E	GPa		115.8	152.5	92.4	[93Alk]
Crystal properties						
Structure		monoclinic				[93Opt]
Space group		C_{2h}^6				[93Opt]
Lattice const.	a/nm	0.8098				[93Opt]
	b/nm	1.0417				[93Opt]
	c/nm	0.7583				[93Opt]
Orientation		⟨010⟩				[93Opt]
T_m	°C	1075				[93Opt]
F_A	10^{20} cm^{-3}/at%	0.633				[93Opt]
F_W	10^{20} cm^{-3}/wt%	3.064				[93Opt]
Mol weight	g	647.2				[93Opt]
Formula units	ZEZ	4				[93Opt]
Supplier data			Nd			
l_{max}	mm		80			[93Alk]
d_{max}	mm		8			[93Alk]
C (ion)	at%		1–8			[93Opt, 93Alk]

4.1.3.9 LICAF (lithium calcium aluminum fluoride)

Material		$LiCaAlF_6$			Ref.
Active ion		Nd^{3+}	Cr^{3+}		
Optical properties			∥ a-axis	∥ c-axis	
dn_{rel}/dT	10^{-6}/°C		−4.2	−4.6	[90Cha]
Thermal properties			∥ a-axis	∥ c-axis	
k	W/(m °C)		4.6	5.1	[90Cha]
α	10^{-6}/°C		22	3.6	[90Cha]

Thermal lensing is very low [90Cha].

4.1.3.10 LNA (lanthanum neodymium hexa-aluminate), LMA (lanthanum magnesium hexa-aluminate)

Material		$LaMgAl_{11}O_{19}$			Ref.
Active ion		Nd^{3+}	Codoping	Cr	
Optical properties			o	e	
n			1.769	1.764	
dn_{rel}/dT	$10^{-6}/°C$		12.5	11.5	[91Aub]
Thermal properties			$\perp c$-axis	$\parallel c$-axis	
c_p	W s/(g °C)	0.715			[91Aub]
k	W/(m °C)		4.58	2.68	[91Aub]
α	$10^{-6}/°C$		8	12	[91Aub]
Mechanical properties			$\perp c$-axis	$\parallel c$-axis	
ρ	g/cm^3	4.18			[91Aub]
E	GPa	38			[91Aub]
P_{max}	MPa	20			
H_K	MPa		14.2	18.2	[91Aub]
Crystal properties			Nd	Cr	
Structure		hexagonal			
Space group		$P6_3/mmc$			[81Kah]
Lattice const.	a/nm	0.558			[81Kah]
	c/nm	2.202			[81Kah]
Orientation		a-axis			[91Ami]
T_m	°C	1760			[81Kah]
F_A at%	10^{20} cm^{-3}	3.4			[81Kah]
Distribution coefficient			≈ 1	≈ 1.3	
Derived data		$\perp c$-axis	$\parallel c$-axis		
ϕ_B	°	60.5			
R_T	kW/m	≈ 0.226	≈ 0.09		
τ/f	s/mm^2	0.653	1.115		
dn_{abs}/dT	$10^{-6}/°C$	≈ 10			
Supplier data		Nd	Nd(Cr)		
C (ion)	wt%	1.5	1.5(1)		[89Ami, 91Ami]

Tunable up to 1083 nm [89Ami]. Can be doped very highly by Nd.
The wavelength depends on the Nd concentration [91Ami].

4.1.3.11 LSB (lanthanum scandium borate)

Material		$LaSc_3(BO_3)_4$			Ref.
Active ion		Nd^{3+}	Codoping	Cr	
Optical properties			x	y	z
n	@ 1 μm		1.828	1.8272	1.828
dn_{rel}/dT	10^{-6}/°C @ 633 nm		4.37		
Thermal properties			$\parallel z$		
c_v	W s/(g °C)	0.62 ± 0.02			[96Bre]
k	W/(m °C)		2.8		[96Bre]
α	10^{-6}/°C	12.3			[96Bre]
T_m	°C	1600			[96Bre]
Mechanical properties			a-axis	b-axis	c-axis
ρ	g/cm^3	3.8			[96Bre]
Crystal properties					
Structure		monoclinic for $x \leq 0.5$, trigonal for $x > 0.5$			[96Bre]
Lattice const.	a/nm	0.9778			[96Bre]
	c/nm	0.7929			[96Bre]
Supplier data		Nd	Nd(Cr)		
l_{max}	mm	1	50		[96Bre]
d_{max}	mm	3	4		[96Bre]
C (ion)	at%	5–25	$7.3(0.5) \times 10^{20}$ cm^{-3}		[96Bre]

4.1.3.12 NYAB (neodymium yttrium aluminum borate)

Material		$YAl_3(BO_3)_4$	Neodymium Yttrium Aluminum Borate		Ref.
Active ion		Nd^{3+}			
Optical properties			n_o	n_e	
n	@ 1062 nm		1.7553	1.6869	[90Lin, 90Wan]
n	@ 531 nm		1.7808	17075	[90Lin, 90Wan]
Frequency doubling			Type I	Type II	
d_{11}	pm/V	1.7			
d_{eff}	pm/V		1.43	0.67	[90Lin]
Phase angle	°		32.9	51	[90Lin]
Crystal properties					
Lattice const.	a/nm	0.9293			[90Wan]
	b/nm	0.9293			[90Wan]
	c/nm	0.7245			[90Wan]
F_A	10^{20} cm^{-3}/at%	0.557			[90Lin]

Self-frequency doubled.

4.1.3.13 Quartz

Material		SiO_2	Ref.
Active ion		Nd^{3+}	
Optical properties			
n	@ 1064 nm	1.44963	
dn_{rel}/dT	$10^{-6}/°C$	10	
ν_d		67.8	
Thermal properties			
c_p	W s/(g °C)	0.772	
k	W/(m °C)	1.5	
α	$10^{-6}/°C$	0.55	
Mechanical properties			
ρ	g/cm^3	2.201	
ν		0.17	
E	GPa	70	
Crystal properties			
Structure		amorphous	
T_g	°C	1600	
F_W	10^{20} cm^{-3}/wt%	0.925	

4.1.3.14 Sapphire

Material		Al_2O_3	Ruby	Sapphire	Ref.
Active ion		Cr	Cr	Ti	
Optical properties			n_e π	n_o σ	
n		1.7638	1.7556	1.76	[89Uni]
dn_{rel}/dT	$10^{-6}/°C$	12.6			
p_{11}		−0.25			[80Ars]
p_{12}		−0.038			[80Ars]
p_{44}		−0.1			[80Ars]
Thermal properties					
c_p	W s/(g °C)	3.98			
k	W/(m °C)	28			[86Kru2]
α	$10^{-6}/°C$	6.7			[86Kru2]
Mechanical properties					
ρ	g/cm^3	3.98			
ν		0.25			[86Kru2]
E	GPa	405			[86Kru2]
P_{max}	MPa	440			[86Kru2]
γ	MPa $m^{1/2}$	2.2			[86Kru2]
Crystal properties					
Structure		hexagonal	rhombohedral		
T_m	°C		2040		[89Uni]
F_W	10^{20} cm^{-3}/wt%	3.24	3.29		
Derived data					
R_T	kW/m	3.4	3.4		[86Kru2]
τ/f	s/mm^2	0.56			
C_r		−0.026			
C_ϕ		−0.044			
dn_{abs}/dT	$10^{-6}/°C$	11.02			
M_r	10^{-6} m/W	0.16			
M_ϕ	10^{-6} m/W	0.14			
Supplier data		Cr_2O_3	TiO_2		
l_{max}	mm	100	100		[89Uni]
d_{max}	mm	20	6.35		[89Uni]
C	wt%	0.03–0.05	0.02–0.15		[89Uni]

4.1.3.15 YAG (yttrium aluminum garnet)

Material		$Y_3Al_5O_{12}$				Ref.
Active ions		Er^{3+}	Ho^{3+} (Cr, Tm)	Nd^{3+}	Yb^{3+}	
Optical properties						
n		1.82	1.818			[90All1, 88Lit2, 92Lit1]
dn_{rel}/dT	$10^{-6}/°C$	7.3–8.9				[88Lit2, 92Lit1, 90Cha]
n_2	10^{-13} esu	3				[89Ami]
p_{11}		−0.0290				[80Ars]
p_{12}		0.0091				[80Ars]
p_{44}		−0.0615				[80Ars]
λ_{FZ}	nm	475				
Thermal properties			⟨100⟩	⟨110⟩	⟨111⟩	
c_p	W s/(g °C)	0.6				[90All1]
k	W/(m °C)	10–14				[86Kru2, 90All1]
α	$10^{-6}/°C$	6.9–7.5	8.2	7.7	7.8	[88Lit2, 92Lit1, 90All1, 88Uni1, 88Uni2]
Mechanical properties						
ρ	g/cm^3	4.56				[90All1]
ν		0.25–0.28				[88Lit2, 92Lit1, 86Kru2]
E	GPa	282–300				[86Kru2, 90All1]
P_{max}	MPa	130–280				[90All1, 86Kru2]
H_K	MPa	11.9				
γ	MPa $m^{1/2}$	1.4				[86Kru2]
Crystal properties		Nd	Cr	Tm	Ho	
Structure		cubic, isotropic				[85Hoe, 88Hoe]
Space group		O_h^{10}–Ia3d				
Lattice const.	a/nm	1.201				[90All1]
Orientation		⟨111⟩				
T_m	°C	1950				[88Lit2, 92Lit1]
F_W	$10^{20}cm^{-3}$/wt%	1.903				
F_A	$10^{20}cm^{-3}$/at%	1.38				[88Lit2, 92Lit1]
Distribution coefficient		0.18	2.6	1.06	1.0	[86Chi, 92Lit1]
Mol weight	g	593.6				[88Lit2, 92Lit1]
Derived data			Literature values			
R_T	kW/m	0.516–1.254	0.7–1.4, 0.79			[86Kru2, 90All1, 88Lit2, 92Lit1]
τ/f	s/mm^2	0.27				
C_r		0.017				
C_ϕ		−0.003				
dn_{abs}/dT	$10^{-6}/°C$	5.66				
M_r	10^{-6} m/W	0.362				
M_ϕ	10^{-6} m/W	0.282				
Supplier data		Nd	Ho (Cr | Tm)	Er		
l_{max}	mm	250	152			[88Lit2, 92Lit1]
d_{max}	mm	20	9.5			[88Lit2, 92Lit1]
C	at%	0.6–1.4	0.36 (1 | 5.7)	50		[88Lit2, 92Lit1, 88Uni1, 88Uni2]

YAG is the most essential crystal for material processing.

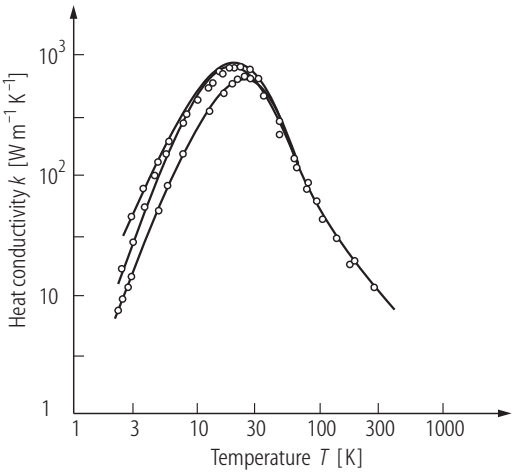

Fig. 4.1.58. Temperature dependence of the heat conductivity of YAG, after [71Sla].

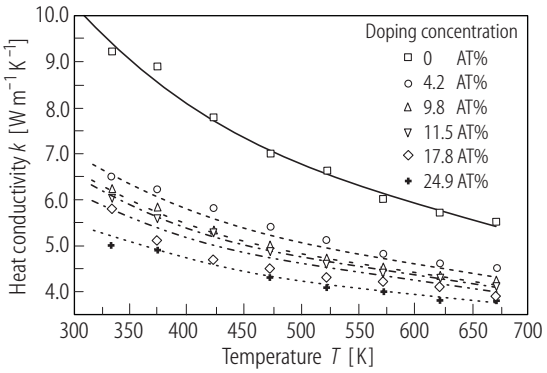

Fig. 4.1.59. Heat conductivity of Yb:YAG and undoped YAG in the temperature range from 330 K to 670 K, after [00Tue].

The temperature dependence of the heat conductivity of YAG, after [71Sla], is shown in Fig. 4.1.58.

The heat conductivity of Yb:YAG and undoped YAG in the temperature range from 330 K to 670 K, after [00Tue], is depicted in Fig. 4.1.59.

The quantum efficiency, the fraction of the absorbed pump photons which contribute to the population of the upper laser level, of Nd in YAG depends on the concentration and is typically between 0.6 at 1.6 at% and 0.8 at 0.9 at% [89Lup]. Some single rods attain 0.87 [89Dev], even at high concentration. The relative dependence on the concentration C/at% is given in [89Lup] with

$$\eta_{\mathrm{r}}(C) = 1 - 18.2\, C\ .$$

Heating the crystal to 1400 °C in I_2 and O_2 (atmosphere) for 8 h reduces the absorption by color centers and improves the efficiency [89Dev].

The thermal lens in the Ho laser is about three times stronger in the Cr co-doped crystal than in Nd without Cr.

4.1.3.16 YAP (yttrium aluminum perovskite), YALO (yttrium aluminum oxide)

Material		$YAlO_3$	Yttrium Aluminum Perovskite			Ref.
Active ion		Nd^{3+}	Er^{3+}	Tm^{3+}		
Codoping				Cr		
Optical properties			*a*-axis	*b*-axis	*c*-axis	
n			1.932	1.923	1.909	[90Zen]
dn_{rel}/dT	$10^{-6}/°C$		8.5–9.75	8.1–9.86	12.8–14.5	[90Zen, 72You]
λ_{FZ}	nm	280				[69Web]
Thermal properties			*a*-axis	*b*-axis	*c*-axis	
c_p	W s/(g °C)	0.418				[80Ars]
k	W/(m °C)	11				[80Ars]
α	$10^{-6}/°C$		9.5	4.3	10.8	[80Ars]
Mechanical properties						
ρ	g/cm^3	4.88–5.35				[72Kei, 80Ars]
E	GPa	220				[80Ars]
Crystal properties						
Structure		orthorhombic				
Space group		D_{2h}^{16}–Pbnm				[80Ars]
Lattice const.	a/nm	0.5176				
	b/nm	0.5307				[72Kei]
	c/nm	0.7355				[72Kei]
Orientation		*b*-axis				
T_m	°C	1850				
F_A	10^{20} cm^{-3}/at%	1.95				[81Her]
Distribution coefficient		0.82				[72Kei]
Derived data		Literature values				
τ/f	s/mm^2	0.185	0.2			[80Ars]
dn_{abs}/dT	$10^{-6}/°C$	6.4–11.1				
Supplier data	Nd					
l_{max}	mm	150				
d_{max}	mm	10				
C	wt%	0.7				[81Her]

The emission wavelength is dependent on the polarization direction and the rod orientation:
$\lambda = 1079$ nm, rod axis $\parallel$ *a*-axis and polarization $\parallel$ *b*-axis,
$\lambda = 1064$ nm, rod axis $\parallel$ *a*-axis and polarization $\parallel$ *c*-axis,
$\lambda = 1064$ nm, rod axis $\parallel$ *b*-axis independent of polarization direction,
$\lambda = 1064$ nm, rod axis $\parallel$ *c*-axis independent of polarization. Without polarization $\parallel$ *a*-axis.

4.1.3.17 YLF (yttrium lithium fluoride)

Material		$LiYF_4$			Ref.
Active ion		Nd	Er	Ho	
Codoping				Er, Tm	
Optical properties			n_e	n_o	
n			1.470	1.448	[88Lit3]
dn_{rel}/dT	$10^{-6}/°C$		−4.1	−2.0	[87Lee]
Thermal properties			a-axis	c-axis	
c_p	W s/(g °C)		0.79		[88Lit3]
k	W/(m °C)	4.3	6		[90Cha, 88Lit3]
α	$10^{-6}/°C$	14	13	8	[86Kru2, 88Lit3]
Mechanical properties					
ρ	g/cm^3	3.95			[88Lit3]
ν		0.33			[86Kru2]
E	GPa	75–77			[88Lit3, 86Kru2]
P_{max}	MPa	33–54			[88Lit3, 86Kru2]
γ	MPa $m^{1/2}$	0.27			[86Kru2]
Crystal properties					
Structure		tetragonal	uniaxial		
Orientation		⟨100⟩	a-axis		[88Lit3]
T_m	°C	825			[88Lit3]
F_A	10^{20} cm^{-3}/at%	1.3			
Distribution coefficient			0.3		[86Chi]
Mol weight	g	171.844			[88Lit3]
Derived data		Literature values			
R_T	kW/m		0.14		[86Kru2]
Supplier data		Nd	Er	(Ho, Er, Tm)	
l_{max}	mm	127			[88Lit3]
d_{max}	mm	9.5			[88Lit3]
C	at%	1	5	(2, 35, 10)	[88Lit3]

The thermal lens is assumed to be smaller than for YAG, due to the negative dn/dT. The focal length is smaller by a factor of 6 for the same pump power [83Mur].

4.1.3.18 YOS (yttrium ortho-silicate)

Material		Y_2SiO_5			Ref.
Active ion		Nd			
Optical properties		n_x	n_y	n_z	
n		1.772	1.773	1.793	[93Com]
Thermal properties					
k	W/(m °C)	4.5			[93Com]
Mechanical properties					
γ	MPa $m^{1/2}$	0.54			[93Com]
Crystal properties					
Structure		monoclinic biaxial			
Space group		c2/2			[93Com]
Orientation		20° relative to ⟨010⟩			[93Com]
Derived data		Literature values			
R_T	kW/m	0.38			[93Com]
Supplier data					
l_{max}	mm	150			[93Com]
d_{max}	mm	25			[93Com]
C	10^{20} cm^{-3}	2			[93Com]

Birefringent, polarized laser.

4.1.3.19 YSAG (yttrium scandium aluminum garnet)

Material		$Y_3Sc_2Al_3O_{12}$	Ref.
Active ion		Nd^{3+}	
Codoping		Cr	
Optical properties			
n		1.86	[90All2]
Thermal properties			
k	W/(m °C)	10.8	[88Duc]
Crystal properties			
Structure		cubic	
Lattice const.	a/nm	1.2271	[90All2]
Orientation		⟨111⟩	[90All2]
T_m	°C	1900	[90All2]
F_W	10^{20} cm^{-3}/wt%	0.189	[90All2]
F_A	10^{20} cm^{-3}/at%		
Distribution coefficient		0.4	[90All2]

4.1.3.20 YSGG (yttrium scandium gallium garnet)

Material		$Y_3ScGa_3O_{12}$			Ref.
Active ion		Nd^{3+}	Ho^{3+}	Er^{3+}	
Codoping		Cr^{3+}	Cr, Tm	Cr^{3+}	
Optical properties					
n		1.9626			[92Kuz]
dn_{rel}/dT	$10^{-6}/°C$	12.3			[92Kuz]
p_{11}		0.40			[92Kuz]
p_{12}		0.42			[92Kuz]
p_{44}		0.77			[92Kuz]
Thermal properties					
c_p	W s/(g °C)	0.534			[92Kuz]
k	W/(m °C)	7.9	8.3		[92Kuz, 88Duc]
α	$10^{-6}/°C$	8.1			[92Kuz]
Mechanical properties					
ρ	g/cm^3	5.36			[92Kuz]
E	GPa	218			[92Kuz]
Crystal properties					
Structure		cubic			
Space group		$Ia3d–O_h^{10}$			
Orientation		⟨001⟩	⟨111⟩		
T_m	°C	1810			[92Kuz]
Derived data		Literature values			
τ/f	s/mm^2	0.362			
C_r		0.079			
C_ϕ		0.206			
dn_{abs}/dT	$10^{-6}/°C$	10.57			
M_r	10^{-6} m/W	1.26			
M_ϕ	10^{-6} m/W	2.2			
Supplier data		Nd(Cr)	Ho(Tm, Cr)	Er(Cr)	
l_{max}	mm	152.4	101	101	[92Kuz]
d_{max}	mm	12.7	5	5	[92Kuz]
C	10^{20} cm^{-3}	2–3 (1–2)	0.5(8, 2.5)	30–40 (1–2)	[92Kuz]

4.1.3.21 YVO(4) (yttrium (ortho)vanadate)

Material		YVO_4	Yttrium orthovanadate		Ref.
Active ion		Nd^{3+}	Nd^{3+}	Ho^{3+}	
Optical properties			o = $a = b$	e = c	
n @ 1064 nm			1.9573	2.16252	[92Lit2, 95Cas]
dn_{rel}/dT	$10^{-6}/°C$		8.5	3.0	
n @ 808 nm			1.9721	2.1858	
n @ 532 nm			2.0210	2.2560	
$n = A + B(\lambda^2 - C) - D\lambda^2$					
A			3.77834	4.59905	[95Cas]
B			0.069736	0.110534	[95Cas]
C			0.04724	0.04813	[95Cas]
D			0.0108133	0.0122676	[95Cas]
Thermal properties			a-axis	c-axis	
k	W/(m °C)	5.2	5.23 ∥ c-axis	5.10 ⊥c-axis	[92Lit2, 95Cas]
α	$10^{-6}/°C$		4.49	11.4	[92Lit2]
Mechanical properties					
ρ	g/cm^3	4.22			[95Cas]
Crystal properties					
Structure		tetragonal	uniaxial		[92Lit2]
Space group		D_{4h}			
Lattice const.	$a = b$/nm	0.712			[92Lit2]
	c/nm	0.629			[92Lit2]
Orientation		a-axis	(c-axis)		[92Lit2]
T_m	°C	1825			[92Lit2]
F_A	10^{20} cm^{-3}/at%	1.54			[92Lit2]
Supplier data					
l_{max}	mm	20			[92Lit2]
d_{max}	mm	5			[92Lit2]
C	wt%	1.5–3			[92Lit2]

The absorption coefficient at 809 nm is α = 40 cm^{-1} for polarization parallel to the c-axis (π). The absorption range is from 801 to 821 nm.

References for 4.1

Overview literature

Charschan, S.S. (ed.): Lasers in Industry, Western Electric Series, New York: Van Nostrand Reinhold Co., 1972.
Gerrad, A., Burch, J.M.: Introduction to Matrix Methods in Optics, London: Wiley, 1975.
Kaminskii, A.A.: Laser Crystals, Berlin: Springer, 1990.
Kneubühl, F.K., Sigrist, M.W.: Laser, Stuttgart: Teubner, 1988.
Koechner, W.: Solid-State Laser Engineering, 5th ed., Berlin, Heidelberg: Springer, 1999.
Nonhof, C.J.: Material Processing with Nd-Lasers, Ayr, Scotland: Electrochem. Publ., 1988.
Naumann, H., Schröder, G.: Bauelemente der Optik, Taschenbuch der technischen Optik, 5. Aufl., München: Hanser Verlag, 1987.
Penzkofer, A.: Solid-State Lasers; Prog. Quantum Electron. **12** (1988) 291–427.
Siegmann, A.E.: An Introduction to Lasers and Masers, New York: Mc Graw Hill, 1971.
Sutter, E., Schreiber, P., Ott, G.: Handbuch Laser-Strahlenschutz, Berlin: Springer, 1989.
Weber, M.J. (ed.): Handbook of Laser Science and Technology, Vol. 1, Chemical Rubber Comp., Boca Raton, Florida: CRC Press, 1982.
Yariv, A.: Introduction to Optical Electronics, Pasadena, California: California Institute of Technology, 1976.
Hodgson, N., Weber, H.: Optical Resonators, London: Springer, 1997.
Saleh, B.E.A., Teich, M.C.: Fundamentals of Photonics, New York: John Wiley & Sons, 1991.

References cited in the text

66Gra Grau, G.K.: Output Laser Mirror for a Special Fundamental Mode Limited Parallel Beam (in German); AEÜ **20** (1966) 704–705.

69Bau Baues, P.: Huygens' Principle in Inhomogeneous Isotropic Media and a General Integral Equation Applicable to Optical Resonators; Opto-Electron. **1** (1969) 37–44.

69Web Weber, M.J., Bass, M., Andringa, K., Monchamp, R.R., Comperchio, E.: Czochralski Growth and Properties of $YAlO_3$ Laser Crystals; Appl. Phys. Lett. **15** (1969) 342–345.

70Fos Foster, J.D., Osterink, L.M.: Thermal Effects in a Nd:YAG Laser; J. Appl. Phys. **41** (1970) 3656–3663.

70Pip Pipes, L.A., Harvill, L.R.: Applied Mathematics for Engineers and Physicists, New York: Mc Graw Hill, 1970.

71Bal Baldwin, G.D.: Output power calculations for a continuously pumped Q-switched YAG:Nd^{+3} laser; IEEE J. Quantum Electron. **7** (1971) 220–224.

71Sla Slack, G.A., Oliver, D.W.: Thermal Conductivity of Garnets and Phonon Scattering by Rare-Earth Ions; Phys. Rev. B **4** (1971) 592–609.

72Kei Keig, G.A., DeShazer, L.G.: Laser Performance of Yttrium-Orthoaluminate Doped with Rare Earthes (in German); Laser Elektro Optik **3** (1972) 45–50.

72Mar Martin, W.S.: Multiple Internal Reflection Face-Pumped Laser; US Patent 3,633,126, 1972.

72Mas Massey, G.A.: Measurement of device parameters for Nd:$YAlO_3$ lasers; IEEE J. Quantum Electron. **8** (1972) 669–674.

72You Young, D.D., Jungling, K.C., Williamson, T.L., Nichols, E.R.: Holographic Interferometry Measurement of the Thermal Refractive Index Coefficient and Thermal Expansion Coefficient of Nd:YAG and Nd:YALO; IEEE J. Quantum Electron. **8** (1972) 720–721.

74DeS DeShaze, L.G., Bass, M., Ranon, U., Guha, J.K., Reed, E.D.: Laser performance of Nd^{3+} and Ho^{3+} in YVO_4 and Nd^{3+} in Gadolinium Gallium Garnet (GGG); Dig. Tech. Pap., 8th Int. Quantum Electron. Conf., 1974, p. 683.

75All Allied Synthetic Crystal Products, Charlotte, North Carolina: Lanthanum Beryllate: A New Laser Host of Great Promise, 1975.

76Jen Jenssen, H.P., Begley, R.F., Webb, R., Morris, R.C.: Spectroscopic properties and laser performance of Nd^{3+} in lanthanum beryllate; J. Appl. Phys. **47** (1976) 1496–1500.

76Kam Kaminskii, A.A., Butaeva, T.I., Ivanov, A.O., Mochalov, I.V., Petrosyan, A.G., Rogov, G.I., Fedorov, V.A.: New data on stimulated emission of crystals containing Er^{3+} and Ho^{3+} ions; Sov. Tech. Phys. Lett. (English Transl.) **2** (1976) 308–310.

76Sar Saruwatari, M., Kimura, T.: LED Pumped Lithium Neodymium Tetraphosphate Lasers; IEEE J. Quantum Electron. **12** (1976) 584–591.

77Mil Milam, D., Weber, M.J., Glass, A.J.: Nonlinear refractive index of fluoride crystals; Appl. Phys. Lett. **31** (1977) 822–825.

77Tuc Tucker, A.W., Birnbaum, M., Fincher, C.L., Erler, J.W.: Stimulated-emission cross section at 1064 and 1342 nm in Nd:YVO_4; J. Appl. Phys. **48** (1977) 4907–4911.

78Bol Boling, N.L., Birnbaum, M., Fincher, C.L., Erler, J.W.: Empirical relationships for predicting nonlinear refractive index changes in optical solids; IEEE J. Quantum Electron. **14** (1978) 601–608.

78Kam Kaminskii, A.A., Osiko, V.V., Sarkisov, S.E., Timoshechkin, M.I., Zharikov, E.V., Bohm, J., Reiche, P., Schultze, D.: Growth, spectroscopic investigations, and some new stimulated emission data of $Gd_3Ga_5O_{12}$:Nd^{3+} single crystals; Phys. Status Solidi (a) **49** (1978) 305–311.

78Rig Rigrod, W.W.: Homogeneously broadened CW laser with uniform distributed loss; IEEE J. Quantum Electron. **14** (1978) 377–381.

79Lin Linford, G.J., Saroyan, R.A., Trenholme, J.B., Weber, M.J.: Measurements and Modeling of Gain Coefficients for Neodymium Laser Glasses; IEEE J. Quantum Electron. **15** (1979) 510–523.

79Sch Schott: Nd-Phosphate glasses for the Laser Technique, LG 703 and LG 706, Product Information Nr. 7515, 1979.

80Ars Arsenjew, P.A., Bagdasarow, Ch.S., Bienert, K., Kustow, E.F., Potjomkim, A.W.: Crystals in Modern Laser Technique (in German), Leipzig: Akademische Verlagsgesellschaft, 1980.

80Sch Schindler, G.M.: Optimum output efficiency of homogeneously broadened lasers with constant loss; IEEE J. Quantum Electron. **16** (1980) 546–549.

80Wal Walling, J.C., Peterson, O.G., Jenssen, H.P., Morris, R.C., O'Dell, E.W.: Tunable alexandrite lasers; IEEE. J. Quantum Electron. **16** (1980) 1302–1315.

80Wax Waxler, R.M., Feldman, A.: Piezooptic Coefficients of Four Neodymium-Doped Laser Glasses; Appl. Opt. **19** (1980) 2481–2482.

81Bro Brown, D.C.: High-Peak-Power Nd:Glass Laser Systems, Berlin: Springer-Verlag, 1981.
81Her Heraeus: Nd:YAP Laser-Crystals, Data sheet, 1981.
81Kah Kahn, A., Lejus, A.M., Madsac, M., Théry, J., Vivien, D., Bernier, J.C.: Preparation, Structure, Optical and Magnetic Properties of Lanthanide Aluminate Single Crystals ($LnMAl_{11}O_{19}$); J. Appl. Phys. **52** (1981) 6864–6869.

82Kni Knights, M.G., Wing, W.F., Baer, J.W., Chicklis, E.P., Jenssen, H.P.: High-efficiency deep-red laser pumped by doubled Nd:YAG; IEEE J. Quantum Electron. **18** (1982) 163–166.
82Pol Pollak, T.M., Wing, W.F., Grasso, R.J., Chicklis, E.P., Jenssen, H.P.: CW laser operation of Nd:YLF; IEEE J. Quantum Electron. **18** (1982) 159–162.
82Web Weber, M.J. (ed.): Handbook of Laser Science and Technology, Vol. 1, Boca Raton, Florida: CRC Press, 1982, pp. 26–35.

83Min Mindak, M., Szydlak, J.: Examples of operating characteristics and power balance in pump cavity of CW Nd:YAG laser; Opt. Appl. **13** (1983) 407–419.
83Mur Murray, J.E.: Pulsed Gain and Thermal Lensing of Nd:LiF_4; IEEE J. Quantum Electron. **19** (1983) 488–490.

84Hor Horowitz, L., Band, Y.B., Kafri, O., Heller, D.F.: Thermal Lensing Analysis of Alexandrite Laser Rods by Moire Deflectometry; Appl. Opt. **23** (1984) 2229–2233.
84Mae Maeda, K., Wada, N., Umino, M., Abe, M., Takada, Y., Nakano, N., Kuroda, H.: Concentration dependence of fluorescence lifetime of Nd^{3+}-Doped $Gd_3Ga_5O_{12}$ lasers; Jpn. J. Appl. Phys. **23** (1984) L759–L760.
84Pet Petermann, K., Huber, G.: Broad band fluorescence of transition metal doped garnets and tungstates; J. Lumin. **31&32** (1984) 71–77.
84Wal Walling, J.C.: Properties of Alexandrite lasers, Manuscript of the talk presented at the Nato meeting, Italy, 1984.

85Alb Albrecht, G.F., Eggleston, J.M., Ewing, J.J.: Measurements of Ti^{3+}:Al_2O_3 as a lasing material; Opt. Commun. **52** (1985) 401–404.
85All Allied Synthetic Crystal Products, Charlotte, North Carolina: YAG Data sheet, 1985.
85Hoe Hoefer, C.S., Kirby, K.W., DeShazer, L.G.: Thermo-Optic Properties of Garnet Laser Crystals; IRD Quarterly Report, Malibu, CA: Hughes Research Labs, 1985.
85Hoy Hoya Optics, Fremont, CA: Data sheet, 1985.
85Kit Kitaeva, V.F., Zharikov, E.V., Chistyi, I.L.: The properties of crystals with garnet structure; Phys. Status Solidi (a) **92** (1985) 475–488.
85Kni Knights, M.G., Mosto, J., Chicklis, E.P.: High power TEM_{00} 2-μm Laser; Conf. Dig. CLEO (1985) 94.
85Kru Krupke, W.F.: Specific Heat Loading in Nd-Glas Lasers; LLNL-Report UCID-20531 DE36 002151, 1985.
85Lac Lacovara, P., Esterowitz, L., Allen, R.: Flash-lamp-pumped Ti^{3+}:Al_2O_3 laser using fluorescent conversion; Opt. Lett. **10** (1985) 273–275.
85Mar Marion, J.E.: Strengthening of Solid-State Laser Materials; Appl. Phys. Lett. **47** (1985) 694–696.
85Rap Rapoport, W.R., Samelson, H.: Alexandrite Slab Laser, LASER 85, Las Vegas, 1985.
85Wal Walling, J.C., Heller, D.F., Samelson, H., Harter, D.J., Pete, J.A., Morris, R.C.: Tunable Alexandrite Lasers: Development and Performance; IEEE J. Quantum Electron. **21** (1985) 1568–1581.

86Bar Barnes, N.P., Allen, R., Esterowitz, L., Chicklis, E.P., Knights, M.G., Jenssen, H.P.: Operation of an Er:YLF laser at 1.73 μm; IEEE J. Quantum Electron. **22** (1986) 337–343.

86Bas Bass, M., Shi W-Q., Kurtz, R., Kokta, M., Diegl, H.: Room Temperature of the 50 % Doped Er:YAG Laser at 2940 nm, Conf. Dig. CLEO, 1986, 3–7.

86Bro Brown, D.C., Lee, K.L.: Methods for Scaling High Average Power Laser Performance; Proc. SPIE **622** (1986) 30–41.

86Chi Chin, T., Morris, R.C., Kafri, O., Long, M., Heller, D.F.: Athermal Nd:BEL Lasers; Proc. SPIE **622** (1986) 53–60.

86Dri Driedger, K.P., Krause, W., Weber, H.: Average Refractive Powers of an Alexandrite Laser Rod; Opt. Commun. **57** (1986) 403–406.

86Hoy Hoya: Data sheet, 1986.

86Ima Imai, S., Ishida, S., Fujimori, Y., Ishikawa, K.: High Power Alexandrite Laser and its Applications, Conf. Dig. CLEO, 1986, 106.

86Kru1 Krupke, W.F.: Spectroscopic, Optical and Thermo-Mechanical Properties of GSGG and its Laser Performance, UCRL 93853 Preprint, 1986.

86Kru2 Krupke, W.F., Shinn, M.D., Marion, J.E., Caird, J.A., Stokowski, S.E.: Spectroscopic, Optical and Thermomechanical Properties of Neodymium- and Chromium-Doped Gadolinium Scandium Gallium Garnet; J. Opt. Soc. Am. B **3** (1986) 102–113.

86Lai Lai, S.T.: Review of Spectroscopic and Laser Properties of Emerald; Proc. SPIE **622** (1986) 146–150.

86Mei Meier, J.V., Barnes, N.P., Remelius, D.K., Kokta, M.: Flashlamp-pumped Cr^{3+}: GSAG Laser; IEEE J. Quantum Electron. **22** (1986) 2058–2064.

86Pay Payne, J.P., Evans, H.W.: Flashlamp-Pumped Lasing of Chromium-Doped GSG Garnet; Conf. Dig. CLEO (1986) 106.

86San Sanchez, A., Fahey, R.E., Strauss, A.J., Aggarwal, R.L.: Room-temperature continuous-wave operation of a Ti:Al_2O_3 laser; Opt. Lett. **11** (1986) 363–364.

86She Shen, H., Zhou, Y., Zeng, R., Yu, G., Ye, Q., Huang, C., Huang, X., Liao, H.: High Power 1.314 μm Nd:YAG Laser; Opt. Laser Technology, Aug. 1986, pp. 193–197.

86Tho Thomas, M.D., Chicklis, E.P.: High power 1.3 μm Nd:YAG Laser; Conf. Dig. CLEO, 1986, p. 214.

86Ucr UCRL-50021-86: High-Average-Power Lasers 7, Laser Program; Annual Report, 1986, pp. 7–151.

86Uni Union Carbide: CZ Ruby Laser Rods, Data sheet, 1986.

86Upp Uppal, J., Monga, J., Bhawalkar, D.: Study of Thermal Effects in an Nd Doped Phosphate Glass Laser Rod; IEEE J. Quantum Electron. **22** (1986) 2259–2265.

87Cer Cerqua, K.A., Lindquiat, A., Jacobs, S.D., Lambropoulos, J.: Strengthened Glass for High Average Power Laser Applications; Proc. SPIE **736** (1987) 13–21.

87Dae Dätwyler, M., Lüthy, W., Weber, H.P.: New wavelengths of the $YAlO_3$:Er laser; IEEE J. Quantum Electron. **23** (1987) 158–159.

87Fan Fan, T.Y., Huber, G., Byer, R.L.: Continuous-wave operation at 2.1 μm of a diode-laser-pumped, Tm sensitized Ho:$Y_3Al_5O_{12}$ laser at 300 K; Opt. Lett. **123** (1987) 678–680.

87Fra Frauchiger, J., Lüthy, W.: Power limits of a YAG:Er laser; Opt. Laser Technol. **19** (1987) 312–315.

87Fuh Fuhrmann, K., Hodgson, N., Hollinger, F., Weber, H.: Effective cross section of the Nd:YAG 1.0641-μm laser transition; J. Appl. Phys. **62** (1987) 4041–4044.

87Hag Hagen, W.F.: Thermal Fracture of Laser Glasses and Crystals; LLL Internal Report LRD 87-170/6061T, 1987.

87Hay Hayakawa, H., Maeda, K., Ishikawa, T., Yokoyama, T., Fujii, Y.: High average power Nd:$Gd_3Ga_5O_{12}$ Slab laser; Jpn. J. Appl. Phys. **26** (1987) L1623–L1625.

87Hod Hodgson, N., Weber, H.: Extraction efficiencies of laser oscillators (in German); Universität Kaiserslautern: Inst. für Physik, April 1987.
87Hof1 Hoffmann, H.J.: Matrix Materials for Laser Technique and Optic (in German); Offenlegungsschrift DE 36 17 362 A1, 1987.
87Hof2 Hoffmann, H.J., Iffländer, R., Weber, H.: A Laser with One Active Medium and Several Pump Sources (in German); Patent Application DE 37 26 279 C2, 1987.
87Hug Hughes, J.L.: High Power Continuous Wave Multi-Slab Laser Oscillator; Int. Patent WO 87/05160, 1987.
87Kel Kelly, J.H., Smith, D.L., Lee, J.C., Jacobs, S.D., Smith, D.J., Lambropoulos, J.C., Shoup III, M.J.: High Repetition Rate Cr-Nd:GSGG Active Mirror Amplifier; Opt. Lett. **12** (1987) 996–998.
87Lai Lai, S.T.: Highly Efficient Emerald Laser; J. Opt. Soc. Am. B **4** (1987) 1286–1290.
87Lee Lee, J.C., Jacobs, S.D.: Refractive Index and $\Delta n/\Delta T$ of Cr:Nd:GSGG at 1064 nm; Appl. Opt. **26** (1987) 777–778.
87Mar Marion, J.E.: Fracture mechanisms and strengthening of Slab lasers; Proc. SPIE **736** (1987) 2–12.
87Neu Neuroth, N.: Laser Glass: Status and Prospects; Opt. Eng. **26** (1987) 96–101.
87Non Nonhof, C.J., Keränen, R.: Pulse to pulse instabilities in a multimode Q-switched ND:YAG-laser; Proc. Laser 87 Optoelectronic, Munich, 1987, pp. 332–338.
87See Seelert, W., Strauss, E.: Absolute excited-state absorption cross section and fluorescence quantum efficiency of Cr^{3+}:Gadolinium Scandium Gallium Garnet; Opt. Lett. **12** (1987) 798–799.
87Web Weber, H.: Optimization of Nd-lasers (in German); Universität Kaiserslautern, Inst. für Physik, Interner Bericht, Feb. 1987.
87Wil Wildmann, D., Junghans, J., Jundt, H.F.: Laser scribing: State of the art (in German); Proc. Laser 87 Optoelectronic, Munich, 1987, pp. 586–589.

88Ber Berger, J., Welch, D.F., Streifer, W., Scifres, D.R., Hoffman, N.J., Smith, J.J., Radecki, D.: Fiber-Bundle Coupled, Diode End-Pumped Nd:YAG Laser; Opt. Lett. **13** (1988) 306–308.
88Dri Driedger, K.P., Iffländer, R.M., Weber, H.: Multirod resonators for high-power solid-state lasers with improved beam quality; IEEE J. Quantum Electron. **24** (1988) 665–674.
88Duc Duczynski, E.W., Heide, H.-J. v.d., Huber, G., Mitzscherlich, P., Petermann, K., Teichmann, H.-O.: Efficient Flashlamp Pumped Cr,Nd:YSAG Laser; Proc. SPIE **1021** (1988) 69–73.
88Fan Fan, T.Y., Huber, G., Byer, R.L., Mitzscherlich, P.: Spectroscopy and diode laser-pumped operation of Tm, Ho:YAG; IEEE J. Quantum Electron. **24** (1988) 924–933.
88Hay Hayden, J.S., Sapak, D.L., Hoffmann, H.J.: Advances in Glasses for High Average Power Laser Systems; Proc. SPIE **1021** (1988) 36.
88Hod1 Hodgson, N., Festkörperlaser-Institut Berlin: Personal communication, 1988.
88Hod2 Hodgson, N., Weber, H.: Measurement of Extraction Efficiency and Excitation Efficiency of Lasers; J. Mod. Opt. **35** (1988) 807–813.
88Hoe Hoefer, C.S., Kirby, K.W., DeShazer, L.G.: Thermo-Optic Properties of Gadolinium Garnet Laser Crystals, J. Opt. Soc. Am. B **5** (1988) 2327–2332.
88Hof Hoffman, H.J., Hayden, J.S.: Glasses as active materials for high average power solid-state lasers; Proc. SPIE **1021** (1988) 42–50.
88Jai Jain, R.K., Sipes, D.L., Pier, T.J., Hulse, G.R.: Diode-Pumped 1.3 μm Nd:YVO_4 Laser, Conf. Dig. CLEO, 1988, THB5.
88Jon Jones jr., W.B.: Slab Geometry Lasers; in: Cheo, P.K. (ed.): Handbook of Solid-State lasers, New York: Marcel Dekker Ltd, 1988, p. 581.
88Lit1 Litton Airtron Morris Plains, New Jersey: GSGG Data sheet GSGG S-4/88, 1988.
88Lit2 Litton Airtron Morris Plains, New Jersey: YAG Data sheet NDYAGS-4/88, 1988.

88Lit3 Litton Airtron Morris Plains, New Jersey: YLF Data sheet YLFS-4/88, 1988.
88Lun Lundt, H., Wacker Chemitronic: Personal communication, 1988/89.
88Man Mann, K., Weber, H.: Surface Heat Transfer Coefficient, Heat Efficiency, and Temperature of Pulsed Solid-State Lasers; J. Appl. Phys. **64** (1988) 1015–1021.
88Pen Penzkofer, A.: Solid-state lasers; Prog. Quantum Electron. **12** (1988) 366–369.
88Sch1 Schott Glass Techn. Inc.: APG-Laser Glass from Schott, Data sheet 2302/88, 1988.
88Sch2 Schott: Laser glass from Schott, Schott Catalog 2301, 1988.
88Tei1 Teichmann, H., Duczynski, E.W., Huber, G.: Efficient Flashlamp Pumped Operation of a Cr, Tm, Ho:YAG Laser at 2.08 μm; Conf. Dig. CLEO, 1988.
88Tei2 Teichmann, H., Duczynski, E.W., Huber, G.: 17 J Ho-Laser at 2 Microns; Proc. SPIE **1021** (1988) 74–81.
88Uni1 Union Carbide: Tm:Ho:Cr:YAG laser rods; Roditi communication, 1988.
88Uni2 Union Carbide: YAG:Nd Data; Data sheet, 1988.

89Ami Aminoff, C.G., Larat, C., Leduc, M., Laloë, F.: Optical Pumping of Helium with Arc Lamp Excited LNA Lasers; Rev. Phys. Appl. **24** (1989) 827–831.
89Car1 Carts, Y.A.: Titanium sapphire's star rises; Laser Focus World **9** (1989) 73–88.
89Car2 Carts, Y.A.: Flashlamp pumps Ti:sapphire laser; Laser Focus World **8** (1989) 21.
89Dev Devor, D.P., DeShazer, L.G., Pastor, R.C.: Nd:YAG Quantum Efficiency and Related Radiative Properties, IEEE J. Quantum Electron. **25** (1989) 1863–1873.
89Kig Kigre Inc. Hilton Head Island: QE-7S Erbium-Doped Phosphate Laser Glass, Data sheet LC500-10-89, 1989.
89Lup Lupei, V., Lupei, A., Georgescu, S.: Effects of Energy Transfer on Quantum Efficiency of YAG:Nd; J. Appl. Phys. **66** (1989) 3792–3797.
89Mar Marion, J.E., Pertica, A.J.: Materials for high average power lasers; Proc. SPIE **1040** (1989) 2–18.
89Qua Quarles, G.J., Rosenbaum, A., Marquadt, C.L., Esterowitz, L.: High efficiency 2.09 μm flashlamp-pumped laser; Appl. Phys. Lett. **55** (1989) 1062–1064.
89Rap Rapoport, W.R., Chin, T.: Laser and Laser Related Characteristics of Nd:BEL; Proc. SPIE **1040** (1989) 19–31.
89Rot Rotman, S.R.: Nonradiative energy transfer in Nd:YAG – evidence for the correlated placement of ions; Appl. Phys. Lett. **54** (1989) 2053–2055.
89Sta Stange, H., Petermann, K., Huber, G., Duczynski, E.W.: Continuous wave 1.6 μm laser action in Er doped garnets at room temperature; Appl. Phys. B **49** (1989) 269–273.
89Uni Union Carbide: Titanium-Doped Sapphire, Tunable Laser Crystals, Data sheet, 1989.
89Wac Wacker Chemitronic: Cr:Nd:GGG Laser Crystals, Data sheet, 1989.

90All1 Allied Synthetic Crystal Products Charlotte, North Carolina: YAG Data sheet, 1990.
90All2 Allik, T.H., Morrison, C.A., Gruber, J.B., Kokta, M.R.: Crystallography, Spectroscopic Analysis, and Lasing Properties of Nd^{3+}:$Y_3Sc_2Al_3O_{12}$; Phys. Rev B **41** (1990) 21–29.
90Arm Armagan, G., Buoncristiani, A.M., Edwards, W.C., Inge, A.T., DiBartolo, B.: Spectroscopic characterization of dynamical process for Tm, HO:YAG lasers; OSA Proc. Adv. Solid State Lasers **6** (1990) 144–149.
90Bae Baer, T.M.: High Efficiency Mode-Matched Solid-State Laser with Transverse Pumping and Cascaded Amplifier Stages; US Patent 4,894,839, 1990.
90Bor Borik, M.A., Gorbunov, P.V., Danileĭko, Y.K., Denker, B.I., Ivanov, A.D., Ilíchev, N.N., Larikov, A.V., Lebedeva, T.P., Maksimova, G.V., Motsartov, V.V., Musatov, A.G., Osiko, V.V., Pashinin, P.P.: High-Power Pulse-Periodic Neodymium Glass Laser with a Plate-Shaped Active Element; Sov. J. Quantum Electron. **20** (1990) 332–336.
90Cha Chase, L.L., Payne, S.A., Hughes, R.S., Davis, L.E.: Measurement of Thermal Lensing for the $LiCaAlF_6$:Cr^{3+} Laser Material; OSA Proc. Adv. Solid State Lasers **6** (1990) 83–85.

90Fil Filer, E.D., Morrison, C.A., Turner, G.A., Barnes, N.P.: Theoretical branching ratios for the $^5I_7 \rightarrow {}^5I^7$ levels of Ho^{3+} in the garnets $A_3B_2C_3O_{12}$ (A = Y, La, Lu, Gd; B = Al, Lu, SC, Ga; C = Al, Ga); OSA Proc. Adv. Solid State Lasers **6** (1990) 354–362.

90Hon Hongyuan, S., Yuping, Z., Ruirong, Z., Guifang, Y., Chenghui, H., Hong, L., Zhendong, Z.: New Advances in Nd:YAP-Lasers; Fujian Institute of Research on the Structure of Matter, Fuzhou, Fujian, China, 1990.

90Hov Hovies, F.E., Stuff, M., Kennedy, C.J., Vivian, B.: Low-level relaxation of Nd:YAG; OSA Proc. Adv. Solid State Lasers **9** (1990) 227–229.

90Ima Imai, S., Yamada, T., Fujimori, Y., Ishikawa, K.: A 20 W Cr^{3+}, Tm^{3+}, Ho^{3+}:YAG laser; Opt. Laser Technol. **22** (1990) 351–353.

90Kam Kaminskii, A.A.: Laser Crystals, Berlin: Springer-Verlag, 1990, p. 327.

90Kig Kigre Inc., Hilton Head Island: Glass Laser Rods, Data sheet Rods 500-10-90, 1990.

90Kur Kurtz, R., Fathe, L., Birnbaum, M.: New laser lines of erbium in yttrium aluminum garnet; OSA Proc. Adv. Solid State Lasers **6** (1990) 247–250.

90Lin Lin, J.T.: Doubled Jeopardy: The Blue-Green Race's New Players, Laser Optronics **12** (1990) 40.

90Moc Mochizuki, T., Unternährer, J.R., Amano, S., Tajima, H., Nakajima, S., Moriyama, M.: Development of High Power Solid-State Lasers at Hoya Corp., 1990.

90Qua1 Quarles, G.J., Marquardt, C.L., Esterowitz, L.: Efficient room-temperature operation of a flashlamp-pumped Cr;Tm:YAG laser at 2.014 μm; OSA Proc. Adv. Solid State Lasers **6** (1990) 150–153.

90Qua2 Quarles, G.J., Rosenbaum, A., Marquardt, C.L., Esterowitz, L.: Flash pumped, room-temperature 2 μm laser with 5 % slope efficiency; Proc. SPIE **1223** (1990) 221–229.

90Sch Schütz, I., Freitag, I., Wallenstein, R.: Minature self-frequency-doubling CW Nd:YAB laser pumped by a diode-laser; Opt. Commun. **77** (1990) 221–225.

90Wan Wang, S.C., Stone, R.E.: Characteristics of Neodymium Yttrium Aluminium Borate as a Diode-Pumped Laser Material; OSA Proc. Adv. Solid State Lasers **6** (1990) 23–25.

90Won Wong, S.K., Mathieu, P., Pace, P.: Eye-safe Nd:YAG laser; Appl. Phys. Lett. **57** (1990) 650–652.

90Zen Zeng, Z., Shen, H., Huang, M., Xu, H., Zeng, R., Zhou, Y., Yu, G., Huang, C.: Measurement of the Refractive Index and Thermal Refractive Index Coefficients of Nd:YAP Crystal; Appl. Opt. **29** (1990) 1281–1286.

91Ami Aminoff, C.G., Larat, C., Leduc, M., Viana, B., Vivien, D.: Characterization and Laser Properties of Lanthanum Magnesium Hexa-Aluminate Activated by Neodymium and Chromium; J. Lumin. **50** (1991) 21–29.

91Arm Armagan, G., Buoncristiani, A.M., Inge, A.T., DiBartolo, B.: Comparison of spectroscopic properties of Tm and Ho in YAG and YLF crystals; OSA Proc. Adv. Solid State Lasers **10** (1991) 222–226.

91Aub Aubert, J.J., LETI C.E.N.G., Grenoble: Personal communication, 1991.

91Bow Bowman, S.R., Winings, M.J., Auyeung, R.C.Y., Tucker, J.E., Searles, S., Feldmann, B.J.: Upconversion studies of flashlamp-pumped Cr, Tm, Ho: YAG; OSA Proc. Adv. Solid State Lasers **10** (1991) 172–177.

91Cha1 Chase, L.L., Payne, S.A., Smith, L.K.: Emission cross sections of the mid-infrared laser transitions of Ho^{3+}, Er^{3+} and Tm^{3+} in fluoride and oxide crystals; Adv. Solid State Lasers Tech. Dig. (1991) 118–120.

91Cha2 Chase, L.L., Payne, S.A., Smith, L.K., Kway, W.L., Krupke, W.F.: Emission cross sections and energy extraction for the mid-infrared transitions of Er, Tm and Ho in oxide and fluoride crystals; OSA Proc. Adv. Solid State Lasers **10** (1991) 161–165.

91Com Comaskey, B., Beach, R., Albrecht, G., Benett, B., Freitas, B., Petty, C., VanLue, D., Mundinger, D., Solarez, R.: High Average Power Diode Pumped Slab Laser; UCRL-JC-108447 Preprint, IEEE J. Quantum Electron., 1991.

91Coy Coyle, D.B.: Design of a High-Gain Laser Diode-Array Pumped Nd:YAG Alternative Precessive Slab Amplifier; IEEE J. Quantum Electron **27** (1991) 2327–2331.
91Hoy Hoya: Laser Glass, Data sheet E 9005-1A010D, 1991.
91Jey Jeys, T.H.: Suppression of laser spiking by intracavity second harmonic generation; Appl. Opt. **30** (1991) 1011–1018.
91Kam Kaminskii, A.A.: Achievements of modern crystal-laser physics; Ann Phys. **16** (1991) 639–706.
91Lac1 Lacovara, P., Choi, H.K., Wang, C.A., Aggarwal, R.L., Fan, T.Y.: Room-temperature diode-pumped Yb:YAG laser; Opt. Lett. **16** (1991) 1089–1091.
91Lac2 Lacovara, P., Choi, H.K., Wang, C.A., Aggarwal, R.L., Fan, T.Y.: Room-temperature InGaAs diode-pumped Yb:YAG laser, Adv. Solid State Lasers Conf. Dig. (1991) 220–222.
91Mar Marion, J.E., Weber, M.J.: Phosphate Laser Glasses; Eur. J. Solid State Inorg. Chem. **28** (1991) 271–287.
91Min Miniscalco, W.J., Quimby, R.S.: General procedure for the analysis of Er^{3+} cross sections; Opt. Lett. **16** (1991) 258–260.
91Ohi Ohishi, Y., Kanamori, T., Kitagawa, T., Takahashi, S., Snitzer, E., Sigel jr., G.H.: Pr^{3+}-doped fluoride fiber amplifier operating at 1.31 μm; Opt. Lett. **16** (1991) 1747–1749.
91Pet Petricevic, A.S., Alfano, R.R., Seas, A.: Slope efficiency measurements of a chromium-doped forsterite laser; Opt. Lett. **16** (1991) 811–813.
91Qua Quarles, G., Pinto, J.F., Esterowitz, L.: Broad tunability of flash-pumped, Tm-Activated garnet lasers; OSA Proc. Adv. Solid State Lasers **10** (1991) 167–171.

92Ara Arahira, S., Watanabe, K., Shinozaki, K., Ogawa, Y.: Successive excited-state absorption through a multistep process in highly Er^{3+}-doped fiber pumped by a 1.48-μm laser diode; Opt. Lett. **17** (1992) 1679–1681.
92Com Comaskey, B., Beach, R., Albrecht, G., Benett, B., Freitas, B., Petty, C., VanLue, D., Mundinger, D., Solarez, R.: Diode Pumped 275 Watt Average Power Nd:YAG Slab Laser; UCRL-JC-109185 Preprint, SPIE OE LASE 92, 1992.
92Kuz Kuzmin, O., FIRN, Krasnodar, USSR: Personal communication, 1992.
92Lit1 Litton Airtron Charlotte, North Carolina: Calculated Cr, Tm, Ho: YAG compositions; Technical Brief 0813, 1992.
92Lit2 Litton Airtron Charlotte, North Carolina: Nd: Yttrium Vanadate; Technical Brief, 1992.
92Pay Payne, S.A., Krupke, W.F., Smith, L.K., DeLoach, L.D., Kway, W.L.: Laser properties of Yb-doped fluorapatite; Adv. Solid State Lasers Conf. Dig. (1992) Pd8-1–Pd8-4.

93Alk Alkor Techn. Inc., St. Petersburg, 198035 Russia: Nd:KGW laser Rods, Data sheet, 1993.
93Bur Burnham, R., Bournes, P., Kasinski, J., Le, K., DiBiase, D.: High-Power-Diode-Pumped Solid-State Industrial Laser; OSA Conf. Dig. Adv. Solid State Lasers (1993) AMA3-1.
93Cao Cao, J.D., Laliberte, B.M., Minns, R.A., Po, H., Robinson, R.F., Rockney, B.H., Tricca, R.R., Zhang, Y.H.: Five Watt Single Transverse Mode Neodymium-Doped Fiber Laser, Conf. Dig. CLEO, 1993, p. 622.
93Com Comaskey, B., Albrecht, G.F., Beach, R.J., Moran, B.D., Solerz, R.W.: Flash-Lamp-Pumped Laser Operation of Nd^{3+}:Y_2SiO_5 at 1.074 μm; Opt. Lett. **18** (1993) 2029–2031.
93Cth Conf. Dig. CLEO CthF-4, 1993, p. 409.
93DeL DeLoach, L.D., Payne, S.A., Chase, L.L., Smith, L.K., Kway, W.L., Krupke, W.F.: Evaluation of Absorption and Emission Properties of Yb^{3+} Doped Crystals for Laser Applications, University of California, LLNL Livermore, 1993.
93Eic Eichler, H.J., Liu, B.: Gepulster $LiYF_4$: Pr^{3+}-Laser, TU-Berlin, 1993.

93Gol Golla, D., Freitag, I., Zellmer, H., Schöne, W., Kröpke, I., Welling, H.: 15 W Single-Frequency Operation of a CW, Diode Laser-Pumped Nd:YAG Ring Laser; Opt. Commun. **98** (1993) 86–90.

93Hod Hodgson, N., Golding, D.J.: High power 1.444 μm Nd:YAG laser and its medical applications; Laser Optoelektronik **25** (1993) 38–47.

93Hol Hollinger, F., Laser Institute FLI-Berlin: Personal communication, 1993.

93Kam Kaminskii, A.A., Eichler, H.J., Liu, B., Meindl, P.: $LiYF_4:Pr^{3+}$ Laser at 639.5 nm with 30 J flashlamp pumping and 87 mJ output energy; Phys. Status Solidi (a) **138** (1993) K45–K48.

93Mor Morris, P.J., Lüthy, W., Weber, H.P.: Operation of Resonantly Pumped Tm:Ho:YAG in Active Mirror Mode; Opt. Commun. **104** (1993) 97–101.

93Nak Nakatsuka, M., Naito, K., Fujimoto, Y., Yamanaka, M., Nakai, S., Takeuchi, T., Sonehara, T.: Nd:Quartz Laser Rod Produced by the Sol-Gel Method with no Additives; Conf. Dig. CLEO, 1993, p. 590.

93Net Neto, J.A.M., Hewak, D.W., Pearson, A.D., Samson, B.N., Tate, H., Deol, R.S., Brocklesby, W.S., Payne, D.N.: Radiative and Nonradiative Properties of Prasodymium-Doped Glasses; Conf. Dig. CLEO, 1993, p. 498.

93Opt Optron Technology Ltd, 1000 Sofia Bulgaria, 67 Vassil Levsky Blvd.: Nd:KGW Data sheet, 1993.

93Ram Ramet Ltd, Moscow 109017: Product Data sheet, 1993.

93Tho Thogersen, J., Bjerre, N.: Multiphoton absorption and cooperative upconversion excitation in Er^{3+}-doped fibers; Opt. Lett. **18** (1993) 197–199.

94Bra1 Brand, T.: Excitation Efficiency and Heat Transfer Efficiency of Diode-pumped High-Power Solid-State Lasers (in German); Dissertation TU-Berlin, 1994.

94Bra2 Brand, T.: Solid-State Laser Setup; Offenlegungsschrift DE 44 11 599 A1, 1994.

94Gie Giesen, A., Hügel, H., Voss, A., Wittig, K., Brauch, U., Opower, H.: Scalable concept for diode-pumped high-power solid-state lasers, Appl. Phys. B **58** (1994) 365.

94Hof Hoffstädt, A.: High-average-power flash-lamp-pumped Ti:sapphire laser; Opt. Lett. **19** (1994) 1523.

94Pet Petermann, K., Universität Hamburg: Personal communication, 1994.

95Cas Castech Crystals: Data sheet, 1995.

95Esm Esmeria, J.M., Ishii, H., Sato, M., Ito, H.: Efficient continous-wave lasing operation of $Nd:KGd(WO_4)_2$ at 1.067 μm with diode and Ti:sapphire laser pumping; Opt. Lett. **20** (1995) 1538–1540.

95Sum1 Sumida, D.S., Fan, T.Y.: Radiation trapping in solid-state laser media and its impact on fluorescence lifetime and emission cross section measurements; OSA Proc. Adv. Solid State Lasers **24** (1995) 542–544.

95Sum2 Sumida, D.S., Fan, T.Y., Hutcheson, R.: Spectroscopy and diode-pumped lasing of Yb^{3+}-doped $Lu_3Al_5O_{12}$ (Yb:LuAG); OSA Proc. Adv. Solid State Lasers **24** (1995) 348–350.

95Zel Zellmer, H., Willamowski, U., Tünnermann, A., Welling, H., Unger, S., Reichel, V., Müller, H.-R., Kirchhof, J., Albers, P.: High Power CW Neodymium-Doped Fiber Laser Operating at 9.2 W with High Beam Quality; Opt. Lett. **20** (1995) 578–580.

96Bre Bremlas Lasertechnik, Bremen: Data Sheet, 1996.

96Gol Golla, D., Bode, M., Schöne, W., Tünnermann, A.: 62-W CW TEM_{00} Nd:YAG Laser Side-Pumped by Fiber-Coupled Diode Lasers; Opt. Lett. **21** (1996) 210–212.

96Klo Klocek, P.: Inorganic Optical Materials, Critical Rev., Opt. Sci. Technol.; Proc. SPIE **CR64** (1996) 30.

99Dom Dominic, V., MacCormack, S., Waarts, R., Sanders, S., Bicknese, S., Dohle, R., Wolak, E., Yeh, P.S., Zucker, E.: 110 W Fibre Laser; Electr. Lett. **35** (1999) 1158.

99Koe Koechner, W.: Solid-state laser engineering, 5th ed., Berlin, Heidelberg: Springer-Verlag, 1999.

00Alv Alvarez-Chavez, J.A., Offerhaus, H.L., Nilsson, J., Turner, P.W., Clarkson, W.A., Richarson, D.J.: High-Energy, High-Power Ytterbium-Doped Q-switched Fiber Laser; Opt. Lett. **25** (2000) 37.

00Tue Tünnermann, A., Zellmer, H., Schöne, W., Giesen, A., Contag, K.: Solid-State Lasers; in: Diehl, R. (ed.): High-Power Diode Lasers, Berlin: Springer-Verlag, 2000.

01Aki Akiyama, Y., Takada, H., Yuasa, H., Nishida, N.: High-Power All-Solid-State Laser Technology: Rod-Type Laser; Proc. 5th Symp. of Adv. Phot. Proc. and Meas. Techn., Tokyo, 2001, Poster 1.

01Fuj1 Fujikawa, S., Futura, K., Kojima, T., Takaneda, Y., Yasui, K., Tanaka, M.: Development of a 1-kW High-Beam-Quality, Highly-Efficient Diode-Pumped Solid-State Laser; Proc. 5th Symp. of Adv. Phot. Proc. and Meas. Techn., Tokyo, 2001, Poster 9.

01Fuj2 Fujikawa, S., Futura, K., Yasui, K.: Highly Efficient, High-Brightness Diode Stacks-Side-Pumped Nd:YAG Rod Laser; Proc. SPIE **4267** (2001) 96.

01Hoe Höfer, S., Liem, A., Limpert, J., Zellmer, H., Tünnermann, A., Unger, S., Jetschke, S., Müller, H.-R., Freitag, I.: Single-frequency Master-Oscillator Fiber Power Amplifier System Emitting 20 W of Power; Opt. Lett. **26** (2001) 1326–1328.

01Iff Iffländer, R.: Solid-State Lasers for Materials Processing, Berlin: Springer, 2001.

01Sat Sato, M., Naito, S.: Development of High Power Slab-Type Laser; Proc. 5th Symp. of Adv. Phot. Proc. and Meas. Techn., Tokyo, 2001, Poster 3.

01Sek Sekiguchi, H., Ito, K., Yamaura, H., Tanaka, A., Senda, Y., Okada, K., Toranati, H., Kann, H., Ueda, K.: Developments of High Average Power Fiber lasers; Proc. 5th Symp. of Adv. Phot. Proc. and Meas. Techn., Tokyo, 2001, Poster 5.

02Der Dergachev, A., Wall, K., Moulton, P.F.: A CW Side-Pumped TM:YLF Laser; Proc. ASSL (2002) WA1-1.

02Hod Hodgson, N., Hoffmann, H.J., Ter-Mikirtychev, V., Jordan, W.: Diode-Pumped, 220 W Ultra-Thin Nd:YAG Slab Laser with Near-Diffraction Limited Beam Quality; Proc. ASSL (2002) PD2-1.

02Hua Hua, R., Liao, Y., Franjic, K., Bruner, B., Miller, R.J.D.: A 49.5 W Nd:YVO_4 Laser Using the Disc-Anvil Configuration; Proc. ASSL (2002) TuC1-1.

02Lai Lai, K.S., Xie, W.J., Lim, Y.L., Lau, E., Chia, L., Phua, P.B.: A 150 W 2-micron Diode-Pumped Tm:YAG Laser; Proc. ASSL (2002) WE6-1.

02Lie Lieto, A.D., Minguzzi, P., Pirastu, A., Sanguinetti, S., Toncelli, A., Magni, V.: High-Power Diffraction-Limited Diode-Pumped Nd:YVO_4 CW Laser at 1.34 μm; Proc. ASSL (2002) PD6-1.

02Lu Lu, J., Murai, T., Takaichi, K., Uematsu, T., Ueda K.: 1.46 kW CW Nd:YAG Ceramic Laser; Proc. ASSL (2002) WE1-1.

02Mac Machan, J.P., Long, W.H., Zamel, J., Marabella, L.: 5.4 kW Diode-Pumped, 2.4x Diffraction-Limited Nd:YAG Laser for Material Processing; Proc. ASSL (2002) PD1-1.

02Ost Ostermeyer, M., Klemz, G., Kubina, P., Menzel, R.: Enhanced Brightness and Extraction Efficiency of Nd:YAG Rod Laser Resulting in 180 W Output Power with $M^2 < 1.2$; Proc. ASSL (2002) WE7-1.

02Pla Platonov, N.S., Gapontsev, D.V., Gapontsev, V.P., Shumilin, V.: 135 W CW Fiber Laser With Perfect Single Mode Output; Proc. CLEO (2002) CPDC3-2.

02Sch Schnitzler, C., Schmidt, G., Höfer, M., Hoffmann, D., Poprawe, R.: A 500 W High Brightness Diode End-Pumped Nd:YAG Slab Laser; Proc. ASSL (2002) WE2-1.

4.2 Glasses

H.-J. Hoffmann

4.2.1 General properties of laser glasses

4.2.1.1 Basic considerations

Glasses are solids. Thus, in principle one observes absorption and fluorescence bands of laser active ions in glasses as matrices similar to those in crystals. In fact, soon after the first observation of laser action with ruby (i.e. Al_2O_3 doped with chromium) by Maiman in 1960 [60Mai1, 60Mai2], Snitzer reported on laser emission of a barium crown glass doped with neodymium in 1961 [61Sni1, 61Sni2]. However, there are specific differences between crystals and glasses: In crystals, the laser active ions occupy lattice sites with the same environment irrespective of the individual ion due to the periodicity. Depending on the symmetry of the respective lattice site and on the selection rules to be obeyed, some transitions between the ionic levels may be forbidden. The influence of the lattice on the individual active ion is seen in good crystals essentially by relatively small effects, such as the lattice vibrations and the macroscopic stress fields. This causes some broadening of sharp absorption and fluorescence lines.

In contrast to most crystals, the stoichiometry and the arrangement of the constituents are statistically varying in glasses. Thus, the local environment of the individual ions changes from site to site in the glassy network, even if the coordination of a given kind of ion is the same. This can result in a strong inhomogeneous broadening of otherwise sharp absorption and fluorescence lines. (As an example, the absorption spectrum of a Nd-doped phosphate glass is shown in Fig. 4.2.1. For comparison with crystalline materials see Figs. 4.1.47 and 4.1.48 in Sect. 4.1.2, e.g.) Furthermore, the symmetry of the energy levels can be disturbed and otherwise forbidden transitions may be

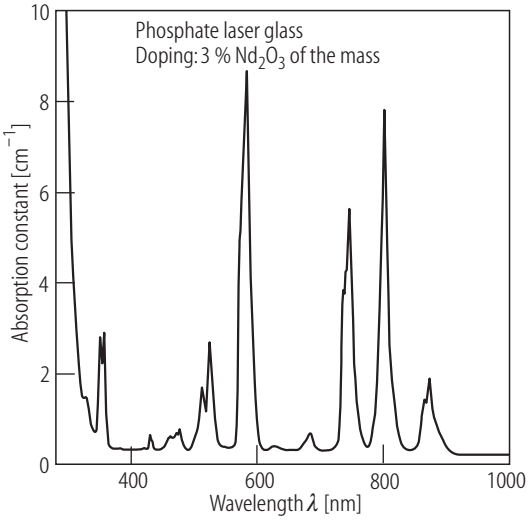

Fig. 4.2.1. Absorption spectrum of neodymium in a phosphate laser glass.

allowed. The broadening of the energy levels (including the laser active levels) facilitates the optical pumping by flashlights. It reduces the average cross section for stimulated emission resulting in a smaller loss due to Amplified Spontaneous Emission (ASE) and allows tuning over a larger interval of wavelength.

Glasses can be melt in large quantities with excellent homogeneity. In this respect, the homogeneity of crystals may be disturbed by stacking faults and other mismatch during crystal growth. The time to grow large volumes of single crystals may be prohibiting long, since the crystals must necessarily grow layer by layer.

4.2.1.2 Lanthanides as active ions

The rare-earth or lanthanide ions in their two-, three- or four-valence state (lanthanum La^{3+}, cerium Ce^{3+}/Ce^{4+}, praseodymium Pr^{3+}/Pr^{4+}, neodymium Nd^{3+}, promethium Pm^{3+}, samarium Sm^{2+}/Sm^{3+}, europium Eu^{2+}/Eu^{3+}, gadolinium Gd^{3+}, terbium Tb^{3+}/Tb^{4+}, dysprosium Dy^{3+}, holmium Ho^{3+}, erbium Er^{3+}, thulium Tm^{2+}/Tm^{3+}, ytterbium Yb^{2+}/Yb^{3+}, and lutetium Lu^{3+}) are generally considered as suitable laser active ions if they show electronic transitions in the inner shielded 4f-shell. The 6s-, 5d- and some of the 4f-orbitals are used for the bonding states to neighboring atoms. The transitions between the inner 4f-levels (f–f transitions) usually correspond to rather sharp absorption and emission lines of these ions. The sharp emission lines favor laser action. The electronic configuration of the outer atomic shells is given in Table 4.2.1. There are in total 7 different 4f-orbitals if one neglects the spin quantum number. According to Hund's rule, these 4f-orbitals are filled with increasing order number first by just one electron each. Thereafter the double occupancy starts with the terbium until all orbitals are occupied by two electrons for the ytterbium. For a survey of the relevant energy levels see [63Dic, 68Die, 81Kam, 90Fra].

Table 4.2.1. Electron configuration of the outer shells of the rare-earth atoms and oxide valence states.

Rare earth element	La	Ce	Pr	Nd	Pm	Sm	Eu	Gd	Tb	Dy	Ho	Er	Tm	Yb	Lu
Order number	57	58	59	60	61	62	63	64	65	66	67	68	69	70	71
4f shell	–	2	3	4	5	6	7	7	9	10	11	12	13	14	14
5d shell	1	–	–	–	–	–	–	1	–	–	–	–	–	–	1
6s shell	2	2	2	2	2	2	2	2	2	2	2	2	2	2	2
Oxide valence states	3+	3+	3+	3+	3+	2+	2+	3+	3+	3+	3+	3+	2+	2+	3+
		4+	4+			3+	3+		4+				3+	3+	

Laser action of many rare-earth ions has been observed in the visible and infrared spectral regions (with the exception of Gd^{3+}, which lases in the UV) using bulk glasses or glass fibers [86Poo, 88Ain1]. The doping is usually achieved by adding a suitable rare-earth compound to the batch of the glass melt or by rather special elaborated doping techniques mainly to produce preforms of fibers [86Poo, 87Tow, 88Ain2, 89Mor]. Fibers have the advantage of being pumped longitudinally with other laser sources, such as diode lasers, and of guiding the laser beam.

For lanthanum and lutetium ions f–f transitions are absent, since the 4f-shell is empty or completely filled. Ce^{3+} has f–f transitions in the IR at about 2500 cm^{-1}. This transition is masked in oxide glasses by the excitation of ionic vibrations of the matrix. Gd^{3+} does not show suitable pumping bands in the visible spectrum but in the UV. Promethium has no stable isotopes. The possibility and early attempts to use transitions of Dy^{3+} ions in glassy matrices have been reported in [94Hew, 94Sam, 99Tan, 00Flo]. A survey of rare-earth ions in different glasses (silicates, phosphates, fluorides, e.g.) used successfully for lasing is given in Table 4.2.2.

Table 4.2.2. Laser active rare-earth ions in glasses, approximate laser wavelengths, possible sensitizing ions and references.

Ion	Laser wavelength [nm]	Sensitizing ions	References
Pr^{3+}	890, 1080, 1310		[89Per, 91Oho]
Nd^{3+}	1060, 920, 1340, 1310–1360	Ce^{3+}, Cr^{3+}, Mn^{2+}, Tb^{3+}, Eu^{3+}, UO_2^{2+}, Yb^{3+}	[61Sni1, 61Sni2, 63Mau, 64Cab, 64Gan1, 64Gan3, 64Mau, 64Pea2, 65Kar, 65Shi, 74Sto, 90Miy]
Pm^{3+}	933, 1098		[87Kru]
Sm^{3+}	650		[88Far]
Gd^{3+}	312.5		[62Gan1]
Tb^{3+}	542		[68And]
Dy^{3+}	2900		[03Jac]
Ho^{3+}	1380, 2080, 2830–2950	Er^{3+}, Yb^{3+}, Tm^{3+}	[62Gan2, 65Gan1, 88Bri, 89Han2, 90Web, 90Wet]
Er^{3+}	1540, 850, 990, 1660, 1720, 2750, 2670–2830	Cr^{3+}, Yb^{3+}, Mo^{3+}	[65Gan2, 65Sni, 66Dau, 91Wet, 90Sma, 01Phi]
Tm^{3+}	820, 1470, 1780–2056, 1650–2000, 2300	Er^{3+}, Yb^{3+}	[67Gan, 88Est, 89Han1, 89All, 90Han, 90Bar]
Yb^{3+}	1000–1060, 1015–1140, 980	Nd^{3+}, Ce^{3+}, Cr^{3+}	[62Etz, 62Gan3, 64Gan2, 64Pea1, 66Dau, 66Sni, 88Han, 89Arm]

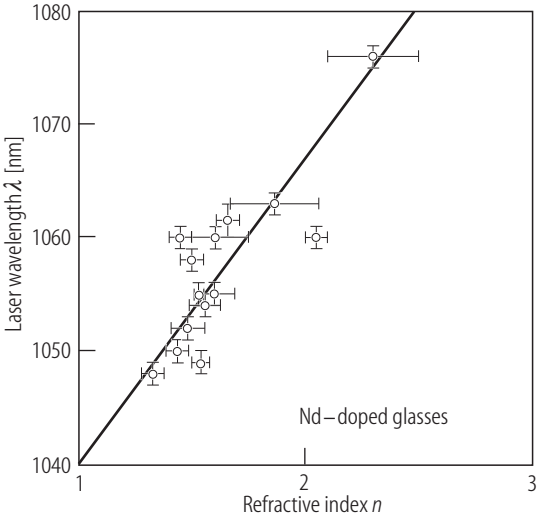

Fig. 4.2.2. The laser wavelength of the $^4F_{3/2} \rightarrow {}^4I_{11/2}$ transition of Nd^{3+} in different glasses as a function of the refractive index n. Data from Table 4.2.3. The solid line shows $\lambda_{max} = (1013 + 27 \cdot n)$ nm.

The laser lines given in Table 4.2.2 are approximate only, since the wavelengths depend on the specific glass composition and on the respective configuration of the laser. An example of the shift of the laser line with the refractive index (which depends on the polarizability of the ions of the matrix and thus also on the local environment of the laser active ions) is shown for the $^4F_{3/2} \rightarrow {}^4I_{11/2}$ transition of Nd^{3+} in Fig. 4.2.2. The shape and the intensities of the absorption and emission lines are evaluated according to a theory given by Judd [62Jud] and Ofelt [62Ofe] to calculate the cross sections for stimulated emissions, σ_{se}. It was first applied to laser glasses by Krupke [74Kru]. The spectroscopic properties of trivalent rare-earth ions in fluorophosphate glasses have been analyzed recently in [98Bin]. A survey of the Judd–Ofelt parameters in different matrices is given by Görller-Walrand and Binnemans [98Goe].

Useful transitions for absorption and laser action of the rare-earth ions in glasses are mostly the same as those in crystals (see Chap. 4.1). The glasses have also been co-doped with other ions or sensitized (using e.g. other rare-earth ions or chromium ions) in order to absorb a larger part of the pumping spectrum. However, the maximum thermal load per excited active ion is larger, since the energy transfer from the sensitizing ions to the lasing ions is less than 100 %. Thus, the maximum laser emission to be admitted without breaking of the active material is decreased, although the total pumping power may be decreased considerably by the co-doping. Using laser diodes, however, the pumping occurs with a very large efficiency. In this case, the co-doping does not play an important role any longer, except that the pumping of the active laser ions occurs essentially via the sensitizing ions.

4.2.1.3 Glasses doped with Nd^{3+}

Among the ions listed in Table 4.2.2, neodymium is the most prominent 4-level-system used to lase. The cross sections for absorption and stimulated emission of Nd^{3+} as the active ions as well as many other parameters have been investigated for many different glass compositions. The glass systems are usually named according to their most characteristic component. In Table 4.2.3 many of these glass systems which have been used as matrices for the most widely investigated Nd^{3+} ion with its $^4F_{3/2} \rightarrow {}^4I_{11/2}$ transition are listed together with the range of some important parameters to characterize the lasing properties, i.e., the cross section for stimulated emission σ_{se}, the radiative lifetime τ_0, the wavelength of the fluorescence maximum λ_{max}, the full width at half maximum or FWHM, and the product of the refractive index n_0 with the nonlinear refractive index γ.

Glasses doped with neodymium are commercially available in large quantities. Among the Nd^{3+}-doped glasses, the phosphate glasses are favorites, since the overall performance seems to be an optimum with respect to many technical parameters. Some types of phosphate glasses show a minimum thermal lensing. If laser glass is produced in contact with platinum special care has to be taken to avoid in the glass platinum particles, which may act as the origin of cracks at very high fluence levels [88Hay]. Because of their transmittance in the IR spectral region, heavy-metal fluoride or – more generally – halide glasses have found widespread interest in the technical literature [75Pou, 77Pou, 78Luc, 83Pou, 84Tra, 85Dre, 89Per, 90Fra, 98Bin]. A prominent example of this type of glass is ZBLAN (55 ZrF_4·18 BaF_2·6 LaF_3·4 AlF_3·17 NaF, quantities in mol %) [89Luc]. The expected properties, however, have not yet been fully achieved.

The most powerful lasers used for nuclear fusion experiments possess neodymium-doped glasses as active materials with the lasing line at about 1060 nm, whereas the other possible laser lines of Nd^{3+} (with minor efficiency) at about 920 nm and 1340 nm are not used but for special low-power applications. Performance data achieved by one of the ten arms of the Nova laser at the Lawrence Livermore National Laboratory (California) until 1999 are 680 J within 440 femtoseconds, which results in more than one petawatt power [00Per]. This high power is achieved by stretching a short pulse and large diameter before amplification in a laser amplifier made of active laser glass and subsequent pulse compression before focusing on the target. The stretching of the pulse is necessary in order to avoid destruction of the optical components due to high power density during the pulse. The pulse compression is done in vacuum without optical elements in the final path. The power density of the focused beam is nearly 10^{21} W/cm^2 with an energy density of $3 \cdot 10^{10}$ J/cm^3 [00Per]. A laser with an optical energy of 2 MJ and optical peak power in excess of 500 TW (long pulses of several ns) using Nd-doped phosphate glasses is currently (present year: 2007) under construction [00Cam] and will be in operation in the near future.

Table 4.2.3. Important parameters of the $^4F_{3/2} \rightarrow {}^4I_{11/2}$ transition of the Nd^{3+} ion in different glass systems.

Glass type	Range of refractive indices n_0 [90Wet]	σ_{se} [10^{-20} cm^2]	Fluorescence parameters of the $^4F_{3/2} \rightarrow {}^4I_{11/2}$ transition			Typical $n_0\gamma$ [10^{-20} m^2/W]	References
			τ_0 [10^{-6} s]	λ_{max} [nm]	FWHM [nm]		
silicate	1.46–1.75	1–3.5	300–1000	1060	30–40	5.9–6.7	[81Sto, 76Jac]
borate	1.51–1.69	1–2	50–400	1055	30–40	3.8	[81Sto]
silicoborate	1.45–1.55*	0.8–3	200–800	1058	30	5	[81Sto]
phosphate	1.49–1.63	1.8–4.7	100–500	1054	20–30	3.8–5	[81Sto, 76Jac]
tellurite	2.0–2.1	3–5.1	140–240	1060	25–30	41.9	[81Sto, 81Web2]
fluorosilicoborate	1.4–1.5*	1–1.7	300	1060	30	3.4–4.6	[81Sto]
fluorophosphate	1.41–1.56	1.7–3.8	350–500	1052	25–31	2.1–2.9	[81Sto, 80Sto]
fluoroberyllate	1.28–1.38	1.6–4	460–900	1048	18–28	1.3	[81Sto, 79Cli, 79Vid]
fluorozirconate	1.50–1.58*	2.9–3	430–450	1049	26	5	[75Pou, 78Luc]
fluoroaluminate	1.39–1.49	2.2–2.9	400–600	1050	30–33	2.1	[81Sto]
chloride	1.67–2.06	6–6.3	180–220	1063	20	> 29.3	[82Web]
chlorophosphate	1.51–1.55	5.2–5.4	290–300	1055	20–23	> 5.9	[81Web1]
sulphide	2.1–2.5	6.9–8.2	60–100	1076	21	> 29.3	[77Luc, 80Auz, 82Bor]
germanate	1.61–1.71	1.7–2.5	300–460	1060–1063	36–43		[90Web]

* Estimated range of the refractive index.

σ_{se} : cross section for stimulated emission of the $^4F_{3/2} \rightarrow {}^4I_{11/2}$ transition,
τ_0 : limiting radiative lifetime for low concentrations,
λ_{max} : wavelength of the fluorescence maximum,
FWHM : full width at half maximum of the $^4F_{3/2} \rightarrow {}^4I_{11/2}$ transition,
$n_0\gamma$: product of the refractive index n_0 with the nonlinear refractive index γ (adopted from [87Neu]).
The data of FWHM are partly replaced by the effective line width defined by $\Delta\lambda_{eff} = \frac{1}{I(\lambda_{max})} \int I(\lambda) d\lambda$, which is close to FWHM ($I(\lambda)$ is the intensity at the wavelength λ and $I(\lambda_{max})$ is the intensity of the fluorescence maximum of the line).

4.2.1.4 Radiative lifetime and concentration quenching

Nd-doped glasses are used mainly to produce high-energy pulses. Prerequisite to achieve this is a large number of excited active ions. Thus, one might assume that this problem can be solved simply by increasing the doping concentration. The effect of concentration quenching of the fluorescence and clustering of the active ions, however, becomes effective at high doping level, thus limiting the useful range of their concentration. Figure 4.2.3 shows how the *radiative lifetime*, τ, of the upper lasing level decreases with increasing concentration of the active ions due to additional radiationless transitions according to

$$\tau = \frac{\tau_0}{1 + \left(\frac{C}{C_{1/2}}\right)^2} , \tag{4.2.1}$$

wherein τ_0 is the lifetime at low concentration, C is the doping concentration and $C_{1/2}$ is the characteristic quenching concentration, for which the lifetime decreases to $\tau_0/2$. $C_{1/2}$ is a characteristic of the glass type. For the $^4F_{3/2} \rightarrow {}^4I_{11/2}$ transition of Nd^{3+} ions in phosphate glasses, $C_{1/2}$ is in the order of $(7-10) \cdot 10^{20}$ cm^{-3}. It is interesting to note that concentration quenching occurs for phosphate glasses at relatively large concentrations of the laser active ions. The emission of photons decreases with decreasing radiative lifetime, since an additional non-radiative deexcitation channel opens at large concentrations. Thus, the radiative quantum yield, η, which can be expressed by the ratio of the probability of radiative transitions to the probability of all transitions from the upper lasing level

$$\eta = \frac{\tau_0^{-1}}{\tau^{-1}} = \frac{1}{1 + \left(\frac{C}{C_{1/2}}\right)^2} , \tag{4.2.2}$$

is of the same type as shown in Fig. 4.2.3. In addition to the concentration quenching (or self-quenching) radiationless energy transfer from the upper lasing level to OH^- groups and transition-metal ions, which usually possess rather broad absorption bands in glasses, is possible and may degrade the quantum yield and the lifetime, which is not necessarily an exponential in this case. Thus, special care has to be taken to avoid such impurities and to produce the glasses under special "dry" conditions. Furthermore, the transition metals may cause absorption bands at the laser lines, which reduces the gain (see [88Sap], e.g.). Unfortunately, very often the specific residual absorption is not characterized clearly in the literature, since "absorption coefficients" or "absorbance" or "absorption" or "attenuation coefficients" are used without specifying the procedure the numbers have been obtained.

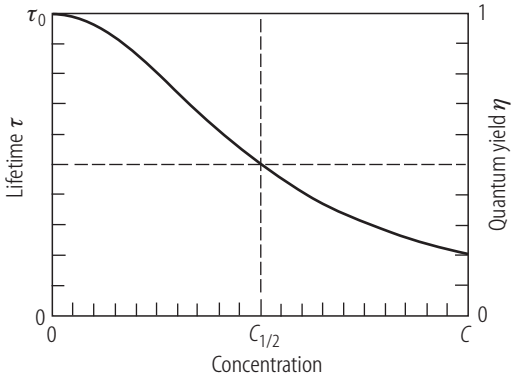

Fig. 4.2.3. Concentration quenching of the lifetime and of the quantum yield.

4.2.1.5 Glasses doped with other active ions, codoping

For application as a so-called eye-safe range-finder one uses erbium-doped glasses lasing at about 1540 nm as a 3-level-system, which are commercially available. Erbium-doped laser glasses are also used preferentially for amplifiers in optical communication networks [89Des, 94Des, 00Bea]. Glasses doped with rare-earth ions other than neodymium and erbium are not generally commercially available, except in small quantities for research purposes and from research laboratories, such as special rare-earth-doped fibers (see Chap. 4.3). To facilitate the pumping, one often uses (co-doped) double-clad fiber lasers with suitably increasing refractive index towards the axis, such as stepwise increasing from the outer to the inner clad and from the inner clad to the core. This means that the pumping light is guided by the first cladding to pump the inner core doped with laser-active ions [01Aue]. Usually the pumping is done by laser diodes to yield transversal mono-mode laser power in the fiber. The pumping power does not need to be of high quality (low diameter–aperture angle product). Co-doping is used for energy transfer from the excited state of sensitizing ions to the laser active ions. This is favorable if the laser active ions do not possess sufficient and sufficiently strong absorption bands. Then, the co-doped ions facilitate the pumping and the energy of the pumping sources is better utilized. However, the co-doping does not generally reduce but rather increases the thermal load due to the pumping and to loss mechanisms in the active material, as has been mentioned already above.

The lasing properties have been investigated thoroughly for many different ions in various glass systems. However, the neodymium ion is still proven to be most interesting because of its pumping levels and of the emission wavelengths.

Several attempts have been tried to use ions other than the rare-earths as active ions, especially chromium [91Izu]. However, these attempts have not yet been successful. Some 5f–5f transitions of actinides might also be considered as active ions. But, since these ions are radioactive and unstable, they are not useful in practice.

4.2.2 Temperature effects

4.2.2.1 Thermal load of cylindrical rods

For data see Sects. 4.2.4.2–4.2.4.4.

The coefficient of thermal conductivity κ for glasses is much smaller than for crystals (typically at least one order of magnitude at room temperature). Therefore, effective cooling is important if glasses are used as active materials. Details of the construction of solid-state laser devices are given in Chap. 4.1 and e.g. [99Koe, 01Iff]. Cooling by a liquid at temperature T_f, preferentially water, is mandatory for cw-lasers in order to obtain reasonably laser power. Due to the cooling a temperature difference ΔT occurs between the interior and the surface of the active medium. In the case of a constant uniform heating rate P effective in the volume of a cylindrical laser rod of radius r_0 and length L, the temperature is given as a function of the radius r from the symmetry axis in the steady state approximately by

$$T(r) - T_\mathrm{f} = \frac{P}{4\pi r_0^2 L\kappa}\left(r_0^2 - r^2\right) + \frac{P}{2\pi Lh} \tag{4.2.3}$$

(see Fig. 4.2.4) yielding a temperature difference between the surface and the symmetry axis of the rod of

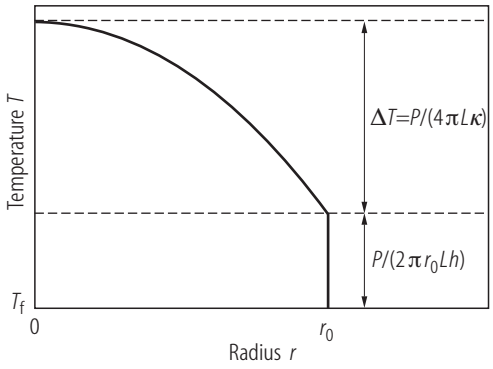

Fig. 4.2.4. Radial temperature profile of a laser rod, schematically.

$$\Delta T = \frac{P}{4\pi L\kappa} \,, \tag{4.2.4}$$

wherein T_f is the temperature of the liquid, κ is the coefficient of thermal conductivity, and h is the heat transfer coefficient from the rod to the cooling medium.

This temperature difference causes tensile stresses on the surface unless the coefficient of linear thermal expansion α is zero. If the thermal stresses are too large, the active material breaks. To characterize the material with respect to the acceptable thermal stresses, the thermo-mechanical figure of merit

$$FOM = \frac{K_{1\mathrm{c}}\kappa(1-\mu)}{\alpha E} \tag{4.2.5}$$

is used with the fracture toughness $K_{1\mathrm{c}}$, Poisson's ratio μ, the coefficient of linear thermal expansion α, and Young's modulus E. Equation (4.2.5), however, is only a rule of thumb, since the fracture cannot be predicted properly but determined experimentally. The stress to cause fracture of a given part made of glass is strongly dependent on the surface quality and a possible pre-stressing in a surface layer by ion exchange or thermal quenching. The maximum stress σ induced in a glassy material by temperature differences ΔT is roughly estimated by

$$\sigma = \frac{E\alpha\Delta T}{1-\mu} \,. \tag{4.2.6}$$

The thermal load of the active material is critical, if it is pumped by flash lights. The heat load is mainly due to

- the relaxation energies from the different optically excited states into the upper lasing level and from the lower lasing level into the ground state,
- absorption by impurities and by the matrix,
- radiationless transitions, and
- absorption of the excited states.

With the advent of diode laser pumping, however, the heat load during the pumping is considerably reduced. One has to point out that for constant total heat rate, P, the temperature difference, ΔT, between the surface and the symmetry axis of the rod does not depend on the radius of the rod, r_0, but on its length, L. Thus, it is favorable to use the active material in the shape of long rods or even fibers.

4.2.2.2 Thermal lensing

Due to the temperature profile the effect of *thermal lensing* occurs in the rod. According to Koechner [99Koe] the refractive power of the thermal lens into radial and azimuthal direction of the

plane of vibration of the laser wave, $1/f_r$ and $1/f_\varphi$ respectively, is given in the steady state by

$$\frac{1}{f_{r,\varphi}} = \frac{1}{K}\left(\frac{1}{2}\frac{\mathrm{d}n}{\mathrm{d}T} + \alpha C_{r,\varphi} n^3 + \frac{\alpha r_0 (n-1)}{L}\right)\frac{P}{A}\,. \tag{4.2.7}$$

In (4.2.7) n means the absolute refractive index, $\mathrm{d}n/\mathrm{d}T$ the temperature coefficient of the absolute refractive index, r_0 the radius, L the length, A the cross section of the laser rod, and P the total average heating power. The first term in the brackets of (4.2.7) is due to the temperature dependence of the absolute refractive index. The second term with the functions

$$C_r = \frac{(17\mu - 7)p_{11} + (31\mu - 17)p_{12} + 8(\mu + 1)p_{44}}{48(\mu - 1)} \tag{4.2.8}$$

and

$$C_\varphi = \frac{(10\mu - 6)p_{11} + 2(11\mu - 5)p_{12}}{32(\mu - 1)} \tag{4.2.9}$$

takes into account the change of the refractive index by the thermal stresses in the cylindrical rod. These changes are in general different for the radial and azimuthal component of an electromagnetic wave. C_r and C_φ depend on the elasto-optic coefficients p_{11}, p_{12}, and p_{44} and Poisson's ratio μ. Since glasses are statistically isotropic materials, one has furthermore $2p_{44} = p_{11} - p_{12}$. The third term in (4.2.7) considers the deformation of the end faces of the rod. There are minor additional contributions due to the change of the refractive index caused by the excitation of the laser active ions and the nonlinear refractive index at very large intra-cavity power, which may vary as a function of the position inside the rod. The effect of thermal lensing can be compensated by additional elements in the cavity or even by a suitable choice of the resonator configuration. This compensation is possible very precisely for a given heat load. Since a huge variety of different glass compositions is in principle available, one can custom tailor some of the properties of the active materials. Material engineers succeeded in developing laser glasses with a minimized value of the bracket in (4.2.7), i.e., minimized thermal lensing for a standard geometry of a rod (see the laser glass LG-750 in Sect. 4.2.4.2).

4.2.2.3 Increasing the maximum laser power

To obtain a large figure of merit (4.2.5) or to reduce the thermal stresses considerably, glass ceramics with approximately zero coefficient of linear thermal expansion α have been tested as a suitable active material for solid-state lasers [73Mue, 00Bea]. Although such a material can be pumped very strongly, the overall lasing properties have not yet been promising, probably because of the relatively large scattering losses and too low a cross section for stimulated emission. Ceramics as the active material have also been developed and tested [73Gre, 74Gre, 95Ike1, 95Ike3, 95Ike2, 96Ike]. The homogeneity of the material did not seem to be sufficient causing too large scattering losses. Recently, however, remarkable progress has been achieved, when a diode-laser-pumped Nd:YAG-ceramic laser rod (length: 104 mm, diameter: 3 mm) delivered 72 W output. The pump power was 290 W at 808 nm [01Lu].

Several possibilities are described and tested to solve the problems of the thermal load: In a simple concept, the surface for heat removal by the cooling liquid should be increased. For this reason a granulate laser, i.e., powder of laser glass immersed in an index matching fluid, has been proposed [84Mue]. Unfortunately, the scattering losses are too large for a granulate in an index matching fluid, similar to the ceramic active material. To avoid these losses at the interfaces, the surface around the active volume should be enlarged, however, only the surface with the normal perpendicular to the propagation of the laser wave. Thus, the active material in shape of a tube

with both the outer and the inner surface being cooled has been successfully developed and used [97Hod].

In a second concept, the thermal load is reduced by changing the active medium in the resonator. This can be done by moving a slab or by rotating a laser tube or by turning a disk of active material, where only a part of the whole volume of the active medium is pumped and activated and subsequently exchanged by a new cool part. Since the resonator must be adjusted to a fraction of the laser wavelength, the mechanical problems for a moving part in the resonator are difficult to solve. Nevertheless, lasers with moving parts have been built in the laboratory [86Bas, 90Bas, 88Red, 94Che, 94Far, 91Kor, 97Hod].

Equation (4.2.3) in mind one can reduce the temperature difference within the active material considerably by choosing the diameter of the rod as small as possible and leaving the total active volume constant, in order to have the output power for a given pumping rate constant. This leads to a fiber laser. In this case, the active volume is the core surrounded by an inactive cladding. If the diameter of the core is sufficiently small for a given difference of the refractive indices, one can achieve laser action within a single-mode fiber. If the fiber is very long even mirrors are not necessary. Instead one can use the inverted system as an amplifier.

To reduce the thermal load, the transport of heat has been made more effective by using a fiber bundle with a much larger surface than a single rod [87Zap]. However, the beam quality is also reduced, since it is determined in this case by the sum of the beams of all fibers used. The product of the full aperture angle and the diameter of the beam at the output mirror of the laser is at minimum about $2\lambda/\pi$ for a single cylindrical rod or a mono-mode fiber. (If $2\pi\, a\lambda_0^{-1}\sqrt{n_1^2(\lambda_0) - n_2^2(\lambda_0)} < 2.405$ is valid for a step-index fiber, one mode can propagate in the fiber, only. λ_0 is the wavelength, a the radius of the core, n_1 and n_2 are the refractive indices of the core and the cladding material, respectively.) This corresponds to the optimum beam quality. For a fiber bundle, however, this value must be multiplied by the ratio of the diameter of the bundle to the diameter of the active core of a single fiber, which is typically in the order of $\sqrt{N}$ with N being the number of fibers of the bundle. Thus, the low product of the beam diameter and the divergence of a single fiber laser is degraded by the same factor and the outstanding good focusing property of the laser beam is lost in this concept.

Degradation of the beam quality by the thermal distortions of the active medium (change of the refractive index, stresses and deformation caused by the temperature field in the active material) is strongly reduced if the concept of the slab laser is applied. (For a survey of different resonator configurations see [97Hod].) In its clearest version, several thin plane-parallel plates are arranged one behind the other and the laser beam traverses the plates under Brewster's angle. (Brewster's angle – against the normal at the boundary surface – is defined by $\alpha_B = \arctan(n_g/n_m)$, where n_g and n_m are the absolute refractive indices of the active glassy material and the surrounding medium. For this angle of incidence, an electromagnetic wave with its plane of vibration parallel to the plane expanded by the vector of incidence and the normal of the surface does not experience reflection but refraction only. Such an electromagnetic wave incident under Brewster's angle has no reflection losses at each boundary.) Then each portion of the laser sees approximately the same temperature and stress field, since the heat removal occurs essentially perpendicular to the large areas of the plates. In another version, the laser beam is propagating in the slab in a zigzag line caused by the reflection on the surfaces (see Sects. 4.1.1.12 and 4.1.1.13). One can take profit of the total internal reflection (which occurs for angles of incidence $\varphi > \varphi_{lim} = \arcsin(n_m/n_g)$ against the normal of the surface) by choosing suitable angles for a given difference between the refractive indices of the active medium and the cooling fluid.

4.2.3 Quantities to characterize properties of laser glasses

For data see Sects. 4.2.4.2–4.2.4.4, and for a general overview on the properties of optical glasses including laser glasses see [98Bac].

4.2.3.1 Density of ions

As an example it is shown how the density of active ions in a solid-state laser material is calculated. Usually, the manufacturers of oxide laser glasses give the quantities of active ions in units of mass % (or weight %) of the corresponding oxides, e.g. X% Nd_2O_3. If the mass density of the glass is ρ, then neodymium ions are present in the glass corresponding to $X\rho/100$ mass of Nd_2O_3 per volume. In order to obtain the density of Nd^{3+} ions per volume, we have to multiply $X\rho/100$ by the ratio of Avogadro's number N_A divided by half of the molar mass of Nd_2O_3, i.e. $2N_A/M_{Nd_2O_3}$, since with each formula unit Nd_2O_3 we increase the number of Nd ions by 2. In total, we have the density of Nd^{3+} ions

$$N_{Nd^{3+}} = X\rho\, 2N_A/\left(100\, M_{Nd_2O_3}\right) = X \cdot F_w \tag{4.2.10}$$

with $N_A = 6.022\,136\,7 \cdot 10^{23}$/mol [89Coh] and $M_{Nd_2O_3} = 336.48$ g/mol. (The corresponding molar mass for Er is $M_{Er_2O_3} = 382.52$ g/mol.) The factor $F_w = \rho\, 2N_A/\left(100\, M_{Nd_2O_3}\right)$ in (4.2.10) is given in Sects. 4.2.4.2–4.2.4.4, if available. If ρ is inserted in g/cm^3 and X is the percentage, one obtains the concentration per cm^3.

In a stoichiometric crystal the laser active ions are located on lattice sites replacing the respective ions. In this case, the concentration of the doping ions is expressed in a stoichiometric formula as, e.g., $Y_{(3-x)}Nd_xAl_5O_{12}$ or Nd:YAG, wherein $x/3$ is the relative amount of Yttrium ions being replaced by neodymium ions. The mass per mole of the formula unit is

$$\begin{aligned} M_{Nd:YAG} &= M_{Y_{(3-x)}\cdot Nd_x\cdot Al_5\cdot O_{12}} \\ &= (3-x)M_Y + xM_{Nd} + 5M_{Al} + 12M_O = (593.6182 + x \cdot 55.3341)\ \text{g/mol}\,, \end{aligned} \tag{4.2.11}$$

wherein the M_I are the molar masses of the ions. If the mass density of the crystal is $\rho_{Nd:YAG}$, we have $N_A\rho_{Nd:YAG}/M_{Nd:YAG}$ formula units per volume and hence we have the density of Nd^{3+} ions per volume:

$$N_{Nd^{3+}} = xN_A\rho_{Nd:YAG}/M_{Nd:YAG}\,. \tag{4.2.12}$$

With the density of active ions $N_{Nd^{3+}}$ one calculates readily the absorption cross section per ion from the absorption constant k

$$\sigma_{abs} = k/N_{Nd^{3+}} \tag{4.2.13}$$

and the molar absorption coefficient (absorption constant divided by mol per volume)

$$\varepsilon_{abs} = kN_A/N_{Nd^{3+}}\,. \tag{4.2.14}$$

4.2.3.2 Refractive index

One has to distinguish between the *absolute refractive index* n_{abs} (i.e. with respect to vacuum) and the *relative refractive index* n_{rel} (i.e. the surrounding medium is dry air under standard conditions:

pressure $p_0 = 0.101325 \cdot 10^6$ Pa and 0.03 % CO_2 of the volume at 15 °C). The general relation between both refractive indices is

$$n_{\mathrm{rel}} = n_{\mathrm{abs}}/n_{\mathrm{air}} \ , \tag{4.2.15}$$

wherein n_{air} is the *absolute refractive index of air*. It can be calculated for different temperatures T_{c} (in °C) and different pressures (in Pa) as well as different partial pressures of water vapor w from the relations [68Koh]

$$n_{\mathrm{air}}(15\ ^\circ\mathrm{C}, p_0) = 1 + 10^{-8}\left(6432.8 + \frac{2\,949\,810\ \mu\mathrm{m}^{-2}\cdot\lambda^2}{146\ \mu\mathrm{m}^{-2}\cdot\lambda^2 - 1} + \frac{25\,540\ \mu\mathrm{m}^{-2}\cdot\lambda^2}{41\ \mu\mathrm{m}^{-2}\cdot\lambda^2 - 1}\right) \tag{4.2.16}$$

and

$$n_{\mathrm{air}} = 1 + \frac{n_{\mathrm{air}}(15\ ^\circ\mathrm{C}, p_0) - 1}{1 + \dfrac{\alpha_{\mathrm{air}}(T_{\mathrm{c}} - 15^\circ\mathrm{C})}{1 + 15\ ^\circ\mathrm{C}\cdot\alpha_{\mathrm{air}}}}\ \frac{p}{p_0} - \frac{413\cdot 10^{-12}\ \mathrm{Pa}^{-1}\cdot w}{1 + \alpha_{\mathrm{air}} T_{\mathrm{c}}} \ , \tag{4.2.17}$$

where $\alpha_{\mathrm{air}} = 3.67\cdot 10^{-3}/^\circ\mathrm{C}$ is the thermal expansion coefficient of the volume of air. The manufacturers of glass usually provide data of the refractive index at 20 °C relative to air under standard conditions. Data are given for selected wavelengths, only, typically for the line d with a wavelength of 587.5618 nm. Thus, one has to consider the dispersion of n. If it is not given, only a rough estimate of n for other wavelengths is possible using the *Abbe number*

$$\nu_{\mathrm{d}} = \frac{n_{\mathrm{d}} - 1}{n_{\mathrm{F}} - n_{\mathrm{C}}} \tag{4.2.18}$$

(the indices d, F, and C stand for the wavelengths 587.5618 nm, 486.1327 nm, and 656.2725 nm). The data on the refractive index are average data over many different melts. The accuracy of 10^{-3} corresponds approximately to the reproducibility of the melts, if one neglects deviations for very large concentrations of neodymium ions. If a better accuracy is needed, measurement of n for the individual melt is recommended.

4.2.3.3 The refractive index as a function of the temperature

To calculate the refractive indices for a given wavelength of the laser as a function of the temperature one needs the corresponding *temperature coefficients* $\mathrm{d}n_{\mathrm{rel}}/\mathrm{d}T$ and $\mathrm{d}n_{\mathrm{abs}}/\mathrm{d}T$ of the refractive index. Both quantities are related by (differentiation of (4.2.15))

$$\frac{\mathrm{d}n_{\mathrm{abs}}}{\mathrm{d}T} = n_{\mathrm{air}}\frac{\mathrm{d}n_{\mathrm{rel}}}{\mathrm{d}T} + n_{\mathrm{rel}}\frac{\mathrm{d}n_{\mathrm{air}}}{\mathrm{d}T} \ , \tag{4.2.19}$$

which can be simplified to

$$\frac{\mathrm{d}n_{\mathrm{abs}}}{\mathrm{d}T} = \frac{\mathrm{d}n_{\mathrm{rel}}}{\mathrm{d}T} + n_{(\mathrm{abs\ or\ rel})}\frac{\mathrm{d}n_{\mathrm{air}}}{\mathrm{d}T} \ , \tag{4.2.20}$$

since $n_{\mathrm{air}} \approx 1$ and $n_{\mathrm{abs}} \approx n_{\mathrm{rel}}$. Care must be taken, if the manufacturers do not specify their data on the refractive index and its temperature coefficient with respect to air or to vacuum. (Unfortunately, the wavelengths for some optical data, such as the temperature dependence of the refractive index and the photoelastic data (see below), are often not specified either. Obviously, one needs the data in general for the laser wavelengths. Only in these cases where the dispersion of the respective quantity is small or within the limit of the accuracy one can use data determined at other wavelength than the laser wavelength.)

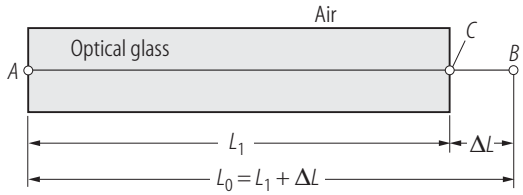

Fig. 4.2.5. Optical path length, see text.

The temperature coefficients of the refractive index are given as average data for specified temperature intervals and a given wavelength, from which the required increments Δn of the refractive index at the design temperature T with respect to the standard data of n have to be calculated. The increments and decrements as a function of the temperature can be calculated also using a dispersion formula developed recently for optical glasses [90Hof]

$$\Delta n_{\mathrm{abs}}(\lambda, T) = \frac{n^2(\lambda, T_0) - 1}{2n(\lambda, T_0)} \times \left[D_0(T - T_0) + D_1(T - T_0)^2 + D_2(T - T_0)^3 + \frac{E_0(T - T_0) + E_1(T - T_0)^2}{\lambda^2 - \lambda_{\mathrm{tc}}^2} \right] , \tag{4.2.21}$$

where D_i, E_i, and λ_{tc} are fitting parameters, and T_0 is the reference temperature. For $n(\lambda, T_0)$ one can insert either the absolute or the relative refractive index, since the pre-factor of (4.2.21) is nearly independent of small variations of n.

The *temperature coefficient of the optical path length* w is usually defined by

$$\frac{\mathrm{d}w}{\mathrm{d}T} = \alpha(n - 1) + \frac{\mathrm{d}n}{\mathrm{d}T} \tag{4.2.22}$$

with the linear thermal expansion coefficient α. Glasses for which $\mathrm{d}w/\mathrm{d}T \approx 0$ are sometimes called *athermal* glasses. Since $\alpha(n - 1) > 0$ the second term $\mathrm{d}n/\mathrm{d}T$ in (4.2.22) must be negative. This occurs for phosphate and fluorophosphate glasses. Thus, commercial athermal laser glasses may be found.

The manufacturers use in (4.2.22) often $\mathrm{d}n_{\mathrm{rel}}/\mathrm{d}T$, which is not useful to characterize $\mathrm{d}w/\mathrm{d}T \approx 0$. Instead, $\mathrm{d}n_{\mathrm{abs}}/\mathrm{d}T$ has to be inserted into (4.2.22). Then, (4.2.22) applies for the optical path between the points A and B in Fig. 4.2.5 with $L_1 \approx L_0$ and L_0 fixed. This is shown by the following consideration: The optical path length between A and B is given by $W = n_{\mathrm{abs}} L_1 + n_{\mathrm{air}}(L_0 - L_1)$, which yields

$$\frac{\mathrm{d}W}{\mathrm{d}T} = \frac{\mathrm{d}n_{\mathrm{abs}}}{\mathrm{d}T} L_1 + n_{\mathrm{abs}} \frac{\mathrm{d}L_1}{\mathrm{d}T} + \frac{\mathrm{d}n_{\mathrm{air}}}{\mathrm{d}T}(L_0 - L_1) + n_{\mathrm{air}} \frac{\mathrm{d}(L_0 - L_1)}{\mathrm{d}T} \quad \text{or}$$

$$\frac{\mathrm{d}W}{\mathrm{d}T} = \frac{\mathrm{d}n_{\mathrm{abs}}}{\mathrm{d}T} L_1 + (n_{\mathrm{abs}} - n_{\mathrm{air}}) \frac{\mathrm{d}L_1}{\mathrm{d}T} + \frac{\mathrm{d}n_{\mathrm{air}}}{\mathrm{d}T}(L_0 - L_1) , \quad \text{since}$$

$$\frac{\mathrm{d}(L_0 - L_1)}{\mathrm{d}T} = -\frac{\mathrm{d}L_1}{\mathrm{d}T} .$$

Hence, one obtains

$$\frac{\mathrm{d}W}{L_1 \mathrm{d}T} = \frac{\mathrm{d}w}{\mathrm{d}T} = \frac{\mathrm{d}n_{\mathrm{abs}}}{\mathrm{d}T} + (n_{\mathrm{abs}} - n_{\mathrm{air}}) \frac{\mathrm{d}L_1}{L_1 \mathrm{d}T} + \frac{\mathrm{d}n_{\mathrm{air}}}{\mathrm{d}T} \frac{(L_0 - L_1)}{L_1} \approx \alpha(n_{\mathrm{abs}} - 1) + \frac{\mathrm{d}n_{\mathrm{abs}}}{\mathrm{d}T}$$

with $n_{\mathrm{air}} \approx 1$ and neglecting the term $\dfrac{\mathrm{d}n_{\mathrm{air}}}{\mathrm{d}T} \dfrac{(L_0 - L_1)}{L_1}$ since $(L_0 - L_1) \ll L_1$.

If, on the other hand, the optical path just from one surface of the piece of glass to the second surface (from A to C in Fig. 4.2.5) should be independent of the temperature, then (4.2.22) has to be replaced by

$$\frac{\mathrm{d}\bar{w}}{\mathrm{d}T} = \alpha n_{\mathrm{abs}} + \frac{\mathrm{d}n_{\mathrm{abs}}}{\mathrm{d}T} \ , \tag{4.2.23}$$

which apparently is much more difficult to fulfill, since the first term (αn) is about 3 times as large as $\alpha(n-1)$ in (4.2.22).

The term "athermal" may be misleading, if thermally induced stress-optical effects have to be included (see below). It may also be misleading for a different reason: Deriving (4.2.22), the whole geometrical path has been considered to be constant or independent of the temperature and a part of that geometrical path has been assumed to consist of a piece of glass. Thus, the increase in the geometrical path length within the glass sample is partly compensated by the decrease of the path length of the environment. This is not necessarily true as shown in a simple example leading to (4.2.23) or in the case $(L_0 - L_1) \gg L_1$.

4.2.3.4 Photoelastic coefficients

Applying stress to a glass changes its refractive index. In the case of uniaxial stress and the electric field vector of the electromagnetic wave parallel (perpendicular) to the direction of stress σ, the refractive index n changes into $n_\parallel = n + \Delta n_\parallel$ ($n_\perp = n + \Delta n_\perp$). Thus, the glass becomes optically uniaxially anisotropic. The changes of the refractive index are proportional to the stress, i.e.

$$\Delta n_\perp = \frac{\mathrm{d}n_\perp}{\mathrm{d}\sigma}\sigma = K_\perp \sigma \quad \text{and} \quad \Delta n_\parallel = \frac{\mathrm{d}n_\parallel}{\mathrm{d}\sigma}\sigma = K_\parallel \sigma \ , \tag{4.2.24}$$

over quite a large interval nearly to the fracture limit. The coefficients K_i are the photoelastic coefficients. Under the convention that a tensile (compressive) stress is positive (negative), the photoelastic coefficients of oxide glasses are negative, i.e. the refractive index decreases (increases) with the tensile (compressive) stress [98Hof]. With the exception of glasses with large content of lead oxide $\left|K_\parallel\right| < |K_\perp|$. Thus, the stress-optical coefficients $K = K_\parallel - K_\perp$ are positive in most cases. The quantities $K_{\parallel,\perp}$ are related to other coefficients by the following relationships

$$K_\parallel = \frac{\mathrm{d}n_\parallel}{\mathrm{d}\sigma} = -\frac{n^3}{2} q_{11} = \frac{n^2}{Ec}(q - 2\mu p) = \frac{n^3}{2E}(p_{11} - 2\mu p_{12}) \tag{4.2.25}$$

and

$$K_\perp = \frac{\mathrm{d}n_\perp}{\mathrm{d}\sigma} = -\frac{n^3}{2} q_{12} = \frac{n^2}{Ec}(-\mu q + (1-\mu)p) = \frac{n^3}{2E}(-\mu p_{11} + (1-\mu)p_{12}) \ , \tag{4.2.26}$$

wherein q_{11} and q_{12} are the piezo-optic coefficients, q and p are Neumann's coefficients, p_{11} and p_{12} are the elasto-optic (strain-optical) coefficients, E is Young's modulus, μ Poisson's ratio, c the velocity of light in vacuum and n is the refractive index without stress.

4.2.3.5 Nonlinear effects

Besides the change of the refractive index by temperature variation and stresses one must consider that the transitions from the ground state to an excited state also changes the optical polarizability $\left(n^2(\lambda) - 1\right)$ of a material, since the properties (concentrations, resonance wavelengths and the oscillator strengths) of the accessible states change. These changes are roughly estimated by the ratio of the density of the excited ions to that of all ions. Assuming 10^{22} ions/cm^3 in total, one expects 10^{17} excited ions/cm^3 needed to change the refractive index by 10^{-5}. Such a concentration

of excited ions or even more is possible under strong pumping of the active material. A relative change in length of the material can also be expected under the same condition [67Bal].

The ions in their excited state can induce rearrangement of their environment, since some restraints for rearrangement and structural relaxation can be overcome more easily in the excited state and a different arrangement of the nearest neighbors may decrease the free energy of the system. This may result in permanent changes of the refractive index [87Dur].

Usually, the electric field strength of an electromagnetic wave is much smaller than the field strength in the interior of the ions. With increasing intensity of the electromagnetic wave, however, the optical field strength approaches the order of the inner ionic fields. In this case, the refractive index cannot be considered as a constant but is a function of the electric field strength E and of the intensity $I = \varepsilon_0 c n_0 \overline{E^2}$ of the electromagnetic wave in the glass (with the velocity of the electromagnetic wave in vacuum $c = 299\,792\,458$ m/s and the permittivity of the vacuum $\varepsilon_0 = 8.854\,187\,817 \cdot 10^{-12}$ As/Vm, $\overline{E^2}$ is the mean square of the amplitude of the electric field strength):

$$n(I) = n_0(\lambda) + \gamma I \ , \tag{4.2.27}$$

wherein $n_0(\lambda)$ is the usual linear refractive index at low intensity and γ is the nonlinear refractive index (in m^2/W). If the refractive index is expressed as a function of $\overline{E^2}$, (4.2.27) reads

$$n(\overline{E^2}) = n_0(\lambda) + n_2 \overline{E^2} \tag{4.2.28}$$

with

$$\gamma = n_2 \frac{\overline{E^2}}{I} = \frac{n_2}{\varepsilon_0 c n_0} \ . \tag{4.2.29}$$

Often, the nonlinear refractive index n_2 is given in reciprocal electrostatic units (esu) of the electric field strength squared. Using n_2 in esu, (4.2.29) is rewritten

$$\gamma = \frac{40\,\pi}{c n_0} \left(\frac{n_2}{\text{esu}}\right) \left(\frac{\text{m}}{\text{W s}}\right) = \frac{4.19169 \cdot 10^{-7}}{n_0} \left(\frac{n_2}{\text{esu}}\right) \left(\frac{\text{m}^2}{\text{W}}\right) \tag{4.2.30}$$

to yield γ in units $\left(\text{m}^2/\text{W}\right)$.

For oxide laser glasses, the nonlinear coefficient γ is in the order of $4 \cdot 10^{-20}$ m^2/W. Thus, the refractive index is changed in the sixth decimal place by intensities I of the electromagnetic wave of several 10^9 W/cm^2. Since the power density is distributed from the center to the border of the laser beam, self-focusing of the beam can be observed, which may cause self-destruction. Care must be taken, however, to distinguish between self-focusing by the nonlinear refractive index and focusing by the variation of the temperature as function of the distance from the center of the beam, which is caused simply by linear and two-photon absorption. In any case, high optical power may be destructive for the laser material.

In principle, the nonlinear changes of the refractive index by strong intensities as has been discussed in the last paragraphs have to be included into (4.2.7). There, however, they have been neglected, since the nonlinear effects play a minor role, only, and the data of the effects considered are not so accurate that the nonlinear effects can a priori be taken into account quantitatively.

On the other hand, nonlinear effects of crystals can be exploited for frequency conversion under phase matching condition: Doubling, tripling or quadrupling of the frequency of Nd-lasers is possible, thus shifting the standard wavelength from 1060 nm to 530 nm, 353 nm, and even 265 nm.

Nonlinear effects play also an important role in fibers with and without doping by laser active ions. The nonlinear refractive index changes the group-velocity and causes self-phase modulation. Pulse compression and the creation of ultra-short laser pulses in fibers are based on nonlinear effects. The propagation of solitons has been studied [92Tay] as well as stimulated Raman and Brillouin scattering, and parametric processes such as frequency doubling and four-wave mixing,

mode locking or the creation of Bragg gratings in fibers. In this respect, however, it is worth mentioning that the information transfer capacity of fibers including amplification seems to be limited by nonlinear effects [01Kah, 01Mit].

Co-doping of the fibers (see Table 4.2.2) increases the pumping efficiency, as has been mentioned already above. More important, however, is the possibility to transfer the energy of low-energy photons to higher energy levels by co-pumping and take profit of this effect in up-conversion lasers [90All]. It is not possible to give credit to all researchers in these fields. A survey on these effects can be obtained from [95Agr]. From a technical point of view one has to mention that the refractive index profile of fibers as well as the doping with laser active ions can be adjusted to specific requirements. The core with the active laser ions, e.g., may be centered in a first cladding guiding the pumping radiation, or an asymmetry may be introduced with respect to the core in order to maintain the polarization status of the radiation. These effects will be treated elsewhere in the present series. (See also Chap. 4.3.)

4.2.4 Properties of commercial laser glasses doped with Nd^{3+} (Er^{3+}) ions from different manufacturers

The data in this section are adopted from catalogues of the manufacturers and partially from [01Iff]. If the temperature is relevant and not specified, the data are mostly given for 20 °C or the range above room temperature.

4.2.4.1 Meaning of the symbols

For the meaning of the symbols see also text.

T_g :	glass transformation temperature;
F_w :	factor to calculate the concentration of active ions from the relative mass content of the oxide; see (4.2.10);
$C_{1/2}$ and $C'_{1/2}$:	quenching concentration ($C_{1/2}$: RE ions per cm^3; $C'_{1/2}$: % RE_2O_3 of the mass density or mass) to decrease the lifetime of the upper lasing level by a factor of 2;
λ_{max} :	wavelength of the maximum of the fluorescence transition between the laser levels;
$\Delta\lambda_{eff}$:	effective width of the fluorescence line;
σ_{se} :	cross section for stimulated emission;
τ_0 :	limiting radiative lifetime of the upper lasing level at low concentrations;
$n(\lambda_{max})_{rel}$:	refractive index at laser wavelength relative to standard air;
$n_{d,rel}$:	refractive index relative to standard air for the d-line ($\lambda = 587.5618$ nm);
ν_d :	Abbe number of the d-line (see (4.2.18));
dn_{rel}/dT :	temperature coefficient of the relative refractive index, mostly for the laser wavelength;
n_2 :	nonlinear refractive index in esu;
γ :	nonlinear refractive index in m^2/W, mostly for the laser wavelength;
p_{11}, p_{12}, and p_{44} :	elasto-optic coefficients, mostly for 632.8 nm;
K :	stress-optical coefficient;
c_p :	specific heat capacity at constant pressure;
κ :	heat conductivity;
α :	coefficient of linear thermal expansion;
ρ :	mass density;
μ :	Poisson's ratio or Poisson's number;
E :	modulus of elasticity (Young's modulus);
HK 0,1/20:	Knoop hardness according to ISO 9385.

4.2.4.2 Manufacturer: Schott Glass Technologies

Address: Schott Glass Technologies, Inc., 400 York Avenue, Duryea, PA 18642-2036, U.S.A.

Designation	**LG-680**	**LG-750**	**LG-760**	**LG-770**	**APG-1**	**APG-2**	**IOG-1**	**IOG-2**	**IOG-10**
kind of active ion	Nd^{3+}	Nd^{3+}	Nd^{3+}	Nd^{3+}	Nd^{3+}	Nd^{3+}	Er^{3+}/Yb^{3+}	Er^{3+}/Yb^{3+}	Er^{3+}/Yb^{3+}
glass type	silicate	phosphate	phosphate	phosphate	phosphate	phosphate	phosphate	phosphate	silicate
T_g [°C]	468	450	350	461	450	540	474	375	569
F_w [10^{20}/cm^3/% RE_2O_3 of mass]	0.91	1.01	0.93	0.925	0.94	0.916	0.86	0.856	0.853
$C_{1/2}$ [10^{20}/cm^3]	5.5	17	10.0	8.8	16.7	10.6			
$C'_{1/2}$ [% RE_2O_3 of mass]	6.0	16.8	10.7	9.5	17.7	11.6			
Properties of the laser transition: Nd^{3+}: $^4F_{3/2} \rightarrow {}^4I_{11/2}$; Er^{3+}: $^4I_{13/2} \rightarrow {}^4I_{15/2}$ and Yb^{3+}: $^2F_{5/2} \rightarrow {}^2F_{7/2}$									
λ_{max} [nm]	1059.7	1053.5	1054	1052.7	1053.9	1054.6	1534/1002	1533/1000	1536/1020
$\Delta\lambda_{eff}$ [nm]	35.9	26.0	24.3	25.4	27.8	31.5			
σ_{se} [10^{-20} cm^2]	2.54	3.7	4.5	3.9	3.4	2.4	0.66/0.54	0.8/0.54	0.58/0.45
τ_0 [µs]	337	356	330	372	370	464	10700/1400	9000/1500	17800/1400
Optical properties of the bulk glass									
$n(\lambda_{max})_{rel}$	1.560	1.516	1.508	1.4996	1.526	1.5032	1.513/1.515	1.508/1.510	1.518/1.520
refractive index $n_{d,rel}$	1.560	1.526	1.519	1.5086	1.537	1.5127	1.523	1.518	1.530
Abbe number ν_d	57.7	68.2	69.2	68.4	67.7	66.9	67.5	66.8	56.6
dn_{rel}/dT [10^{-6}/°C]	2.9	−5.1	−6.8	−4.7	1.2	3.4			
n_2 [10^{-13} esu]	1.6	1.08	1.02	1.13	1.13	1.06			
γ [10^{-20} m^2/W]	4.3	3	2.8	3.2	3.1	3			
p_{11}	0.0853	0.105	0.110	0.0894	0.0839	0.088			
p_{12}	0.1827	0.237	0.234	0.202	0.190	0.206			
p_{44}	−0.0487	−0.066	−0.062	−0.0563	−0.053	−0.059			
K [10^{-6} mm^2/N]	2.0	1.8	2.0	2.1	2.2	2.82			

(continued)

Designation	LG-680	LG-750	LG-760	LG-770	APG-1	APG-2	IOG-1	IOG-2	IOG-10
Thermal properties of the bulk glass									
c_p [W s/(g °C)]	0.92	0.72	0.75	0.77	0.84	0.77	0.78	0.75	0.77
κ [W/(m °C)]	1.35	0.49	0.57	0.57	0.78	0.80	0.67	0.57	0.92
α [10^{-6}/°C]	9.3	11.4	12.5	11.61	7.6	5.07	9.3	12.5	6.8
Mechanical properties of the bulk glass									
mass density ρ [g/cm^3]	2.54	2.83	2.60	2.585	2.633	2.559	2.74	2.72	2.71
Poisson's number μ	0.242	0.256	0.267	0.253	0.238	0.225	0.24	0.27	0.24
Young's modulus E [GPa]	90.1	50.1	53.7	47.29	70	63.8	61.2	54	71
HK 0,1/20	620	290	340	330	450	420	380	340	520
Other properties of the glass									
Mass loss in water [mg/cm^2/day] at 50 °C	0.050	0.016	0.028	0.040	0.006	0.007	0.012	0.028	0.001

4.2.4.3 Manufacturer: Hoya Optics

Address: Hoya Optics, Inc., 3400 Edison Way, Freemont, CA 94538, U.S.A.

Designation	**LHG-80**	**HAP-4**	**LHG-8**	**LHG-5**	**LSG-91H**	**LEG-30**	**LEG-40**
kind of active ion	Nd^{3+}	Nd^{3+}	Nd^{3+}	Nd^{3+}	Nd^{3+}	Er^{3+}	Er^{3+} (Cr^{3+})
glass type	phosphate	phosphate	phosphate	phosphate	silicate	phosphate	phosphate
T_g [°C]	402	486	485	455	465	515	520
F_w [10^{20}/cm^3/% RE_2O_3 of mass]	1.045	0.966	1.01	0.96	1.005	0.973	0.973
$C_{1/2}$ [10^{20}/cm^3]							
$C'_{1/2}$ [% RE_2O_3 of mass]		10.4	8.5	8.5			
Properties of the laser transition: Nd^{3+}: $^4F_{3/2} \rightarrow {}^4I_{11/2}$ and Er^{3+}: $^4I_{13/2} \rightarrow {}^4I_{15/2}$							
λ_{max} [nm]	1054	1054	1054	1054	1062	1535	1535
$\Delta\lambda_{eff}$ [nm]	20.2	27	21.8	22	27.4	32	32
σ_{se} [10^{-20} cm^2]	4.8	3.6	4.2	4.1	2.7	0.77	0.77
τ_0 [μ s]	320	350	315	290	300	8700	8700
Optical properties of the bulk glass							
$n(\lambda_{max})_{rel}$	1.533	1.533	1.520	1.531	1.5498	1.52678	1.52707
refractive index $n_{d,rel}$	1.543	1.543	1.530	1.541	1.56115	1.54191	1.54289
Abbe number ν_d	64.7	64.6	66.5	63.5	56.6	65.4	65.2
dn_{rel}/dT [10^{-6}/°C]	−3.8	1.8	−5.3	−0.4	1.6	−3.0	−2.7
n_2 [10^{-13} esu]	1.24	1.25	1.13	1.28	1.58	1.22	1.23
γ [10^{-20} m^2/W]	3.4	3.4	3.1	3.5	4.3	3.3	3.4
p_{11}	0.107	0.1835	0.1929	0.19			
p_{12}	0.1829	0.241	0.2358	0.26			
p_{44}	−0.038	−0.029	−0.021	−0.035			
K [10^{-6} mm^2/N]	1.8	2.49	1.97	2.3	2.2		

(continued)

Designation	LHG-80	HAP-4	LHG-8	LHG-5	LSG-91H	LEG-30	LEG-40
Thermal properties of the bulk glass							
c_p [W s/(g °C)]	0.63	0.71	0.75	0.71	0.63		
κ [W/(m °C)]	0.63	1.02	0.58	0.77	1.04	0.55	0.55
α [10^{-6}/°C]	10.2	7.2	11.2	8.4	9.0	10.9	11
Mechanical properties of the bulk glass							
mass density ρ [g/cm^3]	2.92	2.7	2.83	2.68	2.81	3.09	3.09
Poisson's number μ	0.267	0.236	0.258	0.237	0.237	0.261	0.259
Young's modulus E [GPa]	50	68.9	50.1	67.8	87.2	55.3	57.8
HK 0,1/20, approximate data	340	470	350	430	590	346	354
Other properties of the glass							
mass loss at 100 °C [%/h] surface area not specified	0.18	0.07	0.13	0.08	0.036	0.06	0.02

4.2.4.4 Manufacturer: Kigre

Address: Kigre, Inc., 5333 Secor Rd., Toledo, Ohio 43623, U.S.A.

Designation	**Q-88**	**Q-98**	**Q-100**	**Q-246**	**QE-7**	**Q-89**
kind of active ion	Nd^{3+}	Nd^{3+}	Nd^{3+}	Nd^{3+}	Er^{3+}	Nd^{3+}
glass type	phosphate	phosphate	phosphate	silicate	phosphate	phosphate
T_g [°C]	366	416	413	470	462	440
F_w [10^{20}/cm^3/% RE_2O_3 of mass]	0.97	1.11	1.07	0.913	0.926	1.12
$C_{1/2}$ [10^{20}/cm^3]						
$C'_{1/2}$ [% RE_2O_3 of mass]	8					
Properties of the laser transition: Nd^{3+}: $^4F_{3/2} \rightarrow {}^4I_{11/2}$ and Er^{3+}: $^4I_{13/2} \rightarrow {}^4I_{15/2}$						
λ_{max} [nm]	1054	1053	1054	1062	1535	1054
$\Delta\lambda_{eff}$ [nm]	22	21	21	28	30	21
σ_{se} [10^{-20} cm^2]	4	4.5	4.4	2.9	0.8	3.8
τ_0 [μ s]	326	308	357	370	8000	308
Optical properties of the bulk glass						
$n(\lambda_{max})_{rel}$	1.536	1.546	1.561	1.561	1.532	
refractive index $n_{d,rel}$	1.550	1.555	1.572	1.572	1.542	1.559
Abbe number ν_d	64.8	63.6	62.1	57.8		
dn_{rel}/dT [10^{-6}/°C]	−0.5	−4.5	−4.6	2.9	−6.3	
n_2 [10^{-13} esu]	1.1	1.2	1.2	1.4		
γ [10^{-20} m^2/W]	3	3.3	3.2	3.8		
p_{11}						
p_{12}						
p_{44}						
K [10^{-6} mm^2/N]						

(continued)

Designation	Q-88	Q-98	Q-100	Q-246	QE-7	Q-89
Thermal properties of the bulk glass						
c_p [W s/(g °C)]	0.81	0.8	0.8	0.93		
κ [W/(m °C)]	0.84	0.82	0.82	1.3		0.82
α [10^{-6}/°C]	10.4	9.9	9.6	9.0	11.4	8.8
Mechanical properties of the bulk glass						
mass density ρ [g/cm^3]	2.71	3.1	3.2	2.55	2.94	3.14
Poisson's number μ	0.24	0.24	0.24	0.24	0.24	
Young's modulus E [GPa]	69.9	70.7	70.1	84.1	70.7	
HK 0,1/20	420	560	550	590		
Other properties of the glass						
mass loss at 100 °C [%/h] surface area not specified	0.2	0.08	0.08	0.04		

References for 4.2

60Mai1 Maiman, T.H.: Br. Commun. Electron. **7** (1960) 674.
60Mai2 Maiman, T.H.: Nature (London) **187** (1960) 493.

61Sni1 Snitzer, E.: J. Appl. Phys. **32** (1961) 36.
61Sni2 Snitzer, E.: Phys. Rev. Lett. **7** (1961) 444.

62Etz Etzel, H.W., Gandy, H.W., Ginther, R.J.: Appl. Opt. **1** (1962) 534.
62Gan1 Gandy, H.W., Ginther, R.J.: Appl. Phys. Lett. **1** (1962) 25.
62Gan2 Gandy, H.W., Ginther, R.J.: Proc. IRE **50** (1962) 2113.
62Gan3 Gandy, H.W., Ginther, R.J.: Proc. IRE **50** (1962) 2114.
62Jud Judd, B.R.: Phys. Rev. **127** (1962) 750.
62Ofe Ofelt, G.S.: J. Chem. Phys. **37** (1962) 511.

63Dic Dicke, G.H., Crosswhite, H.M.: Appl. Opt. **2** (1963) 675.
63Mau Mauer, P.B.: Appl. Opt. **2** (1963) 87.

64Cab Cabezas, A.Y., DeShazer, L.G.: Appl. Phys. Lett. **4** (1964) 37.
64Gan1 Gandy, H.W., Ginther, R.J., Weller, J.F.: Appl. Phys. Lett. **4** (1964) 188.
64Gan2 Gandy, H.W., Ginther, R.J., Weller, J.F.: Appl. Phys. Lett. **5** (1964) 220.
64Gan3 Gandy, H.W., Ginther, R.J., Weller, J.F.: Phys. Lett. **11** (1964) 213.
64Mau Mauer, P.B.: Appl. Opt. **3** (1964) 153.
64Pea1 Pearson, A.D., Porto, S.P.S.: Appl. Phys. Lett. **4** (1964) 202.
64Pea2 Pearson, A.D., Porto, S.P.S., Northorer, W.R.: J. Appl. Phys. **35** (1964) 1704.

65Gan1 Gandy, H.W., Ginther, R.J., Weller, J.F.: Appl. Phys. Lett. **6** (1965) 237.
65Gan2 Gandy, H.W., Ginther, R.J., Weller, J.F.: Phys. Lett. **16** (1965) 266.
65Kar Karapetyan, G.O., Kovalyov, V.P., Lunter, S.G.: Opt. Spectrosc. **19** (1965) 529.
65Shi Shionoya, S., Nakazawa, E.: Appl. Phys. Lett. **6** (1965) 117.
65Sni Snitzer, E., Woodcock, R.: Appl. Phys. Lett. **6** (1965) 45.

66Dau Dauge, G.: IEEE J. Quantum Electron. **2** (1966) LVIII.
66Sni Snitzer, E.: IEEE J. Quantum Electron. **2** (1966) 562.

67Bal Baldwin, G.D., Riedel, E.P.: J. Appl. Phys. **38** (1967) 2726.
67Gan Gandy, H.W., Ginther, R.J., Weller, J.F.: J. Appl. Phys. **38** (1967) 3030.

68And Andreyev, S.I., Bedilov, M.R., Karapetyan, G.O., Likhachev, V.M.: Sov. J. Opt. Technol. (English Transl.) **35** (1968) 819.
68Die Dieke, G.H.: Spectra and Energy Levels of Rare-Earth Ions in Crystals, New York: Interscience, 1968.
68Koh Kohlrausch, F.: Praktische Physik, Lautz, G., Taubert, R. (eds.), Stuttgart: Teubner, 1968, p. 408.

73Gre Greskovich, C., Chernoch, J.P.: J. Appl. Phys. **44** (1973) 4599.
73Mue Müller, G., Neuroth, N.: J. Appl. Phys. **44** (1973) 2315.

74Gre Greskovich, C., Chernoch, J.P.: J. Appl. Phys. **45** (1974) 4495.
74Kru Krupke, W.E.: IEEE J. Quantum Electron. **10** (1974) 450.
74Sto Stone, J., Burrus, C.A.: Appl. Opt. **13** (1974) 1256.

75Pou Poulain, M., Poulain, M., Lucas, J., Brun, P.: Mater. Res. Bull. **10** (1975) 243.

76Jac Jacobs, R.R., Weber, M.J.: IEEE J. Quantum Electron. **12** (1976) 102.

77Luc Lucazeau, G., Barnier, S., Loireau-Lozac'h, A.M.: Mater. Res. Bull. **12** (1977) 437.
77Pou Poulain, M., Chanthanasinh, M., Lucas, J.: Mater. Res. Bull. **12** (1977) 151.

78Luc Lucas, J., Chanthanasinh, M., Poulain, M., Poulain, M., Brun, P., Weber, M.J.: J. Non-Cryst. Solids **27** (1978) 273.

79Cli Cline, C.F., Weber, M.J.: Wiss. Z. Friedrich-Schiller-Univ. Jena, Math.-Naturwiss. Reihe **28** (1979) 351.
79Vid Videau, J.J., Fava, J., Fouassier, C., Hagenmüller, P.: Mater. Res. Bull. **14** (1979) 499.

80Auz Auzel, F., Michel, J.C., Flahaut, J., Loireau-Lozac'h, A., Guittard, M.: C. R. Acad. Sci. (Paris) Ser. **C 291** (1980) 21.
80Sto Stokowski, S.E., Martin, W.E., Yarema, S.M.: J. Non-Cryst. Solids **40** (1980) 481.

81Kam Kaminski, A.A: Laser Crystals, New York: Springer-Verlag, 1981.
81Sto Stokowski, S.E., Savoyan, R.A., Weber, M.J.: Lawrence Livermore National Laboratory, Report M-95, 2nd Rev., 1981.
81Web1 Weber, M.J., Almeida, R.M.: J. Non-Cryst. Solids **43** (1981) 99.
81Web2 Weber, M.J., Myers, J.D., Blackburn, D.H.: J. Appl. Phys. **52** (1981) 2944.

82Bor Bornstein, A., Reisfeld, R.: J. Non-Cryst. Solids **50** (1982) 23.
82Web Weber, M.J., Ziegler, D.C., Angell, C.A.: J. Appl. Phys. **53** (1982) 4344.

83Pou Poulain, M.: J. Non-Cryst. Solids **56** (1983) 1.

84Mue Müller, G.: German Patent DE 3447311 A1, 1984.
84Tra Tran, D.C., Sigel jr., G.H., Bendow, B.: J. Lightwave Technol. **2** (1984) 566.

85Dre Drexhage, M.G.: Heavy-Metal Fluoride Glasses, in: Treatise on Materials Science and Technology, Vol. 26 (Glass IV), Tomozawa, M., Doremus, R.H. (eds.), New York: Academic Press, 1985, pp. 151–243 (ISBN 0-12-341826-7).

86Bas Basu, S., Byer, R.L.: Opt. Lett. **11** (1986) 617.
86Poo Poole, S.B., Payne, D.N., Mears, R.J., Ferman, M.E., Laming, R.I.: J. Lightwave Technol. **4** (1986) 870.

87Ain Ainslie, B.J., Craig, S.P., Davey, S.T.: Mater. Lett. **5** (1987) 143.
87Dur Durville, F.M., Powell, R.C.: J. Opt. Soc. Am. B **4** (1987) 1934.
87Kru Krupke, W.F., Shinn, M.D., Kirchoff, T.A., Finch, C.B., Boatner, L.A.: Appl. Phys. Lett. **51** (1987) 2166.
87Neu Neuroth, N.: Opt. Eng. **26** (1987) 96.
87Tow Townsend, J.E., Poole, S.P., Payne, D.N.: Electron. Lett. **23** (1987) 329.
87Zap Zapata, L.E.: J. Appl. Phys. **62** (1987) 3110.

88Ain1 Ainslie, B.J., Craig, S.P., Davey, S.T.: J. Lightwave Technol. **6** (1988) 287.
88Ain2 Ainslie, B.J., Craig, S.P., Davey, S.T., Wakefield, B.: Mater. Lett. **6** (1988) 139.
88Bri Brierley, M.C., France, P.W., Millar, C.A.: Electron. Lett. **24** (1988) 539.
88Est Esterowitz, L.: Electron. Lett. **24** (1988) 1104.
88Far Farries, M.C., Morkel, P.R., Townsend, J.E.: Electron. Lett. **24** (1988) 709.

88Han Hanna, D.C., Percival, R.M., Perry, I.R., Smart, R.G., Suni, P.J., Townsend, J.E., Tropper, A.C.: Electron. Lett. **24** (88) 1111.
88Hay Hayden, J.S., Sapak, D.L., Marker, A.J.: Proc. SPIE **895** (1988) 176.
88Red Reed, M.K., Kozlovsky, W.J., Byer, R.L.: Opt. Lett. **13** (1988) 204.
88Sap Sapak, D.L., Ward, J.M., Marion, J.E.: Proc. SPIE **970** (1988) 107.

89All Allain, J.Y., Monerie, M., Poignant, H.: Electron. Lett. **25** (1989) 1660.
89Arm Armitage, J.R., Wyatt, R., Ainslie, B.J., Craig-Ryan, S.P.: Electron. Lett. **25** (1989) 298.
89Coh Cohen, E.R., Taylor, B.N.: Physics Today BG 8, August 1989.
89Des Desurvire, E., Simpson, J.R.: J. Lightwave Technol. **7** (1989) 835.
89Han1 Hanna, D.C., McCarthy, M.J., Perry, I.R., Suni, P.J.: Electron. Lett. **25** (1989) 1365.
89Han2 Hanna, D.C., Percival, R.M., Smart, R.G., Townsend, J.E., Tropper, A.C.: Electron. Lett. **25** (1989) 593.
89Luc Lucas, J., Adam, J.-J.: Glastech. Ber. **62** (1989) 422.
89Mor Morse, T.F., Reinhart, L., Kilian, A., Risen jr., W., Cipolla, J.W.: Proc. SPIE **1171** (1989) 72.
89Per Percival, R.M., Phillips, M.W., Hanna, D.C., Tropper, A.C.: IEEE J. Quantum Electron. **25** (1989) 2119.

90All Allain, J.Y., Monerie, M., Poignant, H.: Electron. Lett. **26** (1990) 166.
90Bar Barnes, W.L., Townsend, J.E.: Electron. Lett. **26** (1990) 746.
90Bas Basu, S., Byer, R.: Appl. Opt. **12** (1990) 1765.
90Fra France, P.W.: Fluoride Glass Optical Fibres, Glasgow: Blackie, 1990.
90Han Hanna, D.C., Percival, R.M., Smart, R.G., Tropper, A.C.: Opt. Commun. **75** (1990) 283.
90Hof Hoffmann, H.-J., Jochs, W.W., Westenberger, G.: Proc. SPIE **1327** (1990) 219.
90Miy Miyajima, Y., Komukai, T., Sugawa, T.: Electron. Lett. **26** (1990) 194.
90Sma Smart, R.G., Carter, J.N., Hanna, D.C., Tropper, A.C.: Electron. Lett. **26** (1990) 194.
90Web Weber, M.J.: J. Non-Cryst. Solids **123** (1990) 208.
90Wet Wetenkamp, L.: Electron. Lett. **26** (1990) 883.

91Izu Izumitani, T., Zou, X., Wang, Y.: Proc. SPIE **1535** (1991) 150.
91Kor Korn, T.H., Jeys, T.H., Fan, T.Y.: Opt. Lett. **16** (1991) 1741.
91Oho Ohoshi, Y., Kanamori, T., Kitagawa, T., Takahashi, S., Snitzer, E., Sigel jr., G.H.: Technical Digest Optical Fiber Communnication Conf., Opt. Soc. Am., 1991, p. 10.
91Wet Wetenkamp, L.: Archiv für Elektronik und Übertragungstechnik **45** (1991) 328.

92Tay Taylor, J.R. (ed.): Optical solitons – Theory and Experiment, Cambridge, UK: Cambridge University Press, 1992.

94Che Chen, Y., Zhou, F., Hu, W., Li, Z., Wang, Z.: Chin. J. Lasers B **3** (1994) 405.
94Des Desurvire, E.: Erbium-Doped Fiber Amplifiers – Principles and Applications, New York: Wiley, 1994 (ISBN 0-471-58977-2).
94Far Farinas, A.D., Gustafson, E.K., Byer, R.L.: Opt. Lett. **19** (1994) 114.
94Hew Hewak, D.W., Samson, B.N., Medeiros Neto, J.A., Laming, R.I., Payne, D.N.: Electron. Lett. **30** (1994) 968.
94Sam Samson, B.N., Medeiros Neto, J.A., Laming, R.I., Hewak, D.W.: Electron. Lett. **30** (1994) 1617.

95Agr Agraval, G.P.: Nonlinear Fiber Optics, 2nd Ed., San Diego: Academic Press, 1995 (ISBN 0-12-045142-5).

95Ike1 Ikesue, A., Furusato, I., Kamata, K.: J. Am. Ceram. Soc. **78** (1995) 225.
95Ike2 Ikesue, A., Kamata, K., Yoshida, K.: J. Am. Ceram. Soc. **78** (1995) 2545.
95Ike3 Ikesue, A., Kinoshita, T., Kamata, K., Yoshida, K.: J. Am. Ceram. Soc. **78** (1995) 1033.

96Ike Ikesue, A., Kamata, K., Yoshida, K.: J. Am. Ceram. Soc. **79** (1996) 1921.

97Hod Hodgson, N., Weber, H.: Optical Resonators: Fundamentals, Advanced Concepts and Applications, Berlin: Springer-Verlag, 1997 (ISBN 978-3-540-76137-2).

98Bac Bach, H., Neuroth, N. (eds.): The Properties of Optical Glass, Schott Series on Glass and Glass Ceramics: Science, Technology, and Applications, 2nd corrected printing, Berlin, Springer-Verlag, 1998 (ISBN 978-3-540-58357-8).
98Bin Binnemans, K., Van Deun, R., Görller-Walrand, C., Adam, J.L.: J. Non-Cryst. Solids **238** (1998) 11.
98Goe Görller-Walrand, C., Binnemans, K.: Handbook on the Physics and Chemistry of Rare Earths, Vol. 25, Gscheidner jr., K.A., Eyring, L. (eds.), Amsterdam: Elsevier, 1998, p. 101.
98Hof Hoffmann, H.-J.: Differential Modifications of the Refractive Index, in: Schott Series on Glass and Glass Ceramics: Science, Technology, and Applications: Optical Glasses, Bach, H., Neuroth, N. (eds.), 2nd corrected printing, Berlin: Springer-Verlag, 1998, pp. 96–123 (ISBN 978-3-540-58357-8).

99Koe Koechner, W.: Solid-State Laser Engineering, 5th rev. and updated ed., Berlin: Springer-Verlag, 1999 (ISBN 978-3-540-65064-5).
99Tan Tanabe, S.: J. Non-Cryst. Solids **259** (1999) 1.

00Bea Beall, G.H.: Glastechn. Ber. Glass Sci. Technol. **73 C1** (2000) 3.
00Cam Campbell, J.H., Suratwala, T.I.: J. Non-Cryst. Solids **263&264** (2000) 318.
00Flo Florez, A., Jerez, V.A., Florez, M.: J. Alloys Compounds **303/304** (2000) 355.
00Per Perry, M.: Science & Technology Review, March 2000, California, U.S.A: Lawrence Livermore National Laboratory.

01Aue Auerbach, M., Wandt, D., Fallnich, C., Welling, H., Unger, S.: Opt. Commun. **195** (2001) 437.
01Iff Iffländer, R.: Solid-State Lasers for Materials Processing, Berlin: Springer-Verlag, 2001 (ISBN 978-3-540-66980-7).
01Lu Lu, J., Murai, T., Takaichi, T., Uematsu, T., Misawa, K., Prabhu, M., Xu, J., Ueda, K., Yagi, H., Yanagitani, T., Kaminskii, A.A., Kudryashov, A.: Appl. Phys. Lett. **78** (2001) 3586.
01Kah Kahn, J.M., Ho, Keang-Po: Nature (London) **411** (2001) 1007.
01Mit Mitra, P.P., Stark, J.B.: Nature (London) **411** (2001) 1027.
01Phi Philipps, J.E., Töpfer, T., Ebendorff-Heidepriem, H., Ehrt, D., Sauerbrey, R.: Appl. Phys. B **72** (2001) 399.

03Jac Jackson, S.D.: Appl. Phys. Lett. **83** (2003) 1316.

4.3 Diode-pumped fiber lasers

A. Tünnermann, J. Limpert, A. Bruns

4.3.1 Introduction

The pursuit of highest power together with highest brightness is efficiently fulfilled by diode-pumped rare-earth-doped solid-state lasers. The most common solid-state laser geometry is a rod, with dimensions of few millimeters in diameter and several centimeters in length. However, conventional rod lasers suffer from thermo-optical problems, which restrict simple power scaling by maintaining a good beam quality [99Koe]. Several geometries of the gain media have been developed to overcome this limitation, such as thin disk [94Gie] and slab [72Jon], which reduce thermo-optical distortions due to their special geometry.

A promising alternative to bulk solid-state laser systems are rare-earth-doped fibers, whose properties, achievements and potential in several operation regimes will be reviewed in the following sections.

4.3.2 Historical background of fiber lasers

The guidance of light by total internal reflection in water jets has been demonstrated by D. Colladon in 1841 and J. Tyndall in 1854. Theoretical background describing electromagnetic waves has been developed by Maxwell in 1864, which then has been extended by Hondros and Debye to describe dielectric waveguides. However, the fabrication technology enabling to produce optical waveguides with sufficient properties has not been developed until the 1970s. A breakthrough was the development of the chemical vapor deposition technique to manufacture optical fibers. Before, the large attenuation of fibers only allowed for short transmission devices for instance medical endoscopes or instrument lightning. Nevertheless, optical amplification in fibers doped with rare-earth ions has been reported in the early sixties, just few years after the invention of the laser itself, by Snitzer and Koester [63Sni, 66Koe].

A milestone was the realization of low-loss fused silica fibers by Corning in 1970. These fibers revolutionized the communication on earth, starting in the mid-70s copper wires are replaced by optical fibers for most commercial telecommunication and network systems worldwide. Doping these fibers with rare-earth ions allowed for the amplification of light by stimulated emission, however, the decades after the invention of fiber lasers they were little more than a low-power laboratory curiosity. Recently, however, diode-pumped fiber lasers are entering the realm of kilowatt powers with diffraction-limited beam quality [04Jeo, 05Tue, 07IPG]. This power evolution is made possible by novel fiber designs, such as the double-clad fiber, fabricated by advanced technologies and also the development of powerful diode lasers as pump sources. Figure 4.3.1 illustrates the impressive power evolution of fiber lasers with single-transverse-mode beam quality over the recent years.

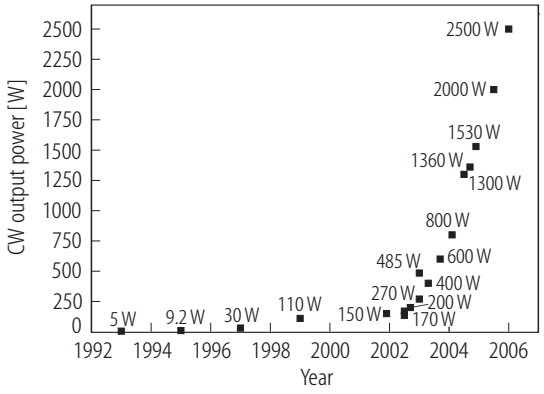

Fig. 4.3.1. Power evolution of fiber lasers with high beam quality ($M^2 < 3$).

4.3.3 Basic principles of a fiber laser

Comparable to conventional solid-state lasers a fiber laser consists of a gain medium, a cavity and a pump source. The gain medium is realized by a rare-earth-doped glass-fiber, which allows for the propagation of light independent of diffraction due to total internal reflection. Figure 4.3.2 illustrates the simple setup of a fiber laser.

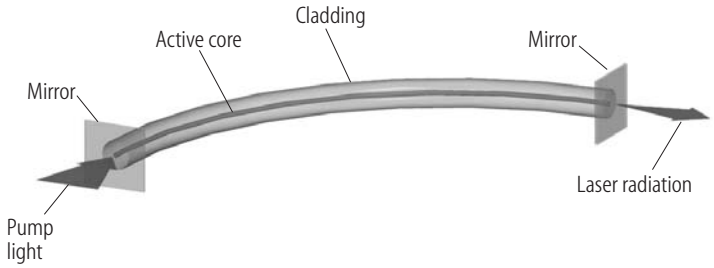

Fig. 4.3.2. Setup of a fiber laser.

A number of glasses are applied as host material of fiber lasers, but the most common host material is fused silica. Fused silica distinguishes oneself by a high mechanical and chemical stability and very low attenuation. However, fused silica possesses high phonon energy, therefore laser transitions which rely on a long lifetime of intermediate states, such as mid-infrared or visible (i.e. up-conversion), are not efficiently possible. For such an extension of emission range of fiber laser typically heavy-metal fluoride glasses or chalcogenide glasses are employed. Table 4.3.1 summarizes realized laser transitions of rare-earth-doped glasses [88Urq, 93Bri], see also Table 4.2.2.

The cavity of a fiber laser can be formed by directly attached (butt-coupled) dielectric mirrors or fiber integrated mirrors, such as fiber Bragg gratings or fiber loop mirrors. The two fiber end facets can be used to launch the pump radiation from a diode laser into the fiber, i.e. longitudinal pumping. However, several techniques have been developed to side-couple (transversal pumping) the pump light, such as Wavelength Division Multiplexers (WDM) or Tapered Fiber Bundles (TFB). In general, both the pump and laser radiation is guided in an active doped waveguide structure. This complete integration of the laser process leads to the inherent compactness and long-term stability of fiber lasers, because no components are necessary in a long free-space cavity.

Table 4.3.1. Laser transitions in rare-earth-doped glasses.

$\lambda_{emission}$ [μm]	RE-ion	$\lambda_{emission}$ [μm]	RE-ion	$\lambda_{emission}$ [μm]	RE-ion
3.4	Er^{3+}	1.31	Pr^{3+}	0.715	Pr^{3+}
2.9	Ho^{3+}	1.2	Ho^{3+}	0.695	Pr^{3+}
2.75	Er^{3+}	1.08	Pr^{3+}	0.651	Sm^{3+}
2.3	Tm^{3+}	1.06	Nd^{3+}	0.635	Pr^{3+}
2.04	Ho^{3+}	1.04	Yb^{3+}	0.61	Pr^{3+}
1.9	Tm^{3+}	0.98	Er^{3+}	0.55	Ho^{3+}
1.72	Er^{3+}	0.975	Yb^{3+}	0.546	Er^{3+}
1.66	Er^{3+}	0.94	Nd^{3+}	0.52	Pr^{3+}
1.55	Er^{3+}	0.91	Pr^{3+}	0.491	Pr^{3+}
1.47	Tm^{3+}	0.88	Pr^{3+}	0.48	Tm^{3+}
1.38	Ho^{3+}	0.85	Er^{3+}	0.455	Tm^{3+}
1.34	Nd^{3+}	0.8	Tm^{3+}	0.38	Nd^{3+}

4.3.4 Fundamentals of fiber optics

In contrast to conventional solid-state lasers in which at least a free optical beam path is formed in a resonator, the beam formation and guiding in a fiber laser device is realized in optical waveguides. Figure 4.3.3 shows the structure of an optical fiber. The fiber consists of a core with a refractive index n_1, generally surrounded by a pure fused silica glass cladding of refractive index $n_2 < n_1$ so that, based on total internal reflection, wave guiding takes place in the core. The fiber is protected against external influence by a polymer coating.

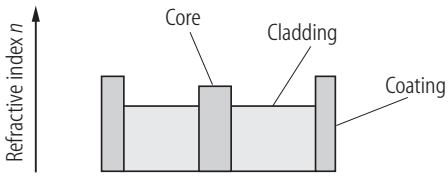

Fig. 4.3.3. Refractive-index profile of an optical fiber.

The characteristics of the refractive index profile of the core determine the number of guided modes. If the fiber core satisfies the condition for the dimensionless normalized frequency parameter (V-parameter) as follows [98Gha]:

$$V = \frac{2 \cdot \pi \cdot a}{\lambda} \cdot \sqrt{n_1^2 - n_2^2} = \frac{2 \cdot \pi \cdot a}{\lambda} \cdot NA < 2.405 \,, \tag{4.3.1}$$

where a is the radius of the core and λ the wavelength of the confined radiation, only the transversal fundamental mode can be guided through the fiber. For these fibers the term monomodal or single-mode fiber is used. The numerical aperture NA, defined by $\sqrt{n_1^2 - n_2^2}$, determines the sine value of the angle to the fiber axis up to which radiation is being coupled into the fiber. Fibers which satisfy the condition $V > 2.405$ are termed multimodal. The number of modes Z propagating in the fiber can be approximated for large values of the V-parameter according to $Z = V^2/2$.

Applying the wave-optical picture, the field distribution (mode) inside the core can de determined in cylindrical optical waveguides by solving the wave equation. For a specific mode LP_{lm} (LP stands for linearly polarized) with mode numbers l and m using cylindrical coordinates r and φ the radial distribution of the electrical field amplitude E_{lm} of the fiber mode is described by Bessel functions (J_l, K_l) and the azimuthal distribution by sine function with phase δ [98Gha]:

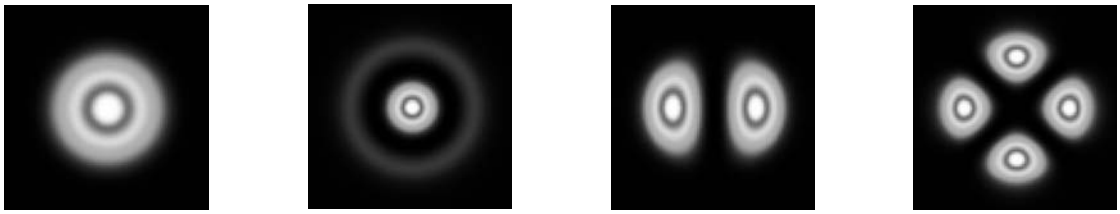

Fig. 4.3.4. 2D-plot of the calculated intensity distribution of transverse modes in a step-index fiber.

$$\begin{aligned} E_{l,m}^{\text{core}} &= a_1 \sin(l\varphi + \delta) J_l(\gamma r) \ , \\ E_{l,m}^{\text{cladding}} &= a_2 \sin(l\varphi + \delta) K_l(\gamma r) \ . \end{aligned} \tag{4.3.2}$$

Using an approximation (similar to the Wentzel-Kramers-Brillouin approximation known in quantum mechanics) it is possible to obtain the missing constants a_1 and a_2 as well as the spreading constant $\gamma(m, l, V)$ for a given fiber. The intensity distribution of the individual modes is obtained by the square of the field strength and is depicted in Fig. 4.3.4 for some low-order LP modes.

Commonly, in order to excite a rare-earth-doped fiber, the pump radiation is coupled through the fiber facet into the laser core. However, in the case of longitudinal pumping the pump radiation has to be launched into a waveguide with dimensions of few microns. Therefore, highly brilliant pump radiation sources are required to excite monomodal fibers, which are so far limited to output powers of few watts. Hence the output power of such a fiber laser is limited to few watts. To scale up the output power one needs a larger fiber diameter that is adapted to the beam-parameter product of a high-power diode-array. However, the enlarged active core of the fiber allows for higher transversal mode propagation, resulting in a reduced beam quality. Such a multimode core would spoil one of the fiber laser's outstanding properties: the power-independent excellent beam quality.

An alternative is to use separate cores for pumping and lasing, the so-called double-clad is described below. With this concept the operation of fiber lasers with output powers of several ten watts was possible for the first time in the early 1990s and nowadays double-clad fiber lasers are the most powerful solid-state lasers with single-transverse-mode beam quality.

4.3.5 Double-clad fiber lasers

In double-clad fiber lasers [74Mau, 88Sni] the pump radiation is not directly launched into the active core (laser core) but into a surrounding highly multimode waveguide known as the pump core or inner cladding. This again is surrounded by a jacket or outer cladding. A double-clad fiber is schematically illustrated in Fig. 4.3.5. In order to realize the pump core which also acts as cladding for the active core with optical waveguide characteristics, the surrounding coating must have a

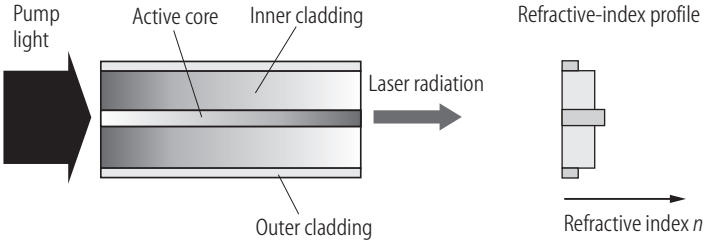

Fig. 4.3.5. The double-clad fiber concept.

smaller refractive index. Normally, a fluorine-doped silica glass or a highly transparent polymer with a low refractive index such as silicone, Teflon or fluorine-doped acrylate is used. The diameter of the pump core is typically a few hundred microns and its numerical aperture NA can be as high as ~ 0.45.

The pump radiation which is launched into the pump core is coupled into the active core over the entire fiber length and is absorbed there by the rare-earth ions, hence the upper laser level is excited. Using this technique the multimodal pump radiation from the high-power diode lasers can be efficiently converted into laser radiation with excellent beam quality. Assuming a typical pump core dimension of 400 μm diameter and an NA of 0.4 the brightness improvement is about 70000 if the fiber laser emission is diffraction-limited.

The efficiency of a fiber laser is strongly dependent on the coupling of the pump radiation from the pump core to the laser core. In conventional double-clad fibers with centered laser cores and circular pump cores the pump radiation is only partly absorbed, and a large portion is transmitted independent of the fiber length and doping concentration. The proportion of the unused pumping power is determined only by the geometry of the double-clad fiber. As an example, for a fiber with 100 μm pump core diameter and 5 μm laser core diameter, only about 30 % of the launched pump radiation is absorbed. To improve the pump absorption and thus achieve a more efficient laser operation, the propagation of the pump radiation in the pump core must be carefully considered. This can be done in a wave-optical approach but also in a ray-propagation approach based on geometrical optics. The wave-optical approach is based on the solution of the wave equation with the boundary condition of the cylindrically symmetric waveguide, as described above. The absorption coefficient for each individual LP mode is obtained from the overlap of its intensity and the rare-earth distribution in the fiber. To perform a quantitative analysis of pump radiation absorption, the overlap of all modes guided in the pump core and the active core has to be considered. As a matter of fact, modes with azimuthal mode number $l > 0$ (by far the majority of fiber modes) show no intensity on the fiber axis, therefore, the absorption coefficient for this kind of modes is negligible. A disadvantage of the method to determine the pump absorption is, however, that it is only applicable to rectilinear fibers with circular pump cores. The description is no longer applicable for the generally used coiled fibers. An essentially more versatile method to describe pump absorption in double-clad fibers is the ray-tracing method. Ray-tracing in optical waveguides is valid as long as the dimensions of the waveguide are greater than the wavelength of the radiation. From the ray-tracing point of view the pump radiation launched into a circular pump core can be divided into two categories: meridional rays and helical rays (see Fig. 4.3.6). In principle only meridional rays pass through the center of the pumping core and thus through the laser core and can be absorbed. Helical rays cannot fall below a certain inner radius r and thus cannot be absorbed. The limitations to fibers with circular pump-core cross sections do not apply to ray-tracing methods, all geometries can be considered.

To improve the pump absorption and accordingly increase the optical efficiency of double-clad fibers, fiber designs have to be developed which prevent the propagation of helical radiation. This can be done by the disturbance of the rotational symmetry of the fiber along the longitudinal axis to hamper the propagation of helical rays. Rectangular and D-shaped pumping-core cross sections enforce a chaotic spreading of the pump radiation and ensure that the pump radiation coupled into the pump core crosses the active core during propagation. Thus complete pump-radiation absorption occurs within a short fiber length. This situation is illustrated in Fig. 4.3.7 for a D-shaped double-clad fiber.

Absorption of helical rays can also be achieved by geometries in which the active core is positioned decentered in the pump core rather than in its center. Such off-center cores then lie in a region crossed by helical radiation which can therefore be absorbed. Figure 4.3.8 compares the calculated pump light absorption in double-clad fiber of different geometries but similar cross-sectional areas and reveals the absorption enhancement by breaking the symmetry. The highest absorption for a given fiber length is observed in D-shaped and rectangular fibers. The above men-

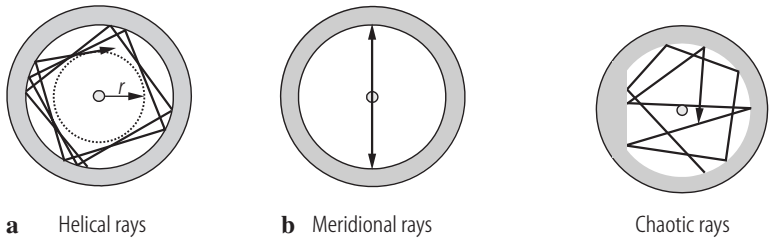

Fig. 4.3.6. Meridional and helical rays in a pump cladding of a double-clad fiber with centered active core.

Fig. 4.3.7. Chaotic rays in a double-clad fiber with D-shaped inner cladding and centered active core.

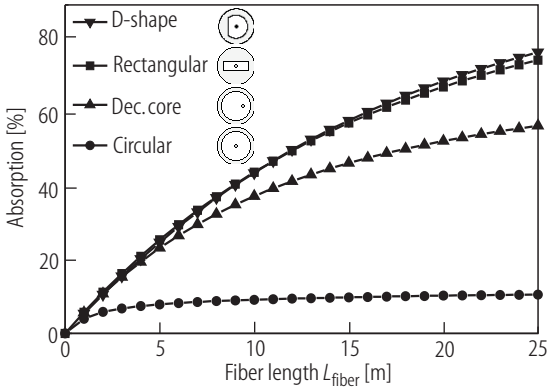

Fig. 4.3.8. Normalized pump-radiation absorption in double-clad fibers with different geometries.

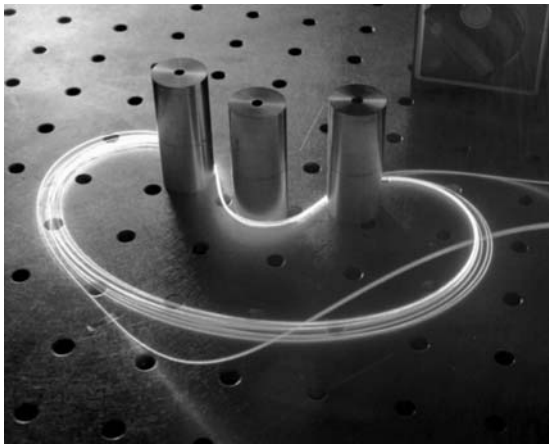

Fig. 4.3.9. Double-clad fiber coiled in kidney shape in order to increase the pump absorption.

tioned absorption saturation in circular pump cores occurs within a short fiber length, hence only a small fraction of the pump radiation is absorbed.

As an alternative to the costly manufacturing of fibers with non-round pumping cores a concept has been developed by which a suitable mode mixing improves the pump light absorption in circular fibers with centered active cores. The curvature in a bend of a fiber causes pump radiation from the outer regions of the pump core to be added to that of the center, or in other words, the bend causes mode mixing from modes which are not absorbed to modes which are. Figure 4.3.9 shows an especially favorable form of bending: the kidney shape.

4.3.6 Ytterbium-doped fiber lasers

As mentioned, a number of rare-earth ions can be doped in several host glasses. Their emission wavelength can cover a spectral range from the visible to the mid-infrared. However, ytterbium-doped fused silica fibers offer unique properties [97Pas] making this configuration preferable for a lot of operation regimes.

The energy level scheme of triply-ionized ytterbium, as shown in Fig. 4.3.10, is characterized by its simplicity. It just consists of two manifolds, the $^2F_{5/2}$ and the $^2F_{7/2}$, that participate in

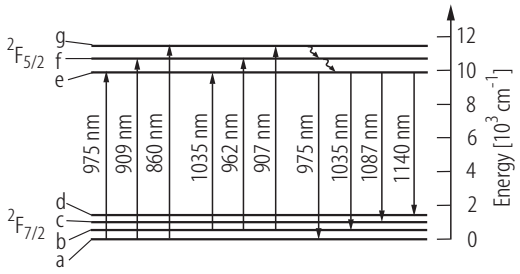

Fig. 4.3.10. Energy level scheme of triply-ionized ytterbium-doped glass.

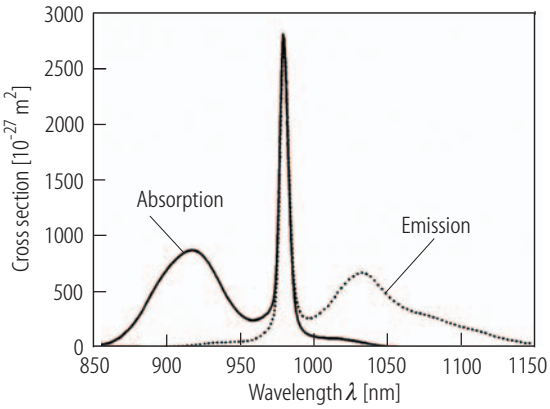

Fig. 4.3.11. Emission and absorption cross section of ytterbium-doped fused silica.

the lasing process. These manifolds are separated by approximately 10 000 cm^{-1} corresponding to a photon wavelength in the 1 μm region. Higher-lying energy levels in the Yb^{3+}-ion are far above the ground state – almost 100 000 cm^{-1} – that they do not affect this transition. Therefore, ytterbium-doped systems do not suffer from any losses caused by Excited State Absorption (ESA).

Furthermore, these transitions are significantly broadened in the glass host, leading to a very broad emission and absorption bandwidth. Figure 4.3.11 shows the emission and absorption cross sections for ytterbium-doped fused silica. The broad emission bandwidth allows for the generation and amplification of ultrashort laser pulses, whereas the broad absorption bandwidth is helpful due to its overlap with the emission wavelength of high-power diode lasers.

Compared to other rare-earth ions the quantum defect of ytterbium is very small, it is depending on the pump and emission wavelength and is less than $\sim$ 15 %. Therefore, very high optical-to-optical efficiencies are possible, values of 80 % are typical. Moreover, the small quantum defect leads to very low thermal load of the fiber, which is an important aspect for high-power operation. The huge saturation fluence of $\sim$ 30 J/cm^2 and the long fluorescence lifetime of $\sim$ 1 ms of Yb-doped fused silica are interesting properties for the generation and amplification of pulsed laser radiation.

4.3.7 Fiber lasers versus bulk lasers

The properties which distinguish a fiber laser from a conventional bulk laser, and making a fiber laser to a power-scalable solid-state laser concept, arise from the fiber geometry itself and the confinement of pump and laser radiation in waveguide structures.

Fiber lasers offer the possibility to overcome the limits in scaling the output power of solid-state lasers while maintaining the beam quality. The beam quality of a fiber laser is mainly determined by the refractive-index profile of the active fiber core. If the core is monomodal, then the laser oscillates in the transverse fundamental mode independent of external influences. This means that compared to conventional (even diode-pumped) solid-state lasers, fiber lasers are to a large extent immune against thermo-optical effects. Effects such as thermally induced lens formation and stress-induced birefringence in the active region resulting in a degradation of the beam quality are not observed even at high output powers. Furthermore, for fiber lasers the thermal load caused by the pumping process is spread over the entire fiber length (typical several meters or even longer), as due to the greater surface-to-volume ratio, heat is more efficiently removed, and thus the observed

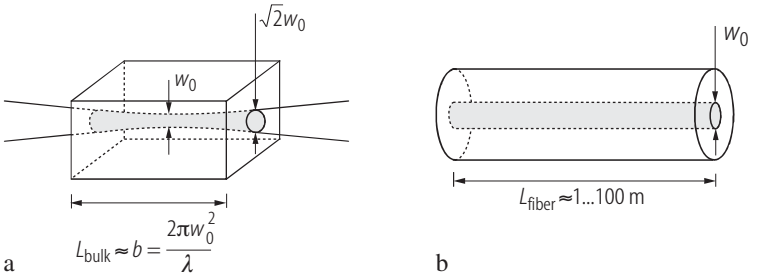

Fig. 4.3.12. Comparison of bulk and fiber laser geometry.

temperature increase in the laser core in comparison to bulk solid-state lasers is small. Therefore, the reduction of the quantum efficiency of the active medium with increasing temperature during laser operation plays a subordinate role in fiber lasers.

Since the length of the active medium needed is determined by the pump absorption requirements when designing an end-pumped bulk laser device, the pump spot size and therefore the pump intensity is limited by the confocal parameter b of the pump radiation, as shown in Fig. 4.3.12. This situation is somewhat different in a fiber laser. Pump radiation which is launched into its waveguide can propagate down the fiber, independent of diffraction, until it is completely absorbed while maintaining the spot size diameter, resulting in large values of pump intensity times interaction length product. This product, which can be orders of magnitude larger in fiber laser geometries compared to bulk solid-state lasers, determines the gain of a laser medium, hence, with fibers a very high gain can be achieved. Depending on the rare-earth ion small-signal gains in the range of 50 dB are possible and even for a saturated high-power fiber amplifier values of 30 dB are feasible. This high gain is responsible for the low threshold values and high efficiencies obtained with fiber laser, but also for the possibility to exploit weak or three-level transitions in continuous-wave operation, which in general cannot easily be achieved in solid-state lasers.

4.3.8 Nonlinearity – the main performance limitation of a fiber laser

The fiber geometry is responsible for the outstanding properties of rare-earth-doped fibers. However, as opposed to conventional diode-pumped solid-state laser systems the significantly longer interaction length and the tight confinement of the laser radiation enforces disturbing nonlinear effects [95Agr], which constitute the main restriction of rare-earth-doped fiber-based laser systems. Because of the isotropy of the glass contributions of the second-order susceptibility vanish for silica glass fibers. Thus, the lowest-order nonlinear effect in optical fibers originates from the third-order susceptibility and is responsible for an intensity-dependent refractive index. Consequently, an optical field propagating through a fiber experiences a self-induced phase shift, a phenomenon referred to as Self-Phase Modulation (SPM). A second important class of nonlinear effects results from stimulated inelastic scattering processes, whereby the radiation transfers a part of its energy to the glass host in the form of excited vibrational modes. Two phenomena known as Stimulated Raman Scattering (SRS) and Stimulated Brillouin Scattering (SBS) fall in this category. Both manifest themselves as a significant power loss mechanism in fiber-based laser systems.

In general, the nonlinearity coefficients in glass fibers are intrinsically small. Both the nonlinear index coefficient n_2 and the gain coefficients of SRS and SBS are at least two orders of magnitude smaller than in other common nonlinear media. Nevertheless, due to the large product of intensity and interaction length inside the fiber core nonlinearity can be observed at very low power levels and basically limits the performance of rare-earth-doped fiber systems before limitations due to

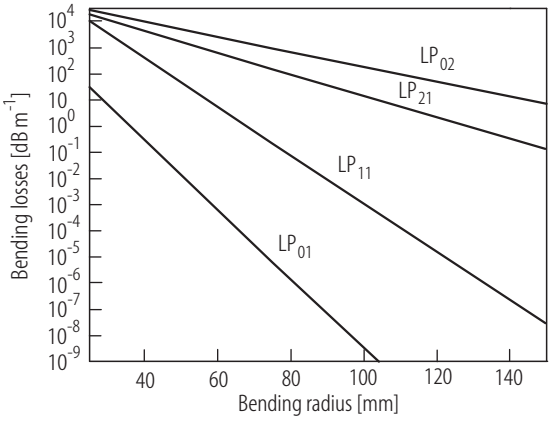

Fig. 4.3.13. Calculated bending losses in a 30 μm LMA fiber ($NA = 0.06$) for the first four transverse modes subject to the bending radius.

thermo-optical effects or fracture of the fiber are reached. This counts even for the generation of continuous-wave radiation.

Basically, as discussed above, the nonlinear effects are proportional to the fiber length and the intensity in the fiber core, and therefore inversely proportional to the mode-field area of the guided radiation in the fiber. Thus, an enlargement of the Mode-Field Diameter (MFD) and a reduction of fiber length would help to avoid disturbing nonlinear effects. Using special techniques and fiber designs the mode-field area of fiber devices in a single transverse mode could be significantly increased in the past years. One approach is to decrease the numerical aperture relative to a standard telecommunication value of about 0.16, which allows an increase in the core size while single-mode operation is maintained, see (4.3.1). The reduction of core numerical aperture to 0.06 allows for an enlargement of single-mode-core size to $\sim$ 15 μm in the 1 μm wavelength region. Such fibers are termed low-numerical-aperture Large-Mode-Area (LMA) fiber. However, a further reduction in the numerical aperture is not tolerable in terms of fabrication accuracy. On the other hand, an increase of core size too at this given numerical aperture would lead to multimode fiber core. But in a multimode fiber laser one of the most important advantages of fiber laser compared to bulk laser would be lost, the power-independent excellent beam quality.

However, the bending losses can be applied to achieve stable fundamental-mode operation of a fiber laser or amplifier characterized by active cores with V-parameters in the range of 5 to 10 [00Kop]. Figure 4.3.13 shows the calculated bending losses [78Sak] of a 30 μm LMA fiber ($NA = 0.06$) for the fundamental and three higher-order modes as a function of bending radius. This calculation reveals a significant discrimination of high-order transverse modes. As an example, at a bending radius of 50 mm the induced bending loss for the LP_{01} mode is 0.01 dB/m and for the first higher-order mode LP_{11} 52 dB/m. This approximately 5 orders of magnitude difference enforces fundamental-mode operation.

Other approaches to increase the core size which allows for single-mode operation depend on a preferential gain to the fundamental mode, created by an optimally overlapping rare-earth dopant distribution. Alternatively, one can optimize the design of a multimode fiber to avoid mode scattering of the fundamental mode to higher-order modes combined with a careful excitation of the fundamental mode at the beginning of the fiber (e.g. by inserting tapered sections). By applying these techniques, experimentalists have extracted diffraction-limited output from a step-index, multimode fiber with a mode-field diameter as large as 30 μm [01Gal]. However, robust and environmentally stable fundamental-mode operation is possible only in a true single-mode fiber. Therefore, a single-mode fiber with large mode areas would be a significant achievement. The following section discusses the achievement of photonic crystal fiber for fiber laser devices.

4.3.9 Photonic crystal structures in a fiber laser

Microstructuring the fiber adds several attractive properties to conventional fibers. The cladding of a photonic crystal or holey fiber consists of a triangular array of air holes with diameter d and pitch Λ, as shown in Fig. 4.3.14 [03Rus]. Intuitively, one can imagine that the "average" refractive index of the cladding is decreased by the air holes, so that light is guided in the core by modified total internal reflection.

In analogy to conventional step-index fibers, a normalized frequency parameter (V-parameter) for a photonic crystal fiber can be defined. For a Photonic Crystal Fiber (PCF) having a core formed from a single missing hole, the V-parameter is given by

$$V_{\mathrm{PCF}} = \frac{2\pi}{\lambda} \cdot \Lambda \cdot \sqrt{n^2_{\mathrm{core}}(\lambda) - n^2_{\mathrm{cladding}}(\lambda)} \,. \tag{4.3.3}$$

The condition for higher-order mode cut-off can be formulated as $V_{\mathrm{PCF}} = \pi$. In contrast to step-index fibers, the effective index of the cladding region of a PCF is strongly wavelength-dependent, as shown in Fig. 4.3.15. If the ratio of wavelengths of the guided mode to hole-to-hole distance, λ/Λ approaches zero, then the effective cladding index approaches the effective core index.

One can show numerically that these unusual dispersion properties of the cladding, taken together with the single-mode condition, lead to the behavior shown in Fig. 4.3.16. Here, the curved line across the lower right side of the plot indicates where the single-mode condition is met; above the line, only single-mode propagation is possible. For any fiber whose d/Λ ratio is less then

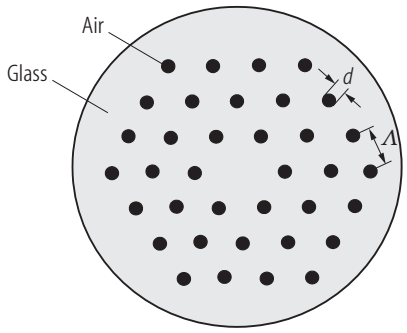

Fig. 4.3.14. Schematic illustration of a photonic crystal fiber [03Rus].

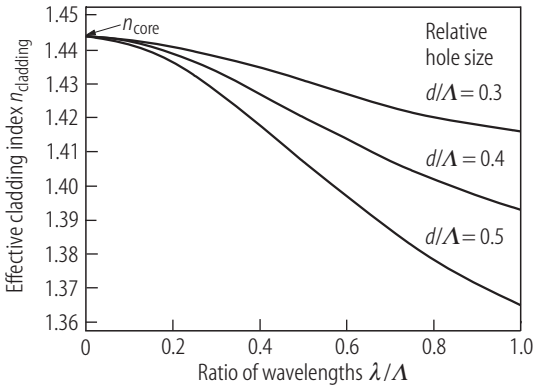

Fig. 4.3.15. Effective index of a photonic crystal cladding.

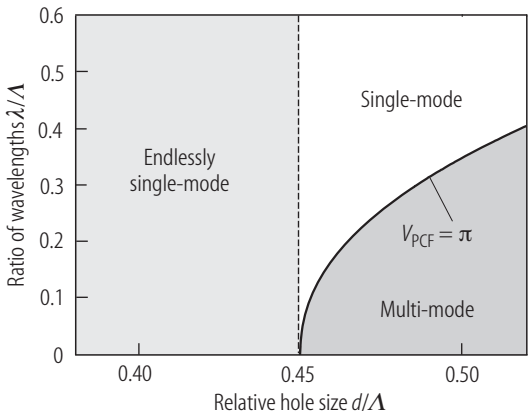

Fig. 4.3.16. Single-mode and multimode parameter space of a photonic crystal fiber.

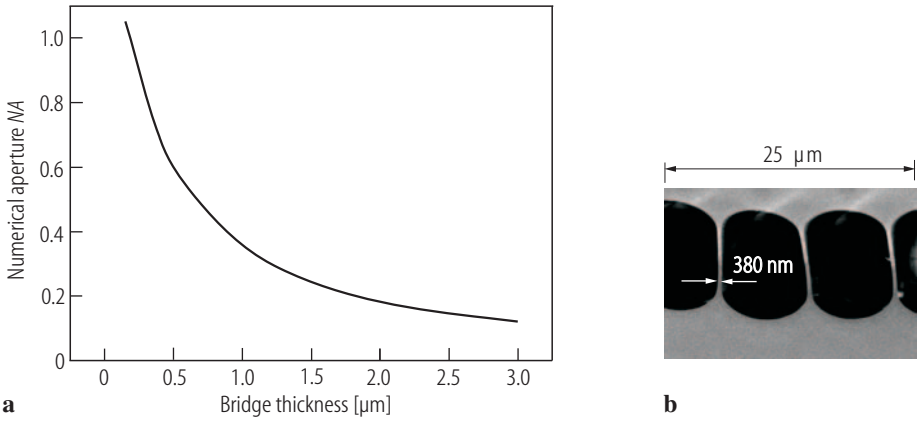

Fig. 4.3.17. (**a**) The numerical aperture of an air-clad fiber ($\lambda_{\text{pump}} = 980$ nm). (**b**) Close-up to the air-cladding.

about 0.45, all wavelengths will propagate in a single mode. Such fibers are termed to be "endlessly single-mode" [96Kni, 97Bir].

A more intuitive explanation of these unusual guiding properties is to consider the air holes (diameter d, spacing Λ) as a modal filter or modal sieve. Due to the evanescence of light in air, the holes are strong barriers and can be analogous to the wire mesh of the sieve. The fundamental transverse mode with a lobe dimension of $\sim 2\Lambda$ fits into the core and can not escape through the too-narrow silica gaps between the air holes. In contrast, the higher-order modes have significantly smaller lobe dimensions and can therefore slip between the gaps. It becomes clear that, if the relative hole size d/Λ increases, more and more higher-order modes become guided. Thus, the cladding geometry alone determines the number of guided modes, and no higher-order modes are guided at all if d/Λ is less than 0.45. This last observation is true independent of wavelength, and independent of core diameter. Thus, if a photonic crystal fiber meets the condition $d/\Lambda < 0.45$, its core can theoretically become arbitrarily large and the fiber will still be single-mode. Of course, the scaling of the core size leads to fibers with reduced effective index difference between the core and the cladding. Hence, controlling the index during fabrication is of high importance. Conventional rare-earth-doped step-index fibers are fabricated by the well-know MCVD process (Modified Chemical Vapor Deposition) followed by solution doping. The smallest refractive-index step which can be precisely created is in the range of $\sim 1 \cdot 10^{-3}$, corresponding to a numerical aperture of 0.06. In microstructured fibers this value can be as small as $\sim 1 \cdot 10^{-4}$, corresponding to a NA of 0.02. Consequently, significantly larger single-mode core can be achieved in photonic crystal fibers [04Lim].

A further advantage of microstructuring a fiber is the possibility of forming an air-cladding region to create double-clad fibers. Double-clad PCFs can be achieved by surrounding the inner cladding with a web of silica bridges which are substantially narrower than the wavelength of the guided radiation. The resulting numerical aperture of the inner cladding is basically given by the thickness of the silica bridges. Figure 4.3.17a shows the numerical aperture of an air-clad fiber as a function of silica bridge width assuming a pump wavelength of 980 nm. Indeed, silica bridges as thin as 400 nm are feasible without loosing the mechanical stability of the fiber, as shown in Fig. 4.3.17b. This bridge width leads to a numerical aperture of the pump core well above 0.6, which is significantly larger than values obtained by low-index polymers.

This high NA allows the diameter of the inner cladding to be reduced while still maintaining sufficient brightness acceptance for efficient pumping with diode lasers. Shrinking the inner cladding diameter is advantageous, because the overlap ratio of the active core to the inner cladding increases, which leads to shorter absorption lengths – or higher thresholds for nonlinear effects.

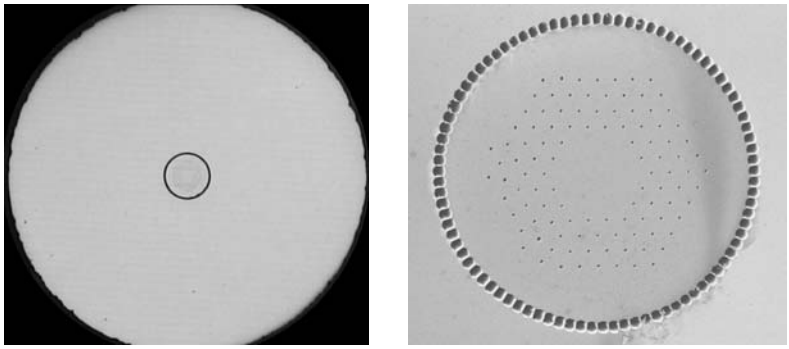

a **b**

Fig. 4.3.18. (**a**) Microscope-image of the extended-mode-area rod-type photonic crystal fiber and (**b**) SEM-picture of the microstructured region.

Table 4.3.2. Comparison of the nonlinearity in different fiber designs.

	Standard step-index fiber	Low-NA LMA fiber	Rod-type PCF
MFD, fiber length	6 μm, 15 m	25 μm, 5 m	50 μm, 0.5 m
$(\text{Nonlinearity})^{-1}$	1	50	2000

Furthermore, no radiation has direct contact to the coating material, which avoids another common problem of conventional fibers in high-power operation.

A fiber design which possesses these two microstructured regions, the air-clad and the photonic crystal cladding, to reduce the nonlinearity has been developed, it is called rod-type photonic crystal fiber [05Lim]. The basic idea of this fiber design is to have outer dimensions of a rod laser, meaning a diameter in the range of a few millimeters and a length of just a few tens of centimeters, but including two important waveguide structures, one for pump radiation and one for laser radiation. Finally, such a fiber has an extremely reduced nonlinearity and therefore allows for significant power and energy scaling. The cross section of this fiber is shown in Fig. 4.3.18. The inner cladding has a diameter of $\sim$ 180 μm. The numerical aperture is as high as 0.6. The ytterbium-doped core has a diameter of 60 μm, which is a significant increase in core size compared to other fiber designs. This fiber possesses a pump light absorption as high as $\sim$ 30 dB/m at 976 nm. Usually, the extraction of high power levels from short fiber lengths is limited by thermo-optical problems. A detailed analysis of the thermo-optical behavior of high-power fiber lasers (including photonic crystal fibers) [03Lim] has revealed that power scaling is restricted by damage to the polymer coating, which occurs at fiber surface temperatures between 100 °C and 200 °C. These temperatures are easily reached if power levels in the 100 W/m range are extracted. In a microstructured air-clad fiber it just serves to protect the fiber from mechanical damage and chemical attack. The most straightforward way to avoid damage of the coating is to remove it. This can be done if the fiber itself has enough mechanical stability, i.e., if the fiber is thick enough. The fiber shown in Fig. 4.3.18 has an outer cladding diameter as large as 2 mm and possesses no coating. In addition, the larger outer diameter improves the heat dissipation capabilities of this fiber and also reduces the propagation loss of weakly guided radiation because of the increased rigidity.

A comparison of nonlinearity between a double-clad ytterbium-doped step-index single-mode fiber, a low-numerical large-mode-area fiber and the described rod-type photonic crystal fiber shows the achievement of this novel fiber design (Table 4.3.2). The nonlinearity, basically given by the effective mode area and the absorption length of the fiber, is normalized to the value of the standard single-mode step-index fiber in the 1 μm wavelength region. This comparison reveals a reduction

of nonlinearity by a factor of about 2000 in the rod-type PCF. As stated above, whenever power or energy scaling is limited by nonlinearity such a fiber offers a significant potential.

4.3.10 Power scaling consideration for cw fiber lasers

The described progress in fiber fabrication technology allows for a significant power scaling of fiber lasers in continuous-wave and pulsed operation. The limit in output power is determined by optical damage, thermal loading and nonlinear effects. For a fiber laser possessing a micro-structured core with a mode-field diameter as large as 35 μm the limits are summarized in Fig. 4.3.19. Such fibers allow for stable fundamental-mode operation even at bending diameters of smaller than 1 m.

Surface damage thresholds in excess of 1.3 GW/cm^2 are experimentally verified for rare-earth-doped fused silica by extracting output powers of 200 W from a 4 μm core fiber laser. This value leads to a damage threshold of about 12.5 kW in a core with a mode-field diameter of 35 μm (the solid line in Fig. 4.3.19). The calculated threshold of nonlinearity (Stimulated Raman Scattering, SRS) as a function of the fiber length is illustrated by the line "SRS threshold" in Fig. 4.3.19. Several experimental results confirm the shown numerical simulations. Detailed investigations of the thermo-optical behavior of air-clad rare-earth-doped microstructured fibers have shown that these fibers have basically the same heat dissipation capabilities as conventional double-clad fibers if the air-cladding region is properly designed. An extracted power of more than 100 W/m is experimentally demonstrated without any thermal problems out of air-cooled fibers. This value is assumed in Fig. 4.3.19 (lower line). This analysis leads to the conclusion that it is possible to extract a power in the range of ∼ 3 kW from an air-cooled, 30-m long single-mode fiber laser. If more sophisticated cooling techniques are applied (e.g. forced air-cooling or passive water cooling) the extracted power can be easily enhanced. Recently, an extracted power level of 550 W/m has been realized in a water-cooled configuration without thermo-optical issues [06Lim]. The left "extracted power" line in Fig. 4.3.19 assumes an average power extraction per unit fiber length of 1 kW/m, which we believe can be obtained by applying advanced active or passive fiber cooling techniques. As can be seen in Fig. 4.3.19, this leads to a possible output power close to 10 kW for diffraction-limited output. It is worth to be mentioned that due to the spectral separation of the laser wavelength and the Raman signal of ∼ 13 THz a suppression of stimulated Raman scattering is possible by spectral filtering. The consequently increased threshold of nonlinearity allows for the use of longer fiber lengths than those shown in Fig. 4.3.19 and thus relax thermo-optical issues by spreading the thermal load. Due to the recent developments of reliable high-brightness all-solid-state pump sources, and to recent advances in fiber manufacturing technology, we fully expect that these power levels will soon be demonstrated in the laboratory.

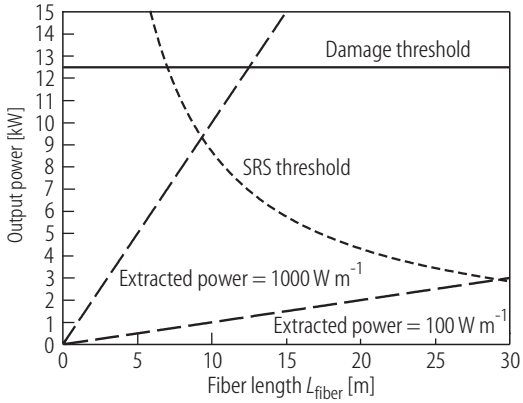

Fig. 4.3.19. Summary of all limitations of a continuous-wave fiber laser with a mode-field diameter of 35 μm.

References for 4.3

63Sni Snitzer, E.: Neodymium glass laser; Proc. of the Third International Conference on Solid Lasers, Paris, 1963, pp. 999–1019.

66Koe Koester, C.J.: Laser action by enhanced total internal reflection; IEEE J. Quantum Electron. **2** (1966) 580–584.

72Jon Jones, W.B., Goldman, L.M., Chernoch, J.P., Martin, W.S.: The Mini-FPL – A Face-Pumped Laser: Concept and Implementation; IEEE J. Quantum Electron. **8** (1972) 534.

74Mau Maurer, R.: Optical waveguide light source; U.S. Patent 3 808 549, Apr. 30, 1974.

78Sak Sakai, J.I., Kimura, T.: Bending loss of propagation modes in arbitrary-index profile optical fibers; Appl. Opt. **17** (1978) 1499–1506.

88Sni Snitzer, E., Po, H., Hakimi, F., Tumminelli, R., McCollum, B.C.: Double-clad, offset core Nd fiber laser, in: Optical Fiber Sensors of 1988 OSA Technical Digest Series, Vol. 2, Washighton, D.C.: Optical Society of America, 1988, postdeadline paper PD5.

88Urq Urquhart, P.: Review of Rare Earth Doped Fibre Lasers and Amplifiers; IEE Proc. J. Optoelectron. **155** (1988) 385.

93Bri Brierley, M.C., Massicott, J.F., Whitley, T.J., Millar, C.A., Wyatt, R., Davey, S.T., Szebesta, D.: Visible Fiber Lasers; BT Technol. J. **11** (1993) 128.

94Gie Giesen, A., Hugel, H., Voss, A., Wittig, K., Braucli, U., Opower, H.: Scalable concept for diode-pumped high power solid-state lasers; Appl. Phys. B **58** (1994) 365–372.

95Agr Agrawal, G.P., in: Nonlinear Fiber Optics, San Diego, NY: Academic Press, 1995.

96Kni Knight, J., Birks, T., Russell, P., Atkin, D.: All-silica single-mode optical fiber with photonic crystal cladding; Opt. Lett. **21** (1996) 1547.

97Bir Birks, T., Knight, J., Russell, P.: Endlessly single-mode photonic crystal fiber; Opt. Lett. **22** (1997) 961–963.

97Pas Paschotta, R., Nilsson, J., Tropper, A.C., Hanna, D.C.: Ytterbium-doped fiber amplifiers; IEEE J. Quantum Electron. **33** (1997) 1049.

98Gha Ghatak, A., Thyagarajan, K.: Introduction to Fiber Optics, Cambridge: Cambridge University Press, 1998.

99Koe Koechner, W.: Solid-State Laser Engineering, Berlin, Heidelberg: Springer-Verlag, 1999.

00Kop Koplow, P., Kliner, D., Goldberg, L.: Single-mode operation of a coiled multimode fiber amplifier; Opt. Lett. **25** (2000) 442–444.

01Gal Galvanauskas, A.: Mode-scalable fiber-based chirped pulse amplification systems; IEEE J. Sel. Topics Quantum Electron. **7** (2001) 504–517.

03Lim Limpert, J., Schreiber, T., Liem, A., Nolte, S., Zellmer, H., Peschel, T., Guyenot, V., Tünnermann, A.: Thermo-optical properties of air-clad photonic crystal fiber lasers in high power operation; Opt. Express **11** (2003) 2982–2990.

03Rus Russell, J.P.: Photonic Crystal Fibers; Science **299** (2003) 358–362.

04Jeo Jeong, Y., Sahu, J.K., Payne, D.N., Nilsson, J.: Ytterbium-doped large-core fiber laser with 1.36 kW continuous-wave output power; Opt. Express **12** (2004) 6088–6092.

04Lim Limpert, J., Liem, A., Reich, M., Schreiber, T., Nolte, S., Zellmer, H., Tünnermann, A., Broeng, J., Petersson, A., Jakobsen, C.: Low-nonlinearity single-transverse-mode ytterbium-doped photonic crystal fiber amplifier; Opt. Express **12** (2004) 1313–1319.

05Lim Limpert, J., Deguil-Robin, N., Manek-Hönninger, I., Salin, F., Röser, F., Liem, A., Schreiber, T., Nolte, S., Zellmer, H., Tünnermann, A., Broeng, J., Petersson, A., Jakobsen, C.: High-power rod-type photonic crystal fiber laser; Opt. Express **13** (2005) 1055–1058.

05Tue Tünnermann, A., Schreiber, T., Röser, F., Liem, A., Höfer, S., Zellmer, H., Nolte, S., Limpert, J.: The renaissance and bright future of fibre lasers; J. Phys. B **38** (2005) 681–693.

06Lim Limpert, J., Schmidt, O., Rothhardt, J., Röser, F., Schreiber, T., Tünnermann, A., Ermeneux, S., Yvernault, P., Salin, F.: Extented single-mode photonic crystal fiber lasers; Opt. Express **14** (2006) 2715–2720.

07IPG `www.ipgphotonics.com`.

4.4 Color-center lasers

R. Beigang

4.4.1 Introduction

Color-center lasers are broadly tunable solid-state lasers which can be operated in cw, pulsed and mode-locked operation. They are optically pumped by coherent light sources and the active material consists of color centers in alkali-halide crystals which have to be cooled down to liquid-nitrogen temperatures. These laser systems have shown to be very efficient, widely tunable laser systems for the near-infrared spectral region which have been used in a wide range of applications. Because of the requirement of cryogenic temperatures and the advent of other coherent tunable solid-state sources in the near-infrared spectral region they are no longer used routinely.

The first color-center laser was already realized in 1965 by Fritz and Menke [65Fri] in pulsed operation. Although the efficiency of this system was rather low and the tunability was not demonstrated the color-center laser was, in principle, the first tunable laser system operated. Only a decade later first cw operation with demonstration of tunability was achieved for F_A(II) centers in KCl [74Mol, 76Mol]. This was the start of a fast development of different color-center lasers spanning a very wide wavelength range [77Lit, 80Sch, 82Mol, 85Pin, 89Gel]. Although several attempts have been made the requirement of cryogenic cooling was never overcome. However, easy to use cryogenic cooling systems for the laser made this system for a long time a very versatile laser for many applications.

In the following sections the basic physics of color centers in alkali-halide crystals, their optical properties and the main characteristics of different laser systems using color centers will be briefly reviewed. Review articles about color-center lasers can be found in the literature [79Mol2, 85Mol1, 85Mol2, 86Pol, 87Mol, 91Gel, 95Mir].

4.4.2 Physics of color centers

4.4.2.1 Classification of color centers

Color centers are electron (or hole) trapping defects in insulating crystals. They are studied very intensively in alkali-halide crystals which are the main material for laser systems. Therefore, in the following we will concentrate on alkali-halide crystals only. The basic color center which is the fundamental building block for a large variety of color centers is the F center (F from the German word *Farbe*, meaning color). It consists of an electron trapped at a halide vacancy. An F_A center is formed if one of the nearest surrounding alkali atoms is replaced by a foreign ion, e.g. a Li^+ in a potassium chloride crystal. If two neighbouring halide ions are replaced by a foreign ion this center is called F_B center. Two F centers next to each other are called F_2 center and the singly ionized counterpart is the F_2^+ center which is an important center for powerful color-center lasers. The

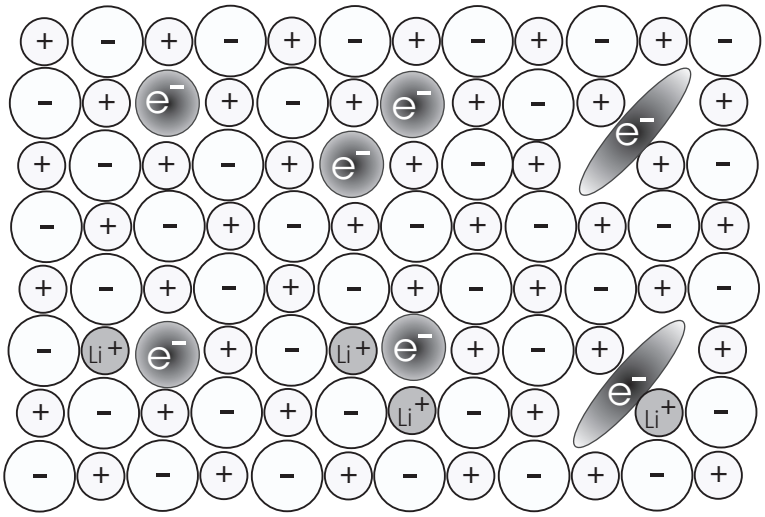

Fig. 4.4.1. Schematic diagram of the ionic configurations of different color centers in alkali-halide crystals. Upper row from left to right: F-center, F_2-center and F_2^+-center. Lower row from left to right: F_A(II)-center, F_B(II)-center and $(F_2^+)_A$-center. The foreign alkali ion is represented by a Li^+-ion.

stability of this center can be greatly improved by adding foreign metal ions (like Li^+ as shown in Fig. 4.4.1) which is then called $(F_2^+)_A$ center. In order to get electrically neutral centers other charged defects replacing a halide ion can be added like O^{2-}. It should also be mentioned that F^+ centers in alkaline earth oxides have shown to be laser-active. A foreign Tl^+-ion leads to a $Tl^0(1)$-center which is a stable and important laser-active center although it is not an F center because the electron is concentrated in the vicinity of the Tl^+-ion making it a neutral atom. All centers listed here are only stable at cryogenic temperatures. The preparation of the centers is different for each type and requires special knowledge of their optical properties. A survey of color-center physics can be found in [68Fow].

4.4.2.2 Preparation of laser-active color centers

The basic building block of all color centers in alkali-halide crystals is the simple F center. F centers can be produced by radiation damage with ionizing radiation. A more controlled way of generation is additive coloration in alkali-metal vapor. This method is based on the fact that there is an equilibrium between alkali ions in the crystal and alkali atoms in the surrounding vapor. As a consequence alkali atoms will move to the crystal surface leaving behind simple vacancies where an electron is trapped, forming an F center. After a certain time there will be an equilibrium density of F centers which only depends on the vapor density whereas the temperature of the crystal determines the speed of diffusion. In a second step an aggregation process has to be performed which combines the F centers with other F centers, defects or foreign ions in the crystal. This aggregation strongly depends on the type of center and is typically a combination of optical excitation and thermal ionization at specific temperatures. Details can be found e.g. in [87Mol, 91Gel]. After aggregation the crystals have to be cooled down to cryogenic temperatures to guarantee stability under optical excitation. Even daylight at room temperatures will destroy the generated centers and will lead to cluster formation of centers due to diffusion in the crystal. For some types of centers the aggregation process can be repeated several times (F_A and F_B centers e.g.) whereas other centers have to be kept at low temperatures after aggregation all the time (F_2^+ centers).

4.4.2.3 Excitation and emission processes

The optical excitation, relaxation and emission properties will be illustrated for the case of an $F_A(II)$ center in KCl:Li. A typical energy level diagram together with the corresponding ionic configuration is shown in Fig. 4.4.2. Because of the symmetry of the $F_A(II)$ center the absorption band is split into two bands. After optical excitation in the visible spectral region a fast relaxation to the upper laser level occurs. This relaxation is accompanied by a dramatic change of the ionic configuration. The $F_A(II)$ center relaxes into a double-well configuration where the electron is spread over a wide area. The laser transmission takes place in this double-well configuration. From the ground state the $F_A(II)$ center relaxes to the original configuration. Both relaxation times are extremely fast ($< 10^{12}$ s) and the lifetime in the upper laser level ranges from several nanoseconds up to microseconds depending on the center type. The fluorescence quantum efficiency η is strongly temperature-dependent with a maximum at low temperatures. For $F_A(II)$ centers in KCl:Li, e.g., it changes from 50 % at 1.6 K to 20 % at 200 K.

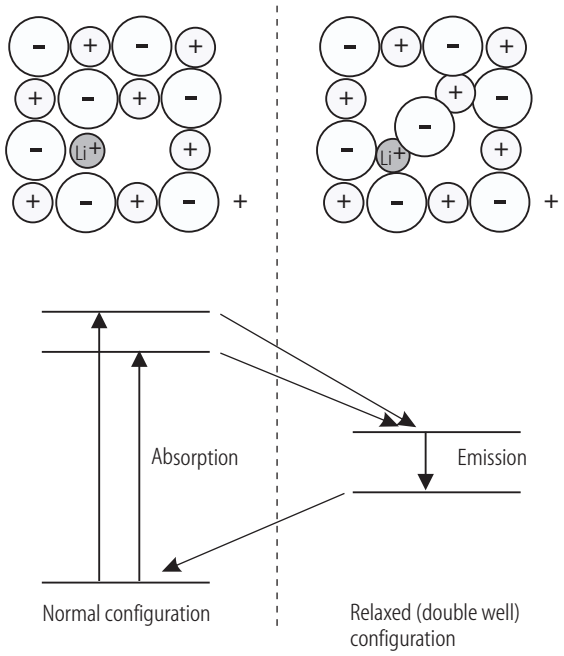

Fig. 4.4.2. Energy levels and optical transitions of the $F_A(II)$ center in KCl:Li. The upper part shows the ionic configuration of the $F_A(II)$ center in its ground and relaxed excited state. After excitation the crystal relaxes to a double-well configuration. The lower part shows the corresponding energy levels associated with absorption and emission bands. The absorption band is split into two bands because of the symmetry of the ionic configuration. The absorption wavelength is in the visible and the emission in the near-infrared between 2.3 μm and 3.1 μm.

The Stokes shift between pump and laser emission wavelength limits the output power, in particular in the case of $F_A(II)$ and $F_B(II)$ centers as there is a ratio of nearly 5:1 between pump and emission photon energies. In this case 80 % of the input pump power is dissipated into heat in the crystal. Properties of different types of centers in various hosts are displayed in Table 4.4.1.

4.4.3 Laser systems

Color-center lasers have been operated pulsed, cw and mode-locked. In principle, the optical cavities used for color-center lasers are very similar to dye laser resonators. However, there is additional need for cryogenic cooling and, as a consequence, also insulating vacuum. Therefore, the actual color-

Table 4.4.1. Performance of typical cw color-center lasers.

Center type	Host	Pump wavelength [μm]	Tuning range [μm]	Output power (cw) [W]	Reference
F^+	CaO	0.351	0.36–0.40	0.2	[81Hen]
F_2^+	LiF	0.647	0.82–1.05	1.8	[79Mol1]
	KF	1.064	1.22–1.50	2.7	[79Mol1]
$(F_2^+)_H$	NaCl:O^{2-}	1.064	1.42–1.85	3	[86Pin, 87Geo, 87Ger, 87Wan2, 87Wan1, 88Bei]
	KBr:O^{2-}	1.58	1.8–2.2	0.15	[94Mol2]
$(F_2^+)_{AH}$	KBr:Na:O^{2-}	1.58	1.9–2.4	0.15	[94Mol2]
	KCl:Na:O^{2-}	1.32	1.7–2.1	0.5	[80Gel]
$Tl^0(1)$	KCl:Tl	1.064	1.4–1.6	1.1	[82Mol, 81Gel]
F_A(II)	KCl:Li	0.514, 0.647	2.3–3.1	0.28	[86Ger]
	RbCl:Li	0.647	3.5–3.65	0.9	[86Ger]
F_B(II)	KCl:Na	0.514, 0.595	2.2–2.7	0.6	[86Ger]

center laser systems are more complex than dye lasers. In the following sections basic operation principles will be discussed and properties of selected systems are described. The whole wavelength range from 1.3 μm up to 5 μm can be covered with color-center lasers using different types of centers in various hosts. However, because of complex procedures to generate the centers and their instability at room temperature there are only a few systems which have been used for applications.

4.4.3.1 Continuous-wave laser systems

A typical optical cavity of a cw color-center laser is shown in Fig. 4.4.3. It basically consists of a folded astigmatically compensated cavity as used with dye lasers. The crystal is placed under

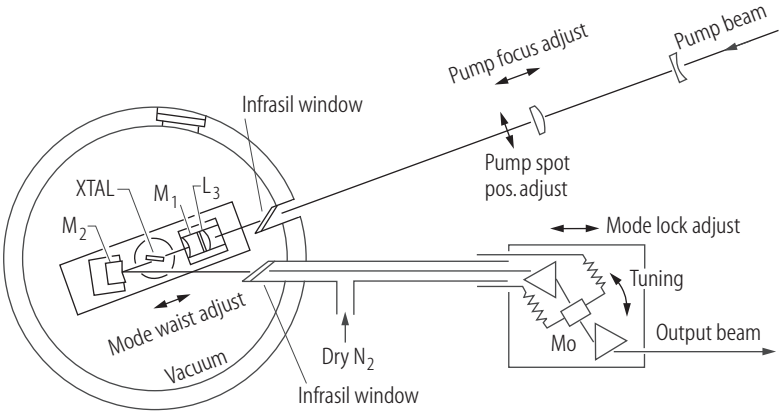

Fig. 4.4.3. Typical set-up of a cw color-center laser [87Mol]. M1 and M2 are concave mirrors with a radius of curvature of −50 mm. The crystal is placed inside a vacuum chamber. Tuning is accomplished with a Brewster prism. The tuning arm is flushed with dry nitrogen to reduce water vapor absorption. The external prism is used for beam walk-off compensation.

Brewster's angle as it cannot be antireflection-coated. Because of the tight focus at the place of the crystal the thickness is limited to 1 to 3 mm. It is cooled with a cryogenic system which has to be very efficient as it determines the maximum pump power to be used [78Lit, 85Mol1]. Tuning is accomplished by use of prisms, gratings [85Vie] or birefringent filters [88Phi]. For single-mode operation also ring cavities have been applied [88Bei]. In this case birefringent filters are preferable to tune the color-center laser. The intrinsic line width of single-mode color-center lasers can be extremely narrow [77Bei] which makes these lasers very attractive for use in frequency-stabilized systems. Typical output powers depend on the type of color center used. It can range from a few mW for color centers with a large Stokes shift up to several watts for $(F_2^+)_H$-centers. The main problem to achieve high output power is an efficient heat removal from the excitation area inside the crystal [78Lit].

The type of pump source depends on the absorption bands of the color center. For cw operation only cw lasers in the visible and near-infrared spectral region can reach the required pump power at threshold. Typical pump lasers are Ar- and Kr-ion lasers, dye lasers and Nd:YAG lasers.

The $(F_2^+)_H$-center laser in O^{2-}-doped NaCl is one of the most powerful color-center lasers operating in the wavelength range from 1.42 μm up to 1.8 μm [86Pin, 87Geo, 87Ger, 87Wan2, 87Wan1, 88Bei] which can be pumped by the powerful Nd:YAG laser. Because of realignment processes of the color centers during the relaxation processes after excitation the crystal has to be pumped simultaneously with additional low-power auxiliary light from a green light source [91Car]. The maximum output power obtained with such a system was 3 W when pumped with 10 W of a Nd:YAG laser and 100 mW of green light from an air cooled Ar-ion laser for reorientation.

4.4.3.2 Pulsed laser systems

Pulsed operation was reported for several color-center laser systems using different pulsed laser pump sources like N_2-pumped dye lasers [81Bei], flashlamp pumped dye lasers [80Bei] and *Q*-switched, frequency-doubled Nd:YAG lasers [81Sub]. As for cw systems the resonator design is in close analogy to pulsed dye lasers. Tuning is accomplished mainly by gratings in Littrow mount [80Bei] or under grazing incidence [81Bei]. Pulse energies of up to 100 μJ have been obtained even with F_A(II) centers in KCl:Li [81Sub]. There are also reports of pulsed color-center lasers at room temperature. In this case pulsed operation is required to guarantee the stability of the centers under laser excitation [87Cul, 04Bas].

Because of the large gain bandwidth of all color-center lasers they are ideally suited for mode-locked operation. Synchronous pumping resulted in pulses with pulse lengths in the order of several picoseconds [79Mol1, 82Mol, 80Mol, 89Kur, 94Mol1]. Self-mode-locking generated pulses below 1 ps [93Ken] and the combination of synchronous pumping with soliton formation led to ultrashort pulses in the near-infrared spectral region down to 18 fs [84Mol, 85Mol2, 86Mit, 87Mit].

References for 4.4

65Fri Fritz, B., Menke, E.: Solid State Commun. **3** (1965) 61.

68Fow Fowler, F. (ed.): Physics of Color Centers, New York: Academic Press, 1968.

74Mol Mollenauer, L.F., Olson, D.H.: Appl. Phys. Lett. **24** (1974) 386.

76Mol Mollenauer, L.F., Olson, D.H.: J. Appl. Phys. **46** (1976) 3109.

77Bei Beigang, R., Litfin, G., Welling, H.: Opt. Commun. **22** (1977) 269.
77Lit Litfin, G., Beigang, R., Welling, H.: Appl. Phys. Lett. **31** (1977) 382.

78Lit Litfin, G., Beigang, R.: J. Phys. E **11** (1978) 984.

79Mol1 Mollenauer, L.F., Bloom, D.M.: Opt. Lett. **4** (1979) 247.
79Mol2 Mollenauer, L.F., in: Quantum Electronics, Part B, Tang, C.L. (ed.), New York: Academic Press, 1979, Chap. 6.

80Bei Beigang, R.: Opt. Gommun. **34** (1980) 249.
80Gel Gellermann, W., Luty, F., Koch, K.P., Litfin, G.: Phys. Status Solidi (a) **57** (1980) 411.
80Mol Mollenauer, L.F., Stolen, R.H., Gordon, J.P.: Phys. Rev. Lett. **45** (1980) 1095.
80Sch Schneider, I., Marquardt, C.L.: Opt. Lett. **5** (1980) 214.

81Bei Beigang, R., Wynne, J.J.: Opt. Lett. **6** (1981) 295.
81Gel Gellermann, W., Luty, F., Pollock, C.R.: Opt. Commun. **39** (1981) 391.
81Hen Henderson, B.: Opt. Lett. **6** (1981) 247.
81Sub Subdo, A.S., Loy, M.M.T., Roland, A., Beigang, R.: Opt. Commun. **37** (1981) 417.

82Mol Mollenauer, L.F., Vieira, N.D., Szeto, L.: Opt. Lett. **7** (1982) 414.

84Mol Mollenauer, L.F., Stolen, R.H.: Opt. Lett. **9** (1984) 13.

85Mol1 Mollenauer, L.F., in: The Laser Handbook, Stich, M., Bass, M. (ed.), Amsterdam: North Holland, 1985, Chap. 3.
85Mol2 Mollenauer, L.F.: Philos. Trans. R. Soc. A (London) **315** (1985) 437.
85Pin Pinto, J.F., Stratton, L.W., Pollock, C.R.: Opt. Lett. **10** (1985) 384.
85Vie Vieira jr., N.D., Mollenauer, L.F.: IEEE J. Quantum Electron. **21** (1985) 195.

86Ger German, K.: J. Opt. Soc. Am. B **3** (1986) 149.
86Mit Mitschke, F.M., Mollenauer, L.F.: IEEE J. Quantum Electron. **22** (1986) 2242.
86Pin Pinto, J.F., Georgiou, E., Pollock, C.: Opt. Lett. **11** (1986) 519.
86Pol Pollock, C.R.: J. Lumin. **35** (1986) 65.

87Cul Culpepper, C.F., Carrig, T.J., Pinto, J.F., Pollock, C.R.: Opt. Lett. **12** (1987) 882.
87Geo Georgiou, E., Pinto, J.F., Pollock, C.: Phys. Rev. B **35** (1987) 7636.
87Ger German, K., Pollock, C.: Opt. Lett. **12** (1987) 474.
87Mit Mitschke, F.M., Mollenauer, L.F.: Opt. Lett. **12** (1987) 407.
87Mol Mollenauer, L.F., in: Topics in Applied Physics, Vol. 59, Mollenauer, L.F., White, J.C. (ed.), Berlin: Springer-Verlag, 1987, p. 225.

87Wan1 Wandt, D., Gellermann, W.: Opt. Commun. **61** (1987) 405.
87Wan2 Wandt, D., Gellermann, W., Luty, F.: J. Appl. Phys. **61** (1987) 864.

88Bei Beigang, R., Klameth, K., Becker, B., Yoon, Z., Welling, H.: Opt. Commun. **65** (1988) 383.
88Phi Phillips, G., Hinske, P., Demtröder, W., Möllmann, K., Beigang, R.: Appl. Phys. B **47** (1988) 127.

89Gel Gellermann, W., Luty, F.: Opt. Commun. **72** (1989) 214.
89Kur Kurobori, T., Nebel, A., Beigang, R., Welling, H.: Opt. Commun. **73** (1989) 365.

91Car Carrig, T.J., Pollock, C.R.: J. Appl. Phys. **69** (1991) 3796.
91Gel Gellermann, W.: J. Phys. Chem. Solids **52** (1991) 249.

93Ken Kennedy, G.T., Grant, R.S., Sibbett, W.: Opt. Lett. **18** (1993) 1736.

94Mol1 Mollmann, K., Gellermann, W.: Opt. Lett. **19** (1994) 490.
94Mol2 Mollmann, K., Schrempel, M., Yu, B.K., Gellermann, W.: Opt. Lett. **19** (1994) 960.

95Mir Mirov, S.B., Basiev, T.: IEEE J. Sel. Topics Quantum Electron. **1** (1995) 1.

04Bas Basiev, T., Papashvilli, A.G., Fedorov, V.V.: Laser Physics **14** (2004) 1.

5.1 Fundamentals of diode lasers

E. Gornik

5.1.1 Introduction

Diode lasers represent a very attractive source of coherent light for a widespread field of applications since they combine high external efficiency and compact size. Typical dimensions of diode lasers are below 500 μm. They appear in laser printers as well as in optical disk storage devices and optical measurement systems. High-power semiconductor laser arrays with cw output powers of ~ 1 W of a single laser are used to pump solid-state lasers. For spectroscopic applications, single-frequency lasers with line widths in the range of several kHz are employed. Moreover, diode lasers are key-components in high-performance, fiber-based optical communication systems.

Diode laser structures are usually made up of epitaxially grown III-V and in some cases of II-VI compound semiconductors. Emission wavelengths range from visible blue lasers based on the GaN/AlGaN/InGaN material system to the mid-infrared lead salt lasers. The "classical" materials for the realization of diode lasers, however, are the GaAs/$Al_xGa_{1-x}As$ system covering the spectral range from 620 nm to 880 nm, and $In_{1-x}Ga_xAs_{1-y}P_y$ for emission wavelengths around 1.3 μm and 1.55 μm which are of special importance for silica-fiber-based optical communication systems.

A powerful feature of diode lasers is that the widespread possibilities of epitaxial growth can be fully exploited in the device design. Structures comprising layers of different materials (so-called heterostructures) can be realized to tailor both the optical properties of the laser cavity and electrical device characteristics. Quantum Wells (QWs) consisting of only a few atomic monolayers have a very high material gain which is used to realize very-low-threshold lasers. The gain spectrum of QWs can be tuned by properly adjusting the QW thickness, allowing the fabrication of laser diodes operating at wavelengths not attainable with bulk material.

5.1.2 Basic diode laser operational principles

Figure 5.1.1 depicts the general structure of a semiconductor laser. It consists of an active zone incorporating the gain region, which amplifies the light propagating back and forth in the direction of the laser axis. In simple Fabry–Perot (FP) lasers, optical feedback is provided by two end mirrors formed by cleaved facets. The active region is placed between two cladding layers which serve two purposes. First, having refractive indices (μ_1 and μ_3) smaller than that of the active region (μ_2), they represent a dielectric waveguide confining the light in the transverse direction [90Tam]. This waveguide is usually designed such that only one transverse mode exists. Second, they possess opposite doping types, allowing the creation of a population inversion in the gain region by simply forward-biasing the diode.

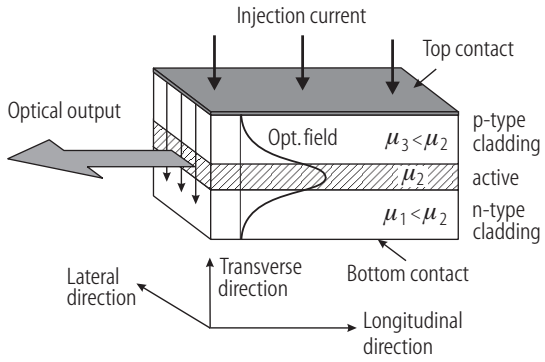

Fig. 5.1.1. Stripe-contact Fabry–Perot laser diode.

5.1.2.1 Gain in semiconductors

One of the most common diode lasers is of the Double-Hetero (DH) type, comprising bulk semiconductor material which provides the gain. Figure 5.1.2 shows the band diagram of a forward-biased DH structure. Electrons and holes are injected into the active layer from the n– and p-doped cladding layer, respectively. The higher bandgap energies of the cladding layer materials create barriers in the band structure which prevent the carriers from escaping the active region, thus greatly improving the conversion efficiency from current to light. The injected carriers can recombine by several mechanisms: nonradiative recombination, bimolecular recombination and Auger processes. These recombination processes are described in terms of a carrier lifetime τ_s which depends on the carrier density n and the nonradiative recombination time τ_nr. The total recombination rate is given by the expression

$$\frac{n}{\tau_\mathrm{s}} = \frac{n}{\tau_\mathrm{nr}} + Bn^2 + Cn^3 \; . \tag{5.1.1}$$

B is found to be in the order of $0.3 \ldots 2 \times 10^{-10}$ cm^3 s^{-1} for both AlGaAs and InGaAsP devices. The recombination coefficient C of the non-radiative Auger process is about $1 \ldots 3 \times 10^{-29}$ cm^6 s^{-1} for InGaAs whereas for AlGaAs Auger recombination can usually be neglected. For lightly doped material and carrier densities of several 10^{18} cm^{-3}, typically required for lasing, carrier lifetimes are a few nanoseconds. For sufficiently high carrier injection population inversion occurs. Gain as a function of photon energy can be written as

$$g(\hbar\omega) \propto \frac{1}{\hbar\omega} |\mathsf{M}_{\mathrm{c}\to\mathrm{v}}|^2 \rho_\mathrm{comb}(\hbar\omega)(f_\mathrm{c} - f_\mathrm{v}) \; , \tag{5.1.2}$$

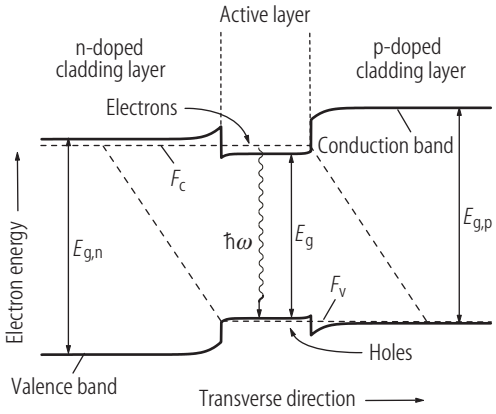

Fig. 5.1.2. Schematic band diagram of a DH structure under forward bias.

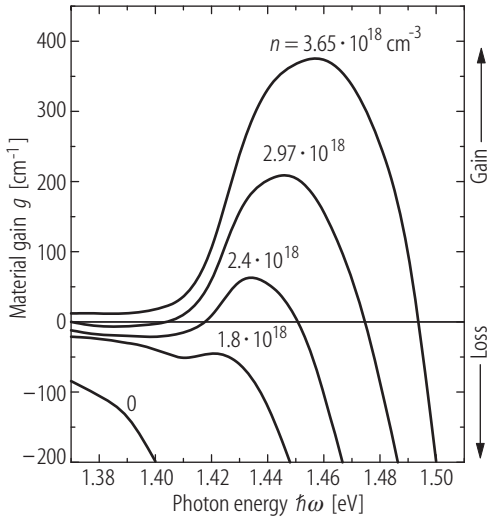

Fig. 5.1.3. Gain in bulk GaAs as a function of photon energy for different carrier densities (after [81Yam]).

where $\mathsf{M}_{c\to v}$ is the transition matrix element and ρ_{comb} the combined density of states [93Zor]. f_c and f_v are the Fermi functions in the conduction- and valence-band, with their related Fermi-energies F_c and F_v. Since gain in semiconductors is due to electronic transitions between energy bands, photons in a relatively wide energy range $F_c - F_v > \hbar\omega > E_g$ are amplified. Figure 5.1.3 shows the calculated material gain for undoped bulk GaAs as a function of the photon energy for different carrier densities. A peak gain of several hundred cm^{-1} can be achieved for carrier densities of several 10^{18} cm^{-1}. The peak gain g_p depends on the carrier density and can be linearized to a good approximation:

$$g_p(n) = a(n - n_t) \,, \tag{5.1.3}$$

where $a = \partial g/\partial n$ is the differential gain and n_t is the transparency density. For GaAs, $a \approx 2 \ldots 3 \times 10^{-16}$ cm^2 and $n_t \approx 10^{18}$ cm^{-3}. Considerably higher material gain of some thousand cm^{-1} can be achieved in QWs because of the enhanced density of states in quantized systems. For bulk material with parabolic bands one finds $\rho_{comb}(\hbar\omega) \propto \sqrt{\hbar\omega - E_g}$, whereas for a QW $\rho_{comb}(\hbar\omega)$ is step-wise constant and non-vanishing at the band-edge. For QW systems the peak gain rather follows a logarithmic law $g_p(n) = A \ln(n/n_t)$ than a linear one.

5.1.2.2 Round-trip condition

When laser oscillation occurs, the optical field reproduces itself after a round-trip through the resonator. Assuming a Fabry–Perot resonator with length L which is terminated by reflectors with an amplitude reflectivity r_1 and r_2 on the left and the right side, respectively, the round-trip condition can be written as follows:

$$r_1 r_2 \, e^{(\Gamma g - \alpha_{wg})L} \exp\left(\frac{4\pi \, i \mu_{eff}}{\lambda} L\right) = 1 \,, \tag{5.1.4}$$

where μ_{eff} is the effective refractive index of the laser waveguide, g the active layer gain and α_{wg} the waveguide loss. The confinement factor Γ accounts for the fact that the optical field in the cladding regions is not amplified. For symmetric dielectric waveguides composed of an active layer with thickness d and refractive index μ_2 embedded in cladding layers with refractive index μ_1, a suitable approximation for Γ is given by

$$\Gamma = \frac{2\nu^2}{1+2\nu^2} , \quad \nu = \frac{\pi d}{\lambda}\sqrt{\mu_2^2 - \mu_1^2} . \tag{5.1.5}$$

For the sake of simplicity we assume r_1 and r_2 to be real and of equal magnitude $r_1 = r_2 = \sqrt{R}$ where R is the intensity reflectivity of the laser facet. From the absolute value of (5.1.4) the gain threshold condition for laser oscillation

$$\Gamma g = \Gamma g_{\mathrm{th}} = \alpha_{\mathrm{wg}} - \frac{1}{L}\ln R \tag{5.1.6}$$

is deduced. This means that the mode gain Γg has to compensate the waveguide loss α_{wg} and the facet loss

$$\alpha_{\mathrm{facet}} = -\frac{1}{L}\ln R . \tag{5.1.7}$$

The phase condition of (5.1.4) yields the longitudinal modes $\lambda_m = 2\mu_{\mathrm{eff}}L/m$ where m is the (integer) mode order. The mode spacing is given by [91Buu]

$$\Delta\lambda = \frac{\lambda^2}{2\mu_{\mathrm{g}}L} , \tag{5.1.8}$$

where $\mu_{\mathrm{g}} = \mu_{\mathrm{eff}} - \lambda(\mathrm{d}\mu_{\mathrm{eff}}/\mathrm{d}\lambda)$ is the group refractive index of the laser waveguide which is somewhat larger than the effective index. For a typical GaAs/AlGaAs Fabry–Perot DH laser diode (L = 380 µm, $R = 0.32$, $\alpha_{\mathrm{facet}} = -(\ln R)/L \approx 30\ \mathrm{cm}^{-1}$, $\alpha_{\mathrm{wg}} \approx 10\ \mathrm{cm}^{-1}$, $\lambda \approx 870$ nm, $\Gamma = 0.4$, $\mu_{\mathrm{eff}} = 3.4$ and $\mu_{\mathrm{g}} = 4$) one obtains a threshold gain $g_{\mathrm{th}} = 100\ \mathrm{cm}^{-1}$ and a mode spacing $\Delta\lambda \approx 2.4$ Å which is roughly two orders of magnitude smaller than the width of the gain spectrum. Under cw-operation, the laser emits into the mode that receives enough gain to start lasing. The adjacent side modes experience a gain only slightly smaller than their threshold gain. Due to amplified spontaneous emission, these side modes also contain some power, although much less than the dominant mode. When the laser is modulated, transient phenomena may raise the gain above the threshold value of the side modes. The emission spectrum will then contain several longitudinal modes.

5.1.2.3 Rate equations

In order to describe laser properties such as threshold behavior, output power and modulation characteristics, rate equations are used. For the sake of simplicity we restrict ourselves to single-mode rate equations – the discussion of multi-mode rate equations may be found elsewhere [86Agr, 91Pet]. The rate equations for the carrier density n and the photon density S of the optical mode are written as follows:

$$\frac{\mathrm{d}n}{\mathrm{d}t} = \frac{j}{ed} - \frac{n}{\tau_{\mathrm{s}}} - a(n-n_{\mathrm{t}})S\frac{c}{\mu_{\mathrm{g}}} , \tag{5.1.9}$$

$$\frac{\mathrm{d}S}{\mathrm{d}t} = \frac{\Gamma K n}{\tau_{\mathrm{s}}} + \Gamma a(n-n_{\mathrm{t}})S\frac{c}{\mu_{\mathrm{g}}} - \frac{S}{\tau} . \tag{5.1.10}$$

The carrier injection rate into the active layer with the thickness d due to the drive current density j is j/ed. The carriers recombine both spontaneously at a rate n/τ_{s} and due to stimulated emission of photons at a rate $a(n-n_{\mathrm{t}})Sc/\mu_{\mathrm{g}}$. The linear approximation (5.1.3) has been used here to describe the carrier dependence of the gain. c/μ_{g} is the group velocity of light in the laser. The photon density increases due to stimulated emission at a rate $\Gamma a(n-n_{\mathrm{t}})Sc/\mu_{\mathrm{g}}$. A fraction $K = 10^{-5} \ldots 10^{-4}$ – which is called spontaneous emission factor – of the spontaneous emission goes into the optical mode yielding an increase of the photon density at a rate $\Gamma K n/\tau_{\mathrm{s}}$. The expression S/τ is the photon decay rate with τ being the photonic lifetime of the resonator. Due to the small laser cavities, τ is in the order of 1 fs and therefore roughly three orders of magnitude smaller than the carrier lifetime.

5.1.2.4 Threshold behavior and optical output

Assuming steady-state conditions ($\mathrm{d}/\mathrm{d}t = 0$) for the rate equations (5.1.9) and (5.1.10) and neglecting spontaneous emission into the optical mode, the following solutions of the rate equations are obtained: Below threshold ($j < j_{\mathrm{th}}$) one gets

$$S = 0\,, \quad n = \frac{\tau_{\mathrm{s}}}{ed}\, j\,. \tag{5.1.11}$$

The cavity contains no photons and the carrier density increases linearly with the pump current density. Above threshold ($j > j_{\mathrm{th}}$) the photon density grows linearly with j and the carrier density is clamped in saturation:

$$S = \Gamma \frac{\tau}{ed}\,(j - j_{\mathrm{th}})\,, \quad n = \frac{\tau_{\mathrm{s}}}{ed}\, j_{\mathrm{th}} = n_{\mathrm{th}}\,. \tag{5.1.12}$$

This behavior is depicted in Fig. 5.1.4. The threshold current density is explicitly given by the expression

$$j_{\mathrm{th}} = \frac{ed}{\tau_{\mathrm{s}}}\left(n_{\mathrm{t}} + \frac{\mu_{\mathrm{g}}}{ca\Gamma\tau}\right)\,. \tag{5.1.13}$$

The threshold current density depends on the carrier lifetime as well as on the differential gain $a = \partial g/\partial n$ and the confinement factor Γ which is a function of the active layer thickness d. For GaAs/AlGaAs DH lasers the optimum active layer thickness is about 0.1 μm where the threshold current shows a minimum taking typical values of roughly 1 kA/cm^2. Considerably lower threshold current densities of less than 0.1 kA/cm^2 have been obtained for strained QW lasers, since the differential gain is considerably larger [88Anh, 94Thi, 93Che], also overcompensating the influence of the lower confinement factor ($\Gamma_{\mathrm{QW}} \sim 1\%$).

The rate of photons leaving the resonator via the facets is $S_{\mathrm{tot}}/\tau_{\mathrm{R}}$ where $S_{\mathrm{tot}} = LwdS$ is the total photon number in the resonator with the volume Lwd (w: resonator width). The inverse outcoupling lifetime of the resonator is given by $1/\tau_{\mathrm{R}} = \alpha_{\mathrm{facet}} c/\mu_{\mathrm{g}}$. Using (5.1.12) the output power is written as

$$P = \eta_{\mathrm{i}} \frac{\hbar\omega}{e}(I - I_{\mathrm{th}})\frac{\tau}{\tau_{\mathrm{R}}} \tag{5.1.14}$$

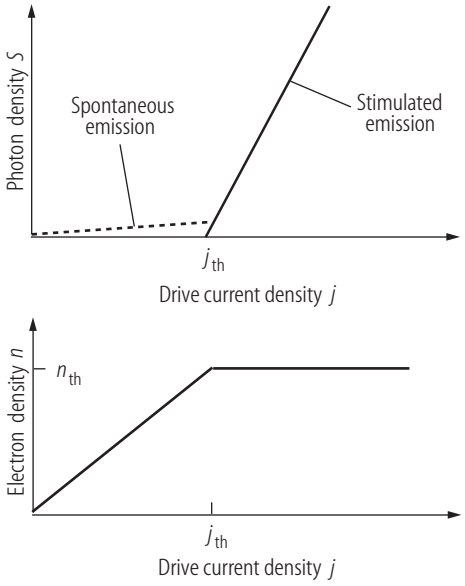

Fig. 5.1.4. Photon and carrier density as a function of drive current density.

with the current $I = Lwj$ and the treshold current $I_{\mathrm{th}} = Lwj_{\mathrm{th}}$. The internal quantum efficiency $\eta_{\mathrm{i}} < 1$ accounts for leakage currents and non-radiative recombination and takes values between 65 % and 90 %. The differential output efficiency is given by

$$\eta_{\mathrm{d}} = \frac{\mathrm{d}(P/\hbar\omega)}{\mathrm{d}(I/e)} = \eta_{\mathrm{i}} \frac{\tau}{\tau_{\mathrm{R}}} = \frac{\eta_{\mathrm{i}}}{1 - \alpha_{\mathrm{wg}} L / \ln R} \tag{5.1.15}$$

and shows values of up to 80 %. The conversion efficiency η describes the fraction of stimulated emission power and input power. Since almost the whole voltage drops at the pn-junction the input power is $\approx I\hbar\omega/e$ and thus

$$\eta = \frac{I - I_{\mathrm{th}}}{I} \eta_{\mathrm{d}} \,. \tag{5.1.16}$$

Conversion efficiencies of up to 60 % can be achieved. Diode lasers show the highest conversion efficiency of all laser types.

5.1.2.5 Thermal aspects

The temperature dependence of the threshold current of FP diode lasers is commonly described by the phenomenological law $I_{\mathrm{th}} \propto \exp(T/T_0)$, where T_0 is the characteristic temperature. Typically, for AlGaAs lasers $T_0 > 120$ K around room temperature, for InGaAsP lasers T_0 is found to be $50 \ldots 70$ K. The first group of mechanisms that jeopardize the laser output at elevated temperatures is related to the properties of the laser material: At higher temperatures, the Fermi-functions of the electrons and holes spread over wider energy ranges, resulting in an overall decrease of the material gain. Nonradiative Auger-recombination becomes more important and plays a dominant role in InGaAsP laser diodes. Absorption losses and leakage currents across the hetero-barriers increase with temperature. More structure-related effects are facet heating, increased surface recombination and temperature-dependent leakage currents flowing around the active region.

Due to their dense modal spectrum, Fabry–Perot lasers emit wavelengths close to the peak gain, which has a temperature-coefficient around 0.5 nm/K. The emission wavelength of other laser types (DFB, DBR, short-cavity lasers, see Sect. 5.1.3.1) is entirely determined by the refractive indices of the laser structure, resulting in a temperature dependence which is reduced by about one order of magnitude.

5.1.3 Lateral light/current confinement

In analogy to the transverse waveguide structure, confinement of both photons and carriers is also desired in the lateral direction in order to achieve lateral single-mode operation and low threshold currents. Lateral optical confinement can be achieved by either gain-guiding or index-guiding.

The simplest design for a gain-guided laser is sketched in Fig. 5.1.5a. Current is injected through a stripe contact formed by a typically $\sim 5 \ldots 20$ µm wide opening of a dielectric insulation layer. The optical field is confined to lateral regions where it experiences gain, i.e. where sufficient carrier injection into the active region occurs. Since no lateral current guiding is present, leakage currents due to current spreading limit device performance, especially for narrow devices. To overcome these problems lateral current confinement has to be introduced, either by proton implantation or (see Fig. 5.1.5b) by the introduction of an n-type blocking layer in the p-type upper cladding. By introducing a refractive index step in the lateral direction, lateral index-guiding can be obtained.

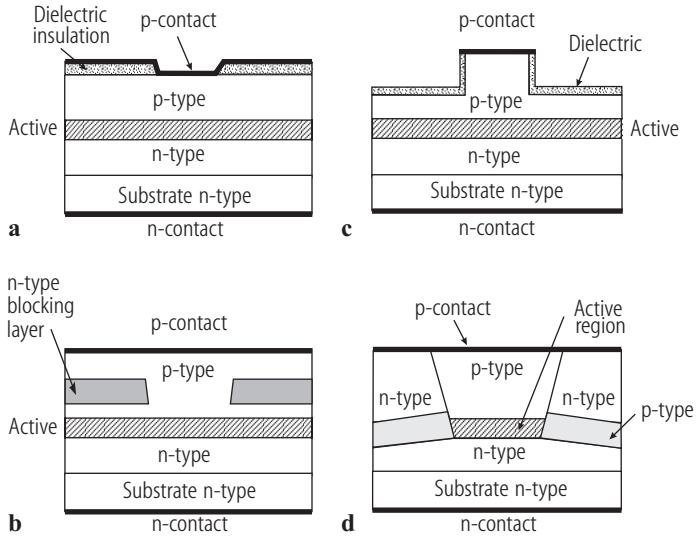

Fig. 5.1.5. Different schemes for lateral light and current confinement.

Weak index-guiding takes place in ridge waveguide lasers (see Fig. 5.1.5c) where the ridge structure causes a small lateral variation of the effective index, which, however, is too weak to dominate gain-guiding. A common feature of gain- and weakly index-guided lasers is, that they are vulnerable to lateral multi-mode behavior especially at high injection levels, resulting in multiple spectral lines and uneven far-field pattern. The physical reason for this can mainly be attributed to the lowering of the refractive index under carrier injection leading to antiguiding and favoring higher lateral modes to lase.

These problems do not occur for strongly index-guided lasers like buried heterostructure lasers, where the laser ridge is embedded in low-index material together with a current-blocking layer (Fig. 5.1.5d). Both strong optical and current confinement is guaranteed in these structures. The typical lateral dimensions are comparable to the emission wavelength, thus favoring low power consumption, good heat dissipation capabilities and stable lateral single-mode emission also at high injection levels. However, strongly index-guided structures require complex device fabrication including diverse epitaxial overgrowth techniques.

5.1.3.1 Longitudinal mode control – single-mode lasers

A laser is said to operate single-mode when the Side-Mode Suppression Ratio (SMSR) which is defined as the intensity ratio of the dominating mode and the strongest side-mode, exceeds 30 dB. It has been shown [83Koy] that these two modes must have a threshold gain difference of about 5 cm^{-1} to achieve dynamic single-mode emission, that is, if the laser is modulated.

The approaches to achieve this modal discrimination can be categorized in four main groups (see Fig. 5.1.6):

1. short-cavity lasers,
2. injection locking,
3. external-cavity and coupled-cavity lasers, and
4. distributed optical feedback.

The longitudinal mode spacing and the associated difference in the gain spectrum can be increased by decreasing the length of the cavity (5.1.8). For single-mode operation, the laser must only be several μm long, and requires very high gain and/or high mirror reflectivities. A representative of this group of lasers is the Vertical Cavity Surface Emitting Laser (VCSEL).

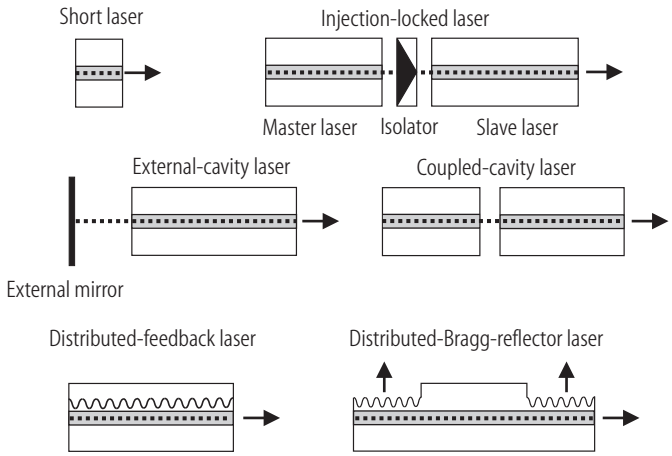

Fig. 5.1.6. Single-mode laser structures.

Injection locking utilizes a low-power, stable, single-mode beam of a master laser being injected into the high-power slave laser thus forcing it to lase at the injected wavelength. In order to prevent "backward" injection locking from the slave laser to the master laser, an optical isolator has to be used, which is a severe problem for the feasibility of compact devices.

In external-cavity [84Zie] and coupled-cavity lasers [83Tsa] the light propagating through the structure experiences multiple reflections that all interfere with each other. This finally results in a wavelength-selective feedback providing sufficient threshold gain difference between the closely spaced longitudinal modes. However, the feedback is very sensitive to variations of the cavity properties, such that mode jumps may occur due to thermal effects when these lasers are modulated with high modulation depths [84Lee].

In Distributed FeedBack (DFB) lasers and Distributed Bragg Reflector (DBR) lasers optical feedback is provided by Bragg reflection due to a periodic variation of the effective refractive index in the laser waveguide structure. Maximum reflectivity occurs at the Bragg wavelength of the waveguide grating structure,

$$\lambda_B = \frac{2\Lambda\,\mu_{\text{eff}}}{M}\ , \tag{5.1.17}$$

where Λ is the grating period, μ_{eff} the effective index of the uncorrugated waveguide structure and $M = 1, 2, \ldots$ the diffraction order. In DBR-lasers the uncorrugated active structure is placed in between passive DBR-regions providing the optical feedback whereas in DFB-lasers the grating expands over the whole resonator. The wavelength-selective feedback from the grating reduces the threshold gain of modes near the Bragg wavelength. Therefore, lasers can be realized in which one mode shows a considerably lower threshold gain than all others.

5.1.4 Laser modulation

One of the most attractive features of diode lasers is that they can be directly modulated via the pump current with modulation bandwidths in the range of several GHz. Since a change of the carrier density also changes the refractive index in the laser, Amplitude Modulation (AM) and Frequency Modulation (FM) always occur simultaneously. In the following sections, we will give a short description of the AM-response of laser diodes. A more comprehensive analysis of both AM and FM can be found in [91Pet, 97Mor, 95Vas].

5.1.4.1 Large-signal amplitude modulation

If, at $t = 0$, the drive current through a laser diode is instantaneously increased from $j_{\mathrm{bias}} = 0$ to $j > j_{\mathrm{th}}$, the laser output and the carrier density in the active zone show the typical spiking depicted in Fig. 5.1.7. Laser operation starts after a delay time t_{d}, which is required to build up the threshold carrier density. Both the laser output and the carrier density then show damped relaxation oscillations, which are also well known in other laser types. Due the extremely short photonic life times, the relaxation oscillations in diode lasers are some orders of magnitude faster as compared with gas- or solid-state lasers. The frequency of these oscillations is typically some GHz, the delay time for bias-free operation is in the range from $0.5 \ldots 10$ ns. Assuming a bias current $j_{\mathrm{bias}} < j_{\mathrm{th}}$, an expression for the delay time can be derived from (5.1.9) and (5.1.10):

$$t_{\mathrm{d}} = \tau_{\mathrm{s}} \ln\left(\frac{j - j_{\mathrm{bias}}}{j - j_{\mathrm{th}}}\right) . \tag{5.1.18}$$

Applying a bias current can thus greatly reduce the turn-on delay. For the same reason, a small threshold current is required.

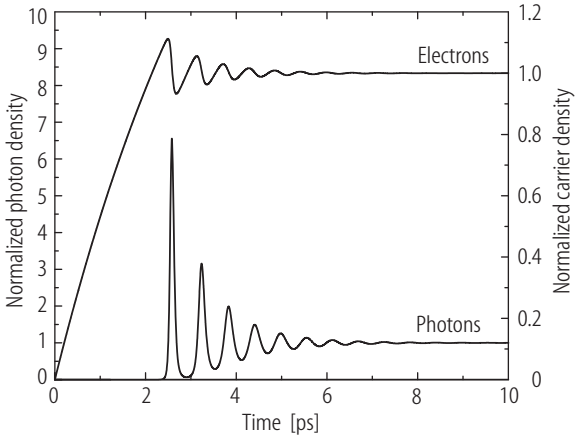

Fig. 5.1.7. Temporal evolution of photon and carrier density upon increasing the drive current from $j = 0$ to $j > j_{\mathrm{th}}$ at $t = 0$.

5.1.4.2 Small-signal amplitude modulation

IfindexSmall-signal amplitude modulation operated at a constant current j_0 above threshold, the steady-state solutions for the photon density S_0 and the carrier density n_0 are given by (5.1.12). Using the small-signal expansions for time-depending quantities

$$j(t) = j_0 + \Delta j(t) , \quad S(t) = S_0 + \Delta S(t) , \quad n(t) = n_0 + \Delta n(t) \tag{5.1.19}$$

the rate equations can be linearized and solved analytically using Fourier transformation. The solutions in the frequency regime are given by

$$\Delta S(\nu) = \frac{4\pi^2 {\nu_{\mathrm{r}}}^2 \tau \Gamma/(ed)}{4\pi^2 {\nu_{\mathrm{r}}}^2 + 2\pi\,\mathrm{i}\gamma\nu - 4\pi^2\nu^2} , \tag{5.1.20}$$

$$\Delta n(\nu) = \frac{2\pi\,\mathrm{i}\nu/(ed)}{4\pi^2 {\nu_{\mathrm{r}}}^2 + 2\pi\,\mathrm{i}\gamma\nu - 4\pi^2\nu^2} . \tag{5.1.21}$$

In (5.1.20) and (5.1.21), the following abbreviations were used for the damping constant γ and the relaxation oscillation frequency ν_{r}:

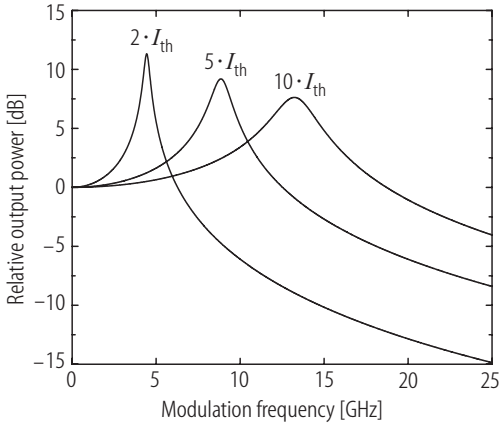

Fig. 5.1.8. Small signal AM-response of a laser diode biased at various currents above threshold.

$$\gamma = \frac{1}{\tau_s} + \frac{aS_0c}{\mu_g} , \tag{5.1.22}$$

$$\nu_r = \frac{1}{2\pi}\sqrt{\frac{aS_0c}{\mu_g\tau} + \frac{K}{\tau\tau_s}} . \tag{5.1.23}$$

Neglecting the spontaneous emission and using (5.1.13) and (5.1.12), ν_r can be expressed in terms of the current density:

$$\nu_r \approx \frac{1}{2\pi}\sqrt{\frac{aS_0c}{\mu_g\tau}} = \frac{1}{2\pi}\sqrt{\frac{(a\Gamma\tau n_t C/\mu_g)+1}{\tau\tau_s}\left(\frac{j_0}{j_{th}} - 1\right)} . \tag{5.1.24}$$

The transfer function (5.1.20) has a maximum at $\sqrt{{\nu_r}^2 - \gamma^2/(8\pi^2)}$, which shifts to higher frequencies for increasing bias currents, as shown in Fig. 5.1.8. The damping of the relaxation oscillations also increases with the bias current, resulting in a suppression of the resonance peak in the AM-response. From (5.1.24) it follows that high-speed modulation requires high differential gain in the active zone and a short photonic lifetime. A more accurate description of the modulation characteristics also includes the presence of nonlinear gain, resulting in a stronger damping of the relaxation oscillations [75Bog, 88Agr, 89Ara]. In practical devices, the modulation bandwidth is often limited by parasitic resistances and stray capacitances of the device and/or the packaging rather than by the intrinsic laser properties.

5.1.5 Line width

The finite value of the laser line width in semiconductor laser diodes is caused by spontaneous emission resulting in phase fluctuations of the electric field in the cavity [83Hen, 83Vah]. The line width $\delta\nu$ is generally described by the Henry-formula:

$$\delta\nu = \frac{R_{sp}}{4\pi S}\left(1 + \alpha^2\right) . \tag{5.1.25}$$

Where R_{sp} is the spontaneous emission rate, S is the number of photons in the active zone, and α is the line width enhancement factor [87Osi]. α describes how carrier fluctuations in the active layer are transformed into frequency fluctuations of the emission wavelength. α is wavelength-dependent and takes values from 1 . . . 6. Typical values of $\delta\nu$ for single-mode laser diodes range from 100 kHz to 50 MHz. Even smaller line widths can be obtained using optical feedback effects [83Wya, 91Pet].

References for 5.1

75Bog Bogatov, A.P., Eliseev, P.G.: IEEE J. Quantum Electron. **11** (1975) 510.

81Yam Yamada, M., Suematsu, Y.: J. Appl. Phys. **52** (1981) 2653.

83Hen Henry, C.: IEEE J. Quantum Electron. **19** (1983) 1391.
83Koy Koyama, F., Suematsu, Y., Arai, S., Tawee, T.-E.: IEEE J. Quantum Electron. **19** (1983) 1042.
83Tsa Tsang, W.T., Olsson, N.A., Logan, R.A.: Appl. Phys. Lett. **42** (1983) 650.
83Vah Vahala, K., Yariv, A.: IEEE J. Quantum Electron. **19** (1983) 1101.
83Wya Wyatt, R., Devlin, W.J.: Electron. Lett. **19** (1983) 110.

84Lee Lee, T.-P., Burrus, C.A., Liu, P.-L., Sessa, W.B., Logan, R.A.: IEEE J. Quantum Electron. **20** (1984) 374.
84Zie Van der Ziel, J.P., Mikulyak, R.M.: IEEE J. Quantum Electron. **20** (1984) 223.

86Agr Agrawal, G.P., Dutta, N.K.: Long-wavelength Semiconductor Lasers, New York: Van Nostrand Reinhold Company Inc., 1986.

87Osi Osinski, M., Buus, J.: IEEE J. Quantum Electron. **23** (1987) 9.

88Agr Agrawal, G.P.: J. Appl. Phys. **63** (1988) 1232.
88Anh Anh, D., Chuang, S.L.: IEEE J. Quantum Electron. **24** (1988) 2400.

89Ara Arakawa, Y., Takahashi, T.: Electron. Lett. **25** (1989) 169.

90Tam Tamir, T. (ed.): Guided-Wave Optoelectronics, Berlin: Springer-Verlag, 1990.

91Buu Buus, J.: Single Frequency Semiconductor Lasers, Bellingham, Washington: SPIE – The International Society for Optical Engineering, 1991.
91Pet Petermann, K.: Laser Diode Modulation and Noise, Dordrecht, Boston, London: Kluwer Academic Publishers, 1991.

93Che Chen, T.R., Eng, L.E., Zhao, B., Zhuang, Y.H., Yariv, A.: Appl. Phys. Lett **63** (1993) 2621.
93Zor Zory, P.S. (ed.): Quantum Well Lasers, San Diego, London: Academic Press, 1993.

94Thi Thijs, P.J.A., Tiemeijer, L.F., Binsma, J.J.M., Van Dongen, T.: IEEE J. Quantum Electron. **30** (1994) 477.

95Vas Vasil'ev, P.: Ultrafast Diode Lasers, Boston, London: Artech House, 1995.

97Mor Morthier, G., Vankwikelberge, P.: Handbook of Distributed Feedback Laser Diodes, Boston, London: Artech House, 1997.

5.2 Diode lasers in the visible spectral region

H. Wenzel

5.2.1 Introduction

Diode lasers emitting in the visible spectral region can be made from ternary or quaternary alloys between III-V or II-VI semiconductor compounds. There is an additional alloy based on I-III-VI_2 semiconductor compounds which could be possibly used, too. Table 5.2.1 gives a general overview of the compounds.

Table 5.2.1. Overview of semiconductor compounds and its constituent elements that can be used in light-emitting devices ($\lambda < 1000$ nm). For every element, the corresponding group in the period table is denoted. The crystal structure first noted is exploited in laser structures.

Wavelength λ [nm]	Type of compound	Group: cation	Group: anion	Crystal structure
200–1500	III-V (nitrides)	III A: Al, Ga, In	V A: N	wurtzite, zincblende, rocksalt
400–600	II-VI (wide-gap sulfo-selenides)	II A: Be, Mg II B: Zn, Cd	VI A: S, Se, Te	zincblende, rocksalt, wurtzite
500–800	I-III-VI_2	I B: Cu III A: Al, Ga, In	VI A: S, Se, Te	chalcopyrite
600–2000	III-V (phospho-arsenides)	III A: Al, Ga, In	V A: P, As	zincblende

With the existing semiconductor compounds and their alloys the spectral region above 350 nm is covered. However, there are still some gaps where no or no reliable diode lasers are available. This refers especially to the wavelength range between 450 and 600 nm. Although the visible spectral region extends only to wavelengths of about 800 nm, we include also the spectral region up to 1000 nm because basically the same alloys are used.

All current diode lasers emitting in this spectral region are based on multiple heterostructures. Mostly, the active region consists of unstrained or strained, single or multiple QWs the thickness of which is between 3 and 20 nm. The basic mechanism leading to stimulated emission of photons is due to radiative recombination of electrons in the conduction band and holes in the valence band (band-to-band recombination). The shorter the wavelength, the more important are excitonic effects due to the Coulomb interaction between electrons and holes. In nitride-based diode lasers, additionally localization effects due to compositional disordering have an impact on the optical gain.

5.2.2 Diode lasers based on III-nitrides

These diode lasers cover the violet–blue spectral region. The first room-temperature cw operation was reported 1996 [96Nak2]. See [97Pea, 98Gil, 99Kap2, 99Nak1, 00Nak1] for overviews.

5.2.2.1 Material properties

In Fig. 5.2.1, the energy gaps of the constituent binary compounds are depicted versus the lattice constants. The lattice constants of some substrates are indicated by dashed perpendicular lines. See [82Mad, 94Edg, 96Mad, 97Pea, 99Edg, 99Mor, 99Pan, 00Jai, 03Vur, 03Pip, 07Pip] for compilations of material properties and physical data.

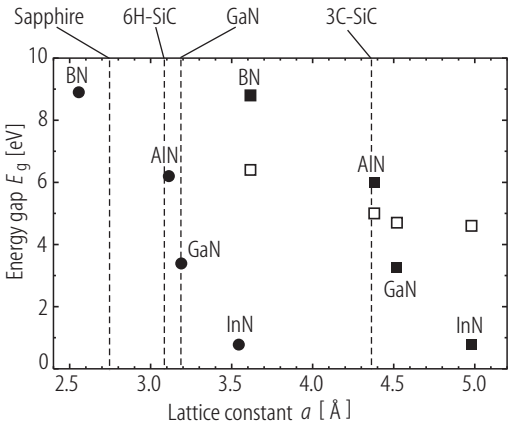

Fig. 5.2.1. III-N compounds: Energy gaps versus lattice constant for the constituent binaries. $T = 300$ K. The zincblende and wurtzite structures are denoted by squares and circles, respectively. Full and empty symbols denote the energy gaps at Γ and X, respectively.

The crystal structure is of wurtzite type, at equilibrium. However, with Molecular Beam Epitaxy (MBE) or Metal-Organic Vapor-Phase Epitaxy (MOVPE) the zincblende structure can be grown successfully depending on the substrate used. All nitride-based diode lasers reported so far are based on the wurtzite structure.

Wurtzite GaN, AlN and InN are direct semiconductors with the minimum of the conduction band situated at the center of the Brillouin zone (Γ). Wurtzite BN is an indirect semiconductor with the minima of the conduction band situated at K. The topmost valence band is split due to crystal field and spin-orbit coupling into three spin-degenerate states (heavy, light and crystal-field split-off holes). The exact band gap of InN is still a matter for debate [03Bhu, 05But]. Strain and quantum-size effects modify the band structure.

A peculiarity of wurtzite nitrides is the macroscopic polarization, comprising a spontaneous and a piezoelectric component [97Ber]. The former is absent in zincblende materials and is independent on strain. The latter appears in the presence of strain (e.g., in an InGaN/GaN quantum well) along certain crystallographic directions, for example along the most commonly used [0001] direction. For other crystallographic directions the spontaneous polarization effects reduce or vanish resulting in an increase of the optical gain [03Par].

5.2.2.2 Substrate

Before the availability of GaN substrates in sufficient size and low dislocation density, sapphire (Al_2O_3) was the most frequently used substrate due to its low price, the availability of large-area crystals of good quality and its stability at high temperatures. The surface orientation of the sapphire substrate used is mostly the *c*-plane, i.e. (0001), but growth on other orientations such as *a*-plane ($11\bar{2}0$) and *r*-plane ($1\bar{1}02$) where also conducted. Exact-oriented as well as misoriented sapphire is used [99Nak2].

Reactive ion etching or complicated cleavage techniques must be employed to form mirror cavity facets. A high-reflectivity facet is obtained by coating with quarter-wave dielectric multilayers, such as SiO_2/TiO_2. GaN grown on a-plane sapphire could be cleaved along ($1\bar{1}02$).

Due to the fact that sapphire is an insulator, it does not enable the fabrication of conventional laser structures having a broad-area n-type contact deposited on the backside of the substrate. Another disadvantage of sapphire is the large lattice and thermal expansion coefficient mismatch with GaN and the poor thermal conductivity.

Several alternative substrates have been studied and partially used to fabricate laser diodes, see [98Gil, 99Edg, 02Liu]. Among them is silicon carbide (SiC) which has several advantages over sapphire for GaN epitaxy, for example a smaller lattice constant mismatch and a much higher thermal conductivity. Conductive substrates are available, making electrical contacts on the backside possible, thereby simplifying the device structure compared to sapphire substrates. The crystal planes in epitaxial GaN are parallel to those of the SiC substrate, making facets formation by cleaving easier.

Due to the large lattice mismatch between these substrates and GaN, a large number of threading dislocations with a density larger than 10^8 cm^{-2} arise from the corresponding interfaces. With the introduction of epitaxial lateral over-growth techniques such as ELOG [94Kat], pendeo-epitaxy [99The] or FIELO [00Miz] the high dislocation density was strongly reduced to less than 10^6 cm^{-2}, above the SiO_2 stripe or etched regions, respectively.

GaN itself is the best choice as a substrate for GaN epitaxy and device fabrication, as it eliminates all problems associated with heteroepitaxy. Until now only High Nitrogen Pressure Solution (HNPS) growth and Hydride Vapor Phase Epitaxy (HVPE) have produced large-area crystals [02Liu]. In the latter case, several 100 μm thick GaN films are deposited by HVPE and separated from the substrate. The structural quality of the HVPE substrates is not as good as HNPS GaN crystals but the electrical and optical properties are better. In order to reduce polarization effects, besides the growth of *c*-plane (0001) the growth of *m*-plane ($1\bar{1}00$) or *a*-plane ($11\bar{2}0$) GaN films is also conducted.

5.2.2.3 Doping

N-type dopants are Si, Ge (IV A of the periodic table), O, Se (group VI A). Si is most commonly employed. Potential p-type dopants are, for example, Be, Mg, Ca (group II A of the periodic table), and C (IV A). A drawback to all these acceptors is their large activation energy of order 200 meV. Mg is the p-type dopant of choice. However, thermal annealing or low-energy electron beam irradiation in a hydrogen-free atmosphere is required to activate the acceptor.

5.2.2.4 Active region

Typically the active region consists of one to three QWs. Table 5.2.2 gives an overview of the alloy used.

Table 5.2.2. Alloy used as active material in diode lasers based on III-N compounds.

λ [nm]	Alloy	Strain	Remarks
200–650	$Al_xIn_yGa_zN$ ($z = x + y$)	unstrained for $y_u \approx 0.2x$ (a_{GaN}), compressive for $y > y_u$, tensile for $y < y_u$,	The quaternary alloy ($x > 0$) needs further development to reach device quality.

In general a small amount of InN is needed to obtain strong luminescence from band-to-band recombination. However, QWs with larger InN content ($y > 0.4$) are difficult to grow and their radiative efficiency rapidly decreases.

The exact mechanism responsible for laser action at room temperature is still an open question. It is assumed that radiative recombination between deep localized energy states due to In composition fluctuations or even quantum-dot-like states attribute to the optical gain. Another point to be considered is the large built-in static electric field due to the built-in polarization which is, however, at least partially screened under lasing conditions due to the large electron and hole densities ($> 10^{19}$ cm^{-3}).

5.2.2.5 Waveguide and cladding layers

In Table 5.2.3 there is an overview of the alloy used in waveguide and cladding layers.

Table 5.2.3. Alloy used in waveguide and claddings in diode lasers based on III-N compounds.

Waveguide	Cladding	Conditions	Remarks
$Al_{x_1}In_{y_1}Ga_{z_1}N$ $z_1 = x_1 + y_1$	$Al_{x_2}In_{y_2}Ga_{z_2}N$ $z_2 = x_2 + y_2$	lattice matching to GaN: $y_{1,2} = 0.22x_{1,2}$ $x_1 < x_2$ or $y_1 > y_2$	The quaternary alloy ($y > 0$) needs further development to reach device quality. Currently $x_1 = 0$ and $y_2 = 0$.

GaN is the standard material for waveguide layers, however, compressively strained InGaN has been also employed. Tensile-strained AlGaN is the standard material for cladding layers. In order to prevent cracking during growth due to the lattice and thermal expansion coefficients mismatch, AlGaN/GaN superlattices have been successfully employed. See Sect. 5.2.5 for general remarks on the thickness of the cladding layers to prevent the fundamental light mode to leak into the substrate or to interact with contact layer modes.

5.2.2.6 Contact layer

If insulators are used as substrates, there is an additional n-contact layer made from Si-doped GaN which allows a lateral contacting. The p-contact layer is usually made from Mg-doped GaN covered by Mg-doped InGaN.

5.2.2.7 Distributed Bragg reflectors in VCSELs

Epitaxial distributed Bragg reflectors in VCSELs are made from AlGaN, using either AlN/AlGaN or AlGaN/GaN mirror pairs. Dielectric mirrors, such as SiO_2/TiO_2, can be also used [00Osi]. Room-temperature optically pumped pulsed VCSEL operation at $\lambda = 400$ nm has been reported in [99Som]. The bottom and top mirrors consisted of $Al_{0.34}Ga_{0.66}N$/GaN and SiO_2/ZrO_2, respectively.

5.2.2.8 Epitaxial structure

Figure 5.2.2 shows schematically the transverse cross section of a typical nitride-based edge-emitting laser. Details concerning thicknesses and compositions are contained in Table 5.2.4.

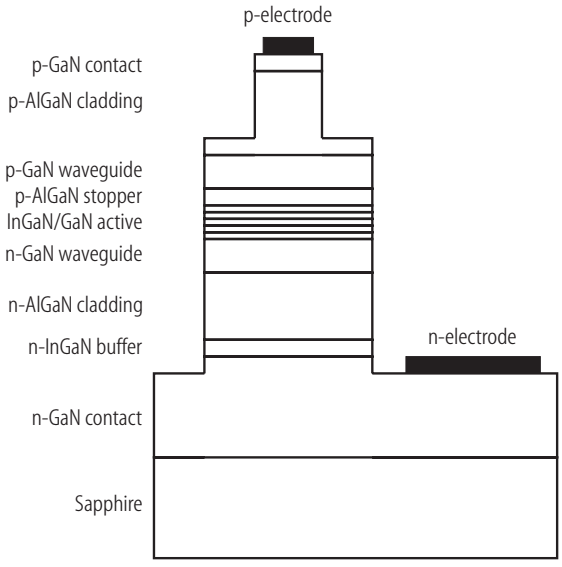

Fig. 5.2.2. Transverse cross section of a nitride-based edge-emitting laser grown on sapphire.

5.2.2.9 Results

The emission wavelength λ ranges currently between 343 nm [04Edm] and 463 nm [03Muk]. Some laser data are compiled in Table 5.2.5.

Table 5.2.4. Epitaxial structure of a nitride-based edge-emitting laser emitting at 450 nm [00Nak2].

Layer	Compound	Thickness [nm]	Doping element
p-contact	GaN	50	Mg
p-cladding	GaN / $Al_{0.14}Ga_{0.86}N$ superlattice	2.5 / 2.5 (100 periods)	Mg
p-waveguide	GaN	100	Mg
p-electron stopper	$Al_{0.2}Ga_{0.8}N$	20	Mg
active layer	$In_{0.3}Ga_{0.7}N$ QWs / $In_{0.02}Ga_{0.98}N$ barriers	3 / 6	undoped / Si
n-waveguide	GaN	100	Si
n-cladding	GaN / $Al_{0.14}Ga_{0.86}N$ superlattice	2.5 / 2.5 (140 periods)	Si
n-buffer	$In_{0.1}Ga_{0.9}N$	100	Si
n-contact	GaN	3000	Si

Table 5.2.5. Data achieved at room temperature with diode lasers based on nitrides. The results refer to continuous-wave operating edge-emitting lasers. The emission wavelength is around 410 nm.

Quantity	Value	Reference	Remark
threshold current density	1.2 . . . 2.8 kA/cm^2	[98Nak1]	ELOG substrate, 3 μm ridge width, 450 μm cavity length
power	420 mW	[98Nak2]	ELOG substrate, 3 μm ridge width, 450 μm cavity length
lifetime	15000 h	[03Muk]	ELOG on GaN substrate, 30 mW optical power, 60 °C heatsink temperature
power	920 mW	[03Got]	GaN substrate, 10 μm ridge width, 600 μm cavity length

5.2.3 Diode lasers based on II-VI sulfo-selenides

These diode lasers cover the blue–green spectral region. The first room-temperature cw operation was reported in 1993 [93Nak]. The lifetime of the diode lasers is still limited due to rapid degradation. See [96Ish, 96Nur, 97Nur, 99Beh, 99Ish, 00Oku] for overviews.

5.2.3.1 Material properties

In Fig. 5.2.3, the energy gaps of the constituent binary compounds are depicted versus the lattice constants. The lattice constants of some substrates are indicated by dashed perpendicular lines. See [97Bha, 98Oku, 97Nur] for compilations of material properties and physical data.

The crystal structure at equilibrium is of zincblende or wurtzite type depending on the compound. All sulfo-selenide-based diode lasers reported so far are based on the zincblende structure.

Zincblende BeSe and BeTe are probably indirect semiconductors with the minima of the conduction band situated near X. The other zincblende binaries are direct semiconductors with the minimum of the conduction band situated at the center of the Brillouin zone (Γ). The topmost valence band is split due to spin-orbit coupling into a fourfold state (light and heavy holes) and a twofold state (spin-orbit split-off holes). Strain and quantum-size effects modify the band structure.

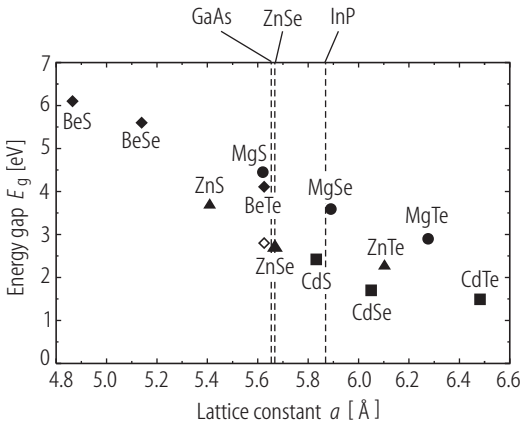

Fig. 5.2.3. Wide-gap II-VI compounds: Energy gaps versus lattice constant for the constituent binaries. Zincblende structure. $T = 300$ K. Cd, Mg and Zn compounds are denoted with full squares, circles, and triangles, respectively. Be compounds are denoted with diamonds. Full and empty symbols denote the energy gaps at Γ and X, respectively.

5.2.3.2 Substrate

ZnSe bulk crystals that can be used as substrates have been not yet available in sufficient size, low dislocation density and high conductivity. Diode lasers grown on ZnSe and GaAs substrates are compared in [99Wen]. Until now, (001)-oriented GaAs is the substrate most frequently employed for II-VI diode lasers. With structures grown on InP substrates, optical pumped lasing action has been achieved [98Zen].

5.2.3.3 Doping

N-type dopants are, for example, Al, Ga (group III A of the periodic table), Cl, I (VII A). Cl or I are most commonly used. Potential p-type dopants are, for example, Li, Na (group I A of the periodic table), N, P, As, Sb (V A). N is most commonly used. However, special nitrogen sources are necessary, such as remote radiofrequency (rf) or Electron-Cyclotron Resonance (ECR) plasma cells or the thermal cracking of nitric oxide (NO). So far it was not possible to prove p-type conductivity in epitaxial layers grown by MOCVD. Reasons are probably the presence of hydrogen, background impurities in the sources and the large growth temperatures, which contribute to the compensation of the p-type dopant nitrogen.

5.2.3.4 Active region

Typically the active region consists of a single or of multiple QWs. Table 5.2.6 gives an overview of the alloys used.

At room temperature, the optical gain is due to radiative recombination of free electrons and holes. However, at temperatures below 120 K stimulated emission due to the radiative recombination of exitonic molecules (biexitons) has been clearly demonstrated [98Kre].

5.2.3.5 Waveguide and cladding layers

In Table 5.2.7 there is an overview of the alloys used in waveguide and cladding layers.

Table 5.2.6. Alloys used as active materials in diode lasers based on wide-gap II-VI compounds.

λ [nm]	Alloy	Strain	Remarks
450–550	$Cd_xZn_{1-x}S_ySe_{1-y}$	unstrained for: $x_u = -0.03 + 0.61y$ (a_{GaAs}), $x_u = 0.61y$ (a_{ZnSe}), $x_u = 0.475 + 0.61y$ (a_{InP}), compressive for $x > x_u$, tensile for $x < x_u$	Mostly used alloy.
450–550	$Be_xCd_yZn_{1-z}Se$ $(z = x + y)$	unstrained for: $x_u = 0.03 + 0.72y$ (a_{GaAs}), $x_u = 0.72y$ (a_{ZnSe}), $x_u = -0.38 + 0.72y$ (a_{InP}), compressive for $x < x_u$, tensile for $x > x_u$	Alternative alloy containing beryllium [98Waa].

Table 5.2.7. Alloys used in waveguide and claddings in diode lasers based on wide-gap II-VI compounds.

Waveguide	Cladding	Conditions	Remarks
$ZnS_{y_1}Se_{1-y_1}$	$Mg_{x_2}Zn_{1-x_2}S_{y_2}Se_{1-y_2}$	lattice matching to GaAs: $y_1 = 0.06$, $x_2 = -0.0685 + 1.227y_2$ lattice matching to ZnSe: $y_1 = 0$, $x_2 = 1.227y_2$	Mostly used alloys. Strongly decreased p-type conductivity with increasing MgSSe content due to increase of the N activation energy [97Han]. Tendency of spontaneous ordering along specific crystallographic directions such as [110] [94Oku].
$Be_{x_1}Zn_{1-x_1}Se$	$Be_{x_2}Mg_{y_2}Zn_{z_2}Se$ $(z_2 = x_2 + y_2)$	lattice matching to GaAs: $x_1 = 0.03$, $x_2 = 0.03 + 0.42y_2$	Alternative alloy containing beryllium [98Waa].
$Mg_{x_1}Cd_{y_1}Zn_{z_1}Se$ $(z_1 = x_1 + y_1)$	$Mg_{x_2}Cd_{y_2}Zn_{z_2}Se$ $(z_2 = x_2 + y_2)$	lattice matching to InP: $x_{1,2} = 0.90 - 1.72y_{1,2}$ $y_1 < y_2$	Alloy used in [98Zen] to grow optical pumped laser structures on InP.

Beryllium chalcogenides are promising in respect to lattice hardening due to their pronounced covalent bonding, which is supposed to have an important impact on the defect generation and propagation and therefore the lifetime [98Waa]. See Sect. 5.2.5 for general remarks on the thickness of the cladding layers to prevent the fundamental light mode to leak into the substrate or to interact with contact layer modes.

5.2.3.6 Contact layer

The deep Γ-point valence band edge and the limited p-dopability produces a Schottky barrier of at least 1 eV when contacting p-ZnSe with a metal [99Wen]. Several schemes have been proposed to minimize this barrier. They include CdSe, HgSe, BeTe or ZnTe or a combination of those. The mostly utilized methods appear to be the insertion of ZnTe layers in ZnSe to form a pseudo-graded alloy or the use of ZnSe/ZnTe superlattice [99Wen]. A disadvantage of these contacting schemes is

the large lattice mismatch between ZnTe and ZnSe or GaAs. An alternative approach to achieve an Ohmic contact is to perform a postgrowth diffusion of Li_3N [94Lim].

5.2.3.7 Distributed Bragg reflectors in VCSELs

Epitaxial distributed Bragg reflectors in VCSELs can be made from ZnSe/ZnS, ZnSe/MgS or ZnSSe/ZnMgSSe, for example. With dielectric mirrors, such as SiO_2/TiO_2, optically pumped vertical-cavity lasing has been observed in CdZnSeS. An electrically driven CdZnSeS VCSEL emitting at 484 nm at 77 K has been fabricated [95Yok] using dielectric mirror pairs.

5.2.3.8 Epitaxial structure

Figure 5.2.4 shows schematically the transverse cross section of a typical sulfo-selenide-based edge-emitting laser. Details concerning thicknesses and compositions are contained in Table 5.2.8.

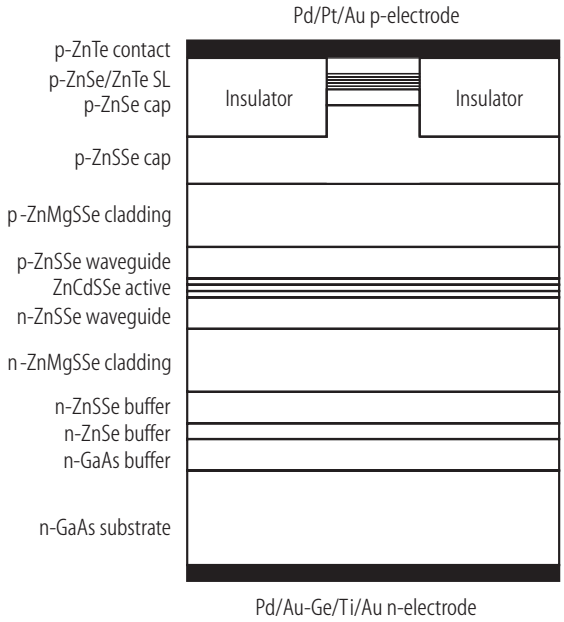

Fig. 5.2.4. Transverse cross section of a typical sulfo-selenide-based edge-emitting laser (ridge-waveguide structure).

5.2.3.9 Results

The longest lifetime reported so far is 400 h [00Oku]. Threshold current densities of about 200 A/cm^2 and threshold voltages below 4 V have been achieved. A maximum output power of 75 mW in cw operation has been reported in [00Klu].

Table 5.2.8. Epitaxial structure of a sulfo-selenide-based edge-emitting laser emitting around 500 nm [00Ito].

Layer	Compound	Thickness [nm]	Doping element
p-contact	ZnTe	4	N
p-superlattice	ZnSe/ZnTe	7	N
p-cap	ZnSe	90	N
p-cap	ZnSSe	1800	N
p-cladding	MgZnSSe	1000	N
p-waveguide	ZnSSe	100	N
active layer	ZnCdSe QW	3.5	undoped
n-waveguide	ZnSSe	100	Cl
n-cladding	MgZnSSe	1000	Cl
n-buffer	ZnSSe	260	Cl
n-buffer	ZnSe	30	Cl
n-buffer	GaAs	250	Si
n-substrate	GaAs		

5.2.4 Diode lasers based on I-III-IV$_2$ compounds

Double heterostructures of the Cu(Al,Ga)(S,Se)$_2$ system can be grown on GaP substrates and possibly also on Si substrates. The ternary alloys $CuInSe_2$ and $CuGaSe_2$ are well-known photovoltaic materials [93Moe]. LEDs have been realized, and optical-pumped laser action has been achieved [99Ack].

In Fig. 5.2.5, the energy gaps of the constituent ternary compounds are depicted. The lattice constants of some substrates are indicated by dashed perpendicular lines. See [75Sha, 82Mad, 96Mad] for a compilation of material properties and physical data.

The crystal structure is of chalcopyrite type. The ternaries are direct semiconductors with the minimum of the conduction band situated at the center of the Brillouin zone (Γ). The topmost valence band is split due to crystal field and spin-orbit coupling into three spin-degenerate states.

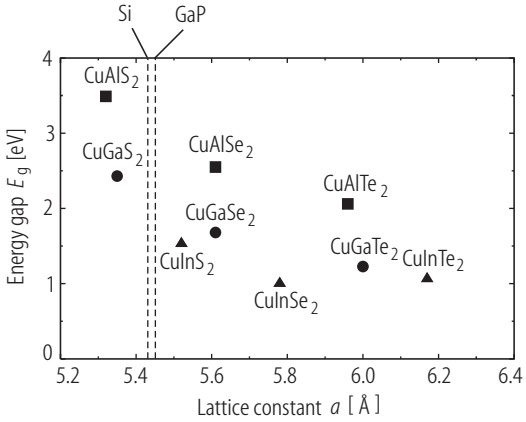

Fig. 5.2.5. I-III-IV$_2$ compounds: Energy gaps versus lattice constant for the constituent ternaries. $T = 300$ K. Al, Ga and In compounds are denoted with squares, circles and triangles, respectively.

5.2.5 Diode lasers based on phospho-arsenides

These diode lasers cover the red to near-infrared spectral region. With GaAs/AlGaAs double heterostructures the first room-temperature cw-operation of diode lasers at all has been achieved [70Alf, 70Hay]. The first room-temperature GaAs/AlGaAs QW diode laser grown by MOVPE has been reported in [78Dup]. Another milestone was the demonstration of an InGaAs/AlGaAs strained-layer QW diode laser in [84Lai]. Since then, an extremely large variety of diode lasers, differing in the used alloys and their compositions and in the lateral or longitudinal structurization have been demonstrated. A lot of them are commercially available. See [93Eva, 93Zor, 95Sal, 99Kap1, 99Kap2, 99Wil, 00Die] for overviews.

5.2.5.1 Material properties

In Fig. 5.2.6, the energy gaps of the constituent binary compounds are depicted versus the lattice constants. The lattice constants of the GaAs substrate is indicated by dashed perpendicular lines. See [82Mad, 92Ada, 93Ada, 93Bha, 96Bha, 96Bro, 96Mad, 01Vur] for compilations of material properties and physical data.

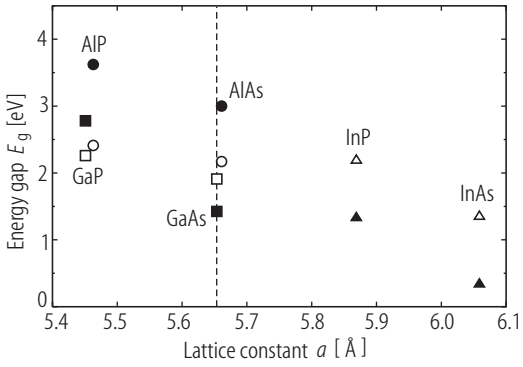

Fig. 5.2.6. Arsenides and phosphides: Energy gaps versus lattice constant for the constituent binaries. $T = 300$ K. Al, Ga and In compounds are denoted with circles, squares and triangles, respectively. Full and empty symbols denote the energy gaps at Γ and X, respectively.

The crystal structure is of zincblende type. AlAs, AlP and GaP are indirect semiconductors with the minima of the conduction band situated near X. The other binaries are direct semiconductors with the minimum of the conduction band situated at the center of the Brillouin zone (Γ). The topmost valence band is split due to spin-orbit coupling into a fourfold state (light and heavy holes) and a twofold state (spin-orbit split-off holes). Strain and quantum-size effects modify the band structure.

5.2.5.2 Substrate

The mostly used substrate is (001)-oriented GaAs. Sometimes (for example, for the AlGaInP alloy), slightly misoriented substrates towards (111)A are used. As can be seen from Fig. 5.2.6, the ternary alloy AlGaAs can be almost grown lattice-matched on GaAs, the maximum lattice mismatch is about $\Delta a/a = 1.3 \times 10^{-3}$. The quaternary alloys GaInAsP and AlGaInP can be grown perfectly

lattice-matched. For special applications other crystal orientations are used, for example (311)B-oriented GaAs for polarization-stable VCSELs.

Edge-emitting lasers grown on (001) substrates are cleaved along the (011) planes. The corresponding facets have a reflection coefficient of about 30 % with respect to air. The precise value depends on the waveguide structure used and the polarization of the emitted light (the reflection coefficient for TM modes is usually smaller than that for TE modes).

Other available substrates are GaP and InGaAs. Mostly, n-doped substrates are used. However, p-doped substrates are also available.

5.2.5.3 Doping

N-type dopants are, for example, Sn, Si (group IV A of the periodic table), S, Se, Te (VI A). Si is most commonly used. P-type dopants are, for example, Be, Mg (group II A of the periodic table), Zn, Cd (II B), C (IV A), Mn (VII B). The preferred p-type doping depends strongly on the growth method. In MBE, Be is the p-dopant of choice. In MOVPE, Zn, Mg and C are mostly used, depending on the material to be doped [00Die].

5.2.5.4 Active region

Typically the active region consists of a single or of multiple QWs. Table 5.2.9 gives an overview of the alloys used.

Table 5.2.9. Alloys used as active materials in diode lasers based on phospho-arsenides.

λ [nm]	Alloy	Strain	Remarks
580–750	$Al_xGa_yIn_{1-z}P$ ($z = x + y$)	unstrained for $z_u \approx 0.52$ compressive for $z < z_u$ tensile for $z > z_u$	Indirect for $x > 0.3$. Strong tendency to order In and Al/Ga atoms on alternate (111)B planes.
670–890	$Al_xGa_{1-x}As_{1-y}P_y$	tensile for $y > 0$	Indirect for energy gaps > 1.95 eV ($x > 0.4$ if $y = 0$).
610–1200	$Ga_xIn_{1-x}As_yP_{1-y}$	unstrained for $x_u \approx 0.515 + 0.485y$ compressive for $x < x_u$ tensile for $x > x_u$	Direct for all $x = x_u$. Strong tendency to order In and Ga atoms on alternate (111)B planes (especially for $y \approx 0$). Miscibility gap.
670–1200	$Al_xGa_yIn_{1-z}As$ ($z = x + y$)	compressive for $z < 1$	Indirect for $x > 0.4$ if $z = 1$.

Diode lasers having unstrained and compressively strained QWs as active regions usually emit TE-polarized light, where the main component of the electric field is parallel to the epitaxial layers. If the tensile strain is high enough, the emission is TM-polarized, where the main component of the electric field is perpendicular to the layers.

The optimum QW thickness and number can be hardly given for the general case. For example, for unstrained and compressively strained QWs, the threshold current decreases with QW thickness until there is only one conduction subband (typically for thicknesses of 4 to 8 nm). Decreasing the

QW thickness further, the threshold current increases again, due to loss of carrier confinement and increased influence of thickness fluctuations. In tensile-strained QWs the situation is different due to the crossing of the light and heavy-hole subband edges occurring at a certain QW thickness. Thus, in this case the optimum thickness ranges typically from 9 to 20 nm.

The thickness of strained QWs is limited by the so-called critical thickness, where strain relaxation takes place and lattice defects arise [74Mat, 85Peo, 94Dun]. In order to compensate partially or totally for the strain, the QWs can be surrounded by barriers strained into the opposite direction resulting in so-called strain-compensated active regions.

The optimum number of QWs for minimum threshold current depends strongly on the optical losses. For example, shorter cavities (larger out-coupling loss) require more QWs. However, in MQWs with a large number of QWs (5 and more), the electron and hole density distributions between different QWs can be nonuniform leading to a deterioration of the laser performance.

5.2.5.5 Waveguide and cladding layers

The alloys used in the waveguide and cladding layers must be nearly lattice-matched to the GaAs substrate because their thicknesses are usually much larger than the corresponding critical thicknesses. In Table 5.2.10 there is an overview of the alloys used in waveguide and cladding layers.

Table 5.2.10. Alloys used in waveguides and claddings in diode lasers based on phospho-arsenides.

Waveguide	Cladding	Conditions	Remarks
$Al_{x_1}Ga_{1-x_1}As$	$Al_{x_2}Ga_{1-x_2}As$	$x_1 < x_2$	So far best controlled and investigated material system for diode lasers.
$(Al_{x_1}Ga_{1-x_1})_{0.52}In_{0.48}P$	$(Al_{x_2}Ga_{1-x_2})_{0.52}In_{0.48}P$	$x_1 < x_2$	Standard alloy for red-emitting diode lasers. If $x_1 = 0$ aluminum-free active area diode lasers if GaInAsP QWs are used.
$Ga_{x_1}In_{1-x_1}As_{y_1}P_{1-y_1}$	$Ga_{x_2}In_{1-x_2}As_{y_2}P_{1-y_2}$	$x_{1,2} = 0.515 + 0.485y_{1,2}$ $y_1 < y_2$	Aluminum-free diode lasers if GaInAsP QWs are used. Very good reliability if growth is properly controlled.
$Ga_{x_1}In_{1-x_1}As_{y_1}P_{1-y_1}$	$Al_{x_2}Ga_{1-x_2}As$	$x_1 = 0.515 + 0.485y_1$ $x_2 > 0.5$, if $y_1 = 0$, otherwise x_1 can be smaller	Combination of well-established AlGaAs material system and aluminum-free InGaAsP waveguide layers.
$(Al_{x_1}Ga_{1-x_1})_{0.52}In_{0.48}P$	$Al_{x_2}Ga_{1-x_2}As$	$x_2 > 0.5$, if $x_1 = 0$, otherwise x_2 must be larger	Combination of well-established AlGaAs material system and large-energy-gap alloy AlGaInP.

A common problem of all GaAs-based lasers is the small band gap and the large refractive index of the GaAs substrate, which could lead to a leakage of the fundamental light mode into the substrate. The enhanced optical loss connected with a too small thickness of the cladding layer following the substrate leads to a high threshold current and a low external efficiency. If the substrate is transparent ($\lambda > 880$ nm), the amplified spontaneous emission spectrum emitted at

the facets below threshold shows a characteristic modulation superposing the longitudinal mode spectrum. If the difference between the effective index of the lasing mode and the refractive index of the substrate is sufficiently small, a secondary peak in the far field occurs.

5.2.5.6 Contact layer

The p-contact layer is made of GaAs and is usually highly doped with Zn or C (in the order of 10^{19} cm^{-3}). If the thickness exceeds a certain value depending on emission wavelength and alloy used, light modes are guided in the contact layer. For certain thicknesses, one of these modes interacts strongly with the lasing mode leading to an enhanced optical loss if the corresponding cladding layer is too thin. The reason is again the small band gap and large refractive index of the GaAs.

5.2.5.7 Distributed Bragg reflectors in VCSELs

The first room-temperature cw operation of a VCSEL at all has been achieved in 1988 [88Koy]. Most commonly, epitaxial distributed Bragg reflectors in VCSELs are made from $Al_xGa_{1-x}As$, due to the high-refractive index contrast ($\Delta n = 0.6$ at $\lambda = 900$ nm) that can be reached between GaAs (high index) and AlAs (low index) and the small lattice mismatch. Another advantage is that $Al_xGa_{1-x}As$ with high AlAs content ($x > 0.9$) can be easily oxidized at temperatures between 350 and 500 °C in a steam environment. Oxide layers obtained in this way can serve to confine both the electrical current and the emitted light laterally.

Decreasing the wavelength below 880 nm necessitates an increase in of the AlAs content in the high-index mirror layer (up to $x = 0.5$ at $\lambda = 650$ nm). This leads to a reduced index contrast which must be compensated for by a larger number of mirror pairs.

Another possibility is the use of dielectric mirrors with a large index contrast. Thus, a few mirror pairs often suffice. Disadvantage is, that more complicated contacting schemes must be employed, and that the thermal resistance is larger.

For general discussion of the design, fabrication and performance of VCSELs see [95Sal, 99Wil].

5.2.5.8 Epitaxial structure

Figures 5.2.7 and 5.2.8 show schematically the transverse cross sections of edge-emitting lasers based on AlGaInP and AlGaAs, respectively. Details concerning thicknesses and compositions are contained in Tables 5.2.11 and 5.2.12.

5.2.5.9 Results

Due to the huge amount of data, we must refer to the bibliography. Some results are collected in Table 5.2.13.

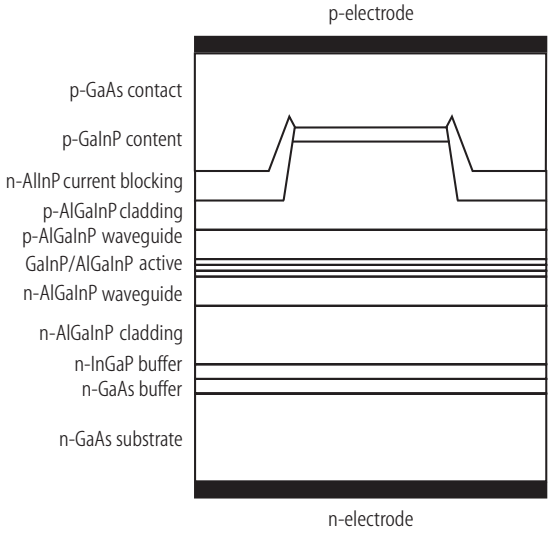

Fig. 5.2.7. Transverse cross section of an AlGaInP-based edge-emitting laser (real-index-guided self-aligned structure).

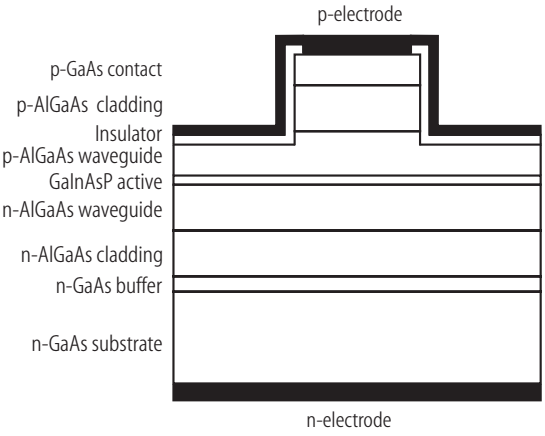

Fig. 5.2.8. Transverse cross section of an AlGaAs-based edge-emitting laser (ridge-waveguide structure).

Table 5.2.11. Epitaxial structure of a typical AlGaInP-based edge-emitting laser grown in two steps. The emission wavelength is 659 nm [04Oni].

Layer	Compound	Thickness [nm]	Doping element
p-contact	GaAs	300	Zn
p-contact	$Ga_{0.5}In_{0.5}P$	50	Mg
n-current blocking	$Al_{0.5}In_{0.5}P$	300	Si
p-cladding	$Al_{0.35}Ga_{0.15}In_{0.5}P$	1200	Mg
p-waveguide	$Al_{0.25}Ga_{0.25}In_{0.5}P$	250	undoped
active	3 compr. strained GaInP QWs / $Al_{0.25}Ga_{0.25}In_{0.5}P$ barriers	6 / 5	undoped
n-waveguide	$Al_{0.26}Ga_{0.25}In_{0.5}P$	250	undoped
n-cladding	$Al_{0.35}Ga_{0.15}In_{0.5}P$	2000	Si
n-buffer	$Ga_{0.5}In_{0.5}P$		Si
n-buffer	GaAs		Si
n-substrate	GaAs		

Table 5.2.12. Epitaxial structure of an AlGaAs-based edge-emitting laser emitting at 800 nm [00Wen].

Layer	Compound	Thickness [nm]	Doping element	Doping concentration [10^{18} cm^{-3}]
p-contact	GaAs	300	C	20
p-cladding	$Al_{0.70}Ga_{0.30}As$	800	Zn	1
p-waveguide	$Al_{0.45}Ga_{0.55}As$	1000	Zn	0.1
active	$GaAs_{0.85}P_{0.15}$ QW	14	undoped	
n-waveguide	$Al_{0.45}Ga_{0.55}As$	1000	Si	0.1
n-cladding	$Al_{0.70}Ga_{0.30}As$	400	Si	1
n-buffer	GaAs	300	Si	2
n-substrate	GaAs			

Table 5.2.13. Data achieved at room temperature with diode lasers based on phospho-arsenides (wavelength $\lambda < 1000$ nm). If not otherwise stated, the results refer to edge-emitting lasers.

Quantity	Values	λ [nm]	Ref.	Remarks
threshold current density [A cm^{-2}]	65	980	[90Cho]	Strained InGaAs single QWs and long cavities.
	56	980	[91Cha]	
	45	980	[91Wil]	
threshold current [μA]	145	980	[95Zha]	Strained InGaAs single QW grown on the tip of a mesa structure on a patterned substrate, submicron-wide active region, short cavity and HR-coated facets.
	8.7	980	[95Yan]	Strained InGaAs single QW, VCSEL with an optical and electrical aperture made by selective wet oxidation.
cw optical power [W]	6	626	[98Osi]	1-cm laser bar, cavity length 1 mm, filling factor 7–10 %, emitter width 50 μm, water-cooled heatsink.
	15	635	[98Osi]	1-cm laser bar, cavity length 1 mm, filling factor 7–10 %, emitter width 50 μm, water-cooled heatsink.
	7	644	[04Ima]	1-cm laser bar, cavity length 1.4 mm, 25 emitters, emitter width 60 μm.
	2.1	650	[04Toi]	Cavity length 1 mm, stripe width 150 μm.
	7	730	[99Kna]	
	15	810	[05Kna]	Small vertical far-field divergence (18 ° FWHM).
	11	870	[98OBr]	
	0.89	980	[01Mil]	Large-area bottom-emitting VCSEL.
	16	980	[05Sch]	
conversion efficiency [%]	73	940	[05Kni]	At 70 W output power, heatsink temperature 25 °. 1-cm laser, cavity length 1.5 mm, 19 emitters, emitter width 150 μm.
	73	970	[05Kan]	At 50 W output power, heatsink temperature 10 °. 1-cm bar, cavity length 1 mm, 19 emitters, emitter width 100 μm.
single-spatial-mode power [mW]	120	635	[98Lu]	Small vertical far-field divergence (20 ° FWHM).
	150	659	[04Oni]	High-temperature operation (70 ° C).
	200	660	[05Ma]	Small vertical far-field divergence (15 ° FWHM), high-temperature operation (70 ° C).
	240	780	[01Hir]	Real-index-guided self-aligned stripe.
	1200	980	[05Sch]	Ridge-waveguide.
	5000	980	[05Web]	Tapered laser.
single-frequency power [mW]	2200	854	[97OBr]	Monolithically integrated MOPA with a DBR laser as power amplifier.
	700	980	[06Wen]	Single section DFB RW laser.
	1500	980	[99Lam]	Monolithically integrated MOPA with a DFB laser as power amplifier.
3-db modulation band width [GHz]	40	980	[96Wei]	Strained InGaAs multi QW.
wavelength tuning range [nm]	170	980	[90Eng]	Grating-coupled external cavity.

References for 5.2

70Alf Alferov, Zh.I., Andreev, V.M., Portnoi, E.L.: Sov. Phys. Semicond. (English Transl.) **3** (1970) 1107.

70Hay Hayashi, I., Panish, M.B., Foy, P.W., Sumski, S.: Appl. Phys. Lett. **17** (1970) 109.

74Mat Matthews, J.W., Blakeslee, A.E.: J. Cryst. Growth **27** (1974) 118.

75Sha Shay, J.L., Wernick, J.H.: Ternary Chalcopyrite Semiconductors; Oxford: Pergamon Press, 1975.

78Dup Dupuis, R.D., Dapkus, P.D., Holonyak, N., Rezek, E.A., Chin, R.: Appl. Phys. Lett. **32** (1978) 295.

82Mad Madelung, O., Schulz, M., Weiss, H. (eds.): Numerical Data And Functional Relationships In Science And Technology, Landolt-Börnstein, Group III, Vols. 17 and 22; Berlin, Heidelberg, New York, Tokyo: Springer-Verlag, 1982–1989.

84Lai Laidig, W.D., Caldwell, P.J., Lin, Y.F., Peng, C.K.: Appl. Phys. Lett. **44** (1984) 653.

85Peo People, R., Bean, J.C.: Appl. Phys. Lett. **47** (1985) 322.

88Koy Koyama, F., Kinoshita, S., Iga, K.: Trans. Inst. Electron. Inf. Commun. Eng. (IEICE) Sect. E **E71** (1988) 1089.

90Cho Choi, H.K., Wang, C.A.: Appl. Phys. Lett. **57** (1990) 321.

90Eng Eng, L.E., Mehuys, D.G., Mittelstein, D.G., Yariv, A.: Electron. Lett. **26** (1990) 1675.

91Cha Chand, N., Becker, E.E., van der Ziel, J.P., Chu, S.N.G, Dutta, N.K.: Appl. Phys. Lett. **58** (1991) 1704.

91Wil Williams, R.L., Dion, M., Chatenoud, F., Dzurko, K.: Appl. Phys. Lett. **58** (1991) 1816.

92Ada Adachi, S.: Physical Properties of III-V Semiconductor Compounds; New York: Wiley, 1992.

93Ada Adachi, S. (ed.): Properties of Aluminum Gallium Arsenide, No. 7 of EMIS Datareviews Series; London: INSPEC IEE, 1993.

93Bha Bhattacharya, P. (ed.): Properties of Indium Gallium Arsenide, No. 8 of EMIS Datareviews Series; London: INSPEC IEE, 1993.

93Eva Evans, G.A., Hammer, J.M.: Surface Emitting Semiconductor Lasers and Arrays; San Diego, London, Boston: Academic Press, 1993.

93Moe Möller, H.J.: Semiconductors for Solar Cells; Boston, London: Artech House, 1993.

93Nak Nakayama, N., Itoh, S., Ohata, T., Nakano, K., Okuyama, H., Ozawa, M., Ishibashi, A., Ikeda, M., Mori, Y.: Electron. Lett. **29** (1993) 1488.

93Zor Zory, P.S. (ed.): Quantum Well Lasers; San Diego, London, Boston: Academic Press, 1993.

94Dun Dunstan, J.D., Kidd, P., Fewster, P.F., Andrew, N.L., Grey, R., David, J.P.R., Gonzalea, L., Gonzales, Y., Sacedon, A., Gonzales-Sanz, F.: Appl. Phys. Lett. **65** (1994) 839.

94Edg Edgar, J.H. (ed.): Properties of Group III nitrides, No. 11 of EMIS Datareviews Series; London: INSPEC IEE, 1994.

94Kat Kato, Y., Kitamura, S., Hiramatsu, K., Sawaki, N.: J. Cryst. Growth **144** (1994) 133.
94Lim Lim, S.W., Hondo, T., Koyama, F., Iga, K., Inoue, K., Yanashima, K., Munekata, H., Kukimoto, H.: Appl. Phys. Lett. **65** (1994) 2437.
94Oku Okuyama, H., Itoh, S., Kato, E., Ozawa, M., Nakayama, N., Nakano, K., Ikeda, M., Ishibashi, A., Mori, Y.: Electron. Lett. **30** (1994) 415.

95Sal Sale, T.E.: Vertical Cavity Surface Emitting Lasers; Taunton: Research Studies, 1995.
95Yan Yang, G.M., MacDougal, M.H., Dapkus, P.D.: Electron. Lett. **31** (1995) 886.
95Yok Yokogawa, T., Yoshii, S., Tsujimura, A., Sasai, Y., Merz, J.: Jpn. J. Appl. Phys. **34** (1995) L751.
95Zha Zhao, H.M., Cheng, Y., Macdougal, M.H., Yang, G.M., Dapkus, P.D.: IEEE Photon. Technol. Lett. **7** (1995) 593.

96Bha Bhattacharya, P. (ed.): III-V Quantum Wells and Superlattices, No. 15 of EMIS Datareviews Series; London: INSPEC IEE, 1996.
96Bro Brozel, M.R., Stillman, G.E. (eds.): Properties of Gallium Arsenide, No. 16 of EMIS Datareviews Series; London: INSPEC IEE, 1996.
96Ish Ishibashi, A.: J. Cryst. Growth **159** (1996) 555.
96Mad Madelung, O. (ed.): Semiconductors – Basic Data; Berlin, Heidelberg, New York, Tokyo: Springer-Verlag, 1996.
96Nak1 Nakamura, S., Senoh, M., Nagahama, S., Iwasa, N., Yamada, T., Matsushita, T., Kiyoku, H., Sugimoto, Y.: Jpn. J. Appl. Phys. **35** (1996) L217.
96Nak2 Nakamura, S., Senoh, M., Nagahama, S., Iwasa, N., Yamada, T., Matsushita, T., Sugimoto, Y., Kiyoku, H.: Appl. Phys. Lett. **69** (1996) 4056.
96Nur Nurmikko, A.V., Heonsu, J., Gunshor, R.L., Han, J.: J. Cryst. Growth **159** (1996) 645.
96Wei Weisser, S., Larkins, E.C., Czotscher, K., Benz, W., Daleiden, J., Esquivias, I., Fleissner, J., Ralston, J.D., Romero, B., Sah, R.E., Schoenfelder, A., Rosenzweig, J.: IEEE Photon. Technol. Lett. **8** (1996) 608.

97Ber Bernadini, B., Fiorentini, V., Vanderbilt, D.: Phys. Rev. B **56** (1997) R10024.
97Bha Bhargava, R. (ed.): Properties of Wide-bandgap II-VI Semiconductors, No. 17 of EMIS Datareviews Series; London: INSPEC IEE, 1997.
97Han Han, J., Gunshor, R.L.: Semicond. Semimet. **44** (1997) 1.
97Nur Nurmikko, A., Gunshor, R. (eds.): II-VI Semiconductor Blue/Green Light Emitters, Semiconductors and Semimetals, Vol. 44; San Diego, London, Boston: Academic Press, 1997.
97OBr O'Brien, S., Lang, R., Parke, R., Major, J., Welch, D.F., Mehuys, D.: IEEE Photon. Technol. Lett. **9** (1997) 440.
97Pea Pearton, S.J. (ed.): GaN and Related Materials, Optoelectronic Properties of Semiconductors and Superlattices, Vol. 2; Amsterdam: Gordon and Breach, 1997.

98AlM Al-Muhanna, A., Mawst, L.J., Botez, D., Garbuzov, D.Z., Martinelli, R.U., Conolly, J.C.: Appl. Phys. Lett. **73** (1998) 1869.
98Gil Gil, B. (ed.): Group III Nitride Semiconductor Compounds; Oxford: Clarendon, 1998.
98Kre Kreller, F., Wünsche, H.-J., Puls, J., Henneberger, F.: J. Cryst. Growth **184/185** (1998) 614.
98Lu Lu, B., Osinski, J.S., Vail, E., Pezeshki, B., Schmitt, B., Lang, R.J.: Electron. Lett. **34** (1998) 272.
98Nak1 Nakamura, S., Senoh, M., Nagahama, S., Iwasa, N., Yamada, T., Matsushita, T., Kiyoku, H., Sugimoto, Y., Kozaki, T., Umemoto, H., Sano, M., Chocho, K.: Jpn. J. Appl. Phys. **37** (1998) L627.

98Nak2 Nakamura, S., Senoh, M., Nagahama, S., Iwasa, N., Yamada, T., Matsushita, T., Kiyoku, H., Sugimoto, Y., Kozaki, T., Umemoto, H., Sano, M., Chocho, K.: Jpn. J. Appl. Phys. **37** (1998) L1020.
98OBr O'Brien, S.O., Zhao, H., Lang, R.J.: Electron. Lett. **34** (1998) 184.
98Oku Okuyama, H., Kishita, Y., Ishibashi, A.: Phys. Rev. B **57** (1998) 2257.
98Osi Osinski, J.S., Lu, B., Zhao, H., Schmitt, B.: Electron. Lett. **34** (1998) 2336.
98Waa Waag, A., Litz, Th., Fischer, F., Lugauer, H.-J., Baron, T., Schüll, K., Zehnder, U., Gerhard, T., Lunz, U., Keim, M., Reuscher, G., Landwehr, G.: J. Cryst. Growth **184/185** (1998) 1.
98Zen Zeng, L., Yang, B.X., Cavus, A., Lin, W., Luo, Y.Y., Tamargo, M.C., Guo, Y., Chen, Y.C.: Appl. Phys. Lett. **72** (1998) 3136.

99Ack Acket, G.A., Valster, A., van der Poel, C.J.: Visible-Wavelength Laser Diodes, in: Kapon, E. (ed.): Semiconductor Lasers II, San Diego, London, Boston: Academic Press, 1999, p. 1.
99Beh Behringer, M., Wenisch, H., Fehrer, M., Großmann, V., Isemann, A., Klude, M., Heinke, H., Ohkawa, K., Hommel, D.: Growth and Characterization of II-VI Semiconductor Lasers, in: Kramer, B. Festkörperprobleme, Advances in Solid State Physics, Vol. 38, Braunschweig, Wiesbaden: Vieweg und Sohn, 1999, p. 47.
99Edg Edgar, J.H., Strite, S., Akashi, I., Amano, H., Wetzel, C. (eds.): Gallium Nitride and Related Semiconductors, No. 23 of EMIS Datareviews Series; London: INSPEC IEE, 1999.
99Ish Ishibashi, A.: Proc. SPIE **3625** (1999) 19.
99Kap1 Kapon, E. (ed.): Semiconductor Lasers I; San Diego, London, Boston: Academic Press, 1999.
99Kap2 Kapon, E. (ed.): Semiconductor Lasers II; San Diego, London, Boston: Academic Press, 1999.
99Kna Knauer, A., Erbert, G., Wenzel, H., Bhattacharya, A., Bugge, F., Maege, J., Pittroff, W., Sebastian, J.: Electron. Lett. **35** (1999) 638.
99Lam Lammert, R.M., Ungar, J.E., Osowski, M.L., Qi, H., Newkirk, M.A., Chaim, N.B.: IEEE Photon. Technol. Lett. **11** (1999) 1099.
99Mor Morkoc, H.: Nitride Semiconductors and Devices, in: Springer Series in Materials Science, Vol. 32; Berlin, Heidelberg, New York: Springer-Verlag, 1999.
99Nak1 Nakamura, S.: Semicond. Sci. Technol. **14** (1999) R27.
99Nak2 Nakamura, S., Senoh, M., Nagahama, S., Matsushita, T., Kiyoku, H., Sugimoto, Y., Kozaki, T., Umemoto, H., Sano, M., Mukai, T.: Jpn. J. Appl. Phys. Part 2 **38** (1999) L226.
99Pan Pankove, J.I., Moustakas, T.D. (eds.): Gallium Nitride; San Diego, London, Boston: Academic Press, 1999.
99Som Someya, T., Werner, R., Forchel, A., Arakawa, Y.: Phys. Status Solidi (a) **176** (1999) 63.
99The Theleva, T., Smith, S., Thomson, D., Linthicum, K., Rajagopal, P., Davis, R.F.: J. Electron. Mater. **28** (1999) L5.
99Wen Wenisch, H., Behringer, M., Fehrer, M., Klude, M., Isemann, A., Ohkawa, K., Hommel, D.: Jpn. J. Appl. Phys. **38** (1999) 2590.
99Wil Wilmsen, C.W., Temkin, H., Coldren, L.A.: Vertical-Cavity Surface-Emitting Lasers; Cambridge: Cambridge University Press, 1999.

00Die Diehl, R. (ed.): High-Power Diode Lasers: fundamentals, technology, applications, with contributions by numerous experts; Berlin, Heidelberg, New York: Springer-Verlag, 2000.
00Ito Itoh, S., Nakano, K., Ishibashi, A.: J. Cryst. Growth **214/215** (2000) 1029.

00Jai Jain, S.C., Willander, M., Narayan, J., Overstraeten, R. van: J. Appl. Phys. **87** (2000) 965.
00Klu Klude, M., Fehrer, M., Hommel, D.: Phys. Status Solidi (a) **180** (2000) 21.
00Miz Mizuta, M.: Phys. Status Solidi (a) **180** (2000) 163.
00Nak1 Nakamura, S., Fasol, G.: The Blue Laser Diode: The Complete Story; Berlin, Heidelberg, New York: Springer-Verlag, 2000.
00Nak2 Nakamura, S., Senoh, M., Nagahama, S., Iwasa, N., Matsushita, T., Mukai, T.: Appl. Phys. Lett. **76** (2000) 22.
00Oku Okuyama, H.: Trans. Inst. Electron. Inf. Commun. Eng. (IEICE) Sect. E **E83-C** (2000) 536.
00Osi Osinski, M., Smagley, V.A., Chun-Sheng, F., Smolyakov, G.A., Eliseev, P.G.: Proc. SPIE **3944** (2000) 40.
00Wen Wenzel, H., Erbert, G., Bugge, F., Knauer, A., Maege, J., Sebastian, J., Staske, R., Vogel, K., Tränkle, G.: Proc. SPIE **3947** (2000) 32.

01Hir Hiroyama, R., Nomura, Y., Furusawd, K., Okamoto, S., Hayashi, N., Shono, M., Sawada, M.: Electron. Lett. **37** (2001) 30.
01Mil Miller, M., Grabherr, M., King, R., Jäger, R., Michalzik, R., Ebeling, K.J.: IEEE J. Sel. Topics Quantum Electron. **7** (2001) 210.
01Vur Vurgaftman, I., Meyer, J.R., Ram-Mohan, L.R.: J. Appl. Phys. **89** (2001) 5815.

02Liu Liu, L., Edgar, J.H.: Mater. Sci. Eng. R **37** (2002) 61.

03Bhu Bhuiyan, A.G., Hashimoto, A., Yamamoto, A.: J. Appl. Phys. **94** (2003) 2779.
03Got Goto, S., Ohta, M., Yabuki, Y., Hoshina, Y., Nagnuma, K., Tamamura, K., Hashizu, T., Ikeda, M.: Phys. Status Solidi (a) **200** (2003) 122.
03Muk Mukai, T., Nagahama, S., Sano, M., Yanamoto, T., Morita, D., Mitani, T., Narukawa, Y., Yamamoto, S., Niki, I., Yamada, M., Sonobe, S., Shioji, S., Deguchi, K., Naitou, T., Tamaki, H., Murazaki, Y., Kameshima, M.: Phys. Status Solidi (a) **200** (2003) 52.
03Par Park, S.-H.: Jpn. J. Appl. Phys. **42** (2003) 5052.
03Pip Piprek, J.: Semiconductor Optoelectronic Devices; San Diego, London: Academic Press, 2003.
03Vur Vurgaftman, I., Meyer, J.R.: J. Appl. Phys. **94** (2003) 3675.

04Edm Edmond, J., Abare, A., Bergman, M., Bharathan, J., Bunker, K.L., Emerson, D., Haberern, K., Ibbetson, J., Leung, M., Russel, P., Slater, D.: J. Cryst. Growth **272** (2004) 242.
04Ima Imansihi, D., Sato, Y., Naganuma, K., Ito, S., Hirata, S.: Conf. Digest 19th IEEE Internat. Semicond. Laser Conf., 2004, p. 49.
04Oni Onishi, T., Inoue, K., Onozawa, K., Takayama, T., Yuri, M.: IEEE J. Quantum Electron. **40** (2004) 1634.
04Toi Toikkanen, L., Dumitrescu, M., Tukiainen, A., Viitala, S., Suominen, M., Erojärvi, V., Rimpiläinen, V., Rönkkö, R., Pessa, M.: Proc. SPIE **5452** (2004) 199.

05But Butcher, K.S.A., Tansley, T.L.: Superlatt. Microstructures **38** (2005) 1.
05Kan Kanskar, M., Earles, T., Goodnough, T.J., Stiers, E., Botez, D., Mawst, L.J.: Electron. Lett. **41** (2005) 245.
05Kna Knauer, A., Erbert, G., Staske, R., Sumpf, B., Wenzel, H., Weyers, M.: Semicond. Sci. Technol. **20** (2005) 621.
05Kni Knigge, A., Erbert, G., Jönsson, J., Pittroff, W., Staske, R., Sumpf, B., Weyers, M., Tränkle, G.: Electron. Lett. **41** (2005) 250.

05Ma Ma, B., Cho, S., Lee, C., Kim, Y., Park, Y.: IEEE Photon. Technol. Lett. **17** (2005) 1375.

05Sch Schmidt, B.E., Sverdlov, B., Pawlik, S., Lichtenstein, N., Mueller, J., Valk, B., Baettig, R.K., Mayer, B., Harder, C.S.: Proc. SPIE **5711** (2005) 201.

05Web Weber, J., Kelemen, M.T., Mikulla, M., Weimann, G.: Conference Digest CLEO Europe, 2005, CB6-3-WED.

06Wen Wenzel, H., Fricke, J., Klehr, A., Knauer, A., Erbert, G.: IEEE Photon. Technol. Lett. **18** (2006) 1.

07Pip Piprek, J. (ed.): Nitride Semiconductor Devices – Principles and Simulation; Weinheim: WILEY-VCH Verlag, 2007.

6.1 Free-electron lasers

M.J. Kelley, G.R. Neil

6.1.1 Overview

The Free-Electron Laser (FEL) is a device for direct conversion of electrical energy to a laser-like beam of light. The direct conversion is in contrast to lamps and to other lasers, where electrical energy is first deposited in a medium, which then emits a portion as light. The FEL is based on the combined action of three physical effects:

1. radiation by an oscillating charge;
2. strong peaking, Lorentz contraction and a Doppler shift of radiation from a relativistic electron beam into the direction of the beam;
3. bunching of a beam of electrons traveling in a strong optical radiation field so that they radiate coherently with the field.

The required major hardware (Fig. 6.1.1) consists of a source of high-energy electrons, a magnetic wiggler, and a means of providing strong interaction between the electrons and the light in the wiggler. Many embodiments of the technology and a wide range of applications have been explored. Reviews of experimental studies and FEL theory are available [90Bra, 95Sal, 96Fre, 99Fre]. A recent review describes 46 active and 24 proposed FELs of all wavelengths worldwide [99Col].

Future FEL development seems to be taking three directions:

1. machines with high average power in the IR through the VUV based on energy-recovering linacs [00Nei] for signal-intensive fundamental studies and materials-processing R&D utilizing sub-picosecond pulses and multiple simultaneous wavelengths out for pump-probe studies;
2. extreme UV to X-ray FELs for advanced lithography, and fundamental studies of atomic and molecular physics;

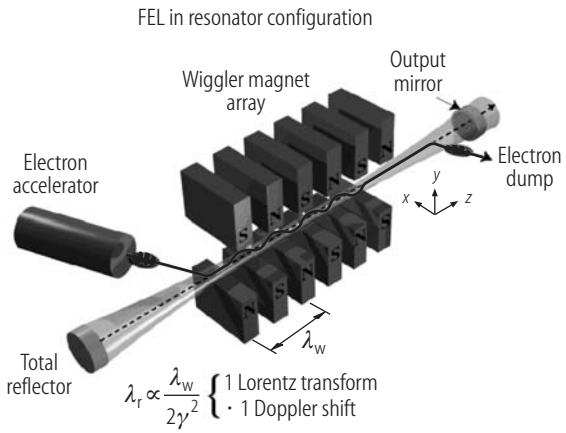

Fig. 6.1.1. Schematic of a typical free-standing FEL.

3. "table-top" low-power machines for fundamental atomic and molecular, and solid-state science studies operating at IR wavelengths longer than mid-microns, where solid-state wavelength conversion technology (Optical Parametric Oscillator – OPO) has not proven effective.

For all but synchrotron storage rings, the dominant electron source is a photocathode followed by an RF linac. For all but the proposed VUV/EUV/X-ray machines, the means of achieving an intense optical beam within the wiggler is to place mirrors at each end, forming an optical cavity oscillator which allows the optical pulses to build to saturation. All but the table-top FEL machines are large, occupying a building rather than a laboratory room.

The output format for most of the operating and proposed FELs consists of a continuous train or bursts ("macropulses") of picosecond pulses of highly polarized, single-wavelength light. Routine operation is presently in the IR; visible and UV light are available at the storage-ring FELs and a few high-energy linac facilities and X-ray sources are being actively developed. The maximum time between the individual pulses (micropulses) in oscillators is set by the hardware and is less than a few tens of nanoseconds, in contrast with many familiar solid-state and gas lasers. The maximum micropulse energy of oscillators is also typically hardware-limited to less than a few tens of microjoules per pulse, as discussed in more detail later. Maximum sustained average output power is now in excess of 10 kilowatts [04Beh, 00Nei] and, unlike other laser and lamp sources, physics or technology upper limits to attainable average output power should be substantially in excess of this value. Very much the same hardware components are needed for any size FEL, so that the multimillion-dollar cost increases little as output power increases. Estimates suggest that the unit cost of light from a more-than-25-kW FEL should not be greater than from a comparably powerful CO_2 laser [96Nei].

Interest in the direct generation of electromagnetic radiation by interaction of an electron beam with an alternating magnetic field began with the pioneering work of Motz [51Mot] a half-century ago. The first demonstration of an FEL recognizable in present terms was by Madey [77Dea] some 25 years later. Defense interests drove the field for the next several years. Theoretical issues were addressed and a consensus understanding achieved that, while not resolving all issues, provides an adequate basis for the reliable design of machines [90Bra, 95Sal, 96Fre, 99Fre]. Options in electron source and accelerator technology were explored, converging on optimized strategies for different objectives, but with substantial commonality amongst the hardware. The FEL hardware upstream of the wiggler must produce and deliver a high-quality electron beam over the desired energy range, typically a factor of 1.5 to 2. A key measure of beam quality is the emittance; the transverse emittance is the product of the beam radius and its divergence angle. Roughly speaking, the numerical value of the emittance (meters, radians) must not significantly exceed the intended wavelength (meters)/4π. The physical meaning is that the output optical beam cannot be brighter than the electron beam which makes it.

6.1.2 Components of a FEL

6.1.2.1 Injector

The beginning of the FEL is the injector, comprising the cathode, the electron gun within which the cathode is mounted and the pre-accelerator (Fig. 6.1.2). The electron source must simultaneously deliver high charge per bunch, small energy spread, and short bunch length. The once-commonplace thermionic source is being displaced by the laser-driven photocathode, typically a cesiated semiconductor such as gallium arsenide or indium antimonide. Metallic cathodes may also be used but have a lower quantum efficiency and require an ultraviolet drive laser due to a higher work function

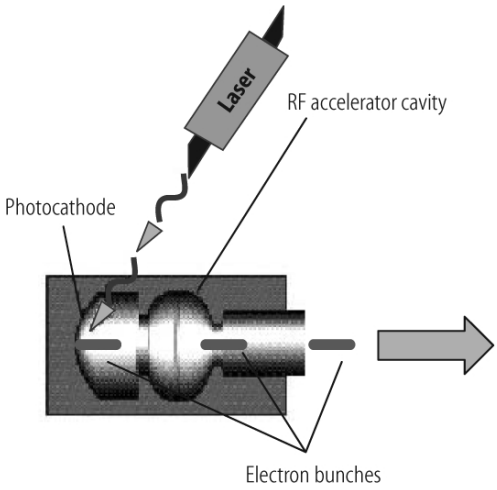

Fig. 6.1.2. Schematic of an RF FEL injector. Light from a modelocked laser impinges on a photocathode inside a RF cavity. The electrons emitted from the cathode are accelerated by the RF fields in the cavity. See Fig. 6.1.3.

of the surface. A more robust materials system continues to be sought to increase performance, to avoid the need for recesiation and to escape from the fragility of semiconductor wafers. Design of the electron gun seeks to raise the energy of the photoelectrons rapidly to avoid emittance growth by applying the highest tolerable voltage and voltage gradient to the photocathode. The performance of present DC guns is limited by field emission as operating voltage increases beyond a few hundred kilovolts. RF guns bring a significant improvement in emittance, but further development is needed before such systems can provide cw beams. Following the gun assembly is the pre-accelerator to bring the electrons up to injection energy, typically about 10 MeV.

6.1.2.2 Accelerator

For the main accelerator (Fig. 6.1.3), only the microwave-driven RF linac (or RF drive cavity on a synchrotron storage ring) yields a beam in the desired energy range to produce near IR light with sufficiently high quality to lase. RF accelerator technology has been developed for more than fifty years for nuclear and high-energy-physics research [86Hum, 98Pad, 98Wan]. Drive frequencies ranging from 180 MHz to 17 GHz have been employed. Low frequencies have the advantages that the current transport stability limit varies as the inverse square of the frequency [99Mer] and the larger internal physical dimensions make alignment a little less critical. However, larger accelerator elements for a fixed output energy are a disadvantage for accelerator cost, a consideration that looms larger as Superconducting RF (SRF) structures replace the long-used room-temperature copper. Superconducting technology offers the advantages of 100 % versus 1 % duty cycle and increasingly higher gradients, now installing at 18 MeV/meter [99Mer]. The gains in average power and machine compactness more than offset the more complex accelerator and addition of a liquid-helium supply, making SRF the lowest-total-cost accelerator technology for medium to high average power and high-energy machines. Room-temperature copper cavities suffice for table-top FELs.

The accelerator output energy for IR FELs is typically a few tens of MeV and a few hundred to thousands of MeV for the proposed DUV and shorter wavelength machines. The storage-ring FELs work with the available ring energy. The design of table-top machines seeks to utilize beam energies below 10 MeV, to minimize the prospects for making the materials of construction radioactive by photonuclear activation.

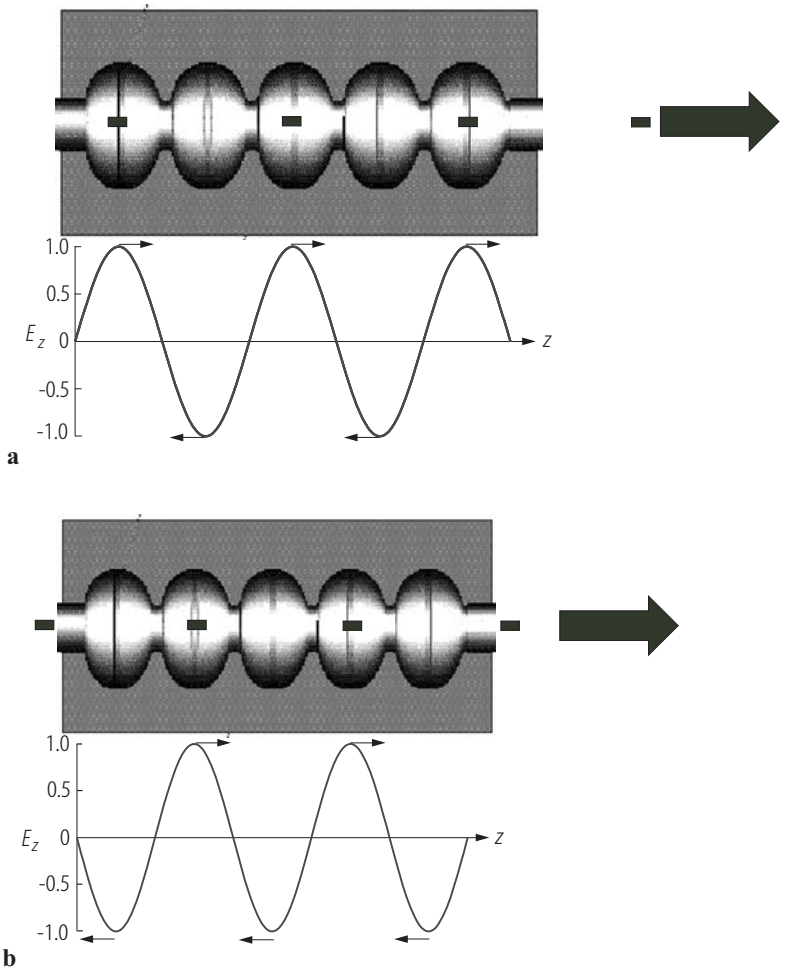

Fig. 6.1.3. Schematic of RF accelerator cavity. (**a**) Electron bunches spaced by an integral number of RF periods enter the accelerating structure in phase with the RF fields so that the electric field accelerates the electrons. (**b**) A half RF cycle later the electrons have moved to the next cavity while the RF field has reversed phase so now this next cavity also accelerates the electrons. The process continues down the linac.

6.1.2.3 Wiggler

The wiggler (Fig. 6.1.4) accomplishes conversion of electron-beam energy to light. It is an alternating array of magnets, whose field deflects the beam first to one side and then the other in a plane perpendicular to the magnetic field of the array. In terms of hardware, for cost and simplicity most FELs to date have used permanent magnets with a gap of perhaps 1 cm between opposing faces. A precise gap control mechanism may be used to adjust field strength over a limited range. Special pole face contours to optimally shape the magnetic field have been explored as have helical designs, but the resulting performance advantages have not proven sufficient to offset the increased cost and manufacturing complexity. Electromagnetic wigglers offer the advantage that the magnetic field strength can be adjusted by means of the power supply current providing an easy means of tuning wavelength. Typical wiggler parameters are 30–100 periods (N_w) of a few centimeters wavelength (λ_w) for permanent magnets, somewhat longer periods for electromagnets. The parameters may be constant for the whole length of the wiggler or may vary ("taper") so as to extract more energy

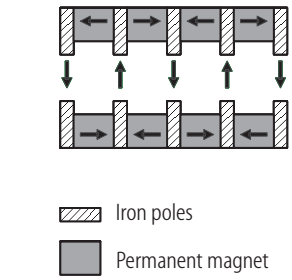

Fig. 6.1.4. Schematic of a typical permanent-magnet hybrid wiggler. Permanent magnets provide the flux that is channeled through iron pole pieces to make a sinusoidal transverse field on axis.

from the electron beam. Increased energy extraction entails increased beam degradation, however, so that FELs which recycle the beam (synchrotron storage rings) or its energy (energy recovering linac FELs) limit energy extraction to about a percent.

6.1.2.3.1 Processes in the wiggler

Among the fruits of the intense theoretical effort in the late 1980's was a thorough understanding of what takes place in the wiggler. Fortunately, for the conditions of most interest, it is sufficient to consider classical electrons (no quantum effects) interacting with each other only through the optical field (no space-charge effects) [76Col]. The developers of synchrotron light sources addressed in detail the problem of the spectral distribution of light spontaneously generated by an electron beam traversing a wiggler (strictly, an undulator). An electron traverses the array at nearly the speed of light, so that in its frame the wavelength of the wiggler is Lorentz-contracted by a factor of $1/\gamma$ accordingly ($\gamma = 1 + E\,(\mathrm{MeV})/0.511$). Further, the wavelength of the emitted light is reduced by Doppler shift for a stationary observer by a factor $(1+\beta)\gamma \sim 2\gamma$, so that the primary wavelength for emission is given by:

$$\lambda_{\mathrm{FEL}} = \lambda_{\mathrm{w}}(1 + a_{\mathrm{w}}^2)/2\gamma^2 \; ; \quad a_{\mathrm{w}} = eB_{\mathrm{w}}\lambda_{\mathrm{w}}/2\pi mc \; , \tag{6.1.1}$$

where quantities subscripted "w" refer to the wiggler, λ_{w} is the wiggler wavelength. The wavelength correction factor of $(1 + a_{\mathrm{w}}^2)$ accounts for the fact that the electron beam is not traveling straight down the axis but oscillating to each side. The electron beam energy enters through γ and the magnetic field strength B_{w} through the wiggler parameter, a_{w}. The other symbols have their usual meanings. The expression applies to both spontaneous emission from the FEL and from a synchrotron undulator. The line shape has the functional form $\sin^2(u)/u^2$, where $u = \pi N_{\mathrm{w}}(\lambda - \lambda_{\mathrm{FEL}})/\lambda_{\mathrm{FEL}}$, so that the linewidth varies as $1/N_{\mathrm{w}}$. Further, the beam at the primary wavelength is contained within a cone centered on the axis having an opening angle of $1/(\gamma\sqrt{N_{\mathrm{w}}})$. Harmonics of the fundamental are also produced but the even harmonics vanish along the axial direction. In spontaneous emission, each electron emits independently with no fixed phase relationship to emission arising from any other electron. Total intensity therefore depends linearly on the number of electrons participating, i.e., the beam current.

In the FEL under lasing conditions, as distinguished from spontaneous emission conditions, a high-intensity optical beam co-propagates with the electron beam. It can be achieved by placing a highly reflective mirror at each end of the wiggler to form a resonant optical cavity in which optical beam intensity builds up. An alternative approach when an adequate mirror technology is unavailable is to design the wiggler with high gain to generate the optical beam itself – Self-Amplified Spontaneous Emission – "SASE". The requirement to have the two beams occupy exactly the same space over their region of co-propagation emphasizes the importance of electron beam quality and of precision in the construction of the wiggler. The electron oscillations in the wiggler must now occur in response to both the optical field and the magnetic field.

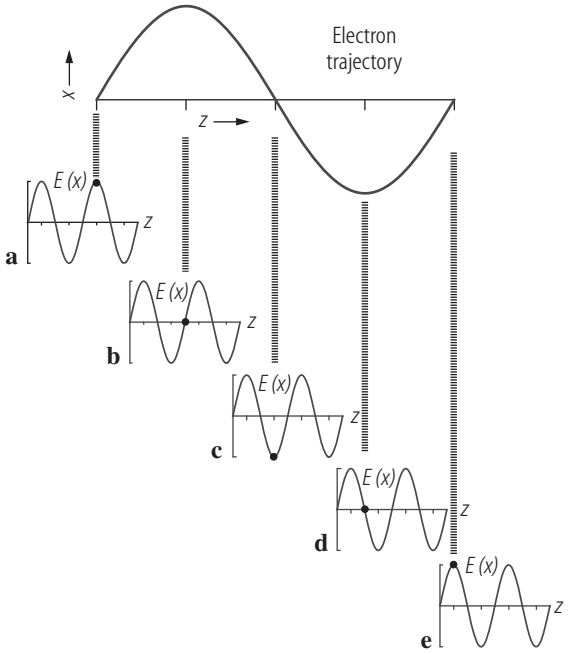

Fig. 6.1.5. A net transfer of energy between the electron and the co-propagating electromagnetic wave occurs because of the resonance condition. The resonance condition says that for one particular wavelength there is exactly one wavelength of slip between the optical field and the electrons for each wiggler wavelength due to the fact that the optical wave travels at the speed of light c and the electron travels at βc along the oscillating trajectory determined by the wiggler. This is illustrated in this figure. In (**a**) the direction of the electron's transverse motion is in the same direction as the electric field so the electron does work on the field, that is, gives up some of its energy to the field. In (**b**) the motion and electric field are at right angles so no work is done. In (**c**) both the direction of motion and the sense of the field has reversed so again there is transfer of energy from the electron to the field. In (**d**) it is neutral again. Finally in (**e**) the electron is shown slipped backward by exactly one optical wavelength and again is able to transfer energy to the wave. This process continues down the wiggler. In addition to this energy transfer which occurs for single electrons there is longitudinal bunching of the electrons at the optical wavelength due to the ponderomotive potential of the beating wiggler field and electromagnetic wave. This results in a gradual build up of coherence in the field as the electron bunches radiate in an increasingly coherent fashion as they bunch while traveling down the wiggler.

The axial distribution of electrons entering the wiggler is random with respect to the optical field. The combination of the optical field and the wiggler magnetic field forms a co-propagating ponderomotive potential wave moving with the electrons. As the electrons traverse the wiggler, they experience an accelerating or decelerating force according to the degree to which they lead or lag the moving ponderomotive field, transforming an initially continuous electron beam to a train of bunches uniformly spaced at the optical wavelength. The major result of this fixed phase relationship is that their emission adds coherently. That is, proportional to the number of electrons squared.

A schematic illustration of the energy-transfer process for a wiggler with planar symmetry is shown in Fig. 6.1.5. Electrons moving in synchronism with the ponderomotive wave are said to be in *resonance* with it and will experience an average decelerating force which can give rise to coherent amplification. Equating the phase velocity of the ponderomotive wave ($v_{\mathrm{ph}} = \omega/(k + k_{\mathrm{w}})$, where ω and k are the angular frequency and wavenumber of the optical wave and k_{w} is the wiggler wavenumber) with the electron beam velocity parallel to the propagation axis, v_{b}, we obtain the resonance condition

$$\omega = (k + k_w)v_b \ . \tag{6.1.2}$$

For waves propagating in free space $\omega = ck$ and this condition yields a wavelength of

$$\lambda = \frac{\lambda_w}{2\gamma_b^2} \ , \tag{6.1.3}$$

where λ_w is the wiggler period, and $\gamma_b = (1 - v_b^2/c^2)^{1/2}$.

In order to understand how a wiggler and a forward-propagating electromagnetic wave (whose electric and magnetic fields are oriented transversely to the electron beam) give rise to a ponderomotive force which extracts energy from the electrons, we consider the particle motion in a sinusoidal wiggler field. The wiggler field determines the electron trajectories. An electron propagating through the wiggler experiences a force which acts at right angles to both the direction of the field and to its own velocity. The resulting orbit is sinusoidal. The magnitude of the transverse wiggle velocity, denoted by v_w, is proportional to the product of the wiggler amplitude and period. This relationship may be expressed in the form

$$\frac{v_w}{c} = \frac{a_w}{\gamma_0} = 0.934\frac{B_w\lambda_w}{\gamma_0} \ , \tag{6.1.4}$$

where the wiggler period is expressed in units of centimeters, and B_w denotes the wiggler field strength in Tesla.

Since the motion is sinusoidal the resonant wavelength is given by

$$\lambda = (1 + a_w^2)\frac{\lambda_w}{2\gamma_0^2} = (1 + 0.872\ B_w^2\lambda_w^2)\frac{\lambda_w}{2\gamma_0^2} \ , \tag{6.1.5}$$

where the magnetic field is understood to be the Root Mean Square (RMS) field amplitude. This is just the same condition as expressed in (6.1.1) for the peak of the spontaneous emission. This synchronism is illustrated in Fig. 6.1.5 demonstrating that under resonance the electron feels on average a decelerating force and the electromagnetic field takes on energy from the electron.

The net transfer of energy from the electron beam to the optical beam results in optical gain. Madey showed that the small-signal gain G_S varies as the derivative of the spectral intensity [79Mad]:

$$G_S = K[(\lambda_{FEL}\lambda_w)^{1/2}/A_{FEL}][a_w^2/(1 + a_w^2)^{3/2}]I_p N_w^3 I'_{spon}(1/\lambda) \ , \tag{6.1.6}$$

where K is a group of constants, A_{FEL} is the cross-sectional area of the laser beam within the wiggler, I_p is the peak current during the electron pulse, $I'_{spon}(1/\lambda)$ is the derivative of the spontaneous emission line profile and the other terms have their previous meanings. Factors that contribute to high gain are tight laser beam focus, high peak current, long wiggler (up to saturation) and narrow spontaneous emission peak. Factors which degrade the gain can include inhomogeneities in the wiggler field and energy spread in the electron beam. The electron beam continues to transfer energy to the optical beam until the induced energy spread on the electrons reduces the gain below the cavity losses: saturation.

6.1.3 Output

Homogeneous and inhomogeneous broadening of the output spectrum do not occur in the same manner in an FEL as with conventional lasers since they are the result of different physical processes. The bandwidth of an FEL is typically Fourier transform bandwidth limited, i.e., by the

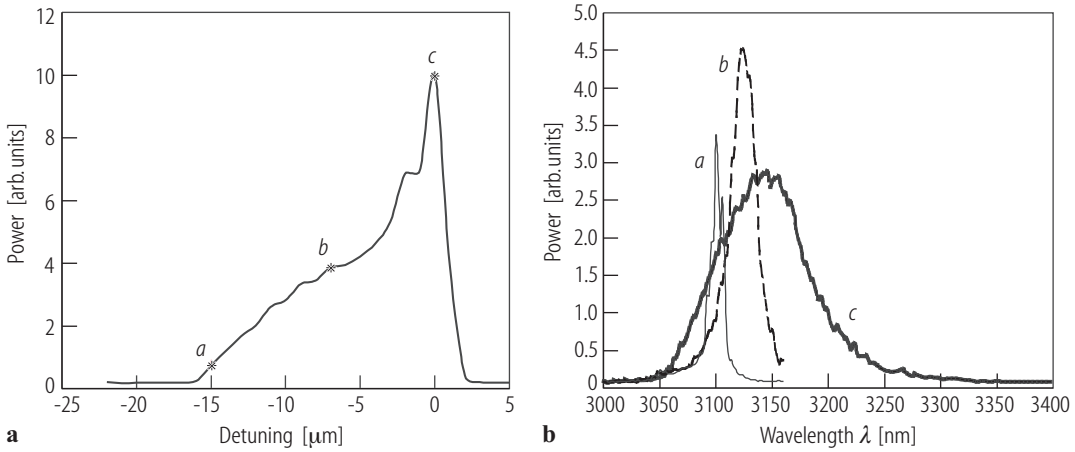

Fig. 6.1.6. (**a**) Typical detuning curve of the FEL, i.e., power as a function of cavity length. The spectra in (**b**) show the increase in bandwidth as the peak in power is approached. By the Fourier bandwidth transform this indicates an increasingly shorter optical output pulse near the peak. Data from the Jefferson Lab IR Demo.

number of cycles of oscillation in the FEL light so that $\Delta\omega\,\tau = 1$. For Gaussian pulses this means that $c\tau(\Delta\lambda/\lambda^2) = 0.44$ and the coherence length is given by $L = \lambda^2/(2\Delta\lambda)$. The bandwidth of the output from a given device can be made to vary over a large range depending on how hard the FEL is driven into saturation.

In FEL oscillators the degree to which the FEL is driven into saturation depends on the extent to which the small-signal gain exceeds the cavity losses including outcoupling. If the small-signal gain exceeds three times the losses the oscillator may be driven well into saturation and the extraction efficiency (conversion of electron beam power to light) can exceed $1/2N_\mathrm{w}$. The oscillator depends on overlap of the optical pulses bouncing in the optical cavity and electron pulses produced by the accelerator. The degree to which these overlap exactly is called synchronism or detuning. Since the electron pulse slips back exactly one optical wavelength each wiggle period in the wiggler the output pulse length can be longer (or shorter) than the electron pulses producing it depending on the relative overlap of the returning optical pulse and the subsequent electron pulse. As the synchronism is changed from the round-trip time of the optical pulse being exactly the same as the electron interpulse spacing to longer than that the FEL power goes from the highest power with the shortest pulse length (and widest bandwidth) to lower power with longer pulses and narrower bandwidth. An example of this is shown in Fig. 6.1.6 with the power and bandwidth at three detunings.

Similar behavior exists in Self-Amplified Spontaneous Emission (SASE) FELs, but in this case, since the FEL signal grows from noise (hence the name), it may exhibit fluctuation behavior set by the gain length in number of wiggler periods and operating wavelength. The bandwidth of the output again becomes set by Fourier transform limits but the pulse intensity exhibits spiking behavior in the frequency domain. The average wavelength spacing between these intensity spikes can be used to estimate the bunch length of the pulse through the relation $\tau = \lambda^2/(0.64\,c\Delta\lambda)$. The details of this behavior are beyond the scope of this article. We refer the reader to [98Hog]. In a SASE case the saturation power is determined by the length of the wiggler, however, the gain rate typically drops rapidly as the conversion efficiency reaches a fraction of a percent of the electron beam power and reaches a state of diminishing returns.

For oscillators placing an inward-facing mirror at each end of the wiggler affords the simplest optical cavity. One of the mirrors may be made a few percent transmissive to outcouple the laser light or alternately have a hole to outcouple the light. Although the hole outcoupling is simple to implement, diffraction losses from the hole typically mean that less than 50 % of the power losses in

the cavity are delivered in a useful optical mode. The mirror surfaces typically have some curvature so that the beam at the mirror face spreads over a larger area than within the wiggler, to reduce the risk of damage from the high intra-cavity power. The mirror loading associated with few-watt and lower average power output can be accommodated with broad-band metal mirrors. Kilowatt and higher output powers require wavelength-specific dielectric stack coatings on a water-cooled substrate. Continuing fundamental and practical advances in optical coatings will hopefully open a path to highly reflective broad-band coatings, eliminating loss of operating time to mirror changes. Alignment tuning of the present several-meter long, opposed-mirror cavities requires care, but is routinely accomplished. Designs for high-average-power UV FELs envision optical cavities perhaps ten times as long and may use active alignment.

The electron pulse exiting the wiggler still typically carries more than 99 % of the original energy, but its beam energy spread is degraded to a degree that depends on the extent of energy extraction. The effect is most critical for storage-ring FELs, where sustained lasing requires beam quality to be restored ("cooling") before the next pass through the wiggler. In practice, this means that storage-ring FELs either lase at low efficiency or in a relaxation oscillation with high peak power followed by beam cooling. High-average-power FELs depend on recycling the beam energy, though not the electron pulse itself. By keeping energy extraction in the wiggler to about a percent, sufficient beam quality can be maintained to transport the beam back to the accelerator. A valuable feature of RF accelerator technology is that bringing the electron bunch back into the original accelerator cavity in reverse-phase causes energy transfer from the bunch to the RF field, where it is available to accelerate a fresh pulse from the injector [00Nei]. A further benefit is that the energy remaining in the original pulse can be brought below the threshold for photonuclear activation (about 10 MeV), greatly simplifying the beam dump. For EUV/X-ray FEL SASE, discussion continues about whether to make the investment needed for energy recovery or to dump the beam at full unextracted power.

As noted in the overview, the optical beam from the FEL consists of discrete pulses, approximately a picosecond long. Micropulse separation in a SASE machine is the same as the separation of the electron beam pulses, but is at most the optical round-trip time of the cavity in an oscillator FEL. For the machines that use optical cavities, even high average power will not mean micropulse energies much greater than several tens of millijoules. The FEL also produces light at the harmonics of the primary wavelength, but with much less than 1 % of the primary power unless special arrangements are made to enhance harmonic lasing. A further issue arises when the FEL operates in macropulse mode. Depending on the optical cavity gain, the optical field in the cavity reaches steady-state over a number of micropulses: The laser takes a number of micropulses to turn on.

6.1.4 Summary and outlook

All in all, an FEL delivers a reasonably well-defined range of output parameters dependent on the accelerator driving it. Operation much outside the range takes considerable effort or cannot yet be achieved at all. Accordingly FEL researchers have given attention to optical beam conditioning, achieving the desired beam characteristics by downstream manipulations while the FEL operates in its native mode. The isolation of individual micropulses from a continuous stream ("pulse picking") is practiced in mainstream laser science by means such as Electro-Optic (EO) – Pockels – cell switching. Applying it to an FEL beam requires EO cells that work at the desired wavelength and can handle the power load. The power handling issue can be helped by operating the FEL in a macropulse mode, delivering beam to the EO cell only for a time slice surrounding the "on" time. Changing the length of individual micropulses has been addressed in a manner analogous to "ultrafast" solid-state lasers. The FEL is operated so as to produce a wavelength chirp in the output

by slewing the beam energy within each micropulse [95Sza], followed by a grating or prism pair to accomplish about a tenfold compression or stretch. Increased individual micropulse energy has been achieved by adding a downstream optical cavity equipped with a switchable mirror, a pulse stacker. A demonstration of pulse stacking in the IR used a silicon wafer at the center of the cavity, which was rendered reflective to dump the cavity by a pulse from a Ti:sapphire laser [97Smi]. For components of the beam conditioning equipment and further downstream optics, no damage issues have been reported beyond those which may be anticipated from general laser experience.

To have a lasting role, the FEL must find important applications in a world where many other laser technologies (most of which are less complex and capital-intensive than the FEL) are competing for resources. Present applications are reported at the leading conferences describe the using the FEL to gain access to otherwise-unavailable wavelengths to probe chemistry, electronic properties, etc. An analysis by the U.S. National Research Council [94Ano] saw a rich menu of such opportunities in the far-IR (10–1000 μm) where other lasers are notably absent or weak, and in the VUV (10 nm to 200 nm). Table 6.1.1 shows the capabilities of a few of the FELs worldwide that are operated as established user facilities. A great opportunity for contribution to medicine is attributed to the FEL's wavelength tunability that provides access to IR bands associated with biologically significant molecular entities, such as the amide bands of proteins. Despite a number of scientifically interesting studies, a truly striking result has yet to emerge.

The ability to selectively sever molecular bonds in organic molecules arises from the combination of wavelength tuning, short pulse length and high peak power. Selective bond scission makes possible intact ablation oligomers from polymers, which can then deposit as molecularly faithful films, e.g. [01Bub, 02Bub, 04Tof]. The FEL appears to be finding a unique role as a drive laser for versatile pulsed laser deposition of organics.

An assessment of the potential industrial applications saw opportunity in micromachining, pulsed laser deposition and large-area thermal processing [98Kel]. All have been shown to be technologically and functionally attractive using Ti:sapphire or excimer lasers, but they have not gone forward because these lasers lack sufficient capacity and/or are too costly to support wide deployment. The FEL's ability to be made large and, if made large, the expected low cost of its light were seen as decisive advantages. Defense applications originally envisioned defense against ballistic missiles. Interest has now turned toward defending ships against sea-skimmer missiles [97Tod, 00Tod] or as an airborne antimissile system [05Whi], more significant issues in the smaller conflicts of the post-cold-war world. The breadth of possibilities envisioned for an FEL user facility based on energy recovery can be sampled in the 4GLS science case.

In the last few years substantial progress in the development of electron injectors has led to the launching of several substantial projects aimed at developing incredibly intense X-ray FELs based on SASE. The exciting prospect of a laser operating at 0.1 nm with a brightness exceeding existing sources by 6 orders of magnitude has invigorated and challenged the user community. The wealth of new physics studies enabled by such a source is only exceeded by the daunting array of new techniques which must be developed to make the source a practical scientific tool.

The most important point, however, is that new and vastly more capable FELs are being brought into operation as user facilities for scientific and applied technical studies. FELs are moving from an exotic tool of a few specialists to something broadly available providing photon characteristics unobtainable from more conventional sources.

Table 6.1.1. A partial list of currently available FEL user facilities. Also shown are the major X-ray FEL facilities under construction at Stanford Linear Accelerator Center, the high-average-power UV machine at Jefferson Lab, and the Energy Recovering Linac facility in prototyping at Daresbury. See [06Col] for a more complete and up-to-date list of FELs. Also visit the web FEL page hosted by University of California at Santa Barbara `http://sbfel3.ucsb.edu/www/vl_fel.html`. Under accelerator the type is indicated as RTRF: Room Temperature Radio Frequency linac, SCRF: SuperConducting Radio Frequency linac, SR: Storage Ring, and VDG: Van De Graff accelerator. The accelerator type tends to determine the temporal characteristics, e.g., cw train of short pulses in SCRF, limited-duration bunch train of short pulses in RTRF, a long pulse or DC beam in a VDG, and a long pulse at high repetition rate or a gain-switched high-peak-power pulse in SR.

Country	Institution	Device	λ [μm]	τ_p [ps]	E_b [MeV]	I_b [A]	P_{peak} [MW]	P_{avg} [W]	Accelerator
USA	Stanford	FIREFLY	15–80	0.3–10	15	25	0.3	0.4	SCRF
	Vanderbilt	FELI	2–10	0.7	43	50	10	10	RTRF
	Duke	Mark III	2.7–6.5	3	31–41.5	20	2	3	RTRF
		OK-5	0.45	0.1–10	270–800	35	1000	0.1	SR
	JLab	IR upgrade	0.7–10	0.2–1	145	270	100	14000	SCRF
		UV upgrade	*0.3–1*	*0.1–1*	*145*	*270*	*10*	*1000*	*SCRF*
	UCSB	FIR-FEL	60	25000	6	2	0.004	0.08	VDG
	BNL	SDL	0.2–1.0	0.5–1	100–250	400	400	0.1	RTRF
	SLAC	*LCLS*	*0.0001*	*0.1*	*15000*	*5000*			*RTRF*
Japan	Osaka	FELI 1	5.5	10	33	42	5	2	RTRF
		FELI 2	1.9	10	68	42	5	0.5	RTRF
		FELI 3	0.3–0.7	5	155	60	5	0.5	RTRF
		FELI 4	18–40	10	33	40	5	1	RTRF
		ISIR	32–150	20–30	13–19	50	2	1	RTRF
	Tsukuba	KHI-FEL	0.2–0.6	14	310	10			
England	*Daresbury*	*4GLS*	(*multiple FELs, IR to VUV*)	*1*	*600*	*300*			*SCRF*
NL	FOM	FELIX	3–250	1	50	50	2	1	RTRF
Germany	Dresden	U-100	15–150	0.3–10	15	240	2	0.5	RTRF
	Dresden	ELBE	3–22	1–10	34	30			SCRF
	DESY	Flash	0.013	0.025	700	2000	2000	10	SCRF

References for 6.1

51Mot Motz, H.: J. Appl. Phys. **22** (1951) 527–535.

76Col Colson, W.B.: Phys. Lett. A **59** (1976) 187–189.

77Dea Deacon, D.A.G., Elias, L.R., Madey, J.M.J., Ramian, G.J., Schwettnan, H.A., Smith, T.I.: Phys. Rev. Lett. **38** (1977) 892–894.

79Mad Madey, J.M.J.: Nuovo Cimento **50B** (1979) 64–88.

86Hum Humphries jr., S.: Principles of Charged Particle Acceleration, New York: John Wiley, 1986.

90Bra Brau, C.A.: Free Electron Lasers, San Diego: Academic Press, 1990.

94Ano Anonymous: Free Electron Lasers and Other Advanced Sources of Light – Scientific Research Opportunities, Washington, DC: National Academy Press, 1994.

95Sal Saldin, E.L., Schneidmiller, E.A., Yurkov, M.V.: Phys. Rep. **260** (1995) 187–327.

95Sza Szarmes, E.B., Madden, A.D., Madey, J.M.J.: Nucl. Instrum. Methods Phys. Res. Sect. A **358** (1995) 220–223.

96Fre Freund, H.P., Antonsen jr., T.M.: Principles of Free Electron Lasers, 2nd Edn., London: Chapman & Hall, 1996.

96Nei Neil, G.R.: Proc. 1995 Particle Accelerator Conference, IEEE, 1996, pp. 137–139.

97Smi Smith, T.I., Haar, P., Schwettman, H.A.: Nucl. Instrum. Methods Phys. Res. Sect. A **393** (1997) 245–251.

97Tod Todd, A.M.M., Colson, W.B., Neil, G.R., in: Free-Electron Laser Challenges. Proc. SPIE **2988** (1997) 176.

98Hog Hogan, M., Anderson, S., Bishofberger, K., Frigola, P., Murokh, A., Osmanov, N., Pellegrini, C., Reiche, S., Rosenzweig, J., Travish, G., Tremaine, A., Varfolomeev, A.: Nucl. Instrum. Methods Phys. Res. Sect. A **407** (1998) 257–260.

98Kel Kelley, M.J.: Nucl. Instrum. Methods Phys. Res. Sect. B **144** (1998) 186–192.

98Pad Padamsee, H., Knobloch, J., Hays, T.: RF Superconductivity for Accelerators, New York: John Wiley, 1998.

98Wan Wangler, T.: Principles of RF Linear Accelerators, New York: Wiley Interscience, 1998.

99Col Colson, W.B.: Nucl. Instrum. Methods Phys. Res. Sect. A **429** (1999) 37–40.

99Fre Freund, H.P., Neil, G.R.: Proc. IEEE **87** (1999) 782–803.

99Mer Merminga, L., Alexeev, P., Benson, S., Bolshakov, A., Doolittle, L., Neil, G.: Nucl. Instrum. Methods Phys. Res. Sect. A **429** (1999) 58–64.

00Nei Neil, G.R., Bohn, C.L., Benson, S.V., Biallas, G., Douglas, D., Dylla, H.F., Evans, R., Fugitt, J., Grippo, A., Gubeli, J., Hill, R., Jordan, K., Li, R., Merminga, L., Piot, P., Preble, J., Shinn, M., Siggins, T., Walker, R., Yunn, B.: Phys. Rev. Lett. **84** (2000) 662–665.

00Tod Todd, A.M.M., in: Gas, Chemical and Electrical lasers and Intense Beam Control and Applications. Proc. SPIE **3931** (2000) 234.

01Bub Bubb, D.M., Horwitz, J.S., Callahan, J.H., McGill, R.A., Houser, E.J., Chrisey, D.B., Papatonakis, M.R., Haglund, R.F., Galicia, M.C., Vertes, A.: J. Vac. Sci. Technol. A **19** (2001) 2698.

02Bub Bubb, D.M., Papatonakis, M.R., Toftman, B., Horwitz, J.S., McGill, R.A., Chrisey, D.B., Haglund, R.F.: J. Appl. Phys. **91** (2002) 9809.

02Poo Poole, M.W., Clarke, J.A., Seddon, E.A., in: Proc. EPAC 2002, available at `http://accelconf.web.cern.ch/AccelConf/` (2002).

04Beh Behre, C., Benson, S., Biallas, G., Boyce, J., Curtis, C., Douglas, D., Dylla, H.F., Dillon-Townes, L., Evans, R., Grippo, A., Gubeli, J., Hardy, D., Heckman, J., Hernandez-Garcia, C., Hiatt, T., Jordan, K., Merminga, L., Neil, G., Preble, J., Rutt, H., Shinn, M., Siggins, T., Toyokawa, H., Waldman, D.W., Walker, R., Wilson, N., Yunn, B., Zhang, S.: Nucl. Instrum. Methods Phys. Res. Sect. A **528** (2004) 19–22.

04Sal Saldin, E.L., Schneidmiller, E.A., Yurkov, M.V., in: Proc. FEL 2004, available at `http://accelconf.web.cern.ch/AccelConf/` (2004).

04Tof Toftman, B., Papatonakis, M.R., Auyeung, R.C.Y., Kim, W., O'Malley, S.M., Bubb, D.M., Horwitz, J.S., Schou, J., Johansen, P.M., Haglund, R.F.: Thin Solid Films **453–454** (2004) 177.

05Whi Whitney, R.L., Douglas, D., Neil, G.R., in: Laser Source and System Technology for Defense and Security. Proc. SPIE **5792** (2005) 119.

06Col Colson, W.B., Blau, J., Kampouridis, A., in: Proc. FEL 2006, Paper THPPH071, available at `http://accelconf.web.cern.ch/AccelConf/` (2006).

06Wu Wu, J., Emma, P., in: Proc. LINAC 2006, available at `http://accelconf.web.cern.ch/AccelConf/` (2006).

7.1 X-ray lasers

P.V. Nickles, K.A. Janulewicz, W. Sandner

7.1.1 Introduction

The breakthrough bringing experiment by Maiman demonstrating in 1960 the first laser at 694.3 nm [60Mai1, 60Mai2] was immediately followed by a dramatic progress on the way towards new laser schemes and their emission parameters.

Despite all this progress it is interesting to note that the spectral range of lasers has not much expanded since 1960, at least not by orders of magnitude (such as most other emission parameters) and particularly not towards the short-wavelength range. Today, almost half a century later, the shortest wavelength of commercial lasers is still at 157 nm, less than a factor of five below Maiman's first ruby laser. Laboratory prototypes reached further wavelength reduction by one or two orders of magnitude, however, the problems are still large enough to make novel concepts like huge, accelerator-based free-electron lasers as a competitive and commonly used alternative. On the other hand, the last few years have seen considerable progress towards new concepts for laboratory-sized (so called "table-top") EUV- or X-ray lasers with the real prospect of reaching acceptable average powers for applications. Applications are pressing in many areas, since X-rays offer radiation with a wavelength well adapted to the micro- and nano-technologies of the present century. Some of these new laser concepts will be covered in the present chapter.

One of the most fascinating research areas in this field are sources of a coherent short-wavelength radiation with the wavelength between 2 and 60 nm. As this spectral range touches soft X-rays these sources have been termed as soft X-Ray Lasers (XRLs) even if the research was dominantly performed in the EXtreme UltraViolet (XUV or EUV). The quoted spectral range of the emitted wavelengths indicates that the population inversion has to be created between the energy levels lying deeply inside the atomic core. This means the atoms before excitation have to be stripped of much of the electrons (i.e. highly ionized) and as a consequence a plasma has become a naturally preferred active medium.

The first X-ray laser scheme dates back to 1963, when the pump method relying on collisional recombination in a plasma was proposed [63Gud]. This first excitation method was followed by proposals of inner-shell photoionization in 1967 [67Dug] and electron collisional excitation several years later [72Mol, 72Zhe, 75Elt]. Simple estimates of the energetic balance in the medium give a scaling rule for the applied pump power density with the emitted wavelength as $P \sim \lambda^{-4}$ [90Elt, 99Roc]. The latter sets an enormous energetic requirement on the pump lasers and therefore the first soft X-ray lasers within the collisional and recombination schemes could not be demonstrated until 1985 [85Mat, 85Suc].

The large size, complexity and costs of the pump lasers for those X-ray lasers made a wide dissemination of those devices hardly possible. The following decade resulted in numerous successful soft X-ray laser experiments and proof-of-principle demonstrations based mostly on the dramatic progress in the technology of the laser drivers. Since then the research was focused on more efficient pump techniques and new excitation schemes utilizing these new abilities, with the ultimate goal of drastic reduction in the necessary pump energy. Advent of the short-pulse high-intensity lasers based on the Chirped Pulse Amplification (CPA) resulted in further progress on the way towards

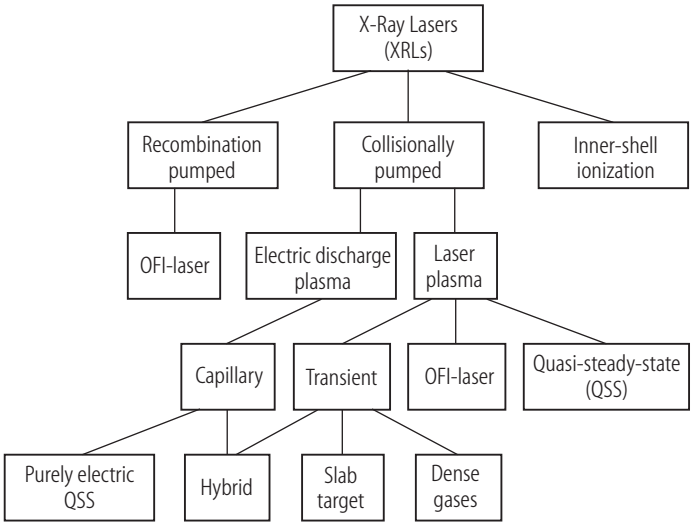

Fig. 7.1.1. Pump-mechanism-based classification of X-ray lasers [04Jan1].

very compact systems, so-called table-top X-ray lasers. The transient inversion scheme applied in the slab target geometry resulted in the fastest progress along this way. The first saturated soft X-ray laser in Ni-like palladium working at 14.7 nm with the pump energy of $\sim$ 7 J in double-pulse structure was demonstrated in the year 2000 [00Dun]. Two years later a saturated lasing with the output at 13.9 nm (Ni-like silver) has been achieved with the pump energy lower than 3 J in a single picosecond laser pulse [03Jan]. Moreover, the results on repetitive GRazing Incidence Pumping (GRIP) scheme, reported in 2004, demonstrated further dramatic reduction in the pump energy down to a few hundreds of millijoules [04Dun1, 04Roc]. These results promise a reasonable average output power from real table-top class soft X-ray lasers, which can become reality in the nearest future. Additionally, soft X-ray lasers with the active medium created by Optical-Field-Ionization (OFI), so called OFI-lasers, have been very actively pursued since the year 2000, whereby an important progress in the development of these lasers has been achieved [01Seb, 02Seb1, 03But].

Very promising and attractive sources of the coherent short-wavelength radiation, using capillary discharge plasma as an active medium, were developed parallel to the laser plasma sources. Such an X-ray laser, demonstrated for the first time in 1994 [94Roc], has the advantage of simplicity, delivering the radiation with only a small number of devices between the wall socket and the laser output. Hence, these devices offer relatively high efficiency, they work with an increased repetition rate, exhibit easily controllable high coherence levels and have the highest energy output among the compact X-ray lasers [98Ben, 01Liu]. On the other hand, there is at the moment only one working wavelength (46.9 nm), scaling towards shorter wavelengths appears to be difficult, the radiation pulses are still relatively long ($\sim$ 1 ns), and the capillary lifetime is limited.

The diagram seen in Fig. 7.1.1 presents an XRL classification based on the pump mechanisms. A survey of the X-ray laser physics accompanied by practical realizations of the most common pumping schemes and some prospective applications are presented below.

7.1.2 Principles of X-ray lasers

7.1.2.1 Active medium

7.1.2.1.1 Pump energy absorption

A highly ionized plasma is a common X-ray laser active medium for the reasons sketched above. This plasma consists of highly charged ions and free electrons with a reasonable density between 10^{19} cm^{-3} and 10^{21} cm^{-3}, conserving global neutrality. The electron temperature varies from a few electron volts (eV) to above one keV, depending on the pumping scheme applied. Transitions between the energy levels of the ions are responsible for the observed short-wavelength emission. Plasma is usually created either by material ablation from solids or by optical breakdown in dense gases. Typically, the pump laser intensities of an X-ray laser driver are in the range between 10^{11} and 10^{15} W/cm^2, but sometimes well above 10^{17} W/cm^2. Any plasma creation process needs energy which is delivered either by a laser beam or an electric discharge. The delivered energy is converted and redistributed with some losses into the thermal energy appearing as a temperature. Losses include ionization energy and kinetic energy connected with expansion of the ablated plasma. The material vaporized in the ablation process is dominantly heated by the energy absorbed from the laser by the *Inverse Bremsstrahlung* (IB) mechanism and ionized by collisional impact or directly through tunneling or multi-photon ionization. The density of the created plasma plume, initially high, will decrease due to the expansion while the temperature gradually increases, it achieves a maximum and then decreases due to cooling by adiabatic expansion and thermal conduction.

Typical electron density and temperature profiles are given in Fig. 7.1.2a. Once the plasma is created the pump laser pulse with the wavelength λ_p and the angular frequency ω_p penetrates it but only through the region of underdense plasma ending at the *critical electron density* n_c determined as (with m_e denoting electron mass)

$$n_c = (\varepsilon_0 m_e / e^2)\, \omega_p^2 \tag{7.1.1}$$

or in a more practical form

$$n_c\ [\mathrm{cm}^{-3}] = 1.1 \times 10^{21} / \lambda_p^2\ [\mu\mathrm{m}]\ . \tag{7.1.2}$$

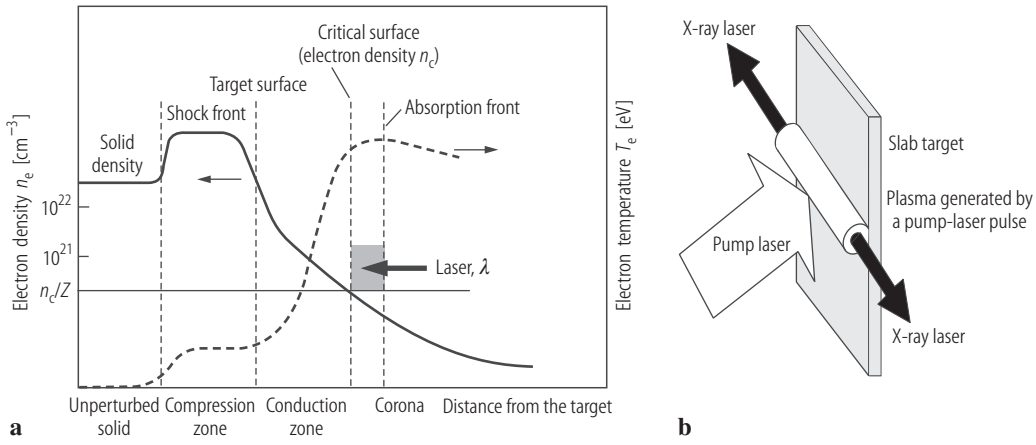

Fig. 7.1.2. (**a**) Typical electron density and temperature distributions in a laser-produced plasma in the direction normal to the target surface (the region suitable for X-lasing has been marked). (**b**) XRL arrangement: Typical elongated plasma produced at the target surface by a cylindrically focused laser pulse emitting X-ray laser pulses in both directions.

The laser energy is dominantly absorbed near the critical surface due to the high density existing there and, hence, the electrons are mostly heated in this area referred to as a *coronal zone*. Whereas the electron density decreases in the coronal zone with the distance from the target, the electron temperature achieves its maximum there. A shock wave is created in the interaction process, propagating inwards the target. The region where the X-ray amplification preferentially takes place is the coronal plasma characterized by both a sufficient electron density and temperature.

In contrast, the plasma of the electric discharge is created usually in a limited cylindrical space (capillary) and has a different history as compared to that created in the slab target geometry, as it reaches the required temperature and the density by compression on the capillary axis, followed by a stagnation process. Ohmic heating of the capillary walls leads to material ablation, and on the way to the capillary axis the plasma compression is supported by the pinching effect caused by very fast changes of the discharge current. Slower discharges used in some experiments show rather a wall-sustained character.

7.1.2.1.2 Population inversion and gain

The plasma as a gain medium containing ions of different ionization stages is very unstable in time. A given composition of ion species has a typical lifetime of several nanoseconds. One of the species which is expected to be a lasing one has to appear in the plasma in excess, as an abundance. In order to create a population inversion in the abundance of specific ions (the fundamental pre-requisite of gain) the ionization balance has to be reasonably stable. Therefore, ions with closed electronic shells or sub-shells are best suited as an X-ray laser medium when collisional excitation is applied. The recombination laser can use also one dominant ionization stage to produce the laser effect and this has to show a reasonably efficient collisional-radiative cascade after the recombination process, with a long-lived level at the end of this cascade. This level becomes the upper laser level.

The most important ion isoelectronic sequences fulfilling these requirements and characterized by the number of remaining electrons, are shown in Table 7.1.1.

Table 7.1.1. XRL-relevant and most frequently used isoelectronic sequences of ions.

Ion type	Closed shell n = main quantum number	Number of bound electrons	Fundamental electronic structure
Helium-like	$n = 1$	2	$1s^2$
Neon-like	$n = 2$	10	$1s^2 2s^2 2p^6$
Ni-like	$n = 3$	28	$1s^2 2s^2 2p^6 3s^2 3p^6 3d^{10}$

Population inversion is usually realized in a three- or four-level scheme. Each of these basic schemes is embedded in a reservoir of energy levels and exchanges energy with it in the relaxation process. Examples of the energy level diagrams of Ne-like and Ni-like ions used within the collisional pump schemes are shown in Fig. 7.1.6 and Fig. 7.1.8. The upper laser level is pumped by electrons from the ground-state level. The population inversion can be produced between the two excited levels lying above the ground state. Direct transition from the upper laser level into the ground level is forbidden (metastable or long-lived level), while the lower lasing level empties rapidly by radiative or collisional processes.

In the case of the recombination mechanism three-body recombination populates high-energy levels which subsequently relax to low-lying levels by the collisional-radiative cascade. This process has to be sufficiently fast (effective) in order to avoid population of the lower laser level by other recombination processes (dominantly radiative). This is especially important for the laser transitions ending at the ground state, which are available in the recombination lasers under specific conditions.

The gain, here in a form of a small-signal gain coefficient $g(\nu)$ depending on the frequency, describes the beam amplification in a system without considering for the origin of this amplification. Similarly to the optical laser, a product of the stimulated emission cross section σ and the density of the population inversion ΔN for the lasing transition determines the gain factor [72Zhe, 90Elt].

With

$$\Delta N = (N_\mathrm{u} - N_\mathrm{l}\,\frac{g_\mathrm{u}}{g_\mathrm{l}})\;, \tag{7.1.3}$$

where N_u, N_l denote densities of the upper and lower laser level populations and g_u, g_l account for the corresponding level degeneracy factors, we can obtain

$$g(\nu) = \sigma \times \Delta N \cong \left(A_\mathrm{ul}\lambda^2/8\pi\,\Delta\nu\right)(N_\mathrm{u} - N_\mathrm{l}\,\frac{g_\mathrm{u}}{g_\mathrm{l}})\;[\mathrm{cm}^{-1}]\;, \tag{7.1.4}$$

where A_ul is the Einstein coefficient for the spontaneous emission, it scales along the isoelectronic sequence as $A_\mathrm{ul} \sim \lambda^{-2}$. For a transition with the natural linewidth $\Delta\nu \sim A_\mathrm{ul}^{-1}$ it follows that

$$g(\nu) \sim \Delta N\,\lambda^2 \cong N_\mathrm{u}\lambda^2\;. \tag{7.1.5}$$

In general, the gain increases with the plasma electron density n_e and this is controlled by the pump process. An upper limit is set by electron collisions that can thermalize the populations of the laser levels destroying the population inversion ΔN.

7.1.2.1.3 Pump power requirements for soft X-ray lasers in plasmas

The minimum pump power density required to maintain a certain N_u scales as

$$P = N_\mathrm{u}A_\mathrm{ul}\,\frac{hc}{\lambda} \sim N_\mathrm{u}\lambda^{-3}\;. \tag{7.1.6}$$

Here A_ul is a total upper-level decay rate. The actual power density required to obtain a certain gain coefficient depends on the line profile. For natural broadening it scales according to (7.1.6) as

$$P \propto g \times \lambda^{-5}\;. \tag{7.1.7}$$

The required and disposable pump power densities constitute one of the fundamental limits for the operation of an X-ray laser. Given a finite energy and power of the driving source they limit the volume V of the gain medium. Assuming that the upper level decays only radiatively one can estimate the requirements of the pump power density for hydrogenic lasing ion [90Elt]

$$P = 16\pi\,l \times (gl)hc^2\,\frac{\Delta\lambda_\mathrm{ul}/\lambda_\mathrm{ul}}{\lambda_\mathrm{ul}^3\lambda_\mathrm{u0}} \tag{7.1.8}$$

with $\lambda_\mathrm{ul} = \lambda_\mathrm{x}$ the lasing wavelength, λ_u0 the wavelength of the transition from the upper level into the ground state, gl the product of the gain and active-medium length.

Within a rough approximation that $\lambda_\mathrm{ul} \approx 6\lambda_\mathrm{u0}$, $gl = 10$ (where l is the length of gain medium) and $\Delta\lambda_\mathrm{ul}/\lambda_\mathrm{ul} = 3 \times 10^{-4}$, (7.1.8) gives numerically

$$P = \text{energy}/(\text{pulse duration} \times \text{irradiated area}) \approx 4 \times 10^{19}/\lambda_\mathrm{ul}^4\;[\mathrm{W\;cm}^{-2}]$$

or more general

$$P \sim \left(\lambda_\mathrm{ul}\;[\text{Å}]\right)^{-4}\;. \tag{7.1.9}$$

Equation (7.1.9) shows a dramatic increase in the required pump power density (proportional to the pump intensity at a constant irradiation area) with decreasing the wavelength of the laser transition. Examples of consequences arising out of this relation are given in Table 7.1.2.

It is clearly seen from Table 7.1.2 that shorter pump pulses drastically reduce the pump energy requirements. An additional increase in the required pump power density for XRLs is frequently caused by refraction in the plasma which significantly reduces the gain coefficient available in some pump arrangements.

Table 7.1.2. Approximate dependence of the pump parameters on the emitted XRL wavelength with the assumption that 1 % of the pump energy will be transferred from the pump pulse to the plasma.

λ_{ul} [Å]	10	100	1000
Plasma area of (0.1×10) mm^2 and pump pulse duration 1 ps			
Pump intensity [W cm^{-2}]	10^{17}	10^{13}	10^{9}
Pump energy [J]	10^{3}	10^{-1}	10^{-5}
Plasma area of (0.1×10) mm^2 and pump pulse duration 1 ns			
Pump energy [J]	10^{6}	10^{2}	10^{-2}

7.1.2.1.4 Kinetics of the active medium – working regimes

The kinetics describes temporal changes in the populations of the ion levels in the plasma creating the active medium. In general, different processes such as ionization, recombination, collisional excitation and de-excitation, as well as radiative decay are included in the rate equations describing the population density N_{nZ} of such an energy level

$$\frac{\mathrm{d}N_{nZ}}{\mathrm{d}t} = \sum_i N_{iZ}\Gamma_{in} - N_{nZ}\sum_i \Gamma_{ni} + R_{nZ^+} - R_{nZ^-} \ , \tag{7.1.10}$$

where n denotes an electronic state of ions with charge Z.

The temporal change of the population of the n-th level of the Z-times charged ion is given by 4 terms on the right side of (7.1.10). The first term describes the positive contribution of electrons from other levels of the same ion, and the second one the loss of electrons to those levels. The rates are Γ_{in} and Γ_{ni}, respectively. Here, Γ_{kl} describes the probability of the transition per second of an electron from the level of interest to another specific level. When multiplied by the initial population of electrons at the level of interest it gives the number of transitions per second. As various excitation and de-excitation paths can be included in the transitions the total rate Γ_{in} in (7.1.10) is the sum of specific rates of all processes included. The third and fourth terms account for the rates of the population changes of the given level caused by ionization and recombination.

For modeling of the collisionally excitated schemes one can simplify (7.1.10) by taking into account only collisional ionization and recombination and neglecting the radiative variant of these processes. A further frequently used simplification relies on choosing only the ion species of interest (for example Ne- or Ni-like) and separating the rate equations including creation of other ion species. Then one can write for the chosen ions the reduced rate equations as follows:

$$\frac{\mathrm{d}N_n}{\mathrm{d}t} = \sum_i N_i S_{in} - N_n \sum_i S_{ni} \ , \tag{7.1.11}$$

where N_n is the population of the n-th level of the given ion species, and $S_{in} = S_{in}(Z, n_\mathrm{e}, T_\mathrm{e})$ the total probability of the transition $i \to n$ caused by various processes that do not change the ion stage.

If the concentration of the ion species ε_Z is the ratio of the density of a given ion species to the total ion density, it can be described as

$$\varepsilon_Z = \frac{\sum_n N_{nZ}}{\sum_n \sum_Z N_{nZ}} \tag{7.1.12}$$

and consequently the dynamics of the ion creation (excitation and recombination of different ion species) can be written in the form

$$\frac{\mathrm{d}\varepsilon_Z}{\mathrm{d}t} = [\varepsilon_{Z-1} C^{\mathrm{I}}_{Z-1} + \varepsilon_{Z+1} C^{\mathrm{R}}_{Z+1} - \varepsilon_Z (C^{\mathrm{I}}_Z + C^{\mathrm{R}}_Z)]\, n_{\mathrm{e}} \,, \tag{7.1.13}$$

where C^{I}_Z is the ionization rate and C^{R}_Z the recombination rate.

Equations (7.1.12) and (7.1.13) describe fully the ionic system. They must be solved in combination with the hydrodynamic equations for a given n_{e} and T_{e} distribution, which is very difficult in a general case. It is therefore useful to distinguish between three different approximations applicable in three characteristic limiting cases corresponding to different working regimes [89Afa, 90Elt].

Which approximation is suitable for a given situation depends on the characteristic times of the processes involved:

τ_{hyd} : characteristic time of hydrodynamic changes in the plasma,
τ_{I} : characteristic time of ionization,
τ_{r} : characteristic time of the relaxation of excited electronic levels.

It is worth noting, that all three characteristic times can be considered partially independent. Since both the ionization and the excitation result by collisions with free electrons, the characteristic times change with the electron density and temperature. The characteristic time needed to get a plasma with the necessary n_{e} and T_{e}, is determined by the pump laser parameters. Hence, slowing down or speeding up plasma heating by choosing the amplitude and duration of the pump pulse, one can realize different combinations between τ_{hyd}, τ_{I} and τ_{r} and in this way different plasma conditions.

7.1.2.1.4.1 Steady-state approximation

The electron density n_{e} and the electron temperature T_{e} of the plasma, as well as the charge Z, are stationary, i.e. independent of time for all values of Z. Hence, it holds

$$\frac{\mathrm{d}\varepsilon_Z}{\mathrm{d}t} = 0 \quad \text{and} \quad \frac{\mathrm{d}N_n}{\mathrm{d}t} = 0 \,.$$

The steady-state approximation can be used for a system where the population is already stabilized, i.e. close to equilibrium so that the number of electrons coming to a given energetic level in the excitation process virtually equals to the number of electrons escaping from that level. The same holds for the changes in the ionization states. The number of the ions of interest that are ionized into a higher ionization state or recombine to a lower one is almost equalized by the number of ions that recombine to the appropriate ion state from a higher ionization stage or are advanced from a lower ionization stage to the discussed one. This condition can also be expressed in terms of characteristic times as the situation where the characteristic times of changes in ionization and excitation are much shorter than the characteristic times of changes in the plasma parameters:

$$(\tau_{\mathrm{I}}, \tau_{\mathrm{r}}) < \tau_{\mathrm{hyd}} \,.$$

It is characteristic for the steady–state regime, that no population inversion neither for recombination nor for collisional X-ray laser schemes is possible.

7.1.2.1.4.2 Quasi-steady-state approximation

The ion species concentration changes in time, but the population of all levels within the species does not change. This means that the population re-allocates immediately with changes of ion concentration ε_Z. As a consequence

$$\frac{\mathrm{d}\varepsilon_Z}{\mathrm{d}t} \neq 0 \quad \text{and} \quad \frac{\mathrm{d}N_n}{\mathrm{d}t} = 0 \,.$$

In other words the population is in the steady-state, while the relative ion concentration ε_Z is non-stationary or *transient*. It means that the populations N_n of the excited levels follow the temporal changes of the ion concentration ε_Z.

The quasi-steady-state case occurs if the relaxation times of the population are shorter than the time needed for full stabilization of the concentration of the ions species. Here, the level populations follow changes in the concentration of ion species ($\tau_\mathrm{I} > \tau_\mathrm{r}$). Importantly, the characteristic time of the population relaxation is still shorter than the time scale of changes in plasma parameters and the ionization cannot follow the plasma changes. As a result $\tau_\mathrm{I} > \tau_\mathrm{hyd} > \tau_\mathrm{r}$. In real XRL experiments, the quasi-steady-state regime has resulted in the maximum small-signal gain about 10 cm^{-1} [90Mac1, 92Mac, 93Max, 94Koc, 95Nil2, 95Nil3, 96Dai, 96Zha2, 98Pra].

7.1.2.1.4.3 Non-stationary or transient approximation

This is the most general case, in which changes in ε_Z introduce changes in populations N_n:

$$\frac{\mathrm{d}\varepsilon_Z}{\mathrm{d}t} \neq 0 \quad \text{and} \quad \frac{\mathrm{d}N_n}{\mathrm{d}t} \neq 0 \,.$$

The electron density n_e and temperature T_e are still assumed to be constant.

The non-stationary or transient approximation applies for the case, when neither the populations nor the ionization stages have enough time to stabilize on a time scale of the hydrodynamic evolution of the plasma. Therefore this problem requires not only solution of the above formulated equations, but also hydrodynamic equations to determine the temporal dependence of $n_\mathrm{e}(t)$ and $T_\mathrm{e}(t)$. Transient approximation means that at $t = 0$ the electron temperature abruptly increases from $T_\mathrm{e} = T_1$ to $T_\mathrm{e} = T_2$ (see Fig. 7.1.3). The characteristic time of this change should be very short (jumping character) and after this rise time one can use the values $T_\mathrm{e} = \text{const.}$ and $n_\mathrm{e} = \text{const.}$ as $\tau_\mathrm{hyd} \leq (\tau_\mathrm{I}$ and $\tau_\mathrm{r})$, i.e. the rise time of the excitation is comparable to the interatomic relaxation time. The XRLs realized in this regime are characterized by the highest gain. Simulations predict values of $g \sim 10^2 \ldots 10^3$ cm^{-1} and the gain reported in the experiments is equal to several tens of cm^{-1} [97Hea, 97Nic, 99Nil, 00Dun, 03Jan].

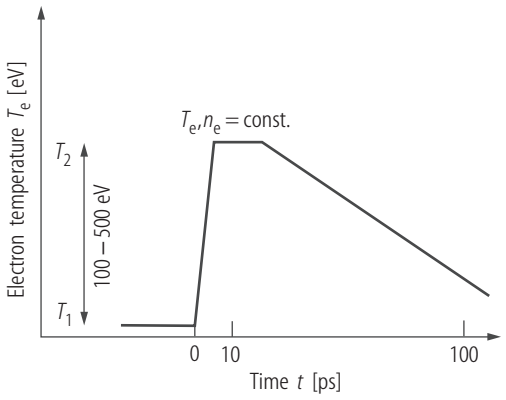

Fig. 7.1.3. The history of the electron temperature T_e for the transient excitation: The electron temperature abruptly increases at $t = 0$ from $T_\mathrm{e} = T_1$ to $T_\mathrm{e} = T_2$. After that one can use the approximation of $T_\mathrm{e} = \text{const.}$, $n_\mathrm{e} = \text{const.}$ and $\tau_\mathrm{hyd} \leq (\tau_\mathrm{I}$ and $\tau_\mathrm{r})$.

7.1.2.1.5 Medium size and output geometry – refraction

The very large pump power densities and the usual requirement of a small *optical thickness* in the transverse direction of the elongated plasma column [90Elt] result in the gain volume that is small

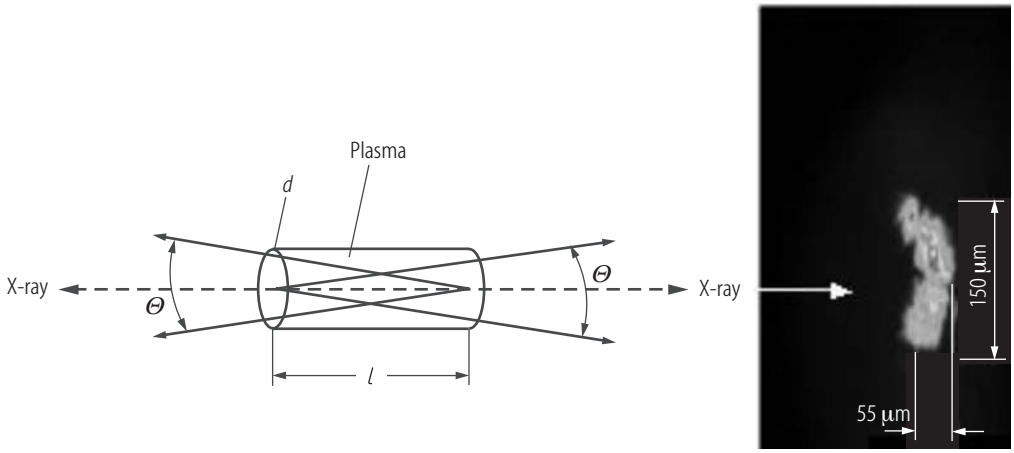

Fig. 7.1.4. Size of the XRL gain medium and aspect ratio d/l determining the divergence of the output beam of a transversely pumped XRL. Θ: divergence of the XRL beam, d: diameter of the amplification zone in the plasma, l: length. Additionally, an output beam image of a transverse collisional XRL (Ni-like Ag-XRL) registered in the near-field zone is shown on the right side.

in comparison to that of classic (UV, VIS, IR) lasers with longer (above 100 nm) wavelengths. Therefore the lasing medium has typically a width of $d = 10 \ldots 200$ µm and a length of $l = 0.1 \ldots 2$ cm (these parameters for the capillary discharges are usually one order of magnitude higher), corresponding to the maximum aspect ratio of $\approx 1:1000$.

The dimensions strongly depend on the pump power used for the excitation process and most frequently limit the effective length of the active medium. In the case of the capillary discharge XRL which includes guiding elements the aspect ratio may therefore reach higher values than those quoted above. Generally, it is aspired to increase the aspect ratio values by increasing the length of the gain media and hence to improve the transverse spatial coherence and to operate the XRL in saturation regime. In the realized XRL schemes amplification in the active medium was achieved by single- and very rarely by double-pass arrangements. Gain lifetimes ($t_{\mathrm{gain}} \sim 10$ ps) of the modern XRLs put some severe constraints on the length of the active medium. The aspect ratio will also in principle determine the maximum geometrical beam divergence Θ. For $l = 1$ cm and $d = 50$ µm the expected beam divergence is $\Theta = d/l \approx 5$ mrad (Fig. 7.1.4).

With a retro-mirror M (at a distance l_M from the active medium) realizing the double-pass geometry, the length l must be substituted by l_M. The divergence is then reduced for the second pass according to the increased length of the optical path. Typical divergences for a single-pass arrangement are in the range between 3 and 10 mrad.

7.1.2.1.5.1 Refraction

Once the amplifying plasma has been created, the amplification process demands propagation of the X-ray beam in the elongated amplifying zone. It means the plasma parameters should allow propagation over a sufficiently long distance to ensure high level of the output X-ray laser signal and its reasonable collimation. At the same time the plasma should be dense since the gain increases with the plasma density (equivalent to the electron density) n_{e}. An upper density limit is set by electron collisions that can destroy the population inversion. Inhomogeneities of the density should be minimized as any plasma density gradients (∇n_{e}) reflect in the gradients of the refraction index ∇n according to

$$\nabla n = -\frac{1}{n}\,\frac{\nabla n_{\mathrm{e}}}{2n_{\mathrm{c}}} \tag{7.1.14}$$

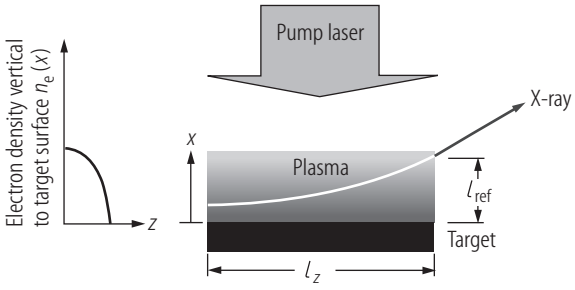

Fig. 7.1.5. Refraction of the X-ray beam in a plasma with the density gradient normal to the amplification direction.

with the refraction index in the plasma

$$n = \left(1 - \frac{n_e}{n_c}\right)^{-1/2} , \tag{7.1.15}$$

where n_e is the plasma electron density and n_c the critical plasma density. Typically, in the region of high electron density and high gain the electron density gradient is in the order of $\nabla(n_e/n_c) \sim 10^{-3} \ldots 10^{-4}$ μm^{-1}. Any gradient of the refraction index causes refraction (or ray deviation) which can bend the X-ray beam out of the gain medium. The refraction problem is especially crucial for X-ray lasers pumped laterally in the slab target geometry where the gradients appear inherently in the direction of the pump laser beam, i.e. perpendicular to the X-ray beam propagation in the plasma and normal to the target (see Fig. 7.1.5).

Since the high-density region in the plasma, characterized by high gain has only a narrow spatial extent (about several tens of microns) the X-ray beam suffering refraction is bent out of this region over a distance shorter then the maximum amplification length l. As a result the effective gain is also reduced. The typical distance l_{ref} (refraction length) the X-photon travels in the propagation direction z before it refracts out of the gain region is given for a parabolic density profile [88Lon] by

$$l_{ref} = l_x (n_c/n_{0e})^{1/2} , \tag{7.1.16}$$

where the maximum electron density $n_{0e} < n_c$, and l_x is the transversal extension of the high-gain region. The corresponding angle of refraction θ_{ref} can be described as $\theta_{ref} = (n_c/n_{0e})^{1/2}$. In the one-dimensional treatment, refraction reduces the gain roughly by $1/l_{ref}$. For large plasma length $l_z > l_{ref}$ the real amplification is then determined by an effective gain coefficient

$$g_{eff} = g - \frac{1}{l_{ref}} . \tag{7.1.17}$$

In a cylindrical plasma geometry which corresponds better to the situation in an axially (longitudinally) pumped laser plasma or discharge pumped system, the refraction index shows gradients symmetric to the plasma axis. Refraction introduces here the loss term $1/l_{ref}$ for each direction and the effective gain is given by [96Chi]

$$g_{eff} = g - \frac{2}{l_{ref}} . \tag{7.1.18}$$

Several techniques have been successfully introduced to reduce the unwanted effect of refraction. They include softening of sharp density gradients by use of foil targets [93Max], curved target structures [95Plo] and a prepulse in the laser-pumped systems [95Nil2]. A plasma waveguide being a medium characterized by a density minimum on the axis became a promising scheme for a future table-top XRL.

Additionally, the index gradient affects the direction and the intensity distribution of the output X-ray beam increasing its pointing and divergence. One of the plausible solutions could be the use

of low-density targets like aerogel foam. Aerogels are made by a solution-gel polymerization process. They can be fabricated from a variety of metal oxides, with densities in the range $0.03 \ldots 0.5$ g/cm^3 and pore sizes between 20 and 50 nm [91Hru, 92Liv]. Simulations have shown, that similarly to the solid slab target, the gain region for the foam target is narrow. However, a much flatter density gradient is present in the gain area. It was estimated using (7.1.16), that the refraction length should be about 300 μm, which is by a factor of 6 larger than in the usual slab targets.

7.1.2.2 Excitation mechanisms

7.1.2.2.1 Electron collisional excitation

The first demonstration of a collisional-excited XRL in a laser-produced plasma dates back to 1985 (Ne-like selenium [85Mat]). Collisional excitation, especially in its transient version, became today, owing to its robustness, the most frequently explored pumping mechanism among all operating X-ray lasers. The excitation process can be described as

$$Z_0^{i+} + \text{electron} \rightarrow Z_\mathrm{u}^{i+} \,. \tag{7.1.19}$$

Here Z^{i+} represents an i-times ionized atom of an element Z in which the excitation occurs from the ground state (0) to the upper state (u).

This excitation is accomplished by energetic (high-temperature) free electrons that collide with the ion Z_0^{i+} in the plasma, transfer part of its energy to this ion and cause the ion levels, including the upper lasing level, to be populated. The colliding electron should have a kinetic energy higher than the energetic gap between the ground state and the given level. Usually the lower laser level with a smaller energy gap $\Delta E_{0\mathrm{l}}$ is more rapidly populated than the upper level. Hence, the lower level (l) must be efficiently depopulated to achieve a reasonable population inversion between the upper (u) and lower (l) lasing levels. This can happen if the lower level (l) is depopulated by a fast radiative decay into the ground state and the upper level is sufficiently resistant against radiative and collisional decay into other levels, i.e. it possesses a metastable character.

The pumping rate by collisions is proportional to the second power of the electron density. Two groups of ions, namely those from the Ne-like (3p–3s transitions) and Ni-like (4d–4p transitions) isoelectronic sequences, constitute sets of well suited lasants because they fulfill both the above discussed conditions and the expected stability of the ionization balance. Taking into account the fact that the levels included in the laser action are split in a multilevel fine structure several lasing lines will be possible for each ion type (see Fig. 7.1.6).

7.1.2.2.1.1 Ne-like scheme

In the neon-like scheme lasing is possible on the $1s^2 2s^2 2p^5 3p \rightarrow 1s^2 2s^2 2p^5 3s$ transition. As the core electron configuration ($1s^2 2s^2 2p^5$) remains unchanged it is usually omitted in the level description, and only the position of the outer (valence) electron is given. According to the level fine structure the largest population can be generated for the $n = 3$ transitions, i.e. $3p(1/2, 1/2)_{J=0} \rightarrow 3s(1/2, 1/2)_{J=1}$, $3p(1/2, 3/2)_{J=2} \rightarrow 3s(1/2, 1/2)_{J=1}$ and $3p(3/2, 3/2)_{J=2} \rightarrow 3s(3/2, 1/2)_{J=1}$. The common jj-coupling referring to the angular momenta of the core and of the excited electrons, with J being the total angular momentum of the level (j, j), is used in this notation (Fig. 7.1.6).

In general, the population inversion between the levels involved in the mentioned transitions is created by a combination of electron collisional excitation from the Ne-like ground state $2p^6$ to the upper laser level $2p^5 3p$ and dielectronic recombination from the higher-lying energetic levels of F-like ions followed by radiative-collisional cascades to the same level. The inversion population

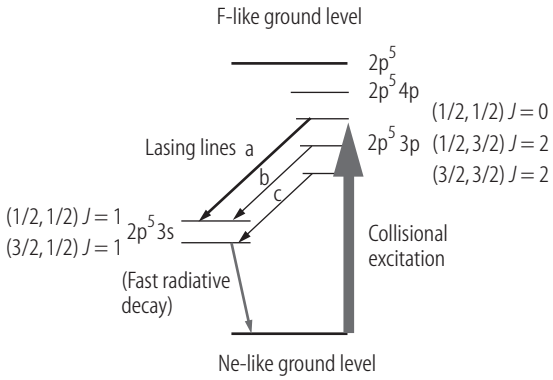

Fig. 7.1.6. Schematic of the energy levels of a neon-like Ti-XRL plasma.

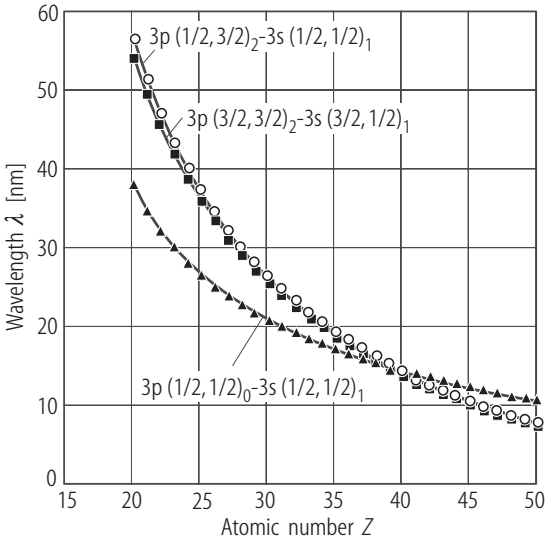

Fig. 7.1.7. Wavelength scaling of the Ne-like isoelectronic sequence for the 3p ($J = 0$)–3s ($J = 1$) and 3p ($J = 2$)–3s ($J = 1$) transitions [01Kub].

for the $J = 0$–1 transition is dominantly produced by the collisional excitation, while both effects are responsible for the inversion on the $J = 2$–1 transition [96Hea]. Despite the large gain and gain–length product values obtained in Ne-like X-ray lasers, their scaling to shorter wavelengths is not favorable, since the lasing levels are closely spaced and ions with higher Z are necessary to improve these situation. This requires, however, enormous increase in the pump power. The latter can be estimated from the empirical formula (for a 500 ps pulse at 530 nm) reported in [92Mac]

$$I_\mathrm{p}\ [\mathrm{W/cm^2}] \sim 1.2 \times 10^{16} (4.5/\lambda\ [\mathrm{nm}])^{3.5}\ . \tag{7.1.20}$$

An approximation for the wavelength of neon-like XRL was given in [90Elt]

$$\lambda_\mathrm{las}\ [\mathrm{Å}] = 4.6 \times 10^3/(Z - 9)\ , \tag{7.1.21}$$

where Z is the nuclear charge.

Figure 7.1.7 shows the scaling curves of the Ne-like isoelectronic sequence for the 3p ($J = 0$)–3s ($J = 1$) and 3p ($J = 2$)–3s ($J = 1$) transitions [01Kub].

7.1.2.2.1.2 Ni-like schemes

Ni-like X-ray lasers were first demonstrated in 1987 in a laser-produced plasma of Eu at 7.1 nm with an observed gain–length product equal to 4 [87Mac]. The diagram of Ni-like laser transitions (Fig. 7.1.8) includes the group of the lasing transitions between the $3d^9 4d$–$3d^9 4p$ level manifolds within the shell with $n = 4$.

The 4d-levels are metastable regarding radiative decay to the $3d^{10}$ Ni-like ground state, while the 4p-levels are rapidly emptied to the ground state. The upper laser state is dominantly pumped (over 90 %) by the collisional excitation from the $3d^{10}$ ground level. Other transitions predicted to have a significant gain include a second $J = 0$–1 transition, $J = 2$–1 and a $J = 1$–1 transition – all within the general 4d–4p manifold of the transitions [84Hag]. The energy gap between the Ni-like ground state and the upper lasing level is twice as large as the electron temperature which maximizes Ni-like-abundance. In experiments the Ni-like XRLs show significant gain only on the $J = 0$–1

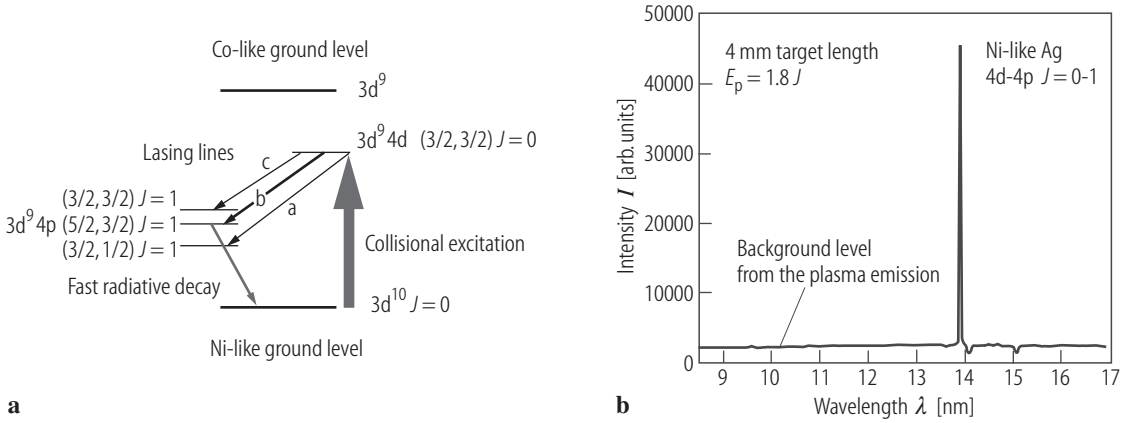

Fig. 7.1.8. (**a**) Energy level diagram of a Ni-like XRL plasma. (**b**) Typical emission spectra of an X-ray laser (here the 4d–4p 13.9 nm emission line of a Ni-like Ag-XRL). The plasma emission is fully dominated by the lasing line [03Jan].

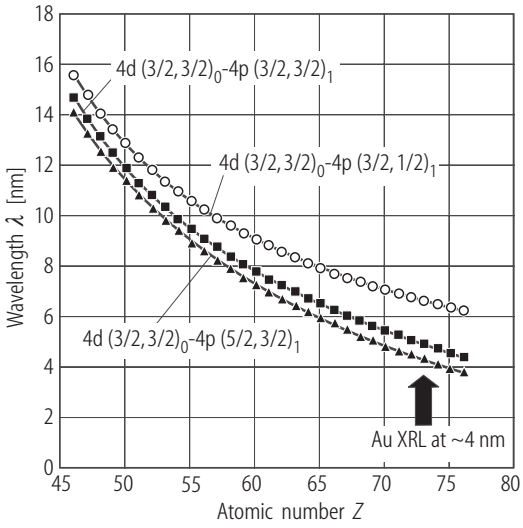

Fig. 7.1.9. Wavelength scaling of collisional XRL Ni-like isoelectronic sequence of the transitions $4d\,(J = 0)$–$4p\,(J = 1)$. The arrow marks the shortest collisional XRL realized [92Sco, 01Kub].

lines while the $J = 2$–1 and $J = 1$–1 transitions have little or no gain. The strongest signals can be expected on the transitions: $4d(3/2, 3/2)_0 \rightarrow 4p(3/2, 1/2)_1$, $4d(3/2, 3/2)_0 \rightarrow 4p(5/2, 1/2)_1$ and $4d(3/2, 3/2)_0 \rightarrow 4p(3/2, 3/2)_1$. The Ni-like ions show also favorable scaling to shorter wavelengths in comparison to Ne-like ones (Fig. 7.1.9).

The empirical scaling law for Ni-like isoelectronic sequence calculating the required pump intensity (again for a 500 ps, 530 nm, single pulse) is given in [92Mac]

$$I_\mathrm{p}\ [\mathrm{W/cm^2}] \sim 2.5 \times 10^{14} (4.5/\lambda\ [\mathrm{nm}])^{3.5}\ . \tag{7.1.22}$$

The required pump intensities for Ne-like and Ni-like ions differ only by the multiplication factor that is, however, remarkably smaller for the Ni-like ions. Therefore, the Ni-like X-ray lasers can, in principle, work at shorter wavelengths than the Ne-like ones for the comparable amount of the pump energy.

In summary the most important requirements for efficient collisional pumping include:

– an abundance of the lasing ions (Ne-, Ni-, Pd-like or other ions of moderate or high Z),
– sufficiently high electron density, because the collisional pumping rate depends on the electron density,

– electron temperature sufficient to pump the system efficiently by collisions (it means that the most probable energy of the electron reservoir should be comparable with or in fact, slightly higher than the excitation energy from the ground state to the upper laser level),
– the depopulation of the lower laser level should be very fast, i.e. the opacity of the plasma has to be small for this emptying radiative transition to the ground level (4p–3d for Ni-like ions and 3s–2p for Ne-like),
– the plasma density must not be too high, otherwise the de-excitation of the upper laser level would be dominated by collisions with free electrons,
– the electron density gradient within the active region should be as smooth as possible in order to prevent the X-ray beam from refraction out of the gain region.

7.1.2.2.2 Recombination X-ray lasers

The recombination laser is conceptually very simple. It consists of four basic stages. The population inversion is promoted by cold free electrons which recombine by the three-body recombination and subsequently populate the upper laser level by an effective and fast collisional-radiative cascade, while the lower level remains less, if at all, populated. Low plasma temperature being favorable for the three-body recombination should also minimize the limited population of the low-energy levels. This scheme is very frequently considered with the lasing transition to the ground state. It gives shorter wavelength but also increases the constraints on the plasma temperature. The excitaton process can be described by the relation:

$$Z_0^{(i+1)+} + 2 \text{ electrons} \rightarrow Z_n^{i+} + \text{electron} \rightarrow Z_\mathrm{u}^{i+} + \text{electron} \,. \tag{7.1.23}$$

The principle level diagram for a electron-collisional recombination scheme, followed by a cascade, in a collisionally ionized plasma is shown in Fig. 7.1.10.

Recombination-pumped laser systems require electron–ion recombination to occur on a time scale short if compared with the natural lifetime of the laser transition. This is equivalent to the requirement of the plasma with a high electron density n_e and a low electron temperature T_e. An efficient recombination process requires low electron temperature (usually $T_\mathrm{e} < 50$ eV) and a high density (at least $n_\mathrm{e} \geq 10^{18}$ cm^{-3}). In the specific case of the H-like scheme (other approaches like He- or Li-like schemes are directly analogs of that), a fully stripped ion recombines in a rapidly cooled plasma, dominantly by a *three-body process* with a rate proportional to $T_\mathrm{e}^{-9/2}$ [90Elt]. It preferentially fills up high-lying states which subsequently relax in a combination of very fast collisional and radiative transitions between adjacent levels. The generation of an inversion between the rapidly populated $n_\mathrm{u} = 3$ and the radiatively unstable $n_\mathrm{l} = 2$ levels takes place if cooling and the following relaxation are sufficiently fast to avoid significant population of the lower laser level by other processes, for example radiative recombination. Gain has been observed in many systems,

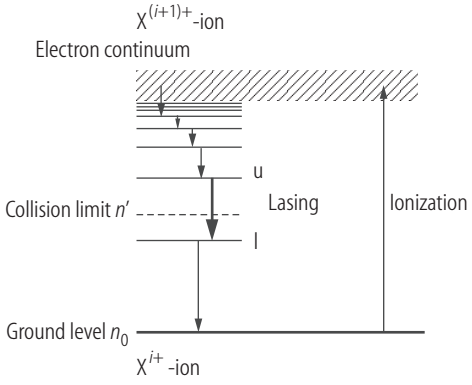

Fig. 7.1.10. Simplified energy level scheme explaining pumping by the electron collisional recombination and the following radiative-collisional cascade. For higher levels than the collision limit level n', collisional excitation dominates over radiative decay. For quantum states lower than n' radiative decay dominates.

such as expansion-cooled H-like [87Che, 90Car, 92Dai], Li-like and Na-like [1887Jae, 92Ste, 94Ste] and radiatively cooled H-like systems [85Suc, 86Suc].

Recombination schemes have the important advantage of being more favorable than collisional systems for both shorter wavelengths and a high quantum efficiency [85Jam, 86Suc]. This is a result of operation on transitions involving a change in the principal quantum number (e.g. $n = 3$–2 or $n = 2$–1). Recombination X-ray lasers require a short pump pulse since only in this case rapid heating of nearly solid density plasma can be realized which, in turn, makes *adiabatic cooling* of the plasma during the following expansion phase more efficient. The requirement that the expansion has to be very fast but simultaneously sufficiently long for efficient collisional ionization defines, in principle, an optimum pulse duration for high-gain operation of recombination lasers. Rapid cooling leads to high gain in recombination lasers. If the scheme does not include adiabatic cooling the driving laser pulse has to be shortened to minimize collisional absorption during the ionization (see OFI XRLs, Sect. 7.1.4.3).

Lasing to the ground state (usually denoted as the $n = 2$–1 transition) allows for a good scaling to shorter wavelengths. Since the energy of a level scales as $1/n^2$, the wavelength of a transition decreases with n. For instance, the wavelength of a $n = 2$–1 transition in a given ion is 5 times shorter than that for the $n = 3$–2 one.

On the contrary, the systems working on the $n = 3$–2 transitions have the advantage of the applicability of longer pumping laser pulses (nanosecond range). This is caused by the fact that radiative transition between these levels is about one order of magnitude slower than the transition to the ground level, and because the population inversion between them can exist even if the population of the ground level is 2–3 orders of magnitude higher than the population of these levels. This makes it possible to use low-power driving lasers (e.g. compact and quite inexpensive commercially available YAG lasers).

7.1.2.2.3 Inner-shell photoionization (ISPI)

The Inner-Shell PhotoIonization Scheme (ISPIS) was one of the first XRL schemes proposed [67Dug]. In this system the inner-shell ionization is realized by incoherent X-rays emitted from a neighbor auxiliary plasma source that is produced by heating a high-Z target (e.g. Au) with a high-intensity ultrashort laser pulse. Whereas photons with the energy below the inner-shell binding energy have to be removed from the pumping beam by appropriate filtering to avoid pumping of the lower laser level, the remaining hard X-rays (with an energy above the inner-shell ionization threshold) preferentially remove inner-shell electrons from the ions of the lasant. The generation of population inversion by this mechanism is possible because at the photon energies just above the threshold for inner-shell photoionization the cross section for this process can be an order of magnitude larger than that for the outer-shell electrons. Unfortunately, in most atoms inner-shell vacancies decay primarily through Auger decay rather than radiatively. Typical Auger decay rates are of the order of 10 fs^{-1} or higher. This puts a severe constraint on the time gap for building up a population of the upper laser level and also on the duration of the pumping photon burst.

The advantage of the ISPIS approach is a potentially very short emitted wavelength. Using low-Z elements from Ne to Cl [92Kap, 93Str, 94Str] the wavelength can be shortened down to 0.5 nm and the system is able to operate at a reasonable (~ 10 cm^{-1}) gain supported by a very low temperature (less than 1 eV). The latter results in a very weak Doppler broadening estimated to be about $\Delta\lambda/\lambda \leq 10^{-6}$.

The optimum filter material cleaning the high-energetic pump radiation and its thickness depend on the bremsstrahlung spectrum and the lasing material. In the spectral range between 800 eV and 2.8 keV the filters made of Li, Be or B with a thickness of $2 \ldots 5$ μm would be effective in blocking the low-energy X-rays with a minimal reduction in the higher-energy X-rays that can ionize the inner-shell electrons.

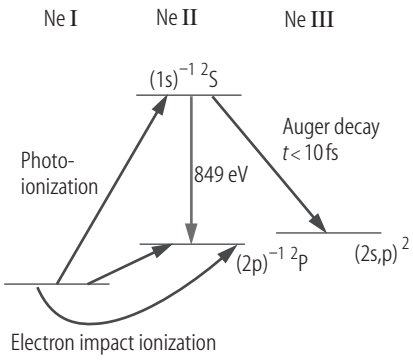

Fig. 7.1.11. Energy-level scheme of an Inner-Shell Photo Ionization (ISPI) XRL based on Ne II. Fast Auger decay reduces the population inversion [88Kap].

In contrast to the OFI scheme, which also requires a high-intensity short-pulse driving laser and is now accessible in several laboratories, the pump energy requirements of the inner-shell X-ray lasers are significantly higher, as the ionization mechanism is more indirect than that of the OFI scheme or conventional collisional lasers. The required pump energy of the K_α line for Ne II at 1.5 nm in a traveling-wave arrangement necessary to produce an output of 3 J was estimated to be equal to 10 J during 50 fs [92Kap]. Even if the real ISPI-pumped X-ray laser has not been demonstrated up to now, there are several lasers in the visible range of the spectrum or in Vacuum UltraViolet (VUV), like the 109 nm laser in Xe^{2+} or the 96.9 nm laser in Cs, pumped by auxiliary X-rays [87Sil, 88Kap, 93Tot].

Figure 7.1.11 shows the energy-level scheme of an ISPI XRL based on Ne II as the active medium.

7.1.2.2.4 Photoresonant pumping

The simplest description of the pump process in photoresonantly pumped XRLs can be given by

$$Z_0^{i+} + h\nu \rightarrow Z_u^{i+} \,. \tag{7.1.24}$$

The level diagram is quite similar to that of the electron collisional excitation but here the excitation by a photon replaces the electron impact. As a result, this scheme requires one source (plasma) of an intense line with a wavelength well matched to the energy gap of the transition to be excited in a second plasma plume including lasant. In principle this could be an advantage since the pumping rate and the specific upper laser level could be controlled by the photon flux at a chosen wavelength. Conceptually, the separated photon source resembles the pump laser or flash-lamp, common among the conventional optical lasers. However, the requirements of an exact line matching as well as a high flux of pumping photons are difficult to be fulfilled in practice. Although numerous line coincidences have been found (for example, between the potential lasing lines of various ions and strong pump lines from H-like, He-like and Li-like ions [90Elt]) it is difficult up to now to realize efficient photon coupling between both plasmas which could lead to a high amplification on the lasing transition. In an experiment, gain of $g \sim 1$ cm^{-1} and gain–length product of $gl \sim 2$ were demonstrated on the 3p–4f and 3d–4f transitions of Li-like Mg ions, pumped by a Si plasma created by a laser pulse of 400 ps duration and 120 J energy [92Fil].

In 1996 another type of photopumping called *self-pumping of a strong emission line* in an optically thick plasma was proposed [96Nil1]. It predicts strong lasing at the corresponding line for neon-like ions (3d $^1P_1 \rightarrow$ 3p $^1P_1$). The same mechanism allows also for lasing in Ni-like ions with gain $g \leq 13$ cm^{-1} (in Ni-like Mo, Nb, and Zr ions) [90Boe, 90Mac1, 92Fie] (see Fig. 7.1.12). However, this new line was never observed to be stronger than the principal, collisionally excited 4d $^1S_0 \rightarrow$ 4p $^1P_1$ line. The self-photopumping mechanism is based on the assumption that a strong radiation from one ion photopumps another one of the same ion species, and therefore the resonance

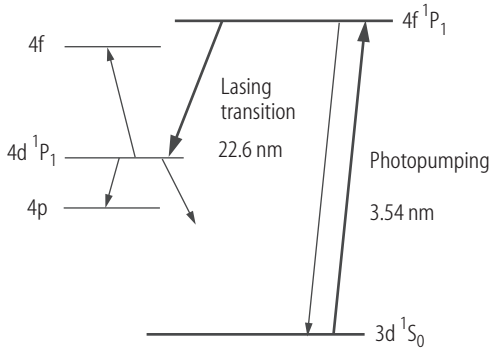

Fig. 7.1.12. Energy-level diagram for a Ni-like 4f $^1P_1$ – 4d $^1P_1$ Mo-XRL at 22.6 nm. Lasing is caused by the strong photopumping from the 3d $^1S_0$ ground level to the 4f $^1P_1$ upper laser level [99Nil].

Table 7.1.3. Realized self-photo-pumped Ni-like XRLs at 4f $^1P_1 \rightarrow$ 4d $^1P_1$ [96Nil1, 96Nil2].

Target, Z	Transition	Wavelength λ [nm]	Ref.
Zr, 40	4f $^1P_1 \rightarrow$ 4d $^1P_1$	27.10	[96Nil1]
Nb, 41	4f $^1P_1 \rightarrow$ 4d $^1P_1$	26.64	[96Nil1]
Mo, 42	4f $^1P_1 \rightarrow$ 4d $^1P_1$	22.60	[96Nil1]
Ag, 47	4f $^1P_1 \rightarrow$ 4d $^1P_1$	16.05	[99Jam]

is perfect. The upper laser level 4f $^1P_1$ is populated by a combination of self-photopumping and collisional excitation from the Ni-like ground state 3d $^1S_0$. As the plasma is optically thick for the transition 4f $^1P_1 \rightarrow$ 3d$^1S_0$, the radiative trapping allows to build up a relatively strong radiation field. In principle, the self-photopumping rate can become of one order of magnitude larger than the standard collisional pumping at this transition. To create an inversion of population, the lower state has to be efficiently depopulated, which is primarily satisfied owing to the collisional transfer to the adjacent 4p- and 4f-levels [96Nil1].

The realized self-photo-pumped Ni-like XRLs on the 4f $^1P_1 \rightarrow$ 4d $^1P_1$ transition are listed in Table 7.1.3.

7.1.2.2.5 Other excitation schemes

The excitation schemes discussed above are by far the most intensely investigated, and include all soft X-ray lasers demonstrated to date. However, other schemes for creation of X-ray population inversion based on different atomic processes such as charge-transfer schemes and a concept for lasing without inversion have also been proposed [98Hag]. It is worth noting that in spite of much effort no reasonable gain was reported up to now within these schemes.

7.1.2.2.5.1 Charge-transfer schemes

Charge-exchange collisions between atoms and ions as well as between ions and ions have been proposed as an effective pumping scheme for XRLs [73Vin, 77Dix, 90Elt]. In this method the ion acquires an electron in an upper laser level from other collision partner, rather than from a reservoir of free electrons. The scheme resembles in some respects recombination pumping described earlier. In general, a non-resonant charge-exchange collision process can be described as follows:

$$Z^{i+} + Y^{j+} \rightarrow Z^{(i+m)+} + Y^{(j-m)+*} + \Delta\varepsilon \,, \tag{7.1.25}$$

where Z and Y are the colliding ions with the charges $i > 0$, $j > 0$ and $\Delta\varepsilon$ is an energy defect which is small in case of quasi-resonant collisions. During the collision, m electrons change from

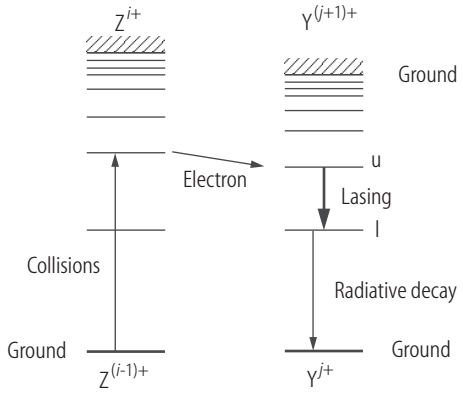

Fig. 7.1.13. Simplified level scheme of a colliding-ion charge-transfer XRL.

ion Z to ion Y, which is now excited (marked by *). A principle energy level diagram for pumping by charge transfer is shown in Fig. 7.1.13.

If the relative velocities of the ions are high enough, large cross sections for the process are expected in spite of the Coulomb repulsion of both ions. This is the case for charge-exchange reactions between fully ionized carbon atoms and beryllium-like carbon ions [94Kun]

$$C^{6+} + C^{2+}(2s^2) \rightarrow C^{5+}(n = 3) + C^{3+} , \tag{7.1.26}$$

$$C^{6+} + C^{2+}(2s2p) \rightarrow C^{5+}(n = 3) + C^{3+} . \tag{7.1.27}$$

This reaction can lead to a selective population of the $n = 3$ level and subsequent population inversion between $n = 3$ and $n = 2$ levels in hydrogenlike carbon. It was reported in [97Ruh] on an experiment with two counter-streaming plasmas including a hot, dominantly fully stripped (C^{6+}) plasma and a cold C^{2+} one. Even if no real gain could be deduced, it was encouraging to see a strongly enhanced emission of the 3p–3d line at 18.2 nm in hydrogenlike C^{5+} and the 4d–4p line at 13.5 nm. However, a collisional system based on the charge exchange with a significant gain has not been demonstrated.

7.1.3 Output characteristics

7.1.3.1 Output intensity

XRLs operate in a single- or double-pass arrangement by Amplification of the Spontaneous Emission (ASE) in the gain medium of length l. Thus, they belong to the class of mirrorless lasers. In such ASE amplifiers the spectrally integrated intensity of the laser signal increases exponentially with plasma length l, until saturated, according to the Linford formula, which for sharply peaked line profiles, including Doppler, can be approximated by [90Elt]

$$I = \frac{\varepsilon_s (e^{g_0 l} - 1)^{3/2}}{g_0 (g_0 l\, e^{g_0 l})^{1/2}} , \tag{7.1.28}$$

where g_0 and ε_s are the gain coefficient at the line center and the emissivity (spontaneous emission) per length unit, respectively. The emissivity here is the spectrally integrated emitted energy per volume and time unit and can be expressed as $N_u A_{ul}$. It has been taken into account that in experiments, only the intensity integrated over the line emission profile can usually be observed. For this reason (7.1.28) has been derived by integration over the spectral profile.

7.1.3.2 Output energy and conversion efficiency

Efficiency $\eta = E_x/E_p$ of the pump energy (E_p) conversion into the X-ray laser output energy (E_x) is presently in the range between 5×10^{-6} and 10^{-6}. Interestingly, this value is rather insensitive to the XRL wavelength, in sharp contrast to non-linear frequency conversion schemes (High Harmonic Generation – HHG), where efficiency decreases approximately with the inverse fifth power of the output wavelength. Hence, there exists a spectral range (presently lying below 30 nm) in which XRLs are inherently more efficient than HHG schemes.

Assuming pumping powers in the TW range, which corresponds well to the real experimental conditions, the XRL peak output power achieves typically several megawatts. There has been much effort to increase the XRL efficiency by optimizing the excitation conditions. The use of only one mirror redirecting the beam again into the amplifying medium can increase the total output by more than a factor of two. The output energy in the saturation regime, favorable for stabilization of the output parameters, is approximately equal to the product of the saturation intensity, the lasing duration and the cross-sectional area of the lasing region:

$$E_{out} \cong I_{sat} \times \tau_x \times \text{area}_x \ . \tag{7.1.29}$$

7.1.3.3 Saturation

Most efficient energy extraction from a laser medium (independent of the spectral range) is achieved in the operation regime of gain saturation [86Sie]. Importantly, saturation puts constraints on the exponential increase of the output intensity with plasma length. At a certain level of the output signal – defined as saturation intensity I_s – the intensity gradually starts to depend on length changes in a linear way. Quantitatively the saturation intensity is defined as the intensity, where the actual gain $g(\nu_0)$ is reduced to the half of its original small-signal-gain value $g_0(\nu_0)$, where ν_0 is the central frequency. Physically, this intensity restriction begins if the stimulated emission rate becomes non-negligible in comparison to the pump rate. The saturation intensity is found by equating the stimulated emission rate to the total pump rate R_{out} of the upper laser level [88Lon]. Assuming again a line profile with a width of $\Delta\nu$, one can find in the most general case

$$I_s = 8\pi h\nu^3 \Delta\nu / c^2 \ , \tag{7.1.30}$$

where $\Delta\nu$ is the FWHM of the atomic line profile and ν the laser frequency.

In real XRLs the saturation intensity varies strongly. Collisionally pumped lasers working at high densities are characterized by saturation intensities between 10^{10} W/cm^2 and 10^{11} W/cm^2. In contrast, the recombination lasers working at significantly lower densities and usually with low-Z elements show significantly lower saturation intensity being in the range between 10^8 and 10^9 W/cm^2. The atomic structure of the elements used in the recombination schemes offers high gain and at the same time high rate of the spontaneous emission A_{ul}. The latter evidently causes (see (7.1.30)) a significant reduction in the saturation-intensity value. It should be stressed that the saturation parameter does not mean the upper limit on the output but just the starting point at which extraction of the energy accumulated in the active medium becomes efficient.

Typically, the optical feedback provided by a cavity at wavelengths well above 100 nm facilitates reaching saturation intensity by increasing the length of the optical path. However, this method is not applicable to the X-ray lasers. The gain duration at XRLs is usually shorter than the time required for the necessary number of round-trips to extract efficiently the energy stored. This short-lived gain is a result of either the difficulty in maintaining the stringent plasma conditions during a sufficiently long period necessary for amplification in quasi-steady-state scheme [85Mat, 86Suc, 87Che, 89Lon, 90Mac1, 92Car, 92Koc, 92Mac] or the fast self-terminated nature of the

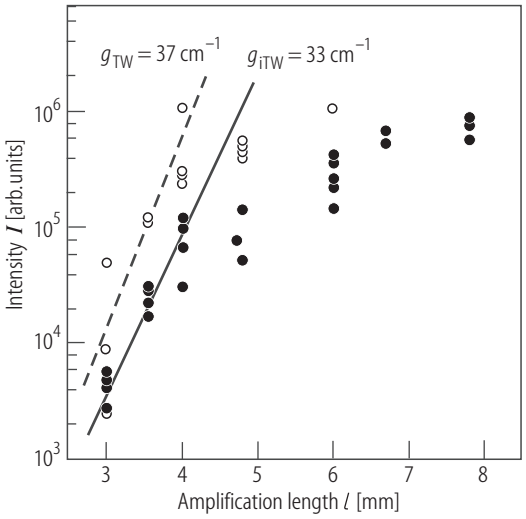

Fig. 7.1.14. Output signal versus the amplification length l in a transient collisional soft XRL (Ni-like Ag at 13.9 nm), showing saturation-like behavior for $l \geq 4 \ldots 5$ mm [03Jan]. Two cases are shown: unmatched (intrinsic) traveling-wave velocity with a small-signal gain value of $g_{iTW} = 33\ cm^{-1}$, and the matched traveling-wave velocity with $g_{TW} = 37\ cm^{-1}$.

population inversion in the transient schemes [96Kor, 97Dun, 02Kaw, 04Jan3, 04Kaw], OFI- and inner-shell-XRLs. Typically, the gain saturation of the mirrorless lasers is achieved when the gain–length product $gl \geq 15$ [92Car, 92Koc, 92Mac]. Figure 7.1.14 shows the amplification of the signal of a collisional XRL at 13.9 nm. In this case the saturation limit has been reached for the medium length between 4 and 5 mm. Saturated X-ray amplification in a single-pass or double-pass amplifier requires, depending on the length of the active medium, a gain coefficient 1–3 orders of magnitude higher than that in a conventional visible or IR lasers.

7.1.3.4 Wavelength

It follows from Bohr's model of a hydrogen-like ion that the transition energies scale as

$$h\nu_x = Z^2 \times h\nu_H \times n\ , \tag{7.1.31}$$

where Z is the charge number of the nucleus, $h\nu_H$ is the transition energy in a hydrogen atom ($Z = 1$), and n is the main quantum number ($n \geq 1$). The transition $n = 3 \rightarrow n = 2$ (Balmer-α line) of hydrogen-like carbon with $Z = 6$ emits photons with energy of 68 eV, with the common conversion formula $h\nu_x$ [eV] $= 12.4 \times 10^3/\lambda_x$ [Å] corresponding to a wavelength of $\lambda = 182.3$ Å. Usually ions are described by the number of electrons that have been removed, i.e. C^{5+} is a hydrogen-like (H-like) carbon ion that is produced by removing five electrons from the carbon atom and leaving only one electron bound to the positive nucleus. This ion belongs to the isoelectronic (having the same number of bound electrons) sequence as the hydrogen atom.

In case of the neon-like (Ne-like) isoelectronic sequence 10 electrons remain bound to the nucleus, i.e. Ne-like titanium Ti^{12+} ion contains 10 electrons. In principle all atoms from He ($Z = 2$) up to uranium ($Z = 92$) can be used as a gain medium for an XRL assuming that the required pump energy for the excitation mechanism can be supplied and the plasma is transparent to the X-rays. Collisional X-ray lasers with wavelengths between 3.56 nm (Ni-like Au) and 60.8 nm (Ne-like S) have already been demonstrated (see Table 7.1.4). Extension to shorter wavelengths seems to be possible (for example hydrogen-like Na with the lasing transition 2p $\rightarrow$ 1s into the ground state at $\sim$ 1 nm) but it is connected with a considerable and hardly predictable increase in the pump energy.

7.1.3.5 Spectral linewidth

The linewidth of the laser transition is mostly dominated by Doppler broadening due to the random thermal motion of the lasing ions with a velocity determined by the ion kinetic energy kT_i. Doppler broadening results typically in a Gaussian-shaped line profile with a half width given by the ratio [92Fie, 88Apr]

$$\begin{aligned}\Delta\lambda_\mathrm{d}/\lambda_\mathrm{d} &= 2(2\ln 2)^{1/2}(kT_\mathrm{i}/M)^{1/2} \\ &= 7.7\times 10^{-15}(kT_\mathrm{i}/\mu)^{1/2}\ ,\end{aligned} \tag{7.1.32}$$

where kT_i is in eV, M is the atomic mass, $\mu \approx 2Z$ and Z is the atomic number. For a high-temperature transient plasma with typical values of $kT_\mathrm{i}/\mu \approx 15$ this ratio is equal to 5×10^{-4}. Gain narrowing can reduce the linewidth and the values $\Delta\lambda_\mathrm{d}/\lambda_\mathrm{d}$ lower than 10^{-4} were anticipated and measured. The narrowest laser line with $\Delta\lambda_\mathrm{d}/\lambda_\mathrm{d} \sim 2\times 10^{-5}$ has recently been measured in the collisionally pumped Ni-like palladium laser working at 14.7 nm. In the case of a low-temperature plasma, as it is expected for Optical-Field-Ionized recombination scheme (OFI) a further reduction down to $\Delta\lambda_\mathrm{d}/\lambda_\mathrm{d} \approx 10^{-6}$ seems to be realistic.

However, the problem of the linewidth is much more complex. It has been shown that even a small contribution of the homogeneous broadening would cancel the rebroadening effect present in amplification of a purely Doppler (inhomogeneous) broadened line [94Koc, 94Per]. On the other hand, mixed line profiles (Voigt profile) and additional broadening mechanisms included as power broadening [95Jan] or Stark broadening, can contribute to the achievement of a reasonable agreement between the experiment and theory.

7.1.3.6 Pulse duration

The length of the XRL output pulse strongly depends on the gain duration which, in turn, depends on the kinetics of the level population. This, on the other hand, depends on the excitation regime and hence on the pump pulse parameters. Nanosecond pumping of a quasi-stationary scheme resulted in nanosecond duration of the XRL output pulses. The significant pulse length was caused by a dominance of the strong relaxation in the excitation process. Picosecond or femtosecond pumping of a transient or self-terminating ASE scheme, as well as application of a traveling-wave configuration will tend to emit picosecond XRL pulses. It has to be stressed that within this pump scheme with clean (high contrast) pulses there is a very weak correlation between the length of the pump pulse and the length of the output pulse [04Dun2, 04Jan2]. This general rule can be changed by pump pulse shaping which could also affect broader aspects of the kinetics. The shortest to date measured XRL-pulse duration – a transient Ni-like Ag XRL pulse at 13.9 nm – was about 2 ps [02Kli].

7.1.3.7 Coherence

Degree of coherence of the radiation is determined by the complex process of propagation of the X-rays in plasma. Coherence is crucial for any measurement or application involving the interference mechanism. It is also important in setting the brightness and focusability of the X-ray beam. Two kinds of coherence are usually distinguished, the spatial and temporal ones.

7.1.3.7.1 Transverse (spatial) coherence

Spatial coherence, in the direction transverse to the X-ray laser beam axis, is characterized by the extent D_{coh} of a region of coherence at a distance L_{d} if illuminated by a source with a diameter d_{s} emitting at the wavelength λ_{x}:

$$D_{\mathrm{coh}} \approx L_{\mathrm{d}}\lambda_{\mathrm{x}}/d_{\mathrm{s}} \; . \tag{7.1.33}$$

As a consequence, an XRL at $\lambda_{\mathrm{x}} = 10$ nm with an output aperture (source size) of $d_{\mathrm{s}} = 100$ μm illuminates coherently at a distance of $L_{\mathrm{d}} = 1$ m an object with a diameter of $D_{\mathrm{coh}} = 0.1$ mm. Such a range of the spatial coherence is of interest for applications requiring a small focal region (microscopy or holography). However, comparing the area of coherence (Fig. 7.1.15) to the total beam area with the diameter D a kind of efficiency for the coherent irradiation can be estimated [01Liu, 04Luc]

$$D_{\mathrm{coh}}^2/D^2 = (L_{\mathrm{d}}\lambda_{\mathrm{x}}/d_{\mathrm{s}}D)^2 \; . \tag{7.1.34}$$

It is seen that for $L_{\mathrm{d}} = 1$ m, and the assumed very low divergence of 1 mrad this ratio is equal to 10^{-2}. This suggests that the number of fully coherent photons in the beam is reduced to about 1 % of the total number of photons. The spatial coherence as well as the power in a single transverse mode can be increased by reducing the diameter of the gain region, i.e. minimizing the *Fresnel-number* (less than unity) of the beam launched from the active medium [99Bor].

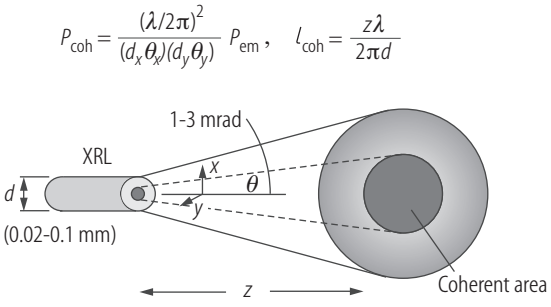

Fig. 7.1.15. Sketch explaining geometry and quantitative estimate of the transverse coherence. Formulae are given for the coherence area of an XRL with the transversal coherence length l_{coh} and the relationship between the totally emitted power P_{em} enclosed in the beam and the coherently emitted power P_{coh} [04Jan1].

As a consequence, the improvement of the spatial coherence of an XRL can be realized by the active medium elongation. This includes either use of a half- cavity arrangement or a MOPA (Master Oscillator–Power Amplifier) setup, where the output of an XRL oscillator is injected into an X-ray amplifier. Such an arrangement can deliver a fully coherent output beam [87Ros1, 03Nis]. In case of the capillary discharge XRLs also control over refraction at steep density gradients can reduce the effective transverse source size and tend towards essentially full spatial coherence. The latter was demonstrated in a capillary discharge XRL with a plasma column length of 36 cm and a length to diameter (aspect) ratio exceeding 1000 : 1 [01Liu].

7.1.3.7.2 Longitudinal (temporal) coherence

The longitudinal coherence length is characterized by

$$L_{\mathrm{coh}} = \lambda_{\mathrm{x}}^2/\Delta\lambda_{\mathrm{x}} \; , \tag{7.1.35}$$

which with a laser wavelength of $\lambda_{\mathrm{x}} = 10$ nm and $\Delta\lambda_{\mathrm{x}}/\lambda_{\mathrm{x}} = 10^{-4}$ gives $L_{\mathrm{coh}} = 100$ μm. Such a longitudinal coherence length is sufficient for imaging objects larger than 1 μm. Further reduction of the linewidth would increase the longitudinal coherence and $L_{\mathrm{coh}} = 1$ mm corresponding to

$\Delta\lambda_x/\lambda_x = 10^{-5}$ for the wavelength given above seems to be quite realistic. If an emitter maintains coherence for a period t_{coh} corresponding to the spectral linewidth [90Elt] and assuming $(\lambda_x/\Delta\lambda_x) \sim 10^4$ we will obtain

$$t_{coh} \approx \frac{\lambda_x}{c} \times \frac{\lambda_x}{\Delta\lambda_x} \approx (3 \times 10^{-7}) \times (\lambda_x\,[\mathrm{cm}])\,[\mathrm{s}]\,, \tag{7.1.36}$$

which is equivalent to a coherence time $t_{coh} = 0.3$ ps for the wavelength of 10^{-6} cm (10 nm).

7.1.4 Practical X-ray laser schemes

7.1.4.1 Collisionally pumped X-ray lasers

7.1.4.1.1 Quasi-steady state (QSS) scheme

In the Quasi-Steady State (QSS) regime exploding foil (no more in use) or solid slab targets are irradiated by energetic, long (nano- or subnanosecond) laser pulses. The laser pulse incident on the target is to achieve two goals:

1. producing a plasma with a high abundance ≥ 30 % of the desired ions (Ne- or Ni-like),
2. creation of the population inversion within the ion abundance.

The first X-ray laser demonstrated in 1985 [85Mat] was operating in the quasi-stationary regime with a laser pulse length of 450 ps and the energy of 1 . . . 1.5 kJ from the huge LLNL NOVA glass laser system. The beam was focused to a line focus with dimensions of 200 μm × 11 mm. Strong amplification at 20.6 and 29.9 nm in Ne-like selenium on 3p–3s ($J = 2$–1) transitions have been reported. The selenium atoms where deposited on a thin 0.5 μm CH-foil. Foil explosion due to high energy of the pump laser pulse resulted in a hydrodynamical smoothing of the electron density gradients in the coronal plasma – an important factor supporting a high gain × length product. Several other X-ray lasers on 3p–3s transition in Ne-like atomic configuration of different elements followed this experiment and all of them demanded an extraordinary large pump laser energy. The first Ni-like X-ray laser demonstrated in 1987 on a 4d–4p transition in Eu at 7.1 nm was also a quasi-steady state system with an enormous pump energy consume [87Mac]. Therefore, many activities between 1990 and 2000 were concentrated on understanding and optimization of the pumping mechanisms and development of new more efficient pumping techniques. It was proposed to separate the plasma preforming and medium excitation by irradiating the target with two or more separated laser pulses (*double-* or *multi-pulse pumping*) (Fig. 7.1.16a) [93Max, 95Nil2]. Within this working regime two irradiation schemes have been successfully applied.

7.1.4.1.2 Low-energy prepulse pumping

One or several low-intensity pulses precede the main pulse (all pulses are of the same duration) within this pump technique. Usually, the prepulse level is of 10^{-1} . . . 10^{-3} of that of the main pulse. In this technique the energy of the first pulse (*low-level prepulse*) can be significantly lower than that of the second pulse because requirements for the level of the electron temperatures are reduced due to separation of the ionization and heating processes. Pumping with a low-intensity prepulse helped to succeed in operation of many quasi-stationary X-ray lasers either in Ne-like or Ni-like ions with targets of various atomic numbers. This enabled many low-Z neon-like ions to lase for the

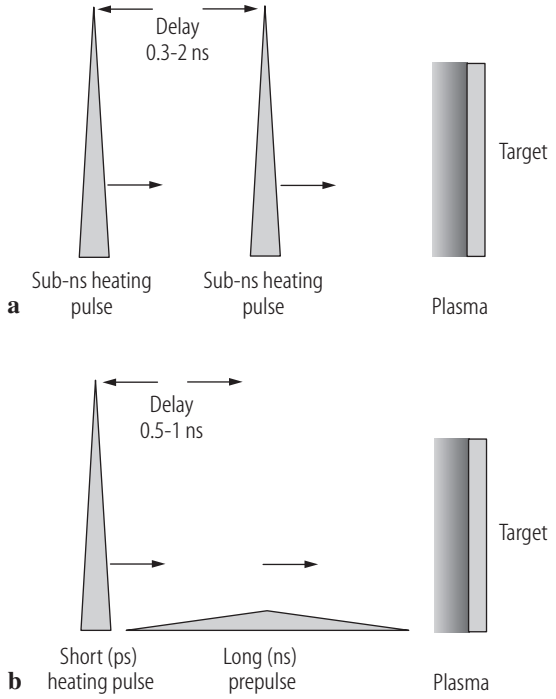

Fig. 7.1.16. Scheme explaining sequential pumping applying softening of plasma density gradient by the pump pulse structure. (**a**) Multi-pulse pumping with pulses of equal length (sub-ns). (**b**) Transient pumping with a long pulse (ns) and a short one (ps).

first time. In those experiments conducted mostly at LLNL on the NOVA laser using $\lambda = 530$ nm and at RAL on the VULCAN laser system, the $J = 0$–1 laser line dominated the spectra as it was originally predicted but never observed in the previous experiments applying single-pulse pumping (usually only weak traces of $J = 0$–1 laser lines were seen). Application of this method resulted in the first *saturated* Ni-like X-ray laser in Ni [97Zha1].

7.1.4.1.3 Multi-pulse pumping

This pump technique is an extended variant of that described above. The first laser pulse heats the target and causes the plasma expansion to result in soft density gradients. The consecutive pulses of the same duration and intensity ionize the preformed plasma to the required ionization stage and create by heating optimum conditions for efficient excitation. This results in improvement of the overall efficiency by reducing both the radiative and thermal losses as well as refraction of the X-ray pulse on the softened density gradients during the hydrodynamic expansion. As a consequence, the gain is higher and the necessary pump pulse energy can be remarkably reduced. Multi-pulse technique was shown to be a very efficient one for moderate-Z Ne-like ions, but lasing within this technique was also demonstrated in many Ni-like as well as some Co-like ions (ytterbium) [90Mac1].

7.1.4.1.4 Transient excitation scheme

In spite of the remarkable reduction in the pump laser energy to the levels well below 100 J by using multi-pulse or low-prepulse pumping techniques, both these schemes required still an amount of the pump energy which could be obtained only with the laser drivers being far from the compact laboratory class.

The situation changed dramatically when an earlier proposal of a *transient excitation* [89Afa] was taken up to achieve operation of the collisional XRL schemes within the table-top class [93Shl,

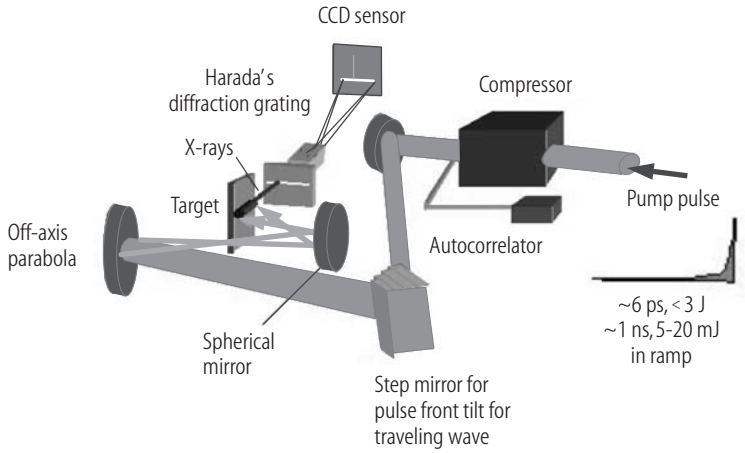

Fig. 7.1.17. Experimental arrangement of a Ni-like Ag-XRL at 13.9 nm pumped only by a shaped ps-pulse [03Jan].

95Nic]. The first transient X-ray laser on the 3p–3s transition in Ne-like Ti was demonstrated in 1995 at MBI Berlin with a pump energy drastically reduced down to 15 J [97Nic]. Presently, this excitation scheme is successfully applied in many experiments and in different variants it dominates the activities in the X-ray laser field.

The transient collisional excitation scheme utilizes two laser pulses, similar to the multi-pulse pumping, however with dramatically different pulse parameters and, hence, completely different excitation kinetics. First, a long nanosecond pulse produces a plasma with abundance of ions with the expected ionization stage (Ne-like or Ni-like). After an optimized delay necessary for plasma expansion which is expected to optimize both pumping and X-ray beam propagation along the plasma column, a short *picosecond laser pulse* generates a transient population inversion via fast electron collisional heating (see Fig. 7.1.16b).

Fast heating allows efficient excitation without perturbing the ionization balance and with negligible both kinetic relaxation and hydrodynamic expansion. Therefore, high gain is possible in this scheme within a very short period (usually about 10 . . . 15 ps) until collisional redistribution of the excited-states population influences the gain. That means, the population inversion is in this period of transient or non-stationary character and the gain factors greater then 100 cm^{-1} are predicted theoretically. As a result, saturation for target lengths of less then 1 cm is possible even if refraction reduces the effective value of the gain coefficient. Therefore, the pulse duration of a transient XRL pulse is intrinsically short (several ps).

The enormous advantage of this scheme relies on the fact that less than 10 J of total laser energy is sufficient to saturate the transitions working at the wavelengths between 10 and 15 nm. Transient collisional pumping was used for Ne-, Ni-like ions where effective gain coefficients up to $g = 70$ cm^{-1} were measured and many systems were driven into saturation. For example, saturated gain with $gl \sim 14 \ldots 18$ on the 4d–4p ($J = 0$–1) transition in Ni-like XRLs at the wavelengths between 13.9 and 20.3 nm was demonstrated with a further reduction in the necessary pump energy down to $\sim 5 \ldots 7$ J. The pumping conditions were optimized with the traveling-wave excitation arrangement [98Dun]. This was the first demonstration of the gain saturation in an X-ray laser pumped by a table-top-class laser driver (glass laser system COMET at LLNL). The progress observed in the development of the table-top XRLs took credit from an enormous progress in the development of the laser technology especially by introducing the Chirped-Pulse-Amplification (CPA).

A new variant of the transient scheme, in contrast to the standard technique relying on pumping with only one specifically shaped short laser pulse, was reported in 2002 (Fig. 7.1.17). With only ~ 3 J in a 6 ps pump pulse saturation in a Ni-like Ag X-ray laser at 13.9 nm was demonstrated at MBI [03Jan].

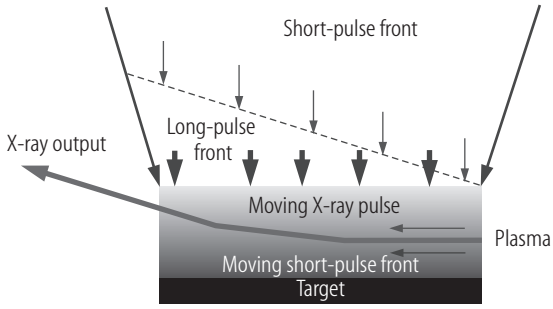

Fig. 7.1.18. Scheme of a transversally pumped XRL with "traveling-wave" of short pump pulses. This is at present the mostly used scheme for transient collisional XRLs.

7.1.4.1.4.1 Traveling-wave pumping

Shortening of the pump pulse in the transient scheme was accompanied by a significant decrease in the gain duration. Gain lifetimes in Ni-like XRLs achieved typically 10 . . . 15 ps. Therefore, the finite propagation time of X-ray photons as they traverse the plasma column can reduce the effective gain of the X-ray laser. It became increasingly important to use a *traveling-wave* pumping arrangement in order to increase the effective length of the high-gain area sampled by the amplified beam, which facilitates energy extraction from the active medium by a *short XRL pulse.*

In Traveling-Wave (TW) pumping geometry (Fig. 7.1.18) the front of the incident pump beam is tilted in a such way that the pumping beam (excited area) travels along the target synchronously (at the same velocity) with the amplified X-rays. The common methods applied to tilt the front of the pumping beam are comprehensively described in [87Ros2, 99Dun, 00Cha].

7.1.4.1.4.2 Grazing incidence pumping (GRIP)

In 2004 a new pump scheme termed as GRazing Incidence Pumping (GRIP) has been successfully demonstrated (Fig. 7.1.19). The total pump energy as low as 150 mJ was sufficient to give lasing at 18.9 nm in molybdenum plasma [04Dun1]. Moreover, the pump energy of about 1 J enabled saturation of the same transition in the same element [04Roc]. Importantly, both results have been achieved in a repetitive regime with the repetition rate of 10 Hz. A repetitive XRL became the fact. This scheme benefits from an oblique (10 . . . 26 degree, optimum about 20 degrees) irradiation of a slab target by a short (a few picoseconds) pulse in the traditional double-pulse scheme. Thus, the pumping beam penetrates a larger volume of the active material and stays there longer what should increase radiation absorption in the medium.

It is well known that one of the most critical points in lateral pumping of X-ray lasers is distribution of energy deposited in the active medium. Most of the delivered energy is absorbed at

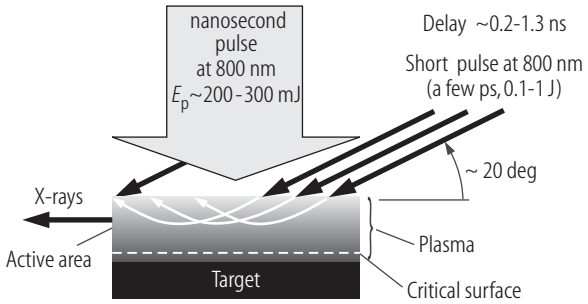

Fig. 7.1.19. Scheme of GRazing Incidence Pumping (GRIP). Low pump energy enables XRL to be operated at 10 Hz.

the critical surface and in its vicinity ($n_e \sim n_c$) due to a very high plasma density present there. However, this region of the ablated plasma is also characterized by high density gradients (see also general characteristics of XRL, Sect. 7.1.2.1.5.1). The latter causes the strongly amplified beam to be severely deflected (bent off) from the axis of the plasma column and it finally escapes from the medium after a short interaction length. The useful radiation comes actually from shallower situated medium areas with a moderate gain.

It was expected that an obliquely incident heating laser pulse should improve the situation and increase the energy absorbed due to a longer way in the plasma plume and partial overlapping of the pumping beams. Such an arrangement was proposed in [98Li, 02Oza] and experimentally tested in [98Li, 01Tom, 02Oza]. However, the incidence angles have been chosen arbitrarily and no lasing was reported. Better justified choice of the incidence angle was reported in 2003 by a LLNL group [03Kee, 03Shl]. The successful experiment was reported in [05Kee] and was confirmed by the results of two other groups [05Lut, 05Tue].

Control over the depth of the pump ray turning point on the density gradients by the choice of the angle of incidence (see Fig. 7.1.19) was the decisive idea behind this experimental layout. Numerical simulations confirmed the expected shift of the energy deposition area and increase in the plasma temperature but the high gain area is still relatively close to the target surface and significantly delayed relative to the onset of the heating laser pulse. The unambiguous optimum pump conditions have not been identified yet. Regardless of this, the total pump energy has been strongly reduced to a level about 1 J. This energy level is available from the commercial titanium-sapphire laser systems working at a wavelength of 800 nm and a repetition rate of 10 Hz. Using such a pump energy saturated lasing has been demonstrated in Ni-like ions of molybdenum (18.9 nm), ruthenium (16.5 nm), palladium (14.7 nm), silver (13.9 nm) and cadmium (13.2 nm). Additionally, strong lasing close to the saturation conditions was reported in Ni-like tin (11.9 nm), antimony (11.4 nm) and tellurium (10.9 nm) [05Roc]. In this experiment two pump laser pulses characterized by energies of 350 mJ and 900 mJ with lengths of 120 ps and 8 ps, respectively, were used to create and heat the medium. The output energy was between 1 and 2 μJ and an estimated pulse length was equal to 2 ps. The average energy for 150 shots showed a standard deviation equal to 23 %. The resulting saturation parameter under the experimental conditions was equal to $(1 \ldots 2) \times 10^{10}$ W/cm^2 [05Lut, 05Wan].

7.1.4.1.4.3 XUV master oscillator–power amplifier (XMOPA)

All X-ray lasers work as single-pass devices due to the short-lived gain with a lifetime depending on the scheme between 10 and 100 ps. This either limits the length of the active medium or forces to apply traveling-wave geometry in the pumping process. Even if the gain is high the spontaneous radiation needs a noticeable length of the medium to be amplified to a level comparable with the saturation parameter. It is well known that the available energy stored in an active medium of volume V, saturation fluence E_S and a small-signal gain coefficient g_0 is equal to $E_{AVAIL} = g_0 E_S V$. Both the saturation fluence and the gain coefficient in an XRL medium are very high and as a consequence the energy stored is high. However, the amplified spontaneous emission mechanism responsible for amplification is, as mentioned earlier, very inefficient.

The search after the efficiency improvement concentrated on the way shown by the lasers in other spectral regions, i.e. an oscillator–amplifier system. Such a scheme we have termed an XUV Master Oscillator–Power Amplifier (XMOPA) . The first attempt to realize such a system, even if many theoretical proposals are dated back to the seventies [72McC, 75Hop], was undertaken in 1995 [95Dit]. However, it failed due to a low seeding signal. High Harmonics (HH) have been used as a seeding source but generated with picosecond laser pulses delivered too little photons to extract efficiently the energy stored in the amplifier. Also the amplifying medium (excited Ga-plasma) was far from optimum. The registered gain was equal to 3. The first successful attempt after a long break to realize such a scheme was reported in [04Zei] and has shown irrefutable amplification of

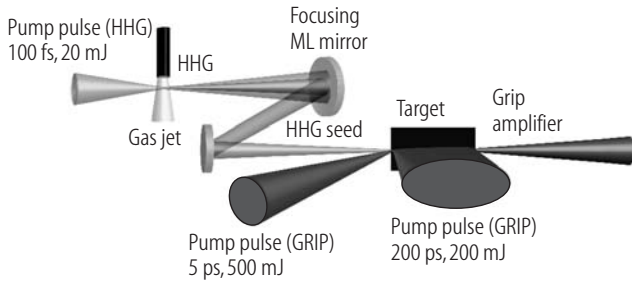

Fig. 7.1.20. The sketch of an XRL based on seeding a GRIP amplifying medium with a high-harmonics signal.

a HH signal in the active medium of an OFI-XRL at 32.8 nm. However, the output energy was very low due to an intrinsically low saturation parameter of an OFI-medium and a huge mismatch between the bandwidths of the seed and that of the amplifying medium. Another variant, developed at MBI predicted seeding a GRIP amplifying medium with high harmonics (see Fig. 7.1.20). The saturation parameter of a GRIP medium is one to two orders of magnitude higher than that of OFI lasers and the energy extracted should be higher. However, the problem of the bandwidth mismatch exists also in this system and has to be solved. One of the interesting features of such a system is the possibility to apply coherent amplification process. The latter was theoretically analyzed in the seventies [69Ics, 70McC, 75Bon]. Such a method should give shortening of the amplified pulses and an increase in its intensity, while the incoherent amplification process (matched bandwidths) results in high extraction efficiency [75Arm]. Very recently such a system has been realized in both Ne-like (Ti) [06Wan] and Ni-like (Ag) active media [07Roc]. The amplifying medium was seeded by 25^{th} harmonic in argon and 59^{th} harmonic in neon of Ti:sapphire laser, respectively. While the energetic amplification factor for Ne-like titanium at 32.6 nm was equal to 64, the amplifier based on Ni-like silver showed a gain factor of 400. Extreme improvement of spatial coherence and reduction in divergence have been observed in both cases.

It is expected that this method will give pulses about 10 μJ of the output energy with a subpicosecond pulse length, a controllable intensity distribution and polarization as well as a very high coherence level at a repetition rate significantly higher than that available now (10 Hz).

The pumping-pulse parameters in those experiments were very relaxed and hence the short-pulse table-top X-ray lasers of reduced size, low cost, and high repetition rate seem to be fairly realistic in the near future.

7.1.4.1.5 Fast capillary discharge

Direct excitation of plasma with an electric discharge has the potential advantage of generating compact and efficient quasi-steady-state X-ray lasers in a relatively simple and cheap way. Fast-capillary-discharge plasma as a lasing medium was first proposed 1988 and demonstrated in 1994 [94Roc]. A capillary-discharge quasi-steady-state XRL is shown schematically in Fig. 7.1.21.

The capillary discharges have proven to be the most efficient plasma sources for soft XRL emission. The fast current rise time of typically 10 . . . 50 ns (between 10 % and 90 % of the maximum value) determines the amount of the material that is ablated from the capillary walls before magnetic field and the radial propagation compress the plasma [96Roc]. The plasma generated in the fast discharges is non-stationary and rapidly contracts, heats up, and expands similarly to a wall-influenced pinch. These discharges with a rapid compression have several advantages beneficial to efficient pumping of small-scale X-ray lasers:

– high pumping efficiency in a high-density and strongly ionized plasma [96Roc],
– high axial uniformity that results from highly uniform initial conditions – a very fast compression [02Kaw],

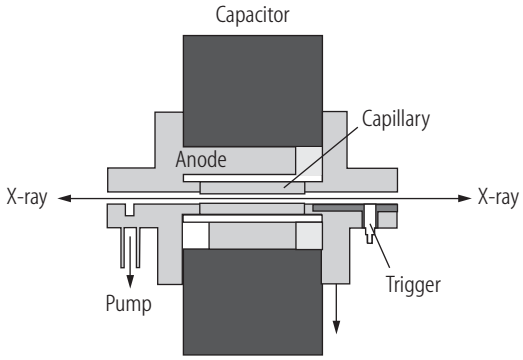

Fig. 7.1.21. Schematic of a capillary-discharge quasi-steady-state XRL. Plasma and inversion population is produced by wall ablation due to a fast current resulting from a fast capacitor discharge.

- plasma columns with very large length to diameter (aspect) ratio (up to 1000 : 1) [96Roc],
- rapid plasma motion at the lasing period which results in a strong dynamical Doppler shift and helps to depopulate radiatively the lower laser level owing to reduction in the radial opacity;
- the radial electron density distribution in the capillary plasma allows for guiding of the traversing X-ray pulses.

The capillary discharge in an argon-filled capillary under the pressure of about 800 mTorr, typically driven by current pulses up to $\sim$ 100 kA of the peak amplitude produces a plasma column with the length of several tens of centimeter. A saturated output in a steady-state regime of neon-like Ar-XRL at 46.9 nm (26.5 eV) has been shown in a 40 cm long capillary with a diameter of 4 mm. Both single- and double-pass configurations were realized. The output pulse duration was about 0.8 ns and the repetitive regime at 4 Hz has been demonstrated as well. This XRL delivers spatially highly coherent pulses with an averaged energy of 0.88 mJ ($\cong 2 \times 10^{14}$ photons/pulse) in a pulse, corresponding to an averaged power of $\cong$ 3.5 mW [91Roc, 97Ben, 03Nis]. With a peak spectral brightness of $\cong 2 \times 10^{25}$ [ph/s $\times$ mm^2 $\times$ mrad^2 $\times$ 0.1 % B_w] (where B_w is the radiation bandwidth) this table-top laser belongs to the brightest existing soft X-ray sources.

No other soft X-ray source, independent of its size, is presently capable to produce simultaneously such a high average coherent power and the peak spectral brightness. Lasing was also demonstrated in a capillary-discharge Ne-like S plasma with a gain–length product of 7.5 on the transition at 60.84 nm [95Roc]. However, in order to shorten the wavelength of these Ne-like XRLs below the presently available 46.9 nm one has to apply much faster and higher discharge currents (200 kA and higher) in order to excite the ions and this is a serious technological challenge. Shortening of the output pulse duration in this inherently quasi-stationary excitation system down to less than 100 picoseconds is not possible.

7.1.4.1.6 Hybrid X-ray lasers

The short-laser-pulse-pumped transient scheme and the quasi-stationary one pumped by the capillary discharge are to some extent complementary and very promising for a further progress in development of compact and efficient XRLs. Capillary discharge is a very compact and cheap source of a plasma with an abundance of Ne-like ions. Hence, it is potentially an excellent source of a preformed symmetric plasma column for transient inversion pumping and it could replace the whole optical laser system delivering the nanosecond pumping pulse. Moreover, the plasma column of the capillary discharge shows a concave radial density profile with the minimum on the capillary axis which is a pre-condition for an efficient guiding effect of the pump beam. Thus the short, guided picosecond pulse could heat rapidly the plasma created by the discharge (Fig. 7.1.22). Moreover, quasi-traveling-wave pumping is inherent for this scheme and guiding in a symmetric plasma pipe eliminates the refraction problems present in the conventional double-pulse transient

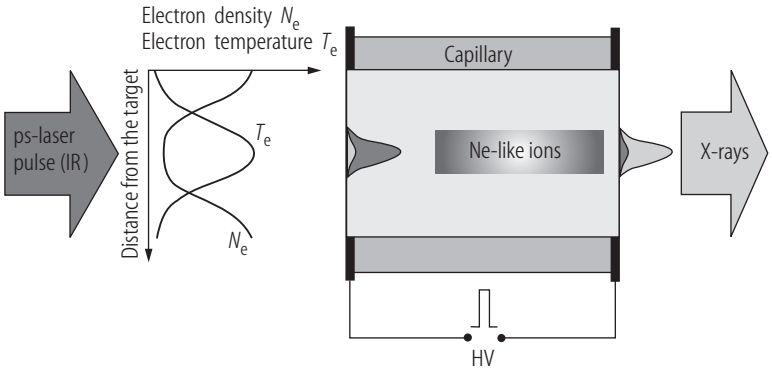

Fig. 7.1.22. The pump method of the hybrid X-ray lasers. Transient collisional capillary X-ray laser pumped (with intrinsic traveling wave) by a short (picosecond) laser pulse. The radial electron density distribution (N_e) has a minimum on the capillary axis to allow guiding of the pump pulse.

system. Additionally, the high-intensity short pulse could easily improve the plasma ionization stage by multiphoton or field ionization.

A proposal to combine both pump methods in one hybrid laser system appeared in [97Shl] and the working scheme was for the first time demonstrated on the 3p–3s, $J = 0$–1 transition in neon-like sulfur at 60.84 nm [01Jan]. The pre-plasma created by the discharge had to fulfill two requirements:

1. It had to be sufficiently dense to ensure strong energy absorption by inverse-bremsstrahlung mechanism.
2. The elongated plasma column should have a density profile that provides efficient guiding for the pumping pulse and enables uniform heating over the whole length of the plasma column.

The maximum gain for a 10 mm longitudinally pumped sulfur capillary by a 2 ps, 1053 nm laser pulse with the energy lower than 0.5 J was equal to 4.7 cm^{-1}. For a 30 mm capillary a gain–length product of $g \times L = 6.8$ was obtained. The ratio (gain-length product $g \times l$)/(pumping energy E_p [J]) was very high and equal to 3.1 J^{-1} (including pumping laser energy as well as the total electrical energy dissipated in the discharge). This belongs to the highest figures of merit obtained for collisionally pumped XRLs. This value was conventionally between $1 \ldots 2$ J^{-1}.

This new type of a transient XRL seems to be a promising scheme for an efficient compact short-pulse-emitting soft XRL if the durability of the capillary against the current pulse can be improved.

7.1.4.1.7 Dense gases

An alternative to the slab target geometry is the use of a gas target with increased density. An electromagnetic valve is used to produce an elongated homogeneous gas puff at high ($\sim$ 100 Hz) repetition rate. The system can be driven by both long single laser pulse and combination (long/short) of the laser pulses (transient regime) (Fig. 7.1.23). Argon irradiated with a single 500 ps long laser pulse of 500 J energy from Asterix laser in Garching showed a gain coefficient of 1.65 cm^{-1} [95Fie]. A high gain of 18 cm^{-1} was demonstrated in the neon-like argon, on the 3p–3s, $J = 0$–1 transition at 46.9 nm [02Lu1] in the transient regime by irradiation with two picosecond laser pulses of different intensity. The shortest achieved lasing wavelength with this technology was 9.9 nm for Ni-like Xe in the transient inversion scheme [02Lu2].

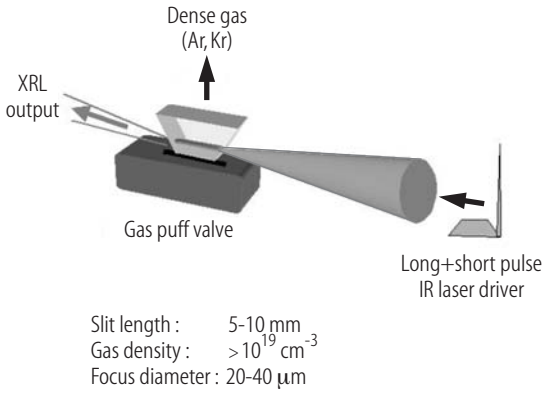

Fig. 7.1.23. Longitudinally pumped collisional X-ray laser applying gas puff technology. A slit nozzle produces an elongated dense gas distribution of the required atoms (Ar, Xe a.o.).

7.1.4.1.8 Review of realized collisional X-ray lasers

A survey of realized and modeled collisional XRLs is given in Table 7.1.4.

7.1.4.2 Recombination-pumped X-ray lasers

Thin fiber targets have been successfully used to realize rapid adiabatical cooling in the cylindrical geometry that allowed for a reasonably high gain obtained in a relatively short plasma column. The first observation of high gain equal to 12.5 cm^{-1} in a CVI (C^{+5}) recombination XRL driven by a 2 ps, 20 J laser pulse was reported in [95Zha]. Carbon fibers of 0.5 cm length and 7 μm diameter supported at one end have been used as targets. Lithium- and sodium-like ions are analogous to H-like ions, having one electron in the outer atomic shell but additionally one or two inner-atomic shells. They have higher quantum efficiency than H-like ions. A high gain at 11.1 nm in sodium-like copper driven by a 2 ps, 20 J laser pulse was reported in [96Zha1].

Very promising results on the way to a table-top recombination XRL were obtained in a fast recombining plasma in a capillary. A carbon plasma was created by ablation of the polyethylene microcapillary walls either by a small prepulse or by the front of the single driving laser pulse, while the main part of the pulse heated the plasma to the temperatures at which carbon atoms were totally stripped of electrons [95Mor]. When the pump laser pulse has passed, the plasma was cooled rapidly creating conditions for a fast recombination process and efficient amplification. An Nd:glass laser pulse with an intensity of approximately 10^{14} W/cm^2 irradiated axially a capillary of 350 μm in diameter and 10 . . . 15 mm in length. A concave radial electron density distribution created in the channel enabled waveguiding of both the pumping as well as the X-ray pulses. The scheme resulted in amplification on the $n = 3$–2 transition in H-like carbon ions (C^{5+}) at 18.2 nm. A more stable set-up is expected in microcapillaries where the pre-plasma is created by a separate laser pulse or high-voltage discharge. A high gain on the $n = 3$–2 transition at 26.2 nm with 1 Hz repetition rate in a table-top system working in H-like boron BV (B^{+4}) was demonstrated by irradiating a 350 μm B_2O_3 capillary in the axial direction first with a 0.2 J KrF-laser pulse followed, after a 400 ns delay, by a 0.45 J YAG-laser pulse [98Kor]. It has been shown that pump pulse propagation is very sensitive to irradiation conditions.

A similar setup as for the boron-based XRL was successfully used for the $n = 2$–1 transition in H-like lithium (Li^{2+}) [97Gol]. Using the radiative lifetime of the upper level $\tau_{21} = 1/A_{21} \approx 27$ ps and taking into account the collisional and photo-recombination rates (radiative decay) to the ground state, it was estimated that the duration of the pumping pulse should not be longer than 10 ps (preferably shorter). Therefore, either picosecond and subpicosecond pump pulses or ionization by

Table 7.1.4. Survey of realized and modeled collisional XRLs.

Target, Z	Ion, Transition, J	Wavelength [nm]	Gain [cm^{-1}], gain × length output	Operation regime	Pumping	Target configuration	Ref.
Chlorine 17	[Ne] 3p–3s $J = 0$–1	52.9	2.5, $gl = 7.5$	qst	1315 nm, 450 ± 50 J, 450 ps, 15 % prepulse	25 mm KCl crystal	[95Fil1]
Argon 18	[Ne] 3p–3s $J = 0$–1	46.9	1.65, $gl = 4.45$	qst	1315 nm, 470 J, 450 ps	2.7 cm long gas-puff nozzle, 5 bar backing pressure	[96Fie]
	3d–3p $J = 1$–1	45.0	observed due to photopumping	qst			
Argon 18	[Ne] 3p–3s $J = 0$–1	46.9	0.6, av. energy/pulse 0.88 mJ, 1.2 ns pulse length, av. power 3.5 mJ, 2×10^{14} ph/pulse, full coherence, 10^{25} ph/s/mm^2/mrad^2/ 0.01 % B_w	qst	electric discharge: peak current 26 kA with a rise time (10–90 %) 40 ns	capillary Al_2O_3, 34.5 cm long and 3.2 mm in dia., filled with 460 mTorr Ar	[94Roc, 99Mac]
Potassium 19	[Ne] 3p–3s $J = 0$–1	42.1	3.4, $gl = 10.2$	qst	1315 nm, 450 ± 50 J, 450 ps, 15 % prepulse	25 mm KCl crystal	[95Fil1]
Calcium 20	[Ne] 3p–3s $J = 0$–1	38.3	3.8, $gl = 11.4$	qst	1315 nm, 450 ± 50 J, 450 ps, 15 % prepulse, 5 ns delay	30 mm CaF_2 crystal	[95Fil1]
Scandium 21	[Ne] 3p–3s $J = 0$–1	35.2	3.8, $gl = 9.8$	qst	1315 nm, 450 ± 50 J, 450 ps, 15 % prepulse	26 mm slab	[95Fil1]
Titanium 22	[Ne] 3p–3s $J = 0$–1	32.6	E_{out}/E_{in} = 64, 50–60 nJ, 0.5–1 ps 2×10^{26} ph/s/mm^2/mrad^2/ 0.01 % B_w, 2.2 mrad diverg.	tr	800 nm, double-prepulse 10 and 300 mJ, 5 ns delay 800 mJ, 6.7 ps, seed 0.5–1 nJ, 2–4 ps delay, 5 Hz rep. rate	4 mm slab target, grazing angle 23 °, seeded by 25th harmonic in Ar	[06Wan]
		30.1	observed (weak)			injector–amplifier	
Titanium 22	[Ne] 3p–3s $J = 0$–1	32.6	19, $gl = 9.5$, 20 ps	tr	1053 nm, long pulse 4 J, 1.5 ns, 10^{12} W/cm^2, 7 J CPA, 0.7 ps	slab 0.5 cm long	[97Nic]
Titanium 22	[Ne] 3p–3s $J = 0$–1	32.6	3.0, $gl = 8.2$	tr	1315 nm, 450 ± 50 J, 450 ps, 15 % prepulse, 5 ns delay	slab 0.5 cm long	[95Fil1]
	$J = 0$–1	28.5					

(continued)

Table 7.1.4 continued.

Target, Z	Ion, Transition, J	Wavelength [nm]	Gain [cm^{-1}], gain × length output	Operation regime	Pumping	Target configuration	Ref.
Vanadium 23	[Ne] 3p–3s $J = 0$–1 $J = 0$–1	30.4 26.1	4.4 ± 0.7, $gl = 11$ 5.0 ± 1.1, $gl = 12.5$	tr	1315 nm, 450 ± 50 J, 450 ps, 15 % prepulse, 5 ns delay	slab 2.5 cm long	[95Fil1]
Chromium 24	[Ne] 3p–3s $J = 0$–1 $J = 2$–1	28.55 40.22	2.6, $gl = 11.2$, 120 ps observed	qst	2×530 nm, 1.1 kJ, 600 ps, 6 J prepulse, 4 ns delay, 34 TW/cm^2	flat slab 4.3 cm long target	[93Nil2]
Chromium 24	[Ne] 3p–3s $J = 0$–1	28.55 24.0	3.9, $gl = 9.6$ 3.0, $gl = 7.4$	qst	1315 nm, 450 ± 50 J, 450 ps, 15 % prepulse, 5 ns delay	flat slab ~ 2.5 cm long	[95Fil1]
Iron 26	[Ne] 3p–3s $J = 0$–1 $J = 0$–1	25.5 20.5	4.1 ± 0.5, $gl = 10.2$ 2.3 ± 0.5, $gl = 5.7$	qst	1315 nm, 450 ± 50 J, 450 ps, 1.5 % prepulse, 5 ns delay	flat slab 2.5 cm long	[95Fil1]
Iron 26	[Ne] 3p–3s $J = 0$–1	25.5	4.5, $gl = 11$, single prepulse 9.2, $gl = 16.5$, double prepulse	qst	1053 nm, 30 J, 100 ps, 12 TW/cm^2, double-prepulse 0.5 %, delayed by 5 and 2 ns	curved ($R = 3$ m) 2.5 cm long	[99Bal]
Nickel 28	[Ne] 3p–3s $J = 0$–1 $J = 2$–1 $J = 2$–1	23.1 29.8 30.4	observed (dominant) observed (weak) observed (weak)	qst	2×530 nm, 1.1 kJ, 600 ps, 6 J prepulse, 7 ns delay, for double-sided energy halved	flat slab 3.8 cm long target, 130 μm thick, one-side or double-sided	[93Nil1]
Zinc 30	[Ne] 3p–3s $J = 0$–1	21.2	7, $gl = 21$, 4 mJ, 90 ps, 3×10^{14} photons 3.5×5.5 mrad, 10^{27} ph/s/mm^2/$mrad^2$	qst	1315 nm, 1.6 J prepulse, 10 ns delay, 1.6×10^{10} W/cm^2, 500 J, 2.8×10^{13} W/cm^2	flat slab, 3 cm long, double-pass	[02Rus]
Zinc 30	[Ne] 3p–3s $J = 0$–1	21.2	5, $gl = 17.3$, 100 ps, 400 μJ	qst	1.06 μm, 350 J, 600 ps, 1.4×10^{13} W/cm^2, train of prepulses 800 mJ, apart 10 ns, the last 170 mJ	slab, 2 cm long, double-pass (half-cavity)	[97Rus]

(continued)

Table 7.1.4 continued.

Target, Z	Ion, Transition, J	Wavelength [nm]	Gain [cm^{-1}], gain × length output	Operation regime	Pumping	Target configuration	Ref.
Zinc 30	[Ne] 3p–3s $J = 0$–1	21.2	4.7	qst	1315 nm, 400 J, 30 TW/cm^2, 450 ps, 5 ns delay, 7.8 % prepulse	flat, 2.5 cm long	[95Fil2]
Zinc 30	[Ne] 3p–3s $J = 0$–1 $J = 2$–1 $J = 2$–1	21.2 26.2 26.7	4.9, $gl = 10$ 2.3 2.6	qst	1.06 μm, 400 J, 600 ps, 1.25×10^{13} W/cm^2	flat slab 2 cm long	[93Jae]
Germanium 32	[Ne] 3p–3s $J = 2$–1	23.6	4, pulse length 250 ps, 10^{14} W/cm^2/sr, div. 3.6 mrad	qst	1053 nm, 500 ps, 1 TW, 2×10^{13} W/cm^2	2×18 mm, double-pass with a Mo/Si mirror	[92Car]
Germanium 32	[Ne] 3p–3s $J = 0$–1	19.6	900 μJ, div. 6.6×30 mrad effic. $= 6 \times 10^{-6}$, brightness 3×10^{27} ph/s/mm^2/$mrad^2$/ 0.01 % B_w, saturated	qst	2×1053 nm, 75 J/beam, 75 ps, 4×10^{13} W/cm^2, prepulse (10–30 %), 2.2 ns delay	2×18 mm (stripe on glass)	[96Zha2]
Germanium 32	[Ne] 3p–3s $J = 0$–1	19.6	8, pulse length 50 ps	qst	530 nm, 400 J/pulse, 100 ps, 3 pulses, 400 ps apart	slab 2.52 cm long	[97Nil]
Germanium 32	[Ne] 3p–3s $J = 0$–1	19.6	30 ± 2, $gl = 18$, 13 μJ, 1.1×10^9 W/cm^2, div. 7 mrad	tr	1053 nm, long pulse $\leq$ 40 J, 600 ps, 5.6×10^{12} W/cm^2, 20 J CPA, 7 ps, 3×10^{14} W/cm^2, delay 300 ps	slab 0.9 cm long	[98War]
Selenium 34	[Ne] 3p–3s $J = 2$–1 $J = 2$–1	20.64 20.96	5.5, $gl = 6.5$, (for both lines) **the first XRL**	qst	532 nm, few kJ, 450 ps, single pulse, 5×10^{13} W/cm^2	foil 1.1 cm, one- and double-sided, up to 2.2 cm	[85Mat]
Selenium 34	[Ne] 3p–3s $J = 0$–1 $J = 2$–1	18.2 20.9	shorter wavelength one order of magnitude more intense	qst	530 nm, multipulse, 110 TW/cm^2, 400 J/pulse, 100 ps, 400 ps apart	3 cm long 100 μm, thick slab, (effective 2.52 cm)	[95Nil2]

(continued)

Table 7.1.4 continued.

Target, Z	Ion, Transition, J	Wavelength [nm]	Gain [cm^{-1}], gain × length output	Operation regime	Pumping	Target configuration	Ref.
Yttrium 39	[Ne] 3p–3s $J = 0$–1	15.5	5, pulse length 45 ps, 30 MW	qst	2×530 nm, 100 ps, $\geq 2 \times 10^{14}$ W/cm^2, multipulse	flat foil 3 cm long	[94DaS]
Yttrium 39	[Ne] 3p–3s $J = 2$–1	15.5	$gl = 20 \pm 2$, 7 mJ, 200 ps, 32 MW, 4×10^{11} W/cm^2, 4.6×10^{17} W/cm^2/sr/nm div. 10 mrad, 120 μm medium dia.	qst	2×530 nm, 500 ps, 1.5×10^{14} W/cm^2	double-sided flat foil 3.8 cm long	[93DaS]
Molybdenum 42	[Ni] 4d–4p $J = 0$–1 4f–4d $J = 0$–1	18.9 22.6	21 ± 2, $gl = 11.6$, 2.5–5 μJ, 4.3 ± 0.9	tr	1053 nm, long pulse 1 J, 600 ps, 5 J CPA, 1 ps, delay 700 ps	flat slab 1 cm long	[99Dun]
Molybdenum 42	[Ni] 4d–4p $J = 0$–1	18.9	55, $gl = 11$–14, 10–20 nJ	tr	800 nm, long pulse 70 mJ, 200 ps, 80 mJ CPA, 1.5 ps, delay 500 ps	flat slab 4 mm long 15 μm width of the line focus, GRIP (14°)	[05Kee]
Molybdenum 42	[Ni] 4d–4p $J = 0$–1 4f–4d $J = 0$–1	18.9 22.6	58, $gl = 15.5$, 150 nJ, 41.1, $gl = 13.5$, div. 10 mrad	tr	800 nm, long pulse 320 mJ, 120 ps, 930 mJ CPA, 8.1 ps, delay 700 ps	flat slab 4 mm long 30 μm width of the line focus, GRIP (14°)	[05Lut]
Palladium 46	[Ni] 4d–4p $J = 0$–1	14.68	65, $gl = 18$, 6–10 ps, 10 μJ, 2–3 mrad diverg., 10^{24} ph/s/mm^2/mrad^2/0.01 % B_w	tr	1053 nm, 1.6 J, 600 ps, CPA 4.8 J, 1.5 ps, 700 ps delay	flat slab 0.9 cm long traveling wave	[99Dun]
Palladium 46	[Ni] 4d–4p $J = 0$–1	14.68	8.3, $gl = 15.8$, 12 μJ, 2 mrad divergence	qst	1053 nm, 30 J, 100 ps, 8 % prepulse, 12 TW/cm^2, delay 1 ns	1.9–2.3 cm slab target	[99Tom]

(continued)

Table 7.1.4 continued.

Target, Z	Ion, Transition, J	Wavelength [nm]	Gain [cm^{-1}], gain × length output	Operation regime	Pumping	Target configuration	Ref.
Silver 47	[Ni] 4d–4p $J = 0$–1	13.89	67.5, $gl = 16.8$, 5 ps, 0.85 μJ, 7 mrad diverg., 2 μW, 5 Hz rep. rate, aver. 10^{13} ph/s/mm^2/mrad^2/0.01 % B_w	tr	800 nm, 10 mJ, 120 ps, 6.7 ns delay, 350 mJ, 120 ps, 2.4×10^{12} W/cm^2, 300 ps delay, 1 J, 8 ps, 10^{14} W/cm^2	flat slab 0.4 cm long target, 20 ° grazing incidence angle, GRIP	[05Wan, 06Wei]
Silver 47	[Ni] 4d–4p $J = 0$–1	13.89	76, $gl = 28.2$, 5–10 ps, 1–2 μJ, 3 mrad diverg.	tr	800 nm, single profiled pulse, CPA 1.5 J, 8 ps	flat slab 0.7 cm long	[06Kim]
Silver 47	[Ni] 4d–4p $J = 0$–1	13.89	33, $gl = 23.1$, 35 ps, 3–5 μJ, 3 mrad diverg.	tr	1053 nm, single profiled pulse, CPA 2.5 J, 4–6 ps,	flat slab 0.7 cm long, focus 80 μm broad	[02Jan, 03Jan]
Silver 47	[Ni] 4d–4p $J = 0$–1	13.89	65, $gl = 18$, 6–10 ps, 10 μJ, 2–3 mrad diverg., 10^{24} ph/s/mm^2/mrad^2/0.01 % B_w	tr	1053 nm, 1.5 J, 600 ps, CPA 4.7 J, 1.5 ps, 700 ps delay	flat slab 0.9 cm long traveling wave	[99Dun]
Silver 47	[Ni] 4d–4p $J = 0$–1 $J = 0$–1	13.89 16.05	33.5, $gl = 12.7$, 10 ps, 10 μJ, 2–3 mrad diverg., defl. 10–12 mrad	tr	1053 nm, 2ω, ∼ 3.5 J, 600 ps, 1ω, ∼ 9 J, 450 fs, 250 ± 50 ps delay	flat slab 1.18 cm long traveling wave	[00Kub]
Silver 47	[Ni] 4d–4p $J = 0$–1	13.89	7.2, $gl = 16$, 34–45 ps, 90 μJ, 4.5 mrad defl., 3 mrad diverg., 10^{25} ph/s/mm^2/mrad^2/0.01 % B_w, 43×57 μm^2 source area	qst	1053 nm, 75 ps, 10–30 % prepulse, 20 TW/cm^2 on target	curved double-slab (each 18–22 mm long)	[97Zha1]
Silver 47	[Ne] 3p–3s $J = 2$–1 $J = 2$–1 $J = 0$–1	9.9 10.4 8.1	9.4 (dominant), $gl = 8.5$, 6.4, $gl = 5.8$ observed	qst	2×530 nm, 500 ps, kJ, $(5$–$15) \times 10^{14}$ W/cm^2 $(8$–$9) \times 10^{14}$ W/cm^2	flat foil 4.5–7 mm flat foil 8.9 mm	[92Fie]

(continued)

Table 7.1.4 continued.

Target, Z	Ion, Transition, J	Wavelength [nm]	Gain [cm^{-1}], gain × length output	Operation regime	Pumping	Target configuration	Ref.
Cadmium 48	[Ni] 4d–4p $J = 0$–1	13.2	69, $gl = 17.6$, 5 ps, 7 mrad diverg., 1 μW, 5 Hz rep. rate, 1.2×10^{10} W/cm^2	tr	800 nm, 1 J, 8 ps, 350 mJ, 120 ps, 300 ps delay, 15 mJ, 120 ps, 5 ns delay	flat slab 0.4 cm long target, 23° grazing incidence angle, GRIP	[05Roc]
Cadmium 48	[Ni] 4d–4p $J = 0$–1	13.15	35–40, close to saturation, divergence 2–3 mrad	tr	1053 nm, 1.7 J, 600 ps, 4.85 J, 1.5 ps, delay 700 ps	slab 0.9 cm long target, traveling wave	[99Dun]
Tin 50	[Ni] 4d–4p $J = 0$–1	11.91	50, $gl = 14.3$, 5 ps, 0.23 μJ, 7 mrad diverg., 5 Hz rep. rate	tr	800 nm, 10 mJ, 120 ps, 6.7 ns delay, 350 mJ, 120 ps, 2.4×10^{12} W/cm^2, 120 ps delay, 1 J, 8 ps, 10^{14} W/cm^2	flat slab 0.4 cm long target, 20° grazing incidence angle, GRIP	[05Wan]
Tin 50	[Ni] 4d–4p $J = 0$–1	11.91	~ 30, $gl \sim 10$	tr	1053 nm, 1.7 J, 600 ps, 5.0 J 1.5 ps, delay 700 ps	slab 0.9 cm long target, traveling wave	[99Dun]
Neodymium 60	[Ni] 4d–4p $J = 0$–1	7.9	1 cm^{-1}, 38 ps	qst	2×530 nm, 150 ps, 600 J/each, triple-pulse, 500 ps apart, 1st 30 %	2 flat slabs, each 2.52 cm traveling wave	[95Nil1]
Neodymium 60	[Ni] 4d–4p $J = 0$–1	7.97	3.1, $gl = 7.8$, 1 μJ, 60 ps	qst	1053 nm, 100 ps, 250 J, 2–3 pulses 400 ps apart 6.9×10^{13} W/cm^2	curved slab 2.5 cm long	[95Dai]
Samarium 62	[Ni] 4d–4p $J = 0$–1	7.32	19, saturated, 1.5 μJ, diverg. 4.9 mrad, 1.7 ps, 10^{10} W/cm^2	tr	1053 nm, 280 ps, 2×10^{13} W/cm^2, 3 ps, 2×10^{25} W/cm^2, delay 130 ps	flat slab 9 mm long target, traveling wave	[01Kin]
Samarium 62	[Ni] 4d–4p $J = 0$–1	7.32 6.8	8.4, saturated, 313 μJ, diverg. 1.2 mrad, 37–49 ps observed	qst	1053 nm, main pulse 75 ps, 10–30 % prepulse, 75 ps, 2.2 ns delay, 4×10^{13} W/cm^2	flat slab, double-target 18 mm/each, 20 mm if single	[97Zha2]
Samarium 62	[Ni] 4d–4p $J = 0$–1	7.32	2.6	qst	1053 nm, 100 ps, 250 J, 2–3 pulses 400 ps apart, 6.9×10^{13} W/cm^2	curved slab 2.5 cm long	[95Dai]

(continued)

Table 7.1.4 continued.

Target, Z	Ion, Transition, J	Wavelength [nm]	Gain [cm^{-1}], gain × length output	Operation regime	Pumping	Target configuration	Ref.
Europium 63	[Ni] 4d–4p $J = 0$–1	7.1 6.58	1.1, $gl \sim 4$ 0.6	qst	2 × 530 nm, 5 kJ, 500 ps, single pulse, 7×10^{15} W/cm^2	flat foil 3 cm	[87Mac]
Gadolinium 64	[Ni] 4d–4p $J = 0$–1	6.92 6.39	2.8 2	qst	1053 nm, 100 ps, 130 J/pulse, 2–3 pulses 400 ps apart, 6.9×10^{13} W/cm^2	curved slab 2.5 cm	[95Dai]
Terbium 65	[Ni] 4d–4p $J = 0$–1	6.67	4.0	qst	1053 nm, 100 ps, 130 J/pulse, 2–3 pulses 400 ps apart, 6.9×10^{13} W/cm^2	curved slab 2.5 cm	[95Dai]
Dysprosium 66	[Ni] 4d–4p $J = 0$–1	5.86	lasing observed	qst	1053 nm, 100 ps, 130 J/pulse two or three pulses, 6.9×10^{13} W/cm^2	curved slab (1 μm stripe on glass), 2.5 cm long	[95Dai]
Dysprosium 66	[Ni] 4d–4p $J = 0$–1	5.86 6.37	9 7.5	qst	2 pulses, 75 ps, 2×10^{13} W/cm^2	double-slab (18 mm each)	[99Smi]
Erbium 68 (theory)	[Ni] 4d–4p $J = 0$–1	5.43 5.99 8.6 8.96 6.48	3.04 5.44 3.45 6.58 6.5 6.91 4.62 8.12 – 7.38	qst	2 pulses, 530 nm, $(0.3–2) \times 10^{15}$ W/cm^2	double sided Eu-Al foil, enhancement by photo-pumping with Ly-α line (7.17 Å) from AlXIII (see second column of the gain values)	[89Nil]
Ytterbium 70	[Ni] 4d–4p $J = 0$–1	5.026	1.2, $gl = 2$	qst	2×530 nm, 500 ps, 1.4×10^{14} W/cm^2	double-sided foil 1.7 cm long	[88Mac]
			2.2	qst	1×530 nm, 500 ps, 3.5×10^{14} W/cm^2	foil 2.5 cm long	[90Mac1]
	[Co] 4d–4p $J = \frac{5}{2} - \frac{7}{2}$	5.176	0.7	qst	3.5×10^{14} W/cm^2	satellite line of a [Ni] line at this intensity	[90Mac1]

(continued)

Table 7.1.4 continued.

Target, Z	Ion, Transition, J	Wavelength [nm]	Gain [cm^{-1}], gain × length output	Operation regime	Pumping	Target configuration	Ref.
Ytterbium 70	[Ni] 4d–4p $J = 0$–1	5.026	6.6, $gl = 11$ divergence 1.5 mrad	qst	1053 nm, 100 ps, 240 J, 2 pulses, 4 % prepulse, delay 1.5 ns	flat double-slab (each 1 cm)	[99Dai]
Hafnium 72	[Ni] 4d–4p J =0–1	4.7	3.6, $gl = 6$	qst	1053 nm, 100 ps, 240 J, 1 pulse, 4 % prepulse, delay 1.5 ns	flat double-slab (each 1 cm)	[99Dai]
Tantalum 73	[Ni] 4d–4p $J = 0$–1	4.48	2.3, gain duration 250 ps	qst	2×530 nm, 5.5 kJ, 500 ps, $I = 1.4 \times 10^{14}$ W/cm^2	foil 2.5 cm long	[90Mac2]
			3.2	qst	1×530 nm, 500 ps, $I = 2.4 \times 10^{14}$ W/cm^2	foil 2.5 cm long	[90Mac1]
			2.3	qst	1×530 nm, 500 ps, $I = 4.6 \times 10^{14}$ W/cm^2	foil 1.7 cm long	[90Mac1]
	[Co] 4d–4p $J = \frac{5}{2} - \frac{7}{2}$	4.609	2.2	qst	1×530 nm, 500 ps, $I = 4.6 \times 10^{14}$ W/cm^2	foil 1.7 cm long, satellite line, disappears at lower intensities	[90Mac1]
Tantalum 73	[Ni] 4d–4p $J = 0$–1	4.48	lasing observed	qst	1053 nm, 100 ps, 240 J, 1 pulse, 4 % prepulse, delay 1.5 ns	flat double-slab (each 1 cm)	[99Dai]
Tungsten 74 (theory)	[Ni] 4d–4p J =0–1	4.32	220, $gl = 20$ $gl = 6$ 8.7, $gl \sim 1$	tr tr tr	1053 nm, 1 ps, 100 ps 250 nm, 1 ps, 40–50 ps prepulse	aerogel curved 1 mm long aerogel slab solid slab 1 mm	[98Dec]
Tungsten 74	[Ni] 4d–4p J =0–1	4.32	2.6, $gl = 7$ 20 μJ, 70 ps	qst	2×530 nm, ~ 5 kJ, 500 ps, $I = 3.1 \times 10^{14}$ W/cm^2	foil 2.5 cm long	[90Mac2, 92Mac]
Gold 79	[Ni] 4d–4p $J = 0$–1	3.56	2.2, $gl = 2.8$	qst	530 nm, 5.6×10^{14} W/cm^2	foil 1.26 cm long	[92Mac]

the Optical-Field-Ionization (OFI) rather than by the electron collisions were used in the most efficient setups of the recombination XRLs working on the transitions to the ground state.

An overview of the realized recombination XRLs is given in Table 7.1.5.

7.1.4.3 Optical-field ionization (OFI) X-ray lasers

7.1.4.3.1 Optical-field ionization as a plasma source

If a high-intensity, ultrashort laser pulse irradiates a gas target, atoms can be ionized in the tunnel regime in which the resulting free-electron energies can be predicted and reasonably well controlled [86Amm, 89Bur, 90Bur, 94Glo]. Optical-Field-Ionization (OFI) occurs when the oscillatory electric field of the laser pulse becomes comparable (or larger) than the Coulomb forces attracting the electrons to the nucleus [86Amm]. The potential barrier will be reduced and under these conditions the ionization process occurs either by tunneling or Barrier Suppression (BS). The electrons released acquire some kinetic energy depending on the phase of the optical field at the release moment. This is the residual energy which determines the temperature of the created plasma and sometimes is termed as ATI (Above-Threshold-Ionization) energy. This energy depends first of all on the polarization of the ionizing optical field but also on the laser intensity or strength of the optical field and its wavelength. Linear polarization causes the residual electron temperature to be very limited while the circular polarization increases the ATI energy enormously. While both ionization variants lead to a non-Maxwellian Electron Energy Distribution Function (EEDF), the character of the latter is dramatically different. The linearly polarized wave leaves the plasma with some excess of cold electrons and a long hot electron tail. It is well approximated by a double-Maxwellian distribution. The circularly polarized wave interacts with the atom/ion during the whole wave period which causes increase in the residual energy and shows very specific, multi-peak EEDF characterized by the quiver energy (energy of the electron in the electromagnetic field). Linearly polarized laser beams produce relatively cold free electrons which are suitable for recombination excitation of X-ray lasers [89Bur, 90Bur, 95Chi, 97Gol]. On the other hand, the circularly polarized laser beam produces higher energetic electrons which can be preferentially used for collisional excitation.

The OFI-X-ray laser scheme has the advantage of strongly reduced pump energy requirements, since the oscillatory high electric field of the driving laser pulse requires high intensity but not energy. As a consequence the low pump energy requirements ($E_{\mathrm{in}} \leq 1$ J) of this XRL scheme make the work at high repetition rates (10 ... 100 Hz) very realistic.

7.1.4.3.2 Propagation issues of OFI

OFI medium is characterized by a very intense ionization process. This results in rapid changes of the electron density which temporally and spatially reflect to some extent the intensity distribution in the ionizing beam. Usually it means, that the maximum plasma density is in the central part of the area traversed by the beam. Hence, as the beam deflection in plasma occurs outward the high-density area the ionization-induced refraction deflects parts of the beam out of the ionized medium. As this process is already present at a relatively low level of the intensity in the convergent beam, it happens at the beginning of the pulse leading edge. Thus, the rest of the beam, including the intensity peak, starts to diverge already before it achieved geometrical focus of the focusing system. As a result the maximum peak intensity in the beam is strongly reduced and its position is shifted towards the focusing system (Fig. 7.1.24).

There are two common approaches to reduce the described effect. The first one tries to place the geometrical focus shifted relative to the medium center to the position determined by compensation

Table 7.1.5. Overview of the realized recombination XRLs (tr – transient/short-lived inversion).

Target, Z	Isoelectronic sequence, Transition	Wavelength [nm]	Gain [cm^{-1}], gain × length output	System	Pumping	Target configuration	Ref.
Lithium, 3	hydrogenlike, $n = 2$–1	13.5	11 $gl = 5.5$	tr, tw		LiF-microcapillary, inherent traveling wave	[97Gol]
Boron, 5	hydrogenlike, $n = 3$–2	26.2	14–19, $gl \sim 5$	tr, tw	248 nm, 20 ns, 0.2 J for plasma forming, 1064 nm, 8 ns, ≤ 450 mJ, 10^{14} W/cm^2	350 µm B_2O-microcapillary, 3.5 mm long, inherent traveling wave	[98Kor]
Carbon, 6	hydrogen-like, $n = 3$–2	18.2	$G = 6.5$ gain per one medium transit averaged over the line profile, enhancement $(\exp(G) - 1)/G = 100$	tr	10.6 µm, 75 ns, 300 J, 5×10^{12} W/cm^2, plasma confined by a magnetic field of 90 kGauss	solid (disc) carbon target with an XUV mirror, plasma column length 1 cm	[85Suc]
Carbon, 6	hydrogenlike, $n = 3$–2 Balmer-α	18.2	12.5	tr	1053 nm, 2 ps, 20 J, 6×10^{15} W/cm^2	7 µm carbon fiber, 0.5 cm long	[95Zha]
Carbon, 6	hydrogenlike, $n = 3$–2 Balmer-α	18.2	$gl \sim 5$	tr, tw	1064 nm, 1.5 ns, ≤ 5 J, 10^{14} W/cm^2, delay 120 ns	350 µm microcapillary, 10–15 mm long, inherent traveling wave	[95Mor]
Nitrogen, 7	heliumlike, $n = 3$–2 3^1D–2^1P	18.52	2.6 space resolved 3.3 time resolved	tr	1053 nm, 100 ps, 15 J, 4×10^{13} W/cm^2	7.8 mm boron nitrade slab	[96Oza]
Copper, 27	sodiumlike, 5g–4f	11.1	8.8	tr		7 µm copper-coated fiber, 0.46 cm	[96Zha1]

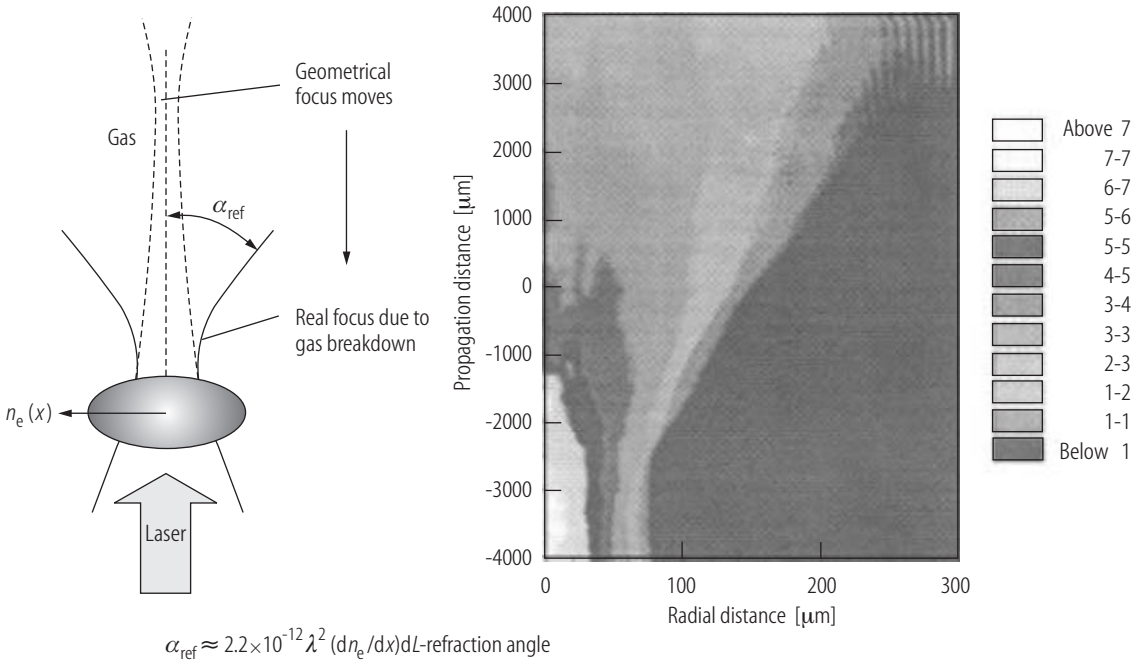

Fig. 7.1.24. The intense laser pulse causes refractive-index changes by modification of the transverse electron density gradient (dn_e/dr) due to field ionization and this leads to reduction in the real focus length in the gas. As a result the beam divergence increases quickly and the geometrical focus is shifted backward. On the right side a contour plot of the distribution of ionization stages in the ionized gas is given showing clearly the changes in pulse focusing. Original geometrical focus is at the position "0". The scale bars on the right side show either the constant level of the ionization stage (a–a, e.g. 1–1) or the range in which the ionization stage varies in the given area (a–b, e.g. 1–2).

of the ionization-induced refraction. This method is applicable to the medium of a limited volume. The second method is based on applying the waveguiding effect which brings the medium elongation and enables its penetration with negligible refraction losses (Fig. 7.1.25).

The ray deviation angle of the ionizing pulse after propagating a distance z in the ionized medium (see Fig. 7.1.5) is equal to $\Theta_R \approx (n_e/n_c)\, z/L_D$ [94Ede], where n_c is the critical density, $L_D = b^2/[r\,(2\ln 2)]$ is the scale length of the transverse intensity gradient for a Gaussian pump pulse and r is the transverse/radial coordinate (n_e is proportional to the intensity distribution in the transverse direction). One can define a distance z_R after which the deviated X-ray radiation propagating in the medium doubles its transverse deviation

$$z_R = b\left(\frac{n_c}{n_e \ln 2}\right)^{1/2} . \tag{7.1.37}$$

In practice, this means that ionization-induced refraction causes a reduction of the effective length of the active medium. The problem of ionization-induced refraction can be reduced by creating a plasma channel with the minimum of the radial density distribution on the axis prior to the field ionization by an intense, short laser pulse [93Dur]. The "waveguiding" effect in such a plasma pipe is sketched in Fig. 7.1.25. The electron density difference δn_e (off-axis density minus on-axis density) which the laser beam "tolerates" over its spatial profile before defocusing is given by

$$\frac{\delta n_e}{n_c} = \frac{\lambda^2}{(\pi w_0)^2} , \tag{7.1.38}$$

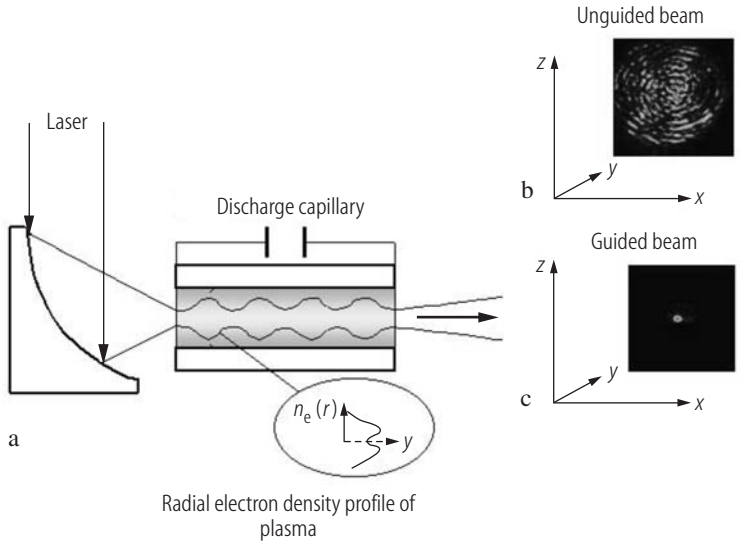

Fig. 7.1.25. (**a**) Sketch of waveguiding in a plasma pipe. Balance between refractive defocusing and self-focusing stabilizes the beam propagation over a length of several cm. The insert shows the radial electron density distribution required for guiding of the pump and X-ray beams. Two images on the right side show a laser beam at the capillary exit for two extreme cases: (**b**) discharge is switched-off and the laser pulse is unguided; (**c**) discharge is on – the beam is guided.

where n_c is the critical density of the plasma at the laser wavelength λ and w_0 is the 1/e-radius (radius at the intensity level equal to I_{max}/e) of the laser beam at focus. For a fixed focal geometry a shorter laser wavelength will permit penetration to a higher plasma density (n_c varies as the inverse square of the wavelength); higher plasma density results in higher gain, especially, of the recombination-pumped laser system.

7.1.4.3.3 OFI with linearly polarized pumping pulse

In contrast to the conventional recombination laser cooling is, in principle, not required in the OFI XRL recombination scheme. The recombination process takes the advantage that a remarkable amount of the low-energetic rapidly recombining electrons is produced in the ionization process applying a linearly polarized laser pulse. Many of the electrons belonging to the hot tail of the EEDF are eliminated by so-called collisional decoupling. They possess a too high energy to collide efficiently, i.e. to transfer significant part of their energy to the ions.

OFI excitation facilitates lasing down to the ground state of the lasant ions. By a suitable choice of the pump laser pulse parameters the ground state can be practically emptied which is extremely important for this type of the laser transitions. Fractional population larger than 10^{-3} remaining in the ground state can significantly reduce the expected gain [92Ede]. The situation complicates the fact that the ground state has only slow energy sink channels. Generally, the population inversion shows a short lifetime and a low saturation intensity.

Unwanted heating of the plasma in the case of a linearly polarized driving pulse can be caused by:

- the electrons that do not return their energy to the laser field (referred to as ATI energy) [89Bur, 90Bur, 91Pen, 92Rae],
- electron–ion collisions in the optical field (inverse-bremsstrahlung process with the efficiency determined by the electron quiver energy),
- stimulated Raman backscattering [94Ede].

Table 7.1.6. Prospects for short-wavelength recombination XRLs pumped by optical field ionization (pumping pulse duration $<\sim$ 250 fs) [93Nag, 94Ede, 97Gol].

Ion		Wavelength [nm]	Radiative transition time for $n = 2$–1 [ps]	Required pump intensity [10^{18} W cm^{-2}]
Li^{2+}	H-like	13.5	26	0.2–0.3
Al^{10+}	Li-like	5.2		1
B^{4+}	H-like	4.8	3.4	1–2
C^{5+}	H-like	3.4	1.6	2–4
N^{6+}	H-like	2.5		30
O^{7+}	H-like	1.8	0.53	7–10
Na^{10+}	H-like	1.0	0.15	20–30

The energy efficiency of OFI systems is significantly lower than 10^{-6} (i.e. at least one order of magnitude lower than that of the conventional collisional scheme) [92Ede]. Therefore, the output energies of OFI-lasers, supposing an input energy of $E_{in} \leq 1$ J, are equal to several tens of nanojoules. Although the output energy per pulse is low compared to conventional collisional XRLs, which have outputs in the μJ ... mJ range, the OFI lasers can operate in principle at much higher repetition rates because of the reduced requirements regarding the driving energy. Additionally, a very narrow emitted line can be important in some applications. Thus, OFI lasers can bridge the gap between conventional XRLs and the high-harmonics generation with a kHz repetition rate or even quasi-continuous output of synchrotrons.

A reasonable gain at 13.5 nm on the Lyman-α transition in Li^{2+} has been reported in [93Nag] for the recombination scheme. Lithium was primarily ablated from a solid metallic target by a long and relatively less intense laser pulse. The resulting plasma plume was then irradiated by a high-intensity, short-pulse laser which generated H-like Li^{3+}. Strong lasing with a gain of 11 cm^{-1} on the $n = 2$–1 transition was observed in this scheme by irradiating a solid LiF-microcapillary with the length between 1 and 5 mm and a diameter of 0.3 mm [97Gol]. The first irradiating laser pulse from a 2 Hz Nd:YAG laser (100 mJ, 5 ns) created and pre-formed the plasma and the second one being a high-intensity KrF-pulse of 60 mJ , 250 fs, arriving a few hundred ns later ionized by tunneling the pre-formed plasma. The short pulse was tightly focused to an intensity of 2×10^{17} W/cm^2 at the capillary entrance. The preformed plasma was created inside the microcapillary (and practically no plasma of significant density was present outside) by the ablation of the capillary walls by a low-power laser (this is in contrast to the discharge-driven capillary).

The prospects for XRLs emitting short wavelengths down to 1 nm are given in the Table 7.1.6. Short, linearly polarized pump pulses are used in the experiment or assumed in numerical simulations [97Gol]. The required driving intensities are now available in several laboratories operating CPA-Ti:sapphire lasers or KrF-lasers.

7.1.4.3.4 OFI with circularly polarized pumping pulse

In this approach, proposed in [88Cor, 94Lem], a very intense, circularly polarized pump laser pulse is used to produce a very hot and highly ionized plasma. The intense circularly polarized femtosecond driving laser pulse ionizes by tunneling a gaseous target with the ionization rates varying exponentially with laser intensity [89Bur, 90Bur]. As a result a non-Maxwellian distribution covering a wide range of energy (from hundreds of eV to several keV) necessary to excite collisionally the ion species is created in the plasma. In contrast to the case of linearly polarized driving pulses the end of the circularly polarized laser pulse retains the electrons with a kinetic energy that is equal to the *quiver energy* ε_q (or ponderomotive potential U_p) at the time of ionization. Quantitatively

$$\varepsilon_q = U_p = e^2 E_p^2/(4 m_e \omega_p^2) \tag{7.1.39}$$

with E_p : averaged laser field, ω_p : laser frequency and m_e : electron mass.

The collisional OFI-scheme allows XRL for scaling to shorter wavelengths in accordance with the isoelectronic scaling rules Ne-, Ni- or Pd-like ions. However, the required intensity has to be very high in order to allow for both the creation of the necessary ion stage and electron heating. For example a Ni-like (Xe^{26+}) XRL at a wavelength of $\lambda \sim 10$ nm would require an intensity of 5×10^{18} W/cm^2 [92Aug, 96Jan].

The first realization of the collisional OFI-XRL in Pd-like Xe [95Lem] was reported in 1995. This result opened a route towards table-top, high-repetition-rate XRLs. However, it took five years to reproduce and improve this original result. Gain saturation on the 5d $^1S_0$–5p $^1P_1$ transition at 41.8 nm was achieved in 2000 by focusing of a 330 mJ, 35 fs circularly polarized Ti:sapphire laser pulse into a gas cell filled with 15 Torr of Xe [01Seb]. The kinetic energy of the released electrons varied from ~ 9 eV for the first electron ionized to ~ 550 eV for the eighth electron ionized. The last four ionized electrons are expected to have energies greater than 104 eV, being suitable to contribute to the collisional excitation of the upper laser level. The collisional OFI-scheme allows for scaling to shorter wavelengths and very recently lasing on the 4d–4p transition in Ni-like Kr at 32.8 nm was demonstrated by focusing of a 760 mJ, 30 fs circularly polarized Ti:sapphire-laser ($\lambda = 800$ nm) pulse into a gas cell filled with 20 Torr. The laser intensity was higher than 1×10^{17} W/cm^2, which is sufficient to create Kr IX ions (the corresponding ionization threshold is 2.6×10^{16} W/cm^2 [91Aug]). A rapid nonlinear increase of the lasing signal with the driving energy and subsequent very high small-signal gain coefficient of 78 cm^{-1} were reported [02Seb1]. However, it is worth noting that the output pulse energy of the system is relatively low and only slightly higher than signals from higher harmonics at comparable wavelengths. One of the most important issues in this scheme is increase in the medium volume enabling boosting of the output.

In Table 7.1.7 an overview of realized OFI XRLs is given.

7.1.4.4 Inner-shell photoionization X-ray lasers

A possible excitation of an Inner-Shell PhotoIonized (ISPI) XRL in neon by K_α radiation was depicted in Fig. 7.1.11. The target is a thin beryllium foil coated on the front side with a high-Z material to emit efficiently hard X-rays of the required energy. The rear side of the target is coated with frozen neon. The beryllium foil acts as an absorber for the low-energy X-rays. Additionally the Be foil should separate the hot region emitting X-rays from the lasing volume in order to prevent thermal ionization of Ne. The X-rays propagating through the foil photoionize (remove) the 1s electrons of the Ne atoms creating a population inversion and gain on the $(1s)^{-1} \rightarrow (2p)^{-1}$ (where "−1" superscript denotes an electron hole) transition of singly ionized neon. Rapid Auger decay depletes the $(1s)^{-1}$ upper laser level. Additionally electron impact ionization can directly populate the lower laser level $(2p)^{-1}$ limiting the gain lifetime or indirectly reduce the population inversion because of a reduction in the neutral population that feeds the upper laser level. Therefore, the primary process that limits the duration of the population inversion is not the self-termination but the ionization process by electron impact.

One of the possible solutions could be mixing of a large amount of hydrogen with the lasant material [92Kap]. The scaling of the required pump energy E_p for a K_α ISPI XRL assuming a 20 fs X-ray pumping pulse can be formulated as E_p [J] $= (4.5/\lambda$ [nm]$)^2$ [96Mat, 98Moo]. According to that a K_α ISPI XRL with a 1 nm wavelength would require an X-ray pulse of ~ 20 J energy.

It was not possible to produce such a short and energetic incoherent X-ray pulse in the past and there is no clarity how to generate it in the future. Experiments using arbitrary focal spots of required intensity can help to get more insight into the kinetic issues of lasers based on inner-shell photoionization and consider other plausible approaches. It was proposed in [92Bor] that relativistic channeling of a short laser pulse in a cylindrical target could expel electrons radially by the charge-displacement effect. The channel surrounded by a high-Z material converter could

Table 7.1.7. Overview of realized OFI XRLs.

Target, Z	Ion, Transition	Wavelength [nm]	Gain [cm^{-1}], gain × length output	System [a]	Pumping configuration	Target configuration	Ref.
Lithium, 3	Li^{2+}, $n = 2$–1 (Lyman-α)	13.5	20 cm^{-1}	recomb.	249 nm, 20 ns, 200 mJ for plasma forming, 50 mJ, 0.5 ps, 10^{17} W/cm^2 for OFI, longit. pumped	flat slab, 2 mm	[93Nag]
Lithium, 3 (predicted)	Li^{2+}, $n = 2$–1 (Lyman-α)	13.5	1–10 cm^{-1} at $T_e = 3$–1 eV	recomb.	400 nm, < 1 ps, 2×10^{17} W/cm^2	gas	[96Don]
Lithium, 3	Li^{2+}, $n = 2$–1 (Lyman-α)	13.5	dominant line	recomb.	1053 nm, 12 ns, 1 J for plasma, 248 nm, 0.4 ps, 100 mJ, 10^{17} W/cm^2 for OFI, longit. pumped	LiF-slab, 2 mm	[93Pol]
Lithium, 3	Li^{2+}, $n = 2$–1 (Lyman-α)	13.5	11 cm^{-1}, 5.5	recomb.	1053 nm, 5 ns, 100 mJ for plasma, 248 nm, 250 fs, 60 mJ, 2×10^{17} W/cm^2 for OFI, longit. pumped	LiF-microcapillary, 5 mm, diamter 0.3 mm	[95Spr]
Carbon, 6	hydrogenlike, C^{5+} $n = 3$–2 $n = 4$–2	 18.2 13.5	7.1 cm^{-1}, 6.5	recomb.	1053 nm, 12 ns, 1 J for plasma, 248 nm, 0.4 ps, 100 mJ, 10^{17} W/cm^2 for OFI, longit. pumped	cylindrical fiber, 6 mm	[93Pol]

(continued)

Table 7.1.7 continued.

Target, Z	Ion, Transition	Wavelength [nm]	Gain [cm^{-1}], gain × length output	System [a]	Pumping configuration	Target configuration	Ref.
Oxygen, 8	nitrogenlike, O^{1+} $2p^2 3s\ ^2P–2p^3\ ^2D$ carbonlike, O^{2+} $2p2s\ ^3P–2p^2\ ^3P$	61.7 37.4	~ 25 cm^{-1}		800 nm, 150 fs, 80 mJ	gas	[95Chi]
Xe, 54	paladiumlike, Xe^{8+} 5p–5d	41.8	13.3 cm^{-1}, 11	coll.	800 nm, 30 fs, circular pol., 3×10^{17} W/cm^2	gas cell, 12 Torr Xe	[95Lem]
Xe, 54	paladiumlike, Xe^{8+} 5p–5d	41.8	67 cm^{-1}, 15, 5×10^9 phot./pulse, saturation	coll.	800 nm, 35 fs, 330 mJ, circular pol., 3×10^{17} W/cm^2, contrast $\geq 10^6$	gas cell, 15 Torr Xe	[01Seb]
Krypton, 36	Ni-like, Kr^{8+} 4d–4p	32.8	78 cm^{-1}, saturated	coll.	800 nm, 35 fs, 600 mJ, circular pol., 5×10^{17} W/cm^2, contrast $\geq 10^6$	gas cell, 20 Torr Kr $l = 5.5$ mm	[02Seb2]
Xe, 54	palladium-like Xe^{8+} 5p–5d	41.8	strengthened by factor 4 in comparison to the experiments with a cell	coll.	800 nm, 37 fs, 240 mJ, 2.5×10^{17} W/cm^2 $C = 4.5$ nF, $I = 105$ A	gas-filled capillary $L = 30$ mm, $d = 210$ µm, $p_{Xe} = 20$ mbar, Xe:$H_2 = 1 : 3$, $p = 120$ mbar	[03But]

[a] recomb.: recombination, coll.: collisions as pump mechanism.

in turn generate the high-flux X-ray pulse. The X-ray pulse would finally photoionize the outer cylinder of lasing material in the traveling-wave regime.

It is worth noting that in contrast to these "pure" inner-shell XRLs there is also another type of X-ray lasers that can work on inner sub-shell transitions. The advantage of these collisional XRLs is a significant shortening of the wavelength for a reasonable increase in the pump laser energy. According to simulations [97Hea] it should be possible to realize a reasonable gain ($g < 20$ cm^{-1}) on the 2p $\rightarrow$ 2s "inner sub-shell" transitions of the Ne-like $1s^2 2s 2p_{1/2}^2 2p_{3/2}^4 3s$ ($J = 0$) to $1s^2 2s^2 2p_{1/2} 2p_{3/2}^4 3s$ ($J = 1$) transition. The calculated gain remains lower than that for the traditional 3p $\rightarrow$ 3s transition and several attempts failed to demonstrate lasing on this inner sub-shell transitions.

The predicted ISPI-XRLs are listed in Table 7.1.8.

7.1.5 Applications

Remarkable progress has been made during the last few years in several crucial aspects of the development of practical table-top soft X-ray lasers operating as both laser-pumped as well as discharge-pumped devices. Saturation has been demonstrated in several transient collisional X-ray lasers in the range from 30 nm down to 13 nm at pumping energy levels between 10 J and less than 1 J generating short X-ray pulses with energies between 1 μJ and several 10 mJ. OFI-XRLs operating at a repetition rate of 10 Hz have been saturated at $\lambda = 41.8$ and 32.8 nm. A very compact capillary discharge system has been operated at 46.9 nm (26.5 eV) producing pulses with the energy at a millijoule level and a 4 Hz repetition rate with an average power per unit bandwidth that is comparable to the values characteristic for synchrotron beam-lines of third generation and a peak coherent power that is several orders of magnitude higher.

Any use of XRLs for applications demands a good knowledge of their radiative properties like pulse energy, duration, bandwidth, source size, beam divergence as well as spatial and temporal coherences. Sometimes brilliance (brightness) B is used to characterize and compare the sources.

The peak brilliance of some soft X-ray sources and the potential of the X-ray laser as a high peak brilliance source are demonstrated in Fig. 7.1.26.

The average brilliance of XRLs is far from the expected high value necessary for many routine applications. This is mainly caused by the lack of short-pulse pump lasers with the desired average power of ≥ 100 W at pulse energies of few Joules. It is expected, that both the optimization of the excitation efficiency of the X-ray lasers as well as the development of pump lasers with higher repetition rate (diode-pumped solid-state lasers) will soon lead to further reduction in the size, complexity, instability and cost of the X-ray lasers with high average power. A widespread use of these coherent sources in numerous scientific and technological applications is therefore expected in the next years. Some of the X-ray lasers have already been used for applications demonstrating their potential as a coherent and (partially) short-pulse X-ray source.

7.1.5.1 Diagnostics with X-ray lasers

Owing to their high brightness, X-ray lasers are well suited as a versatile diagnostics tool in interferometry, microscopy, and reflectometry [98Li, 99Art1, 99Nil, 01Kub, 02Oza]. Short-pulse XRLs are required for probing high-density, laser-produced plasmas. Large plasmas (of 3 mm size) with electron peak densities $n_e \geq 4 \times 10^{21}$ cm^{-3} have been already probed by Moiré-deflectometry [93Res]. At such high densities an optical laser beam cannot propagate through a plasma.

Table 7.1.8. Predicted ISPI-XRLs (tr: transient).

Target, Z	Ion, Transition	Wave-length [nm]	Gain [cm^{-1}], gain × length output	System	Pumping configuration	Target configuration	Ref.
C 6	C^{1+}, 1s–2p (K–L)	4.5	10	tr	20 fs, 1 J	foil	[94Moo]
Neon 10	Ne^{1+}, 1s–2p	1.46	15, 0.4 μJ	tr	X-ray pulse, 100 fs, 5 J, 10^{17} W/cm^2	5 μm × 1 cm area	[94Str]
Neon 10	Ne^{1+}, 1s–2p	1.46	∼ 10	tr	X-ray pulse, 50 fs, 3 J	foil, 10 μm × 1 cm	[92Kap]
Na 11	Na^{+}, $2p^5 3s$–$2p^6$	37.2	≤ 20 at $n_a \sim 10^{18}$ cm^{-3}	tr	X-ray pulse, ≤ 1 ps, 3×10^{13} W/cm^2	100 μm × 1 cm	[67Dug, 97Li]

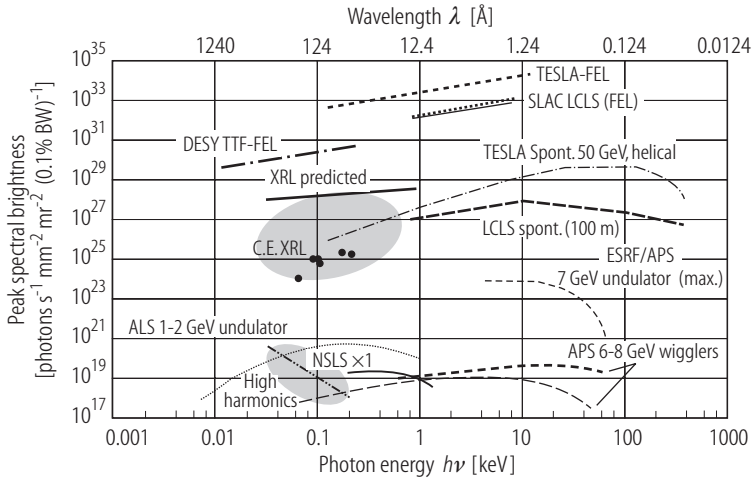

Fig. 7.1.26. Peak brightness of different EUV and X-ray sources – High Harmonics (HH), synchrotrons, Free-Electron Laser (future FEL), and XRLs – showing the great potential of the XRL as small-sized bright coherent source.

Imaging of biological samples requires above all short, close to the "water window" wavelengths that cover the range between 2.3 nm and 4.4 nm. At these wavelengths the contrast between water and carbon-containing substrates (DNA, proteins, etc.) is very high and in-situ microscopy of wet samples is possible.

Some Ni-like QSS X-ray lasers operating within or near the "water window" have been demonstrated [90Mac1, 92Mac]. Wavelengths just longer than the carbon K-edge are also of interest. For X-ray holography, the maximum scattering of carbon-containing structures in water is expected to be just above 4.4 nm [89Lon]. It has been shown that for X-ray holography the X-ray dosage received by the cell is minimized for a given image resolution if the illumination wavelength is in the neighborhood of the long-wavelength-side of the carbon K-edge [89Lon, 82Sol]. This is also a useful wavelength for imaging gold-tagged biological specimens [92DaS] and for the use of carbon-containing multilayer mirrors for the optical elements of an imaging system. Whereas very interesting biological studies could be conducted using the available XRLs at $\lambda = 10 \ldots 20$ nm, crystallography and semiconductor-related research requires compact X-ray lasers operating at 1 nm or shorter wavelengths.

With the upcoming EUV-lithography at wavelengths of approximately 13 nm, X-ray lasers emitting pulses in this range (e.g. collisional Ni-like Ag XRL at 13.9 nm and Ni-like Cd XRL at 13.2 nm) could become attractive as a source for precision reflectometry, interferometry or other types of metrology of samples for lithography facilities. Here, particularly XRLs with high repetition rates could be important. They may also be used for the pump-probe experiments in basic sciences, and for many experiments in material sciences such as photoelectron spectroscopy [01Zei, 94Ede]. Here OFI-XRLs would be very promising sources. A discrete tunability, obtained by using different lasing ions, allows for study of different core levels. Continuous tunability, which is not available at the present XRLs, is not required, because the energy of the ejected photoelectrons is measured to determine the binding energy giving a known photon energy. The photon energy is known accurately because of the narrow bandwidth ($\Delta\lambda/\lambda = 10^{-4} \ldots 10^{-6}$) of the XRL. The number of photons per pulse is expected to be large, but below the limit associated with excessive space-charge effects. A μJ-output energy of the XRL should deliver the necessary number of photons per pulse.

Many experiments like photo-electron spectroscopy or nonlinear optics in the soft X-ray range need a sufficiently high X-ray intensity. Therefore, development of suited focusing optics is necessary

and the first adaptive optics for the wavefront correction of the X-ray laser pulses was reported recently [94Ede, 01Zei].

7.1.5.2 Interferometry

The first XRL-based interferometry of a high-density plasma was reported in 1995 using a Mach–Zehnder-type interferometer working with a neon-like yttrium laser at 15.5 nm [95DaS1, 95DaS2]. The short wavelengths emitted coherently by X-ray lasers enable sampling much higher densities than that possible with a visible coherent radiation

$$(n_{\mathrm{e\ max}})^{1/2} = 3.4 \times 10^{14}/\lambda_{\mathrm{x}} \quad [\text{Å}] \,. \tag{7.1.40}$$

However, this technique based on amplitude division needs X-ray beam splitters of a very high optical quality (flatness $< \lambda/20$ over the aperture). Figure 7.1.27 shows an example layout of such an XUV interferometer.

The currently available efficient reflective optics for the wavelengths between 13 and 15 nm based on the Mo–Si multilayer technology allows for beam transportation with reasonable losses. Membrane beam splitters using some aspects of this technology offer transmission between 10 and 17 %. Another promising method is the wave-front division technique by a shaped mirror, first realized with XUV synchrotron radiation [95Pol]. This method has the advantage of being nearly wavelength-independent, since the reflection occurs under grazing incidence. X-ray beam division can also be realized by an Fresnel bimirror, which however requires a high transverse coherence of the beam to produce well visible interference fringes.

A successful experiment applying a Ne-like zinc XRL working at 21.2 nm and a Fresnel bimirror (two mirrors arranged as a "ridged roof" with a small angle between them) was reported in [97Alb, 03Moc]. An interferometer of this type was used for *in-situ* investigation of electrical-field-induced breakdown on a surface of a niobium-bimorphe mirror [98Zei]. The XUV interferometry gives direct information (in one shot) on the surface shape during any impact on this surface. Influence of the electric field on the surface was observed with the XUV interferometry at 21.2 nm. It was shown that at a field of 14 MV/m perturbations of the interferometer's fringe pattern begin to appear. In principle, XRL-based XUV interferometry appears to be a powerful tool to investigate any stressed surfaces (with high flatness) and could be of great importance for electronic components and for thin-layer technology.

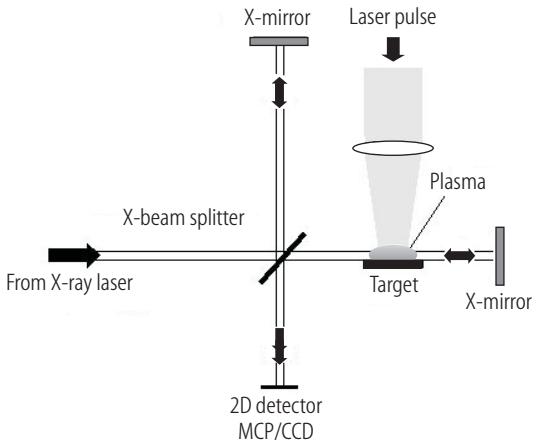

Fig. 7.1.27. Set-up of a Michelson-type interferometer to probe dynamics of a laser plasma.

7.1.5.3 Reflectometry

One of the important applications of the XRL could be determination of XUV optical constants by reflectometry [99Art1]. In this method the optical constants at each wavelength can be found by fitting the measured angular dependence of the reflectivity with the Fresnel formula [97Sou]. A deviation of the experimental data from the calculated curve for the bulk material is a hint that there is an additional contribution to the reflectivity, which is likely due to an additional (oxide) surface layer. This method can in principle provide not only optical constants of the bulk material but also information about the surface characteristics of the sample, and could be a powerful tool for measurement of the quality of EUV-coatings.

In [99Art1] it was shown that when the surface layer is optically thin, the reflection from the bulk material can be separated from the reflection caused by the surface layer. Therefore, the optical constants of solids can be measured even on partially contaminated or oxidized samples. Using a repetitive table-top capillary discharge Ne-like Ar X-ray laser at 46.9 nm (26.5 eV) with an average power of up to 1 mW the optical constants of Si, GaP, InP, GaAs, GaAsP and Ir were determined [99Art2]. The high intensity of an X-ray laser was an advantage for accurate measurements of the reflectivity at near-normal incidence, where the reflectivity of many of the materials is low.

7.1.5.4 Excitation of nonlinear processes

X-ray lasers have, owing to their high brightness, the potential to cause excitation processes not available with conventional incoherent X-ray sources or high-harmonic generation. Multiphoton processes as well as nonlinear laser–matter interaction in the soft X-ray range need high intensities, which to date can be delivered in principle only by XRLs. Among others, multiphoton inner-shell spectroscopy, XUV nonlinear optics to generate new short wavelengths a well as applications of such processes to metrology (measurements of ultrashort XUV pulses using correlation techniques) are in the focus of the activities. For example, an interesting elementary process that needs a demonstration is two-photon ionization of 4d inner-shell electrons in Xe. The removal of an electron from the $4d^{10}$ shell requires an energy of 67.5 eV ($4d_{5/2}$ level) and 69.5 eV ($4d_{3/2}$ level). Therefore, the absorption of two photons of a Ne-like zinc XRL (58.4 eV) is necessary to create the hole. The resulting excitation of the ion with the core-hole would rapidly decay by an Auger process, which together with the accompanying ejection of the second electron would lead to a doubly charged ion in the ground state $5p^4$.

Also macroscopic effects, like pumping of photo-ionization XRLs or inner-shell XRLs might be realized using bright X-ray lasers as a pump source.

It is possible now to produce diffractive optics (e.g. Bragg–Fresnel lenses, which are practically free of geometrical aberrations) or adaptive mirrors in order to realize resolution up to several microns. Therefore, intensities (in a focal spot) higher than 10^{14} W/cm^2 should be possible soon. At these intensities very dense plasmas could be produced with the parameters which may differ from those produced by optical laser pulses. The available XRL intensities will also allow for studies of the excitation of luminescence processes for example in ionic crystals. These crystals are interesting for various practical applications, like scintillation detectors for medical and nuclear application and also for radiography and crystallography. Short-pulse XRL excitation could allow to excite the luminescence "instantaneously" or to study a nonlinear behavior of the luminescence efficiency. It was reported on UV luminescence studies of CsI with 58.4 eV photons of a 21.2 nm zinc XRL [99Jam]. Further experiments are necessary to get more information about creation of the luminescence centers.

7.1.6 Conclusion

The common laser principle rests on stimulated emission in an optically active medium which exhibits population inversion. This principle has been enormously successful during the last 45 years, leading to the control of coherence in visible and infrared light and, thus, to light with unprecedented new properties like stability, monochromaticity, power, or pulse duration. Today, lasers are indispensable tools in almost all areas of science, technology, or medicine.

Although it would be very desirable to extend the principle of stimulated emission towards short wavelengths in the VUV, EUV or X-ray region, this has not been achieved on a broad scale so far. The reasons can be traced back to basic physics, most importantly to the creation of active media with sufficiently high transition frequencies (e.g. atomic ions), and to the power requirements for creating and maintaining a population inversion in such systems. Stability considerations of the active medium (necessarily a dense plasma), power input into the target and beam propagation of the X-radiation are additional issues to be observed.

Considerable progress has been achieved in recent years, mostly driven by an increased understanding of the physics of dense plasmas, and by the availability of new, high-power lasers that can be used as pump sources. The most recent "table-top" X-ray lasers are operating around 10 nm at 10 Hz repetition rates with pump pulse energies of about 1 J. This energy level is easily achievable with laser systems of the laboratory scale. The peak brilliance of XRLs rivals that of the strongest competing sources (free-electron lasers), while the average power can still be scaled up by one or two orders of magnitude even with today's pump laser technologies, and may reach values at the mW level.

Hence, table-top "X-ray lasers" (more correctly EUV- or XUV-lasers) are taking up the challenge to control the coherence of light also in those spectral regions where wavelength matches the geometrical dimensions of the micro- and nano-objects met in the technologies of the new century. First applications have already been achieved and the numbers are expected to increase dramatically with further progress in the laser technology.

References for 7.1

1887Jae Jaegle, P., Jamelot, G., Carillon, A., Klisnick, A.: J. Opt. Soc. Am. B **4** (1887) 563.

60Mai1 Maiman, T.H.: Nature (London) **187** (1960) 493.
60Mai2 Maiman, T.H.: Phys. Rev. Lett. **4** (1960) 564.

63Gud Gudzenko, G.A., Shelepin, L.A.: Zh. Eksp. Teor. Fiz. **45** (1963) 1445.

67Dug Duguay, M.A., Rentzepis, P.M.: Appl. Phys. Lett. **10** (1967) 350.

69Ics Icsevgi, A., Lamb jr., W.E.: Phys. Rev. **185** (1969) 517.

70McC McCall, S.L., Hahn, E.L.: Phys. Rev. A **2** (1970) 861.

72McC McCorkle, R.A.: Phys. Rev. Lett. **29** (1972) 1428 [Erratum: p. 982].
72Mol Molchanov, A.G.: Sov. Phys. Usp. (English Transl.) **15** (1972) 124.
72Zhe Zherikhin, A.N., Koshelev, K.N., Letokhov, V.S.: Sov. J. Quantum Electron. (English Transl.) **6** (1972) 82.

73Vin Vinogradov, A.V., Sobelman, I.I.: Sov. Phys. JETP (English Transl.) **36** (1973) 1115.

75Arm Armandillo, E., Spalding, I.J.: J. Phys. D **8** (1975) 2123.
75Bon Bonifacio, R., Hopf, F.A., Meystre, P., Scully, M.O.: Phys. Rev. A **12** (1975) 2568.
75Elt Elton, R.C.: Appl. Opt. **14** (1975) 97.
75Hop Hopf, F.A., Meystre, P., Scully, M.O., Seely, J.F.: Phys. Rev. Lett. **35** (1975) 511.

77Dix Dixon, R.H., Elton, R.C.: Phys. Rev. Lett. **38** (1977) 1072.

82Sol Solem, J.C., Baldwin, C.G.: Science **218** (1982) 229.

84Hag Hagelstein, P.L.: Phys. Rev. A **34** (1984) 874.

85Jam Jamelot, G., Klisnick, A., Carillon, A., Guennou, H., Sureau, A., Jaegle, P.: J. Phys. B **18** (1985) 4647.
85Mat Matthews, D.L., Hagelstein, P.L., Rosen, M.D., Eckart, M.J., Ceglio, N.M., Hazi, A.U., Medecki, H., MacGowan, B.J., Trebes, J.E., Whitten, B.L., Campbell, E.M., Hatcher, C.W., Hawryluk, A.M., Kauffman, R.L., Pleasance, L.D., Rambach, G., Scofield, J.H., Stone, G., Weaver, T.A.: Phys. Rev. Lett. **54** (1985) 110.
85Suc Suckewer, S., Skinner, C.H., Milchberg, H., Keane, C., Voorhees, D.: Phys. Rev. Lett. **55** (1985) 1753.

86Amm Ammosov, M.V., Delone, N.B., Krainov, V.P.: Sov. Phys. JETP (English Transl.) **64** (1986) 1191.
86Sie Siegman, A.D.: Lasers, Mill Valey, CA: University Science Books, 1986, p. 301.
86Suc Suckewer, S., Skinner, C.H., Kim, D., Valeo, E., Voorhees, D., Wouters, A.: Phys. Rev. Lett. **57** (1986) 1004.

87Che Chenais-Popovics, C., Corbett, R., Hooker, C.J., Key, M.H., Kiehn, G.P., Lewis, C.L.S., Pert, G.J., Regan, C., Rose, S.J., Sadaat, S., Smith, R., Tomie, T., Willi, O.: Phys. Rev. Lett. **59** (1987) 2161.

87Mac Mac Gowan, B.J., Maxon, S., Hagelstein, P.L., Keane, C.J., London, R.A., Matthews, D.L., Rosen, M.D., Scofield, J.H., Whelan, D.A.: Phys. Rev. Lett. **59** (1987) 2157.
87Ros1 Rosen, M.D., Trebes, J.E., Matthews, D.L.: Comments Plasma Phys. Controlled Fusion **10** (1987) 245.
87Ros2 Ross, I.N., Boon, J., Corbett, R., Damerell, A., Gottfeldt, P., Hooker, C., Key, M.H., Kiehn, G., Lewis, C., Willi, O.: Appl. Opt. **26** (1987) 1584.
87Sil Silfast, W.T., Wood, O.R.: J. Opt. Soc. Am. B **4** (1987) 609.

88Apr Apruzese, J.P., Commisso, R.J., Cooperstein, G., et al.: Proc. SPIE **875** (1988) 2.
88Cor Corkum, P.B., Burnett, N.H.: OSA Proc. Short Wavelength Coherent Radiat. **2** (1988) 225.
88Kap Kapteyn, H.C., Falcone, R.W.: Phys. Rev. A **37** (1988) 2033.
88Lon London, R.A.: Phys. Fluids **31** (1988) 184.
88Mac Mac Gowan, B.J., Maxon, S., Keane, C.J., London, R.A., Matthews, D.L., Whelan, D.A.: J. Opt. Soc. Am. B **5** (1988) 1858.

89Afa Afanasiev, Y.V., Shlyaptsev, V.N.: Sov. J. Quantum Electron. (English Transl.) **19** (1989) 1606.
89Bur Burnett, N.H., Corkum, P.B.: J. Opt. Soc. Am. B **6** (1989) 1195.
89Lon London, R.A., Rosen, M.D., Trebes, J.E.: Appl. Opt. **28** (1989) 3397.
89Nil Nilsen, J.: Phys. Rev. A **40** (1989) 5440.

90Boe Boehly, T., Rusotto, M., Craxton, R.S., Epstein, R., Yaakobi, B., Da Silva, L.B., Nilsen, J., Chandler, E.A., Fields, D.J., Mac Gowan, B.J., Matthews, D.L., Scofield, J.H., Shimkaveg, G.: Phys. Rev. A **42** (1990) 6962.
90Bur Burnett, N.H., Enright, G.D.: IEEE J. Quantum Electron. **26** (1990) 1797.
90Car Carillon, A., Edwards, M.J., Grande, M., Henshaw, M.J.C., Jaegle, P., Jamelot, G., Key, M.H., Kiehn, G.P., Klisnick, A., Lewis, C.L.S., O'Neill, D., Pert, G.J., Ramsden, S.A., Regan, C.M.E., Rose, S.J., Smith, R., Willi, O.: J. Phys. B **23** (1990) 147.
90Elt Elton, R.: X-Ray Lasers, London, San Diego: Academic Press, 1990.
90Mac1 Mac Gowan, B.J., Da Silva, L., Fields, D.J., Keane, C.J., Maxon, S., Osterheld, A.L., Scofield, J.H., Shimkaveg, G.: Phys. Rev. Lett. **65** (1990) 2374.
90Mac2 Mac Gowan, B.J., Maxon, S., Da Silva, L., Fields, D.J., Keane, C.J., Matthews, D.L., Osterheld, A., Scofield, J.H., Shimkaveg, G., Stone, G.F.: Phys. Rev. Lett. **65** (1990) 420.

91Aug Augst, S., Meyerhofer, D.D., Strickland, D., Chin, S.L.: J. Opt. Soc. Am. B **8** (1991) 858.
91Hru Hrubish, L.W., Pekala, R.W.: Energy Technol. Rev. **1** (1991) 20 [UCRL 52000-91-1 (Jan.1991)].
91Pen Pentrante, B.M., Bardsley, J.N.: Phys. Rev A **43** (1991) 3100.
91Roc Rocca, J.J., Marconi, M.C., Szapiro, B.T., Meyer, J.: Proc. SPIE **1551** (1991) 275.

92Aug Auguste, T., Monot, P., Lompre, L.A., Mainfray, G., Manus, C.: J. Phys. B **25** (1992) 4181.
92Bor Borisov, A.B., Borovskiy, A.V., Shiryaev, O.B., Korobkin, V.V., Prokhorov, A.M., Solem, J.C., Luk, T.S., Boyer, K., Rhodes, C.K.: Phys. Rev. A **45** (1992) 5830.
92Car Carillon, A., Chen, H.Z., Dhez, P., Dwivedi, L., Jacoby, J., Jaegle, P., Jamelot, G., Zhang, J., Key, M.H., Kidd, A., Klisnick, A., Kodama, R., Krishnan, J., Lewis, C.L.S., Neely, D., Norreys, P., O'Neill, D., Pert, G.J., Ramsden, S.A., Raucourt, J.P., Tallents, G.J., Uhomoibhi, J.: Phys. Rev. Lett. **68** (1992) 2917.
92Dai Daido, H. et al.: X-Ray Lasers 1992, Fill, E.E. (ed.), IOP Conf. Series **125** (1992) 111.

92DaS Da Silva, L.B., Trebes, J.E., Balhorn, R., Mrowka, S., Anderson, E., Attwood, D.T., Barbee jr., T.W., Brase, J., Corzett, M., Gray, J., Koch, J.A., Lee, C., Kern, D., London, R.A., MacGowan, B.J., Matthews, D.L., Stone, G.: Science **258** (1992) 269.

92DiC Di Cicco, D., Kim, D., Rosser, D., Suckewer, S.: Opt. Lett. **17** (1992) 157.

92Ede Eder, D.C., Amendt, P., Wilks, S.C.: Phys. Rev. A **45** (1992) 6761.

92Fie Fields, D.J., Walling, R.S., Shimkaveg, G., Mac Gowan, B.J., Da Silva, L.B., Scofield, J.H., Osterheld, A.L., Phillips, T.W., Rosen, M.D., Matthews, D.L., Goldstein, W.H., Stewart, R.E.: Phys. Rev. A **46** (1992) 1606.

92Fil Fill, E.E., Bergmann, C., Lyras, A., Schlegel, T.: X-Ray Lasers 1992, Fill, E.E. (ed.), IOP Conf. Series **125** (1992) 147.

92Kap Kapteyn, H.C.: Appl. Opt. **31** (1992) 4931.

92Koc Koch, J.A., MacGowan, B.J., Da Silva, L.B., Matthews, D.L., Underwood, J.H., Batson, P.J., Mrowka, S.: Phys. Rev. Lett. **68** (1992) 3291.

92Lee Leemans, W.P., Clayton, C.E., Mori, W.B., Marsh, K.A., Kaw, P.K., Dyson, A., Joshi, C., Wallace, J.M.: Phys. Rev. A **46** (1992) 1091.

92Lew Lewis, C.L.S., Neely, D., O'Neill, D.M., Uhomoibhi, J.O., Key, M.H., Al Hadithi, Y., Tallents, G.J., Ramsden, S.A.: Opt. Commun. **91** (1992) 71.

92Liv Livage, J., Sanchez, C.: J. Non Cryst. Solids **145** (1992) 11.

92Mac MacGowan, B.J., Da Silva, L.B., Fields, D.J., Keane, C.J., Koch, J.A., London, R.A., Matthews, D.L., Maxon, S., Mrowka, S., Osterheld, A.L., Scofield, J.H., Shimkaveg, G., Trebes, J.E., Walling, R.S.: Phys. Fluids B **4** (1992) 2326.

92Rae Rae, S.C., Burnett, K.: Phys. Rev. A **46** (1992) 2077.

92Sco Scofield, J.H., MacGowan, B.J.: Phys. Scr. **46** (1992) 361.

92Ste Steingruber, J., Chen, S., Fill, E.E.: X-Ray Lasers 1992, Fill, E.E. (ed.), IOP Conf. Series **125** (1992) 115.

93Bur Burge, R.E., Browne, M.T., Charalambous, P., Slark, G.E., Smith, P.J., Lewis, C.L.S., Neely, D.: Opt. Lett. **18** (1993) 661.

93DaS Da Silva, L.B., MacGowan, B.J., Mrowka, S., Koch, J.A., London, R.A., Matthews, D.L., Underwood, J.H.: Opt. Lett. **18** (1993) 1174.

93Dur Durfee III, C.G., Milchberg, H.M.: Phys. Rev. Lett. **71** (1993) 2409.

93Hir Hirose, H., Hara, T., Ando, K., Negishi, F., Aoyagi, Y.: Jpn. J. Appl. Phys. Part 2 **32** (1993) L1538.

93Jae Jaeglé, P., Carillon, A., Gauthé, B., Goedtkindt, P., Guennou, H., Jamelot, G., Klisnick, A., Möller, C., Rus, B., Sureau, A., Zeitoun, P.: Appl. Phys. B **57** (1993) 313.

93Max Maxon, S., Estabrook, K.G., Prasad, M.K., Osterheld, A.L., London, R.A., Eder, D.C.: Phys. Rev. Lett. **70** (1993) 2285.

93Nag Nagata, Y., Midorikawa, K., Kubodera, S., Obara, M., Tashiro, H., Toyoda, K.: Phys. Rev. Lett. **71** (1993) 3774.

93Nil1 Nilsen, J., Moreno, M.C., Mac Gowan, B.J., Koch, J.A.: Appl. Phys. B **57** (1993) 309.

93Nil2 Nilsen, J., Mac Gowan, B.J., Da Silva, L.B., Moreno, J.C.: Phys. Rev. A **48** (1993) 4682.

93Pol Polonsky, L., Park, C.O., Krushelnik, K., Suckewer, S.: Proc. SPIE **2012** (1993) 75.

93Res Ress, D., Da Silva, L.B., Barbee, J.T.W., Lehr, D.E., London, R.A., Mrowka, S., Procassini, R.J., Trebes, J.E.: ICF Q. Rep. **3** (1993) 173.

93Shl Shlyaptsev, V.N., Nickles, P.V., Schlegel, T., Kalashnikov, M.P., Osterheld, A.L.: Proc. SPIE **2012** (1993) 111.

93Str Strobel, G.L., Eder, D.C., London, R.A., Rosen, M.D., Falcone, R.W., Gordon, S.P.: Conf. Short-Pulse High-Intensity Lasers and Applications, Los Angeles, 1993, SPIE Bellingham, WA; Proc. SPIE **1860** (1993) 157.

93Tot Toth, C., Young, J.F., Sauerbrey, R.: Opt. Lett. **18** (1993) 2120.

94DaS Da Silva, L.B., London, R.A., Mac Gowan, B.J., Mrowka, S., Matthews, D.L., Craxton, R.S.: Opt. Lett. **19** (1994) 1532.
94Ede Eder, D.C., Amendt, P., Da Silva, L.B.: Phys. Plasmas **1** (1994) 1744 and the references therein.
94Glo Glover, T.E., Donnelli, T.D., Lipman, E.A., Sullivan, A., Falcone, R.W.: Phys. Rev. Lett. **73** (1994) 78.
94Jae Jaegle, P., et al.: X-Ray Lasers 1994, AIP Conf. Series **332** (1994) 25.
94Koc Koch, J.A., Mac Gowan, B.J., Da Silva, L.B., Matthews, D.L., Underwood, J.H., Batson, R.W., London, R.A., Mrowka, S.: Phys. Rev. A **50** (1994) 1877.
94Kun Kunze, H.J., Koshelev, K.N., Steden, C., Uskov, D., Wieschebrink, H.T.: Phys. Lett. A **193** (1994) 183.
94Lem Lemoff, B.E., Barty, C.P.J., Harris, S.E.: Opt. Lett. **19** (1994) 569.
94Moo Moon, S.J., Eder, D.C., Strobel, G.L.: in: X-Ray Lasers 1994, Eder, D.C., Matthews, D.L. (eds.), AIP Conf. Series, AIP, NY, 1994.
94Mor Moreno, J.C., Nilsen, J., Da Silva, L.B.: Opt. Commun. **110** (1994) 585.
94Per Pert, G.J.: J. Opt. Soc. Am. B **11** (1994) 1425.
94Roc Rocca, J.J., Shlyaptsev, V., Tomasel, F.G., Cortázar, O.D., Hartshorn, D., Chilla, J.L.A.: Phys. Rev. Lett. **73** (1994) 2192.
94Ste Steingruber, J., Fill, E.: Appl. Phys. B **58** (1994) 29.
94Str Strobel, G.L., Eder, D.C., Amendt, P.: Appl. Phys. B **58** (1994) 45.

95Chi Chichkov, B.N., Egbert, A., Eichmann, H., Momma, C., Nolte, S., Wellegehausen, B.: Phys. Rev. A **52** (1995) 1629.
95Dai Daido, H., Kato, Y., Murai, K., Ninoniya, S., Kodama, R., Yuan, G., Oshikane, Y., Takagi, M., Takabe, H., Koike, F.: Phys. Rev. Lett. **75** (1995) 1074.
95DaS1 Da Silva, D.B., Barbee, T.W., Cauble, R., Celliers, P., Ciarlo, D., Moreno, J.C., Mrowka, S., Trebes, J.E., Wan, A.S., Weber, F.: Appl. Opt. **34** (1995) 6389.
95DaS2 Da Silva, L.B., Barbee jr., T.W., Cauble, R., Celliers, P., Ciarlo, D., Libby, S., London, R.A., Matthews, D., Mrowka, S., Moreno, J.C., Ress, D., Trebes, J.E., Wan, A.S., Weber, F.: Phys. Rev. Lett. **74** (1995) 3991.
95Dit Ditmire, T., Hutchinson, M.H.R., Key, M.H., Lewis, C.L.S., MacPhee, A., Mercer, I., Neely, D., Perry, M.D., Smith, R.A., Wark, J.S., Zepf, M.: Phys. Rev. A **51** (1995) R4337.
95Fie Fiedorowicz, H., Bartnik, A., Szczurek, M., Fill, E., Li, Y.L., Lu, P.X., Pretzler, G.: Proc. SPIE **2520** (1995) 55.
95Fil1 Fill, E.E., Li, Y., Pretzler, G., Schlögl, D., Steingruber, J., Nilsen, J.: Proc. SPIE **2520** (1995) 21.
95Fil2 Fill, E., Lin, Y., Schlögel, D., Steingruber, J., Nilsen, J.: Opt. Lett. **20** (1995) 374.
95Jan Janulewicz, K.A., Healy, S.B., Pert, G.J.: J. Phys. B **28** (1995) 5237.
95Lem Lemoff, B.E., Yin, G.Y., Gordon III, C.L., Barty, C.P.J., Harris, S.E.: Phys. Rev. Lett. **74** (1995) 1574.
95Mor Morozov, A., Polonsky, L., Suckewer, S.: Proc. of 2nd Int. Symp., Plasma 95, Vol. 2, Warsaw, 1995, p. 247.
95Nic Nickles, P.V., Schnurer, M., Kalashnikov, M.P., Will, I., Sander, W.: Proc. SPIE **2520** (1995) 373.
95Nil1 Nilsen, J., Moreno, J.C.: Opt. Lett. **20** (1995) 1386.
95Nil2 Nilsen, J., Moreno, J.C.: Phys. Rev. Lett. **74** (1995) 3376.
95Nil3 Nilsen, J., Moreno, J.C., Da Silva, L.B., Barbee, T.W., Li, Y., Fill, E., Fiedorowicz, H., Bartnik, A.: UCRL-JC-121199 Preprint, 3. Nov. (1995).
95Plo Plowes, J.A., Pert, G.J., Holden, P.B.: Opt. Commun. **116** (1995) 260.
95Pol Polack, F., Joyeux, D., Svatos, J., Phalippou, D.: Rev. Sci. Instrum. **66** (1995) 2180.

95Roc Rocca, J.J., Marconi, M.C., Chilla, J.L.A., Clark, D.P., Tomasel, F.G., Shlyaptsev, V.N.: IEEE J. Sel. Topics Quantum Electron. **1** (1995) 945.
95Spr Sprangel, P., Ting, A., Esarey, E., Fisher, A.: J. Appl. Phys. **72** (1995) 5032.
95Zha Zhang, J., Key, M.H., Norreys, P.A., Tallents, G.J., Behjat, A., Danson, C., Demir, A., Dwivedi, L., Holden, M., Holden, P.B., Lewis, C.L.S., MacPhee, A.G., Neely, D., Pert, G.J., Ramsden, S.A., Rose, S.J., Shao, Y.F., Thomas, O., Walsh, F., You, Y.L.: Phys. Rev. Lett. **74** (1995) 1335.

96Chi Chilla, J.L.A., Rocca, J.J.: J. Opt. Soc. Am. B **13** (1996) 2841.
96Dai Daido, H., Ninomiya, S., Imani, T., Kodama, R., Takagi, M., Kato, Y., Murai, K., Zhang, J., You, Y., Gu, Y.: Opt. Lett. **21** (1996) 958.
96Don Donnelly, T.D., Da Silva, L.B., Lee, R.W., Mrowka, S., Hofer, M., Falcone, R.W.: J. Opt. Soc. Am. B **13** (1996) 185.
96Fie Fiedorowicz, H., Bartnik, A., Li, Y., Lu, P., Fill, E.: Phys. Rev. Lett. **76** (1996) 415.
96Hea Healy, S.B., Janulewicz, K.A., Pert, G.J.: Opt. Commun. **132** (1996) 442.
96Jan Janulewicz, K.A., Grout, M.J., Pert, G.J.: J. Phys. B **29** (1996) 901.
96Kal Kalantar, D.H., Key, M.H., Da Silva, L.B.: Phys. Rev. Lett. **76** (1996) 3574.
96Kat Kato, Y.: in: X-Ray Lasers 1996, Svanberg, S., Wahlstrom, C.G. (eds.), IOP Conf. Series **151**, Bristol: Inst. of Physics, 1996, p. 275.
96Kor Korobkin, D., Nam, C.H., Suckewer, S., Goltsov, A.: Phys. Rev. Lett. **77** (1996) 5206.
96Mat Matthews, D.L.: in: X-Ray Lasers 1996, Svanberg, S., Wahlstrom, C.G. (eds.), IOP Conf. Series **151**, Bristol: Inst. of Physics, 1996, p. 32.
96Nil1 Nilsen, J.: Phys. Rev. A **53** (1996) 4539.
96Nil2 Nilsen, J., Fiedorowicz, H., Bartnik, A., Li, Y., Lu, P., Fill, E.E.: Opt. Lett. **21** (1996) 408.
96Oza Ozaki, T., Orimo, S., Kuroda, H.: Opt. Quantum Electron. **28** (1996) 187.
96Roc Rocca, J.J., Clark, D.P., Chilla, J.L.A., Shylaptsev, V.N.: Phys. Rev. Lett. **77** (1996) 1476.
96Zha1 Zhang, J., Fill, E.E., Li, Y., Schlögl, D., Steingruber, J., Holden, M., Tallents, G.J., Demir, A., Zeitoun, P., Danson, C., Norreys, P.A., Walsh, F., Key, M.H., Lewis, C.L.S., McPhee, A.G.: Opt. Lett. **21** (1996) 1035.
96Zha2 Zhang, J., Warwick, P.J., Wolfrum, E., Key, M.H., Danson, C., Demir, A., Healy, S., Kalantar, D.H., Kim, N.S., Lewis, C.L.S., Lin, J., MacPhee, A.G., Neely, D., Nilsen, J., Pert, G.J., Smith, R., Tallents, G.J., Wark, J.S.: Phys. Rev. A **54** (1996) R4653.

97Alb Albert, F., Joyeux, D., Jaeglé, P., Carillon, A., Chauvineau, J.P., Jamelot, G., Klisnick, A., Lagron, J.C., Phalippou, D., Ros, D., Sebban, S., Zeitoun, P.: Opt. Commun. **142** (1997) 184.
97Ben Benware, B.R., Moreno, C.H., Burd, D.J., Rocca, J.J.: Opt. Lett. **22** (1997) 796.
97Dun Dunn, J., Osterheld, A.L., Shepherd, R., White, W.E., Shlyaptsev, V.N., Bullock, A., Stewart, R.E.: in: Soft X-Ray Lasers and Applications II, Rocca, J.J., Da Silva, L.B. (eds.); Proc. SPIE **3156** (1997) 114.
97Gol Goltsov, A.Y., Korobkin, D., Nam, C.H., Suckewer, S.: Proc. SPIE **3156** (1997) 204.
97Hea Healy, S.B., Janulewicz, K.A., Pert, G.J.: Opt. Commun. **144** (1997) 24.
97Li Li, Y., Schillinger, H., Ziener, C., Sauerbrey, R.: Opt. Commun. **144** (1997) 118.
97Nic Nickles, P.V., Shlyaptsev, V., Kalachnikov, M., Schnürer, M., Will, I., Sandner, W.: Phys. Rev. Lett. **78** (1997) 2748.
97Nil Nilsen, J., Moreno, J.C., Da Silva, L.B., Barbee jr., T.W.: Phys. Rev. A **55** (1997) 827.
97Ruh Ruhl, F., Aschke, L., Kunze, H.J.: Phys. Lett. A **225** (1997) 107.
97Rus Rus, B., Carillon, A., Dhez, P., Jaegle, P., Jamelot, G., Klisnick, A., Nantel, M., Zeitoun, P.: Phys. Rev. A **5** (1997) 3858.

97Shl Shlyaptsev, V.N., Rocca, J.J., Kalachnikov, M.P., Nickles, P.V., Sandner, W., Osterheld, A.L., Dunn, J., Eder, D.C.: in: Soft X-Ray Lasers and Applications II, Rocca, J.J., Da Silva, L.B. (eds.); Proc. SPIE **3156** (1997) 193.
97Sou Soufli, R., Gullikson, E.: Appl. Opt. **36** (1997) 5499.
97Zha1 Zhang, J., Mac Phee, A.G., Nilsen, J., Lin, J., Barbee, T.W., Danson, C., Key, M.H., Lewis, C.L.S., Neely, D., O'Rourke, R.M.N., Pert, G.J., Smith, R., Tallents, G.J., Wark, J.S., Wolfrum, E.: Phys. Rev. Lett. **78** (1997) 3856.
97Zha2 Zhang, J., MacPhee, A.G., Lin, J., Wolfrum, E., Smith, R., Danson, C., Key, M.H., Lewis, C.L.S., Neely, D., Nilsen, J., Pert, G.J., Tallents, G.J., Wark, J.S.: Science **276** (1997) 1097.

98Ben Benware, B.R., Macchietto, C.D., Moreno, C.H., Rocca, J.J.: Phys. Rev. Lett. **81** (1998) 5804.
98Dec Decker, C.D., London, R.A.: Phys. Rev. A **57** (1998) 1395.
98Dun Dunn, J., Osterheld, A.L., Shepherd, R., White, W.E., Shlyaptsev, V.N., Bullock, A., Stewart, R.E.: Phys. Rev. Lett. **80** (1998) 2825.
98Hag Hagelstein,, P.L.: in: X-Ray Lasers 1998, Kato, Y. (ed.), AIP Conf. Series, 1998.
98Kor Korobkin, D., Goltsov, A., Morozov, A., Suckewer, S.: Phys. Rev. Lett. **81** (1998) 1607.
98Li Li, R., Ozaki, T., Kanai, T., Kuroda, H.: Phys. Rev. E **57** (1998) 7093.
98Moo Moon, S.J., Eder, D.C.: Phys. Rev. A **57** (1998) 1391 and references therein.
98Pra Präg, A., Loewenthal, F., Tommasini, R., Balmer, J.E.: Appl. Phys. B **66** (1998) 561.
98Tom Tommasini, R., Loewenthal, F., Balmer, J.E.: in: X-Ray Lasers 1998, AIP Conf. Series, 1998.
98Ums Umstadter, D.P., Barty, C.P.J., Perry, M., Mourou, G.: Opt. Photonics News **9** (1998) 41.
98War Warwick, P.J., Lewis, C.L.S., Kalachnikov, M.P., Nickles, P.V., Schnürer, M., Behjat, A., Demir, A., Tallents, G.J., Neely, D., Wolfrum, E., Zhang, J., Pert, G.J.: J. Opt. Soc. Am. B **15** (1998) 1808.
98Zei Zeitoun, Ph., Albert, F., Jaeglé, P., Joyeux, D., Boussoukaya, M., Carillon, A., Hubert, S., Jamelot, G., Klisnick, A., Phalippou, D., Lagron, J.C., Ros, D., Sebban, S., Zeitoun-Fakiris, A.: Nucl. Instrum. Methods A **416** (1998) 189.

99Art1 Artioukov, I.A., Benware, B.R., Rocca, J.J., Forsythe, M., Uspenskii, Yu.A., Vinogradov, A.V.: IEEE J. Sel. Topics Quantum Electron. **5** (1999) 1495.
99Art2 Artioukov, I.A., Benware, B.R., Rocca, J.J., Forsythe, M., Uspenskii, Yu.A., Vinogradov, A.V.: in: Soft X-Ray Lasers and Applications III, Rocca, J.J., Da Silva, L.B. (eds.); Proc. SPIE **3776** (1999) 224.
99Bal Balmer, J., Tommasini, R., Löwenthal, F.: Proc. SPIE **3776** (1999) 66.
99Bor Born, M., Wolf, E.: Principles of Optics, 7th Ed., Cambridge: Cambridge University Press, 1999.
99Dai Daido, H., Sebban, S., Sakaya, N., Tohyama, Y., Norimatsu, T., Mima, K., Kato, Y., Wang, S., Gu, Y., Huang, G., Tang, H., Murai, K., Butzbach, R., Uschmann, I., Vollbrecht, M., Förster, E.: J. Opt. Soc. Am. B **16** (1999) 2295.
99Dun Dunn, J., et al.: in: Soft X-Ray Lasers and Applications III, Rocca, J.J., Da Silva, L.B. (eds.); Proc. SPIE **3776** (1999) 2.
99Jam Jamelot, G., et al.: IEEE J. Sel. Topics Quantum Electron. **5** (1999) 1486.
99Mac Macchietto, C.D., Benware, B.R., Rocca, J.J.: Opt. Lett. **24** (1999) 1115.
99Nil Nilsen, J., Dunn, J., Osterheld, A.L., Li, Y.: Phys. Rev. A **60** (1999) R2677.
99Roc Rocca, J.J.: Rev. Sci. Instrum. **70** (1999) 3799.
99Smi Smith, R., Tallents, G.J., Zhang, J., Eker, G., McCabe, S., Pert, G.J., Wolfrum, E.: Phys. Rev. A **59** (1999) R47.

99Tom Tommasini, R., Löwenthal, F., Balmer, J.E.: Phys. Rev. A **59** (1999) 1577.

00Cha Chanteloup, J.-C., Salmon, E., Sauteret, C., Migus, A., Zeitoun, P., Klisnick, A., Carillon, A., Hubert, S., Ros, D., Nickles, P., Kalachnikov, M.: J. Opt. Soc. Am. B **17** (2000) 151.
00Dun Dunn, J., Li, Y., Osterheld, A.L., Nilsen, J., Hunter, J.R., Shlyaptsev, V.N.: Phys. Rev. Lett. **84** (2000) 4834.
00Hul Hulin, S., Auguste, T., D'Oliveira, P., Monot, P., Jacquemot, S., Bonnet, L., Lefebvre, E.: Phys. Rev. E **61** (2000) 5693.
00Kub Kuba, J., Klisnick, A., Ros, D., Fourcade, P., Jamelot, G., Miquel, J.-L., Blanchot, N., Wyart, J.-F.: Phys. Rev. A **62** (2000) 043808-1.

01Jan Janulewicz, K.A., Rocca, J.J., Bortolotto, F., Kalachnikov, M.P., Shlyaptsev, V.N., Sandner, W., Nickles, P.V.: Phys. Rev. A **63** (2001) 033803.
01Kin King, R.E., Pert, G.J., McCabe, S.P., Simms, P.A., MacPhee, A.G., Lewis, C.L.S., Keenan, R., O'Rourke, R.M.N., Tallents, G.J., Pestehe, S.J., Strati, F., Neely, D., Allott, R.: Phys. Rev. A **64** (2001) 053810.
01Kub Kuba, J.: Doctor Thesis, Université Paris XI, 19. Oct 2001.
01Liu Liu, Y., Seminario, M., Tomasel, F.G., Chang, C., Rocca, J.J., Attwood, D.T.: Phys. Rev. A **63** (2001) 033802.
01Seb Sebban, S., Haroutunian, R., Balcou, Ph., Grillon, G., Rousse, A., Kazamias, S., Marin, T., Rousseau, J.P., Notebaert, L., Pittman, M., Chambaret, J.P., Antonetti, A., Hulin, D., Ros, D., Klisnick, A., Carillon, A., Jaeglé, P., Jamelot, G., Wyart, J.F.: Phys. Rev. Lett. **86** (2001) 3004.
01Tom Tommasini, R., Nilsen, J., Fill, E.E.: Proc. SPIE **4505** (2001) 85.
01Zei Zeitoun, P.: Private communication, 2001.

02Jan Janulewicz, K.A., Lucianetti, A., Priebe, G., Sandner, W., Nickles, P.V.: in: X-Ray Lasers 2002, Rocca, J.J., Suckewer, S., Dunn, J. (eds.); AIP Conf. Series **640** (2002) 90.
02Kaw Kawachi, T., Kado, M., Tanaka, M., Sasaki, A., Hasegawa, N., Kilpio, A.V., Namba, S., Nagashima, K., Lu, P., Takahashi, K., Tang, H., Tai, R., Kishimoto, M., Koike, M., Daido, H., Kato, Y.: Phys. Rev. A **66** (2002) 033815.
02Kli Klisnick, A., Kuba, J., Ros, D., Smith, R., Jamelot, G., Chenais-Popovics, C., Keenan, R., Topping, S.J., Lewis, C.L.S., Strati, F., Tallents, G.J., Neely, D., Clarke, R., Collier, J., MacPhee, A.G., Bortolotto, F., Nickles, P.V., Janulewicz, K.A.: Phys. Rev. A **65** (2002) 033810.
02Lu1 Lu, P., Kawachi, T., Suzuki, M., Sukegawa, K., Namba, S., Tanaka, M., Hasegawa, N., Nagashima, K., Daido, H., Arisawa, T., Kato, Y., Fiedorowicz, H.: Jpn. J. Appl. Phys. **41** (2002) L133.
02Lu2 Lu, P., Kawachi, T., Kishimoto, M., Sukegawa, K., Tanaka, M., Hasegawa, N., Suzuki, M., Tai, R., Kado, M., Nagashima, K., Daido, H., Kato, Y., Fiedorowicz, H., Bartnik, A.: Opt. Lett. **27** (2002) 1911.
02Oza Ozaki, T., Yamamoto, K., Kanai, T., Kuroda, H.: J. Phys. Soc. Jpn. **71** (2002) 2963.
02Rus Rus, B., Mocek, T., Präg, A.R., Kozlova, M., Jamelot, G., Carillon, A., Ros, D., Joyeux, D., Phalippou, D.: Phys Rev. A **66** (2002) 063806.
02Seb1 Sebban, S., Mocek, T., Ros, D., Upcraft, L., Balcou, Ph., Haroutunian, R., Grillon, G., Rus, B., Klisnick, A., Carillon, A., Jamelot, G., Valentin, C., Rousse, A., Rousseau, J.P., Notebaert, L., Pittman, M., Hulin, D.: Phys. Rev. Lett. **89** (2002) 253901.
02Seb2 Sebban, S.: Private communication, 2002.

03But Butler, A., Gonsalves, A.J., McKenna, C.M., Spence, D.J., Hooker, S.M., Sebban, S., Mocek, T., Bettaibi, I., Cros, B.: Phys. Rev. Lett. **91** (2003) 205001.

03Jan Janulewicz, K.A., Lucianetti, A., Priebe, G., Sandner, W., Nickles, P.V.: Phys. Rev. A (2003) R051802.

03Kee Keenan, R., Dunn, J., Shlyaptsev, V.N., Smith, R., Patel, P.K., Price, D.F.: Proc. SPIE **5197** (2003) 213.

03Moc Mocek, T., Rus, B., Präg, A.R., Kozlová, M., Jamelot, G., Carillon, A., Ros, D.: J. Opt. Soc. Am. B **20** (2003) 1386.

03Nis Nishikino, M., Tanaka, M., Nagashima, K., Kishimoto, M., Kado, M., Kawachi, T., Sukegawa, K., Ochi, Y., Hasegawa, N., Kato, Y.: Phys. Rev. A **68** (2003) 061802.

03Shl Shlyaptsev, V.N., Dunn, J., Moon, S., Smith, R., Keenan, R., Nilsen, J., Fournier, K.B., Kuba, J., Osterheld, A.L., Rocca, J.J., Luther, B., Wang, Y., Marconi, M.: Proc. SPIE **5197** (2003) 221.

04Dun1 Dunn, J., Keenan, R., Patel, P.K., Price, D.F., Smith, R.F., Shlyaptsev, V.N.: in: X-Ray Lasers 2004, Zhang, J. (ed.), IOP Conf. Series **186** (2004) 305.

04Dun2 Dunn, J.: Private communication, 2004.

04Jan1 Janulewicz, K.A., Lucianetti, A., Priebe, G., Nickles, P.V.: X-Ray Spectrom. **33** (2004) 262.

04Jan2 Janulewicz, K.A., Nickles, P.V., King, R.E., Pert, G.J.: Phys. Rev. A **70** (2004) 013804.

04Jan3 Janulewicz, K.A., Priebe, G., Tümmler, J., Nickles, P.V.: IEEE J. Sel. Topics Quantum Electron. **10** (2004) 1368.

04Kaw Kawachi, T., Sasaki, A., Tanaka, M., Kishimoto, M., Hasegawa, N., Nagashima, K., Koike, M., Daido, H., Kato, Y.: Phys. Rev. A **69** (2004) 033805.

04Luc Lucianetti, A., Janulewicz, K.A., Kroemer, R., Priebe, G., Tümmler, J., Sandner, W., Nickles, P.V., Redkorechev, V.I.: Opt. Lett. **29** (2004) 881.

04Roc Rocca, J.J., Luther, B.M., Heinbuch, S., Wang, Y., Larotonda, M.A., Grisham, M., Alessi, D., Berrill, M., Marconi, M.C., Shlyaptsev, V.N., Dummer, A., Brizuela, F., Menoni, C.S.: in: X-Ray Lasers 2004, Zhang, J. (ed.), IOP Conf. Series **186** (2004) 19.

04Zei Zeitoun, Ph., Faivre, G., Sebban, S., Mocek, T., Hallou, A., Fajardo, M., Aubert, D., Balcou, Ph., Burgy, F., Douillet, D., Kazamias, S., de Lachèze-Murel, G., Lefrou, T., le Pape, S., Mercère, P., Merdji, H., Morlens, A.S., Rousseau, J.P., Valentin, C.: Nature (London) **431** (2004) 426.

05Kee Keenan, R., Dunn, J., Patel, P.K., Price, D.F., Smith, R.F., Shlyaptsev, V.N.: Phys. Rev. Lett. **94** (2005) 103901.

05Lut Luther, B.M., Wang, Y., Larotonda, M.A., Alessi, D., Berrill, M., Marconi, M.C., Shlyaptsev, V.N., Rocca, J.J.: Opt. Lett. **30** (2005) 165.

05Roc Rocca, J.J., Wang, Y., Larotonda, M.A., Luther, B.M., Berrill, M., Alessi, D.: Opt. Lett. **30** (2005) 2581.

05Tue Tümmler, J., Janulewicz, K.A., Priebe, G., Nickles, P.V.: Phys. Rev. E **72** (2005) 037401.

05Wan Wang, Y., Larotonda, M.A., Luther, B.M., Alessi, D., Berrill, M., Shlyaptsev, V.N., Rocca, J.J.: Phys. Rev. A **72** (2005) 053807.

06Kim Kim, H.T., Choi, I.W., Hafz, N., Sung, J.H., Yu, T.J., Hong, K.-H., Jung, T.M., Kim, J.-H., Noh, Y.-C., Ko, D.-K., Tümmler, J., Nickles, P.V., Janulewicz, K.A., Lee, J.: in: X-Ray Lasers 2006, Nickles, P.V., Janulewicz, K.A. (eds.), Springer Proceedings in Physics **115**, Berlin: Springer, 2006, p. 183.

06Wan Wang, Y., Granados, E., Larotonda, M.D., Berrill, M., Luther, B.M., Patel, D., Menoni, C.S., Rocca, J.J.: Phys. Rev. Lett. **97** (2006) 123901.

06Wei Weith, A., Larotonda, M.D., Wang, Y., Luther, B.M., Alessi, D., Marconi, M.C., Rocca, J.J.: Opt. Lett. **31** (2006) 1994.

07Roc Rocca, J.J.: Private communication, 2007.

Index

α line, Balmer 222
3-level system 23
4-level system 22, 23
  rate equations for 5
I–III–VI_2 semiconductor 163
II–VI semiconductor 163
III–V semiconductor 163

Abbe number 47, 108, 113
ABCD law 26
Above-threshold ionization (ATI) 242, 245
Absorption 10, 23, 26
  excited state (ESA) 23, 25, 131
    cross section for 45
  line 97
  loss 25
  saturation 130
  spectrum 97
    of Erbium Er^{3+} 58
  two-photon 111
Accelerator
  cavity, RF 190
  pre- 188
Active
  element 54
  medium 208, 228
  mirror 37
  region 166
    strain-compensated 175
Activity, laser 16
Adiabatic
  cooling 217, 233
  expansion 205
Aerogel foam 213
Alexandrite 56, 69
Alloy
  pseudo-graded 170
  quaternary 163
  ternary 163
AlN, wurtzite 164
AM (amplitude modulation) 158
  large-signal 159
  small-signal 159
Amplification 10, 23, 233
  chirped-pulse (CPA) 227
    Ti:sapphire laser 246
  coherent 192
  energy 7
  factor
    small-signal 10
  intensity 6, 7
  X-ray 206
Amplified spontaneous emission (ASE) 23, 25, 98, 220
  self-terminating 223
Amplifier
  disk 37
  fiber
    saturated high-power 132
  principle 6
Amplitude modulation (AM) 158
  large-signal 159
  small-signal 159
Angle
  Brewster 52, 106, 145
  of incidence 229
  of refraction 212
Anharmonic oscillation 16
Anisotropic, optically uniaxially 110
Antireflection-coated 145
Aperture
  finite 23
  numerical (NA) 127
    core 133
Approximation
  Wentzel–Kramers–Brillouin 128
Area
  mode-field 133
ASE (amplified spontaneous emission) 23, 25, 98, 220
  self-terminating 223
Athermal glass 109
ATI (above-threshold ionization) 242, 245
Atom
  percentage 51
    concentration in 49
  rare-earth 98
Auger
  decay 217
    rate 217
  process 152
    nonradiative 152

Backscattering
  Raman, stimulated 245
Balmer α line 222
Band
  conduction 163
  -to-band recombination 163
  valence 163
Bandwidth limited, Fourier transform 193
Barrier
  potential 242
  suppression (BS) 242
Beam
  divergence 211
  electron, relativistic 187
  molecular, epitaxy (MBE) 164
  parameter
    complex 26
    product 29, 44, 128
  quality 35, 36
  radius 26
BEL (lanthanum beryllate) 70
Bend of a fiber 130
Bending loss 133
Beryllium chalcogenide 170
Bimolecular recombination 152
Biological specimen, gold-tagged 252
Birefringence 33
Birefringent filter 145
Blue
  –green spectral region 168
  laser 151
  –violet spectral region 164
Bohr's model 222
Bragg
  grating 126
    in fibers 112
  reflection 158
  reflector, distributed (DBR), epitaxial 167, 171, 176
Branching of the energy levels 45
Breakdown, electrical-field-induced 253
Bremsstrahlung
  inverse (IB) 205, 232, 245
  spectrum 217
Brewster angle 52, 106, 145
Brightness, spectral 231
Brillouin
  scattering, stimulated (SBS) 111, 132
  zone 164
Broadening
  Doppler 217, 223
  homogeneous 193
  inhomogeneous 97, 193
  natural 207
BS (barrier suppression) 242
Bunching of electrons 187
Buried heterostructure laser 157
Burst, photon 217

Capillary
  discharge 211, 254
    fast-, plasma 230
  plasma 231
Carrier
  injection 154
  lifetime 152, 155
Cascade, collisional-radiative 216
Cavity
  accelerator, RF 190
  coupled-, laser 158
  external-, laser 158
  intra-, power 195
  loss 194
  short-, laser 156
Ce *see* Cerium
Cell switching
  electro-optic (EO) 195
  Pockels *see* Cell switching, electro-optic (EO)
Center
  color 25
  -ed laser core 129
  F 141, 142
  F_2 142
  F_2^+ 142
  $(F_2^+)_A$ 142
  F_A(II) 142, 143
  F_B(II) 142
Cerium
  Ce^{3+} 98
  Ce^{4+} 98
Chalcogenide
  beryllium 170
Charge
  exchange reaction 220
  oscillating 187
  space-, effect 252
  transfer scheme 219
Chemical vapor deposition (CVD) 125
  modified (MCVD) 135
Chirped pulse amplification (CPA) 227
  Ti:sapphire laser 246
Circular
  -ly polarized
    pump laser pulse 246
    Ti:sapphire-laser 247
  pump core 129
Clad, double-
  fiber laser 128
  fiber, D-shaped 129
Cladding
  fiber 41
  layer 166, 175
Coated, antireflection 145

Coefficient
distribution 52
elasto-optic 53, 110, 113
gain 229
effective 227
heat 53
transfer 30
photoelastic 33, 53, 110
saturated gain 6, 24
Sellmeier 46
small-signal gain 6
strain-optical *see* Coefficient, elasto-optic
stress-optical 110, 113
temperature
of the optical path length 109
thermal expansion 31
mismatch 165
Coherence 223
degree of 223
longitudinal 224
spatial *see* Coherence, transverse
temporal *see* Coherence, longitudinal
transverse 224
Coherent amplification 192
Coiled fiber 129
Collisional
decoupling 245
electron-
excitation 218
recombination 216
excitation 206, 208
excited X-ray laser (XRL) 213
pumping
transient 227
-radiative cascade 216
transfer 219
transition 216
Color center 25
laser 141
Column, plasma 231–233
Complex beam parameter 26
Composition
-al disordering 163
fluctuation
In 166
Compound
I-III-VI_2 semiconductor 163
Concentration
doping 53, 102
in atom per cent 49
in weight percentage 49
quenching 102, 113
Condition
oscillator 10
phase matching 111
round-trip 153
Conduction
band 163
thermal 205
Conductivity
heat 31
Configuration
electron 98
Confinement 132
factor 155
optical 156
Confocal parameter 132
Constant
photoelastic 48
Contraction, Lorentz 187, 191
Conversion
efficiency 156
frequency 111
Coolant, temperature of 12
Cooling
adiabatic 217, 233
cryogenic 141
surface 31
unit 24
Core 41
fiber 127
laser, centered 129
numerical aperture 133
pump, circular 129
Coronal
plasma 225
zone 206
Coulomb force 242
Coupled-cavity laser 158
Coupling, spin-orbit 164
CPA (chirped-pulse amplification) 227
Ti:sapphire laser 246
Crack 100
Creation, ion-, dynamics of 208
Criterion
stability 27, 28
Critical
damaging power 47
density 245
electron 205
refracting power 36
surface 206, 229
Cross section
effective 45
for excited state absorption 45
for spontaneous emission 45
for stimulated emission 45, 100
Cryogenic
cooling 141
system 145
Crystal
data 52

photonic 133, 134
fiber (PCF) 134
stoichiometric 107
Crystallography 252, 254
Current
density, threshold 155
threshold- 156
Curvature of the wavefront 26
CVD (chemical vapor deposition) 125
modified (MCVD) 135
cw operation 45

Damage threshold
surface 137
Damaging power
critical 47
Damped
harmonic oscillator 15
oscillation 15
Damping time 15
Data
crystal 52
DBR (distributed Bragg reflector)
epitaxial 167, 171, 176
laser 156, 158
DC gun 189
Decay
Auger 217
rate 217
natural 45
radiative 208
time, resonator 20
Decoupling, collisional 245
De-excitation 208
Defect
quantum 25, 131
trapping 141
Deflectometry, Moiré 250
Defocusing 244
Deformation, endface 33
Degree of coherence 223
Density
critical 245
current, threshold 155
dislocation 165
electron 215
critical 205
saturation energy 24
Deposition, chemical vapor (CVD) 125
modified (MCVD) 135
Depth, flaw 49
Detector
scintillation 254
DFB (distributed feedback) laser 156, 158
DH (double-hetero) type 152
Diameter
mode-field (MFD) 133
Dielectric
mirror 126
multilayer, quarter-wave 165
Diffraction 23, 26
Diode
fiber-coupled 38
laser 38
pumping 104
strained-layer QW 173
-pumped solid-state laser 38
Direct semiconductor 164
Discharge
capillary 211, 254
fast, plasma 230
electric 206
Disk 37, 38
amplifier 37
Dislocation density 165
Disordering, compositional 163
Dispersion 108
Distortion, thermal 106
Distributed
Bragg reflector (DBR)
epitaxial 167, 171, 176
laser 156, 158
feedback (DFB) laser 156, 158
Distribution
coefficient 52
double-Maxwellian 242
function, electron energy (EEDF) 242
of energy 228
Divergence 26
beam 211
multimode 35
Division multiplexer, wavelength (WDM) 126
Doped fiber 40
rare-earth- 103
Doping concentration 53, 102
Doppler
broadening 217, 223
shift 187, 191, 231
Double-clad fiber
D-shaped 129
laser 128
Double-hetero (DH) type 152
Double-Maxwellian distribution 242
Double-pulse scheme 228
Driver
laser, table-top 227
D-shaped double-clad fiber 129
Duration
pulse 19, 20, 24, 223
Dy *see* Dysprosium
Dynamics of the ion creation 208
Dysprosium
Dy^{3+} 98

ECR (electron-cyclotron resonance) 169
Edge-emitting laser
  nitride-based 167
  sulfo-selenide-based 171
EEDF (electron energy distribution function) 242
Effect
  excitonic 163
  lens 31
  localization 163
  photoelastic 33
  space-charge 252
  thermal 37
  waveguiding 244
Effective
  cross section 45
  gain coefficient 227
Efficiency 15, 24, 31, 221
  conversion 156
  excitation 10, 53
  extraction 53, 194
  heat 53
  of solid-state lasers
    lamp-pumped 25
    laser-diode-pumped 25
  optical-to-optical 131
  power 24
  pumping 230
  quantum 25, 46, 188, 233
    fluorescence 143
  resonator 26
  slope 11, 22, 24, 26, 32, 53
Elasticity, modulus of 31, 49
Elasto-optic coefficient 53, 110, 113
Electric discharge 206
Electrical
  -field-induced breakdown 253
  power 24
Electro-optic (EO) cell switching 195
Electromagnetic wave
  forward-propagating 193
Electron
  beam, relativistic 187
  bunching of 187
  collisional
    excitation 218
    recombination 216
  configuration 98
  cyclotron resonance (ECR) 169
  density 215
    critical 205
  energy distribution function (EEDF) 242
  free, laser (FEL) 187
    self-amplified spontaneous emission (SASE) 194
  gun 188
  impact 218
    ionization 247
  photo-, spectroscopy 252
Element
  active 54
Emerald 56, 70
Emission
  amplified spontaneous (ASE) 23, 25, 98, 220
    self-terminating 223
  line, strong, self-pumping of 218
  self-amplified spontaneous (SASE)
    free-electron laser (FEL) 194
  spontaneous 4, 229
    cross section 45
  stimulated 4
    cross section 45, 100
End facet, fiber 126
Endface deformation 33
Endlessly single-mode 135
Energy
  amplification 7
  density, saturation 24
  distribution 228
    function, electron (EEDF) 242
  extraction 221
  injection 189
  laser, rectangular pulse 24
  level
    branching of 45
    diagram of Erbium Er^{3+} 57
  photon, laser 52
  pulse 19, 20, 22
  quiver 242, 245, 246
  threshold 14, 16, 22
EO (electro-optic)
  cell switching 195
Epitaxial
  distributed Bragg reflector (DBR) 167, 171, 176
  growth 151
  overgrowth technique 157
Epitaxy
  hydride vapor phase (HVPE) 165
  metal-organic vapor-phase (MOVPE) 164
  molecular beam (MBE) 164
Equation
  hydrodynamic 209
  rate 4, 154, 208
    for a 4-level system 5
Er *see* Erbium
Erbium
  Er^{3+} 57, 98
    absorption spectrum of 58
    energy level diagram of 57
    in various solids 58
ESA (excited state absorption) 23, 25, 131
Etching
  reactive ion 165

Eu *see* Europium
Europium
  Eu^{2+} 98
  Eu^{3+} 98
EUV (extreme ultraviolet) 203
  interferometer 253
  laser 203
Exchange
  charge, reaction 220
Excitation 23
  collisional 206, 208
    electron 218
  de- 208
  efficiency 10, 53
  longitudinal 40
  multiphoton 25
  source 24
  transient 226
Excited state absorption (ESA) 23, 25, 131
  cross section for 45
Excitonic effect 163
Expansion
  adiabatic 205
  hydrodynamic 226, 227
  thermal 104
    coefficient 31
    coefficient mismatch 165
External-cavity laser 158
Extraction
  efficiency 53, 194
  energy 221
Extreme ultraviolet (XUV or EUV) 203
  interferometer 253
  interferometry 253
  laser 203

F center 141, 142
F_2 center 142
F_2^+ center 142
$(F_2^+)_A$ center 142
F_A(II) center 142, 143
Fabry–Perot (FP)
  laser 151
  resonator 153
Facet, end, fiber 126
Factor
  confinement 155
  gain 227
  loss, per round trip 24
  small-signal
    amplification 10
    gain 6, 24
Fast-capillary-discharge plasma 230
F_B(II) center 142
Feedback
  optical 17, 221
  wavelength-selective 158
FEL (free-electron laser) 187
  self-amplified spontaneous emission (SASE) 194
Fermi function 156
Fiber 38
  amplifier, saturated high-power 132
  bend of 130
  Bragg grating in 112
  bundle, tapered (TFB) 126
  cladding 41
  coiled 129
  core 127
  -coupled diode 38
  D-shaped double-clad 129
  doped 40
  end facet 126
  laser, double-clad 128
  length 40
  loop mirror 126
  low-numerical-aperture large-mode-area (LMA) 133
  optical 125, 127
  photonic crystal (PCF) 134
  rare-earth-doped 103
  silica, low-loss fused 125
  single-mode 127
  step-index 134
Field
  electrical
    induced breakdown 253
  ionization 232
  optical
    ionization (OFI) 204, 242
    ionization (OFI) laser 204
  ponderomotive 192
  radiation
    intensity of 5
  wiggler 193
Filter
  birefringent 145
  modal 135
Finite aperture 23
Flaw depth 49
Fluctuation
  In composition 166
Fluence, saturation 131
Fluorescence
  lifetime 4, 131
  line 97, 113
  maximum, wavelength of 100
  quantum efficiency 143
  transition 113
Flux, saturation 5
FM (frequency modulation) 158
Foam
  aerogel 213

Focusing, self- 47, 111
  length 48
Force
  Coulomb 242
Formula
  Fresnel 254
  Henry 160
  Linford 220
Forward-propagating electromagnetic wave 193
Fourier transform, bandwidth limited 193
FP (Fabry–Perot)
  laser 151
  resonator 153
Fracture
  limit 110
  tension 32, 49
  toughness 104
Fraunhofer line 47
Free-electron laser (FEL) 187
  self-amplified spontaneous emission (SASE) 194
Frequency
  conversion 111
  -doubled Nd:YAG laser 145
  modulation (FM) 158
  parameter V 127, 134
  single-, laser 151
Fresnel
  bi-mirror 253
  formula 254
  number 224
Function
  electron energy distribution (EEDF) 242
  Fermi 156
Fused silica fiber, low-loss 125
Fusion, nuclear 100

Gadolinium
  Gd^{3+} 98
  (ortho)vanadate (GVO(4)) 74
  scandium aluminum garnet (GSAG) 56, 72
  scandium gallium garnet (GSGG) 3, 73
Gain 206
  coefficient 229
    effective 227
  factor 227
  nonlinear 160
  saturated
    coefficient 6, 24
  small-signal 132, 194, 247
    coefficient 6
    factor 6, 24
Gallium gadolinium garnet (GGG) 3, 56, 71
GaN, wurtzite 164
Gd *see* Gadolinium
Generation, high harmonic (HHG) 221, 254
Geometrical path length 110
GGG (gallium gadolinium garnet) 3, 56, 71
Glass
  athermal 109
  laser
    NOVA 225
    oxide 111
  transformation temperature 113
Gold-tagged biological specimen 252
Graded, pseudo-, alloy 170
Gradient
  index 212
  temperature 31
    radial 33
Grating, Bragg 126
  in fibers 112
Grazing incidence pumping (GRIP) 228
  scheme 204
Green–blue spectral region 168
GRIP (grazing incidence pumping) 228
  scheme 204
Group refractive index 154
Growth
  epitaxial 151
  high nitrogen pressure solution (HNPS) 165
GSAG (gadolinium scandium aluminum garnet) 56, 72
GSGG (gadolinium scandium gallium garnet) 3, 73
Guiding, index-
  strong 157
  weak 157
Gun
  DC 189
  electron 188
  RF 189
GVO(4) (gadolinium (ortho)vanadate) 74

Hardness, Knoop 49
Harmonic
  high 247
    generation (HHG) 221, 254
  oscillator, damped 15
Heat
  coefficient 53
  conductivity 31
  efficiency 53
  transfer coefficient 30
Heating 12
  homogeneous
    in rod and slab systems 31
  mechanism 29
  power 31, 105
  rate 103
Helical ray 129
Henry formula 160
Heteroepitaxy 165
Heterostructure, buried, laser 157

HHG (high harmonic generation) 221, 254
High
  harmonic 247
    generation (HHG) 221, 254
  nitrogen pressure solution (HNPS) growth 165
  power fiber amplifier, saturated 132
  repetition rate X-ray laser (XRL) 247
HNPS (high nitrogen pressure solution) growth 165
Ho *see* Holmium
Holmium
  Ho^{3+} 59, 98
Homogeneous
  broadening 193
  heating in rod and slab systems 31
Hund's rule 98
HVPE (hydride vapor phase epitaxy) 165
Hybrid X-ray laser (XRL) 231
Hydride vapor phase epitaxy (HVPE) 165
Hydrodynamic
  equation 209
  expansion 226, 227

IB (inverse bremsstrahlung) 205, 232, 245
Impact, electron 218
  ionization 247
In composition fluctuation 166
Incidence
  angle of 229
  grazing-, pumping (GRIP) 228
    scheme 204
Index
  gradient 212
  guiding
    strong 157
    weak 157
  refractive 33, 46, 100
    absolute 107
    average 134
    group 154
    intensity-dependent 132
    nonlinear 47, 48, 100, 113
    profile 33
    relative 107
    thermal 34
  step-, fiber 134
Induced
  electrical-field-, breakdown 253
  ionization-, refraction 242
  self-, phase shift 132
Inelastic scattering, stimulated 132
Inhomogeneous broadening 97, 193
Injection
  carrier 154
  energy 189
  locking 158
InN, wurtzite 164
Inner-shell
  photoionization (ISPI) 247
    scheme (ISPIS) 217
    X-ray laser (XRL) 250, 251
  vacancy 217
  X-ray laser (XRL) 254
Intensity
  amplification 6, 7
  -dependent refractive index 132
  of the radiation field 5
  saturation 21, 24, 52, 221
Interferometer
  extreme ultraviolet (XUV or EUV) 253
  Mach–Zehnder-type 253
Interferometry 250
  extreme ultraviolet (XUV or EUV) 253
Internal
  loss 10
  reflection
    multiple 37
    total 41, 106, 125
Intra-cavity power 195
Inverse bremsstrahlung (IB) 205, 232, 245
Inversion 5, 21, 24
  population 206, 213, 217, 247
    X-ray 219
  threshold 9, 10, 14, 22, 24
Ion
  creation, dynamics of 208
  etching, reactive 165
  lanthanide 98
  number, absolute 49, 51
  rare-earth 98
    laser active 99
Ionization 208
  above-threshold (ATI) 242, 245
  electron impact 247
  field 232
  -induced refraction 242
  multiphoton 232
  optical-field (OFI) 204, 242
    laser 204
  photo-, X-ray laser (XRL) 254
  stage 206
  thermal 247
  two-photon 254
Isoelectronic
  scaling 247
  sequence 207, 214, 215
ISPI (inner-shell photoionization) 250, 251
ISPIS (inner-shell photoionization scheme) 217
ISPI-XRL (inner-shell photoionization X-ray laser) 250, 251

Judd–Ofelt parameter 99
Junction, pn 156

KCl:Li 143
KGW (potassium gadolinium tungstate) 75
Kinetic relaxation 227
Knoop hardness 49
KrF laser 246

La *see* Lanthanum
Lamp-pumped solid-state laser
  efficiency of 25
Lanthanide ion 98
Lanthanum
  beryllate (BEL) 70
  La^{3+} 98
  magnesium hexa-aluminate (LMA) 76
  neodymium hexa-aluminate (LNA) 76
  scandium borate (LSB) 77
Large-signal amplitude modulation 159
Laser
  active rare-earth ion 99
  activity 16
  blue 151
  color-center 141
  core, centered 129
  coupled-cavity 158
  CPA (chirped-pulse amplification)
    Ti:sapphire 246
  diode 38
    -pumped solid-state laser, efficiency of 25
    pumping 104
    strained-layer QW 173
  distributed Bragg reflector (DBR) 156, 158
  distributed feedback (DFB) 156, 158
  driver, table-top 227
  edge-emitting
    nitride-based 167
    sulfo-selenide-based 171
  energy, rectangular pulse 24
  external-cavity 158
  extreme ultraviolet (XUV or EUV) 203
  Fabry–Perot (FP) 151
  fiber, double-clad 128
  free-electron (FEL) 187
    self-amplified spontaneous emission (SASE) 194
  glass
    NOVA 225
    oxide 111
  heterostructure, buried 157
  KrF 246
  material 6, 10, 45
  mirrorless 222
  multislab 37
  Nd:YAG, frequency-doubled 145
  Nova 100
  optical-field ionization (OFI) 204
  output power 12
  photon energy 52
  power 24
  -produced plasma 213, 250
  pulse, picosecond 227
  pump pulse, circularly polarized 246
  recombination 216, 221
    -pumped 216
  semiconductor 38
  short-cavity 156
  single-frequency 151
  solid-state, diode-pumped 38
    efficiency of 25
  Ti:sapphire
    circularly polarized 247
    CPA (chirped-pulse amplification) 246
  transition 4
  vertical cavity surface emitting (VCSEL) 157
  wavelength 99
  X-ray (XRL) 203, 204
    collisional-excited 213
    high-repetition-rate 247
    hybrid 231
    inner-shell 254
    inner-shell photoionization (ISPI) 250, 251
    photoionization 254
    photoresonantly pumped 218
    pulse 227
    recombination 233
    short-pulse-emitting soft 232
    table-top 227
Lattice mismatch 165
Law
  ABCD 26
Layer
  cladding 166, 175
  waveguide 166, 175
Length
  fiber 40
  path, geometrical 110
  pulse 14
  Rayleigh 27
  rod 36
  self-focusing 48
Lens
  effect 31
  surface 26
  thermal 33
Lensing
  thermal 33, 100, 104
Level
  energy, branching of 45
  low, prepulse 225
  upper, lifetime 24
LICAF (lithium calcium aluminum fluoride) 75
Lifetime 4, 12, 45, 206, 211, 229
  carrier 152, 155
  fluorescence 4, 131

outcoupling 155
radiative 100, 102, 113
upper level 24
Linac, RF, microwave-driven 189
Line
absorption 97
Balmer-α 222
emission, strong, self-pumping of 218
fluorescence 97, 113
Fraunhofer 47
matching 218
profile 223
width 160
Linearly polarized (LP) 127
Linewidth 223
spectral 225
Linford formula 220
LiSAF (lithium strontium aluminum fluoride) 3
Lithium
calcium aluminum fluoride (LICAF) 75
strontium aluminum fluoride (LiSAF) 3
LMA (lanthanum magnesium hexa-aluminate) 76
LMA (large mode area) 133
LNA (lanthanum neodymium hexa-aluminate) 76
Load, thermal 22, 31, 103, 106, 131, 137
safe 32
Localization effect 163
Locking
injection 158
mode 112
Longitudinal
coherence 224
excitation 40
pumping 41, 126
Lorentz contraction 187, 191
Loss
absorption 25
bending 133
cavity 194
factor per round trip 24
internal 10
low-, fused silica fiber 125
of the pump radiation 25
propagation 136
refraction 244
resonator 53
Low
-level prepulse 225
-loss fused silica fiber 125
-numerical-aperture large-mode-area (LMA) fiber 133
LP (linearly polarized) 127
mode 128
LSB (lanthanum scandium borate) 77
Lu *see* Lutetium
Luminescence 166, 254
Lutetium
Lu^{3+} 98

Mach–Zehnder-type interferometer 253
Magnetic wiggler 187
Master oscillator–power amplifier (MOPA) 224
Matching
line 218
phase, condition 111
Material
laser 6, 10, 45
photovoltaic 172
Matrix
for a full round-trip 26
resonator 35
Maximum
fluorescence, wavelength of 100
Maxwellian, double-, distribution 242
MBE (molecular beam epitaxy) 164
MCVD (modified chemical vapor deposition) 135
Mechanical stability 136
Mechanism
heating 29
self-photopumping 218
Medium, active 208, 228
Melting temperature 49
Meridional ray 129
Metal-organic vapor-phase epitaxy (MOVPE) 164
MFD (mode-field diameter) 133
Mg_2SiO_2 56
Micro
crack 49
-wave-driven RF linac 189
Microscopy 250
Mirror 11
-less laser 222
active 37
bi-, Fresnel 253
dielectric 126
fiber loop 126
multilayer 252
output 12
retro- 211
Mismatch
lattice 165
thermal expansion coefficient 165
Mixing, mode 130
Modal filter 135
Mode
field
area 133
diameter (MFD) 133
locking 112
LP (linearly polarized) 128
mixing 130
mono-, transversal 103

Q-switch 17
side-, suppression ratio (SMSR) 157
single- 135
fiber 127
transverse 128
Model
Bohr 222
Modified chemical vapor deposition (MCVD) 135
Modulation
amplitude (AM) 158
large-signal 159
small-signal 159
frequency (FM) 158
self-phase (SPM) 132
Modulus
of elasticity 31, 49
Young's 31, 49, 104
Moiré
deflectometry 250
reflectometry 34
Molecular beam epitaxy (MBE) 164
Mono-mode, transversal 103
MOPA (master oscillator–power amplifier) 224
MOVPE (metal-organic vapor-phase epitaxy) 164
Multi-pulse pumping 225
Multicavity resonator 35
Multilayer
dielectric, quarter-wave 165
mirror 252
Multimode
divergence 35
radius 35
Multiphoton
excitation 25
ionization 232
process 254
Multiple internal reflection 37
Multiplexer, wavelength division (WDM) 126
Multislab laser 37

NA (numerical aperture) 127
core 133
Natural
broadening 207
decay 45
Nd *see* Neodymium
Nd:GGG 30
Nd:YAG 30
laser, frequency-doubled 145
Ne-like zinc 254
Neodymium
Nd^{3+} 60, 98, 100
yttrium aluminum borate (NYAB) 77
Nitride-based edge-emitting laser 167
Nonlinear
gain 160
optics 252
refractive index 47, 48, 100, 113
Nonradiative
Auger process 152
recombination 152, 156
time 152
transition 4, 25
NOVA glass laser 225
Nova laser 100
Nuclear fusion 100
Number
Abbe 47, 108, 113
Fresnel 224
ion, absolute 49, 51
Poisson 31, 49
Numerical aperture (*NA*) 127
core 133
NYAB (neodymium yttrium aluminum borate) 77

OFI (optical-field ionization) 204, 223, 242
laser 204
Opacity, radial 231
Operation
cw 45
pulse 45
OPO (optical parametric oscillator) 188
Optical
confinement 156
feedback 17, 221
fiber 125, 127
field ionization (OFI) 204, 223, 242
laser 204
parametric oscillator (OPO) 188
path length
temperature coefficient of 109
polarizability 110
thickness 210
-to-optical efficiency 131
Optically
thick plasma 218
thin 254
uniaxially anisotropic 110
Optics
nonlinear 252
Oscillating charge 187
Oscillation
anharmonic 16
damped 15
relaxation 15, 159
self- 8
Oscillator
condition 10
harmonic, damped 15
optical parametric (OPO) 188
Outcoupling lifetime 155
Output
mirror 12

power, laser 12
Overgrowth, epitaxial
technique 157
Oxide laser glass 111

Parameter
beam
complex 26
product 29, 44, 128
confocal 132
frequency 127, 134
Judd–Ofelt 99
plasma 210
thermal shock 52
Path length
geometrical 110
optical
temperature coefficient of 109
PCF (photonic crystal fiber) 134
Peak power of a Q-switch pulse 18
Percentage
atom 51
weight 51
Periodical Q-switching 19
Phase
matching condition 111
self-, modulation (SPM) 132
shift, self-induced 132
Photoelastic
coefficient 33, 53, 110
constant 48
effect 33
Photoelectron spectroscopy 252
Photoionization
inner-shell (ISPI) 247
scheme (ISPIS) 217
X-ray laser (XRL) 250, 251
X-ray laser (XRL) 254
Photon
burst 217
energy, laser 52
two-, ionization 254
Photonic crystal 133, 134
fiber (PCF) 134
Photopumping, self-, mechanism 218
Photoresonantly pumped X-ray laser (XRL) 218
Photovoltaic material 172
Picosecond laser pulse 227
Pinch 230
Pipe, plasma 244, 245
Plasma
capillary 231
column 231–233
coronal 225
fast-capillary-discharge 230
laser-produced 213, 250
optically thick 218
parameter 210
pipe 244, 245
temperature 216
waveguide 212
Pm *see* Promethium
pn-junction 156
Pockels cell switching 195
Poisson number 31, 49
Polarizability, optical 110
Polarized
circularly
pump laser pulse 246
Ti:sapphire-laser 247
linearly (LP) 127
Ponderomotive
field 192
wave 192
Population
inversion 206, 213, 217, 247
X-ray 219
thermal 13, 23, 24
Potassium gadolinium tungstate (KGW) 75
Potential barrier 242
Power
damaging, critical 47
efficiency 24
electrical 24
heating 31, 105
intra-cavity 195
laser 24
output, laser 12
peak, of a Q-switch pulse 18
pump 12, 14
threshold 24
refracting 34, 36
scaling 137
transfer diagram 24
Pr *see* Praseodymium
Praseodymium
Pr^{3+} 63, 98
Pr^{4+} 98
Pre-accelerator 188
Prepulse 225
low-level 225
Probability of the transition 208
Process
Auger 152
nonradiative 152
multiphoton 254
Profile
line 223
refractive index 33
Voigt 223
Promethium
Pm^{3+} 98
Propagating, forward-, electromagnetic wave 193

Propagation loss 136
Pseudo-graded alloy 170
Pulse
  chirped, amplification (CPA) 227
    Ti:sapphire laser 246
  double-, scheme 228
  duration 19, 20, 24, 223
  energy 19, 20, 22
  length 14
  multi-, pumping 225
  operation 45
  picosecond, laser 227
  pump laser, circularly polarized 246
  Q-switch
    peak power of 18
  rectangular
    laser energy 24
  repetition rate 19, 20
  shaping 223
  -emitting soft X-ray laser (XRL) 232
  X-ray laser (XRL) 227
Pump
  core, circular 129
  laser pulse, circularly polarized 246
  power 12, 14
    threshold 24
  radiation, loss of 25
  rate 4, 14
    threshold 9
Pumping
  diode laser 104
  efficiency 230
  grazing incidence (GRIP) 228
    scheme 204
  longitudinal 41, 126
  multi-pulse 225
  self-, of a strong emission line 218
  transient collisional 227
  transversal 39, 126
  traveling-wave 228

Q-switch 16
  mode 17
  pulse, peak power of 18
Q-switching, periodical 19
Quality
  beam 35, 36
  of the resonator 17
Quantum
  defect 25, 131
  efficiency 25, 46, 188, 233
    fluorescence 143
  well (QW) 151
  yield, radiative 102
Quarter-wave dielectric multilayer 165
Quartz 78
Quaternary alloy 163
Quenching
  concentration 102, 113
  thermal 104
Quiver energy 242, 245, 246
QW (quantum well) 151
  diode laser, strained-layer 173

Radial
  opacity 231
  temperature gradient 33
Radiation
  field, intensity of 5
  -less transition 102
  pump, loss of 25
Radiative
  collisional-, cascade 216
  decay 208
  lifetime 100, 102, 113
  quantum yield 102
  transition 216
Radiography 254
Radius
  beam 26
  multimode 35
Raman
  backscattering, stimulated 245
  scattering, stimulated (SRS) 111, 132, 137
    threshold 137
Rare earth
  atom 98
  -doped fiber 103
  ion 98
    laser active 99
Rate
  Auger decay 217
  equation 4, 154, 208
    for a 4-level system 5
  heating 103
  pump 4, 14
    threshold 9
  recombination 152
  repetition 228, 232
    high, X-ray laser (XRL) 247
    pulse 19, 20
Ratio, side-mode suppression (SMSR) 157
Ray
  helical 129
  meridional 129
  tracing 129
Rayleigh length 27
Reaction
  charge-exchange 220
Reactive ion etching 165
Recombination 208
  band-to-band 163
  bimolecular 152
  electron-collisional 216

laser 216, 221
nonradiative 152, 156
-pumped laser 216
rate 152
scheme, optical-field-ionized (OFI) 223
surface 156
three-body 216
time, nonradiative 152
X-ray laser (XRL), table-top 233
Rectangular pulse
laser energy 24
Reflection 26
Bragg 158
internal
multiple 37
total 41, 106, 125
Reflectivity 11
Reflectometry 250, 254
Moiré 34
Reflector, distributed Bragg (DBR), epitaxial 167, 171, 176
Refracting power 34
critical 36
Refraction
angle 212
ionization-induced 242
loss 244
Refractive index 33, 46, 100
absolute 107
average 134
group 154
intensity-dependent 132
nonlinear 47, 48, 100, 113
profile 33
relative 107
thermal 34
Region
active 166
strain-compensated 175
spectral
blue–green 168
violet–blue 164
Relative refractive index 107
Relativistic electron beam 187
Relaxation
kinetic 227
oscillation 15, 159
Repetition rate 228, 232
high, X-ray laser (XRL) 247
pulse 19, 20
Resonance
electron-cyclotron (ECR) 169
Resonator 37
decay time 20
efficiency 26
Fabry–Perot (FP) 153
loss 53
matrix 35
multicavity 35
quality of 17
Retro-mirror 211
RF
accelerator cavity 190
gun 189
linac, microwave-driven 189
superconducting (SRF) 189
Rod 38
length 36
system, homogeneous heating in 31
Round trip 10, 26
condition 153
full, matrix for 26
loss factor per 24
Ruby 56
Rule
Hund's 98

Safe thermal load 32
Samarium
Sm^{2+} 98
Sm^{3+} 98
Sapphire 79
SASE (self-amplified spontaneous emission)
free-electron laser (FEL) 194
Saturated
gain coefficient 6, 24
high-power fiber amplifier 132
Saturation 227, 229, 245
absorption 130
energy density 24
fluence 131
flux 5
intensity 21, 24, 52, 221
SBS (stimulated Brillouin scattering) 111, 132
Scaling
isoelectronic 247
power 137
Scattering 10, 23, 26
Brillouin, stimulated (SBS) 111, 132
inelastic, stimulated 132
Raman, stimulated (SRS) 111, 132, 137
threshold 137
Scheme
charge-transfer 219
double-pulse 228
grazing incidence pumping (GRIP) 204
inner-shell photoionization (ISPIS) 217
recombination, optical-field-ionized (OFI) 223
Scintillation detector 254
Second-order susceptibility 132
Self
-amplified spontaneous emission (SASE)
free-electron laser (FEL) 194

-focusing 47, 111
length 48
-induced phase shift 132
-oscillation 8
-phase modulation (SPM) 132
-photopumping mechanism 218
-pumping of a strong emission line 218
-terminating amplified spontaneous emission (ASE) 223
Sellmeier coefficient 46
Semiconductor
direct 164
I-III-VI_2
compound 163
II–VI 163
III–V 163
laser 38
Sequence, isoelectronic 207, 214, 215
Shaping, pulse 223
Shell, inner
photoionization (ISPI) 247
scheme (ISPIS) 217
X-ray laser (XRL) 250, 251
vacancy 217
X-ray laser (XRL) 254
Shift
Doppler 187, 191, 231
phase, self-induced 132
Stokes 143
Shock, thermal, parameter 52
Short-cavity laser 156
Short-pulse-emitting soft X-ray laser (XRL) 232
Side-mode suppression ratio (SMSR) 157
Signal
large-
amplitude modulation 159
small-
amplitude modulation 159
gain 132, 194, 247
Silica fiber
low-loss fused 125
Single-frequency laser 151
Single-mode
endlessly 135
fiber 127
Slab 37, 38, 41
system, homogeneous heating in 31
Slope efficiency 11, 22, 24, 26, 32, 53
Sm *see* Samarium
Small-signal
amplification factor 10
gain 132, 194, 247
coefficient 6
factor 6, 24
SMSR (side-mode suppression ratio) 157
Soft X-ray laser (XRL), short-pulse-emitting 232
Solid-state laser
diode-pumped 38
lamp-pumped
efficiency of 25
laser-diode-pumped
efficiency of 25
Source
excitation 24
Space-charge effect 252
Spatial coherence *see* Transverse coherence
Specimen, biological, gold-tagged 252
Spectral
brightness 231
linewidth 225
region
blue–green 168
violet–blue 164
Spectroscopy
photo-electron 252
Spectrum
absorption 97
of Erbium Er^{3+} 58
bremsstrahlung 217
Spike 16
Spiking 16
Spin-orbit coupling 164
SPM (self-phase modulation) 132
Spontaneous emission 4, 229
amplified (ASE) 23, 25, 98, 220
self-terminating 223
cross section 45
self-amplified (SASE)
free-electron laser (FEL) 194
SRF (superconducting RF) 189
SRS (stimulated Raman scattering) 111, 132, 137
threshold 137
Stability
criterion 27, 28
mechanical 136
Stage
ionization 206
State, excited
absorption (ESA) 23
Step-index fiber 134
Stimulated
Brillouin scattering (SBS) 111, 132
emission 4
cross section 45, 100
inelastic scattering 132
Raman backscattering 245
Raman scattering (SRS) 111, 132, 137
threshold 137
Stoichiometric crystal 107
Stoichiometry 51
Stokes shift 143
Storage ring, synchrotron 188

Strain
-compensated active region 175
-optical coefficient *see* Elasto-optic coefficient
Strained-layer QW diode laser 173
Stress
-optical coefficient 110, 113
thermal 105
thermally induced 110
Strong
emission line, self-pumping of 218
index-guiding 157
Sulfo-selenide-based edge-emitting laser 171
Superconducting RF (SRF) 189
Superlattice 170
Suppression
barrier (BS) 242
ratio, side-mode (SMSR) 157
Surface
cooling- 31
critical 206, 229
damage threshold 137
lens 26
recombination 156
tension 31
Susceptibility
second-order 132
third-order 132
Switching, cell
electro-optic (EO) 195
Pockels *see* Switching, cell, electro-optic (EO)
Synchrotron storage ring 188
System
3-level 23
4-level 22, 23
rate equations for 5
cryogenic 145
rod, homogeneous heating in 31
slab, homogeneous heating in 31

Table-top
laser driver 227
X-ray laser (XRL) 227
recombination 233
Tagged, gold-, biological specimen 252
Tapered fiber bundle (TFB) 126
Tb *see* Terbium
Technique
epitaxial overgrowth 157
Temperature
coefficient of the optical path length 109
gradient 31
radial 33
melting 49
of the coolant 12
plasma 216
threshold 24
transformation, glass 113
Temporal coherence *see* Longitudinal coherence
Tension
fracture 32, 49
surface 31
Terbium
Tb^{3+} 98
Tb^{4+} 98
Ternary alloy 163
TFB (tapered fiber bundle) 126
Thermal
conduction 205
distortion 106
effect 37
expansion 104
coefficient 31
coefficient mismatch 165
ionization 247
lens 33
lensing 33, 100, 104
load 22, 31, 103, 106, 131, 137
safe 32
population 13, 23, 24
quenching 104
refractive index 34
shock parameter 52
stress 105
Thermally
induced stress 110
invariant resonator 37
Thick, optically
plasma 218
Thickness, optical 210
Thin, optically 254
Third-order susceptibility 132
Three-body recombination 216
Threshold
current 156
density 155
energy 14, 16, 22
inversion 9, 10, 14, 22, 24
pump
power 24
rate 9
SRS (stimulated Raman scattering) 137
surface damage 137
temperature 24
Thulium 65
Tm^{2+} 98
Tm^{3+} 98
Ti:sapphire laser, circularly polarized 247
Time
damping 15
decay, resonator 20
nonradiative recombination 152
Tm *see* Thulium
Total internal reflection 41, 106, 125

Toughness, fracture 104
Tracing, ray- 129
Transfer
  charge-, scheme 219
  collisional 219
  heat, coefficient 30
  power, diagram 24
Transformation temperature, glass 113
Transient
  collisional pumping 227
  excitation 226
Transition
  collisional 216
  fluorescence 113
  laser 4
  nonradiative 4, 25
  probability 208
  radiationless 102
  radiative 216
Transversal
  mono-mode 103
  pumping 39, 126
Transverse
  coherence 224
  mode 128
Trapping defect 141
Traveling-wave pumping 228
Tunability 141
Tunneling 246
Two-photon
  absorption 111
  ionization 254

Ultraviolet, extreme (XUV or EUV) 203
  interferometer 253
  interferometry 253
  laser 203
Uniaxially anisotropic, optically 110
Unit
  cooling 24
Upper level lifetime 24

Vacancy, inner-shell 217
Valence band 163
Vapor
  deposition, chemical (CVD) 125
    modified (MCVD) 135
  phase epitaxy, hydride (HVPE) 165
VCSEL (vertical cavity surface emitting laser) 157
Violet–blue spectral region 164
Voigt profile 223

Water window 252
Wave
  electromagnetic, forward-propagating 193
  ponderomotive 192
  traveling-, pumping 228
Wavefront, curvature of 26
Waveguide
  layer 166, 175
  plasma 212
Waveguiding effect 244
Wavelength
  division multiplexer (WDM) 126
  laser 99
  of the fluorescence maximum 100
  -selective feedback 158
  wiggler 191
WDM (wavelength division multiplexer) 126
Weak index-guiding 157
Weight percentage 51
  concentration in 49
Wentzel–Kramers–Brillouin approximation 128
Wiggler 190
  field 193
  magnetic 187
  wavelength 191
Wurtzite
  AlN 164
  GaN 164
  InN 164

X-ray
  amplification 206
  laser (XRL) *see* XRL (X-ray laser)
  population inversion 219
XMOPA (XUV master oscillator–power amplifier) 229
XRL (X-ray laser) 203, 204
  collisional-excited 213
  high-repetition-rate 247
  hybrid 231
  inner-shell 254
  inner-shell photoionization (ISPI) 250, 251
  photoionization 254
  photoresonantly pumped 218
  pulse 227
  short-pulse-emitting soft 232
  table-top 227
    recombination 233
XUV (extreme ultraviolet) 203
  interferometer 253
  laser 203
  master oscillator–power amplifier (XMOPA) 229

YAG (yttrium aluminum garnet) 3, 80
YALO (yttrium aluminum oxide) 82
YAP (yttrium aluminum perovskite) 82
Yb *see* Ytterbium
Yield, radiative quantum 102
YLF (yttrium lithium fluoride) 83
YOS (yttrium ortho-silicate) 84

Young's modulus 31, 49, 104
YSAG (yttrium scandium aluminum garnet) 84
YSGG (yttrium scandium gallium garnet) 85
Ytterbium 67
  Yb^{2+} 98
  Yb^{3+} 98
Yttrium
  aluminum garnet (YAG) 3, 80
  aluminum oxide (YALO) 82
  aluminum perovskite (YAP) 82
  lithium fluoride (YLF) 83
  ortho-silicate (YOS) 84
  (ortho)vanadate (YVO(4)) 86
  scandium aluminum garnet (YSAG) 84
  scandium gallium garnet (YSGG) 85
YVO(4) (yttrium (ortho)vanadate) 86

Zinc, Ne-like 254
Zone
  Brillouin 164
  coronal 206